

Seismic Analysis, Behavior, And Design of Unbonded Post-Tensioned Hybrid Coupled Wall Structures**Qiang Shen****Publication Date**

15-01-2007

License

This work is made available under a All Rights Reserved license and should only be used in accordance with that license.

Citation for this work (American Psychological Association 7th edition)

Shen, Q. (2007). *Seismic Analysis, Behavior, And Design of Unbonded Post-Tensioned Hybrid Coupled Wall Structures* (Version 1). University of Notre Dame. <https://doi.org/10.7274/rr171v55z5p>

This work was downloaded from CurateND, the University of Notre Dame's institutional repository.

For more information about this work, to report or an issue, or to preserve and share your original work, please contact the CurateND team for assistance at curate@nd.edu.

SEISMIC ANALYSIS, BEHAVIOR, AND DESIGN OF UNBONDED
POST-TENSIONED HYBRID COUPLED WALL STRUCTURES

VOLUME I

A Dissertation

Submitted to the Graduate School
of the University of Notre Dame
in Partial Fulfillment of the Requirements
for the Degree of

Doctor of Philosophy

by

Qiang Shen, B.S., M.S.

Yahya C. Kurama, Director

Graduate Program in Civil Engineering and Geological Sciences

Notre Dame, Indiana

December 2006

SEISMIC ANALYSIS, BEHAVIOR, AND DESIGN OF UNBONDED POST-TENSIONED HYBRID COUPLED WALL STRUCTURES

Abstract

by

Qiang Shen

This dissertation focuses on the development of a new type of hybrid coupled wall structure for seismic regions. Coupling of concrete wall piers is achieved by post-tensioning steel beams to the walls using unbonded post-tensioning tendons. Different from conventional hybrid coupled walls, the coupling beams of the new system are not embedded into the walls. Steel top and seat angles are used at the beam-to-wall connections for energy dissipation.

Unbonded post-tensioned hybrid coupling systems offer important advantages over conventional coupling systems, such as simplified construction, ability to undergo large lateral displacements with little damage, and self-centering capability. Analytical investigations are conducted on the nonlinear behavior of floor-level coupled wall subassemblages and multi-story structures under combined lateral and gravity loads. Both finite element and fiber element analytical models are developed. The effects of design parameters (e.g., amount of post-tensioning, beam/wall properties) on the behavior of the structures (e.g., strength, energy dissipation, deformation capacity) are investigated.

Systems with precast concrete walls as well as monolithic cast-in-place concrete walls are considered. The behavior of the proposed coupled wall system is compared with the behaviors of uncoupled walls and conventional systems with embedded steel coupling beams. The analytical results are used to develop approximate procedures to estimate the nonlinear load-deformation behavior of the structures without sophisticated analytical models.

The results from eleven half-scale experiments of floor-level unbonded post-tensioned hybrid coupled wall subassemblages are also summarized in this dissertation. The tests results are used to validate and improve the analytical models, evaluate critical structural components that can limit lateral strength and ductility, and make recommendations for practical applications.

Finally, a performance-based seismic design approach is developed for unbonded post-tensioned hybrid coupled wall structures. Two prototype eight-story hybrid coupled wall systems are designed using the proposed procedures. Evaluations of the global and local behavior of the structures are conducted based on nonlinear static lateral load analyses as well as dynamic time-history analyses under selected ground motion records. The results from these analyses are ultimately used to critically evaluate the validity of the design approach and procedures in achieving the target design performance objectives for the structures.

CONTENTS

VOLUME I

FIGURES.....	xi
TABLES.....	xxxiii
SYMBOLS	xliii
ACKNOWLEDGMENTS.....	lxviii
CHAPTER 1 INTRODUCTION	1
1.1 Problem Statement.....	1
1.2 Proposed Hybrid Coupled Wall System	4
1.3 Research Objectives.....	7
1.4 Research Scope.....	7
1.5 Summary of Approach.....	10
1.6 Research Significance.....	11
1.7 Organization of Dissertation.....	12
CHAPTER 2 LITERATURE REVIEW	15
2.1 Coupled Wall Structural Systems	15
2.2 Concrete Coupled Wall Structures	19
2.2.1 Behavior and Design of Concrete Coupling Beams	20
2.2.2 Analysis and Modeling of Concrete Coupled Wall Structures	20
2.3 Hybrid Structures with Embedded Steel Coupling Beams.....	22
2.3.1 Behavior and Design of Embedded Steel Coupling Beam Subassemblages	24
2.3.2 Embedded Steel Coupling Beams with Concrete Encasement	28
2.3.3 Multi-Story Hybrid Coupled Walls with Embedded Beams	29
2.3.4 Degree of Coupling	31
2.4 Wall Shear Force Demands in Coupled Wall Structures	32
2.5 Unbonded Post-Tensioning In Building Construction	33
2.5.1 Unbonded Post-Tensioning	34
2.5.2 Unbonded Post-Tensioned Precast Concrete Moment Frames	36
2.5.3 Post-Tensioned Steel Moment Frames	44
2.5.4 Unbonded Post-Tensioned Precast Concrete Structural Walls	48
2.6 Behavior of Top and Seat Angles	57
2.6.1 Kishi and Chen (1990) and Lorenz et al. (1993)	59

2.6.2 Sims (2000)	63
2.6.3 Ricles et al. (2001)	65
2.6.4 Garlock et al. (2003)	67
2.7 Chapter Summary	57
CHAPTER 3 ANALYTICAL MODELING OF COUPLED WALL	
SUBASSEMBLAGES	72
3.1 Prototype Subassembly	72
3.1.1 Subassembly Material Properties and Idealizations	76
3.2 Analytical Modeling Assumptions	80
3.3 Fiber Element Subassembly Model	81
3.3.1 Modeling of Wall Regions	82
3.3.2 Modeling of Coupling Beams and Flange Cover Plates	86
3.3.3 Modeling of Gap Opening	93
3.3.4 Modeling of Beam Post-Tensioning Tendons and Anchorages	95
3.3.5 Modeling of Top and Seat Angles	96
3.4 Verification of Fiber Element Subassembly Model	100
3.4.1 Finite Element Subassembly Model	100
3.4.2 Finite Element Analysis Results	103
3.4.3 Comparisons between Finite Element and Fiber Element Model	
Results.....	105
3.5 Advantages and Limitations of Fiber Element Model	108
3.6 Modeling of Embedded Steel Coupling Beams	110
3.7 Chapter Summary	115
CHAPTER 4 NONLINEAR BEHAVIOR OF COUPLED WALL	
SUBASSEMBLAGES.....	116
4.1 Overview of Subassembly Analyses	116
4.2 Behavior under Monotonic Loading	117
4.3 Behavior under Cyclic Loading	123
4.4 Parametric Analyses	125
4.5 Chapter Summary	128
CHAPTER 5 IDEALIZED SUBASSEMBLAGE MOMENT-ROTATION	
RELATIONSHIP.....	131
5.1 Linear-Elastic Behavior	131
5.2 Idealized Nonlinear Relationship	135
5.2.1 Beam Softening State	136
5.2.2 Beam PT-Yielding State	140
5.3 Verification of Idealized Relationship	147
5.4 Chapter Summary	150

CHAPTER 6 ANALYTICAL MODELING OF MULTI-STORY COUPLED WALLS	151
6.1 Prototype Coupled Wall Structures	151
6.1.1 Walls	152
6.1.2 Coupling Beams	156
6.1.3 Material Properties and Idealizations	158
6.2 Analytical Modeling Assumptions	162
6.3 Multi-Story Coupled Wall Models	164
6.3.1 Cast-in-Place Concrete Walls in CIP-UPT system	166
6.3.2 Precast Concrete Walls in PRE-UPT system	170
6.4 Verification of Wall Models	176
6.5 Advantages and Limitations of Analytical Models	177
6.6 Modeling of Walls with Embedded Coupling Beams	179
6.7 Chapter Summary	180
CHAPTER 7 NONLINEAR BEHAVIOR OF MULTI-STORY COUPLED WALLS	181
7.1 Overview of Analyses	181
7.2 Behavior under Monotonic Loading	183
7.2.1 Coupled Wall Base Shear Force versus Roof Drift Behaviors	184
7.2.2 Wall Pier Deflected Shapes	187
7.2.3 Wall Pier Base Flexural Steel Strains and Stresses	187
7.2.4 Wall Pier Base Axial Forces	190
7.2.5 Wall Pier Base Moments	192
7.2.6 Degree of Coupling	193
7.2.7 Wall Pier Base Concrete Strains	195
7.2.8 Coupling Beam Shear Force versus Chord Rotation Behaviors	196
7.2.9 Coupling Beam Axial Forces	201
7.2.10 Coupling Beam End Strains	208
7.2.11 Tension Angle Force versus Deformation Behaviors	208
7.3 Behavior under Cyclic Loading	215
7.3.1 Coupled Wall Base Shear Force versus Roof Drift Behaviors	215
7.3.2 Coupling Beam Axial Forces	218
7.4 Parametric Investigation	223
7.4.1 Base Shear versus Roof Drift Behavior	224
7.4.2 Degree of Coupling	225
7.4.3 Coupling Beam Axial Forces	229
7.5 Chapter Summary	230
CHAPTER 8 IDEALIZED COUPLED WALL LATERAL LOAD-DISPLACEMENT RELATIONSHIPS	234
8.1 Linear-Elastic Behavior	234
8.2 Systems with Cast-In-Place Concrete Walls	239
8.2.1 Coupled Wall Softening State	240

8.2.2 Coupled Wall Ultimate State	245
8.3 Systems with Precast Concrete Walls	252
8.3.1 Coupled Wall Softening State	253
8.3.2 Coupled Wall PT-Yielding State	256
8.3.3 Coupled Wall Ultimate State	265
8.4 Verification of Idealized Relationships	267
8.5 Chapter Summary	275
CHAPTER 9 SUBASSEMBLAGE EXPERIMENTS	276
9.1 Experimental Program	277
9.1.1 Test Set-Up	279
9.1.2 Loading Block and Reaction Block	281
9.1.3 Coupling Beams	285
9.1.4 Beam Post-Tensioning Strands	286
9.1.5 Beam-to-Wall Connection Regions	287
9.1.6 Loading	292
9.1.7 Material Properties	295
9.1.8 Instrumentation	310
9.1.9 Test Procedure	315
9.2 Results of Experiments	319
9.2.1 Behavior of Properly Designed Subassemblages (Tests 1-4)	319
9.2.2 Effect of Coupling Beam Flange Cover Plates (Tests 5-6)	331
9.2.3 Effect of Angle Thickness (Tests 7-8)	335
9.2.4 Effect of Beam Post-Tensioning Steel Area (Test 9)	336
9.2.5 Effect of Beam Depth (Tests 10-11)	338
9.3 Recommendations for Application	343
9.4 Chapter Summary	345
CHAPTER 10 REVISED ANALYTICAL MODEL	346
10.1 Revised Subassemblage Model	346
10.1.1 Modeling of Coupling Beams and Wall-Contact Regions	347
10.1.2 Modeling of Beam Post-Tensioning Tendons	350
10.1.3 Modeling of Top and Seat Angles	352
10.2 Evaluation of Revised Subassemblage Analytical Model	358
10.2.1 Coupling Shear Force versus Chord Rotation Relationships	358
10.2.2 Coupling Beam Post-Tensioning Forces	363
10.2.3 Behavior at Coupling Beam Ends	364
10.2.4 Behavior Along Beam Span	369
10.2.5 Behavior of Top and Seat Angles	370
10.3 Revised Idealized Moment-Rotation Relationship	374
10.3.1 Beam Softening State	374
10.3.2 Beam PT-Yielding State	376
10.4 Chapter Summary	379

VOLUME II

CONTENTS.....	lxx
FIGURES.....	lxxv
TABLES.....	lxxxvi
CHAPTER 11 PERFORMANCE-BASED SEISMIC DESIGN APPROACH	381
11.1 Overview	381
11.2 Performance (Damage) Levels	383
11.2.1 Immediate Occupancy Performance Level	384
11.2.2 Life Safety Performance Level	384
11.2.3 Collapse Prevention Performance Level	385
11.3 Structure Limit States and Capacities	385
11.3.1 Steel Coupling Beam Limit States	386
11.3.2 Concrete Wall Pier Limit States	387
11.4 Seismic Demand Levels	390
11.5 Structure Demands	391
11.6 Relationships between Performance Levels and Limit States	392
11.6.1 Steel Coupling Beams	392
11.6.2 Cast-in-Place Concrete Wall Piers	394
11.6.3 Precast Concrete Wall Piers	394
11.7 Design Objectives	395
11.7.1 Coupling Beams	395
11.7.2 Systems with Cast-in-Place Concrete Wall Piers	396
11.7.3 Systems with Precast Concrete Wall Piers	396
11.8 Seismic Design Criteria	397
11.9 Design Acceleration Response Spectra	397
11.9.1 Design Spectra for the Survival-Level Demand	397
11.9.2 Design Spectra for the Design-Level Demand	399
11.10 Equivalent Nonlinear SDOF Representation	400
11.10.1 Transformation from MDOF System to SDOF System	401
11.10.2 Equivalent Nonlinear SDOF Model	407
11.10.3 Application of Equivalent SDOF BP Model	408
11.10.4 Evaluation of Equivalent SDOF BP Model	415
11.11 Seismic Displacement Demand Relationships	419
11.11.1 Previous Research	420
11.11.2 Displacement Demand Relationships for SDOF BP Model	425
11.12 Nonlinear Static Procedure	431
11.12.1 Coupled Wall Design Base Shear Demand, Q_{wd}	431
11.12.2 Vertical Distribution of Seismic Lateral Forces	434
11.12.3 Horizontal Distribution of Story Forces	435
11.12.4 Load Combinations	437

11.13 Maximum Base Shear Demand	438
11.14 Chapter Summary	442
CHAPTER 12 DESIGN OF PROTOTYPE STRUCTURES	445
12.1 Design Overview	445
12.1.1 Design Material Properties	448
12.1.2 Selection of Initial Dimensions for Structural Members	449
12.1.3 Design Gravity Loads and Seismic Weight	450
12.1.4 Design Load Combination and Capacity Reduction Factors	452
12.1.5 Design Scope and Limitations	453
12.2 Performance-Based Seismic Design Parameters	453
12.2.1 Allowable Target Roof Drift Demands	454
12.2.2 Allowable Inter-story Drift Demands	454
12.2.3 Acceleration Response Spectra Used in Design	455
12.3 Linear-Elastic Structure Properties	457
12.3.1 Linear Elastic Stiffness	457
12.3.2 Period, Mode Shape, and Effective Mass	458
12.4 Design Base Shear Demand	459
12.4.1 Displacement Demand Relationships	459
12.4.2 Strength Ratios	461
12.4.3 Building Design Base Shear Demands	462
12.4.4 Coupled Wall Design Base Shear Demands	463
12.5 Preliminary Design Checks	463
12.5.1 Peak Roof Drift Demands	464
12.5.2 Peak Inter-story Drift Demands	465
12.5.3 Diagonal Tension at Wall Pier Bases	466
12.6 Design of Steel Coupling Beams	468
12.6.1 Design Coupling Beam Shear Force Demand	468
12.6.2 Angle and Post-Tensioning Contributions to Coupling Resistance	470
12.6.3 Coupling Beam Cross Section	475
12.6.4 Beam Post-Tensioning	476
12.6.5 Top and Seat Angles and Connections	481
12.6.6 Coupling Beam Shear Force versus Rotation Behavior	485
12.6.7 Coupling Beam Rotation Demands	486
12.6.8 Yielding of Beam Post-Tensioning Tendons	488
12.6.9 Fracture of Top and Seat Angles	489
12.6.10 Shear Slip at Beam-to-Wall Interfaces	491
12.6.11 Wall-Contact Regions	493
12.7 Design of Wall Piers in Structure P1-CWUPT	496
12.7.1 Wall Pier Flexural Reinforcement	498
12.7.2 Concrete Confinement at Wall Pier Bases	502
12.7.3 Diagonal Tension at Wall Pier Bases	505
12.7.4 Shear Slip at Coupled Wall Base	507
12.8 Design of Wall Piers in Structure P2-PWUPT	509

12.8.1 Wall Pier Post-Tensioning Steel Reinforcement	509
12.8.2 Yielding of Wall Pier Post-Tensioning Steel	513
12.8.3 Concrete Confinement at Wall Pier Bases	515
12.8.4 Diagonal Tension at Wall Pier Bases	518
12.8.5 Shear Slip at Coupled Wall Base	520
12.9 Summary of Design and Final Checks	524
12.9.1 Lateral Load versus Deformation Relationships	524
12.9.2 Design Criteria	526
 CHAPTER 13 BEHAVIOR OF PROTOTYPE STRUCTURES UNDER STATIC	
LATERAL LOADING	532
13.1 Introduction	532
13.2 Behavior under Monotonic Loading	534
13.2.1 Coupled Wall Base Shear Force versus Roof Drift Behaviors	535
13.2.2 Wall Pier Base Flexural Steel Strains and Stresses	541
13.2.3 Wall Pier Base Axial Forces	546
13.2.4 Wall Pier Base Shear Forces	549
13.2.5 Wall Pier Base Moments	553
13.2.6 Degree of Coupling	555
13.2.7 Wall Pier Base Concrete Strains	557
13.2.8 Coupling Beam Shear Force versus Chord Rotation Behaviors	560
13.2.9 Coupling Beam Axial Forces and Post-Tensioning Forces	561
13.2.10 Coupling Beam End Strains	566
13.2.11 Tension Angle Force versus Deformation Behaviors	569
13.3 Behavior under Reversed Cyclic Loading	574
13.3.1 Coupled Wall Base Shear Force versus Roof Drift Behaviors	575
13.3.2 Wall Pier Post-Tensioning Forces in Structure P2-PWUPT	577
13.3.3 Wall Pier Base Axial Forces	579
13.3.4 Wall Pier Base Shear Forces	582
13.3.5 Wall Pier Base Moments	583
13.3.6 Degree of Coupling	586
13.3.7 Wall Pier Base Concrete Strains	588
13.3.8 Coupling Beam Shear Force versus Chord Rotation Behaviors	591
13.3.9 Coupling Beam Axial Forces and Post-Tensioning Forces	591
13.3.10 Coupling Beam End Strains	597
13.3.11 Angle Force versus Deformation Behaviors	597
13.4 Structure with Embedded Steel Coupling Beams	604
13.4.1 Behaviors under Monotonic and Cyclic Loading	605
13.5 Chapter Summary	607
 CHAPTER 14 GROUND MOTION RECORDS FOR DYNAMIC ANALYSES	
14.1 Overview	608
14.2 Design-Level Ground Motion Records	611
14.3 Survival-Level Ground Motion Records	615

CHAPTER 15 BEHAVIOR OF PROTOTYPE STRUCTURES UNDER EARTHQUAKE LOADING	621
15.1 Analytical Model for Dynamic Analyses	621
15.1.1 Building Mass	622
15.1.2 Viscous Damping	622
15.1.3 Time Step	624
15.2 Structure P1-CWUPT	625
15.2.1 Floor/Roof Drifts	625
15.2.2 Inter-Story Drifts	628
15.2.3 Floor/Roof Accelerations	634
15.2.4 Wall Base Axial Forces	636
15.2.5 Wall Base Shear Forces	642
15.2.6 Wall Base Diagonal Tension and Shear Slip Failure	652
15.2.7 Wall Base Moments	653
15.2.8 Wall Base Strains	660
15.2.9 Coupling Beam Chord Rotations	664
15.2.10 Coupling Beam Axial Forces	670
15.2.11 Coupling Beam Post-Tensioning Forces	675
15.2.12 Coupling Beam Shear Forces	677
15.2.13 Coupling Beam Shear Slip Failure	684
15.2.14 Angle Deformations	690
15.3 Structure P2-PWUPT	692
15.3.1 Floor/Roof Drifts	695
15.3.2 Inter-Story Drifts	699
15.3.3 Floor/Roof Accelerations	704
15.3.4 Wall Post-Tensioning Forces	706
15.3.5 Wall Base Axial Forces	714
15.3.6 Wall Base Shear Forces	718
15.3.7 Wall Base Diagonal Tension and Shear Slip Failure	730
15.3.8 Wall Base Moments	736
15.3.9 Wall Base Strains	743
15.3.10 Coupling Beam Chord Rotations	749
15.3.11 Coupling Beam Axial Forces	752
15.3.12 Coupling Beam Post-Tensioning Forces	756
15.3.13 Coupling Beam Shear Forces	763
15.3.14 Coupling Beam Shear Slip Failure	768
15.3.15 Angle Deformations	771
15.4 Uncoupled Concrete Wall Systems	778
15.5 Chapter Summary	781

CHAPTER 16 SUMMARY, CONCLUSIONS AND FUTURE WORK	783
16.1 Summary	783
16.2 Conclusions	788
16.3 Future Work	798
REFERENCES	799

FIGURES

VOLUME I

CHAPTER 1

Fig. 1.1 Eight story coupled wall structure	2
Fig. 1.2 Hybrid coupled wall subassemblage with embedded beam: (a) undeformed configuration; (b) deformed configuration	2
Fig. 1.3 Proposed coupled wall system: (a) subassemblage at a floor level; (b) deformed configuration; (c) coupling forces.....	5

CHAPTER 2

Fig. 2.1 Coupled structural walls	16
Fig. 2.2 Lateral load resisting mechanisms in structural walls (adapted from Paulay and Priestley 1992): (a) uncoupled wall; (b) walls coupled with strong beams; (c) walls coupled with weak beams	17
Fig. 2.3 Shear in concrete coupling beams (from Paulay and Priestley 1992): (a) diagonal tension failure; (b) sliding shear failure; (c) beam with diagonal reinforcement	21
Fig. 2.4 Modeling of coupled wall systems (adapted from Paulay and Priestley 1992): (a) walls with flexible beams; (b) walls with stiff beams.....	22
Fig. 2.5 Hybrid coupled wall subassemblages with embedded steel beams (from Harries et al. 1997): (a) shear-critical beam; (b) beam shear force versus relative end displacement behavior; (c) damage at end of test; (d) flexure-critical beam; (e) beam shear versus relative end displacement behavior; (f) damage at end of test.....	25
Fig. 2.6 Hybrid coupled wall system with embedded steel beams (adapted from Harries 1996): (a) plan view; (b) analytical model.....	30
Fig. 2.7 Unbonded post-tensioned precast concrete frame: (a) elevation; (b) beam-column subassemblage; (c) idealized exaggerated displaced shape	37

Fig. 2.8 Unbonded post-tensioned precast beam-column subassemblages (from Priestley and MacRae1996): (a) interior joint specimen; (b) exterior joint specimen; (c) test setup; (d) photograph of test setup; (e) interior joint behavior; (f) exterior joint behavior; (g) photograph of interior joint.....	39
Fig. 2.9 Unbonded post-tensioned precast beam-column subassemblages (from El-Sheikh et al. 1999, 2000): (a) moment-rotation behavior; (b) analytical model.....	41
Fig. 2.10 Partially post-tensioned precast beam-column subassemblages (adapted from Kurama 2002)	44
Fig. 2.11 Post-tensioned steel exterior beam-column connection (adapted from Ricles et al. 2001)	46
Fig. 2.12 Post-tensioned steel beam-column connection details (from Ricles et al. 2002): (a) specimen with wide flange column; (b) specimen with composite concrete filled steel tube column.....	49
Fig. 2.13 Lateral load versus displacement behavior of post-tensioned steel beam-column subassemblages (from Ricles et al. 2001)	50
Fig. 2.14 Analytical modeling of post-tensioned steel beam-column subassemblages (adapted from Ricles et al. 2001): (a) interior joint region; (b) beam-column subassemblage; (c) modeling of post-tensioning anchorages.....	50
Fig. 2.15 Unbonded post-tensioned precast concrete walls (adapted from Kurama et al. 1999a): (a) wall elevation and cross-section; (b) gap opening and shear slip behavior; (c) analytical model; (d) behavior under cyclic lateral loads; (e) dynamic response.....	51
Fig. 2.16 Experiments of precast concrete walls (from Holden et al. 2003 and Restrepo 2003): (a) test setup; (b) hysteretic response of emulative wall; (c) hysteretic response of partially post-tensioned wall; (d) photograph of partially post-tensioned wall at 3% drift	56
Fig. 2.17 Top-and-seat angle connection: (a) deformed configuration; (b) angle parameters.....	58
Fig. 2.18 Angle model (adapted from Kishi and Chen 1990 and Lorenz et al. 1993): (a) cantilever model of tension angle; (b) assumed yield mechanism; (c) free body diagram of angle horizontal leg	62
Fig. 2.19 Isolated angle experiments (from Sims 2000): (a) plan view of test set up; (b) angle force-deformation relationship of Specimen 9; (c) angle force-deformation relationship of Specimen 11.....	66

Fig. 2.20 Modeling of top and seat angles (from Ricles et al. 2001): (a) fiber Models A and B; (b) fiber model and spring model behaviors; (c) comparisons with test results.....68

CHAPTER 3

Fig. 3.1 Prototype coupled wall subassemblage: (a) elevation; (b) top and seat angle connection details.....75

Fig. 3.2 Subassemblage material properties and idealizations: (a) steel; (b) beam post-tensioning strand; (c) wall unconfined concrete; (d) wall-contact region confined concrete79

Fig. 3.3 Analytical model: (a) subassemblage; (b) wall-contact elements and beam elements83

Fig. 3.4 Fiber element, segments, and fibers84

Fig. 3.5 Schematic showing fiber discretization of wall-contact elements.....87

Fig. 3.6 Length of first beam fiber element segment.....91

Fig. 3.7 Fiber discretization of beam elements91

Fig. 3.8 Cyclic material models: (a) compression-only steel (SC) fiber; (b) compression-only confined concrete (CCC) fiber; (c) compression-tension steel (S) fiber; (d) beam PT element.....94

Fig. 3.9 Angle model: (a) idealized displaced shape; (b) cyclic angle load-deformation model; (c) angle load-deformation behavior for prototype subassemblage.....98

Fig. 3.10 Finite element model: (a) two dimensional (2D) model; (b) three-dimensional (3D) model; (c) close-up view of beam-to-wall interface102

Fig. 3.11 Comparison between 2D and 3D finite element models103

Fig. 3.12 Rigid wall versus deformable wall finite element models104

Fig. 3.13 Maximum principal stress distributions: (a) beam stresses; (b) wall stresses106

Fig. 3.14 Model verification: (a) rigid wall comparison; (b) deformable wall comparison; (c) contact depth comparison107

Fig. 3.15 Modeling of embedded steel coupling beams: (a) Specimen S4 (Harries et al. 1997); (b) analytical model; (c) steel stress-strain relationship112

Fig. 3.16 Modeling of embedded steel coupling beams: (a) Specimen 3 (Remmetter et al. 1992); (b) analytical model; (c) steel stress-strain relationship113

Fig. 3.17 Verification of embedded steel coupling beam model: (a) Specimen S4 (Harries et al. 1997); (b) Specimen 3 (Remmetter et al. 1992)114

CHAPTER 4

Fig. 4.1 Simplified subassemblage model116

Fig. 4.2 Displaced shape: (a) subassemblage; (b) analytical model118

Fig. 4.3 Subassemblage behavior under monotonic loading: (a) beam end moment versus chord rotation behavior; (b) total force in beam post-tensioning tendons; (c) contact depth; (d) maximum beam compression strain; (e) tension angle behavior119

Fig. 4.4 Subassemblage behavior under cyclic loading: (a) with $L8 \times 8 \times 1-1/8$ angles; (b) total force in post-tensioning tendons; (c) with $L8 \times 8 \times 3/4$ angles; (d) without angles124

Fig. 4.5 Subassemblage moment-rotation behaviors from parametric investigation: (a) a_{bt} and f_{bpi} ; (b) a_{bt} ; (c) f_{bpi} ; (d) l_w ; (e) t_c ; (f) t_{bf} ; (g) d_{bw} ; (h) l_b 127

CHAPTER 5

Fig. 5.1 Linear-elastic subassemblage model: (a) model with wall-contact elements; (b) model without wall-contact elements132

Fig. 5.2 Idealized bilinear subassemblage moment-rotation relationship.....135

Fig. 5.3 Coupling beam free body diagram at softening state137

Fig. 5.4 Coupling beam free body diagram at PT-yielding state141

Fig. 5.5 Gap opening at coupling beam PT-yielding state.....143

Fig. 5.6 Second order effects147

Fig. 5.7 Verification of moment estimations: (a) a_{bt} and f_{bpi} ; (b) a_{bt} ; (c) f_{bpi} ; (d) l_w ; (e) t_c ; (f) t_{bf} ; (g) d_{bw} ; (h) l_b 148

Fig. 5.8 Verification of rotation estimations: (a) a_{bt} and f_{bpi} ; (b) a_{bt} ; (c) f_{bpi} ; (d) l_w ; (e) t_c ; (f) t_{bf} ; (g) d_{bw} ; (h) l_b	149
--	-----

CHAPTER 6

Fig. 6.1 Plan view of prototype structures	152
Fig. 6.2 Wall elevation and cross-section at base: (a) CIP-UPT system; (b) PRE-UPT system	153
Fig. 6.3 Floor level details: (a) elevation; (b) top and seat angle connections	156
Fig. 6.4 Wall material properties and idealizations: (a) mild reinforcing steel for CIP-UPT system; (b) post-tensioning bar for PRE-UPT system; (c) concrete	160
Fig. 6.5 Multi-story coupled wall analytical models: (a) CIP-UPT system; (b) PRE-UPT system	165
Fig. 6.6 CIP-UPT wall-height elements: (a) elevation; (b) fiber slice schematic near wall base; (c) fiber slice schematic away from wall base	167
Fig. 6.7 CIP-UPT system cyclic material models: (a) confined concrete (CC) fiber; (b) unconfined concrete (CU) fiber; (c) mild steel reinforcement (S) fiber; (d) steel fiber stress-strain relationship under monotonic loading and envelope relationship under cyclic loading; (e) concrete in tension	169
Fig. 6.8 PRE-UPT wall-height elements: (a) elevation; (b) fiber slice schematic near wall base; (c) fiber slice schematic away from wall base	171
Fig. 6.9 PRE-UPT system cyclic material models: (a) compression-only confined concrete (CCC) fiber; (b) wall PT element	174
Fig. 6.10 Monolithic cast-in-place reinforced concrete wall-height element model verification: (a) Wall RW2 (from Thomsen 1995); (b) measured behavior; (c) predicted behavior	178

CHAPTER 7

Fig. 7.1 Gravity and lateral forces for multi-story coupled wall analyses	182
---	-----

Fig. 7.2 Base shear versus roof drift behaviors under monotonic lateral loads: (a) CIP-UPT system; (b) PRE-UPT system.....	185
Fig. 7.3 Wall deflected shapes: (a) CIP-UPT system; (b) PRE-UPT system	188
Fig. 7.4 Wall pier flexural steel stresses: (a) CIP-UPT system; (b) PRE-UPT system ...	189
Fig. 7.5 Wall pier base axial forces: (a) CIP-UPT system; (b) PRE-UPT system.....	191
Fig. 7.6 Components of wall pier base axial forces: (a) CIP-UPT system; (b) PRE-UPT system	192
Fig. 7.7 Wall base moments: (a) CIP-UPT system; (b) PRE-UPT system.....	194
Fig. 7.8 Degree of coupling	195
Fig. 7.9 Wall pier base neutral axis depths: (a) CIP-UPT system; (b) PRE-UPT system	197
Fig. 7.10 Wall pier base extreme confined concrete compression strains: (a) CIP-UPT system; (b) PRE-UPT system	198
Fig. 7.11 Coupling beam shear force versus chord rotation behaviors for CIP-UPT system	199
Fig. 7.12 Coupling beam shear force versus chord rotation behaviors for PRE-UPT system	200
Fig. 7.13 Calculation of coupling beam chord rotation, θ_b in multi-story coupled wall.....	201
Fig. 7.14 Coupling beam axial forces and post-tensioning forces in CIP-UPT system: (a) 2 nd floor; (b) 3 rd floor; (c) 4 th floor; (d) 5 th floor; (e) 6 th floor; (f) 7 th floor; (g) 8 th floor; (h) roof.....	203
Fig. 7.15 Effect of beam post-tensioning sequence on beam axial forces: (a) 2 nd floor to roof; (b) roof to 2nd floor.....	205
Fig. 7.16 Simulation of beam post-tensioning using external forces.....	207
Fig. 7.17 Coupling beam end neutral axis (i.e., contact) depths for CIP-UPT system....	209
Fig. 7.18 Coupling beam end neutral axis (i.e., contact) depths for PRE-UPT system...	210

Fig. 7.19 Coupling beam end extreme steel compression strains for CIP-UPT system	211
Fig. 7.20 Coupling beam end extreme steel compression strains for PRE-UPT system	212
Fig. 7.21 Coupling beam tension angle force-deformation behaviors for CIP-UPT system	213
Fig. 7.22 Coupling beam tension angle force-deformation behaviors for PRE-UPT system	214
Fig. 7.23 Coupled wall base shear force versus roof drift behaviors under cyclic lateral loads: (a) CIP-UPT system; (b) PRE-UPT system; (c) CIP-EMB system; (d) CIP-UPT system without angles	216
Fig. 7.24 Coupling beam axial forces in CIP-UPT system – cyclic loading: (a) 2 nd floor; (b) 3 rd floor; (c) 4 th floor; (d) 5 th floor; (e) 6 th floor; (f) 7 th floor; (g) 8 th floor; (h) roof	220
Fig. 7.25 Coupling beam post-tensioning forces in CIP-UPT system – cyclic loading: (a) 2 nd floor; (b) 3 rd floor; (c) 4 th floor; (d) 5 th floor; (e) 6 th floor; (f) 7 th floor; (g) 8 th floor; (h) roof	221
Fig. 7.26 Coupling beam axial forces: (a) equilibrium of horizontal forces; (b) wall floor/roof shear forces	222
Fig. 7.27 Base shear versus roof drift behaviors of parametric CIP-UPT systems: (a) l_w ; (b) ρ_{ws} ; (c) t_w ; (d) d_{bw} ; (e) a_{bt} ; (f) f_{bpi} ; (g) l_b ; (h) t_a	226
Fig. 7.28 Base shear versus roof drift behaviors of parametric PRE-UPT systems: (a) l_w ; (b) ρ_{wp} ; (c) f_{wpi} ; (d) d_{bw} ; (e) a_{bt} ; (f) f_{bpi} ; (g) l_b ; (h) t_a	227
 CHAPTER 8	
Fig. 8.1 Eight story linear-elastic coupled wall model	236
Fig. 8.2 Idealized base shear force versus roof drift relationship for prototype CIP-UPT system	239
Fig. 8.3 Coupled wall softening state for systems with cast-in-place concrete walls: (a) free body diagram; (b) coupling beam shear forces; (c) strain and stress distributions at wall bases	241

Fig. 8.4 Coupled wall ultimate state for systems with cast-in-place concrete walls: (a) strain and stress distributions at base of compression-side wall; (b) beam chord rotation; (c) components of beam chord rotation	247
Fig. 8.5 Coupled wall ultimate state for systems with cast-in-place concrete walls: (a) coupling beam shear forces; (b) free body diagram.....	249
Fig. 8.6 Idealized base shear force versus roof drift relationship for prototype PRE-UPT system	252
Fig. 8.7 Coupled wall softening state for systems with precast concrete walls: (a) free body diagram; (b) concrete strain and stress distributions at wall bases	254
Fig. 8.8 Coupled wall PT-yielding state for systems with precast concrete walls: (a) idealized coupled wall displaced shape; (b) beam shear forces.....	259
Fig. 8.9 Coupled wall PT-yielding state for systems with precast concrete walls: (a) free body diagram; (b) concrete stress distributions at base of tension-side wall; (c) concrete stress distributions at base of compression-side wall	262
Fig. 8.10 Coupled wall ultimate state for systems with precast concrete walls – strain and stress distributions at base of compression-side wall	266
Fig. 8.11 Verification of idealized relationship for systems with cast-in-place walls – F_{ws} and F_{wu}	269
Fig. 8.12 Verification of idealized relationship for systems with cast-in-place walls – Δ_{ws} and Δ_{wu}	270
Fig. 8.13 Verification of idealized relationship for systems with precast walls – F_{ws} , F_{wy} , and F_{wu}	271
Fig. 8.14 Verification of idealized relationship for systems with precast walls – Δ_{ws} , Δ_{wy} , and Δ_{wu}	272
Fig. 8.15 Determination of coupled wall softening state in fiber element model: (a) systems with cast-in-place concrete walls; (b) systems with precast concrete walls	273

CHAPTER 9

Fig. 9.1 Photograph of test set-up	277
Fig. 9.2 Elevation of experimental set-up: (a) side view; (b) end view	280

Fig. 9.3 Bracing frame side view	281
Fig. 9.4 Test structure	282
Fig. 9.5 Loading block: (a) 3D view; (b) side view; (c) south end view	283
Fig. 9.6 Reaction block: (a) 3D view; (b) side view; (c) north end view	284
Fig. 9.7 Photograph of steel form for casting of reaction block	284
Fig. 9.8 Beam end view	285
Fig. 9.9 Beam side view.....	286
Fig. 9.10 Photograph of post-tensioning anchorage system	287
Fig. 9.11 Photograph of wall test region prior to casting of concrete.....	288
Fig. 9.12 Photograph of spiral reinforcement used inside wall test region.....	289
Fig. 9.13 Photograph showing shim plates at beam-to-reaction block interface	290
Fig. 9.14 Photograph showing angle-to-beam and angle-to-wall connections.....	291
Fig. 9.15 Displacement history	294
Fig. 9.16 Photograph of mono-strand post-tensioning jack and pump	294
Fig. 9.17 Beam steel stress-strain behavior	296
Fig. 9.18 Cover plate steel specimen	298
Fig. 9.19 Cover plate steel stress-strain behavior	299
Fig. 9.20 Angle steel specimen	301
Fig. 9.21 Angle steel stress-strain behavior: (a) L8x4x1/2 – first heat; (b) L8x4x1/2 – second heat; (c) L8x4x5/8.....	302
Fig. 9.22 Spiral wire specimens.....	303
Fig. 9.23 Spiral wire stress-strain behavior	304
Fig. 9.24 Unloading stiffness of spiral wire steel	306

Fig. 9.25 Post-tensioning strand stress-strain behavior	308
Fig. 9.26 Post-tensioning strand test setup.....	309
Fig. 9.27 Concrete cylinder specimens.....	311
Fig. 9.28 Instrumentation: (a) overall view; (b) beam-to-wall joint region.....	312
Fig. 9.29 Measurement of post-tensioning forces: (a) load cells; (b) placement of load cells	313
Fig. 9.30 DT11-DT15 at displaced position of coupling beam during Test 1	314
Fig. 9.31 Measured coupling shear force versus beam chord rotation ($V_b-\theta_b$) relationships: (a) Test 1; (b) Test 2; (c) Test 3.....	322
Fig. 9.32 Test 3: (a) displaced shape – overall; (b) displaced shape – local.....	324
Fig. 9.33 Test 3 – total beam post-tensioning force.....	325
Fig. 9.34 Test 3 – contact depth.....	327
Fig. 9.35 Test 3 – beam flange steel and wall concrete strains.....	328
Fig. 9.36 Test 3 – angle fracture	330
Fig. 9.37 Angle behavior (Tests 4, 6, 8, and 11): (a) test set-up; (b) deformed shape; (c) $V_b-\theta_b$ relationships	333
Fig. 9.38 Test 5: (a) $V_b-\theta_b$ relationship; (b) beam flange steel strains.....	334
Fig. 9.39 $V_b-\theta_b$ relationship from Test 7.....	336
Fig. 9.40 Test 9: (a) $V_b-\theta_b$ relationship; (b) total beam post-tensioning force; (c) beam flange steel strains.....	339
Fig. 9.41 Test 10: (a) $V_b-\theta_b$ relationship; (b) total beam post-tensioning force; (c) beam flange steel strains.....	341

CHAPTER 10

Fig. 10.1 Revised analytical model: (a) subassemblage; (b) wall-contact elements and beam elements.....	347
Fig. 10.2 Kinking behavior: (a) idealized deformed shape; (b) gap/contact PT kink element.....	351
Fig. 10.3 Angle model: (a) angle displacements and forces; (b) horizontal angle element; (c) vertical angle element.....	355
Fig. 10.4 Coupling shear force versus rotation (V_b - θ_b) behaviors: (a) Test 1; (b) Test 3; (c) Test 5; (d) Test 7; (e) Test 9; (f) Test 10	360
Fig. 10.5 Test 3 predictions using the previous model: (a) V_b - θ_b behavior; (b) angle behavior.....	361
Fig. 10.6 Test 3 predictions using the revised model: (a) horizontal angle element; (b) vertical angle element; (c) model with vertical angle elements removed.....	362
Fig. 10.7 Post-tensioning forces: (a) Test 3; (b) Test 9; (c) Test 10	365
Fig. 10.8 Horizontal displacements of loading block: (a) Test 3; (b) Test 9; (c) Test 10.....	366
Fig. 10.9 Beam cover plate/flange strains: (a) Test 1; (b) Test 3; (c) Test 5; (d) Test 7; (e) Test 9; (f) Test 10.....	367
Fig. 10.10 Average compressive strains at beam end: (a) SG22 from Test 1; (b) calculation of average strains.....	368
Fig. 10.11 Beam web strains: (a) Test 1; (b) Test 3; (c) Test 5; (d) Test 7; (e) Test 9; (f) Test 10.....	371
Fig. 10.12 Calculation of average compressive strains at beam web	372
Fig. 10.13 Angle behavior under monotonic loading-Tests 4, 6, and 8.....	373
Fig. 10.14 Angle behavior under cyclic loading: (a) Tests 1 and 3; (b) difference between Tests 1 and 3 during $\theta_b=6\%$ cycle.....	375

VOLUME II

CHAPTER 11

Fig. 11.1 Outline of the proposed performance-based seismic design approach (adapted from Kurama 1997)	384
Fig. 11.2 Limit states, performance levels, and design objectives: (a) steel coupling beam; (b) coupled wall system with cast-in-place concrete wall piers; (c) coupled wall system with precast concrete wall piers.....	393
Fig. 11.3 Design acceleration response spectra	399
Fig. 11.4 First mode component of roof-displacement time-history	403
Fig. 11.5 BP hysteresis model with $\beta_s=\beta_r<1$ (adapted from Farrow and Kurama 2003)	407
Fig. 11.6 Idealized base shear force versus roof displacement relationships: (a) CIP-UPT system; (b) PRE-UPT system	409
Fig. 11.7 Equivalent SDOF representation of CIP-UPT system: (a) smooth MDOF hysteresis; (b) MDOF BP model; (c) hysteretic energy dissipation; (d) equivalent SDOF BP model.....	413
Fig. 11.8 Equivalent SDOF representation of PRE-UPT system: (a) smooth MDOF hysteresis; (b) MDOF BP model; (c) hysteretic energy dissipation; (d) equivalent SDOF BP model.....	415
Fig. 11.9 Peak SDOF versus MDOF displacements: (a) CIP-UPT system; (b) PRE-UPT system	417
Fig. 11.10a SDOF and MDOF roof-displacement time-histories for CIP-UPT system (SAC LA21-LA30).....	418
Fig. 11.10b SDOF and MDOF roof-displacement time-histories for CIP-UPT system (SAC LA31-LA40).....	419
Fig. 11.11a SDOF and MDOF roof-displacement time-histories for PRE-UPT system (SAC LA21-LA30).....	420
Fig. 11.11b SDOF and MDOF roof-displacement time-histories for PRE-UPT system (SAC LA31-LA40).....	421

Fig. 11.12 Definitions of R_μ and μ (from Farrow and Kurama 2003)	423
Fig. 11.13 Distribution of inertial forces: (a) $H=0.67h_w$; (b) $H=0.3h_w$; (c) bending moment diagrams (adapted from Paulay and Priestley 1992)	440
CHAPTER 12	
Fig. 12.1 Plan view of prototype buildings.....	446
Fig. 12.2 Design-level and survival-level acceleration response spectra	456
Fig. 12.3 Design coupling beam shear force demand.....	469
Fig. 12.4 Angle strength ratio, β_{ar} : (a) $\beta_{ar}=0.66$; (b) $\beta_{ar}=0.91$; (c) $\beta_{ar}=1.27$	473
Fig. 12.5 Post-tensioning contribution to coupling resistance: (a) preliminary; (b) revised	475
Fig. 12.6 Coupling beam and post-tensioning details: (a) Structure P1-CWUPT; (b) Structure P2-PWUPT	478
Fig. 12.7 Angle contribution to coupling resistance.....	482
Fig. 12.8 Top and seat angle and connection details: (a) Structure P1-CWUPT; (b) Structure P2-PWUPT.....	484
Fig. 12.9 Coupling beam shear force versus chord rotation (V_b - θ_b) relationships: (a) Structure P1-CWUPT; (b) Structure P2-PWUPT.....	487
Fig. 12.10 Coupled wall idealized displaced shape	488
Fig. 12.11 Tension angle deformation	490
Fig. 12.12 Wall contact region stresses: (a) side view; (b) beam end view.....	495
Fig. 12.13 Wall-contact region concrete confinement.....	497
Fig. 12.14 Wall pier flexural reinforcement: (a) trial section 1; (b) trial section 2; (c) flexural steel area versus base shear resistance; (d) final wall cross section	500
Fig. 12.15 Concrete confinement at wall pier bases	504
Fig. 12.16 Wall pier post-tensioning steel reinforcement.....	512

Fig. 12.17 Concrete confinement at wall pier bases	517
Fig. 12.18 Prestress losses in wall pier post-tensioning bars	521
Fig. 12.19 Coupled wall base shear force versus roof drift ($F-\Delta$) relationships: (a) Structure P1-CWUPT; (b) Structure P2-PWUPT	525
CHAPTER 13	
Fig. 13.1 Coupled wall base shear force versus roof drift behaviors: (a) Structure P1-CWUPT; (b) Structure P2-PWUPT	536
Fig. 13.2 Wall pier flexural mild steel stresses at base of Structure P1-CWUPT: (a) tension-side wall; (b) compression-side wall	541
Fig. 13.3a Wall pier post-tensioning bar stresses in Structure P2-PWUPT: tension-side wall; (b) compression-side wall	542
Fig. 13.3b Wall pier post-tensioning bar stresses in Structure P2-PWUPT: compression-side wall	543
Fig. 13.4a Wall pier post-tensioning bar stress-strain behaviors for Structure P2-PWUPT: tension-side wall	544
Fig. 13.4b Wall pier post-tensioning bar stress-strain behaviors for Structure P2-PWUPT: compression-side wall	545
Fig. 13.5 Wall pier base axial forces: (a) Structure P1-CWUPT; (b) Structure P2-PWUPT	547
Fig. 13.6 Components of wall pier base axial forces: (a) Structure P1-CWUPT; (b) Structure P2-PWUPT	548
Fig. 13.7 Wall base shear forces: (a) Structure P1-CWUPT; (b) Structure P2-PWUPT	550
Fig. 13.8 Ratio of compression-side wall base shear force to total coupled wall base shear forces: (a) Structure P1-CWUPT; (b) Structure P2-PWUPT	552
Fig. 13.9 Wall base moments: (a) Structure P1-CWUPT; (b) Structure P2-PWUPT	554
Fig. 13.10 Degree of coupling: (a) Structure P1-CWUPT; (b) Structure P2-PWUPT	556

Fig. 13.11 Wall pier base neutral axis (i.e., contact) depths: (a) Structure P1-CWUPT; (b) Structure P2-PWUPT	558
Fig. 13.12 Wall pier base extreme confined concrete compression strains: (a) Structure P1-CWUPT; (b) Structure P2-PWUPT	559
Fig. 13.13 Coupling beam shear force versus chord rotation behaviors for Structure P1-CWUPT.....	562
Fig. 13.14 Coupling beam shear force versus chord rotation behaviors for Structure P2-PWUPT	563
Fig. 13.15 Coupling beam axial forces and post-tensioning forces in Structure P1-CWUPT.....	564
Fig. 13.16 Coupling beam axial forces and post-tensioning forces in Structure P2-PWUPT	565
Fig. 13.17 Coupling beam end neutral axis (i.e., contact) depths for Structure P1-CWUPT	567
Fig. 13.18 Coupling beam end neutral axis (i.e., contact) depths for Structure P2-PWUPT	568
Fig. 13.19 Coupling beam end extreme steel compression strains for Structure P1-CWUPT.....	570
Fig. 13.20 Coupling beam end extreme steel compression strains for Structure P2-PWUPT	571
Fig. 13.21 Coupling beam tension angle force-deformation behaviors for Structure P1-CWUPT.....	572
Fig. 13.22 Coupling beam tension angle force-deformation behaviors for Structure P2-PWUPT	573
Fig. 13.23 Cyclic coupled wall base shear force versus roof drift behaviors: (a) Structure P1-CWUPT; (b) Structure P2-PWUPT	576
Fig. 13.24 Cyclic wall post-tensioning forces for Structure P2-PWUPT: (a) left-side wall pier; (b) right-side wall pier; (c) total coupled wall.....	578
Fig. 13.25 Cyclic wall base axial forces for Structure P1-CWUPT: (a) left-side wall pier; (b) right-side wall pier; (c) total coupled wall	580

Fig. 13.26 Cyclic wall base axial forces for Structure P2-PWUPT: (a) left-side wall pier; (b) right-side wall pier; (c) total coupled wall	581
Fig. 13.27 Cyclic wall pier base shear forces for Structure P1-CWUPT: (a) left-side wall pier; (b) right-side wall pier	582
Fig. 13.28 Cyclic wall pier base shear forces for Structure P2-PWUPT: (a) left-side wall pier; (b) right-side wall pier	583
Fig. 13.29 Cyclic wall base moments for Structure P1-CWUPT: (a) left-side wall pier base moment; (b) right-side wall pier base moment; (c) coupling base moment; (d) total coupled wall base moment.....	584
Fig. 13.30 Cyclic wall base moments for Structure P2-PWUPT: (a) left-side wall pier base moment; (b) right-side wall pier base moment; (c) coupling base moment; (d) total coupled wall base moment.....	585
Fig. 13.31 Degree of coupling: (a) Structure P1-CWUPT; (b) Structure P2-PWUPT	587
Fig. 13.32 Cyclic wall pier base neutral axis (i.e., contact) depths and extreme confined concrete compression strains for Structure P1-CWUPT: (a) left-side wall pier contact depth; (b) right-side wall pier contact depth; (c) left-side wall pier concrete strains; (d) right-side wall pier concrete strains	589
Fig. 13.33 Cyclic wall pier base neutral axis (i.e., contact) depths and extreme confined concrete compression strains for Structure P2-CWUPT: (a) left-side wall pier contact depth; (b) right-side wall pier contact depth; (c) left-side wall pier concrete strains; (d) right-side wall pier concrete strains	590
Fig. 13.34 Cyclic coupling beam shear force versus chord rotation behaviors for Structure P1-CWUPT	592
Fig. 13.35 Cyclic coupling beam shear force versus chord rotation behaviors for Structure P2-PWUPT	593
Fig. 13.36 Cyclic coupling beam axial forces and post-tensioning forces in Structure P1-CWUPT.....	594
Fig. 13.37 Cyclic coupling beam axial forces and post-tensioning forces in Structure P2-PWUPT	595
Fig. 13.38 Cyclic coupling beam end neutral axis (i.e., contact) depths for Structure P1-CWUPT.....	598

Fig. 13.39 Cyclic coupling beam end neutral axis (i.e., contact) depths for Structure P2-PWUPT	599
Fig. 13.40 Cyclic coupling beam end extreme steel compression strains for Structure P1-CWUPT	600
Fig. 13.41 Cyclic coupling beam end extreme steel compression strains for Structure P2-PWUPT	601
Fig. 13.42 Cyclic coupling beam angle force versus deformation behaviors for Structure P1-CWUPT	602
Fig. 13.43 Cyclic coupling beam angle force versus deformation behaviors for Structure P2-PWUPT	603
Fig. 13.44 Coupled wall base shear force versus roof drift behavior of Structure P3-CWEMB: (a) monotonic loading; (b) cyclic loading	606
 CHAPTER 14	
Fig. 14.1a Acceleration time-histories of the SAC design-level ground motions (LA01-LA10)	611
Fig. 14.1b Acceleration time-histories of the SAC design-level ground motions (LA11-LA20)	612
Fig. 14.2a 5%-damped linear-elastic pseudo-acceleration response spectra of the SAC design-level ground motions (LA01-LA10)	613
Fig. 14.2b 5%-damped linear-elastic pseudo-acceleration response spectra of the SAC design-level ground motions (LA11-LA20)	614
Fig. 14.3a Acceleration time-histories of the SAC survival-level ground motions (LA21-LA30)	616
Fig. 14.3b Acceleration time-histories of the SAC survival-level ground motions (LA31-LA40)	617
Fig. 14.4a 5%-damped linear-elastic pseudo-acceleration response spectra of the SAC survival-level ground motions (LA21-LA30)	618

Fig. 14.4b 5%-damped linear-elastic pseudo-acceleration response spectra of the SAC survival-level ground motions (LA31-LA40).....	619
--	-----

CHAPTER 15

Fig. 15.1 Roof drift time history for Structure P1-CWUPT	627
Fig. 15.2 Peak roof drift demands for Structure P1-CWUPT: (a) survival level; (b) design level.....	630
Fig. 15.3 Inter-story drift time histories for Structure P1-CWUPT	632
Fig. 15.4 Peak inter-story drift demands for Structure P1-CWUPT: (a) survival level; (b) design level	633
Fig. 15.5 Floor/roof acceleration time histories for Structure P1-CWUPT	637
Fig. 15.6 Peak floor/roof acceleration demands for Structure P1-CWUPT: (a) survival level; (b) design level.....	638
Fig. 15.7 Wall pier base axial force time histories for Structure P1-CWUPT: (a) left-side wall; (b) right-side wall.....	641
Fig. 15.8 Wall pier base axial force time histories for Structure P1-CWUPT: (a) left-side wall; (b) right-side wall.....	641
Fig. 15.9 Peak wall pier base axial force demands for Structure P1-CWUPT: (a) survival level; (b) design level.....	643
Fig. 15.10 Coupled wall base shear force time history for Structure P1-CWUPT	646
Fig. 15.11 Peak coupled wall base shear force demands for Structure P1-CWUPT: (a) survival level; (b) design level.....	647
Fig. 15.12 Wall pier base shear force time histories for Structure P1-CWUPT: (a) left-side wall; (b) right-side wall	650
Fig. 15.13 Peak wall pier base shear force demands for Structure P1-CWUPT: (a) survival level; (b) design level.....	651
Fig. 15.14 Wall pier base moment time histories for Structure P1-CWUPT: (a) left-side wall; (b) right-side wall.....	656

Fig. 15.15 Peak wall pier base moment demands for Structure P1-CWUPT: (a) survival level; (b) design level.....	657
Fig. 15.16 Coupled wall base moment time history for Structure P1-CWUPT	660
Fig. 15.17 Peak coupled wall base moment demands for Structure P1-CWUPT: (a) survival level; (b) design level.....	661
Fig. 15.18 Wall pier base extreme confined concrete compression strain time histories for Structure P1-CWUPT: (a) left-side wall; (b) right-side wall.....	664
Fig. 15.19 Peak wall base confined concrete compression strain demands for Structure P1-CWUPT: (a) survival level; (b) design level.....	665
Fig. 15.20 Coupling beam chord rotation time histories for Structure P1-CWUPT.....	668
Fig. 15.21 Peak coupling beam chord rotation demands for Structure P1-CWUPT: (a) survival level; (b) design level.....	669
Fig. 15.22 Coupling beam midspan axial force time histories for Structure P1-CWUPT.....	673
Fig. 15.23 Peak coupling beam midspan axial force demands for Structure P1-CWUPT: (a) survival level; (b) design level	674
Fig. 15.24 Coupling beam post-tensioning force time histories for Structure P1-CWUPT ..	678
Fig. 15.25 Peak coupling beam post-tensioning force demands for Structure P1-CWUPT: (a) survival level; (b) design level	679
Fig. 15.26 Coupling beam shear force time histories for Structure P1-CWUPT	682
Fig. 15.27 Peak coupling beam shear force demands for Structure P1-CWUPT: (a) survival level; (b) design level.....	683
Fig. 15.28 Coupling beam shear slip capacity and shear force demand time histories for Structure P1-CWUPT	688
Fig. 15.29 Minimum coupling beam shear slip capacity to shear force demand ratios for Structure P1-CWUPT: (a) survival level; (b) design level	689
Fig. 15.30 Coupling beam connection angle deformation time histories for Structure P1-CWUPT.....	693

Fig. 15.31 Peak coupling beam connection angle tensile deformation demands for Structure P1-CWUPT: (a) survival level; (b) design level	694
Fig. 15.32 Roof drift time history for Structure P2-PWUPT.....	695
Fig. 15.33 Peak roof drift demands for Structure P2-PWUPT: (a) survival level; (b) design level	698
Fig. 15.34 Inter-story drift time histories for Structure P2-PWUPT	702
Fig. 15.35 Peak inter-story drift demands for Structure P2-PWUPT: (a) survival level; (b) design level	703
Fig. 15.36 Floor/roof acceleration time histories for Structure P2-PWUPT	707
Fig. 15.37 Peak floor/roof acceleration demands for Structure P2-PWUPT: (a) survival level; (b) design level.....	708
Fig. 15.38 Total coupled wall post-tensioning force time histories for Structure P2-PWUPT: (a) LA38; (b) LA33	712
Fig. 15.39 Minimum and maximum total coupled wall post-tensioning forces for Structure P2-PWUPT: (a) survival level; (b) design level.....	713
Fig. 15.40 Wall pier base axial force time histories for Structure P2-PWUPT: (a) left-side wall; (b) right-side wall.....	719
Fig. 15.41 Wall pier base axial force time histories for Structure P2-PWUPT: (a) left-side wall; (b) right-side wall.....	719
Fig. 15.42 Peak wall pier base axial force demands for Structure P2-PWUPT: (a) survival level; (b) design level.....	720
Fig. 15.43 Coupled wall base shear force time history for Structure P2-PWUPT	723
Fig. 15.44 Peak coupled wall base shear force demands for Structure P2-PWUPT: (a) survival level; (b) design level.....	725
Fig. 15.45 Wall pier base shear force time histories for Structure P2-PWUPT: (a) left-side wall; (b) right-side wall.....	727
Fig. 15.46 Peak wall pier base shear force demands for Structure P2-PWUPT: (a) survival level; (b) design level.....	729

Fig. 15.47 Coupled wall base shear slip capacity and base shear force demand time histories for Structure P2-PWUPT.....	734
Fig. 15.48 Minimum coupled wall base shear slip capacity to base shear force demand ratio for Structure P2-PWUPT: (a) survival level; (b) design level.....	735
Fig. 15.49 Wall pier base moment time histories for Structure P2-PWUPT: (a) left-side wall; (b) right-side wall.....	738
Fig. 15.50 Peak wall pier base moment demands for Structure P2-PWUPT: (a) survival level; (b) design level.....	740
Fig. 15.51 Coupled wall base moment time history for Structure P2-PWUPT	743
Fig. 15.52 Peak coupled wall base moment demands for Structure P2-PWUPT: (a) survival level; (b) design level.....	744
Fig. 15.53 Wall pier base extreme confined concrete compression strain time histories for Structure P2-PWUPT: (a) left-side wall; (b) right-side wall	747
Fig. 15.54 Peak wall base confined concrete compression strain demands for Structure P2-PWUPT: (a) survival level; (b) design level	748
Fig. 15.55 Coupling beam chord rotation time histories for Structure P2-PWUPT	751
Fig. 15.56 Peak coupling beam chord rotation demands for Structure P2-PWUPT: (a) survival level; (b) design level.....	753
Fig. 15.57 Coupling beam midspan axial force time histories for Structure P2-PWUPT	757
Fig. 15.58 Peak coupling beam midspan axial force demands for Structure P2-PWUPT: (a) survival level; (b) design level	758
Fig. 15.59 Coupling beam post-tensioning force time histories for Structure P2-PWUPT...	761
Fig. 15.60 Peak coupling beam post-tensioning force demands for Structure P2-PWUPT: (a) survival level; (b) design level	762
Fig. 15.61 Coupling beam shear force time histories for Structure P2-PWUPT	766
Fig. 15.62 Peak coupling beam shear force demands for Structure P2-PWUPT: (a) survival level; (b) design level.....	767

Fig. 15.63 Coupling beam shear slip capacity and shear force demand time histories for Structure P2-PWUPT	772
Fig. 15.64 Minimum coupling beam shear slip capacity to shear force demand ratios for Structure P2-PWUPT: (a) survival level; (b) design level.....	773
Fig. 15.65 Coupling beam connection angle deformation time histories for Structure P2-PWUPT	776
Fig. 15.66 Peak coupling beam connection angle tensile deformation demands for Structure P2-PWUPT: (a) survival level; (b) design level.....	777
Fig. 15.67 Peak roof drift demand for uncoupled wall systems: (a) Structure P4-CWUNC; (b) Structure P5-PWUNC	780

TABLES

VOLUME I

CHAPTER 3

Table 3.1 Prototype subassemblage coupling beam properties	73
Table 3.2 Prototype subassemblage beam post-tensioning properties.....	73
Table 3.3 Prototype subassemblage beam-to-wall connection top and seat angle properties.....	73
Table 3.4 Prototype subassemblage wall properties	74
Table 3.5 Prototype subassemblage material properties.....	77
Table 3.6 Wall-contact element fiber discretization	88
Table 3.7 Beam fiber element discretization	92
Table 3.8 Prototype subassemblage beam-to-wall connection top and seat angle design capacities.....	99

CHAPTER 4

Table 4.1 Parametric study of coupled wall subassemblages.....	126
--	-----

CHAPTER 6

Table 6.1 CIP-UPT wall properties	154
Table 6.2 PRE-UPT wall properties	154
Table 6.3 Walls CIP-UPT and PRE-UPT coupling beam properties	157
Table 6.4 Walls CIP-UPT and PRE-UPT beam post-tensioning properties.....	157

Table 6.5 Walls CIP-UPT and PRE-UPT beam-to-wall connection top and seat angle properties.....	158
--	-----

Table 6.6 Wall material properties.....	159
---	-----

Table 6.7 CIP-UPT system wall-height element discretization.....	168
--	-----

Table 6.8 PRE-UPT system wall-height element discretization.....	173
--	-----

CHAPTER 7

Table 7.1 Wall Pier Gravity loads for CIP-UPT and PRE-UPT systems	183
---	-----

Table 7.2 Parametric CIP-UPT systems	224
--	-----

Table 7.3 Parametric PRE-UPT systems	224
--	-----

Table 7.4 Degree of coupling of parametric CIP-UPT systems	225
--	-----

Table 7.5 Degree of coupling of parametric PRE-UPT systems	228
--	-----

Table 7.6 Second floor beam initial axial force divided by total initial PT force in parametric CIP-UPT systems.....	229
--	-----

Table 7.7 Second floor beam initial axial force divided by total initial PT force in parametric PRE-UPT systems.....	230
--	-----

CHAPTER 9

Table 9.1 Subassemblage Test Specimens.....	277
---	-----

Table 9.2 Beam Steel (W10×68) Material Properties.....	297
--	-----

Table 9.3 Cover Plate Steel Material Properties.....	299
--	-----

Table 9.4 Angle Steel Material Properties.....	301
--	-----

Table 9.5 Spiral Wire Steel Material Properties	304
---	-----

Table 9.6 Post-Tensioning Strand Properties.....	309
--	-----

Table 9.7 Concrete Properties.....	310
------------------------------------	-----

VOLUME II

CHAPTER 11

Table 11.1 MDOF System Properties	410
Table 11.2 Idealized MDOF BP Model Properties.....	412
Table 11.3 Equivalent SDOF BP Model Properties	414
Table 11.4 Regression coefficients a and b for BP models (based on IND spectra)	427
Table 11.5 Regression coefficients a and b for BP models (based on DES spectra)	429

CHAPTER 12

Table 12.1 General properties of the prototype structures.....	447
Table 12.2 Seismic weights and gravity loads.....	452
Table 12.3 Acceleration response spectra.....	455
Table 12.4 Linear-elastic stiffnesses.....	458
Table 12.5 Linear-elastic modal analysis results	459
Table 12.6 Displacement demand relationships	460
Table 12.7 Displacement ductility demands and strength ratios	461
Table 12.8 Design base shear demands	462
Table 12.9 Peak roof drift demands.....	464
Table 12.10 Peak inter-story drift demands.....	465
Table 12.11 Diagonal tension at wall pier bases.....	467
Table 12.12 Design coupling beam shear force demands.....	470
Table 12.13 Effect of β_{ar} on coupling beam behavior	474
Table 12.14 Components of coupling beam design forces	474

Table 12.15 Beam post-tensioning	479
Table 12.16 Top and seat angles.....	483
Table 12.17 Coupling beam shear force versus rotation relationships	485
Table 12.18 Coupling beam rotation demands	486
Table 12.19 Tension angle deformation demands	490
Table 12.20 Shear slip at beam-to-wall interfaces.....	493
Table 12.21 Wall-contact regions	496
Table 12.22 Wall pier flexural reinforcement.....	501
Table 12.23 Concrete confinement at wall pier bases	505
Table 12.24 Diagonal tension at wall pier bases.....	507
Table 12.25 Shear slip at coupled wall base	508
Table 12.26 Wall pier post-tensioning steel reinforcement	512
Table 12.27 Yielding of wall pier post-tensioning steel	514
Table 12.28 Concrete confinement at wall pier bases	517
Table 12.29 Diagonal tension at wall pier bases.....	519
Table 12.30 Shear slip at coupled wall base	523
Table 12.31 Idealized F- Δ behaviors for Structures P1-CWUPT and P2-PWUPT	526
Table 12.32 Seismic design criteria for Structures P1-CWUPT and P2-PWUPT	528
CHAPTER 13	
Table 13.1 Wall pier gravity loads in Structures P1-CWUPT and P2-PWUPT	534
Table 13.2 Comparisons between estimation and analytical results.....	540

CHAPTER 14

Table 14.1 SAC design-level ground motions records LA01-LA20	615
Table 14.2 SAC Survival-level ground motions records LA21-LA40	620

CHAPTER 15

Table 15.1 Period and damping ratios for the first eight modes of the prototype structures	624
Table 15.2 Peak roof drift demands for Structure P1-CWUPT under survival level ground motions.....	626
Table 15.3 Peak roof drift demands for Structure P1-CWUPT under design level ground motions.....	626
Table 15.4 Peak inter-story drift demands for Structure P1-CWUPT under survival level ground motions	629
Table 15.5 Peak inter-story drift demands for Structure P1-CWUPT under design level ground motions	629
Table 15.6 Peak floor/roof acceleration demands for Structure P1-CWUPT under survival level ground motions.....	634
Table 15.7 Peak floor/roof acceleration demands for Structure P1-CWUPT under design level ground motions.....	635
Table 15.8 Peak wall pier base tensile axial force demands for Structure P1-CWUPT under survival level ground motions.....	636
Table 15.9 Peak wall pier base tensile axial force demands for Structure P1-CWUPT under design level ground motions.....	639
Table 15.10 Peak wall pier base compressive axial force demands for Structure P1-CWUPT under survival level ground motions.....	639
Table 15.11 Peak wall pier base compressive axial force demands for Structure P1-CWUPT under design level ground motions.....	640

Table 15.12 Peak coupled wall base shear force demands for Structure P1-CWUPT under survival level ground motions.....	644
Table 15.13 Peak coupled wall base shear force demands for Structure P1-CWUPT under design level ground motions	644
Table 15.14 Peak wall pier base shear force demands for Structure P1-CWUPT under survival level ground motions.....	648
Table 15.15 Peak wall pier base shear force demands for Structure P1-CWUPT under design level ground motions	649
Table 15.16 Peak wall pier base shear force distribution ratios for Structure P1-CWUPT under survival level ground motions.....	652
Table 15.17 Peak wall pier shear force distribution ratios for Structure P1-CWUPT under design level ground motions	653
Table 15.18 Peak wall pier base moment demands for Structure P1-CWUPT under survival level ground motions.....	654
Table 15.19 Peak wall pier base moment demands for Structure P1-CWUPT under design level ground motions.....	654
Table 15.20 Peak coupled wall base moment demands for Structure P1-CWUPT under survival level ground motions.....	658
Table 15.21 Peak coupled wall base moment demands for Structure P1-CWUPT under design level ground motions	658
Table 15.22 Peak wall pier base confined concrete compression strain demands for Structure P1-CWUPT under survival level ground motions	662
Table 15.23 Peak wall pier base confined concrete compression strain demands for Structure P1-CWUPT under design level ground motions.....	662
Table 15.24 Peak coupling beam chord rotation demands for Structure P1-CWUPT under survival level ground motions.....	666
Table 15.25 Peak coupling beam chord rotation demands for Structure P1-CWUPT under design level ground motions	666
Table 15.26 Peak coupling beam midspan axial force demands for Structure P1-CWUPT under survival level ground motions.....	670

Table 15.27 Peak coupling beam midspan axial force demands for Structure P1-CWUPT under design level ground motions	671
Table 15.28 Peak coupling beam post-tensioning force demands for Structure P1-CWUPT under survival level ground motions.....	675
Table 15.29 Peak coupling beam post-tensioning force demands for Structure P1-CWUPT under design level ground motions	676
Table 15.30 Peak coupling beam shear force demands for Structure P1-CWUPT under survival level ground motions.....	680
Table 15.31 Peak coupling beam shear force demands for Structure P1-CWUPT under design level ground motions	680
Table 15.32 Minimum coupling beam shear slip capacity-demand ratios for Structure P1-CWUPT under survival level ground motions.....	685
Table 15.33 Minimum coupling beam slip capacity-demand ratios for Structure P1-CWUPT under design level ground motions	685
Table 15.34 Peak angle tensile deformation demands for Structure P1-CWUPT under survival level ground motions.....	690
Table 15.35 Peak angle tensile deformation demands for Structure P1-CWUPT under design level ground motions	691
Table 15.36 Peak roof drift for Structure P2-PWUPT under survival level ground motions	696
Table 15.37 Peak roof drift for Structure P2-PWUPT under design level ground motions ..	696
Table 15.38 Peak inter-story drift for Structure P2-PWUPT under survival level ground motions.....	699
Table 15.39 Peak inter-story drift for Structure P2-PWUPT under design level ground motions.....	700
Table 15.40 Peak floor/roof acceleration for Structure P2-PWUPT under survival level ground motions	704
Table 15.41 Peak floor/roof acceleration for Structure P2-PWUPT under design level ground motions	705

Table 15.42 Minimum total coupled wall post-tensioning forces for Structure P2-PWUPT under survival level ground motions.....	709
Table 15.43 Minimum total coupled wall post-tensioning forces for Structure P2-PWUPT under design level ground motions	709
Table 15.44 Maximum total coupled wall post-tensioning forces for Structure P2-PWUPT under survival level ground motions	710
Table 15.45 Maximum total coupled wall post-tensioning forces for Structure P2-PWUPT under design level ground motions	710
Table 15.46 Minimum wall pier base compression axial force demands for Structure P2-PWUPT under survival level ground motions	715
Table 15.47 Minimum wall pier base compression axial force demands for Structure P2-PWUPT under design level ground motions	716
Table 15.48 Maximum wall pier base compression axial force demands for Structure P2-PWUPT under survival level ground motions	716
Table 15.49 Maximum wall pier base compression axial force demands for Structure P2-PWUPT under design level ground motions	717
Table 15.50 Peak coupled wall base shear force demands for Structure P2-PWUPT under survival level ground motions.....	721
Table 15.51 Peak coupled wall base shear force demands for Structure P2-PWUPT under design level ground motions	721
Table 15.52 Peak wall pier base shear force demands for Structure P2-PWUPT under survival level ground motions.....	726
Table 15.53 Peak wall pier base shear force demands for Structure P2-PWUPT under design level ground motions	726
Table 15.54 Peak wall pier base shear force distribution ratios for Structure P2-PWUPT under survival level ground motions.....	730
Table 15.55 Peak wall pier base shear force distribution ratios for Structure P2-PWUPT under design level ground motions	730

Table 15.56 Minimum coupled wall base shear slip capacity-demand ratios for Structure P2-PWUPT under survival level ground motions	733
Table 15.57 Minimum coupled wall base shear slip capacity-demand ratios for Structure P2-PWUPT under design level ground motions	733
Table 15.58 Peak wall pier base moment demands for Structure P2-PWUPT under survival level ground motions.....	736
Table 15.59 Peak wall pier base moment demands for Structure P2-PWUPT under design level ground motions.....	737
Table 15.60 Peak coupled wall base moment demands for Structure P2-PWUPT under survival level ground motions.....	741
Table 15.61 Peak coupled wall base moment demands for Structure P2-PWUPT under design level ground motions	741
Table 15.62 Peak wall pier base confined concrete compression strain demands for Structure P2-PWUPT under survival level ground motions.....	745
Table 15.63 Peak wall pier base confined concrete compression strain demands for Structure P2-PWUPT under design level ground motions	745
Table 15.64 Peak coupling beam chord rotation demands for Structure P2-PWUPT under survival level ground motions.....	749
Table 15.65 Peak coupling beam chord rotation demands for Structure P2-PWUPT under design level ground motions	750
Table 15.66 Peak coupling beam midspan axial forces demands for Structure P2-PWUPT under survival level ground motion	754
Table 15.67 Peak coupling beam midspan axial force demands for Structure P2-PWUPT under design level ground motions	754
Table 15.68 Peak coupling beam post-tensioning force demands for Structure P2-PWUPT under survival level ground motions	759
Table 15.69 Peak coupling beam post-tensioning force demands for Structure P2-PWUPT under design level ground motions	759
Table 15.70 Peak coupling beam shear force demands for Structure P2-PWUPT under survival level ground motions.....	763

Table 15.71 Peak coupling beam shear force demands for Structure P2-PWUPT under design level ground motions	764
Table 15.72 Minimum coupling beam shear slip capacity-demand ratios for Structure P2-PWUPT under survival level ground motions	769
Table 15.73 Minimum coupling beam slip capacity-demand ratios for Structure P2-PWUPT under design level ground motions	769
Table 15.74 Peak angle tensile deformation demands for Structure P2-PWUPT under survival level ground motions.....	774
Table 15.75 Peak angle tensile deformation in Structure P2-PWUPT under design level ground motions	774
Table 15.76 Peak roof drift demands for Structure P4-CWUNC under survival level ground motions	779
Table 15.77 Peak roof drift demands for Structure P5-PWUNC under survival level ground motions	779

SYMBOLS

a	= regression coefficient for R_{μ} - μ -T relationship
a_{bp}	= area of one coupling beam post-tensioning strand
a_{bsp}	= area of spiral wire in wall pier contact region adjacent to coupling beam
a_{bt}	= area of coupling beam post-tensioning multi-strand tendon
a_f	= area of steel fiber
a_{wp}	= area of wall pier post-tensioning bar
a_{wsp}	= area of spiral wire at wall pier base
A_a	= gross area of angle leg gross cross section
A_{aw}	= total area of post-tensioning steel used in angle-to-wall pier connection
A_b	= area of coupling beam cross section
A_{bc}	= area of coupling beam cross-section including flange cover plates (if any)
A_{bf}	= area of coupling beam flange
A_{bfc}	= area of coupling beam flange plus flange cover plate
A_{bg}	= shear area of coupling beam cross section
A_{bp}	= total area of coupling beam post-tensioning steel per floor/roof level
A_{bw}	= effective area of weld for coupling beam cover plate
A_c	= area of coupling beam flange cover plate
A_w	= area of wall pier gross cross section

A_{wc}	= net concrete area of wall pier cross section
A_{wp}	= total area of wall pier post-tensioning steel reinforcement
A_{ws}	= total area of wall pier boundary flexural mild steel reinforcement
b	= regression coefficient for R_{μ} - μ -T relationship
b_{bf}	= width of coupling beam flange
b_c	= width of coupling beam flange cover plate
c	= regression coefficient for R_{μ} - μ -T relationship
c_b	= neutral axis (contact) depth of coupling beam at beam-to-wall pier interface
$c_{b,pty}$	= value of c_b at coupling beam PT-yielding state
$c_{b,sof}$	= value of c_b at coupling beam softening state
c_{cw}	= neutral axis depth of compression-side wall pier at base
c_{cws}	= value of c_{cw} at coupled wall softening state
c_{cwu}	= value of c_{cw} at coupled wall ultimate state
c_{cwy}	= value of c_{cw} at coupled wall PT-yielding state
c_{tw}	= neutral axis depth of tension-side wall pier at base
c_{tws}	= value of c_{tw} at coupled wall softening state
c_{twy}	= value of c_{tw} at coupled wall PT-yielding state
$[C]$	= damping matrix for structure
C_a	= force in compression angle
C_{asx}	= slip force of angle-to-beam connection bolt group
C_{ax}	= compression force in angle for loading parallel to coupling beam
C_b	= total compression force at end of coupling beam

$C_{b,pty}$	= value of C_b at coupling beam PT-yielding state
$C_{b,sof}$	= value of C_b coupling beam softening state
C_{eq}	= generalized damping for first (fundamental) vibration mode ($\{\phi_1\}^T[C]\{\phi_1\}$)
C_{vx}	= factor for distribution of Q_{sd} over structure height
C_{wc}	= compression force in wall pier contact region adjacent to coupling beam
CC	= confined concrete fiber
CCC	= compression-only confined concrete fiber
CM	= building center of mass at floor/roof level
CS	= building center of stiffness at floor/roof level
CU	= unconfined concrete fiber
CUC	= compression-only unconfined concrete fiber
d_{ab}	= diameter of angle-to-beam or angle-to-column/wall pier connector
d_{abb}	= diameter of angle-to-beam connector
d_{abw}	= diameter of angle-to-column/wall pier connector
d_b	= depth of coupling beam
d_{bc}	= depth of coupling beam including flange cover plates (if any)
d_{bp}	= diameter of coupling beam post-tensioning strand
d_{bsp}	= diameter of spiral wire in wall pier contact region adjacent to coupling beam
d_{bw}	= depth of coupling beam web
d_{wsp}	= diameter of spiral wire at wall pier base
d_{wp}	= distance of wall pier post-tensioning bar from compression end of wall pier
d_{wp1}	= value of d_{wp} for first post-tensioning bar that yields

D	= unfactored design dead loads
D_{bsp}	= center-to-center diameter of spiral in wall pier contact region adjacent to coupling beam
D_m	= coefficient to estimate $Q_{h,max}$
D_{wsp}	= center-to-center diameter of spiral at wall pier base
DOC	= degree of coupling
DOC_{ws}	= value of DOC at coupled wall softening state
DOC_{wu}	= value of DOC at coupled wall ultimate state
e	= eccentricity between floor/roof center of mass (CM) and center of stiffness (CS)
e_{acc}	= accidental eccentricity between floor/roof center of mass (CM) and center of stiffness (CS)
e_{app}	= applied eccentricity between floor/roof center of mass (CM) and center of stiffness (CS)
E	= effect of seismic loads
E_a	= modulus of elasticity of angle steel
E_b	= modulus of elasticity of coupling beam steel
E_{bp}	= modulus of elasticity of coupling beam post-tensioning strand
E_c	= modulus of elasticity of wall pier concrete
E_{hc}	= hysteretic energy dissipation during a base shear force versus roof displacement cycle
E_s	= modulus of elasticity of steel
E_{sp}	= modulus of elasticity of spiral steel
E_{wp}	= modulus of elasticity of wall pier post-tensioning bar
E_{ws}	= modulus of elasticity of wall pier mild steel reinforcement

f	= lateral forces applied at floor/roof levels
f_{am}	= maximum (peak) strength of angle steel
f_{au}	= $0.85f_{am}$
f_{awpi}	= initial stress in angle-to-wall pier connection strands
f_{awpu}	= maximum (peak) strength of angle-to-wall pier connection strands
f_{ay}	= yield strength of angle steel
f_{bi}	= initial compressive stress in coupling beam (including flange cover plates, if any) due to post-tensioning before application of lateral loads
f_{bm}	= maximum (peak) strength of coupling beam steel
f_{bpi}	= initial stress in coupling beam post-tensioning strands before application of lateral loads
f_{bpm}	= maximum (peak) strength of coupling beam post-tensioning strands
f_{bpu}	= f_{bpm}
f_{bpy}	= yield (limit of proportionality) strength of coupling beam post-tensioning strands
f_{bu}	= $0.85f_{bm}$
f_{by}	= yield strength of coupling beam steel
f'_c	= maximum (peak) compressive strength of unconfined concrete
f_{cc}	= maximum (peak) compressive strength of confined concrete
f_{ccw}	= value of f_{cc} for wall pier contact region adjacent to coupling beam
f_{cl}	= linear limit (limit of proportionality) stress of confined concrete in compression
f_{ct}	= tensile strength of unconfined and confined concrete
f_{cwp}	= stress in post-tensioning bar of compression-side wall pier

f_{EXX}	= weld electrode strength
f_{rm}	= maximum (peak) strength of coupling beam flange cover plate steel
f_{ru}	= $0.85f_{rm}$
f_{ry}	= yield strength of coupling beam flange cover plate steel
f_{sm}	= maximum (peak) strength of steel
f_{spm}	= maximum (peak) strength of spiral steel
f_{spu}	= $0.85f_{spm}$
f_{spy}	= yield strength of spiral steel
f_{sy}	= yield strength of steel
f_{twp}	= stress in post-tensioning bar of tension-side wall pier
f_{wpi}	= initial stress in wall pier post-tensioning bar before application of lateral loads
f_{wpm}	= maximum (peak) strength of wall pier post-tensioning bars
f_{wpr}	= residual stress of wall pier post-tensioning bar after losses under cyclic loading
f_{wpu}	= f_{wpm}
f_{wpy}	= yield (limit of proportionality) strength of wall pier post-tensioning bar
f_{wp1}	= stress in wall pier post-tensioning bar layer 1
f_{wp2}	= stress in wall pier post-tensioning bar layer 2
f_{wp3}	= stress in wall pier post-tensioning bar layer 3
f_{wp4}	= stress in wall pier post-tensioning bar layer 4
f_{wp5}	= stress in wall pier post-tensioning bar layer 5
f_{wp6}	= stress in wall pier post-tensioning bar layer 6
f_{wp7}	= stress in wall pier post-tensioning bar layer 7

f_{wp8}	= stress in wall pier post-tensioning bar layer 8
f_{wse}	= extreme tension stress of flexural mild steel reinforcement at compression-side wall pier base
f_{wsm}	= maximum (peak) strength of wall pier mild steel reinforcement
f_{wsy}	= yield strength of wall pier mild steel reinforcement
f_x	= lateral force applied at floor/roof level x
f_ξ	= damping adjustment coefficient
F	= base shear force
F_a	= site coefficient for spectral response acceleration at short periods
F_{be}	= yield strength of BE component of equivalent nonlinear single-degree-of-freedom BP hysteresis model
F_{bp}	= yield strength of equivalent nonlinear single-degree-of-freedom BP hysteresis model
F_{cw}	= base shear force in compression-side wall pier
F_{des}	= base shear force at first “significant” yield of structure
F_{elas}	= linear-elastic lateral force demand for structure
F_{ep}	= yield strength of EP component of equivalent nonlinear single-degree-of-freedom BP hysteresis model
F_{eq}	= force in equivalent single-degree-of-freedom system
$F_{eq,be}$	= yield strength of BE component of equivalent nonlinear single-degree-of-freedom BP hysteresis model
$F_{eq,bp}$	= yield strength of equivalent nonlinear single-degree-of-freedom BP hysteresis model
$F_{eq,ep}$	= yield strength of EP component of equivalent nonlinear single-degree-of-freedom BP hysteresis model
$F_{g,ss}$	= shear friction capacity at base of coupled wall due to gravity loads

F_{nlin}	= lateral force corresponding to u_{nlin}
$F_{p,ss}$	= shear friction capacity at base of coupled wall due to wall pier post-tensioning steel reinforcement
$F_{s,ss}$	= shear friction capacity at base of coupled wall due to wall pier mild steel reinforcement
F_{tw}	= base shear force in tension-side wall pier
F_v	= site coefficient for spectral response acceleration at 1 sec. period
F_{wbs}	= wall pier shear force below floor level
$F_{w,dt}$	= diagonal tension shear force capacity for wall pier
F_{ws}	= coupled wall base shear force at coupled wall softening state
F_{wsi}	= F_{wbs} minus F_{wts}
$F_{w,ss}$	= coupled wall base shear slip capacity
F_{wts}	= wall pier shear force above floor level
F_{wu}	= coupled wall base shear force at coupled wall ultimate state
$F_{w,unc}$	= uncoupled wall base shear force (one wall pier)
F_{wy}	= coupled wall base shear force at coupled wall PT-yielding state
F_y	= base shear force at “global” yield of structure
g	= acceleration of gravity
$g_{b,pty}$	= width of gap opening at coupling beam centerline at beam PT-yielding state
G	= wall floor and roof gravity (dead plus live) forces
G_b	= shear modulus of coupling beam steel
G_c	= shear modulus of wall pier concrete
h_b	= height of coupling beam from wall base

h_s	= height of story
h_w	= height of wall
h_{wp}	= plastic hinge height at base of compression-side wall pier
H	= resultant height of coupled wall lateral forces
H_1	= resultant height of coupled wall first mode inertial forces
I	= occupancy importance factor (ICC 2000)
I_a	= moment of inertia of angle leg cross section
I_b	= moment of inertia of coupling beam cross section
I_w	= moment of inertia of wall pier gross cross section
k_a	= angle fillet length measured from angle heel to toe of angle fillet
k_{be}	= linear-elastic stiffness of single-degree-of-freedom BE hysteresis model
k_{ep}	= linear-elastic stiffness of single-degree-of-freedom EP hysteresis model
K	= linear-elastic stiffness
$[K]$	= stiffness matrix of structure
K_{aixc}	= initial compression stiffness of angle for loading parallel to coupling beam
K_{aixt}	= initial tension stiffness of angle for loading parallel to coupling beam
K_{aiy}	= initial stiffness of angle for loading perpendicular to coupling beam
K_{axs}	= “shooting” stiffness of angle for loading parallel to coupling beam
K_{bi}	= initial linear-elastic lateral stiffness of a coupling beam subassemblage
$[K_{bi}]$	= initial linear-elastic stiffness matrix for coupling beam
$[K_{ci}]$	= initial linear-elastic stiffness matrix of wall pier
K_{eq}	= generalized stiffness for first (fundamental) vibration mode ($\{\phi_1\}^T [K] \{\phi_1\}$)

K_{li}	= initial linear-elastic lateral stiffness of lateral load resisting system
K_{si}	= initial linear-elastic lateral stiffness of entire building
K_{wi}	= initial linear-elastic lateral stiffness of coupled wall
l_a	= length of angle
l_{al}	= length of angle leg
l_b	= length of coupling beam
l_{be}	= embedment length of coupling beam
$l_{b,cr}$	= length of first coupling beam fiber element or segment adjacent to wall pier
$l_{b,eff}$	= effective length for embedded coupling beam
l_{bpu}	= unbonded length of coupling beam post-tensioning tendons
l_c	= length of coupling beam flange cover plate
l_{gh}	= angle-to-beam connection gage length measured from heel of angle to centroid of angle-to-beam connector group
l_{gv}	= angle-to-column/wall pier connection gage length measured from heel of angle to center of innermost angle-to-wall pier connectors
l_{g1}	= length of angle vertical leg (leg perpendicular to coupling beam) assumed to act like a cantilever
l_{g2}	= “effective” gage length of angle vertical leg (leg perpendicular to coupling beam) between two plastic hinges
l_w	= length of wall pier
l_{wc}	= length at each end of a wall pier where concrete confinement is provided
l_{wpu}	= unbonded length of wall pier post-tensioning bar
L	= unfactored design live loads
L_c	= arm for N_{twb} - N_{cwb} axial force couple between tension-side and compression-side wall pier centroids

L_{eq}	= earthquake excitation factor ($\{\phi_1\}^T[M]\{1\}$)
m_{eff}	= effective first mode mass for coupled wall ($m_{eff}=M_{eff}/n_w$)
$m_{eff,2}$	= effective second mode mass for coupled wall
m_w	= seismic mass for coupled wall
M	= seismic mass for entire building
$[M]$	= lumped diagonal mass matrix for structure
M_a	= bending moment in angle leg
M_{ap}	= plastic moment in angle vertical leg (leg perpendicular to coupling beam) considering shear-flexure interaction
M_{a0}	= plastic moment in angle vertical leg (leg perpendicular to coupling beam) without considering shear-flexure interaction
M_b	= coupling beam end moment
$M_{b,bfy}$	= value of M_b at coupling beam flange yielding state
$M_{b,dec}$	= value of M_b at coupling beam decompression state
M_{bp}	= plastic moment of coupling beam cross section
$M_{b,pty}$	= value of M_b at coupling beam PT-yielding state
$M_{b,sof}$	= value of M_b at coupling beam softening state
M_{by}	= yield moment of coupling beam cross section
M_{cw}	= compression-side wall pier base moment
M_{cws}	= value of M_{cw} at coupled wall softening state
M_{cwu}	= value of M_{cw} at coupled wall ultimate state
M_{cwy}	= value of M_{cw} at coupled wall PT-yielding state
M_{eff}	= effective first mode mass for entire building ($M_{eff}=L_{eq}^2/M_{eq}$)

$M_{\text{eff},2}$	= effective second mode mass for entire building
M_{eq}	= generalized mass for first (fundamental) mode of vibration ($\{\phi_1\}^T [M] \{\phi_1\}$)
M_{tw}	= tension-side wall pier base moment
$M_{\text{tw}s}$	= value of M_{tw} at coupled wall softening state
$M_{\text{tw}u}$	= value of M_{tw} at coupled wall ultimate state
$M_{\text{tw}y}$	= value of M_{tw} at coupled wall PT-yielding state
M_w	= total coupled wall base moment
M_{wb}	= contribution of coupling beam shear forces to M_w
M_{wbs}	= contribution of coupling beam shear forces to M_w at coupled wall softening state
M_{ws}	= value of M_w at coupled wall softening state
M_{wu}	= value of M_w at coupled wall ultimate state
$M_{w,\text{unc}}$	= base moment of uncoupled wall (one wall pier)
M_{wy}	= value of M_w at coupled wall PT-yielding state
M_x	= portion of M assigned to floor/roof level x
MIV	= maximum incremental velocity of ground motion record
n	= number of vibration modes
n_{ab}	= number of angle-to-beam or angle-to-column/wall pier connectors
n_{abb}	= number of angle-to-beam connectors
n_{abw}	= number of angle-to-column/wall pier connectors
n_b	= number of coupling beams over wall height
n_{bp}	= number of strands per coupling beam post-tensioning tendon
n_{bt}	= number of coupling beam post-tensioning tendons

n_w	= number of coupled walls in a building
n_{wp}	= number of post-tensioning bars in wall pier
N_{ap}	= axial force in angle vertical leg (leg perpendicular to coupling beam) acting with M_{ap} and V_{ap}
N_b	= axial force in coupling beam at midspan
N_{bi}	= initial axial force in coupling beam before application of lateral loads
N_{cw}	= axial force in compression-side wall pier at base
N_{cwb}	= component of N_{cw} due to coupling beam shear forces
N_{cwg}	= component of N_{cw} due to gravity loads
N_{cwp}	= component of N_{cw} due to wall pier post-tensioning force
N_{cws}	= value of N_{cw} at coupled wall softening state
N_{cwu}	= value of N_{cw} at coupled wall ultimate state
N_{cwy}	= value of N_{cw} at coupled wall PT-yielding state
N_{tw}	= axial force in tension-side wall pier at base
N_{twb}	= component of N_{tw} due to coupling beam shear forces
N_{twg}	= component of N_{tw} due to gravity loads
N_{twp}	= component of N_{tw} due to wall pier post-tensioning force
N_{tws}	= value of N_{tw} at coupled wall softening state
N_{twu}	= value of N_{tw} at coupled wall ultimate state
N_{twy}	= value of N_{tw} at coupled wall PT-yielding state
P_b	= total force in coupling beam post-tensioning tendons
P_{bi}	= total initial force in coupling beam post-tensioning tendons before application of lateral loads

P_{bj}	= total force in coupling beam PT elements before losses
P_{bm}	= maximum total force in coupling beam post-tensioning tendons
$P_{b,pty}$	= value of P_b at coupling beam PT-yielding state
P_{bu}	= total maximum strength of coupling beam post-tensioning tendons
P_{by}	= total yield strength of coupling beam post-tensioning tendons
P_{cw}	= total force in compression-side wall pier post-tensioning bars
P_{cwi}	= total initial force in compression-side wall pier post-tensioning bars before application of lateral loads
P_{cws}	= value of P_{cw} at coupled wall softening state
P_{cwy}	= value of P_{cw} at coupled wall softening state at coupled wall PT-yielding state
P_{tw}	= total force in tension-side wall pier post-tensioning bars
P_{twi}	= total initial force in tension-side wall pier post-tensioning bars before application of lateral loads
P_{tws}	= value of P_{tw} at coupled wall softening state
P_{twy}	= value of P_{tw} at coupled wall PT-yielding state
P_{wi}	= total initial force in wall pier post-tensioning bars
P_{wu}	= maximum post-tensioning tendon force based on design maximum strength of post-tensioning steel ($P_{wu} = \sum a_{wp} f_{wpu}$)
PGA	= peak ground acceleration
PGA _d	= design-level peak ground acceleration
PGA _s	= survival-level peak ground acceleration
Q_{bd}	= design coupling beam shear force demand
$Q_{bd,a}$	= portion of Q_{bd} resisted by top and seat angles
$Q_{bd,p}$	= portion of Q_{bd} resisted by coupling beam post-tensioning force

$Q_{b,max}$	= maximum coupling beam shear force demand
Q_{dd}	= design-level base shear force demand for entire building
Q_{ds}	= survival-level base shear force demand for entire building
Q_E	= effect of horizontal seismic loads
$Q_{h,max}$	= higher mode component of $Q_{w,max}$
Q_{sd}	= design base shear force demand for entire building
Q_{wd}	= coupled wall design base shear force demand
$Q_{w,dt}$	= wall pier diagonal tension shear force demand
$Q_{w,max}$	= coupled wall maximum base shear force demand including higher mode effects
$Q_{l,max}$	= first mode component of $Q_{w,max}$
$\{R\}$	= vector of rigid body displacements of structure in horizontal direction
R_d	= strength ratio based on first “significant” yield of structure
R_n	= nominal weld metal design strength
R_{μ}	= strength ratio based on “global” yield of structure
$R_{\mu d}$	= design-level strength ratio
$R_{\mu s}$	= survival-level strength ratio
s_{bsp}	= pitch for spiral reinforcement in wall pier contact region adjacent to coupling beam
s_l	= distance (perpendicular to strong direction) of lateral load resisting system shear center from center of story stiffness (CS)
s_w	= distance (perpendicular to strong direction) of coupled wall shear center from center of story stiffness (CS)
s_{wsp}	= pitch for spiral reinforcement at wall pier base

S	= compression-tension steel fiber
S_a	= site-adjusted spectral response acceleration
S_{ad}	= site-adjusted design-level spectral response acceleration
S_{as}	= site-adjusted survival-level spectral response acceleration
S_{DS}	= site-adjusted design-level spectral response acceleration at short periods
S_{D1}	= site-adjusted design-level spectral response acceleration at 1 sec. period
S_{MS}	= site-adjusted survival-level spectral response acceleration at short periods
S_{M1}	= site-adjusted survival-level spectral response acceleration at 1 sec. period
S_s	= mapped spectral response acceleration at short periods
S_1	= mapped spectral response acceleration at 1 sec. period
SC	= compression-only steel fiber
t	= time
t_a	= thickness of angle leg
t_{bc}	= thickness of coupling beam flange plus cover plate
t_{bf}	= thickness of coupling beam flange
t_{bw}	= thickness of coupling beam web
t_c	= thickness of coupling beam flange cover plate
t_e	= thickness of wall pier embedded steel plate
t_f	= thickness of concrete fiber
t_{sh}	= thickness of shim plate at coupling beam-to-wall pier interface
t_w	= thickness of wall pier
t_{wc}	= confined thickness of wall pier enclosed by centerline of confinement reinforcement

T	= period
T_a	= tension force in angle
$T_{a,pty}$	= value of T_a at coupling beam PT-yielding state
T_{ax}	= tension force in angle for loading parallel to coupling beam
T_{ayx}	= tension yield force of angle for loading parallel to coupling beam
T_{ayy}	= yield force of angle for loading perpendicular to coupling beam
T_{eq}	= period of equivalent single-degree-of-freedom system
T_m	= period for m^{th} mode
T_n	= period for n^{th} mode
T_s	= S_{M1}/S_{MS}
T_0	= $0.2S_{M1}/S_{MS}$
T_1	= first (fundamental) vibration mode period
u	= lateral displacement of structure at roof level
u_{ad}	= design-level deformation demand for tension angle
u_{as}	= survival-level deformation demand for tension angle
u_b	= vertical displacement of loading block relative to reaction block
u_{be}	= yield displacement of BE component of equivalent nonlinear single-degree-of-freedom BP hysteresis model
u_{bp}	= yield displacement of equivalent nonlinear single-degree-of-freedom BP hysteresis model
$u_{b,pty}$	= elongation of beam post-tensioning tendons at coupling beam PT-yielding state
u_c	= amplitude of roof displacement during loading cycle

u_{des}	= lateral displacement of structure at first “significant” yield
u_{elas}	= linear elastic lateral displacement corresponding to F_{elas}
u_{ep}	= yield displacement of EP component of equivalent nonlinear single-degree-of-freedom BP hysteresis model
u_{eq}	= displacement of equivalent single-degree-of-freedom system
\dot{u}_{eq}	= velocity of equivalent single-degree-of-freedom system
\ddot{u}_{eq}	= acceleration of equivalent single-degree-of-freedom system
$u_{eq,be}$	= yield displacement of BE component of equivalent nonlinear single-degree-of-freedom BP hysteresis model
$u_{eq,bp}$	= yield displacement of equivalent nonlinear single-degree-of-freedom BP hysteresis model
$u_{eq,ep}$	= yield displacement of EP component of equivalent nonlinear single-degree-of-freedom BP hysteresis model
\ddot{u}_g	= horizontal ground acceleration
u_{nlin}	= peak (maximum/minimum) lateral displacement
u_{wpy}	= elongation of extreme wall pier post-tensioning bar at coupled wall PT-yielding state
u_y	= lateral displacement of structure at “global” yield
u_1	= first vibration mode component of roof lateral displacement
$\{U\}$	= relative lateral displacement vector of structure
$\{\dot{U}\}$	= relative lateral velocity vector of structure
$\{\ddot{U}\}$	= relative lateral acceleration vector of structure
V	= force
V_{ap}	= plastic shear force in angle vertical leg (leg perpendicular to coupling beam) considering shear-flexure interaction

$V_{a,ss}$	= contribution of top and seat angles to $V_{b,ss}$
V_{a0}	= plastic shear force in angle vertical leg (leg perpendicular to coupling beam) without considering shear-flexure interaction
V_b	= shear force in coupling beam
$V_{ba,sof}$	= contribution of top and seat angles to $V_{b,sof}$
$V_{bp,sof}$	= contribution of coupling beam post-tensioning force to $V_{b,sof}$
$V_{b,pty}$	= value of V_b at coupling beam PT-yielding state
$V_{b,ss}$	= shear slip capacity of coupling beam at beam-to-wall pier interface
$V_{b,sof}$	= value of V_b at coupling beam softening state
$V_{b,ws}$	= value of V_b at coupled wall softening state
$V_{b,wu}$	= value of V_b at coupled wall ultimate state
$V_{b,wy}$	= value of V_b at coupled wall PT-yielding state
$V_{p,ss}$	= contribution of coupling beam axial force to $V_{b,ss}$
w_{ab}	= width of angle connector head/nut measured across flat sides
w_{abw}	= width of angle-to-column/wall pier connector head/nut measured across flat sides
w_w	= seismic weight for coupled wall
W	= total seismic weight for entire building
$\{Y\}$	= vector of modal amplitudes
Y_i	= amplitude of i^{th} vibration mode shape
Y_1	= amplitude of first vibration mode shape
z_a	= arm for angle force T_a+C_a couple
z_{cb}	= arm for coupling beam compression force C_b couple

α	= post-yield stiffness ratio of equivalent nonlinear single-degree-of-freedom BP hysteresis model
α_a	= post-yield stiffness ratio for angle in tension
α_{bg}	= shear coefficient for coupling beam initial stiffness
α_{cw}	= confined concrete stress-block parameter for compression-side wall pier at base
α_d	= Rayleigh damping factor for mass proportional damping
α_{tw}	= confined concrete stress-block parameter for tension-side wall pier at base
α_{wg}	= shear coefficient for wall pier initial linear-elastic stiffness matrix
α_{wp}	= post-yield stiffness ratio for wall pier post-tensioning bars
β_{ar}	= angle strength ratio
β_{cw}	= confined concrete stress-block parameter for compression-side wall pier at base
β_d	= Rayleigh damping factor for stiffness proportional damping
β_r	= equivalent nonlinear single-degree-of-freedom BP hysteresis model strength ratio
β_s	= equivalent nonlinear single-degree-of-freedom BP hysteresis model stiffness ratio
β_{tw}	= confined concrete stress-block parameter for tension-side wall pier at base
Γ	= participation factor (L_{eq}/M_{eq})
$\delta_{a,pty}$	= value of δ_{ax} at coupling beam PT-yielding state
δ_{ax}	= deformation in tension angle parallel to coupling beam (horizontal displacement of angle heel from column/wall pier)
δ_{ay}	= deformation in tension angle perpendicular to coupling beam
δ_{ayx}	= value of δ_{ax} at yield of angle

δ_{ayy}	= value of δ_{ay} at yield of angle
Δ	= roof drift (roof lateral displacement divided by structure height)
Δ_{ins}	= inter-story drift of coupled wall
Δ_{isd}	= design-level inter-story drift demand of coupled wall
Δ_{iss}	= survival-level inter-story drift of coupled wall
Δ_d	= design-level roof drift demand of coupled wall
Δ_s	= survival-level roof drift demand of coupled wall
Δ_t	= target allowable roof drift demand of coupled wall
Δ_{td}	= design-level target allowable roof drift demand of coupled wall
Δ_{ts}	= survival-level target allowable roof drift demand of coupled wall
Δ_{ws}	= roof drift of coupled wall at coupled wall softening state
Δ_{wu}	= roof drift of coupled wall at coupled wall ultimate state
Δ_{wue}	= linear-elastic component of Δ_{wu}
Δ_{wug}	= component of Δ_{wu} due to gap opening at compression-side wall pier base
$\Delta_{w,unc}$	= roof drift of uncoupled wall (one wall pier)
Δ_{wup}	= component of Δ_{wu} due to plastic hinge rotation at compression-side wall pier base
Δ_{wy}	= roof drift of coupled wall at coupled wall PT-yielding state
ϵ_{am}	= strain of angle steel at f_{am}
ϵ_{au}	= strain of angle steel at f_{au}
ϵ_{ay}	= yield strain of angle steel
ϵ_{be}	= extreme strain of steel at coupling beam end
ϵ_{bm}	= strain of coupling beam steel at f_{bm}

ϵ_{bpu}	= strain of coupling beam post-tensioning strand at f_{bpu}
ϵ_{bpy}	= yield (limit of proportionality) strain of coupling beam post-tensioning strand
ϵ_{bu}	= strain of coupling beam steel at f_{bu}
ϵ_{by}	= yield strain of coupling beam steel
ϵ'_c	= strain of unconfined concrete at f'_c
ϵ_{cc}	= strain of confined concrete at f_{cc}
ϵ_{cce}	= extreme compression strain of confined concrete at compression-side wall pier base
ϵ_{ccu}	= ultimate (crushing) strain of confined concrete
ϵ_{ce}	= extreme compression strain of confined concrete at wall pier base
ϵ_{cu}	= ultimate (crushing) strain of unconfined concrete
ϵ_{cws}	= strain in extreme flexural reinforcement of compression-side wall pier at coupled wall softening state
ϵ_{rm}	= strain of coupling beam flange cover plate steel at f_{rm}
ϵ_{ru}	= strain of coupling beam flange cover plate steel at f_{ru}
ϵ_{ry}	= yield strain of coupling beam flange cover plate steel
ϵ_{sm}	= strain of steel at f_{sm}
ϵ_{spm}	= strain of spiral steel at f_{spm}
ϵ_{spu}	= strain of spiral steel at f_{spu}
ϵ_{spy}	= yield strain of spiral steel
ϵ_{sy}	= yield strain of steel
ϵ_{tce}	= extreme compression strain of confined concrete at tension-side wall pier base
ϵ_{wps}	= strain in wall pier post-tensioning bar under survival-level earthquake

ϵ_{wpi}	= initial strain in wall pier post-tensioning bar before application of lateral loads
ϵ_{wp1}	= strain in wall pier post-tensioning bar layer 1
ϵ_{wp2}	= strain in wall pier post-tensioning bar layer 2
ϵ_{wp3}	= strain in wall pier post-tensioning bar layer 3
ϵ_{wp4}	= strain in wall pier post-tensioning bar layer 4
ϵ_{wp5}	= strain in wall pier post-tensioning bar layer 5
ϵ_{wp6}	= strain in wall pier post-tensioning bar layer 6
ϵ_{wp7}	= strain in wall pier post-tensioning bar layer 7
ϵ_{wp8}	= strain in wall pier post-tensioning bar layer 8
ϵ_{wpu}	= strain of wall pier post-tensioning bar at f_{wpu}
ϵ_{wpy}	= yield (limit of proportionality) strain of wall pier post-tensioning bar
ϵ_{wse}	= extreme tension strain of compression-side wall pier flexural reinforcement at base
ϵ_{wsm}	= strain of wall pier mild steel reinforcement at f_{wsm}
ϵ_{wsy}	= yield strain of wall pier mild steel reinforcement
θ_b	= coupling beam chord rotation (i.e., transverse displacement between tangents at beam ends divided by beam length)
$\theta_{b,bfy}$	= value of θ_b at coupling beam flange yielding state
$\theta_{b,dec}$	= value of θ_b at coupling beam decompression state
$\theta_{be,pty}$	= linear-elastic component of $\theta_{b,pty}$
$\theta_{bg,pty}$	= component of $\theta_{b,pty}$ due to gap opening at coupling beam-to-wall pier interface
$\theta_{b,pty}$	= value of θ_b at coupling beam PT-yielding state
$\theta_{b,sof}$	= value of θ_b at coupling beam softening state

$\theta_{b,wu}$	= value of θ_b at coupled wall ultimate state
$\theta_{b,wy}$	= value of θ_b at coupled wall PT-yielding state
θ_d	= design-level coupling beam chord rotation demand
θ_s	= survival-level coupling beam chord rotation demand
κ	= plastic hinge rotation in angle vertical leg (leg perpendicular to coupling beam)
μ	= peak lateral displacement ductility
μ_{aw}	= coefficient of friction between angle vertical leg and wall pier
μ_{bw}	= coefficient of friction between coupling beam and wall pier
μ_t	= allowable target peak lateral displacement ductility
μ_{td}	= design-level allowable target peak lateral displacement ductility
μ_{ts}	= survival-level allowable target peak lateral displacement ductility
μ_{wf}	= coefficient of friction between wall pier base and foundation
v	= factor for distribution of story shear force in building plan
v'	= value of v due to story translations
v''	= value of v due to applied and accidental torsion effects
ν_b	= Poisson ratio for coupling beam steel
ν_c	= Poisson ratio for wall pier concrete
ξ	= viscous damping ratio
ξ_{eq}	= viscous damping ratio of equivalent single-degree-of-freedom system
ξ_m	= assumed viscous damping ratio for m^{th} mode
ξ_n	= assumed viscous damping ratio for n^{th} mode
ξ_0	= viscous damping ratio for acceleration response spectra used in design

ξ_1	= viscous damping ratio for first (fundamental) vibration mode
ξ_3	= viscous damping ratio for third vibration mode
ρ	= reliability factor based on system redundancy (ICC 2000)
ρ_{bsp}	= spiral reinforcement ratio in wall pier contact region adjacent to coupling beam
ρ_{wp}	= post-tensioning steel reinforcement ratio at wall pier base
ρ_{ws}	= flexural mild steel reinforcement ratio at wall pier base
ρ_{wsp}	= spiral reinforcement ratio at wall pier base
σ_{wc}	= nominal concrete compression stress in wall pier contact region adjacent to coupling beam
ϕ_{cwu}	= curvature of compression-side wall pier base at coupled wall ultimate state
$\{\phi_i\}$	= i th linear-elastic vibration mode-shape
$\{\phi_1\}$	= first (fundamental) linear-elastic vibration mode shape
ϕ_{1x}	= coordinate of $\{\phi_1\}$ at floor/roof level x
ϕ_w	= a resistance factor for fillet weld design
$[\Phi]$	= matrix containing linear-elastic vibration mode shapes
ω_{eq}	= frequency of equivalent single-degree-of-freedom system
ω_1	= first (fundamental) mode frequency

ACKNOWLEDDGMENTS

This investigation was funded by the National Science Foundation (NSF) under Grant No. CMS 98-10067 as a part of the United States-Japan Cooperative Earthquake Research Program on Composite and Hybrid Structures. The support of the NSF Program Director Dr. S. C. Liu and Program Coordinator Dr. S. Goel is gratefully acknowledged.

The author also thanks several individuals for their assistance in the conduct of this work: Keli Engvall, Michael May, Brad Weldon, Julio Escada, and Brent A. Bach.

The opinions, findings, and conclusions expressed in this dissertation are those of the author and do not necessarily reflect the views of the NSF or of the individuals and organizations acknowledged above.

The author gratefully acknowledges the support and advice, and the motivation and encouragement provided by his dissertation advisor, Dr. Yahya C. Kurama. The author thanks his advisor for his invaluable contribution to his personal, academic, and professional growth.

The author thanks his Ph.D. committee members Dr. Kent A. Harries, Dr. Tracy L. Kijewski-Correa, and Dr. David J. Kirkner for providing guidance in his studies.

CHAPTER 1

INTRODUCTION

This chapter provides an introduction for the dissertation as follows: (1) problem statement; (2) proposed hybrid coupled wall system; (3) research objectives; (4) research scope; (5) summary of approach; (6) research significance; and (7) organization of dissertation.

1.1 Problem Statement

Previous earthquakes have shown that reinforced concrete structural walls are one of the most effective primary lateral load resisting systems for seismic regions. The lateral stiffness and strength of these systems can be significantly increased by coupling two or more walls together. Coupling of the walls can be achieved by using reinforced concrete or steel beams at the floor and roof levels. The research described in this dissertation is on “hybrid” systems that use steel beams to couple reinforced concrete walls.

In “conventional” hybrid coupled wall systems, coupling of the walls is achieved by embedding the coupling beams into the walls. As an example, Fig. 1.1 shows a typical eight-story coupled wall system and Fig. 1.2a shows a floor-level hybrid coupled wall subassembly that consists of two concrete wall regions and a steel coupling beam embedded into the walls (indicated by the shaded area in Fig. 1.1). Fig. 1.2b shows an

idealized exaggerated deformed configuration of the subassembly under lateral forces acting on the walls from left to right. The desired behavior of this system can be achieved if the coupling beams “yield” before the walls, behave in a ductile manner, and dissipate energy. This requires that the coupling beams are designed and detailed to develop and sustain their full moment (or shear) capacity under large cyclic deformations.

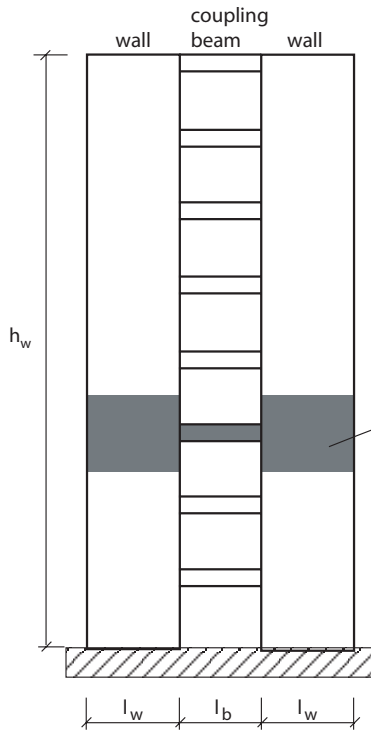


Fig. 1.1 Eight story coupled wall structure

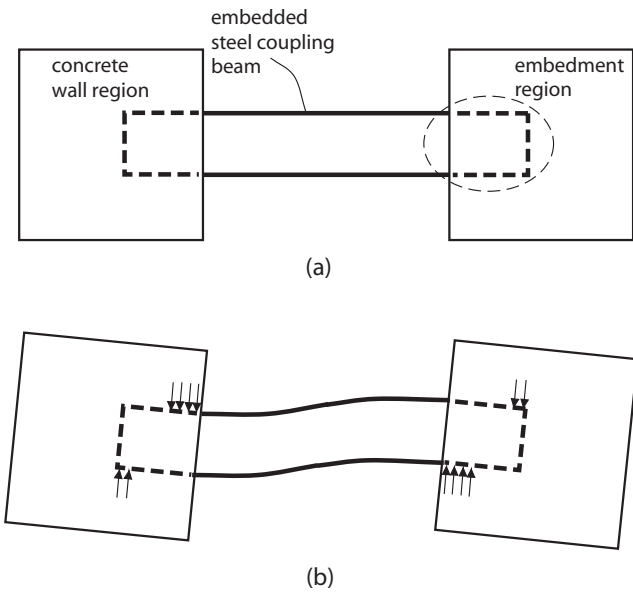


Fig. 1.2 Hybrid coupled wall subassembly with embedded beam: (a) undeformed configuration; (b) deformed configuration

Hybrid coupled wall systems with embedded steel beams have been investigated as part of the National Science Foundation *U.S.-Japan Cooperative Earthquake Research Program on Composite and Hybrid Structures* and other research programs (Harries 1992, 1995, 2001; Harries et al. 1992, 1993, 1994, 1997, 2000; Shahrooz et al. 1992, 1993a, 1993b, 2003; Gong and Shahrooz 1997, 1998, 2001a, 2001b; Gong et al. 1997; Shahrooz

and Gong 1998). Properly-designed and detailed embedded steel coupling beam systems possess large ductility and energy dissipation capacities; however, they are prone to significant damage during lateral displacements in the form of flexural and/or shear yielding in the beams, and spalling and cracking in the wall concrete in the embedment regions (Harries et al. 1997). Furthermore, the selection of the beam shape and dimensions is affected by the wall reinforcement in the embedment regions, often requiring fabricated sections for the beams instead of readily available rolled sections.

In comparison with the system in Fig. 1.2, the coupling beams investigated in this dissertation are not embedded into the walls. Instead, coupling is achieved by post-tensioning the beams and the walls together at the floor and roof levels. Compared with current industry practice and research, the use of post-tensioning to couple structural wall systems is a significant innovation and has the following primary advantages:

(1) The design and detailing requirements for the beams and the wall coupling regions are expected to be simpler than the requirements for conventional systems.

(2) The coupling beams and the wall coupling regions can be designed to remain essentially “damage-free” during a severe ground motion, with most of the damage occurring in certain selected components of the beam-to-wall connections that can be replaced after the earthquake.

(3) The post-tensioning force provides a self-centering capability to the structure (i.e., ability of the structure to return towards the original undisplaced position upon unloading from a large nonlinear lateral displacement).

This dissertation provides a comprehensive study on the seismic behavior and design of this new system.

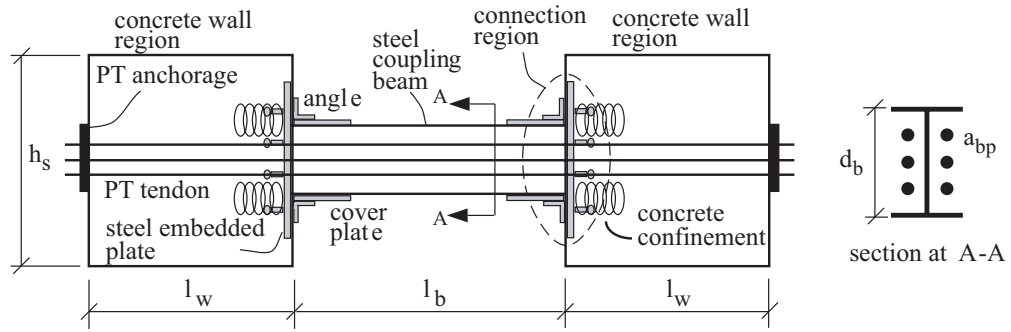
1.2 Proposed Hybrid Coupled Wall System

As an example, Fig. 1.3a shows a subassembly of the proposed hybrid coupled wall system at a floor level. The subassembly consists of a steel coupling beam and two concrete wall regions (as indicated by the shaded area in Fig. 1.1) coupled using post-tensioning. The post-tensioning force is provided by multi-strand high strength tendons that are not in contact with the beam along the span. Inside the walls, the bond between the post-tensioning steel and the concrete is prevented by placing the tendons inside ducts that are not grouted. This type of construction, where the post-tensioning steel is anchored to the coupled wall system only at two locations at the outer ends of the walls, is called “unbonded” post-tensioning. The advantages of using unbonded post-tensioning as compared with bonded post-tensioning are described later.

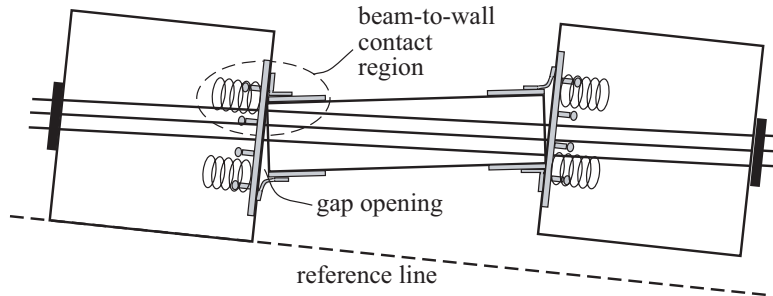
The beam-to-wall connection regions include top and seat angles connected to the beam flanges and to steel plates embedded inside the walls (with welded headed studs) as shown in Fig. 1.3a. Fig. 1.3b shows the expected exaggerated deformed shape of the subassembly under lateral loads acting on the walls from left to right. The nonlinear deformations of the beam occur primarily as a result of gap opening at the beam-to-wall interfaces. Friction develops at the beam-to-wall interfaces due to the post-tensioning force to resist the coupling shear force in the vertical direction.

In a properly-designed subassembly, the desired behavior is yielding of the top and seat angles due to the opening of the gaps, with little yielding and damage in the beam and walls. The purpose of the angles is to provide redundancy and energy

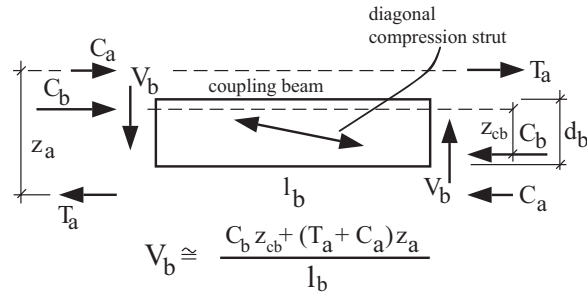
dissipation during an earthquake. The angles also provide a part of the coupling resistance of the subassembly, prevent sliding of the beam at the beam-to-wall interfaces (together with friction resistance against sliding as induced by post-tensioning), and can serve as temporary beam supports during construction. The yielded angles can be replaced after the earthquake.



(a)



(b)



(c)

Fig. 1.3 Proposed coupled wall system: (a) subassembly at a floor level; (b) deformed configuration; (c) coupling forces

As the subassembly deforms, gap opening results in large concentrated compressive stresses in the contact regions near the beam-to-wall interfaces (Fig. 1.3b). Steel cover plates welded to the flanges may be used at the beam ends to stabilize and strengthen the flanges, and prevent or delay the yielding of the flanges in compression. The embedded plates inside the walls distribute the compressive stresses to the concrete. In addition, confinement reinforcement is used behind the embedded plates to transfer and distribute the compressive stresses without excessive deformations in the concrete.

Fig. 1.3c shows the coupling forces that develop from the formation of a diagonal compression strut in the beam upon lateral displacement of the walls, where V_b is the coupling shear force in the beam. The amount of coupling between the walls can be controlled by controlling the total beam post-tensioning force P_b (which controls the total compression force in the beam, C_b), the tension and compression angle forces T_a and C_a , the beam depth d_b , and the beam length l_b .

As a result of post-tensioning, the initial lateral stiffness of the coupled wall subassembly in Fig. 1.3a before the initiation of gap opening is similar to the initial stiffness of a comparable system with embedded steel coupling beams. Gap opening results in a reduction in the lateral stiffness of the subassembly, allowing the system to soften and undergo large nonlinear rotations without significant damage (except for the damage in the angles). The post-tensioning force controls the depth and width of the gaps. As the walls displace laterally, the tensile forces in the post-tensioning tendons increase, resulting in an increase in the compression axial force in the coupling beam. Upon unloading, the post-tensioning tendons provide a restoring force that tends to close the

gaps, thus pulling the beam and the walls back towards their undisplaced position with little or no residual displacement (i.e., self-centering capability).

Unbonding of the post-tensioning tendons has two important advantages: (1) it results in a uniform strain distribution in the tendons between the anchors, and thus, significantly delays the nonlinear straining (i.e., yielding) of the steel (yielding of the post-tensioning steel is not desirable since it results in a loss of prestress under cyclic loading); and (2) it significantly reduces the tensile stresses transferred to the wall concrete, thus reducing damage due to concrete cracking.

1.3 Research Objectives

The broad objective of the research described in this dissertation is to investigate the seismic behavior and design of hybrid coupled wall structures that use unbonded post-tensioning. The research has three specific objectives:

(1) To develop and verify analytical models for the nonlinear behavior of unbonded post-tensioned hybrid coupled wall structures under seismic loading.

(2) To conduct parametric evaluations on the seismic behavior of prototype coupled wall systems.

(3) To develop seismic design procedures, tools, and application guidelines for these structures.

1.4 Research Scope

The research described in this dissertation investigates the seismic behavior and design of reinforced concrete walls coupled using unbonded post-tensioned steel beams.

The investigation is limited to the coupling of two identical walls that are sufficiently slender such that their nonlinear behavior under lateral loads is governed by axial and flexural effects rather than by shear effects. Coupling of more than two walls is not investigated. Note that the research focuses on rectangular cross-sections for the walls and I-shaped cross sections for the coupling beams; however, it may be possible to extend the findings to other types of cross-sections, such as flanged walls and hollow beams.

In order to achieve the research objectives described above, a two-dimensional (in the plane of the walls) analytical model for unbonded post-tensioned hybrid coupled wall structures is developed using the DRAIN-2DX program (Prakash et al. 1993). It is assumed that the earthquake-induced forces at the floor and roof levels of the building are transferred to the primary lateral load resisting structure through rigid diaphragms. Interactions between the coupled wall systems and the rest of the building (i.e., the floor system/diaphragm, columns, foundation-soil system) are not included in the analytical model. The DRAIN-2DX model is verified by comparing the analytical results with results obtained using the ABAQUS program (Hibbitt et al. 1998) as well as with results obtained from experiments of floor-level unbonded post-tensioned hybrid coupled wall subassemblages and experiments of uncoupled walls.

The analytical models are used to conduct parametric nonlinear static push-over analyses and nonlinear cyclic lateral load analyses of isolated unbonded post-tensioned hybrid coupled wall subassemblages and multi-story coupled wall structures. The following parameters are considered in the analyses: (1) amount of post-tensioning; (2) location of the post-tensioning steel; (3) length of the coupling beams; (4) cross-sectional

properties of the coupling beams; (5) properties of the beam-to-wall connection angles; (6) cross-sectional properties of the walls; (7) precast concrete walls versus monolithic cast-in-place reinforced concrete walls; and (8) coupling degree of coupled wall system.

The results from the parametric investigations are used to develop simplified closed-form procedures and tools that can be used in the seismic design and nonlinear response evaluation of unbonded post-tensioned hybrid coupled wall structures. A performance-based seismic design approach is proposed with the primary objective of limiting the peak lateral displacements of the structure during a design level and/or survival level earthquake to below selected values of allowable target displacement.

Two eight-story prototype unbonded post-tensioned hybrid coupled wall structures are designed using the proposed seismic design approach as follows: (1) a structure with monolithic cast-in-place reinforced concrete walls; and (2) a structure with precast concrete walls. Both structures are designed for a region with high seismicity (Los Angeles) and a site with a “medium” soil profile [Site Class D in IBC 2000 (ICC 2000)]. The seismic behavior of the structures is assessed and the proposed design approach is critically evaluated based on nonlinear static and nonlinear dynamic time-history analyses. Ductility demands on the coupling beams and on the walls are established. The seismic behavior of the prototype structures is compared with the behavior of conventional hybrid coupled wall structures that use embedded steel beams.

1.5 Summary of Approach

The research described in this dissertation consists of the following eight tasks:

(1) Conduct a literature survey of previous analytical and experimental research on the seismic behavior and design of coupled wall structures, as well as structures with unbonded post-tensioning.

(2) Develop and verify analytical models that describe the nonlinear hysteretic behavior of hybrid coupled wall structures with unbonded post-tensioned steel beams and structures with embedded steel beams.

(3) Using the analytical models, conduct parametric investigations on the behavior of unbonded post-tensioned hybrid coupled wall subassemblages as well as multi-story coupled wall systems under lateral loads.

(4) Using the results from the parametric investigations, develop simplified closed-form procedures to estimate the nonlinear behavior of unbonded post-tensioned hybrid coupled wall structures under lateral loads.

(5) Develop a performance-based approach for the seismic design of unbonded post-tensioned hybrid coupled wall structures.

(6) Use the design approach developed in Task (5) to design prototype building structures that use unbonded post-tensioned hybrid coupled walls as the primary lateral load resisting system.

(7) Select a set of ground motion records representative of the seismic regions and site soil characteristics used in the design of the prototype structures.

(8) Evaluate the seismic response of the prototype coupled walls, including comparisons with walls that use embedded steel beams, based on nonlinear static and

nonlinear dynamic time-history analyses using the analytical models developed in Task (2) and the ground motions selected in Task (7).

These research tasks are described fully in the following chapters of the dissertation. Each task addresses one or more of the project objectives outlined above. Tasks (1), (2), and (4) are needed to achieve Objective (1). Tasks (3), (7), and (8) achieve Objective (2). Finally, Tasks (1), (4) (5), (6), (7), and (8) are used to achieve Objective (3).

1.6 Research Significance

Compared with current industry practice and current research, the use of unbonded post-tensioning to couple structural walls is a significant innovation. The research results described in this dissertation are needed to demonstrate that unbonded post-tensioned steel beams can provide significant and stable levels of coupling between concrete walls over large nonlinear cyclic deformations and to develop seismic building design recommendations for this new type of hybrid structural system.

It may also be possible to use the proposed system to couple existing walls as part of a seismic retrofit and strengthening scheme. The post-tensioning tendons can be placed outside the walls for this purpose. The use of post-tensioning allows the designer to control the amount of coupling between the walls as shown in Fig. 1.3c. This may be particularly important for the strengthening of existing walls since additional axial forces (both tension and compression) develop in the walls as a result of coupling. Thus, the amount of coupling may be limited by the existing design details of the foundations and the walls near the base.

This research, which was conducted as a part of the *U.S.-Japan Cooperative Earthquake Research Program on Composite and Hybrid Structures* funded by the National Science Foundation, is essential and fundamental to the study of the seismic behavior and design of unbonded post-tensioned hybrid coupled wall systems. Results from the research can be used as the foundation on which future experimental research on multi-story structures can be built and codified building design specifications can be formulated.

1.7 Organization of Dissertation

The remainder of this dissertation is organized into the following fifteen chapters (Chapters 2-16) in accordance with the research approach summarized above (Tasks 1-8).

Chapter 2 presents a literature survey of previous analytical and experimental research on the seismic behavior and design of coupled wall structures as well as structures with unbonded post-tensioning.

Chapter 3 describes analytical models to investigate the nonlinear behavior of floor-level hybrid coupled wall subassemblages.

Chapter 4 describes a parametric investigation on the nonlinear lateral load behavior of unbonded post-tensioned hybrid coupled wall subassemblages using the analytical models in *Chapter 3*.

Chapter 5 presents simplified closed-form procedures to estimate the nonlinear behavior of unbonded post-tensioned hybrid coupled wall subassemblages under lateral loads.

Chapter 6 describes analytical models for multi-story hybrid coupled wall structures based on the subassembly models in *Chapter 3*.

Chapter 7 describes a parametric investigation on the nonlinear lateral load behavior of multi-story unbonded post-tensioned hybrid coupled wall structures using the analytical models in *Chapter 6*.

Chapter 8 presents simplified closed-form procedures to estimate the nonlinear behavior of multi-story unbonded post-tensioned hybrid coupled wall structures under lateral loads.

Chapter 9 describes an experimental investigation on the nonlinear behavior of floor-level unbonded post-tensioned hybrid coupled wall subassemblages.

Chapter 10 compares the results from the experimental investigation in *Chapter 9* with estimations using the subassembly analytical models from *Chapter 3*, and recommends modifications to the analytical models based on these comparisons.

Chapter 11 proposes a performance-based approach for the seismic design of unbonded post-tensioned hybrid coupled wall structures.

Chapter 12 describes the design of prototype structures using the design approach proposed in *Chapter 11*.

Chapter 13 evaluates the behavior of the prototype structures under static lateral loading and provides comparisons with coupled wall structures that use embedded steel coupling beams.

Chapter 14 describes the selection and properties of a set of ground motion records representative of the seismic regions and site soil characteristics used in the design of the prototype structures.

Chapter 15 presents an evaluation of the seismic response of the prototype structures based on nonlinear dynamic time-history analyses, including comparisons with uncoupled wall structures.

Finally, *Chapter 16* presents a summary and conclusions from this dissertation, and discusses future research.

CHAPTER 2

LITERATURE REVIEW

This chapter provides an overview of previous research related to this dissertation as follows: (1) coupled wall structural systems; (2) concrete coupled wall structures; (3) hybrid structures with embedded steel coupling beams; (4) wall shear force demands in coupled wall structures; (5) unbonded post-tensioning in building construction; and (6) behavior of top and seat angles.

2.1 Coupled Wall Structural Systems

In concrete structural walls, a regular pattern of openings is often required to accommodate windows, doors, and/or mechanical penetrations. Efficient seismic structural systems particularly suited for ductile response with very good energy dissipation characteristics can be achieved when these openings are arranged in a rational pattern (Park and Paulay 1975; Paulay and Priestley 1992). Examples are shown in Fig. 2.1 where a number of walls are interconnected or coupled to each other by beams at the floor and roof levels. These systems are generally referred to as coupled structural walls with the implication that the connecting (i.e., coupling) beams, which may be relatively short and deep, are substantially weaker than the walls. The walls, which behave predominantly as cantilevers, can then impose sufficient rotations on the coupling beams

to make them yield. If suitably detailed, the beams can dissipate a significant amount of energy distributed over the entire height of the structure.

The behavior and mechanisms of lateral resistance of a single (i.e., uncoupled) wall and two coupled wall structures are compared in Fig. 2.2. The gravity loads acting on the walls are ignored for this example and it is assumed that a lateral force in the plane of the walls is applied at the top. The base moment resistance, $M_{w,unc}$ of the uncoupled wall (Fig. 2.2a) is developed in the traditional form by flexural stresses, while axial forces as well as moments are resisted in the coupled wall systems (Figs. 2.2b and 2.2c). When a coupled wall structure is pushed from left to right under lateral loads, tensile axial forces (N_{twb}) develop in the left wall and compressive axial forces ($N_{cwb}=N_{twb}$) develop in the right wall due to the coupling effect. The magnitude of these wall axial forces is equal to the sum of the shear forces of all the coupling beams at the upper floor and roof levels, and thus, depends on the stiffness and strength of those beams.

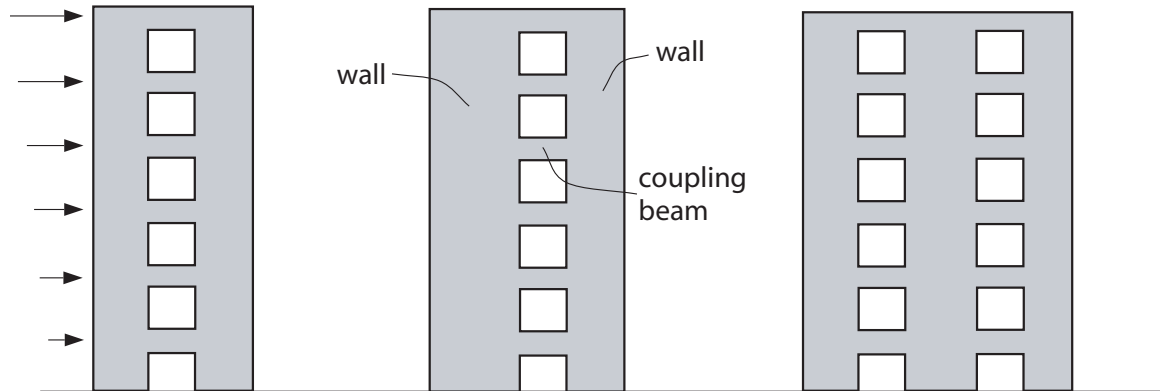


Fig. 2.1 Coupled structural walls

As a result of the axial forces that develop in the walls, the lateral stiffness and strength of a coupled wall system are significantly larger than the combined stiffness and strength of the individual constituent walls (i.e., wall piers) with no coupling. The total base moment, M_w of the coupled wall structures in Figs. 2.2b and 2.2c can be written as:

$$M_w = M_{tw} + M_{cw} + N_{cwb}L_c \quad (2.1)$$

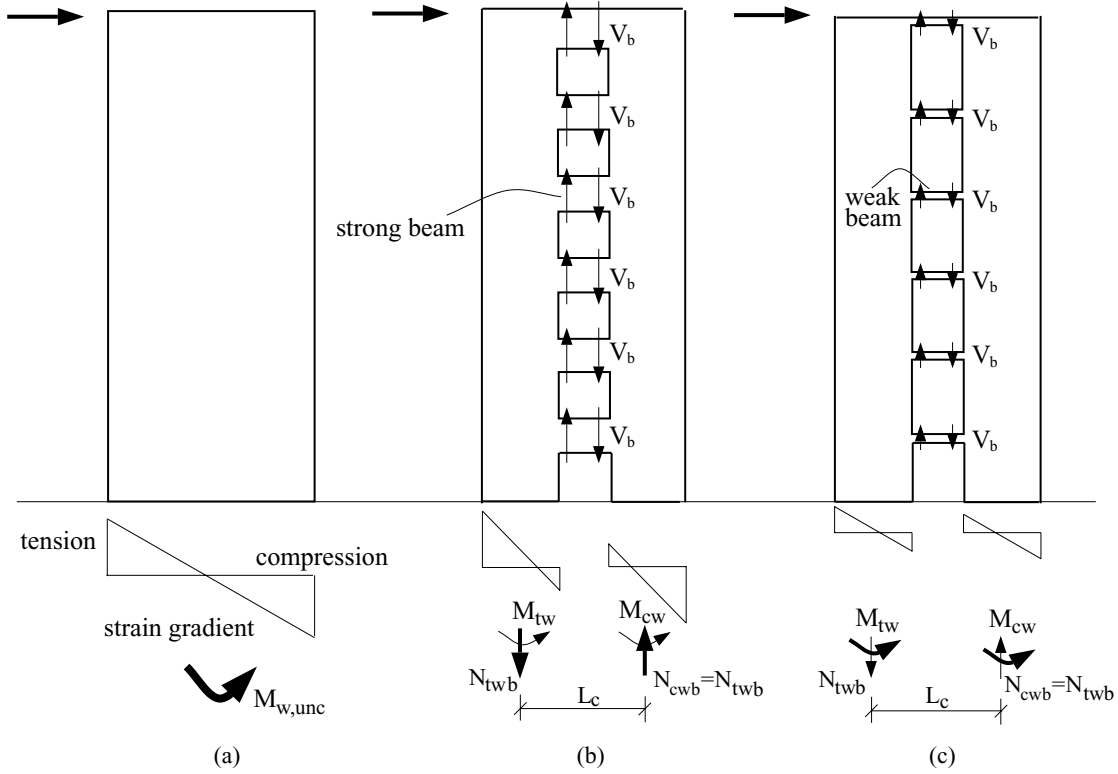


Fig. 2.2 Lateral load resisting mechanisms in structural walls (adapted from Paulay and Priestley 1992): (a) uncoupled wall; (b) walls coupled with strong beams; (c) walls coupled with weak beams

where, M_{tw} and M_{cw} are the base moments in the tension-side and compression-side walls, respectively, $N_{cwb} = N_{tw}$, and L_c is the distance between the centroids of the tension-side and compression-side walls. Then, the contribution of the wall axial forces due to

coupling to the total lateral resistance of the structure can be expressed by the degree (or level) of coupling as

$$DOC = \frac{N_{cwb}L_c}{M_w} = \frac{N_{cwb}L_c}{M_{tw} + M_{cw} + N_{cwb}L_c} \quad (2.2)$$

The degree of coupling, DOC, can be controlled by changing the strength and stiffness of the beams relative to the walls as shown in Figs. 2.2b and 2.2c. Note that the degree of coupling varies as the wall deforms into the nonlinear range of behavior under lateral loading. This is discussed in more detail later in the dissertation.

The coupling degree is a key parameter in the seismic behavior and design of coupled wall structures. Too little coupling (i.e., too small a coupling degree) yields a system that behaves in a manner similar to uncoupled walls and the benefits due to coupling are minimal. Too much coupling (i.e., too large a coupling degree) will add excessive stiffness to the system, causing the coupled walls to perform as a single pierced wall with little or no energy dissipation provided by the beams. The desirable “range” for the amount of coupling lies in between these two extremes and should be selected properly in seismic design.

Coupling beams are analogous to, and serve the same structural role as link beams in eccentrically braced frames. To achieve desirable performance, the failure mechanism should involve the formation of plastic hinges in most or all of the coupling beams and also at the base of each wall. In this manner, the dissipation of seismic input energy is distributed over the height of the structure (rather than being concentrated in a few stories), similar to the strong column-weak beam design philosophy for ductile moment resisting frames.

Despite their structural advantages such as increased lateral strength and stiffness and good energy dissipation, coupled wall systems are not used to their full potential in current design practice. This may be because of the complex characteristics of these structures where achieving a code compliant design and optimizing the global system behavior are often difficult.

2.2 Concrete Coupled Wall Structures

In the last three to four decades, an extensive amount of experimental and analytical research has been conducted on the seismic behavior and design of monolithic cast-in-place reinforced concrete coupled wall structural systems (e.g., Paulay 1971, 1977, 1986; Paulay and Binney 1974; Santhakumar 1974; Aristizabal-Ochoa and Sozen 1976; Srichatrapimuk 1976; Paulay and Santhakumar 1976; Lybas and Sozen 1977; Shiu et al. 1978, 1981; Aristizabal-Ochoa et al. 1979; Fintel and Ghosh 1980, 1982; Aktan and Bertero 1981, 1984, 1987; Aktan et al. 1982; Aristizabal-Ochoa 1982, 1987; Saatcioglu et al. 1987; Pekau and Cistra 1989; Subedi 1991a, 1991b; Chaallal 1992; Chaallal and Gauthier 1995, 2000, 2001; Chaallal and Ghlamallah 1996; Chaallal et al. 1996a, 1996b, 1997; Tassios et al. 1996; Chaallal and Nollet 1997; Harries et al. 1998; Teshigawara 1998; Sugaya et al. 1999; Harries et al. 2000; Munshi and Ghosh 2000; Harries 2001; Cosenza and Pecce 2001; Nollet and Chaallal 2002; Paulay 2002). The behavior and design of the monolithic cast-in-place reinforced concrete coupling beams in these structures are significantly different than the behavior and design of the unbonded post-tensioned steel coupling beams investigated in this research, and thus, a complete review of the previous research listed above is beyond the scope of this dissertation. However,

some of the important findings and conclusions regarding the seismic modeling, behavior, and design of monolithic cast-in-place reinforced concrete coupled wall structures are summarized below.

2.2.1 Behavior and Design of Concrete Coupling Beams

The primary role of coupling beams during an earthquake is the transfer of forces from one wall pier to the other. In considering the seismic behavior and design of coupled wall structures, it should be noted that significantly larger nonlinear deformations can occur in the coupling beams than in the walls that are coupled. Previous research has shown that short monolithic cast-in-place reinforced concrete coupling beams with conventional transverse steel reinforcement (i.e., vertical hoops) inevitably fail in diagonal tension or sliding shear (Figs. 2.3a and 2.3b), with limited or no ductility capacity (Paulay and Priestley 1992). The displacement capacity of these structures is often exceeded by the demand (Harries 2001). The consideration of large seismic ductility demands under many load reversals has led to the development of concrete coupling beams that use diagonal steel reinforcement as shown in Fig. 2.3c. This allows for the transfer of diagonal tension and compression forces to the reinforcement during the lateral displacements of the structure, resulting in a considerably ductile behavior with good energy dissipation characteristics.

2.2.2 Analysis and Modeling of Concrete Coupled Wall Structures

Previous research has often adopted an “equivalent frame” analogy for the nonlinear inelastic hysteretic modeling and analysis of coupled wall structural systems as

shown in Fig. 2.4. The cross-sectional properties of the walls and the beams are concentrated at the centerline of each member. Where the coupling beams frame into the walls, it is usually necessary to use rigid end zones (or kinematic constraints) in the analytical model. Rigid end zones may also be needed in the walls depending on the stiffness of the coupling beams. Nonlinear shear deformations in walls with aspect ratios, h_w/l_w (as shown in Fig. 2.4) larger than 4 are often neglected (Paulay and Priestley 1992).

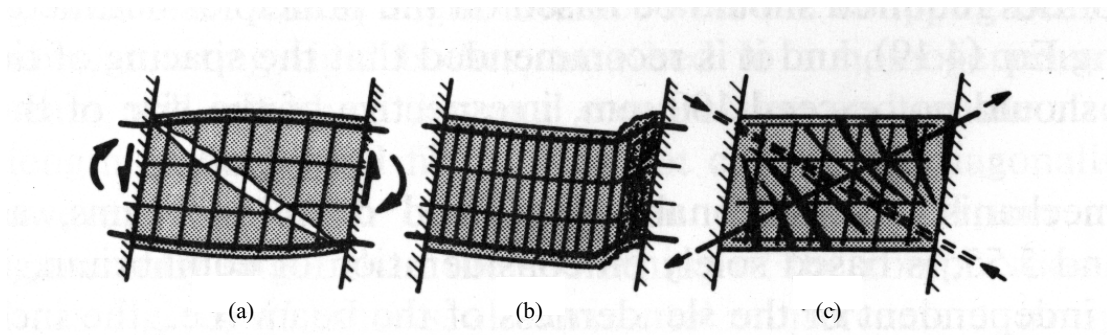


Fig. 2.3 Shear in concrete coupling beams (from Paulay and Priestley 1992):
 (a) diagonal tension failure; (b) sliding shear failure;
 (c) beam with diagonal reinforcement

It is emphasized that the validity of the frame analogy used to model the behavior of coupled wall structures can vary considerably depending on the stiffnesses assumed for the members (including the effect of concrete cracking) and the lengths of the rigid end zones. Furthermore, axial “elongation” and “shortening” of the tension and compression side walls due to axial-flexural interaction cannot be represented using frame analogy. As a result, the modeling of the coupled wall structures in this dissertation is done using fiber beam-column elements as described in Chapter 3. A significant advantage of using fiber-based elements instead of frame analogy is that a reasonably

accurate model can be constructed accounting for axial-flexural interaction including axial as well as flexural deformations in the members, nonlinear behavior of concrete and steel, and gap opening at the beam-to-wall interfaces.

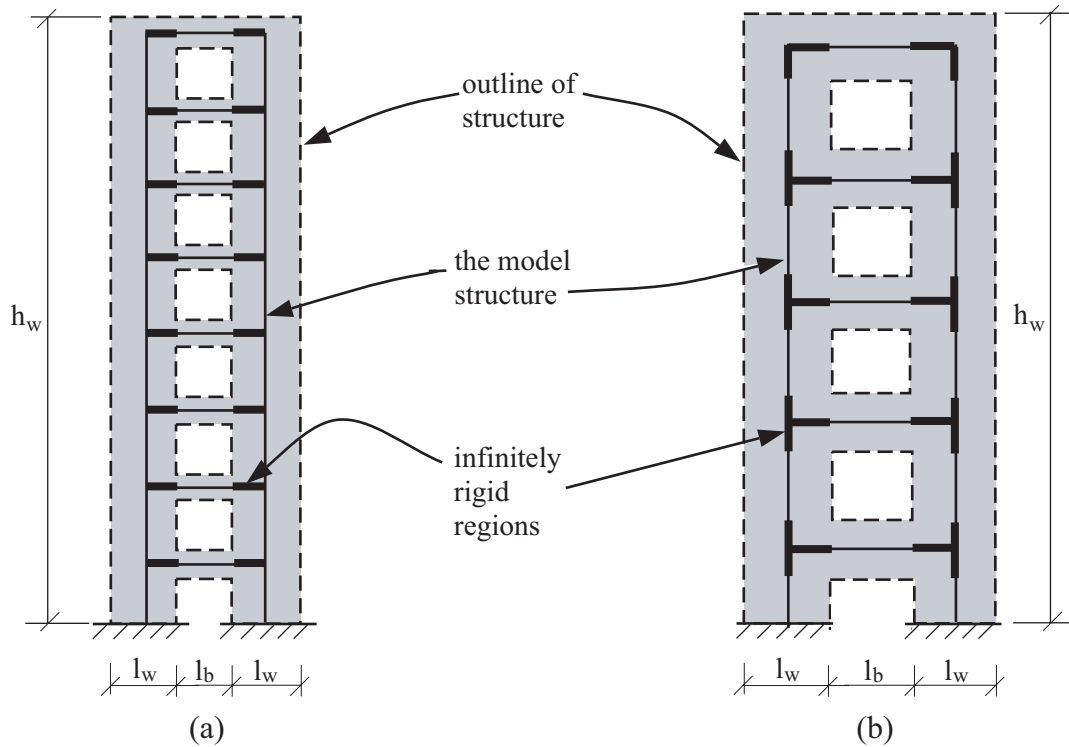


Fig. 2.4 Modeling of coupled wall structures (adapted from Paulay and Priestley 1992): (a) walls with flexible beams; (b) walls with stiff beams

2.3 Hybrid Structures with Embedded Steel Coupling Beams

As described above, ductility is an important issue to be considered in the seismic design of coupled wall structures. The coupling beams in a coupled wall structure must behave in a ductile manner and dissipate energy during the cyclic displacements of the walls during a severe earthquake. While reinforced concrete coupling beams can be designed and detailed to behave in a relatively ductile manner by using diagonal

reinforcement as shown in Fig. 2.3c, the construction of these beams is cumbersome and it is difficult to design a constructible diagonally reinforced coupling beam especially for larger span-to-depth ratios (e.g., larger than 1.5, see Harries et al. 2005). In an attempt to address the limitations of reinforced concrete coupling beams, previous research carried out by Rath (1974), Marcakis and Mitchell (1980), and Mattock and Gaafar (1982) on precast concrete connections with embedded steel members led to the use of embedded steel beams (see Fig. 1.2) to couple reinforced concrete walls (e.g., Harries 1992, 1995; Harries et al. 1992, 1993, 1994, 1997, 2000; Remmetter et al. 1992; Shahrooz et al. 1992, 1993a, 1993b, 2003; Gong and Shahrooz 1997, 1998, 2001a, 2001b; Gong et al. 1997; Shahrooz and Gong 1998; El-Tawil et al. 2002; El-Tawil and Kuenzli 2002; Hassan and El-Tawil 2004).

Using embedded steel coupling beams, it is possible to achieve better ductility and energy dissipation with relatively simpler design and detailing requirements than reinforced concrete coupling beams. Furthermore, reinforced concrete coupling beams with diagonal reinforcement often result in impractically deep cross sections. The depth of the beams can be considerably reduced by using steel cross sections as compared with concrete beams, which is particularly desirable in high-rise apartment buildings. Thus, the advantages of embedded steel coupling beams become especially apparent in cases where height restrictions do not permit the use of deep reinforced concrete beams, or where the required strength, stiffness, or deformation capacity cannot be developed economically with a concrete beam, as demonstrated in recent construction projects (Harries and Shahrooz 2005).

2.3.1 Behavior and Design of Embedded Steel Coupling Beam Subassemblages

Harries et al. (1993) and Shahrooz et al. (1993a) showed that properly-designed and detailed embedded steel coupling beam systems possess large ductility and energy dissipation capacities; however, they are prone to significant damage during lateral displacements in the form of flexural and/or shear yielding in the beams, and spalling and cracking in the wall concrete in the embedment regions.

Harries et al. (1997) conducted floor-level subassemblage experiments of embedded steel coupling beams as depicted in Fig. 2.5a. The test results showed that the seismic design and detailing of these systems should include: (1) moment and shear strength requirements for the beams; (2) laterally unsupported length requirements to prevent lateral instability of the beams; (3) stiffener requirements for the beams within the clear span between the walls; (4) minimum embedment length requirements for the beams; and (5) additional detailing requirements for the embedment regions. The embedment regions are designed and detailed for large cyclic nonlinear-inelastic deformations under shear forces and bending moments that correspond to the full capacity of the beam cross-section. The design requirements for the embedment regions aim to ensure that these regions remain essentially linear-elastic while the coupling beams undergo inelastic deformations in their clear span. These requirements include: (1) full-depth stiffeners on both sides of the beam web; (2) cover plates for the beam flanges; (3) increased thickness for the beam web; and (4) additional wall reinforcement. A full description of the design and detailing requirements for embedded steel coupling beams is given in Harries et al. (1997).

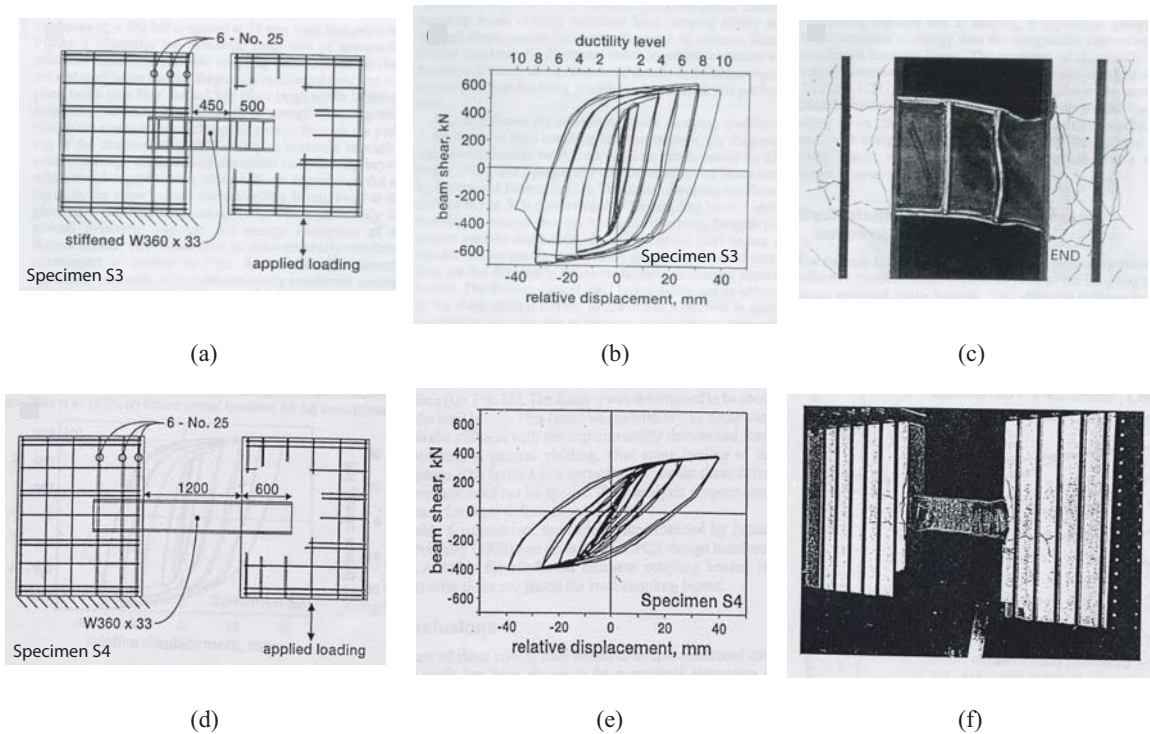


Fig. 2.5 Hybrid coupled wall subassemblages with embedded steel beams (from Harries et al. 1997); (a) shear-critical beam; (b) beam shear force versus relative end displacement behavior; (c) damage at end of test; (d) flexure-critical beam; (e) beam shear force versus relative end displacement behavior; (f) damage at end of test.

The nonlinear behavior of embedded steel coupling beams can be characterized as “shear critical” or “flexure critical.” Shear-critical beams behave in a predominantly shear mode, remaining essentially elastic in flexure. Similarly, flexure-critical beams behave in a predominantly flexural mode. It is typically more advantageous to design steel coupling beams as shear yielding members since such members exhibit a more desirable mode of energy dissipation (Harries et al. 1997).

As an example, Figs. 2.5a and 2.5b show the design details and the beam shear force versus relative end displacement behavior, respectively, of a shear-critical embedded steel coupling beam (Harries et al. 1997). As a result of proper seismic

detailing, the behavior of the test specimen shows stable hysteresis loops with large ductility capacity and large energy dissipation. However, as shown in Fig. 2.5c, the specimen has significant damage at the end of the test in the form of excessive yielding of the beam over the entire clear span and pronounced concrete cracking in the walls. Extensive spalling of the cover concrete was also observed in another test specimen. Earlier tests conducted by Harries et al. (1993) on specimens without proper detailing exhibited premature local flange and web buckling and a more pinched hysteretic behavior.

Similarly, Fig. 2.5d shows a flexure critical coupling beam. The reversed cyclic loading behavior of the specimen in Fig. 2.5e illustrates relatively large and stable hysteresis loops throughout the test. Fig. 2.5f shows the flexural hinges that form in the beam near the face of each wall, with significant concrete cover spalling and cracking in the embedment regions. In order to reduce the amount of damage in the embedment regions, a recent study by Shahrooz et al. (2003) has investigated steel coupling beams with “shear fuses” to concentrate the inelastic deformations in a repairable or replaceable component placed at the beam midspan. In this manner, the wall embedment regions are protected from damage due to the coupling forces.

The experiments conducted by Harries et al. (1997) and Shahrooz et al. (1993a) are used later in this dissertation to develop analytical models for hybrid coupled wall systems with embedded steel beams. These models are then used to compare the behavior of embedded systems with the unbonded post-tensioned system investigated in this dissertation. As described above, despite excellent performance in terms of energy

dissipation and ductile hysteretic behavior, the connection regions of embedded steel coupling beams are prone to significant damage under lateral loading. In such cases, repair is expensive and may be impractical. The unbonded post-tensioned hybrid coupled wall system described in this dissertation has three important advantages over systems with embedded beams as follows:

(1) The selection of the section shape and size for an unbonded post-tensioned steel coupling beam is not affected by the reinforcement details inside the walls, and the use of widely available rolled cross sections is recommended. In comparison, the wall reinforcement inside the embedment regions and the seismic detailing requirements in the form of stiffener and cover plates often result in the use of fabricated beam cross sections in embedded systems.

(2) The nonlinear deformations in unbonded post-tensioned steel coupling beams occur primarily as a result of the opening of gaps at the beam ends. Thus, corresponding to a given nonlinear wall lateral displacement level, the amount of damage in the walls and beams of an unbonded post-tensioned system is expected to be much smaller than the corresponding damage in systems with embedded beams.

(3) The post-tensioning tendons used for coupling at the floor and roof levels provide a restoring force that pulls the entire coupled wall structure back towards its original undisplaced position (with little residual displacements) during and at the end of an earthquake, thus providing self-centering capability (i.e., ability of the structure to return towards zero displacement upon unloading from a nonlinear displacement). In comparison, embedded hybrid coupled wall structures have relatively small self-centering

capability, indicating that significant permanent displacements (i.e., residual lateral displacements from plumb position) can remain at the end of a severe earthquake.

2.3.2 Embedded Steel Coupling Beams with Concrete Encasement

As part of the NSF-funded *U.S.-Japan Cooperative Earthquake Research Program on Composite and Hybrid Structures*, Gong and Shahrooz (1997, 1998) and Gong et al. (1997) investigated the seismic behavior and design of embedded steel coupling beams with concrete encasement. Steel coupling beams are often encased inside concrete members such as door lintels. However, current design guidelines ignore the effect of this encasement on the behavior of the beams. For example, stiffener details for the beams are determined ignoring the effect of the encasement, and the embedment length is determined based on the capacity of the steel beam cross section alone.

Experiments conducted by Gong and Shahrooz (1997, 1998, 2001a, 2001b) showed that nominal concrete encasement around embedded steel coupling beams has the following effects: (1) concrete encasement provides an effective means of preventing web buckling, thus, web stiffeners in the clear span can be eliminated; (2) concrete encasement increases the beam moment and shear capacities, thus, the embedment regions have to be designed based on the capacity of the composite section including the encasement; and (3) concrete encasement increases the stiffness of the beams, which affects the degree of coupling and, thus, the distribution of forces between the walls.

Further information on steel coupling beams with concrete encasement is not within the scope of this dissertation.

2.3.3 Multi-Story Hybrid Coupled Walls with Embedded Beams

Compared with research on floor-level coupled wall subassemblages, previous research on multi-story hybrid coupled wall structures is limited and includes analytical investigations only (e.g., Harries 1996, 2001; El-Tawil and Kuenzli 2002; El-Tawil et al. 2002; Hassan and El-Tawil 2004; Harries and McNeice 2006). Harries (1996) conducted an analytical investigation of the seismic behavior of two eighteen story hybrid coupled walls with embedded steel beams (Fig. 2.6a). The structures were modeled as two-dimensional “equivalent frames” (Fig. 2.6b) using beam-column frame elements located at the wall centerlines and beam elements located at the beam centerlines. The dynamic response of the structures under four ground motion records was obtained from nonlinear dynamic time-history analyses.

As part of a conventional strength-based design approach, Harries (2001) conducted an assessment of the seismic behavior of coupled wall structures with different types of coupling beams (i.e., conventionally reinforced concrete beams, diagonally reinforced concrete beams, and embedded steel beams). Through a review of available experimental investigations on coupling beam subassemblages and analytical investigations on multi-story coupled wall systems, it was concluded that the estimated coupling beam ductility demands from nonlinear dynamic time-history analyses often exceed the expected available ductility capacities from the experiments. Therefore, coupled wall structures are prone to premature failure in the course of a significant seismic event. Limits to the degree of coupling, DOC, were proposed as follows:

- $\text{DOC} \leq 50\%$ for conventionally reinforced concrete coupling beams;
- $\text{DOC} \leq 55\%$ for diagonally reinforced concrete coupling beams;

- $DOC \leq 60\%$ for shear critical embedded steel coupling beams; and
- $DOC \leq 65\%$ for flexure critical steel coupling beams.

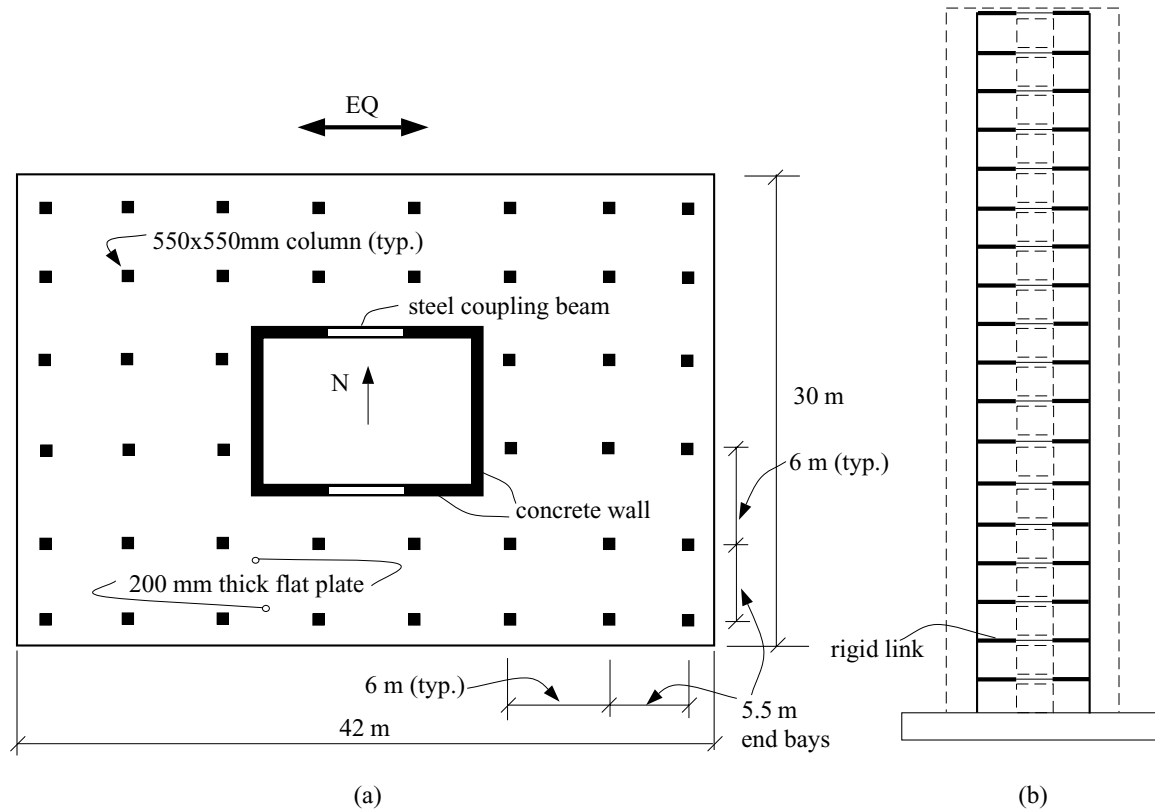


Fig. 2.6 Hybrid coupled wall system with embedded steel beams (adapted from Harries 1996): (a) plan view; (b) analytical model

The higher coupling levels allowed for steel beams were based on previous experimental results that these beams are capable of sustaining larger levels of ductility than reinforced concrete coupling beams.

Harries (2001) also observed that an increase in the degree of coupling causes an increase in the strength of the beams relative to the strength of the individual walls. If the degree of coupling is too high, this may lead to an undesirable structural response where

the walls act as the primary energy dissipating components, rather than the coupling beams. It was argued that in order to ensure that the coupling beams act as the primary energy dissipating members, the walls should be sufficiently strong to allow all of the coupling beams to achieve their probable strengths. Thus, a lower limit of 1.5 was recommended for the wall overstrength factor used in design (applied to the required wall strength to achieve the probable strengths of the coupling beams).

2.3.4 Degree of Coupling

From the above discussion, it is clear that the degree of coupling, DOC, is an important parameter and its effect on the behavior of coupled wall systems must be understood before the successful design of a coupled wall structure can be achieved. As a part of the NSF-funded *U.S.-Japan Cooperative Earthquake Research Program on Composite and Hybrid Structures*, El-Tawil et al. (2002) investigated the effect of the coupling degree on the behavior of hybrid coupled wall systems comprised of three reinforced concrete walls with embedded steel beams.

Pushover lateral load analyses of a series of walls with different amounts of coupling were conducted. It was concluded that moderately coupled hybrid wall systems (DOC=30% to 45%) are well suited for use in regions of high seismic risk. Overcoupling (e.g., DOC=60%) can lead to problems due to the development of large shear forces and compressive axial loads in the compression-side wall, and tension forces in the tension-side wall. Large tension forces, for example, can lead to more widespread cracking and

yielding in the walls, reduce the axial-flexural and shear strength of the walls, and cause foundation uplift.

El-Tawil et al. (2002) recommended that a target level of coupling should be selected as part of the design approach in order to ensure structures with desirable seismic characteristics. Assuming that the coupling beam properties are uniform over the height of the structure, the coupling axial force acting on the compression-side wall can be expressed as:

$$N_{cwb} = n_b V_b \quad (2.3)$$

where, n_b is the total number of coupling beams at the floor and roof levels and V_b is the coupling beam shear strength.

Then, with a target design value for the degree of coupling, DOC, design coupled wall base moment, M_w , and distance between the wall centroids, L_c , known, the required design shear strength of the coupling beams, V_b can be determined by considering Equations (2.2) and (2.3) together as follows:

$$V_b = \frac{DOC \cdot M_w}{n_b L_c} \quad (2.4)$$

2.4 Wall Shear Force Demands in Coupled Wall Structures

Due to the effect of higher modes of response during an earthquake, base shear force demands of coupled wall structures can be much greater than the forces predicted from a static analysis (Harries, 2001; Chaallal and Gauthier 2000). This is similar to the effect of higher modes on the base shear demands of uncoupled wall structures as investigated by many researchers including Aktan and Bertero (1984, 1985), Keintzel

(1990), Ghosh and Markevicius (1990), Aoyama (1993), Eberhard and Sozen (1993), Kabeyasawa (1993), and Otani et al. (1994).

In addition, there can be a significant redistribution of shear forces from the tension-side wall to the compression-side wall, further increasing the shear demands on individual wall piers. As much as 80% redistribution of shear forces between the tension and compression side walls was observed by a recent experimental research program on multi-story reinforced concrete coupled wall structures in Japan (Teshigawara et al. 1998; Sugaya et al. 2000). Chaallal et al. (2000) investigated the effect of the coupling degree on the distribution of the total wall base shear between individual wall piers.

The seismic design of a coupled wall structure should consider both of these effects. More information on the wall shear demands in coupled wall structures is provided in Chapter 11.

2.5 Unbonded Post-Tensioning in Building Construction

In the last decade, a significant amount of research has been conducted on the use of unbonded post-tensioning in precast concrete and steel moment frames and precast concrete walls for building construction in seismic regions. Important findings from this previous research are summarized in this section. Applications of unbonded post-tensioning in bridge construction have also been investigated previously; however, an overview of this research is outside the scope of this dissertation.

Note that the lateral load behavior of unbonded post-tensioned steel frames and precast concrete frames is governed by the opening of gaps at the beam-to-column joints,

similar to the opening of gaps at the beam-to-wall joints of the proposed coupled wall system (see Fig. 1.3b). Thus, there are similarities in the analytical modeling and seismic design of these different types of structures.

2.5.1 Unbonded Post-Tensioning

In unbonded post-tensioned concrete structures, the post-tensioning tendons can be placed either internal or external to the structural members (e.g., beams). Internal tendons are placed inside ducts that, unlike the ducts in bonded post-tensioned construction, are not filled with grout. This way, the bond between the post-tensioning tendons and concrete is intentionally prevented. Greased tendons may be used to reduce the friction forces that may develop between the ducts and the tendons. Furthermore, the ducts can be oversized to prevent the tendons from coming into contact with the ducts during the lateral displacements of the structure. The elimination of the grouting operation offers considerable advantages in the application of post-tensioning. Therefore, unbonded post-tensioned construction often has a lower unit cost than bonded post-tensioned construction.

Internal and external unbonded post-tensioned construction types differ in the displaced shape of the tendon. The displaced shape of internal tendons follows the displaced shape of the structural member, unless the ducts are sufficiently oversized. The displaced shape of external tendons is generally different from that of the member except at deviator or saddle point locations anchored to the structure. Note that the use of

deviator points in seismic applications is not recommended in order to achieve symmetric behavior under reversed cyclic loading.

There is a fundamental difference in the flexural behavior of an unbonded post-tensioned structural member and a bonded post-tensioned member. For a bonded post-tensioned member, it is reasonable and customary to assume that the change in the tendon strain is the same as the change in the concrete strain adjacent to the tendon. In other words, after grouting, an assumption of strain compatibility between the tendon and the adjacent concrete can be made. If it is assumed that plane sections remain plane during flexural deformations, the strain at any point in the tendon can be calculated from the deformations of the corresponding section (i.e., curvature and average axial strain), because the change in strain at any point in a bonded tendon depends only on the deformations at that section.

For an unbonded post-tensioned member, the usual assumption of strain compatibility between the tendon and the adjacent concrete cannot be made. Rather, the change in the tendon strain is uniform (ignoring friction forces) over the unbonded length of the tendon. The change in strain at any point in an unbonded tendon is the average change in strain in the concrete over the entire unbonded length. In other words, the tendon strain depends on the total change in the length of the concrete over the unbonded length. This makes the tendon strain (and stress) dependent on member deformations rather than section deformations. As a result of the uniform distribution of strains, unbonded tendons reach the inelastic strain range at larger overall member deformations

than bonded tendons, which is one of the reasons why they are preferred for seismic applications.

The application of unbonded post-tensioning in steel structural members is similar to the application of external post-tensioning in concrete members. The post-tensioning tendons can be placed outside or inside (as in the case of hollow cross-sections) the steel member.

2.5.2 Unbonded Post-Tensioned Precast Concrete Moment Frames

In the last decade, a significant amount of research has been conducted on the seismic behavior and design of unbonded post-tensioned precast concrete frame structures (e.g., Cheok and Lew 1991, 1993; Cheok et al. 1993; Priestley and Tao 1993; MacRae and Priestley 1994; Priestley and MacRae 1996; El-Sheikh et al. 1997, 1999, 2000).

As a part of the *PREcast Seismic Structural Systems (PRESSS) Research Program* funded by the National Science Foundation (NSF), the Precast/Prestressed Concrete Institute (PCI), and the Precast/Prestressed Concrete Manufacturers Association of California (PCMAC), Priestley and Tao (1993) analytically investigated the concept of joining precast concrete beam and column members using post-tensioning tendons unbonded over a length of each beam through and on either side of the column as shown in Figs. 2.7a and 2.7b. The nonlinear behavior of these structures occurs primarily due to the opening of gaps at the beam-to-column interfaces (Fig. 2.7c).

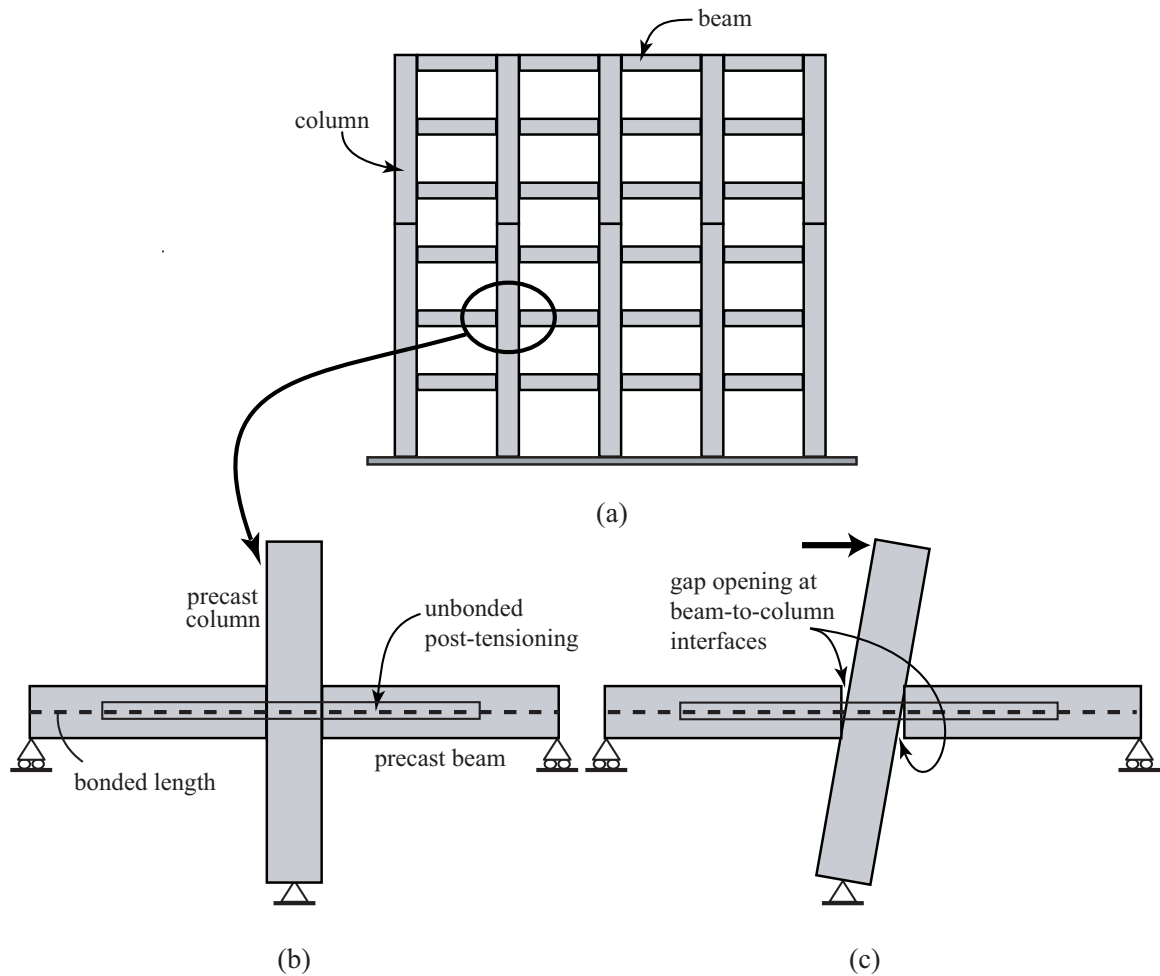


Fig. 2.7 Unbonded post-tensioned precast concrete frame: (a) elevation; (b) beam-column subassembly; (c) idealized exaggerated displaced shape.

Cheok and Lew (1991, 1993) and Cheok et al. (1993) conducted reversed cyclic lateral load experiments of 1/3-scale unbonded post-tensioned precast interior beam-column joint subassemblages at the National Institute of Standards and Technology (NIST). MacRae and Priestley (1994) and Priestley and MacRae (1996) conducted additional cyclic lateral load experiments on two 2/3-scale unbonded post-tensioned precast beam-column subassemblages representing an interior and an exterior joint. The subassemblages from this research program are illustrated in Figs. 2.8a and 2.8b with the

test setup shown in Figs. 2.8c and 2.8d. El-Sheikh et al. (1997, 1999, 2000) developed analytical models and a performance based seismic design approach for multi-story unbonded post-tensioned precast concrete frame structures.

Some of the important conclusions from the previous research on unbonded post-tensioned precast concrete frame structures are summarized below.

(1) As a result of post-tensioning, the initial linear-elastic lateral stiffness of an unbonded post-tensioned precast concrete beam-column joint is similar to the initial stiffness of a monolithic cast-in-place reinforced concrete joint.

(2) Unbonded post-tensioned precast concrete frames can soften (indicating a significant reduction in the lateral stiffness) and go through large nonlinear cyclic lateral displacements without significant damage, and thus, without significant strength degradation (as compared to precast concrete frames with bonded tendons or monolithic cast-in-place reinforced concrete frames). The lateral load versus displacement behaviors of the interior and exterior beam-column joint specimens tested by Priestley and MacRae (1996) are shown in Figs. 2.8e and 2.8f, respectively, with the interior joint at 2.8% drift shown in Fig. 2.8g. The nonlinear displacements occur primarily through the opening of gaps at the beam-to-column interfaces as shown in Fig. 2.7c.

(3) The use of unbonded post-tensioning tendons results in a uniform strain distribution in the steel, and thus, delays the nonlinear straining (i.e., yielding) of the tendons. As long as the post-tensioning tendons remain elastic and the anchors for the tendons do not deteriorate, the initial level of prestress can be maintained during the cyclic lateral displacements of the structure.

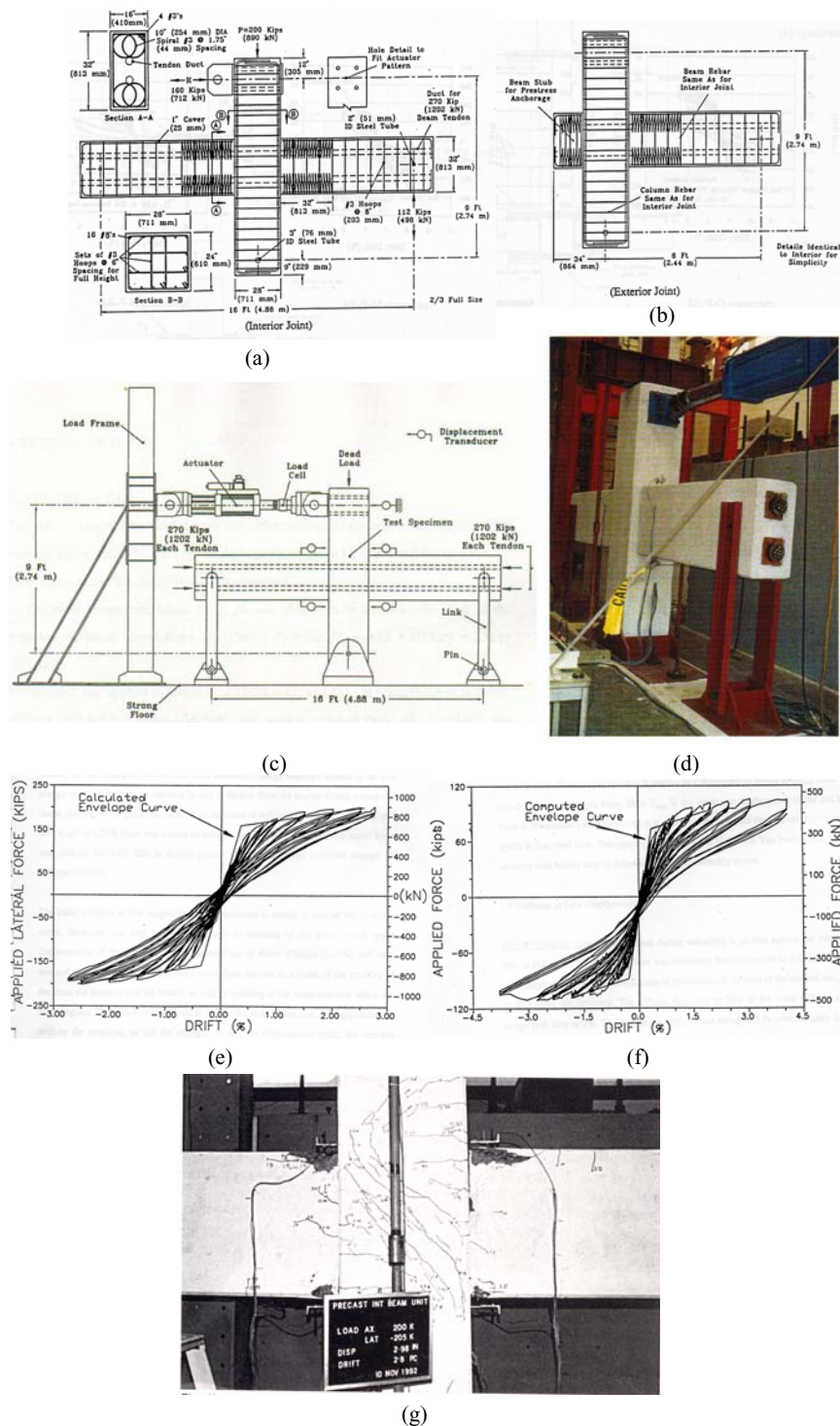


Fig. 2.8 Unbonded post-tensioned precast beam-column subassemblages (from Priestley and MacRae 1996): (a) interior joint specimen; (b) exterior joint specimen; (c) test setup; (d) photograph of test setup; (e) interior joint behavior; (f) exterior joint behavior; (g) photograph of interior joint

(4) Unbonding of the post-tensioning tendons significantly reduces the amount of tensile stresses transferred to the concrete, thus reducing damage due to concrete cracking.

(5) Large compression strains develop at the corners of the beams near the beam-to-column interfaces due to gap opening and post-tensioning. Therefore, transverse reinforcement (e.g., spiral or closed hoop reinforcement) is necessary to confine the concrete near the ends of the beams (see test specimen details with spiral reinforcement in Figs. 2.8a and 2.8b).

(6) Upon unloading from a large nonlinear lateral displacement, the post-tensioning force provides a restoring effect (i.e., self-centering capability) that tends to close the gaps and pull the frame back towards its original undeformed (i.e., plumb) position without significant residual lateral displacements. The resulting hysteretic behavior of the structure is close to nonlinear-elastic as indicated by the loading and unloading cycles that are close to each other for the subassemblages in Figs. 2.8e and 2.8f.

(7) The friction resistance that develops due to post-tensioning is sufficient to prevent shear slip at the beam-to-column interfaces and to transfer the shear forces from gravity and lateral loads without the need for corbels or shear keys at the beam ends. As long as the post-tensioning force is maintained, the shear slip resistance at the beam-to-column interfaces is maintained during large cyclic lateral displacements of the structure.

(8) Unbonded post-tensioning alters the shear resistance mechanism in the beams and in the beam-to-column joint panel regions (as compared with bonded post-tensioned and monolithic cast-in-place reinforced concrete structures), in which the shear force is transferred by a diagonal compression strut, greatly simplifying the design of the beam and joint shear reinforcement and reducing damage.

(9) Because of the small amount of damage, the inelastic energy dissipation of unbonded post-tensioned precast concrete frame structures is small (see Figs. 2.8e and 2.8f) as compared to monolithic cast-in-place reinforced concrete frame structures.

(10) The nonlinear moment versus rotation behavior of a properly-designed unbonded post-tensioned precast beam-column joint subassembly can be idealized using a trilinear relationship as shown in Fig. 2.9a from El-Sheikh et al. (1999). The five limit states marked on the smooth moment-rotation relationship (developed using a fiber element based analytical model) are as follows: Point (1) represents the initiation of gap opening (i.e., decompression) at the beam-to-column interfaces; Point (2) represents a significant reduction in the stiffness of the subassembly (i.e., softening), which occurs primarily due to increased gap opening at the beam-to-column interfaces; Point (3) represents the initiation of cover concrete spalling at the beam ends; Point (4) represents the initiation of yielding (i.e., nonlinear straining) of the unbonded post-tensioning steel; and Point (5) represents the axial-flexural failure of the subassembly due to the crushing of the confined concrete at the beam ends.

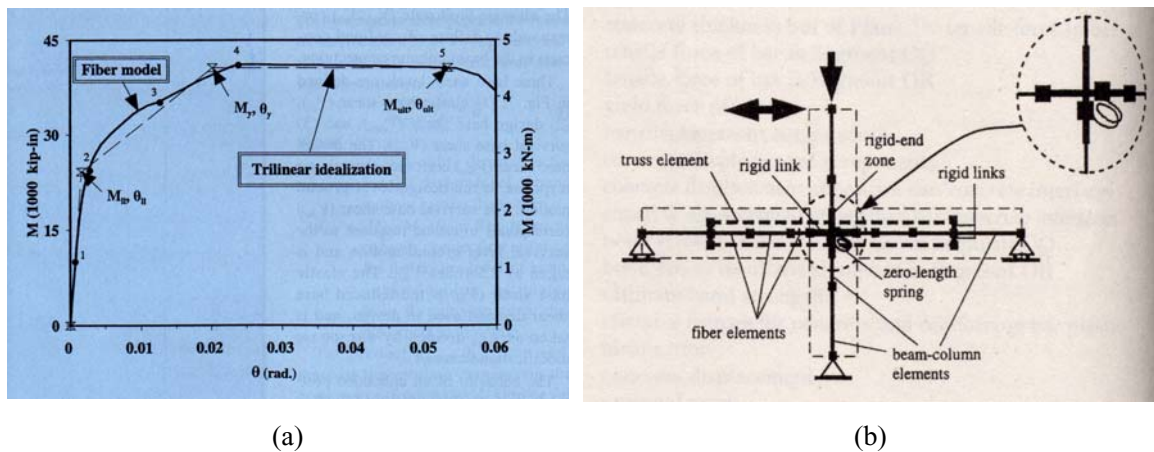


Fig. 2.9 Unbonded post-tensioned precast beam-column subassemblies (from El-Sheikh et al. 1999, 2000): (a) moment-rotation behavior; (b) analytical model

Fig. 2.9b shows the analytical model of an interior unbonded post-tensioned precast concrete beam-column joint subassembly developed by El-Sheikh et al. (1999, 2000). This model, which was used to generate the smooth subassembly moment-rotation relationship in Fig. 2.9a, includes the following elements in the DRAIN-2DX structural analysis program (Prakash et al. 1993): (1) fiber beam-column elements to model the lengths of the beams with unbonded post-tensioning steel; (2) linear-elastic frame beam-column elements to model the column as well as the lengths of the beams with bonded post-tensioning steel, where only linear-elastic deformations are expected to occur; (3) truss elements to model the unbonded length of the post-tensioning tendons; (4) a zero-length rotational spring element to model the joint panel zone shear deformations of the column member; (5) kinematic constraints (rigid links) for the beam elements and rigid end zones for the column elements to model the axial and flexural stiffnesses (assumed to be infinitely large) within the panel zone; and (6) kinematic constraints to model the ends of the unbonded length of the post-tensioning tendons. The gap opening behavior at the beam-to-column interfaces is modeled using compression-only stress-strain relationships for the fibers at the beam ends. The results obtained from the analytical model were found to compare well with experimental results reported by Cheok and Lew (1993).

The greatest setback to the use of unbonded post-tensioned precast concrete frame structures in seismic regions is that their lateral displacement demands during a severe earthquake may be larger than acceptable as a result of small energy dissipation. Previous research (e.g., Priestley and Tao 1993) has shown that the peak lateral displacements of these structures can be, on average, 1.35-1.40 times the peak displacements of

comparable monolithic cast-in-place reinforced concrete frame structures. In order to reduce the lateral displacement demands during a seismic event, the use of bonded mild (e.g., Grade 60) steel reinforcement through the precast beam-column joints, in addition to the unbonded post-tensioning steel, has been investigated (Cheok and Stone 1994; Cheok et al. 1996, 1998; Stanton et al. 1997; Stone et al. 1998; Nakaki et al. 1999; Priestley et al. 1999; Stanton and Nakaki 2002).

These partially prestressed systems are often referred to as “hybrid” precast concrete frame structures due to the mixed use of mild steel and post-tensioning steel reinforcement across the beam-column joints as shown in Fig. 2.10. Properly designed and detailed mild steel reinforcement would yield in tension and compression during the cyclic gap opening displacements that occur at the beam-to-column interfaces, thus dissipating energy. The bond between the mild steel bars and the concrete may be prevented over a predetermined length at the ends of the beams (by wrapping the bars) to prevent fracturing of the mild steel and to reduce the cracking of the concrete during the deformations of the bars in tension.

The concept of combining post-tensioning steel for flexural strength and self-centering with mild steel for inelastic energy dissipation was recently demonstrated through 0.60-scale tests of a five-story precast concrete building structure as part of the final phase of the PRESSS (PREcast Seismic Structural Systems) Research Program (Nakaki et al. 1999; Priestley et al. 1999), leading to the development of design recommendations (ACI Innovation Task Group 1 and Collaborators 2001a, 2001b, 2003) and the successful application of this new structural system in a 39-story precast-

prestressed concrete apartment building in San Francisco, California (Englekirk 2002). Note that in most recent applications, the post-tensioning tendons are typically left unbonded over the entire length of the frame (i.e., without any bonded regions within the beam spans) and are anchored only at the outer ends of the exterior joints.

Additional efforts to reduce the seismic displacement demands of post-tensioned precast concrete frame structures include a new type of friction damper developed for use locally at the beam ends (Morgen and Kurama 2003, 2004a, 2004b, 2005).

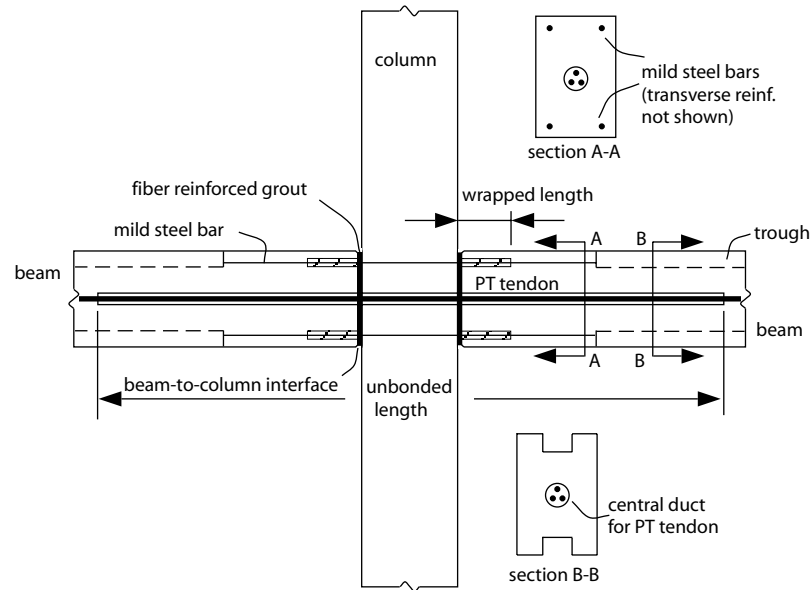


Fig. 2.10 Partially post-tensioned precast beam-column subassemblages (adapted from Kurama 2002)

2.5.3 Post-Tensioned Steel Moment Frames

The use of post-tensioning in steel moment resisting frames for seismic regions was recently investigated by Peng et al. (2000), Ricles et al. (2000, 2001, 2002), Peng (2001), Christopoulos et al (2002), Garlock (2002), and Rojas et al. (2002). Similar to the

unbonded post-tensioned precast concrete frame system described above, these frame structures are constructed by post-tensioning steel beams to steel columns using high strength post-tensioning strands. The strands extend over the entire length of the frame and are anchored only at the outer ends of the exterior joints as shown in Fig. 2.11. Top and seat angles are used at beam-to-column connections to provide energy dissipation and redundancy under seismic loading (analogous to the use of mild steel reinforcement in the partially prestressed precast concrete system in Fig. 2.10).

The nonlinear behavior of post-tensioned steel frame structures is governed by the opening of gaps at the beam-to-column interfaces, similar to the gaps shown in Figs. 1.3b and 2.7c. Reinforcing cover plates are used at the beam ends (analogous to the spiral concrete confinement in Fig. 2.8) to strengthen and control the yielding of the flanges under the high compressive stresses that develop due to post-tensioning and gap opening. Shim plates are used between the columns and the beam flanges to force the bearing between the beams and the columns to occur at the flanges, so that one or both flanges remain in contact with the column after the flanges yield in compression under cyclic loading. The shim plates are terminated at the beam web, thus preventing contact between the web and the column. Moreover, Ricles et al. (2001) used washer plates in the angle-to-column connections (see Fig. 2.11) to better control the location of the plastic hinge in the angle vertical leg near the column bolts and to reduce the prying forces on the bolts. The role of the washer plates on the behavior of the angles is described later.

The beams in a post-tensioned steel moment frame system are similar to the coupling beams investigated in this dissertation. The primary differences between these two types of beams are: (1) the beams in a frame structure are post-tensioned to adjacent

steel columns with the post-tensioning steel anchored at the outer ends of the frame; whereas, the beams in a coupled wall structure are post-tensioned to adjacent concrete walls; and (2) the beam length to depth aspect ratios in a frame structure are typically much larger than the beam aspect ratios in a coupled wall structure.

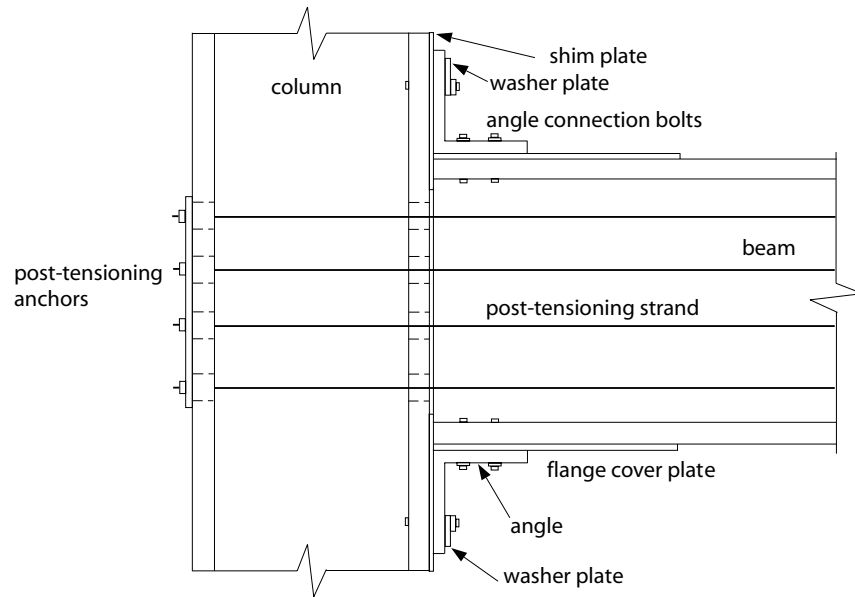


Fig. 2.11 Post-tensioned steel exterior beam-column connection
(adapted from Ricles et al. 2001)

As a result of the similarities between these two types of post-tensioned steel beams, the previous experimental and analytical research on post-tensioned steel frame structures is important for the research described in this dissertation. The experimental program conducted by Ricles et al. (2001, 2002) involved the testing of full-scale interior beam-column subassemblages. Each cruciform shaped specimen (Fig. 2.12) consisted of two wide flange steel beams post-tensioned to a steel column. Several parameters were investigated including angle leg thickness, angle gage length, beam flange cover plates, connection shim plates, and post-tensioning force.

The experimental results from Ricles et al. (2001) shown in Fig. 2.13 demonstrate that properly-designed post-tensioned steel frame beam-column subassemblages possess exceptional cyclic lateral strength and ductility, where yielding mainly occurs in the top and seat angles while the beam and column members remain essentially linear-elastic. The initial linear-elastic lateral stiffness of a post-tensioned steel beam-column connection is comparable to that of a conventional fully-restrained (welded) connection, and no significant permanent deformations remain in the structure following the application of several nonlinear cycles of drift (indicating a large self-centering capability due to the post-tensioning force). The compression yielding that occurs in the beam flanges should be controlled in order to maintain the lateral stiffness, strength, and self-centering capability of the structure. The angle geometry has a significant effect on the connection moment capacity, energy dissipation, and ductility.

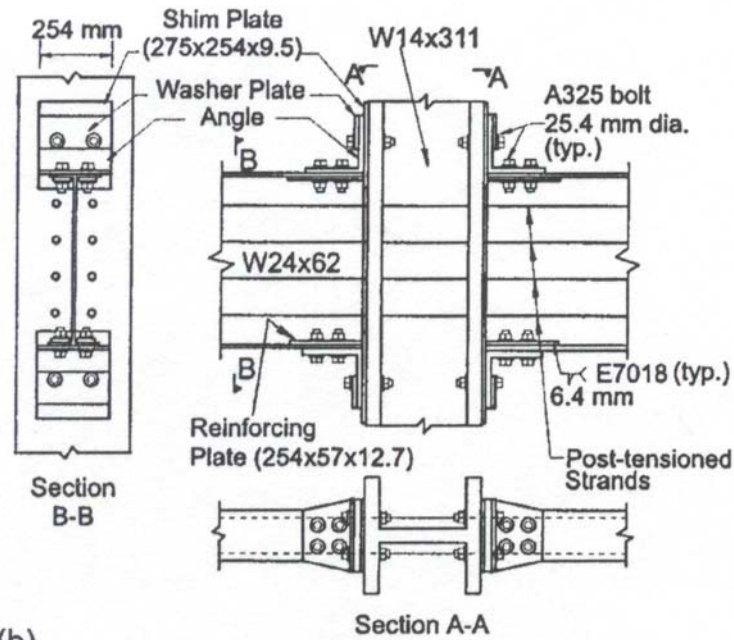
Ricles et al. (2002) used the subassemblage experimental results to develop simple procedures for estimating the connection behavior. Similarly, Ricles et al. (2001) used DRAIN-2DX (Prakash et al. 1993) to develop an analytical model for post-tensioned steel frame beam-column subassemblages. As an example, Fig. 2.14 shows the model for an interior subassemblage. Fiber beam-column elements are used to represent the beam and column members, and two parallel bilinear truss elements are used to represent each angle. The modeling of the top and seat angles is discussed in more detail later. The post-tensioning tendons in the subassemblage are also modeled using truss elements. The post-tensioning anchorages are represented by kinematically constraining (i.e., slaving) the displacements of the nodes at the ends of the truss elements to corresponding nodes at the

ends of the beam fiber elements (Fig. 2.14). The flexibility of the column panel zone in shear is modeled by placing a zero-length rotational spring element at the center of the panel. The moment-rotation behavior of the rotational spring represents the shear stiffness of the panel zone. Gap opening behavior at the beam-to-column interfaces is modeled by using compression-only stress-strain relationships for the steel fibers near the beam ends. This is similar to the modeling of gap opening in unbonded post-tensioned precast concrete frame and wall structures (El-Sheikh et al. 1999, 2000; Kurama et al. 1996, 1999a) and the modeling of gap opening at the beam-to-wall interfaces of the hybrid coupled wall structure investigated in this dissertation.

2.5.4 Unbonded Post-Tensioned Precast Concrete Structural Walls

As part of the NSF-funded PRESSS Research Program, Kurama et al. (1996, 1997, 1998a, 1998b, 1999a, 1999b, 2002) conducted an analytical investigation on the seismic behavior and design of structural walls that are constructed by post-tensioning precast concrete wall panels across horizontal joints using unbonded high strength post-tensioning bars (Fig. 2.15a). The expected seismic characteristics of properly-designed walls were found to be similar to the behavior of unbonded post-tensioned precast concrete frames described previously, with an ability to soften and undergo large nonlinear lateral displacements with little damage. The nonlinear displacements of the walls occur primarily due to the opening of gaps at the horizontal joints between the wall panels and between the base panel and the foundation, as shown in Fig. 2.15b. Shear slip along the horizontal joints (Fig. 2.15b) is not a desired mode of lateral displacement and is prevented by design.

(a)



(b)

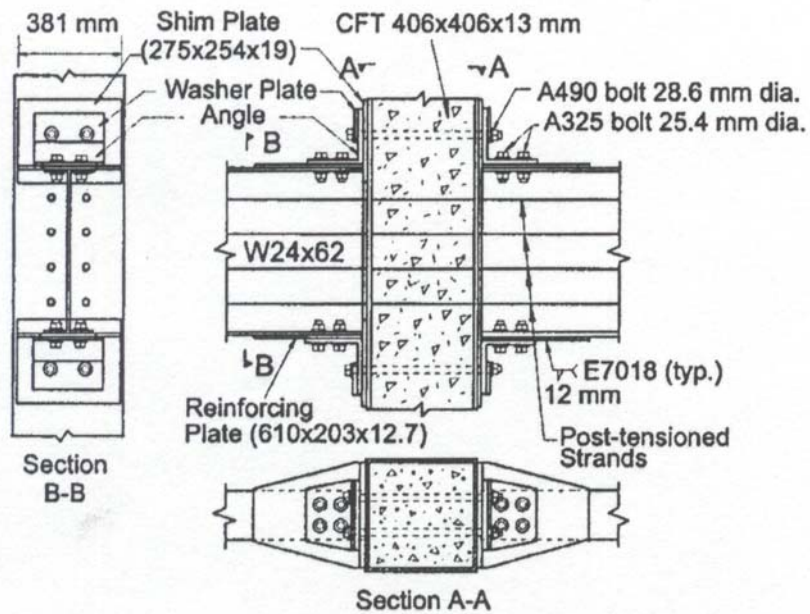


Fig. 2.12 Post-tensioned steel beam-column connection details (from Ricles et al. 2002): (a) specimen with wide flange column; (b) specimen with composite concrete filled steel tube column

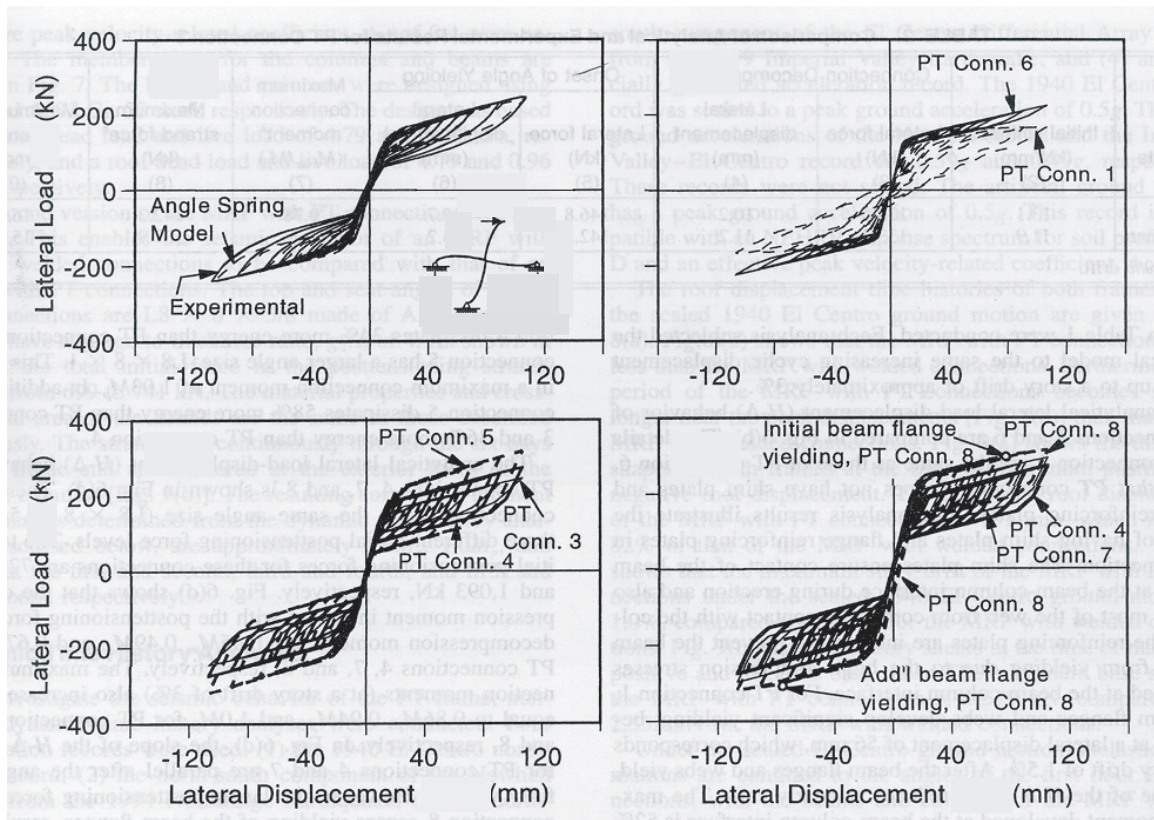


Fig. 2.13 Lateral load versus displacement behavior of post-tensioned steel beam-column subassemblages (from Ricles et al. 2001)

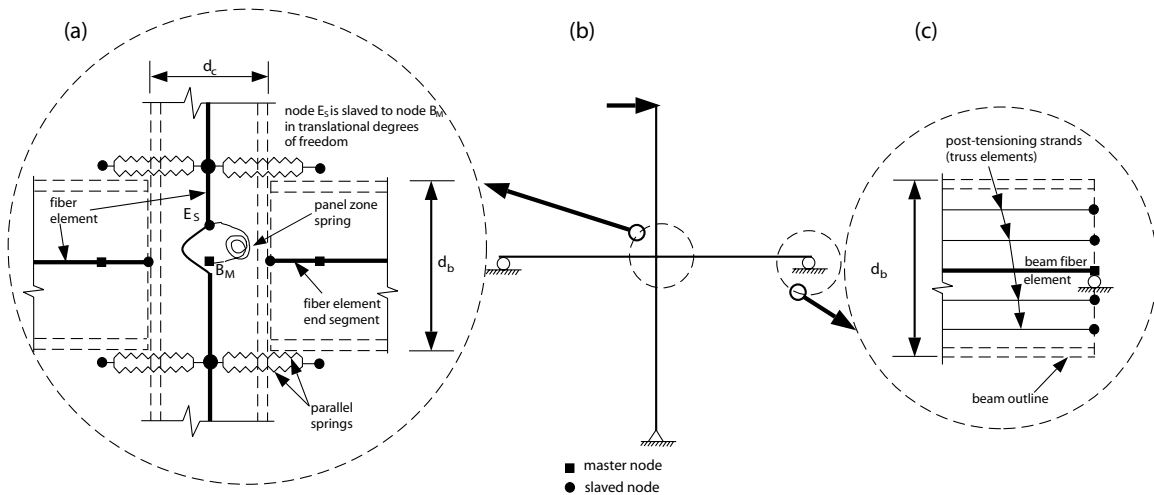


Fig. 2.14 Analytical modeling of post-tensioned steel beam-column subassemblages (adapted from Ricles et al. 2001): (a) interior joint region; (b) beam-column subassemblage; (c) modeling of post-tensioning anchorages

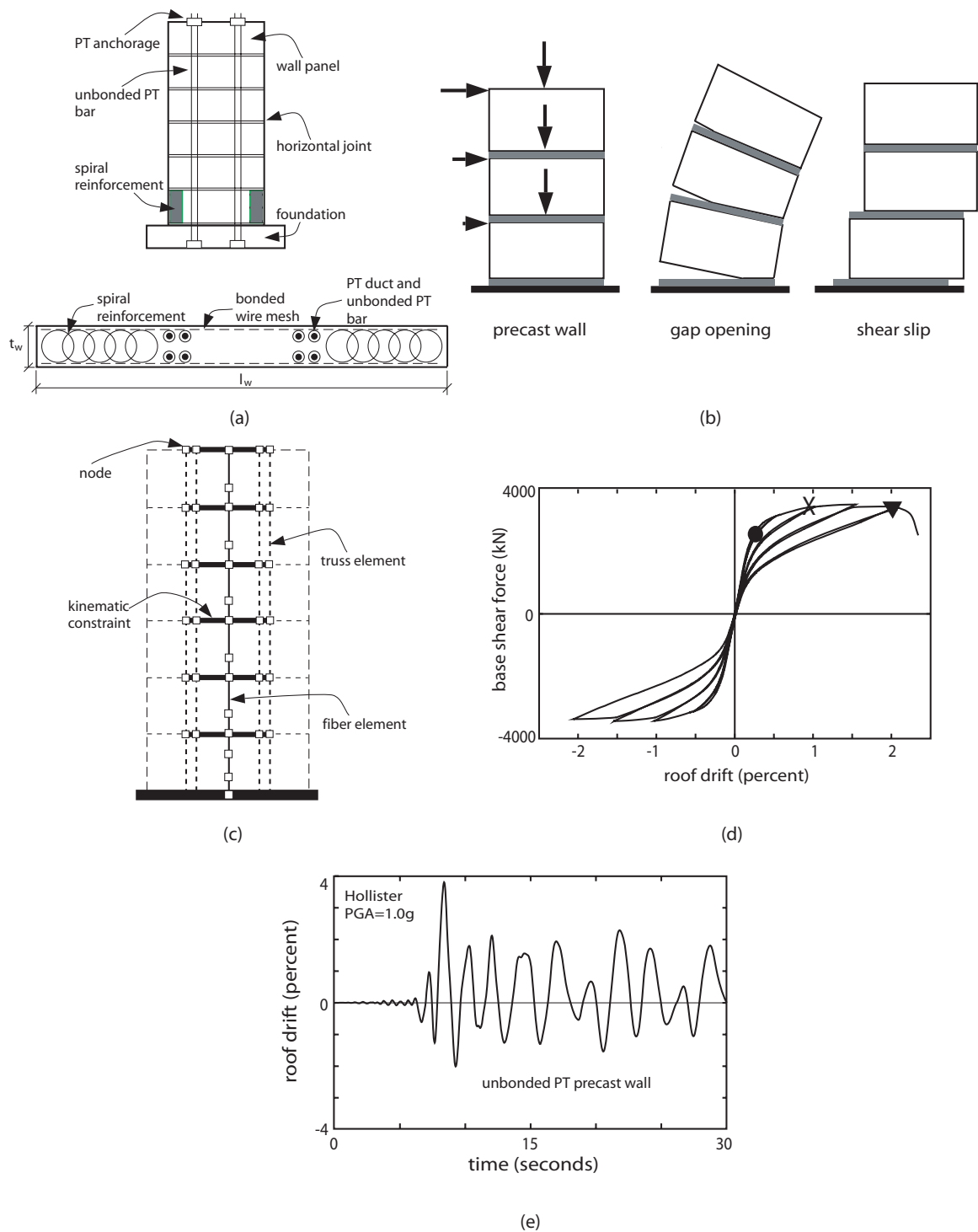


Fig. 2.15 Unbonded post-tensioned precast concrete walls (adapted from Kurama et al. 1999a): (a) wall elevation and cross-section; (b) gap opening and shear slip behavior; (c) analytical model; (d) behavior under cyclic lateral loads; (e) dynamic response

An analytical model (Fig. 2.15c) was developed using the DRAIN-2DX program (Prakash et al. 1993) to investigate the lateral load behavior of the walls (Kurama et al. 1996, 1999a). Fiber beam-column elements were used to model the precast concrete wall panels and truss elements were used to model the unbonded post-tensioning bars. Anchorages to the post-tensioning bars were modeled by kinematically constraining (i.e., slaving) the displacements of the truss element nodes to the wall fiber element nodes at the roof and at the foundation. Gap opening behavior along the horizontal joints was represented by using compression-only stress-strain relationships for the fibers used to model the wall panels.

The fiber wall model in Fig. 2.15c accounts for axial-flexural interaction, nonlinear hysteretic behavior of the post-tensioning steel and concrete including crushing of concrete, and gap opening behavior along the horizontal joints. Comparisons of analysis results obtained from the fiber wall model with results obtained from ABAQUS (Hibbitt, Karlsson, and Sorensen) finite element models that use gap/contact elements to model gap opening (Allen and Kurama 2002a, 200b) indicate that the fiber wall model is capable of predicting both the global (e.g., base shear versus roof lateral displacement) behavior and the local (e.g., gap opening and contact) behavior of the walls reasonably well (Kurama 2000).

A performance based seismic design approach for the walls was developed by Kurama et al. (1997, 2002) with two objectives: (1) to resist design level ground motions without significant damage; and (2) to resist severe survival level ground motions with damage, but without collapse. The seismic response of a series of prototype walls was evaluated based on nonlinear static push-over and reversed cyclic lateral load analyses as

well as nonlinear dynamic time-history analyses. As an example, Fig. 2.15d shows the expected base shear force versus roof lateral drift (i.e., roof lateral displacement divided by the wall height) behavior of a six-story wall designed for a region with high seismicity and a site with a “medium” soil profile (corresponding to Site Class D in IBC 2000) under cyclic lateral loads (Kurama et al. 1997). The behavior of the wall is nearly nonlinear-elastic with a large self-centering capability (i.e., small residual displacements) but with little inelastic energy dissipation.

The dynamic analyses were conducted under an ensemble of recorded and generated ground motions selected for the seismic regions and site soil characteristics used in the design of the walls (Kurama et al. 1997). As an example, Fig. 2.15e shows the roof drift time history of the wall in Fig. 2.15d under the Hollister ground motion (recorded on a site with a medium soil profile during the 1989 Loma Prieta earthquake), scaled to a peak acceleration of 1.0g to represent a survival level ground motion. Based on the results of the dynamic analyses, recommendations were made for the peak nonlinear lateral displacement demands and peak base shear demands for the walls.

Based on these analytical investigations, Kurama et al. (1996, 1997, 1998a, 1998b, 1999a, 1999b, 2002) concluded that unbonded post-tensioned precast concrete walls provide a feasible primary lateral load resisting structural system for use in regions with high seismicity. Similar to unbonded post-tensioned precast frames, the greatest disadvantage of these wall structures is that their lateral displacement demands during a severe earthquake may be larger than acceptable as a result of small inelastic energy dissipation. In order to reduce the seismic displacement demands, Perez (1998), Perez et al. (2004a, 2004b), and Priestley et al. (1999) investigated the use of ductile yielding

connectors along vertical joints between two or more walls. The use of supplemental viscous fluid-dampers and friction dampers to reduce the displacements of the walls was investigated by Kurama (2000, 2001). More recently, partially post-tensioned walls that use bonded mild (e.g., Grade 60) steel reinforcement crossing the horizontal joints in addition to the unbonded post-tensioning steel were investigated experimentally by Rahman and Restrepo (2000), Holden et al. (2001, 2003), and Restrepo (2003), and analytically by Kurama (2002, 2004). Additional research on unbonded post-tensioned walls with supplemental energy dissipation includes an analytical study on the use of dampers in series with the post-tensioning tendons at the wall base, including different tendon profiles (Ajrab et al. 2004).

Kurama (2002) conducted an analytical parameter study to investigate the effect of mild steel reinforcement on the lateral displacement response of unbonded post-tensioned precast concrete walls during earthquakes. A total of 12 wall structures with different amounts of mild steel and post-tensioning steel reinforcement were analyzed considering regions with high seismicity (e.g., coastal California) as well as regions with moderate seismicity (e.g., eastern U.S.). The effect of the number of stories on the behavior of the walls was examined by including ten-story, six-story, and four-story walls in the investigation.

It was shown that the energy dissipation of the walls can be increased considerably by using mild steel reinforcement, while maintaining a high level of self-centering capability. The use of mild steel has two important advantages on the dynamic behavior of the walls: (1) the maximum roof drift decreases; and (2) the number of large roof drift cycles decreases because the response of the wall decays faster. Based on the parametric

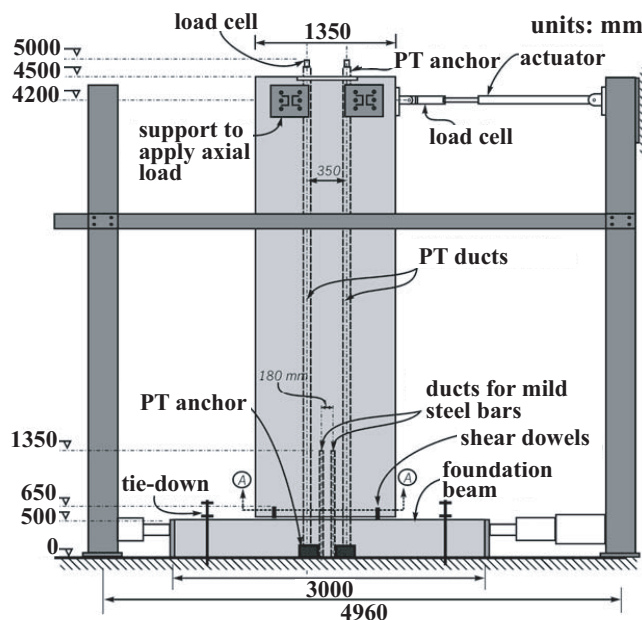
investigation, a seismic design approach was developed for partially post-tensioned precast walls (Kurama 2004), with the main objective of limiting the lateral displacements of a wall to a predetermined allowable displacement.

Rahman and Restrepo (2000), Holden et al. (2001, 2003), and Restrepo (2003) tested three half-scale partially post-tensioned precast concrete wall specimens, representative of a four story building under quasi-static reversed cyclic lateral loading. Fig. 2.16a shows the test set-up. Two of the specimens were identical, with the exception that gravity load was applied on one specimen but not on the other. The specimens were reinforced with two 0.5 inch diameter low relaxation post-tensioning strands and two 62 ksi mild steel bars crossing the horizontal joint between the wall and the foundation. The mild steel bars had a diameter of 0.79 in. but they were milled down to a diameter of 0.63 in. near the base of the wall in order to control yielding. The third specimen used steel fiber reinforced concrete for the wall and unbonded carbon fiber tendons instead of high-strength steel tendons to apply the post-tensioning force. A fourth specimen was also tested as a code compliant conventionally reinforced specimen designed to emulate the behavior of a ductile monolithic cast-in-place reinforced concrete wall.

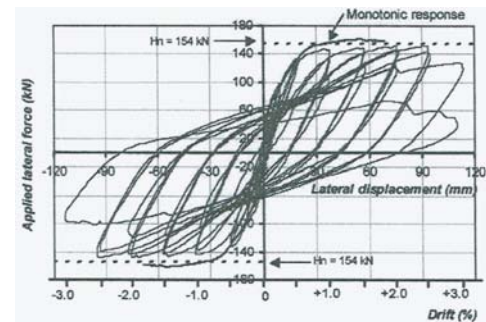
The experimental results showed that the specimen emulating monolithic cast-in-place reinforced concrete construction dissipated more energy than the partially post-tensioned systems; however, it sustained significant structural damage and residual displacements (see Fig. 2.16b). In contrast, the amount of structural damage was markedly reduced in the partially post-tensioned specimens and the residual displacements upon unloading were negligible. Figs. 2.16c and 2.16d show the hysteretic

lateral load versus drift behavior of one of the partially post-tensioned specimens and the extent of damage in the structure at 3% drift (Restrepo 2003).

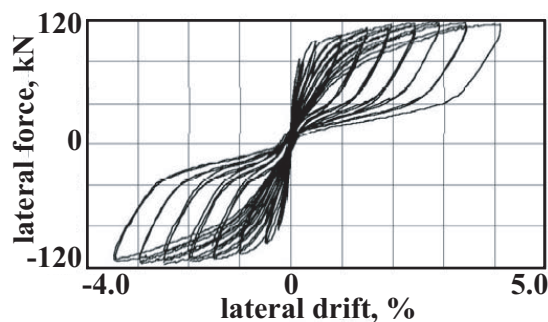
The analytical and experimental research efforts summarized above have recently led to the development of draft acceptance criteria for the use of post-tensioned precast concrete structural walls in seismic regions (ACI Innovation Task Group and Collaborators 2004).



(a)



(b)



(c)



(d)

Fig. 2.16 Experiments of precast concrete walls (from Holden et al. 2003 and Restrepo 2003): (a) test setup; (b) hysteretic response of emulative wall; (c) hysteretic response of partially post-tensioned wall; (d) photograph of partially post-tensioned wall at 3% drift

2.6 Behavior of Top and Seat Angles

As discussed in the preceding sections, it is possible to reduce the lateral displacement demands of unbonded post-tensioned frame and wall structures by using supplemental passive energy dissipation, without losing the desirable characteristics of these structures. Using steel top and seat angles at the frame or wall joints where gap opening occurs is one way of providing energy dissipation and increasing structural redundancy as shown in Figs. 1.3 and 2.11.

A significant amount of previous research has been conducted on steel frame beam-to-column connections that use top and seat angles (e.g., Azizinamini 1985; Aktan et al. 1989; Youssef-Agha et al. 1989; Kishi and Chen 1990; Lorenz et al. 1993; Bernuzzi et al. 1994, 1997; Leon and Shin 1994; Mander et al. 1994; Sarraf and Bruneau 1996; Bernuzzi 1998; Kasai 1998; Kukreti and Abolmaali 1999; Swanson and Leon 1999; Shen and Astaneh-Asl 1999, 2000; Sims 2000; Ricles et al. 2000, 2001; Garlock 2002; Garlock et al. 2003). Fig. 2.17a shows the idealized exaggerated deformed configuration of a top-and-seat-angle steel frame connection, which is a semi-rigid connection comprised of a pair of steel angles bolted to the flanges of the beam and the column. Fig. 2.17b shows some of the design parameters for the connection angles.

The flexural stiffness, strength, and ductility of a top-and-seat-angle beam-to-column connection are influenced by many design parameters, including: (1) beam depth, d_b ; (2) angle length, l_a (which is usually equal to the beam flange width); (3) angle leg thickness, t_a ; (4) angle steel yield strength, f_{ay} ; (5) angle-to-column connection gage

length, l_{gv} , measured from the heel of the angle to the center of the innermost angle-to-column connectors; (6) angle-to-beam connection gage length, l_{gh} , measured from the heel of the angle to the centroid of the angle-to-beam connector bolt group; (7) angle fillet length, k_a , measured from the angle heel to the toe of the angle fillet; (8) angle connector bolt type and diameter, d_{ab} ; (9) bolt head/nut width measured across flat sides, w_{ab} ; and (10) number of bolts, n_{ab} . The previous research conducted by Kishi and Chen (1990) and Lorenz et al. (1993), Sims (2000), Ricles et al. (2001), and Garlock et al. (2003) on the behavior of the connection angles is described below.

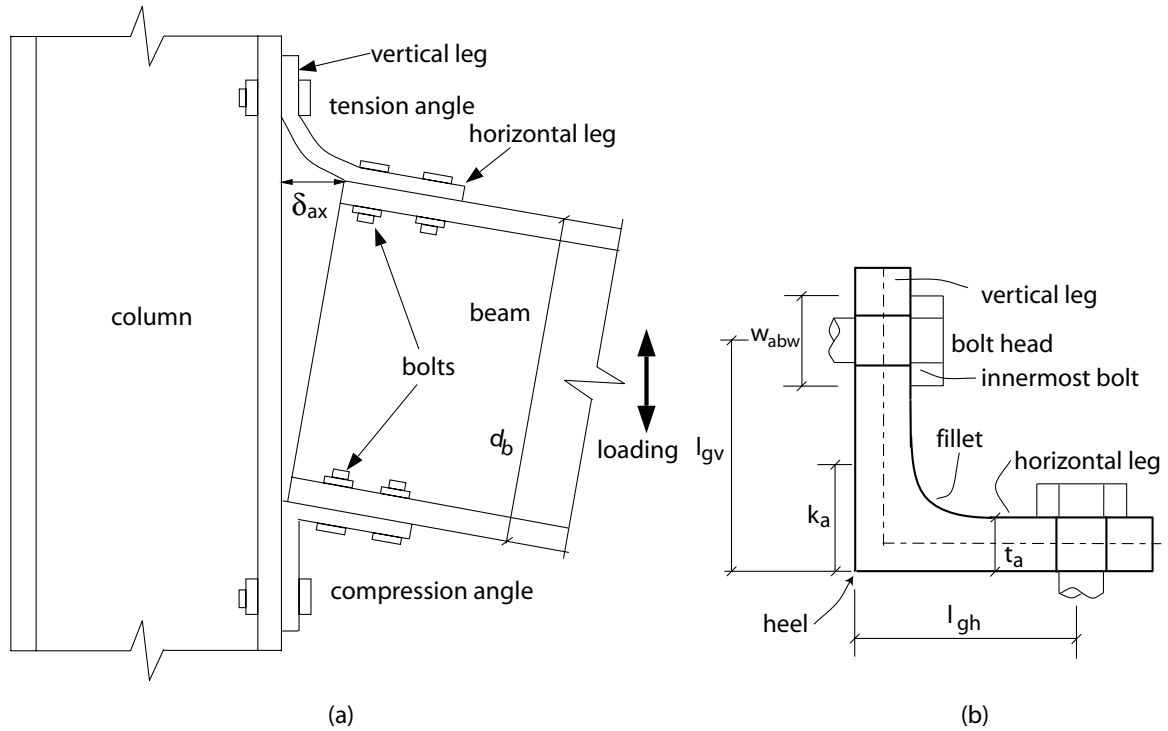


Fig. 2.17 Top-and-seat angle connection:
(a) deformed configuration; (b) angle parameters

2.6.1 Kishi and Chen (1990) and Lorenz et al. (1993)

Kishi and Chen (1990) and Lorenz et al. (1993) developed a model for the analysis and design of steel top-and-seat-angle beam-to-column connections based on equilibrium considerations with assumed internal force distributions and boundary conditions for the angles. An overview of their model is given below since it is used to describe the behavior of the angles at the beam-to-wall connections in this dissertation. Other researchers (e.g., Goto et al. 1991; Matsuoka et al. 1993) have also used this model to investigate the behavior of semi-rigid steel frame connections. Several other similar top-and-seat angle connection models exist (e.g., Sarraf and Bruneau 1996; Aktan et al. 1989).

Note that the model developed by Kishi and Chen (1990) and Lorenz et al. (1993) can only be used to estimate the initial stiffness and yield force capacity of the tension angle (see Fig. 2.17a) in a top-and-seat angle connection under monotonic loading. The post-yield behavior of the tension angle, the behavior of the compression angle, and the behavior of the connection under cyclic loading are not addressed in their investigation.

Tension angle initial stiffness, K_{aixt}

The initial linear-elastic stiffness of the tension angle is determined by assuming that the vertical leg of the angle is fixed along the innermost edge of the line of angle-to-column connection bolt heads and is pulled as a cantilever by the beam flange as shown in Fig. 2.18. Considering the shear deformations of the vertical angle leg, it can be shown that the initial linear-elastic stiffness of the angle, K_{aixt} is given as:

$$K_{aixt} = \frac{T_{ax}}{\delta_{ax}} = \frac{3E_a I_a}{l_{gl}(l_{gl}^2 + 0.78t_a^2)} \quad (2.5)$$

where, T_{ax} is the force in the tension angle parallel to the beam, δ_{ax} is the horizontal displacement of the heel of the angle (see Fig. 2.17a), $E_a I_a$ is the flexural stiffness of the angle vertical leg cross section, t_a is the thickness of the angle, and l_{gl} is the length of the vertical leg that is assumed to act as a cantilever beam. Using centerline dimensions for the angle legs and referring to Fig. 2.18a,

$$l_{gl} = l_{gv} - \frac{w_{abw}}{2} - \frac{t_a}{2} \quad (2.6)$$

where, w_{abw} is the width (across flats) of the angle-to-column connector bolt head/nut and l_{gv} is the angle vertical leg connection gage length measured from the heel of the angle to the center of the innermost angle-to-column connectors as shown in Fig. 2.18a.

Tension angle yield force capacity, T_{ayx}

The yield force capacity, T_{ayx} of the tension angle is determined based on an assumed plastic hinge mechanism in the vertical leg as shown in Fig. 2.18b. One of the plastic hinges is located along the innermost edge of the angle-to-column connection bolt heads/nuts and the other plastic hinge is located along the toe of the fillet. The work equation for the tension angle at this plastic mechanism state is given by

$$2M_{ap}\kappa = V_{ap}l_{g2}\kappa \quad (2.7)$$

where, M_{ap} is the plastic moment and V_{ap} is the plastic shear force in the vertical leg, and κ is the plastic hinge rotation as shown in Fig. 2.18b. Based on the free body diagram of

the angle horizontal leg in Fig. 2.18c, the tension angle yield force, T_{ayx} is equal to the plastic shear force V_{ap} in the vertical leg.

The distance l_{g2} in Equation (2.7) is the “effective” gage length for the assumed plastic hinge mechanism equal to the distance between the two plastic hinges as:

$$l_{g2} = l_{gv} - \frac{w_{abw}}{2} - k_a \quad (2.8)$$

where, w_{abw} is the width of angle-to-column connection bolt head/nut measured across flat sides and k_a is the distance from heel to toe of fillet of the angle. Since l_{g2} is usually rather short, a shear-flexure interaction equation is considered in the calculation of the capacity of the angle as follows:

$$\frac{M_{ap}}{M_{a0}} + \left(\frac{V_{ap}}{V_{a0}} \right)^4 = 1 \quad (2.9)$$

where, M_{a0} and V_{a0} are the plastic moment and plastic shear force in the vertical leg without considering shear-flexure interaction, respectively as

$$M_{a0} = \frac{f_{ay} l_a (t_a)^2}{4} \quad (2.10)$$

$$V_{a0} = \frac{f_{ay} l_a t_a}{2} \quad (2.11)$$

in which f_{ay} is the yield strength of the angle steel and l_a is the length of the angle. Substituting Equations (2.7), (2.10), and (2.11) into Equation (2.9), the angle yield force $T_{ayx}=V_{ap}$ can be determined from

$$\frac{l_{g2}}{t_a} \left(\frac{V_{ap}}{V_{a0}} \right) + \left(\frac{V_{ap}}{V_{a0}} \right)^4 = 1 \quad (2.12)$$

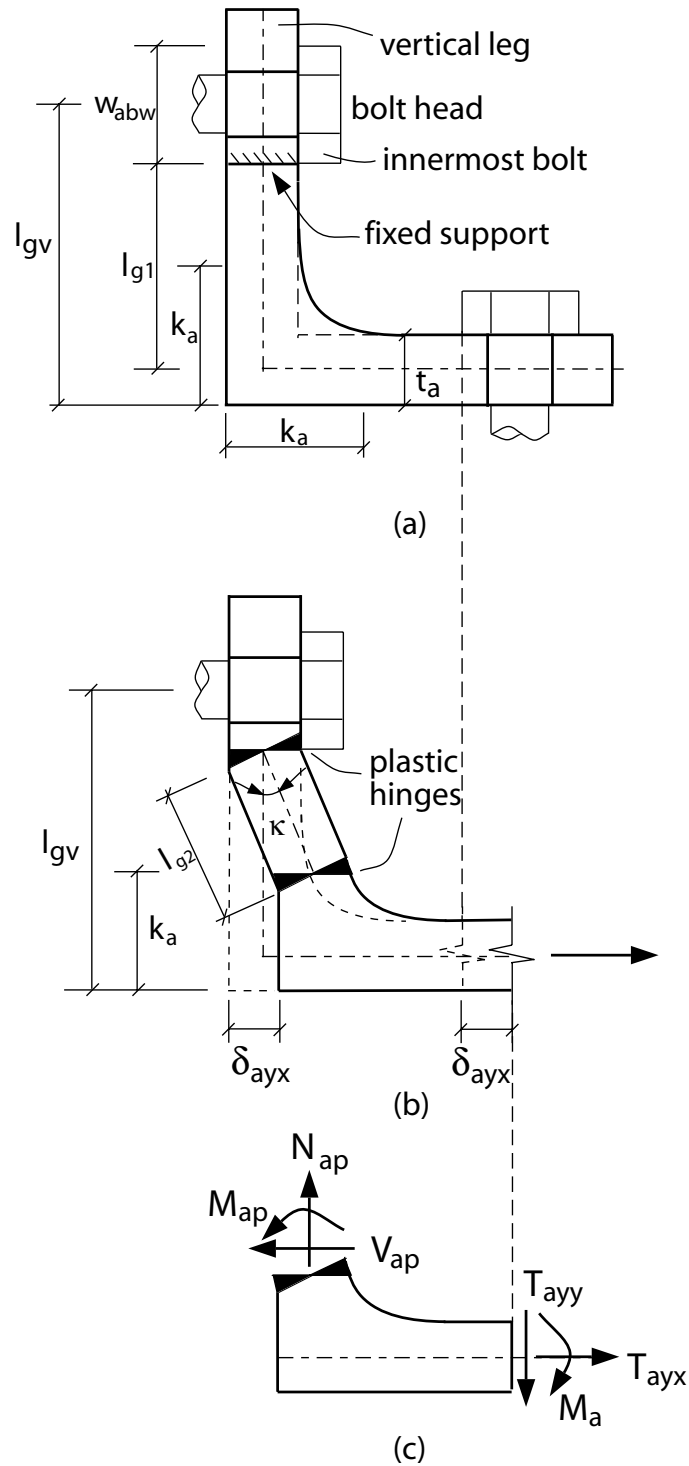


Fig. 2.18 Angle model (adapted from Kishi and Chen 1990 and Lorenz et al. 1993):
 (a) cantilever model of tension angle; (b) assumed yield mechanism;
 (c) free body diagram of angle horizontal leg

Note that in Fig. 2.18c, the horizontal leg of the angle is cut along the innermost edge of the angle-to-beam connection bolt heads/nuts. At this location, it is assumed that the moment M_a is small, and is ignored. Moreover, the shear force of the horizontal leg, T_{ayy} and the corresponding axial force, N_{ap} at the plastic hinge are also ignored.

2.6.2 Sims (2000)

Sims (2000) conducted a parametric finite element investigation of top-and-seat-angle beam-to-column connections. The column was assumed to be rigid and fixed, and reversed cyclic transverse displacements were applied at the beam end. A companion experimental program was also conducted. The finite element model, which was developed using the ANSYS program (Swanson Analysis Systems 1997), included material and geometric nonlinearities and captured aspects of bolt behavior such as pre-load, slip, axial and flexural flexibility, and inelasticity.

Five failure modes for the angles were identified from the finite element analyses: (1) bolt thread failure; (2) bolt/angle flexural mechanism; (3) shear mechanism; (4) vertical-leg/horizontal-leg combination mechanism; and (5) vertical-leg mechanism. The vertical-leg mechanism is similar to the failure mechanism in Fig. 2.18b. According to Sims (2000), this failure mechanism represents an ideal mode with a relatively more uniform distribution of strain, resulting in the lowest maximum strain in the angle. It was found that for angle configurations with vertical-leg mechanism failure modes, the model developed by Kishi and Chen (1991) and Lorenz et al. (1993) can be used to estimate the angle yield force, T_{ayx} . However, since the plastic deformations in the horizontal leg (i.e.,

leg parallel to the beam) and the effect of bolt response are neglected in this analytical model, the angle yield force for the other failure modes can not be estimated especially for angle configurations with non-negligible bolt response (e.g., bolt elongation, slip, yielding, fracture).

The following additional conclusions were made based on the finite element analyses:

(1) Bolt response reduces the strength, stiffness, and ductility of the angle system. Due to the less ductile properties of high strength bolts compared to angle sections, configurations with bolt fracture are less ductile than those with angle fracture. Thus, failure of the bolts should be avoided.

(2) For short effective gage length l_{g2} values, the maximum strain in the angle occurs along the innermost edge of the vertical leg connection bolt heads/nuts. For long l_{g2} values, the maximum strain occurs along the toe of the fillet in the vertical leg. For intermediate l_{g2} values, the maximum strain in the angle occurs along the toe of the fillet in the horizontal leg (leg parallel to the beam). “Strong” and “ductile” top and seat angle configurations exist between l_{g2} values of 1 to 2 in. This range represents an actual gage length l_{gv} of between 3 to 4 in., depending on the angle and bolt sizes. In this range, optimal efficiency of the angle in terms of the amount of angle strength per plastic strain (i.e., maximum force capacity of the angle for a given plastic strain demand) could be reached.

(3) The boundary condition of the horizontal leg connection bolts is an important factor affecting the behavior of the angles. Neglecting the rotations of the horizontal leg results in an overestimation of the tension angle yield force capacity.

(4) Catenary effects at large angle deformations play a very significant role on the angle behavior. Inclusion of large deflections (i.e., second order geometric effects) in the analytical model is necessary to accurately capture these effects.

The isolated angle experiments conducted by Sims (2000) showed good agreement with the finite element analytical results. The plan view of the experimental setup is shown in Fig. 2.19a. Two angles were placed back-to-back and loaded against a support fixture modeling a rigid column, where the applied force of $2T_{ax}$ represents the combined resistance of the angle pair. Three monotonic and eleven cyclic loading experiments were conducted. Figs. 2.19b and 2.19c show representative angle force versus deformation (T_{ax} - δ_{ax}) relationships from two cyclic experiments, each with a “vertical-leg” angle failure mechanism. One of the important conclusions from this experimental program was that bolt slip in the angle horizontal leg is a cause of significant stiffness reduction of the angle. One option for eliminating this bolt slip is to weld the angle horizontal leg to the beam flange. In the absence of this measure, a large number of slip critical bolts may be required for the angle-to-beam connections.

2.6.3 Ricles et al. (2001)

As described previously in Fig. 2.14, Ricles et al. (2001) modeled each angle in their post-tensioned steel beam-column connection using two parallel bilinear truss

element springs in the DRAIN-2DX program (Prakash et al. 1993). The truss element springs represent the behavior of the angle when gap opening occurs at the beam-to-column interface. Elongation and shortening of the springs result in forces that are equivalent to the shear force in the vertical leg of the angle. The combined force-deformation behavior of the two parallel bilinear springs produces a trilinear force-deformation relationship for each angle as described below.

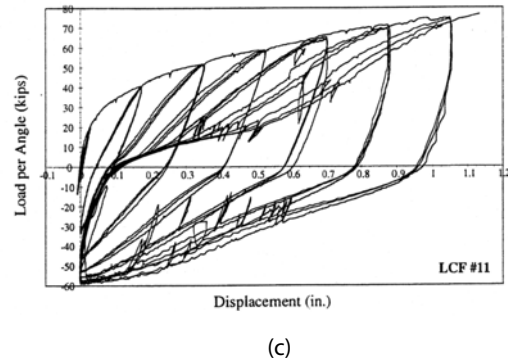
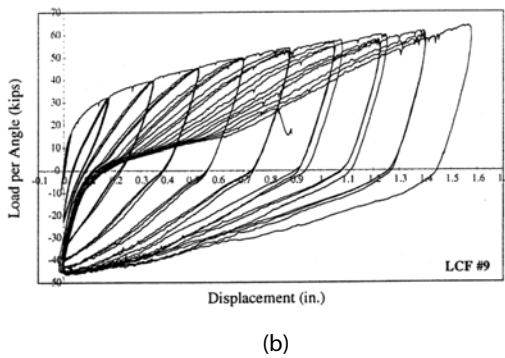
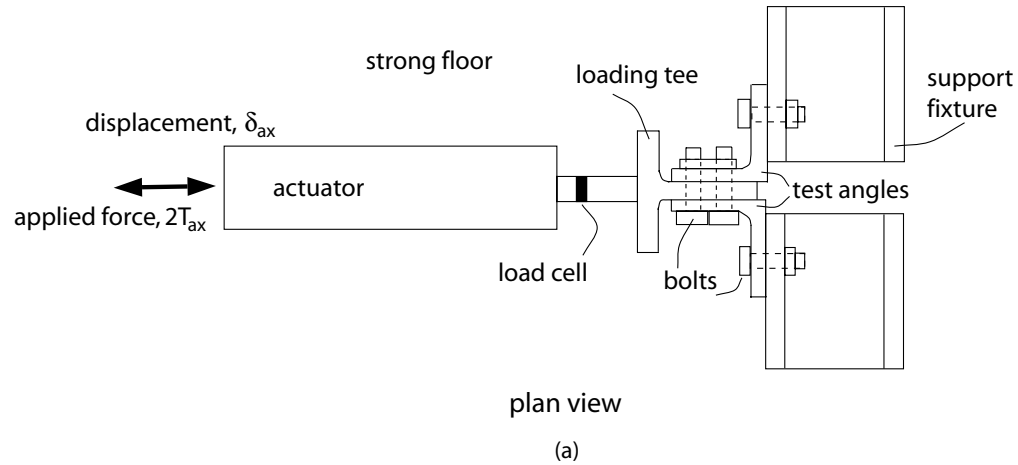


Fig. 2.19 Isolated angle experiments (from Sims 2000): (a) plan view of test setup; (b) angle force-deformation relationship of Specimen 9; (c) angle force-deformation relationship of Specimen 11

Ricles et al. (2001) determined the properties of the parallel spring model by fitting a trilinear curve to the expected force-deformation behavior of the angles, where the angle deformation is equivalent to δ_{ax} in Fig. 2.17. The expected angle force-deformation behavior was obtained from analyses of a model of the angle using fiber beam-column elements in the DRAIN-2DX program. Each angle leg was modeled using one fiber element having several segments, accounting for shear and flexural deformations. Fig. 2.20a shows two angle fiber element models (Models A and B) and the loading and boundary conditions used to determine the angle force-deformation behavior. The effects of prying forces were anticipated to be small due to the relatively long angle gage lengths, and thus, were ignored.

The angle force-deformation behaviors from Models A and B and the corresponding trilinear parallel spring models are shown in Fig. 2.20b. The accuracy of the angle models was verified by comparing the analytical results with experimental results for post-tensioned steel beam-column connection subassemblages (Fig. 2.13a). As shown in Fig. 2.20c, the analytical results for the subassemblages were found to be not too sensitive to the differences between Models A and B. The behavior and modeling of the angles under cyclic loading are not discussed in detail by Ricles et al. (2001).

2.6.4 Garlock et al. (2003)

Garlock et al. (2003) experimentally investigated the behavior of the angles in a bolted top-and-seat angle beam-to-column connection under cyclic loading. Seven specimens were tested to determine how the angle size, gage length, and angle-to-column

connection washer plate (see Fig. 2.11) affect the connection stiffness, strength, energy dissipation, and resistance to low cycle fatigue. All seven specimens developed a yield mechanism with three plastic hinges – two hinges in the angle leg attached to the column (similar to the hinges in Fig. 2.18b) and one hinge along the toe of the fillet in the angle leg attached to the beam. An analytical model was developed based on the experimental results to predict the angle initial stiffness, force at yield mechanism, post-yield stiffness, and unloading behavior. The main conclusions from this research include:

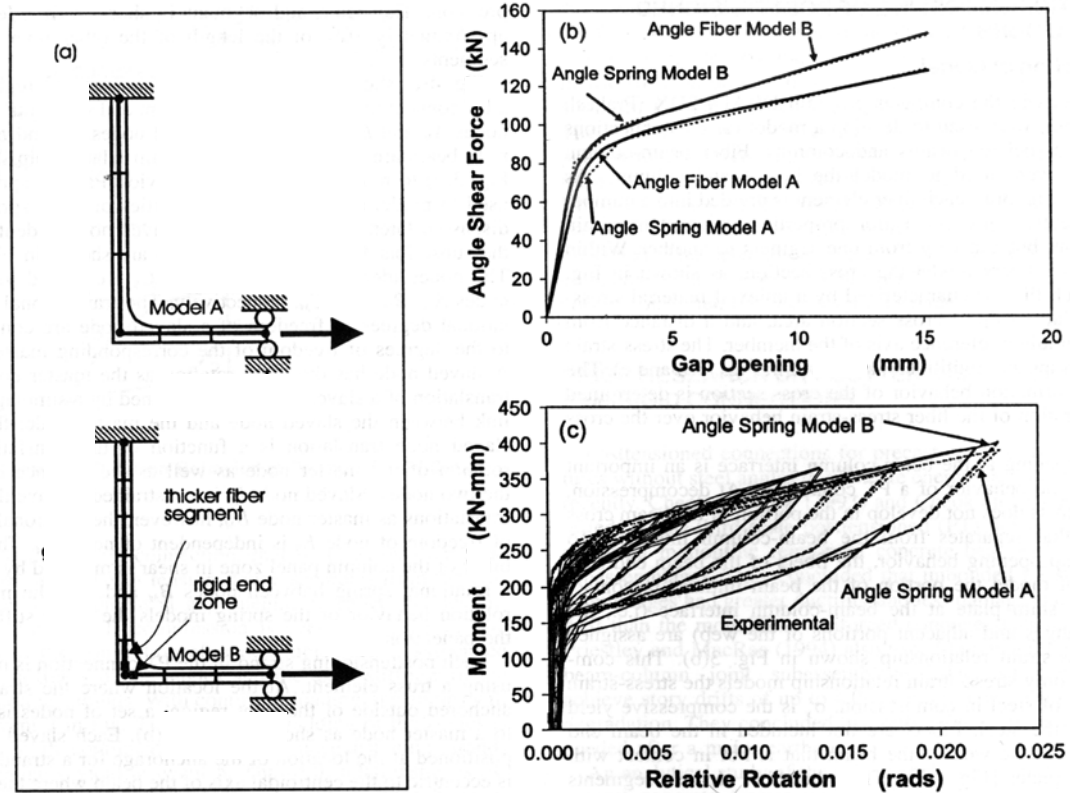


Fig. 2.20 Modeling of top and seat angles (from Ricles et al. 2001): (a) fiber Models A and B; (b) fiber model and spring model behaviors; (c) comparisons with test results.

(1) Following the formation of the plastic hinge mechanism, the angle stiffness greatly decreases but does not become zero. This post-yield stiffness is nearly linear and is comprised of both geometric hardening and material hardening. The geometric hardening accounts for slightly less than half of the total post-yield stiffness.

(2) Angles with smaller ratios of gage length to angle thickness (l_{g2}/t_a) dissipate more energy for a given value of angle displacement and are stronger and stiffer than angles with larger l_{g2}/t_a ratios. However, angles with smaller l_{g2}/t_a ratios have less resistance to low-cycle fatigue. Thus, the angle gage length and thickness must be selected considering the stiffness, strength, energy dissipation, and ductility requirements of the connection.

(3) The washer plates that were used in the angle-to-column connections have no significant influence on the bolt prying forces and are not effective in influencing the location of the plastic hinge for angles with small l_{g2}/t_a ratios. Furthermore, angles without washer plates are capable of undergoing several more cycles until failure, implying that the small decrease in gage length caused by the washer plates reduces the angle's resistance to low-cycle fatigue. Thus, washer plates are not recommended for use in bolted top-and-seat angle connections.

2.7 Chapter Summary

A summary of the important findings from the literature review presented in this chapter is given below.

(1) Coupled wall structural systems are effective primary lateral load resisting systems for seismic regions. The coupling degree is an important parameter for the seismic behavior and design of these structures.

(2) Concrete coupling beams require the use of diagonal reinforcement to prevent premature failure modes due to diagonal tension and sliding shear.

(3) Embedded steel coupling beams possess large ductility capacity and energy dissipation; however, they are prone to significant damage during a large earthquake, possibly resulting in considerable residual deformations after unloading.

(4) Unbonded post-tensioning has been successfully applied to different types of building systems in seismic regions. In an unbonded post-tensioned structure, the nonlinear behavior occurs primarily as a result of the opening of gaps along the joints between the structural members, and not as a result of material nonlinearity. Thus, these structures can undergo large lateral displacements with little damage and possess large self-centering capability due to the restoring effect of the post-tensioning force. The greatest setback to the use of unbonded post-tensioned structures in seismic regions is that their lateral displacement demands during a severe earthquake may be larger than acceptable as a result of small energy dissipation.

(5) Fiber beam-column elements has been successfully used to model the nonlinear hysteretic behavior of different types of unbonded post-tensioned structures, including the opening of gaps at the joints between the structural members.

(6) Steel top and seat angles are effective structural components that can be used at the gap opening connections to provide energy dissipation and structural redundancy

during an earthquake. In a properly-designed post-tensioned top and seat angle connection, the only components to receive significant damage are the angles, which can be replaced after the earthquake.

CHAPTER 3

ANALYTICAL MODELING OF COUPLED WALL SUBASSEMBLAGES

This chapter describes the analytical modeling of hybrid coupled wall subassemblages as follows: (1) prototype subassemblage; (2) analytical modeling assumptions; (3) fiber element subassemblage model; (4) verification of fiber element subassemblage model; (5) advantages and limitations of fiber element model; and (6) modeling of embedded steel coupling beams. The subassemblage models described in this chapter are later used to construct analytical models of multi-story coupled wall structures in this dissertation.

3.1 Prototype Subassemblage

A prototype floor-level unbonded post-tensioned hybrid coupled wall subassemblage (similar to Fig. 1.3) was designed as part of an eight-story structure for a site with a “stiff” soil profile (Site Class *D* in IBC-2000) in a region with high seismicity (coastal California). The structural design properties of the subassemblage are summarized in Tables 3.1-3.4 and described below.

TABLE 3.1

PROTOTYPE SUBASSEMBLAGE COUPLING BEAM PROPERTIES

Coupling Beam Properties	
Section	W21×182
Beam length, l_b	3.05 m (10 ft)
Beam depth, d_b	577 mm (22.72 in.)
Flange thickness, t_{bf}	37.6 mm (1.48 in.)
Flange width, b_{bf}	318 mm (12.5 in.)
Web thickness, t_{bw}	21 mm (0.83 in.)
Beam cross section area, A_b	34581 mm ² (53.6 in ²)
Beam moment of inertia, I_b	19.7 m ⁴ (4730 in ⁴)
Flange cover plate thickness, t_c	38.1 mm (1.5 in.)
Flange cover plate width, b_c	318 mm (12.5 in.)
Flange cover plate length, l_c	406 mm (16 in.)

TABLE 3.2

PROTOTYPE SUBASSEMBLAGE BEAM POST-TENSIONING PROPERTIES

Beam Post-Tensioning Properties	
Beam post-tensioning strand diameter, d_{bp}	15.2 mm (0.6 in.)
Number of strands per beam post-tensioning tendon, n_{bp}	3
Beam post-tensioning tendon area, a_{bt}	420 mm ² (0.651 in ²)
Number of beam post-tensioning tendons, n_{bt}	6
Total beam post-tensioning steel area, A_{bp}	2520 mm ² (3.906 in ²)
Unbonded length of beam post-tensioning tendons, l_{bpu}	9.14 m (30 ft)
Initial stress in beam post-tensioning steel, f_{bpi}	0.6 f_{bpu}

TABLE 3.3

PROTOTYPE SUBASSEMBLAGE BEAM-TO-WALL CONNECTION

TOP AND SEAT ANGLE PROPERTIES

Beam-to-Wall Connection Top and Seat Angle Properties	
Section	L8×8×1-1/8
Angle length, l_a	318 mm (12.5 in.)
Angle leg length, l_{al}	203 mm (8 in.)
Angle leg thickness, t_a	28.6 mm (1.125 in.)
Angle fillet length, k_a	44.5 mm (1.75 in.)
Number of angle-to-wall connection bolts, n_{abw}	8
Number of angle-to-beam connection bolts, n_{abb}	8
Angle-to-wall connection bolt diameter, d_{abw}	22.2 mm (7/8 in.)
Angle-to-beam connection bolt diameter, d_{abb}	25.4 mm (1 in.)
Angle-to-wall connection bolt head width across flats, w_{abw}	36.5 mm (1.4375 in.)
Angle-to-wall connection gage length, l_{gv}	106 mm (4.1875 in.)
Angle-to-beam connection gage length, l_{gh}	127 mm (5 in.)

TABLE 3.4
PROTOTYPE SUBASSEMBLAGE WALL PROPERTIES

Wall Properties	
Wall length, l_w	3.05 m (10 ft)
Wall thickness, t_w	356 mm (14 in.)
Wall storey height, h_s	3.96 m (13 ft)
Wall-contact region embedded plate thickness, t_e	31.8 mm (1.25 in.)
Wall-contact region spiral diameter, D_{bsp}	292 mm (11.5 in.)
Wall-contact region spiral wire diameter, d_{bsp}	12.8 mm (0.504 in.)
Wall-contact region spiral pitch, s_{bsp}	31.8 mm (1.25 in.)
Wall-contact region spiral reinforcement ratio, ρ_{bsp}	5.57%

The elevation view of the prototype subassembly is shown in Fig. 3.1a, with the top and seat angle connection details provided in Fig. 3.1b. The design of similar subassemblies is described in detail in Chapter 12. The story height $h_s = 3.96$ m (13 ft), wall length $l_w = 3.05$ m (10 ft), wall thickness $t_w = 356$ mm (14 in.) uniform, and coupling beam length $l_b = 3.05$ m (10 ft).

The coupling beam has a W21×182 cross section and the top and seat angles have a L8×8×1-1/8 cross section. Note that the steel section designations in this dissertation follow standard U.S. nomenclature. Also note that this research focuses on beams with I sections; however, the findings can be extended to other types of steel beams, such as with hollow (e.g., box-shaped) sections. One of the advantages of unbonded post-tensioned coupling beams over embedded steel beams is that the selection of the beam cross section is not affected by the reinforcing details inside the walls. The beam flange width is limited to the wall thickness.

The prototype subassembly is post-tensioned using six multi-strand tendons, three tendons on each side of the beam web as shown in Fig. 3.1a. Each tendon consists of three 15.2 mm (0.6 in.) nominal diameter high-strength seven-wire strands with a total area of $a_{bt} = 420 \text{ mm}^2$ (0.651 in²). The tendons are prestressed to $f_{bpi} = 0.60f_{bpu}$, where $f_{bpu} = 1862 \text{ MPa}$ (270 ksi) is the design maximum strength of the post-tensioning strands. The stress $f_{bpi} = 0.60f_{bpu}$ represents the design initial stress assumed to act in the beam post-tensioning tendons just before the application of lateral loads. The initial stress at the ends of the coupling beam (including the flange cover plates) due to post-tensioning is $f_{bi} = 48 \text{ MPa}$ (6.96 ksi), which is equal to $0.13f_{by}$ where $f_{by} = 362 \text{ MPa}$ (52.5 ksi) is the assumed yield strength of the beam steel.

Two steel spirals are used to confine the concrete in each wall region, one spiral near each beam flange as shown in Fig. 3.1a. The spiral center-to-center diameter $D_{bsp} = 292 \text{ mm}$ (11.5 in.), spiral W20 wire diameter $d_{bsp} = 12.8 \text{ mm}$ (0.504 in.), and spiral pitch $s_{bsp} = 31.8 \text{ mm}$ (1.25 in.), resulting in a spiral reinforcement ratio of $\rho_{bsp} = 5.57\%$ (defined as the ratio of the volume of spiral reinforcement to the volume of spiral confined concrete core).

The angle-to-wall connections consist of eight 22.2 mm diameter ASTM A490 bolts and the angle-to-beam connections consist of eight 25.4 mm diameter slip-critical ASTM A490 bolts as shown in Fig. 3.1b.

3.1.1 Subassembly Material Properties and Idealizations

This section describes assumed material properties for: (1) the steel used in the coupling beam, angles, cover plates, and wall embedded plates; (2) the beam post-

tensioning strands; and (3) the unconfined and spiral confined concrete in the wall-contact regions. Multi-linear idealizations to the assumed smooth uniaxial material stress-strain relationships are also provided for modeling purposes.

The subassembly material design properties are listed in Table 3.5.

TABLE 3.5
PROTOTYPE SUBASSEMBLY MATERIAL PROPERTIES

Beam, Angle, Cover Plate, Wall Embedded Plate Steel		Beam Post-Tensioning Strands		Wall-Contact Region Spiral Wire		Wall-Contact Region Concrete			
						Unconfined Concrete		Spiral Confined Concrete	
Yield strength, f_{sy}	362 MPa (52.5 ksi)	Yield strength, f_{bpy}	1689 MPa (245 ksi)	Yield strength, f_{spy}	414 MPa (60 ksi)	Linear-elastic stiffness, E_c	30441 MPa (4415 ksi)	Linear-elastic stiffness, E_c	30441 MPa (4415 ksi)
Yield strain, ϵ_{sy}	0.00181	Yield strain, ϵ_{bpy}	0.00860	Yield strain, ϵ_{spy}	0.00207	Maximum strength, f_c'	41.4 MPa (6 ksi)	Maximum strength, f_{cc}	91.0 MPa (13.2 ksi)
Maximum strength, f_{sm}	470 MPa (68.2 ksi)	Maximum strength, f_{bpu}	1862 MPa (270 ksi)	Maximum strength, f_{spm}	621 MPa (90 ksi)	Strain at max. strength, ϵ_c'	0.002	Strain at max. strength, ϵ_{cc}	0.0140
Strain at max. strength, ϵ_{sm}	0.14	Strain at max. strength, ϵ_{bpu}	0.05	Strain at max. strength, ϵ_{spm}	0.08	Ultimate strain, ϵ_{cu}	0.003	Ultimate strain, ϵ_{ccu}	0.0323

Fig. 3.2a shows the assumed smooth (dashed line) and idealized tri-linear (solid line) stress-strain relationships of the steel used in the coupling beam, angles, cover plates, and wall embedded plates. The yield strength and maximum strength of the steel are equal to $f_{sy} = 362$ MPa (52.5 ksi) and $f_{sm} = 470$ MPa (68.2 ksi), respectively. The post-yield stiffness of the idealized stress-strain relationship is determined from the portion of the smooth stress-strain relationship between the yield strain, ϵ_{sy} , and a strain of $\epsilon_{sm} = 0.14$ at which the maximum strength, f_{sm} , is assumed to be reached. The ratio of the idealized post-yield stiffness to the initial linear-elastic stiffness $E_s = 199955$ MPa (29000 ksi) is equal to 0.00393.

The assumed smooth (dashed line) and idealized bi-linear (solid line) stress-strain relationships of the post-tensioning strands are shown in Fig. 3.2b. The yield strength and maximum strength of the post-tensioning strands are equal to $f_{bpy}=1689$ MPa (245 ksi) and $f_{bpu}=1862$ MPa (270 ksi), respectively. The yield strength f_{bpy} is assumed to be equal to the linear limit stress (i.e., the limit of proportionality) of the smooth stress-strain relationship. Since the post-tensioning tendons are not bonded to the concrete, the peak strains in the strands during an earthquake are expected to remain small. Thus, the post-yield stiffness of the idealized bi-linear stress-strain relationship in Fig. 3.2b was determined by assuming that the maximum strength, $f_{bpu}=1862$ MPa (270 ksi) is reached at a strain of 0.0116, to represent the portion of the smooth stress-strain relationship between the yield strain, ϵ_{bpy} , and the largest strain expected in the strands as the subassembly is displaced. The ratio of the idealized post-yield stiffness to the initial linear-elastic stiffness $E_{bp}=196508$ MPa (28500 ksi) of the post-tensioning strands is equal to 0.292.

The wall unconfined concrete maximum compressive strength is assumed to be $f'_c=41.4$ MPa (6 ksi) reached at a strain of $\epsilon'_c=0.002$, and the concrete initial linear-elastic stiffness is assumed to be $E_c=4730\sqrt{f'_c}=30442$ MPa (or $E_c=57000\sqrt{f'_c}=4415201$ psi). It is assumed that the crushing of the unconfined concrete occurs at a strain of $\epsilon_{cu}=0.003$. Fig. 3.2c shows the smooth (dashed line) and idealized multi-linear (solid line) compressive stress-strain relationships of the unconfined concrete.

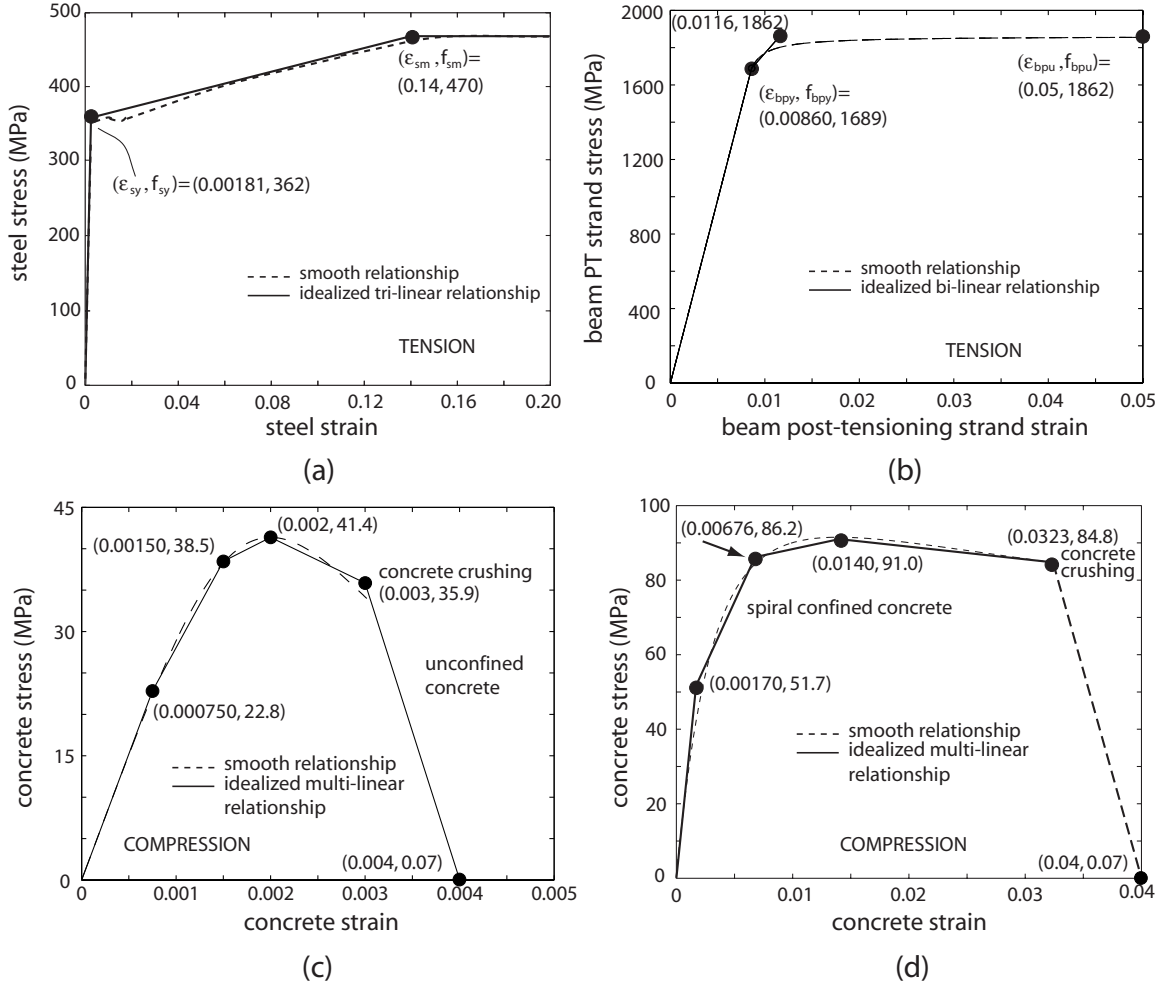


Fig. 3.2 Subassembly material properties and idealizations: (a) steel; (b) beam post-tensioning strand; (c) wall unconfined concrete; (d) wall-contact region confined concrete

Similarly, Fig. 3.2d shows the smooth (dashed line) and idealized multi-linear (solid line) compressive stress-strain relationships of the spiral confined concrete in the wall-contact regions of the prototype subassembly. The maximum compressive strength of the spiral confined concrete is $f_{cc}=91.0$ MPa (13.2 ksi) reached at a strain of $\epsilon_{cc}=0.014$, and the ultimate (i.e., crushing) strain is $\epsilon_{ccu}=0.0323$.

The smooth concrete stress-strain relationships in Figs. 3.2c and 3.2d were determined using a concrete model developed by Mander et al. (1988). The spiral

confined concrete stress-strain parameters, which include the maximum strength, f_{cc} , strain at maximum strength, ϵ_{cc} , and ultimate (i.e., crushing) strain, ϵ_{ccu} , were calculated based on the unconfined concrete properties and the amount, distribution, yield strength [assumed as $f_{spy}=414$ MPa (60 ksi)], and strain at maximum strength (assumed as $\epsilon_{spm}=0.08$) of the spiral reinforcement. According to the concrete confinement model by Mander et al. (1988), the ultimate (crushing) strain ϵ_{ccu} of the confined concrete is reached when the spiral reinforcement fractures, resulting in a complete loss of confinement and a sudden loss in the compression resistance of the concrete. The concrete confinement provided by the wall transverse reinforcement other than the spirals (e.g., wire mesh) was ignored.

In general, the slopes of the first segment of the idealized multi-linear stress-strain relationships in Fig. 3.2 match the linear-elastic stiffness of the smooth relationships. Furthermore, the maximum compressive strength, strain at maximum strength, and ultimate strain of the concrete are matched by the idealized stress-strain relationships in Figs. 3.2c and 3.2d.

3.2 Analytical Modeling Assumptions

The following assumptions are made for the subassembly analytical modeling:

(1) The objective of this research is to investigate the behavior of isolated coupled wall structures under earthquake induced lateral loads. The interaction between the coupled walls and other structural members (e.g., slabs supported by the coupling beams and the walls) is not within the scope of the analytical model, and thus, is ignored. Note

that the floor and roof slabs may affect the expected and desired behavior of a coupled wall structure; however, this is not investigated in the dissertation.

(2) The coupled wall system undergoes in-plane deformations only. Torsional and out-of-plane deformations are not modeled.

(3) Local and/or global instability of the coupling beams is prevented by proper design and detailing.

(4) Shear slip of the coupling beams at the beam-to-wall interfaces is prevented by proper design and detailing.

(5) The welds between the cover plates (if used) and the coupling beam flanges are properly designed and detailed for the maximum forces and deformations. The cover plates are sufficiently long such that yielding of the coupling beam where the plates are terminated does not occur.

(6) The anchorages for the coupling beam post-tensioning tendons are properly designed and detailed for the maximum post-tensioning forces.

(7) The top and seat angles are loaded in the horizontal direction parallel to the coupling beam and the angles form a ductile vertical-leg failure mechanism as shown in Fig. 2.18.

(8) The angle-to-beam and angle-to-wall connections are properly designed and detailed for the maximum angle forces and deformations.

3.3 Fiber Element Subassemblage Model

This section describes a fiber element based analytical model for unbonded post-tensioned hybrid coupled wall subassemblages as follows: (1) modeling of wall regions;

(2) modeling of coupling beams and flange cover plates; (3) modeling of gap opening; (4) modeling of beam post-tensioning tendons and anchorages; and (5) modeling of top and seat angles. The DRAIN-2DX program (Prakash et al. 1993) is used as the analytical platform. As an example, the model for the prototype subassemblage in Fig. 3.1 is shown in Fig. 3.3. The verification of the subassemblage model is described later.

3.3.1 Modeling of Wall Regions

The wall regions are modeled using the fiber beam-column element in DRAIN-2DX. As shown in Fig. 3.4, each fiber element is divided into a number of segments. The cross-section properties remain constant within a fiber segment, but can vary from one segment to another. Within a segment, parallel fibers in the direction of the element model the cross-section (or “slice”) at the mid-length of the segment. Each fiber is characterized by a uniaxial multi-linear material stress-strain relationship (similar to the relationships in Fig. 3.2), a cross section area, and a distance from the longitudinal reference axis of the element. The force versus deformation behavior of the slice is determined by the integration of the stress versus strain behavior of the fibers over the cross section. The theoretical formulations for the development of the fiber element in DRAIN-2DX are described by Prakash et al. (1993), and thus, are not discussed here in further detail.

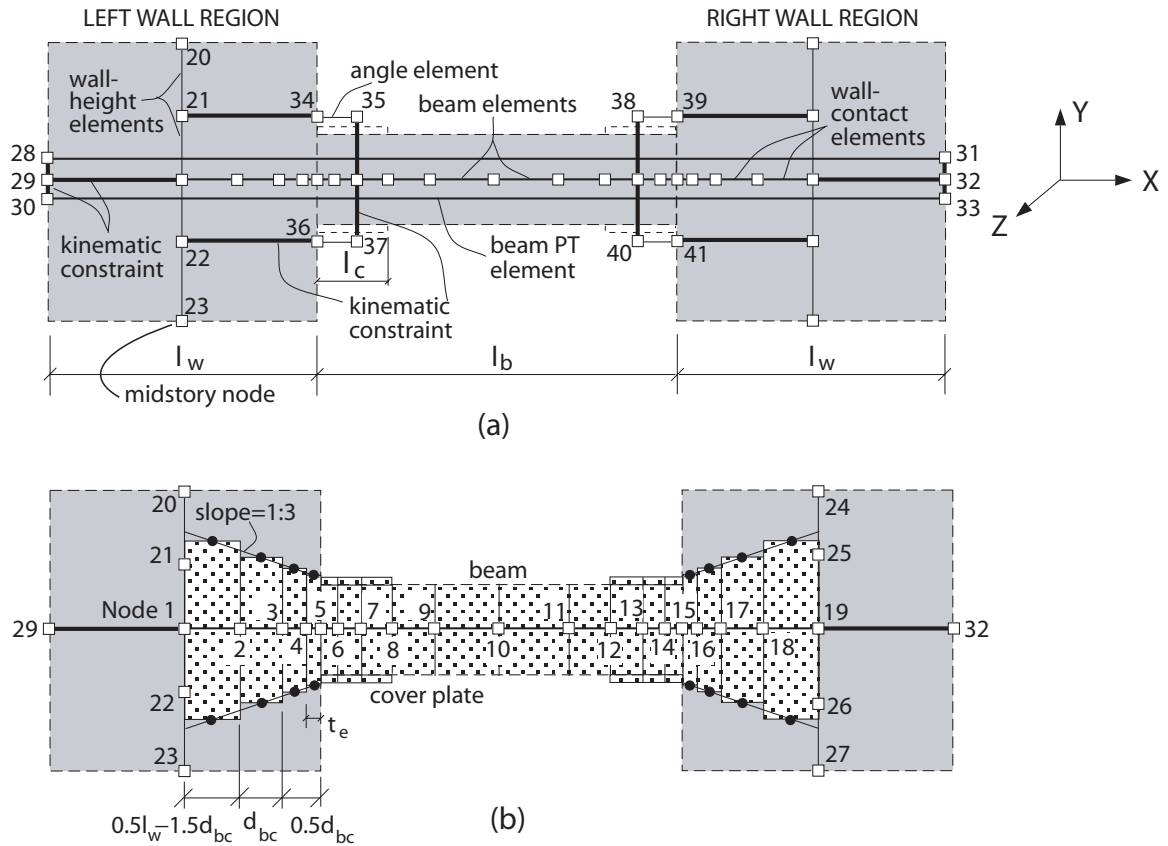


Fig. 3.3 Analytical model: (a) subassembly;
(b) wall-contact elements and beam elements

Each wall region in an unbonded post-tensioned hybrid coupled wall subassembly is modeled using two sets of fiber beam-column elements as shown in Fig. 3.3a. The first set consists of elements that are in the vertical direction to model the axial-flexural and shear behavior of the wall region along its height. These elements, referred to as the “wall-height” elements, are used to model the cross section of each wall in the horizontal X-Z plane. More detailed information on the wall-height elements is provided in Chapter 6.

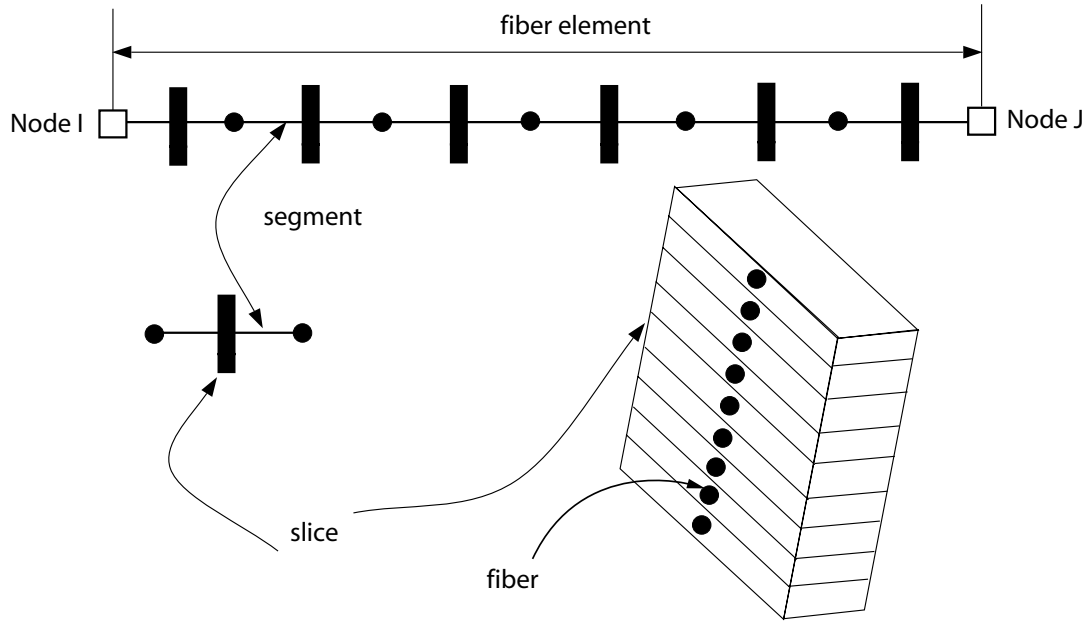


Fig. 3.4 Fiber element, segments, and fibers

The second set of fiber elements is used to model the local behavior of the wall-contact regions to the left and right of the coupling beam. These elements, referred to as the “wall-contact” elements, are in the horizontal direction. As indicated in Fig. 1.3, large concentrated compression stresses develop in the contact regions between the beam and the walls upon gap opening. The wall-contact elements model the deformation of the concrete in the wall-contact regions under these large stresses. The fiber cross section properties of the wall-contact elements are determined from the properties of an “effective” wall cross section in the vertical Y-Z plane as described below.

The thickness of the effective wall cross section is assumed to be equal to the wall thickness, t_w including the unconfined cover concrete. The depth of the effective wall cross section is equal to the beam depth, d_b plus two times the thickness of the cover plate, t_c (denoted as $d_{bc} = d_b + 2t_c$) at the beam-to-wall interface and is assumed to increase away

from the interface (with a slope of 1:3) as shown in Fig. 3.3b. The compression stresses in the wall-contact region decrease away from the interface as a result of an increase in the depth of the compression region inside the wall. The increase in the depth of the effective wall cross section represents this increase in the depth of the compression region away from the interface.

Four wall-contact elements are used between the center of the left wall region (Node 1) and the beam-to-wall interface (Node 5). The Y-translational degree-of-freedom (DOF) of Node 5 is kinematically constrained to that of Node 1. The rotational and X-translational DOFs of Node 5 are not constrained. It is assumed that no slip occurs at the beam-to-wall interface (Assumption 4). The total length of the first two wall-contact elements adjacent to Node 5 is equal to $0.5d_{bc}$. The first element represents the embedded steel plate and has a length equal to the embedded plate thickness, t_e . The length of the third element is equal to d_{bc} . The total length of the wall-contact elements between Nodes 1 and 5 is equal to one half of the wall length, l_w . Note that if $1.5d_{bc} \geq 0.5l_w$, only three wall-contact elements should be used and the length of the third element should be adjusted accordingly. The modeling of the right wall region between Nodes 19 and 15 is similar to the modeling of the left wall region between Nodes 1 and 5.

Fig. 3.5 shows a schematic of the fiber discretizations used in the four wall-contact elements of the prototype subassembly model in Fig. 3.3b. The first fiber element representing the embedded plate (between Nodes 5 and 4) includes steel fibers only (with no concrete fibers) with the trilinear steel stress-strain relationship in Fig. 3.2a. The other wall-contact elements include concrete fibers only (with no steel fibers) with the multi-

linear concrete stress-strain relationships in Figs. 3.2c and 3.2d. The steel and concrete fibers used in the wall-contact elements model the transfer of compression stresses between the coupling beam and the walls, and, are assumed to have no resistance in tension to represent the opening of gaps at the beam-to-wall interfaces. In Fig. 3.5, “CUC” refers to “compression-only unconfined concrete” fibers, “CCC” refers to “compression-only confined concrete” fibers, and “SC” refers to “compression-only steel” fibers. More information on the modeling of gap opening at the beam-to-wall interfaces, as well as on the assumed cyclic behaviors of the compression-only steel and compression-only concrete fibers is provided later.

The actual number of fibers and the thickness of each fiber, t_f used in the wall-contact elements modeling the prototype subassembly are given in Table 3.6. Note that refinement studies using models with larger numbers of elements/segments/fibers than the discretization in Table 3.6 showed no appreciable differences in the analysis results.

3.3.2 Modeling of Coupling Beams and Flange Cover Plates

Fiber beam-column elements are used to model the axial-flexural and shear behavior of the coupling beams. The fiber cross section properties of these elements, which are referred to as the “beam elements,” are determined from the properties of the coupling beam cross section. The beam elements near the beam ends also include fibers

to model the flange cover plates, assuming that the welds between the cover plates and the beam flanges are properly designed and detailed for the maximum forces and deformations (Assumption 5). Second order effects (often referred to as “P-Δ” effects) in the coupling beam (due to the rotation of the beam with respect to the left and right wall regions) are included in the fiber beam elements.

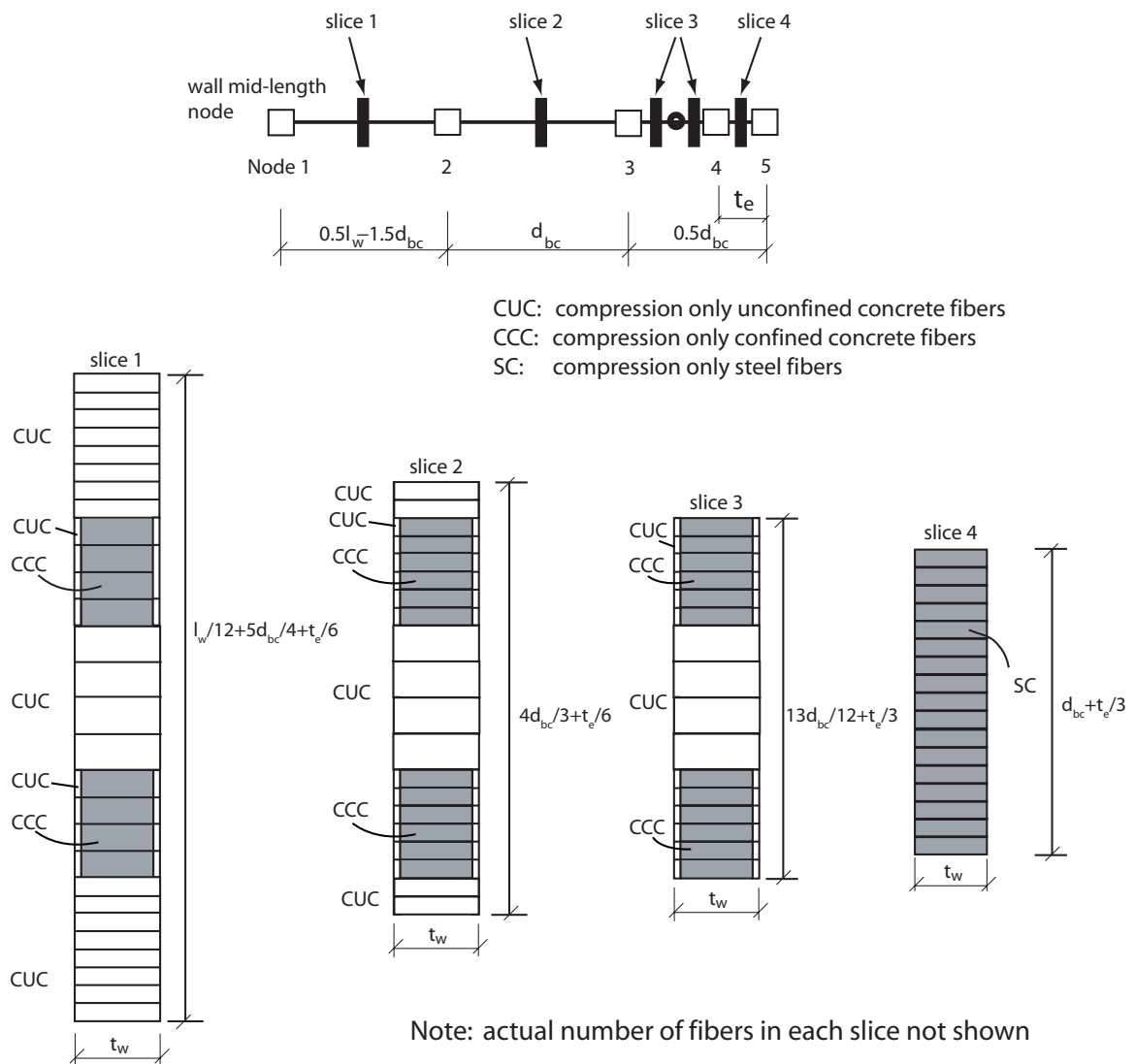


Fig. 3.5 Schematic showing fiber discretization of wall-contact elements

TABLE 3.6

WALL-CONTACT ELEMENT FIBER DISCRETIZATION

Element Nodes	Element Length	Number of Segments and Slices	Segment Length/Element Length and Slice Number	Fiber Thickness, t_f mm (in.)	Depth of Cross Section	Total Number of Fibers in Slice
1-2	544 mm (21.42 in.)	1	1 (Slice 1) (see Fig. 3.5)	1 CUC fiber; $t_f=7.37(0.29)$ 22 CUC fibers; $t_f=12.7(0.5)$ 1 CUC fiber; $t_f=22.4(0.88)$ 1 CUC fiber; $t_f=3.05(0.12)$ 1 CCC fiber; $t_f=3.05(0.12)$ 2 CUC fibers; $t_f=12.7(0.5)$ 2 CCC fibers; $t_f=12.7(0.5)$ 6 CUC fibers; $t_f=25.4(1)$ 6 CCC fibers; $t_f=25.4(1)$ 2 CUC fibers; $t_f=50.8(2)$ 2 CCC fibers; $t_f=50.8(2)$ 1 CUC fiber; $t_f=9.65(0.38)$ 1 CCC fiber; $t_f=9.65(0.38)$ 1 CUC fiber; $t_f=15.7(0.62)$ 1 CUC fiber; $t_f=25.4(1)$ 2 CUC fibers; $t_f=50.8(2)$	1488 mm (58.58 in.)	104
2-3	653.3 mm (25.72 in.)	1	1 (Slice 2)	1 CUC fiber; $t_f=10.9(0.43)$ 6 CUC fibers; $t_f=12.7(0.5)$ 1 CUC fiber; $t_f=22.35(0.88)$ 1 CUC fiber; $t_f=3.05(0.12)$ 1 CCC fiber; $t_f=3.05(0.12)$ 2 CUC fibers; $t_f=12.7(0.5)$ 2 CCC fibers; $t_f=12.7(0.5)$ 6 CUC fibers; $t_f=25.4(1)$ 6 CCC fibers; $t_f=25.4(1)$ 2 CUC fibers; $t_f=50.8(2)$ 2 CCC fibers; $t_f=50.8(2)$ 1 CUC fiber; $t_f=9.65(0.38)$ 1 CCC fiber; $t_f=9.65(0.38)$ 1 CUC fiber; $t_f=15.7(0.62)$ 1 CUC fiber; $t_f=25.4(1)$ 2 CUC fibers; $t_f=50.8(2)$	1089 mm (42.86 in.)	72
3-4	294.9 mm (11.61 in.)	2	0.6 (Slice 3) 0.4 (Slice 3)	1 CUC fiber; $t_f=5.33(0.21)$ 1 CCC fiber; $t_f=5.33(0.21)$ 10 CUC fibers; $t_f=12.7(0.5)$ 10 CCC fibers; $t_f=12.7(0.5)$ 4 CUC fibers; $t_f=25.4(1)$ 4 CCC fibers; $t_f=25.4(1)$ 1 CUC fiber; $t_f=9.65(0.38)$ 1 CCC fiber; $t_f=9.65(0.38)$ 1 CUC fiber; $t_f=15.7(0.62)$ 5 CUC fibers; $t_f=25.4(1)$	773 mm (30.42 in.)	76

TABLE 3.6 (Continued)

Element Nodes	Element Length	Number of Segments and Slices	Segment Length/Element Length and Slice Number	Fiber Thickness, t_f mm (in.)	Depth of Cross Section	Total Number of Fibers in Slice
4-5	31.75 mm (1.25 in.)	1	1 (Slice 4)	1 SC fiber; $t_f=1.78(0.07)$ 8 SC fibers; $t_f=6.35(0.25)$ 6 SC fibers; $t_f=12.7(0.5)$ 8 SC fibers; $t_f=25.4(1)$	664 mm (26.14 in.)	46

Notes:

(1) Only fiber discretization for top half of cross section is given for each slice, listed in order from extreme fiber to innermost fiber. Fiber discretization for bottom half of each cross section is symmetric about mid-depth of section.

(2) Modeling of wall-contact elements between Nodes 19-15 is similar to modeling between Nodes 1-5.

Typically, a larger number of fiber elements/segments/fibers are used near the ends of a coupling beam where the nonlinear behavior is expected to concentrate as compared with the midspan regions. The exact discretization of the fiber elements along the length of the beam is flexible with the following exceptions: (1) there are two beam element nodes (Nodes 7 and 13 in Fig. 3.3b) located at the same X-coordinates as the angle element Nodes 35, 37 and 38, 40, respectively (the angle element nodes are kinematically constrained to these beam element nodes as described later); and (2) new fiber elements or segments are used where the beam cover plates are terminated (in order to define the change in beam geometry).

Furthermore, the length of the first beam fiber element segment adjacent to the beam-to-wall interface is important in modeling the compression deformations that occur at the beam ends. The length where significant yielding of the steel in compression occurs in an unbonded post-tensioned coupling beam is quite different than an embedded steel coupling beam due to the gap opening behavior and the compression stresses from

post-tensioning. El-Sheikh et al. (1997) provide recommendations for the confined concrete crushing length at the ends of unbonded post-tensioned precast concrete beams. Similar to their recommendation, a length of $l_{b,cr}=2c_{b,sof}$ (Fig. 3.6) is used for the length of the first fiber element segment in this research, where $c_{b,sof}$ is the estimated depth of the compression (i.e., contact) region at the beam softening state (see Chapters 4 and 5).

The middle portion of the coupling beam between the cover plates can be modeled using a relatively smaller number of fiber elements (e.g., four elements as shown in Fig. 3.3). It is recommended that a node is placed at the beam mid-span (Node 10 in Fig. 3.3b).

Fig. 3.7 shows a schematic of typical fiber discretizations used at the beam ends and near the beam midspan of the prototype subassembly model in Fig. 3.3. The beam elements include steel fibers only with the tri-linear steel stress-strain relationship shown in Fig. 3.2a. In order to model the effect of gap opening, the steel fibers used in the first beam element segment adjacent to each beam-to-wall interface are assumed to have no resistance in tension. The other beam fiber element segments use full tension-compression steel fibers. In Fig. 3.7, “SC” refers to “compression-only steel” fibers and “S” refers to “compression-tension steel” fibers. More information on the modeling of gap opening at the beam-to-wall interfaces, as well as on the assumed cyclic behaviors of the compression-only and tension-compression steel fibers used in the beam elements is provided later.

The actual number of fibers and the thickness of each fiber, t_f used in the beam elements modeling the prototype subassembly are given in Table 3.7. Note that

refinement studies using models with larger numbers of elements/segments/fibers than the discretization in Table 3.7 showed no appreciable differences in the analysis results.

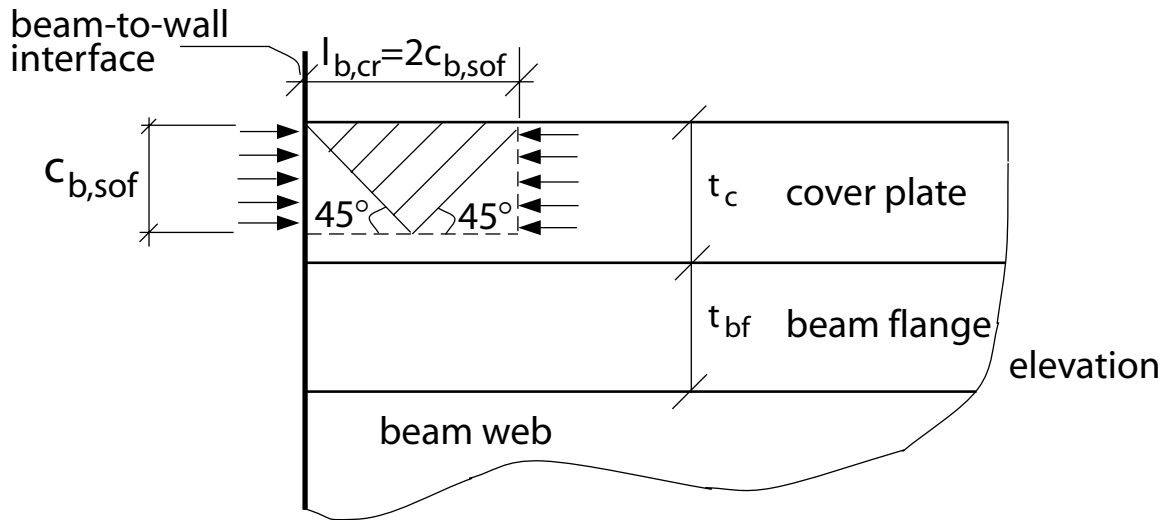
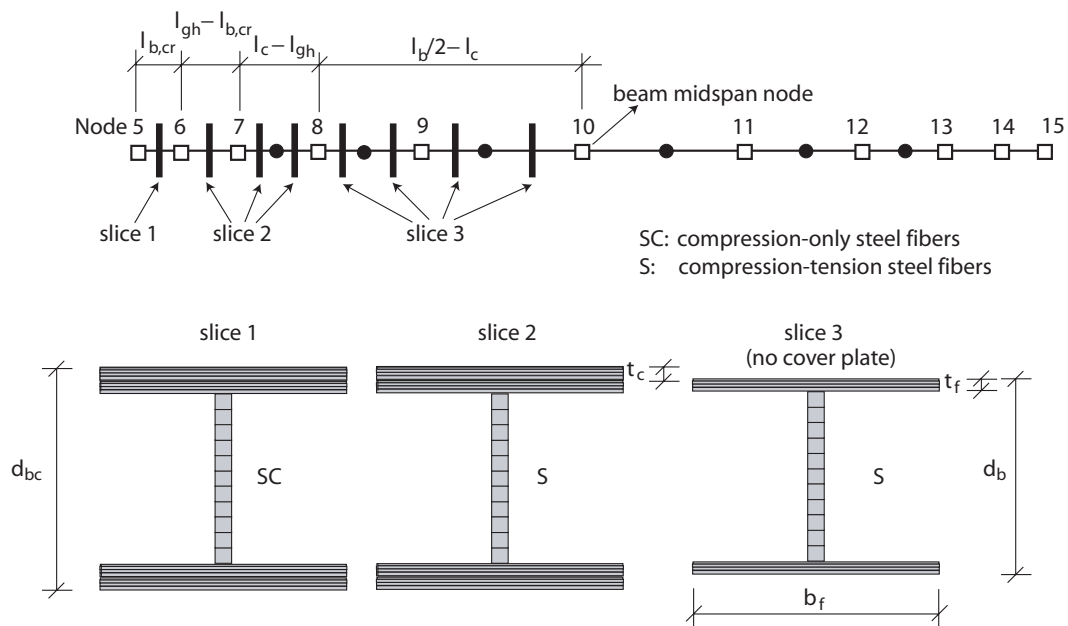


Fig. 3.6 Length of first beam fiber element segment



Note: actual number of fibers in each slice not shown

Fig. 3.7 Fiber discretization of beam elements

TABLE 3.7

BEAM FIBER ELEMENT DISCRETIZATION

Element Nodes	Element Length	Number of Segments and Slices	Segment Length/Element Length and Slice Number	Fiber Thickness, t_f mm (in.)	Depth of Cross Section	Total Number of Fibers in Slice
5-6	76.2 mm (3 in.)	1	1 (Slice 1) (see Fig. 3.7)	15 SC fibers; $t_f=2.54(0.1)$ 1 SC fiber; $t_f=2.03$ (0.08) 14 SC fibers; $t_f=2.54(0.1)$ 1 SC fiber; $t_f=7.11(0.28)$ 12 SC fibers; $t_f=20.32(0.8)$	653.3 mm (25.72 in.)	86
6-7	50.8 mm (2 in.)	1	1 (Slice 2)	15 S fibers; $t_f=2.54(0.1)$ 1 S fiber; $t_f=2.03$ (0.08) 14 S fibers; $t_f=2.54(0.1)$ 1 S fiber; $t_f=7.11(0.28)$ 12 S fibers; $t_f=20.32(0.8)$	653.3 mm (25.72 in.)	86
7-8	279.4 mm (11 in.)	2	0.5 (Slice 2) 0.5 (Slice 2)	15 S fibers; $t_f=2.54(0.1)$ 1 S fiber; $t_f=2.03$ (0.08) 14 S fibers; $t_f=2.54(0.1)$ 1 S fiber; $t_f=7.11(0.28)$ 12 S fibers; $t_f=20.32(0.8)$	653.3 mm (25.72 in.)	86
8-9	508 mm (20 in.)	2	0.5 (Slice 3) 0.5 (Slice 3)	1 S fiber; $t_f=2.03(0.08)$ 14 S fibers; $t_f=2.54(0.1)$ 1 S fiber; $t_f=7.11(0.28)$ 12 S fibers; $t_f=20.32(0.8)$	577 mm (22.72 in.)	56
9-10	609.6 m (24 in.)	2	0.417 (Slice 3) 0.583 (Slice 3)	1 S fiber; $t_f=2.03(0.08)$ 14 S fibers; $t_f=2.54(0.1)$ 1 S fiber; $t_f=7.11(0.28)$ 12 S fibers; $t_f=20.32(0.8)$	577 mm (22.72 in.)	56

Notes:

1) Only fiber discretization for top half of cross section is given for each slice, listed in order from extreme fiber to innermost fiber. Fiber discretization for bottom half of each cross section is symmetric about mid-depth of section.

2) Modeling of beam elements between Nodes 15-10 is similar to modeling between Nodes 5-10.

3.3.3 Modeling of Gap Opening

Gap opening at the beam-to-wall interfaces is one of the most important characteristics governing the behavior of unbonded post-tensioned coupling beams. As a result of the opening of gaps and due to post-tensioning, large compression stresses develop in the beam-to-wall contact regions, while the tensile stresses in the coupling beam and the wall region on either side of a gap are equal or close to zero. The compression behavior in the contact regions is modeled using the nonlinear uniaxial compressive stress-strain relationships of the fibers. To model the gap opening behavior, the tensile strength and stiffness of the fibers adjacent to the beam-to-wall interfaces are set to zero.

The steel fibers of the first beam element and first wall-contact element (with length t_e to model the embedded plate) adjacent to the beam-to-wall interfaces are assigned the “compression-only” steel stress-strain relationship in Fig. 3.8a (i.e., the SC fiber type in Figs. 3.5 and 3.7). Similarly, the concrete wall-contact elements between the embedded plate and the center of each wall region use the “compression-only” concrete stress-strain relationship in Fig. 3.8b (i.e., the CCC and CUC fiber types for confined concrete and unconfined concrete, respectively, in Fig. 3.5). Only the confined concrete (CCC) fiber behavior is shown in Fig. 3.8b – the cyclic behavior of the unconfined concrete (CUC) fiber has similar characteristics. More details on the cyclic stress-strain relationship of the concrete fiber in DRAIN-2DX can be found in Kurama et al. (1996) and Kurama (1997). The beam elements away from the beam-to-wall

interfaces have the full compression-tension steel stress-strain relationship in Fig. 3.8c (i.e., the S fiber type in Fig. 3.7). Note that Bauschinger effect is not modeled in the compression-tension steel fibers since the beam elements away from the interfaces remain essentially linear-elastic.

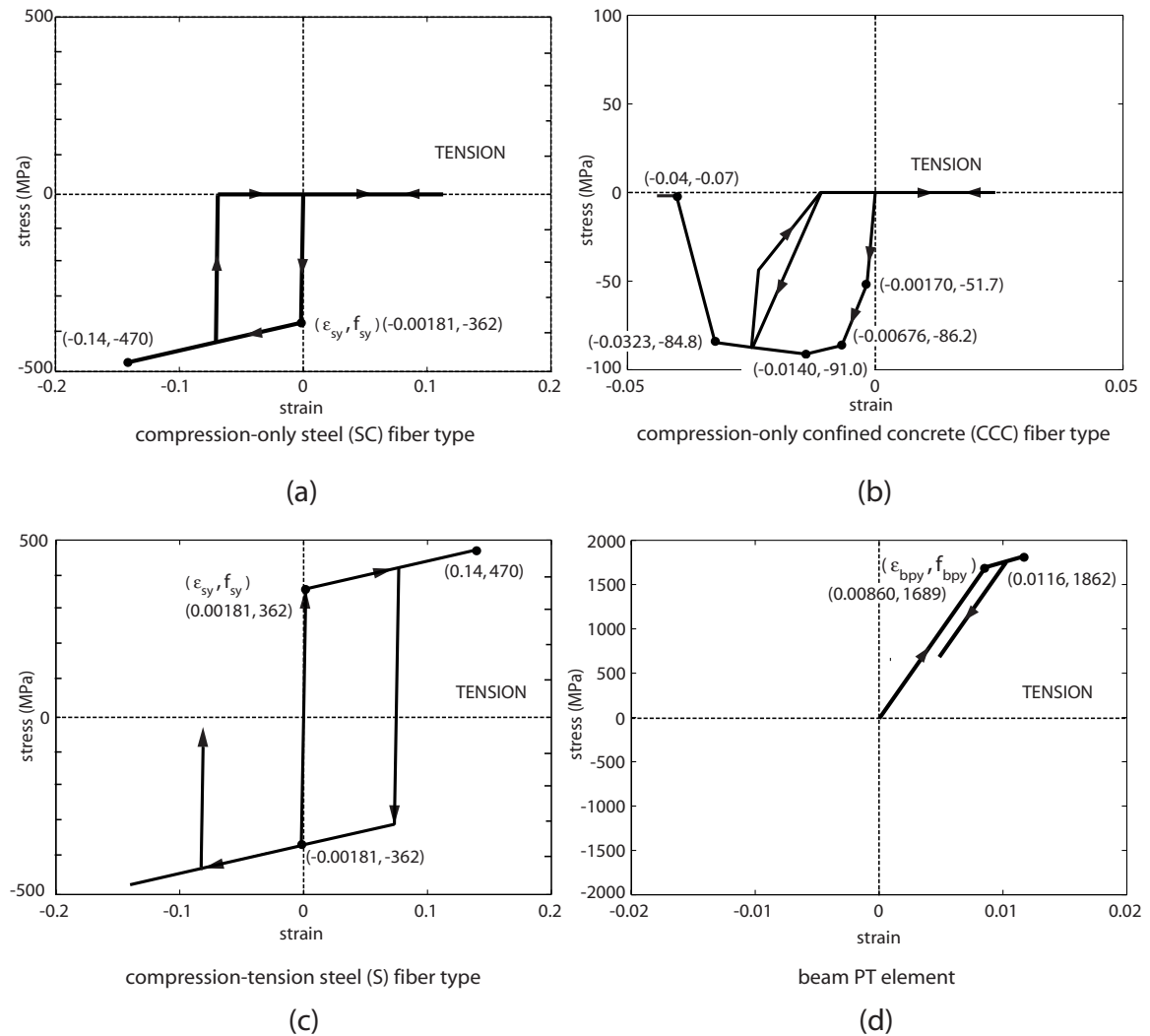


Fig. 3.8 Cyclic material models: (a) compression-only steel (SC) fiber; (b) compression-only confined concrete (CCC) fiber; (c) compression-tension steel (S) fiber; (d) beam PT element

Through this model, the gap opening displacements that occur at the beam-to-wall interfaces are represented as distributed tensile deformations that occur in the adjacent beam and wall-contact elements. The reduction in the lateral stiffness of the subassembly as a result of gap opening is modeled by the zero stiffness of the fibers that go into tension near the interfaces when the precompression stresses due to the post-tensioning force are overcome by the flexural stresses that develop due to the lateral loads (i.e., when decompression occurs).

The process of gap opening/closing under the action of lateral loading/unloading causes softening/re-stiffening at the beam-to-wall interface regions. This process is captured in the fiber element model by having an increasing number of fibers subjected to tension during loading, and then by having the fibers subjected to tension go back into compression during unloading.

3.3.4 Modeling of Beam Post-Tensioning Tendons and Anchorages

Each beam unbonded post-tensioning (PT) tendon is modeled using a truss element, referred to as the “beam PT element.” Post-tensioning tendons located at the same elevation within the beam cross section are modeled using the same truss element. The cyclic stress-strain behavior of the truss elements, based on the bi-linear relationship in Fig. 3.2b, is shown in Fig. 3.8d. The post-tensioning loads are simulated by tensile forces in the truss elements, which are equilibrated by compressive forces in the beam and wall-contact elements. Note that the compression forces that develop in the beam and wall-contact elements result in an elastic shortening and subsequent loss in the forces in the

truss elements modeling the PT tendons. Thus, larger tensile forces are applied to the truss elements in order to achieve the desired amount of initial force (i.e., force just before the application of lateral loads) in the post-tensioning tendons after elastic shortening takes place.

Each beam PT element is connected to two nodes representing the anchorages between the post-tensioning tendons and the walls at the outer ends (e.g., Nodes 28-31, 29-32, and 30-33 for the three pairs of post-tensioning tendons in Fig. 3.3). Based on Assumption 6, the displacements of each anchorage node are kinematically constrained to the node at the center of the corresponding wall region (Nodes 1 and 19) as shown in Fig. 3.3. Second order effects (often referred to as “P- Δ ” effects) in the post-tensioning tendons (due to the relative displacements of the tendon nodes in a direction perpendicular to the tendon) are modeled in the beam PT elements.

3.3.5 Modeling of Top and Seat Angles

The behavior of the top and seat angles at the beam-to-wall interfaces is also modeled using fiber elements, referred to as “angle elements.” Each angle element is connected to two nodes as shown in Fig. 3.3 (Nodes 34-35, 36-37, 38-39, and 40-41 for the four angles). Both nodes are located at the same elevation as the middle of the horizontal leg of the angle parallel to the beam. Based on Assumption 8, the first angle node (e.g., Node 34), which is located at the wall face, is kinematically constrained to a wall-height element node at the same elevation (Node 21). The second angle node (Node

35) is located at the centroid of the bolt group connecting the angle to the beam flange and is kinematically constrained to a corresponding beam node (Node 7).

The angle elements represent the expected behavior of the top and seat angles under loading parallel to the beam flanges as shown in Fig. 3.9a. As described in Chapter 2, the behavior of steel angles under similar loading conditions has been investigated experimentally and analytically by other researchers (e.g., Kishi and Chen 1990; Lorenz et al. 1993; Swanson and Leon 1999; Shen and Astaneh-Asl 1999, 2000; Sims 2000; Garlock et al. 2003). The angle load versus deformation relationship is governed by many factors including the size and gage length of the connection bolts, number and layout of bolts, and angle leg thickness.

The cyclic load-deformation relationship used to model the behavior of each angle in a coupled wall subassembly is shown in Fig. 3.9b. This cyclic behavior is obtained by using two fibers in parallel – fiber 1 is a tension-only concrete fiber and fiber 2 is a tension-compression steel fiber. The combination of the load-deformation relationships of these two fibers in parallel models the expected behavior of an angle under cyclic loading. Under tensile loading, the “yield” strength T_{ayx} and initial stiffness, K_{aixt} for an angle are determined as described by Kishi and Chen (1990) and Lorenz et al. (1993) and as summarized in Chapter 2. The vertical leg of the angle is assumed to be fixed along the innermost edge of the line of bolt heads and is pulled by the coupling beam flange (Fig. 3.9a). The yield strength of the angle is reached when the vertical-leg plastic hinge mechanism shown in Fig. 3.9a develops, considering the interaction between the bending moment and shear in the vertical leg. The “yield” deformation of the angle is assumed to

be $\delta_{ayx} = T_{ayx} / K_{aixt}$. The post-yield stiffness in tension is assumed to be equal to $\alpha_a K_{aixt}$ with $\alpha_a = 0.02$ based on previous experimental results reported by Sims (2000).

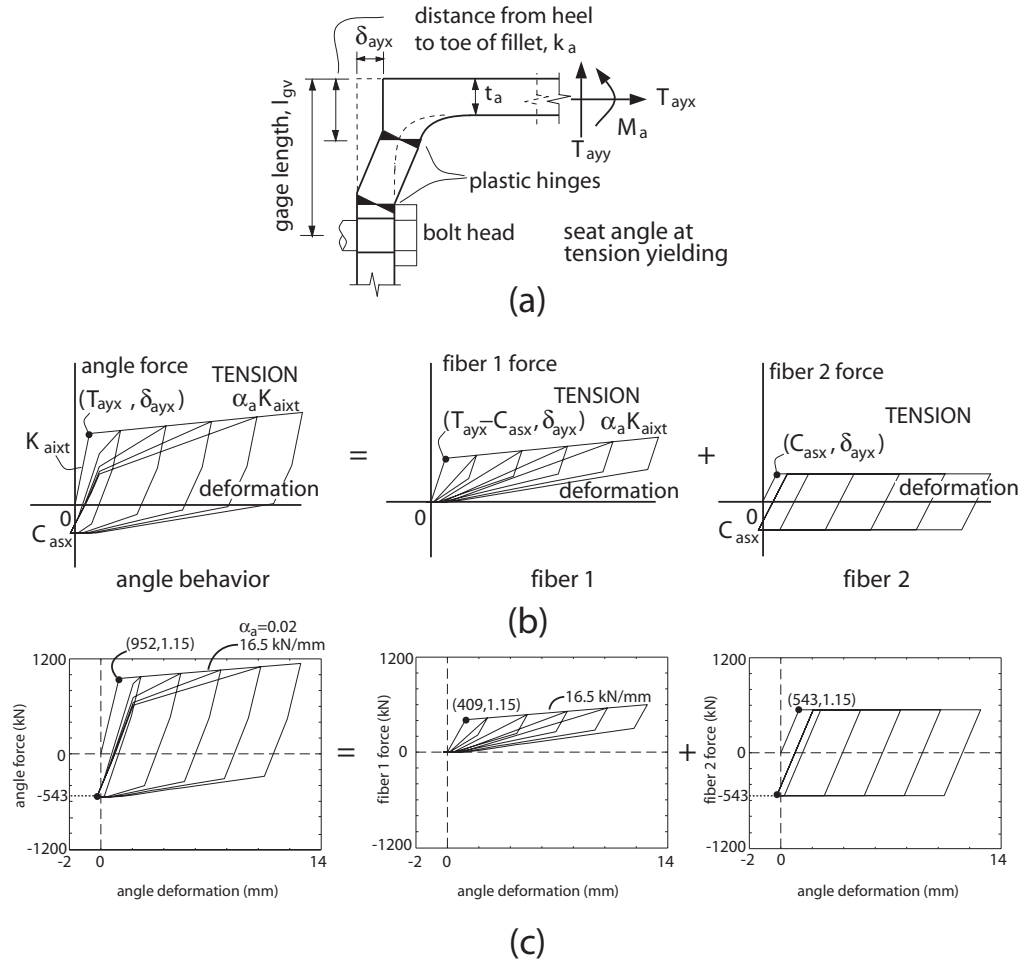


Fig. 3.9 Angle model: (a) idealized displaced shape; (b) cyclic angle load-deformation model; (c) angle load-deformation behavior for prototype subassembly

Under compression loading, the “yield” strength of an angle is assumed to be equal to the slip force C_{asx} for the bolts connecting the horizontal leg of the angle to the beam flange. The subassembly analyses described in Chapter 4 show that extremely small deformations occur in the angle once the beam flange comes in contact with the wall. Thus, the development of the shear/bearing strength of the angle-to-beam connection

bolts or the development of the compression bearing capacity of the angle horizontal leg cross section is not expected and is not modeled.

Based on the angle model described above, Fig. 3.9c shows the load-deformation relationship developed for the top and seat angles in the prototype subassembly. Some of the angle design capacities are given in Table 3.8. The design slip-critical strength, shear strength, and tension strength of the angle-to-beam and angle-to-wall connection bolts were determined based on the recommendations of the American Institute of Steel Construction (AISC 1998).

TABLE 3.8
PROTOTYPE SUBASSEMBLAGE BEAM-TO-WALL CONNECTION
TOP AND SEAT ANGLE DESIGN CAPACITIES

Beam-to-Wall Connection Top and Seat Angle Design Capacities	
Angle initial stiffness in tension, K_{aixt}	824 kN/mm (4707 kips/in.)
Angle yield strength in tension, T_{avx}	952 kN (214 kips)
Total design slip-critical strength of angle-to-beam connection bolts at factored loads, C_{asx}	68 kN(8)= 543 kN (122.1 kips)
Total design shear strength of angle-to-beam connection bolts	196.6 kN(8)= 1573 kN (353.6 kips)
Total design tension strength of angle-to-wall connection bolts	226.8 kN(8)= 1814 kN (408 kips)

The shape of the idealized angle cyclic behavior in Fig. 3.9c resembles the experimentally observed behavior in Fig. 2.19 by Sims (2000). Note that this angle model represents a simplified idealization of the actual behavior of the angles in a coupled wall subassembly. The ultimate failure of the angles is not modeled. The effect of bolt response (e.g., yielding of the bolts) on the behavior of the angles is ignored (Assumption 8) and the angles are assumed to form a ductile plastic mechanism with two hinges in the vertical leg as shown in Fig. 3.9a. The rotation of the horizontal angle leg with respect to

the vertical leg, which occurs as a result of the rotation of the beam with respect to the walls, is not considered. Furthermore, only the axial force in the angle horizontal leg parallel to the beam is represented by the model, ignoring the other angle forces transferred to the beam (e.g., the shear force in the horizontal leg). Similar assumptions have been made by other researchers (e.g., Ricles et al. 2001).

3.4 Verification of Fiber Element Subassembly Model

The coupled wall subassembly model described above (referred to as the fiber element model) is verified using a finite element model developed with the ABAQUS program (Hibbitt et al. 1998).

3.4.1 Finite Element Subassembly Model

Two finite element models of the prototype coupled wall subassembly described previously were developed: (1) a two-dimensional (2D) model using nonlinear rectangular plane stress elements to represent the wall regions and the coupling beam; and (2) a three-dimensional (3D) model using nonlinear brick elements to represent the wall regions and the coupling beam. In both models, truss elements were used to represent the post-tensioning tendons and gap/contact surfaces were used to represent the opening of gaps at the beam-to-wall interfaces. Adequate friction was provided at the gap/contact surfaces to prevent sliding of the beam with respect to the walls.

Fig. 3.10 shows the 2D and 3D finite element models of the prototype subassembly in exaggerated deformed configurations. Discrete gaps form between the

beam and the walls as a result of the gap/contact surfaces. The left wall region is referred to as the reaction block and is fixed along the top and bottom horizontal surfaces. The right wall region, referred to as the loading block, is allowed to translate in the horizontal and vertical directions, but not allowed to rotate assuming that the left and right wall regions do not rotate relative to each other. A force V is applied on the loading block in the vertical direction. These boundary conditions result in deformations in the subassembly that are similar to the deformations with respect to the “reference line” in Fig. 1.3b.

Note that the flange cover plates and the top and seat angles are not included in the finite element models. Thus, the verification of the fiber element model is done based on the prototype subassembly with the flange cover plates and the angles removed. Other researchers have shown the difficulties in the finite element modeling of the nonlinear behavior of top and seat angle connections, in particular the boundary conditions for the angle legs, prying, friction, slip, and interaction between the angles, bolts, and nuts (Sims 2000). Thus, the modeling of the angles using results from previous research as described in Section 3.3.5 is considered to be satisfactory. An improved angle model based on large-scale experiments of unbonded post-tensioned hybrid coupled wall subassemblies is described later in Chapter 10.

Fig. 3.11 compares the load-deformation relationships of the prototype subassembly using the 2D and 3D finite element models. Note that this comparison is based on an approximately half-scale model of the prototype subassembly in Fig. 3.1. The load is equal to the coupling shear force in the beam, $V_b=V$, and the deformation is

equal to the beam chord rotation, θ_b , which is calculated as the vertical displacement of the right end of the beam divided by the beam length. The results obtained using the 2D model (with plane stress elements) and the 3D model (with brick elements) are very similar. Thus, the 2D model is adopted for further finite element analyses of the subassembly due to its relative simplicity.

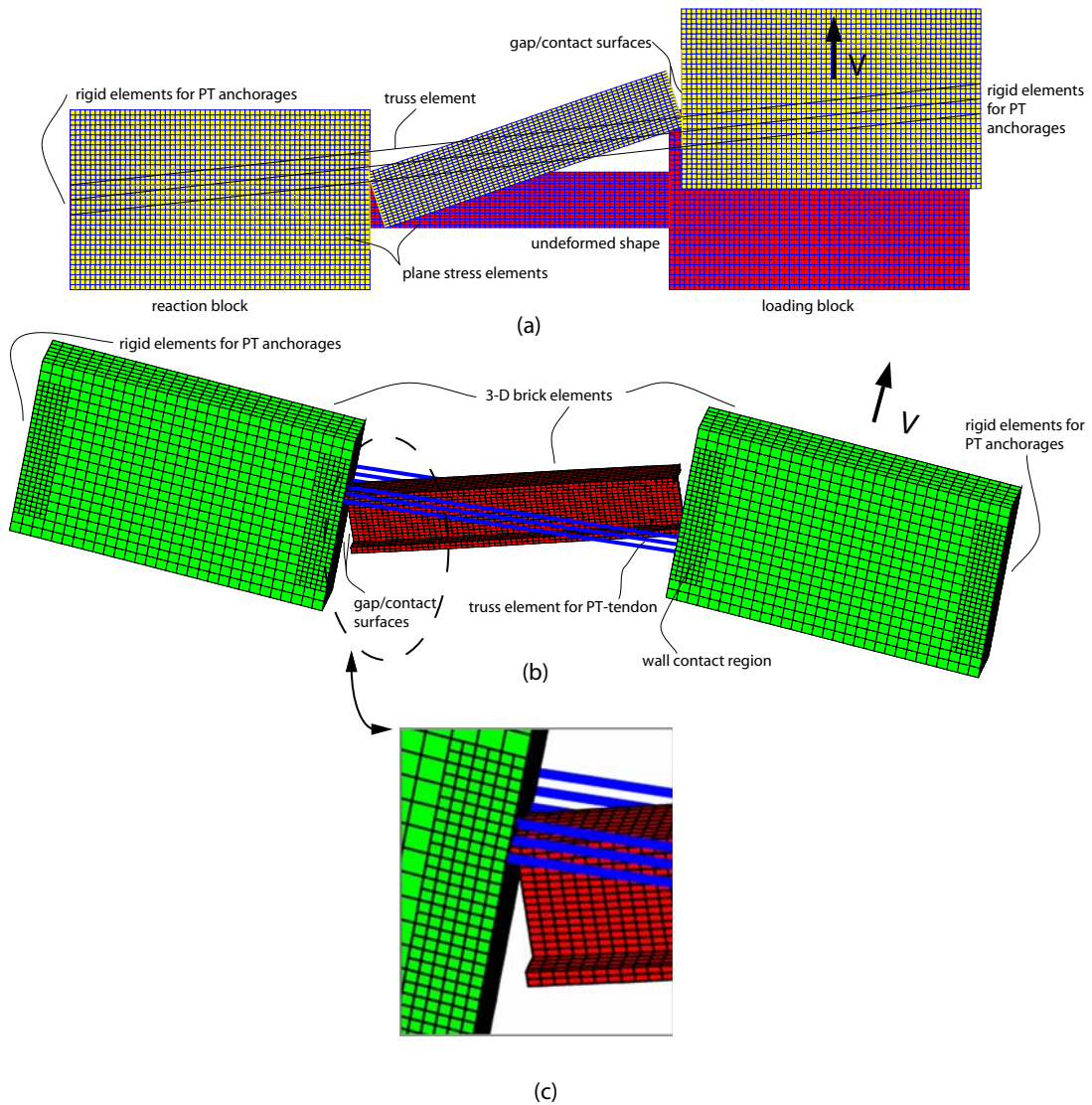


Fig. 3.10 Finite element models: (a) two dimensional (2D) model; (b) three-dimensional (3D) model; (c) close-up view of beam-to-wall interface

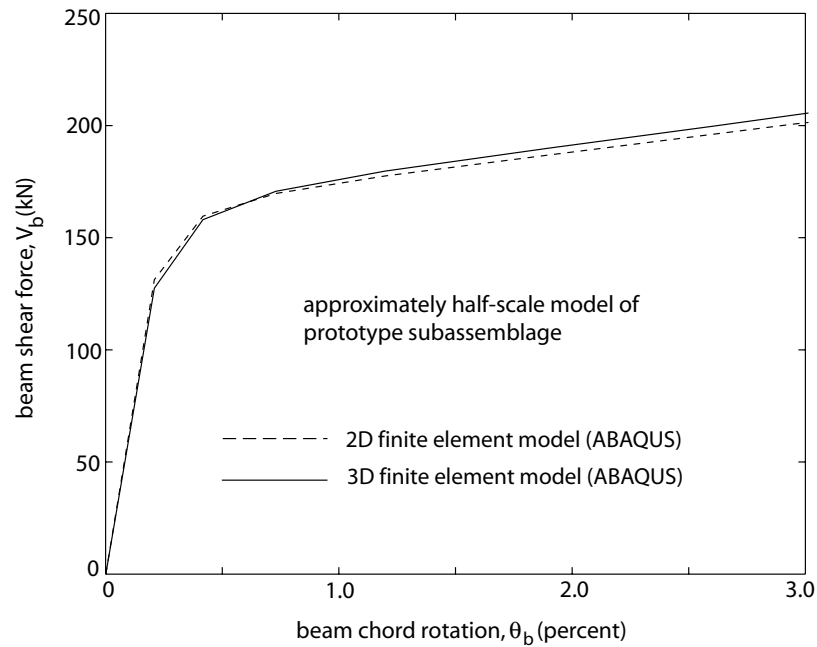


Fig. 3.11 Comparison between 2D and 3D finite element models

3.4.2 Finite Element Analysis Results

Two 2D finite element models of the full-scale prototype subassembly were developed: (1) a “rigid” wall model in which the deformations in the reaction and loading blocks are prevented; and (2) a “deformable” wall model in which the deformations in the wall regions are included. Fig. 3.12 compares the load-deformation relationships of the subassembly using the rigid wall and deformable wall finite element models. The deformations in the wall regions have a considerable effect on the initial stiffness of the subassembly. Most of these deformations occur in the wall-contact regions near the beam-to-wall interfaces, demonstrating the need for modeling the deformations in the wall-contact regions and the need for using concrete confinement in these regions as described previously. The deformations in the walls away from the contact regions remain small.

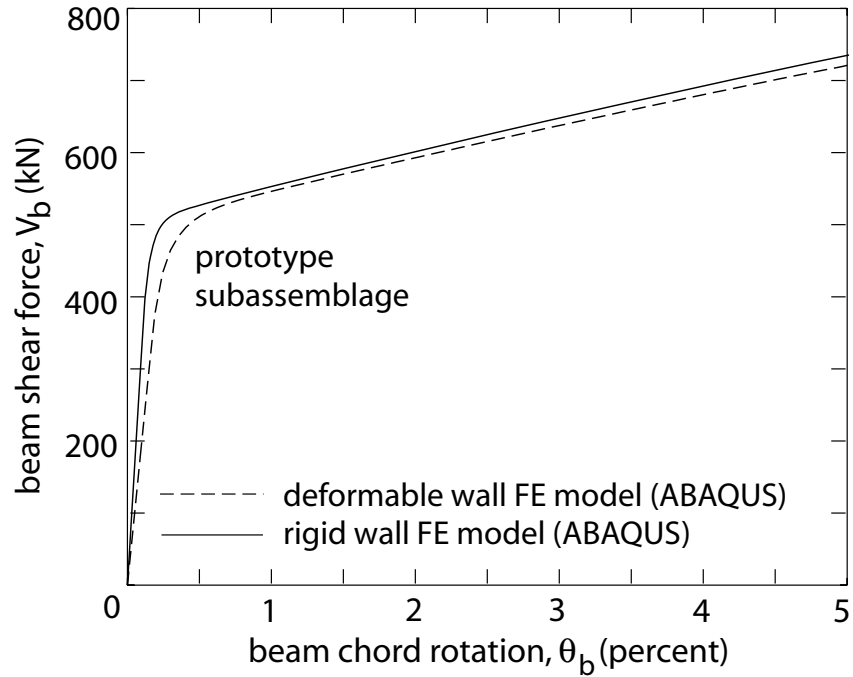


Fig. 3.12 Rigid wall versus deformable wall finite element models

Fig. 3.13 shows the maximum principal stress distributions corresponding to a beam chord rotation of $\theta_b=5\%$ from the deformable wall finite element model. The maximum principal stresses remain mostly compressive, demonstrating the effect of gap opening and post-tensioning on the behavior of the structure. The coupling beam stresses in Fig. 3.13a clearly show the formation of a diagonal compression strut along the beam span, with the maximum principal stresses at the beam end reaching close to 414 MPa (60 ksi) in compression. The stresses outside the diagonal compression strut remain small as a result of gap opening.

Similarly, Fig. 3.13b shows the maximum principal stresses in the reaction block, where the stress concentrations in the post-tensioning anchorage region and the wall-

contact region can be seen. The wall-contact region stresses are similar to the beam flange stresses near the beam-to-wall interface (demonstrating the need for the steel embedded plates and the concrete confinement) and quickly diminish away from the interface as assumed in the wall-contact elements used in the fiber element model. As a result of gap opening, the concrete stresses outside the wall-contact region remain small.

3.4.3 Comparisons between Finite Element and Fiber Element Model Results

Fig. 3.14a compares the load-deformation relationships of the prototype subassembly using rigid wall fiber element and finite element models. In this comparison, the wall regions are assumed to be rigid so that the modeling of the coupling beam and gap opening at the beam-to-wall interfaces can be evaluated. The results indicate that the fiber element model provides a remarkable representation of the nonlinear behavior of the beam including the effect of gap opening.

Similarly, Fig. 3.14b compares the load-deformation relationships of the fiber element and finite element models including the deformations in the wall regions. The objective of this comparison is to evaluate the modeling of the wall regions, in particular, the local deformations in the wall-contact regions using the wall-contact elements. Comparisons are provided for two subassemblies with different beam depths: $d_b = 577$ mm (i.e., the prototype subassembly) and $d_b = 718$ mm. Again, a reasonable agreement between the two models is observed.

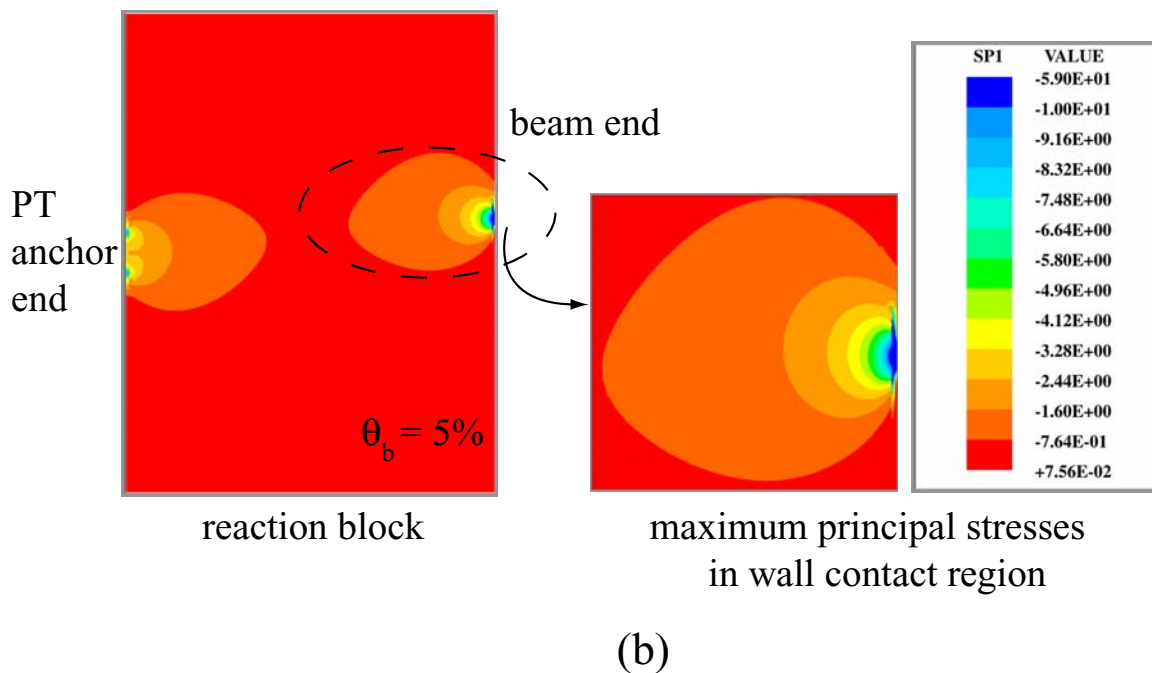
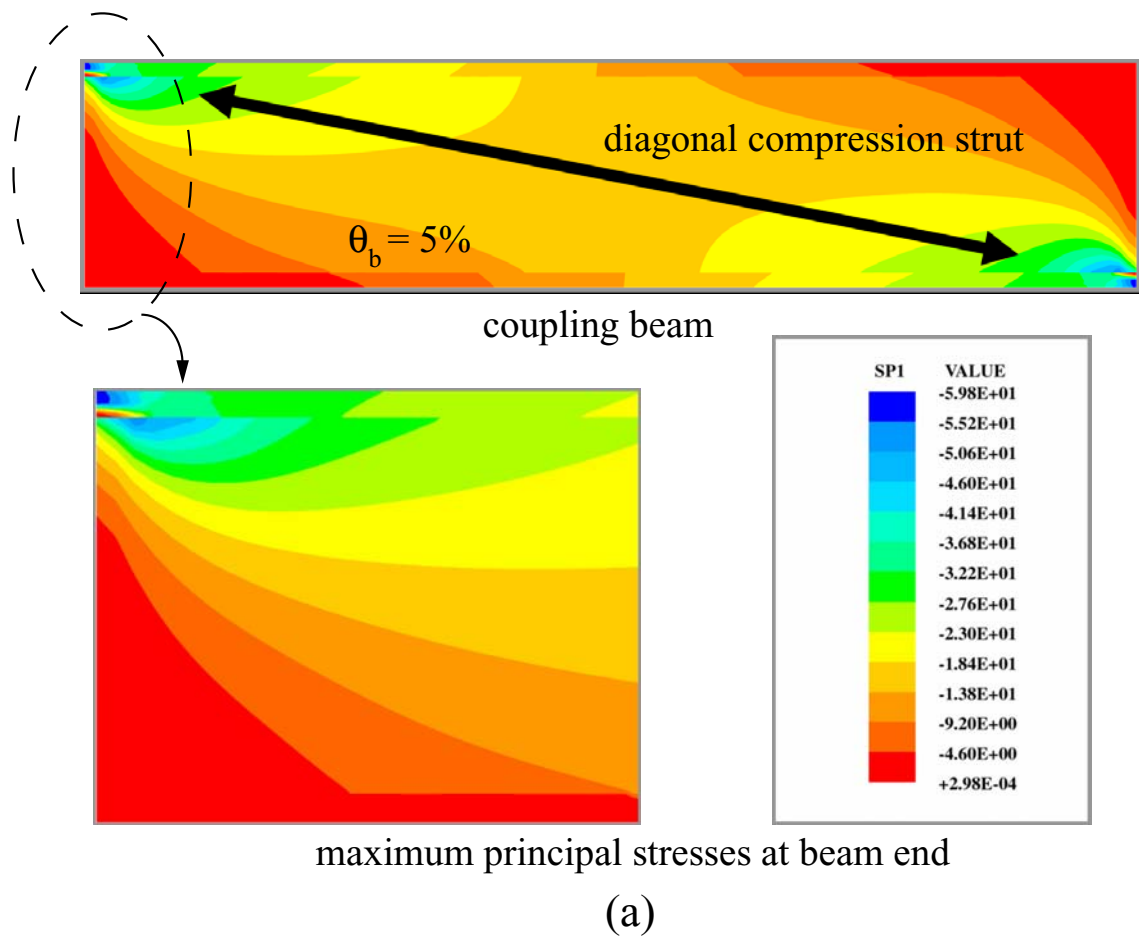


Fig. 3.13 Maximum principal stress distributions: (a) beam stresses; (b) wall stresses

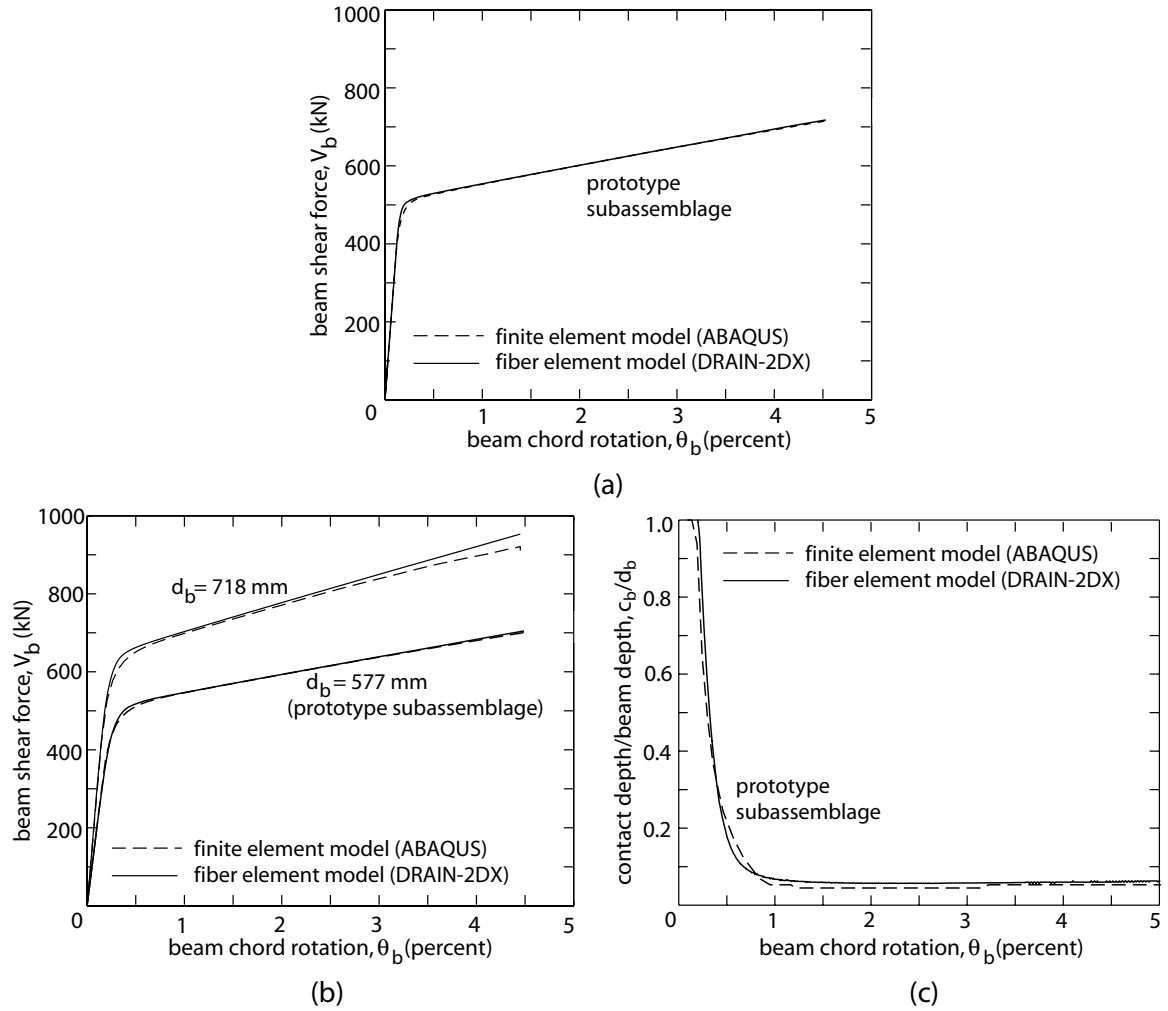


Fig. 3.14 Model verification: (a) rigid wall comparison; (b) deformable wall comparison; (c) contact depth comparison

Finally, Fig. 3.14c compares the contact depth, c_b between the beam and the reaction block in the prototype subassembly using the deformable wall fiber element and finite element models. The contact depth is normalized with respect to the beam depth, d_b .

The results in Fig. 3.14 show that the fiber element model is capable of predicting both the global (e.g., load-deformation) behavior and the local (e.g., gap opening and

contact) behavior of unbonded post-tensioned hybrid coupled wall subassemblages remarkably well. The fiber element model is used to conduct the analyses described in the remainder of this dissertation because of its simplicity and computational efficiency as compared with the finite element model.

3.5 Advantages and Limitations of Fiber Element Model

A significant advantage of the fiber element model described in this chapter is that a reasonably accurate representation of the behavior of the coupling beams, the post-tensioning tendons, the wall-contact regions, and the beam-to-wall connection regions can be developed using uniaxial stress-strain models for concrete, wall steel, beam steel, and post-tensioning steel, the properties of the top and seat angles, and the geometry and dimensions of the coupling beam and wall regions. The fiber element model provides an effective tool to conduct nonlinear monotonic and cyclic load analyses of unbonded post-tensioned hybrid coupled wall subassemblages accounting for: (1) nonlinear axial-flexural interaction in the coupling beams; (2) linear-elastic shear behavior in the coupling beams; (3) local deformations in the wall-contact regions; (4) nonlinear cyclic behavior of the angles; (5) nonlinear cyclic behavior of the steel and concrete, including yielding of the steel and crushing of the concrete; (6) gap opening and closing at the beam-to-wall interfaces; and (7) elongation of the post-tensioning tendons due to gap opening. Analytical models of multi-story coupled wall structures can be constructed by combining the subassemblage fiber element models for the floor and roof levels as described in Chapter 6.

The main limitations of the fiber element subassembly model are as follows:

(1) The desired behavior of unbonded post-tensioned coupling beams is governed, primarily, by the opening of gaps at the beam-to-wall interfaces. Shear slip at the beam-to-wall interfaces should be prevented by design, and thus, is not modeled.

(2) The fiber element model accounts for the linear and nonlinear axial-flexural deformations (including gap opening) and linear shear deformations of the coupling beams; however, nonlinear shear deformations are not modeled. Nonlinear shear deformations are not expected to occur in the coupling beams investigated in this dissertation as a result of the gap opening behavior and the transfer of shear forces through the formation of a diagonal compression strut in the beam. Note that nonlinear shear deformations may be significant in beams with small span-to-depth aspect ratios and with thin webs. Modeling of these types of beams is not within the scope of this dissertation.

(3) The degradation (if any) in the coupling stiffness and resistance of the subassemblages due to increasing lateral displacements is modeled; however, any additional degradation under repeated displacement cycles to a constant amplitude is not captured.

(4) Local and/or global instability of the coupling beams should be prevented by design, and thus, is not modeled.

(5) As discussed in Chapter 2, the nonlinear behavior of top and seat angles is complicated and the modeling of the angles in this dissertation has a number of limitations. Angle plastic hinge mechanisms other than the vertical-leg mechanism in Fig. 3.9a can be modeled by changing the assumed angle force-deformation behavior;

however, this is not investigated. Nonlinear behavior and/or failure of the angle-to-beam and angle-to-wall connections should be prevented by design, and thus, is not modeled. Similarly, low cycle fatigue fracture of the angle legs at the plastic hinges is not modeled.

(6) The model assumes that the post-tensioning tendons remain straight during the lateral displacements of a subassemblage. Kinking of the tendons at the beam-to-wall interfaces can occur if the tendons come into contact with the ducts under large displacements of the subassemblage or if the ducts are not oversized (in which case kinking would occur as soon as gap opening occurs). A revised analytical model is presented in Chapter 10 based on the subassemblage experiments described in Chapter 9. The revised model includes the kinking of the post-tensioning tendons at the beam-to-wall interfaces, as well as other improvements to the analytical model described in this chapter.

3.6 Modeling of Embedded Steel Coupling Beams

This section describes an analytical model for hybrid coupled wall subassemblages with embedded steel beams, similar to the subassemblage in Fig. 2.5d. This analytical model is used later in the dissertation to compare the behaviors of hybrid coupled wall structures with unbonded post-tensioned beams and with embedded beams.

As described in Chapter 2, the nonlinear behavior of embedded steel coupling beams can be characterized as “shear critical” or “flexure critical.” The analytical model described below is limited to flexure critical beams with a predominantly flexural, rather than shear, mode of behavior. As an example, Fig. 3.15a shows a flexure critical embedded steel coupling beam subassemblage (Specimen S4 as shown in Figs, 2.5d, 2.5e,

and 2.5f) tested by Harries et al (1997). The beam has a W14×22 (U.S. designation) section with a clear span length of $l_b=1200$ mm and an embedment length of $l_{be}=600$ mm. Flange cover plates with 5 mm thickness are used over the embedded lengths of the beam.

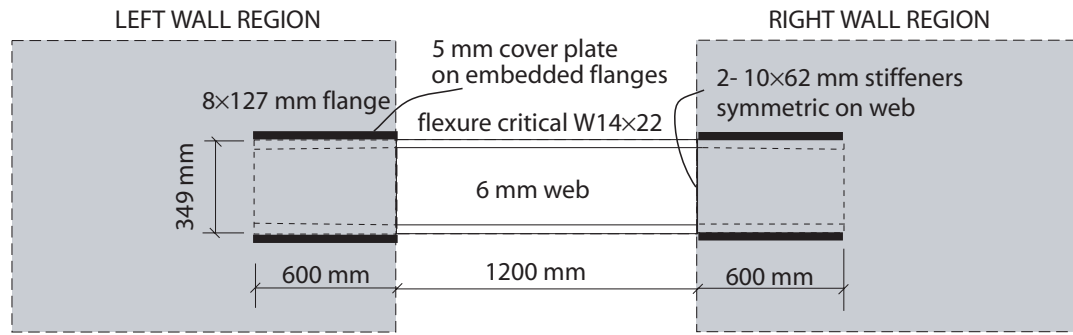
Fig. 3.15b shows a fiber element analytical model for Specimen S4. Similar to the modeling of unbonded post-tensioned subassemblages, the DRAIN-2DX program (Prakash et al. 1993) is used as the analytical platform. Fiber beam-column elements are used to model the coupling beam and the wall regions (referred to as beam elements and wall elements, respectively, in Fig. 3.15b). Previous researchers (Shahrooz et al. 1993a, 1993b; Gong et al. 1997, 1998; Harries et al. 1997) have shown that the flexibility inside the embedment regions needs to be taken into account to ensure that the subassemblage forces and displacements are computed with reasonable accuracy. Based on previous experimental results (Shahrooz et al. 1993a, 1993b, Gong et al. 1997, 1998), the effective length, $l_{b,eff}$ of the coupling beam is assumed to be equal to the clear span length, l_b plus one-third of the embedment length, l_{be} at each end as

$$l_{b,eff} = l_b + (2/3)l_{be} \quad (3.1)$$

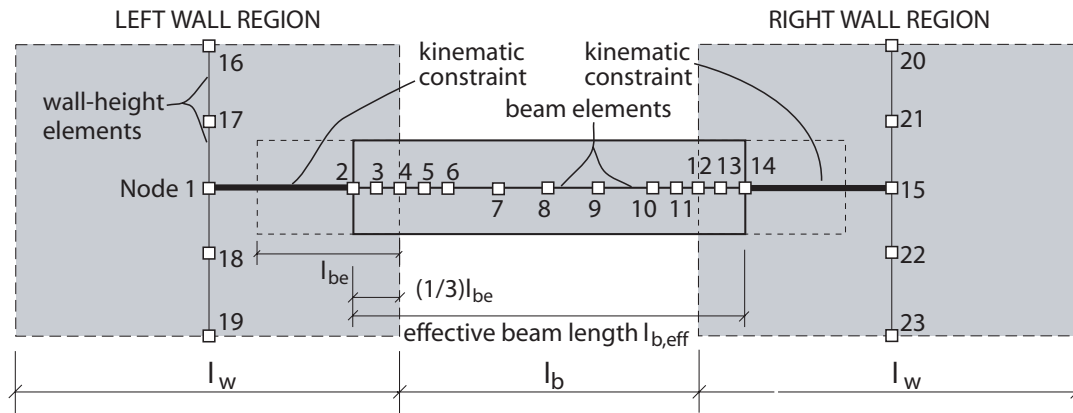
Nodes 2 and 14 represent the effective length of the coupling beam in Fig. 3.15b. The displacements and rotations of these nodes are kinematically constrained to corresponding nodes at the center of each wall region (Nodes 1 and 15, respectively).

Fig. 3.15c shows the cyclic stress-strain relationship used for the steel fibers modeling the coupling beam. Note that the Bauschinger effect of the steel is considered in this model under cyclic loading.

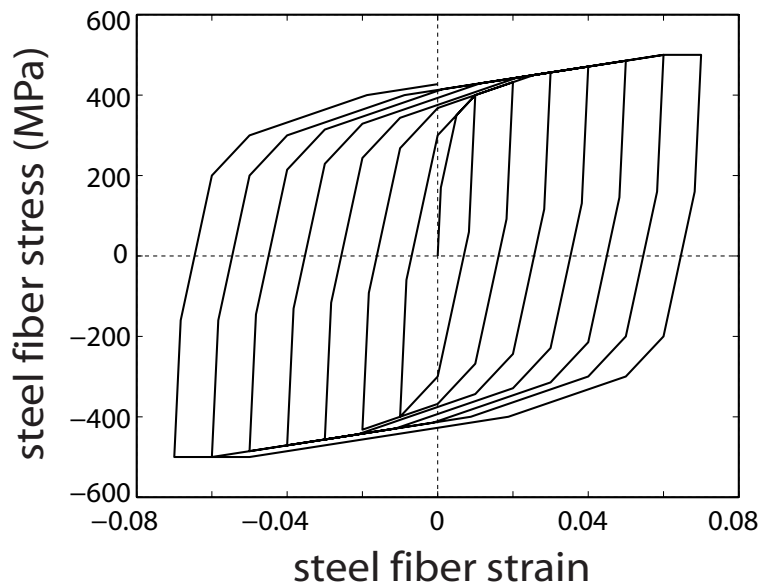
Similarly, Fig. 3.16 shows the analytical model for an embedded steel coupling beam specimen tested by Remmetter et al. (1992). Only one half the length of the beam is tested embedded inside a wall specimen.



(a)



(b)



(c)

Fig. 3.15 Modeling of embedded steel coupling beams: (a) Specimen S4 (Harries et al. 1997); (b) analytical model; (c) steel stress-strain relationship

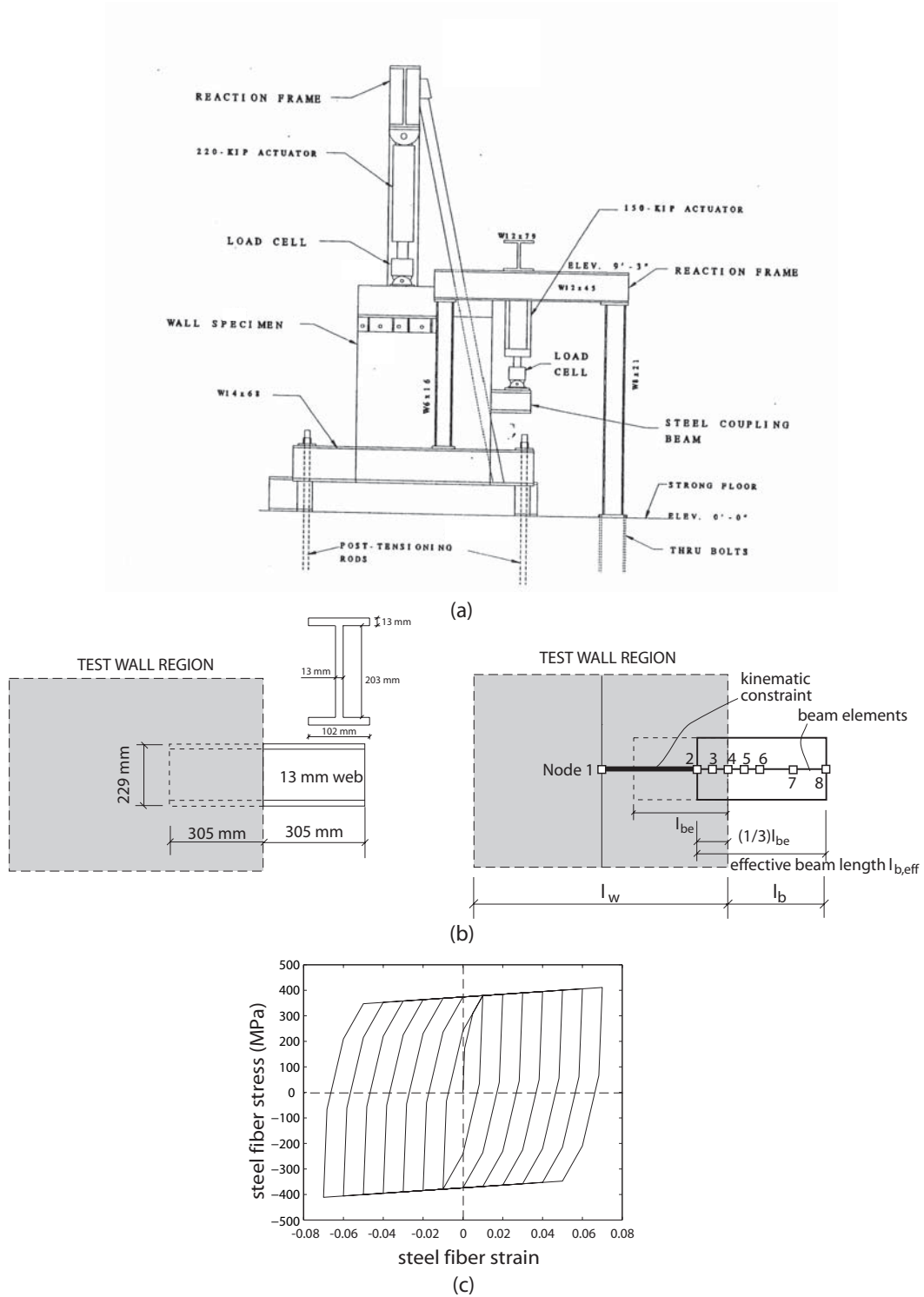


Fig. 3.16 Modeling of embedded steel coupling beams: (a) Specimen 3 (Remmetter et al. 1992); (b) analytical model; (c) steel stress-strain relationship

Fig. 3.17a compares the measured hysteretic load versus displacement behavior of Specimen S4 (Harries et al. 1997) with the predicted behavior from the analytical model. Similarly, Fig. 17b compares the measured and predicted behaviors of Specimen 3 tested by Remmetter et al. (1992). Good agreement is observed between the analytical model and the test results for both specimens.

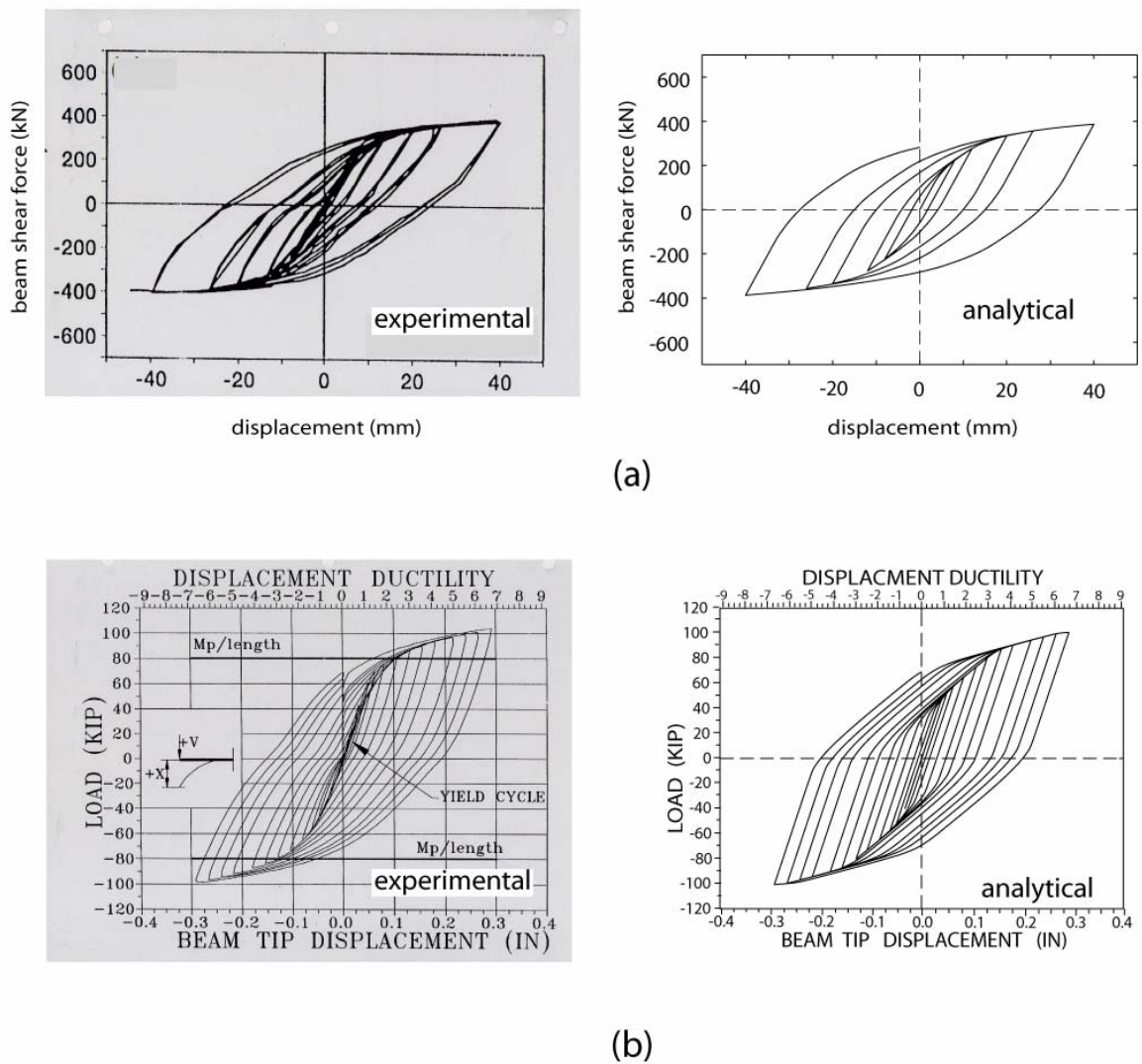


Fig. 3.17 Verification of embedded steel coupling beam model: (a) Specimen S4 (Harries et al. 1997); (b) Specimen 3 (Remmetter et al. 1992)

3.7 Chapter Summary

This chapter describes a fiber element analytical model to investigate the nonlinear behavior of floor-level unbonded post-tensioned hybrid coupled wall subassemblages. The details of a prototype coupled wall subassemblage are also presented. The purpose of the analytical model is to provide a basis for comparisons with subassemblage experimental results as described later in the dissertation and to provide a basis for the modeling of multi-story coupled wall structures. A preliminary verification of the fiber element subassemblage model is done based on comparisons with finite element models. An analytical model for embedded steel coupling beam subassemblages is also developed in the chapter to investigate the differences in the seismic behaviors of coupled wall structures with unbonded post-tensioned and embedded steel beams later in the dissertation.

CHAPTER 4

NONLINEAR BEHAVIOR OF COUPLED WALL SUBASSEMBLAGES

This chapter describes an analytical investigation on the nonlinear moment versus rotation behavior of unbonded post-tensioned hybrid coupled wall subassemblages as follows: (1) overview of subassemblage analyses; (2) behavior under monotonic loading; (3) behavior under cyclic loading; and (4) parametric analyses. These subassemblage analyses are necessary to form a foundation for the investigation of multi-story coupled wall behavior later in the dissertation. The prototype subassemblage and the fiber element model presented in Chapter 3 are used to conduct the analyses.

4.1 Overview of Subassemblage Analyses

Based on the fiber element and finite element analysis results described in Chapter 3, it was found that the deformations in the wall-height elements of the subassemblage model are not significant. Thus, as shown in Fig. 4.1, the wall-height elements are removed from the fiber element model for the purpose of the subassemblage analyses. The reaction block is assumed to be fixed at Node 1 (see also Fig. 3.3), and the loading block (Node 19) is allowed to translate in the horizontal and vertical directions, but not allowed to rotate. The degrees of freedom (DOFs) of angle element Nodes 34 and 36 are constrained to Node 1 and the DOFs of Nodes 39 and 41 are constrained to Node 19.

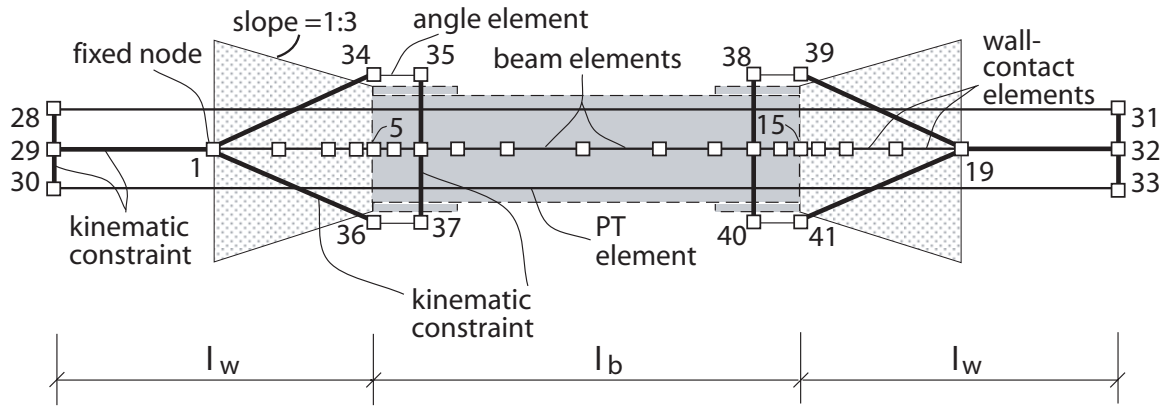


Fig. 4.1 Simplified subassembly model

Following the application of the beam post-tensioning forces, a vertical force V is applied at Node 19. The subassembly analyses are conducted in displacement control based on the relative displacement, u_b (see Fig. 4.2a) of the loading block (Node 19) in the vertical direction with respect to the reaction block (Node 1). Note that since the loading and reaction blocks are not allowed to rotate, the relative vertical displacement between Nodes 5 and 15 at the beam ends is equal to the control displacement u_b as shown in Fig. 4.2b.

4.2 Behavior Under Monotonic Loading

Fig. 4.3a shows the beam end moment versus chord rotation ($M_b-\theta_b$) behavior of the prototype subassembly in Chapter 3 as determined using the simplified fiber element model described above. The corresponding total force in the beam post-tensioning tendons, P_b is shown in Fig. 4.3b, contact depth at the beam-to-wall interfaces, c_b is shown in Fig. 4.3c, extreme beam flange and cover plate compression strains are shown in Fig. 4.3d, and tension angle force versus deformation behavior is shown in Fig.

4.3e. The beam end moment is equal to the coupling moment calculated as $M_b = V l_b / 2$ and the beam chord rotation is calculated as $\theta_b = u_b / l_b$. The contact depth, c_b is normalized with respect to the beam depth, d_{bc} including the flange cover plates. The dashed horizontal lines in Figs. 4.3b, 4.3c, and 4.3d represent, respectively, the total initial force in the beam post-tensioning tendons, P_{bi} , the thickness of the beam flange, t_{bf} plus the cover plate thickness, t_c , and the assumed yield strain of the beam steel, ϵ_{sy} .

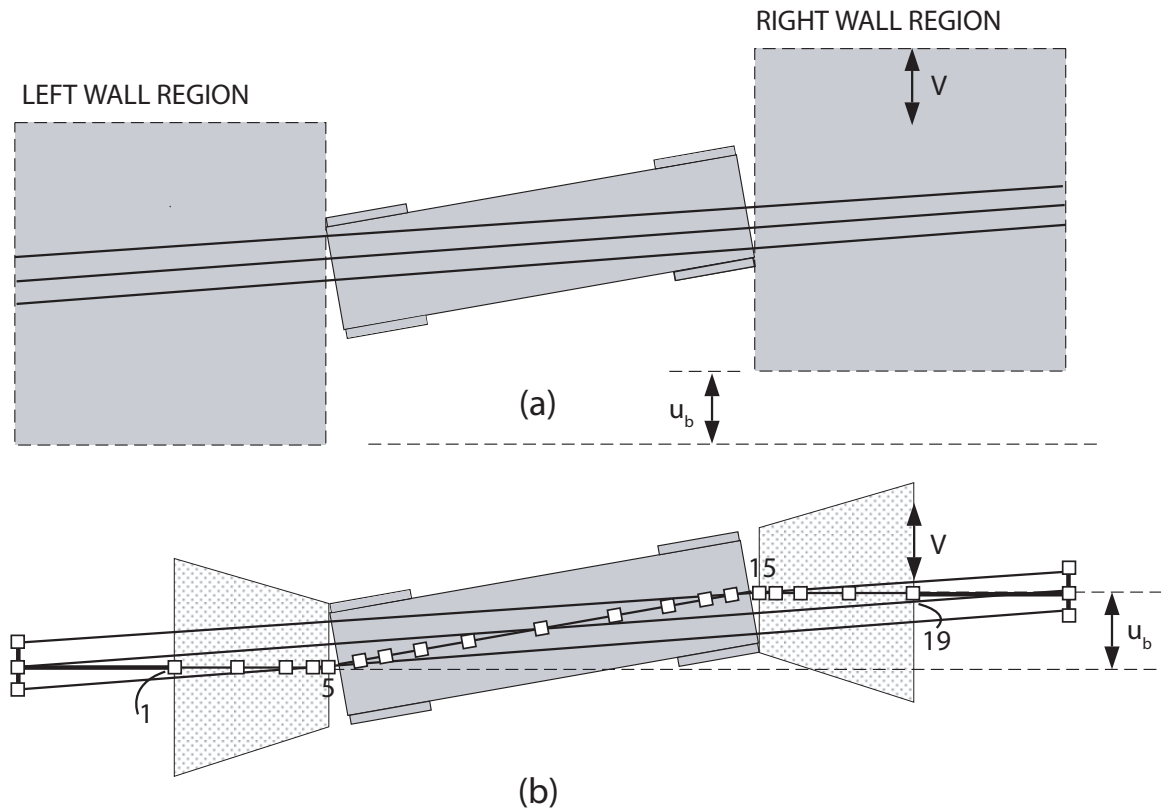


Fig. 4.2 Displaced shape: (a) subassembly; (b) analytical model

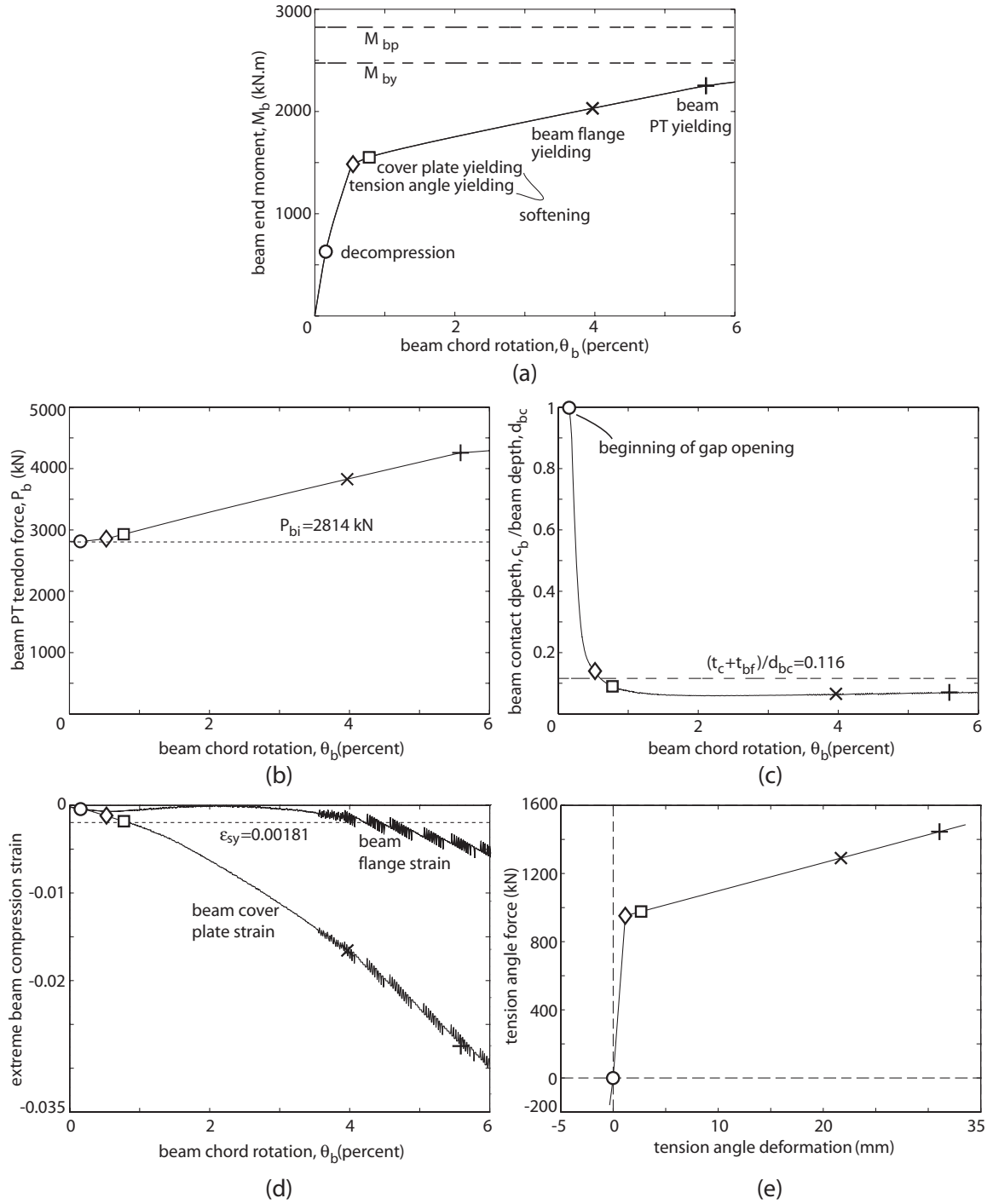


Fig. 4.3 Subassembly behavior under monotonic loading: (a) beam end moment versus beam chord rotation behavior; (b) total force in beam post-tensioning tendons; (c) contact depth; (d) maximum beam compression strain; (e) tension angle behavior

As the subassembly deforms, it goes through five states of response: (1) decompression (i.e., initiation of gap opening), as shown by the circle markers in Fig. 4.3; (2) yielding of the angles in tension, as shown by the diamond markers; (3) yielding of the flange cover plates in compression at the beam-to-wall interfaces, as shown by the square markers; (4) yielding of the beam flanges in compression at the beam-to-wall interfaces, as shown by the “×” markers; and (5) yielding of the beam post-tensioning tendons, as shown by the “+” markers.

The first state in the moment-rotation behavior of the subassembly is decompression at the beam-to-wall interfaces. The beam moment and rotation at this state are referred to as $M_{b,dec}$ and $\theta_{b,dec}$, respectively. Decompression represents the beginning of nonlinear behavior due to gap opening (as indicated by a reduction in the contact depth in Fig. 4.3c) when the precompression due to post-tensioning is overcome by the applied lateral load. The lateral stiffness of the subassembly in Fig. 4.3a before the decompression state is similar to the stiffness of a comparable subassembly with an embedded steel beam. The results indicate that the effect of gap opening (i.e., reduction in contact depth) on the subassembly stiffness is small until the gaps extend over a significant portion of the beam depth and reach close to the compression flange of the beam.

Fig. 4.3a shows that a significant reduction in the stiffness of the subassembly occurs between 0.5% and 0.7% rotation due to a combined effect of increased gap opening, local deformation of the walls in the contact regions, yielding of the angles in tension, and yielding of the flange cover plates in compression. This combined state is referred to as the beam softening state, where the term “softening” is used to describe the

reduction in the stiffness of the structure. The beam moment and rotation at the softening state are referred to as $M_{b,sof}$ and $\theta_{b,sof}$, respectively. It is observed in Fig. 4.3b that the increase in the beam post-tensioning force due to gap opening at the softening state is relatively small. Furthermore, the results in Fig. 4.3c indicate that the beam contact depth remains relatively constant after the softening state is reached.

The moment resistance of the subassemblage continues to increase beyond the softening state. This occurs as a result of the post-yield stiffness of the tension angles and the stiffness of the post-tensioning tendons (which are still linear-elastic). The softening state is followed by the yielding of the beam flanges in compression (at the beam-to-wall interfaces) at a beam moment $M_{b,bfy}$ and rotation $\theta_{b,bfy}$. It is observed in Fig. 4.3d that the maximum compression strains in the flange cover plates are significantly larger than the maximum beam flange strains.

The subassemblage is designed such that the yielding of the post-tensioning tendons, referred to as the beam PT-yielding state, occurs at a large rotation (as shown in Fig. 4.3b). The linear limit point on the stress-strain relationship of the post-tensioning strands (corresponding to $f_{bpy}=1689$ MPa in Fig. 3.2b) is used to identify the yielding of the tendons. Note that the elongations in the tendons due to the deformation of the subassemblage are the same regardless of their location in the beam cross section since the left and right wall regions are not allowed to rotate relative to each other as shown in Fig. 4.2. Thus, the tendons yield at the same beam rotation as long as they are prestressed by the same amount. The beam moment and rotation at the PT-yielding state are referred to as $M_{b,pty}$ and $\theta_{b,pty}$, respectively.

As described in Chapter 3, the prestressing of the beam post-tensioning tendons is simulated by tensile forces in the beam PT elements, which are equilibrated by compression forces in the beam and wall-contact elements. Since a small amount of post-tensioning force is lost due to the elastic shortening of the beam and wall-contact elements, a larger amount of tensile force is applied to the beam PT elements in order to achieve the desired amount of initial force (i.e., force just before the application of lateral loads) in the post-tensioning tendons after elastic shortening. For the prototype subassembly, a total force of $P_{bj}=2906$ kN (653.4 kips) is applied in the beam PT elements to achieve the desired initial post-tensioning force of $P_{bi}=n_{bt}a_{bt}f_{bpi}=2814$ kN (633 kips) where, $a_{bt}=420$ mm² is the beam post-tensioning tendon area, $n_{bt}=6$ is the number of beam post-tensioning tendons, and $f_{bpi}=0.6f_{bpu}$ (with $f_{bpu}=1862$ MPa) is the desired initial stress in the tendons.

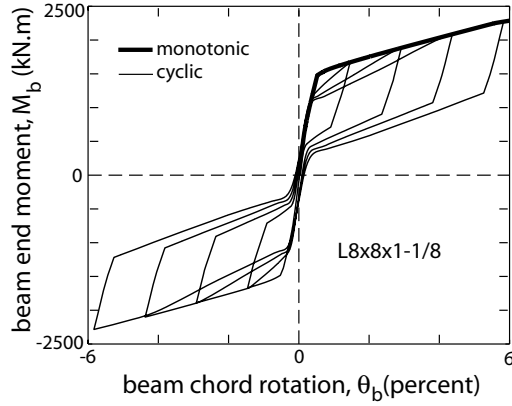
The behavior of the subassembly beyond the beam PT-yielding state is not investigated in Fig. 4.3. The dashed horizontal lines in Fig. 4.3a show the yield moment, M_{by} and the plastic moment, M_{bp} of the W21×182 section used for the prototype beam. The unbonded post-tensioned subassembly reaches the beam softening state at approximately $M_{b,sof} = 0.60M_{by}$ and the PT-yielding state at approximately $M_{b,pty} = 0.80M_{bp}$ (or $M_{b,pty} = 0.91M_{by}$). The beam moment $M_{b,sof}$ is taken as the moment when the tension angles yield. The results indicate that, as a result of gap opening, the strength of an unbonded post-tensioned subassembly is smaller than the strength of a comparable subassembly with a properly-designed and detailed embedded steel beam that achieves the full yield and plastic capacity of the beam cross-section.

4.3 Behavior Under Cyclic Loading

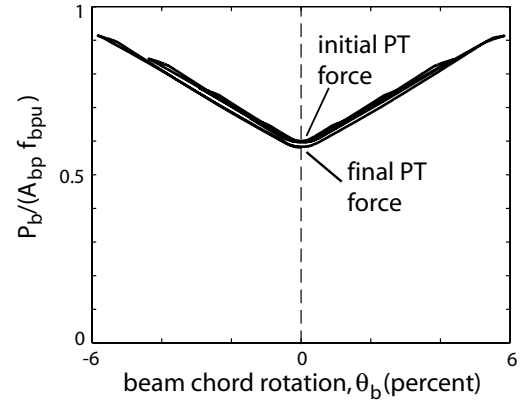
Fig. 4.4a shows the hysteretic moment-rotation behavior of the prototype subassembly under reversed cyclic loading, as determined using the fiber element model in Fig. 4.1. The subassembly has stable behavior under large nonlinear cyclic rotations. The thick curve represents the behavior under monotonic loading as described above. The hysteresis loops show that the subassembly has smaller inelastic energy dissipation but larger self-centering capability as compared to systems with embedded steel coupling beams (e.g., see Fig. 3.17).

The large self-centering capability of the subassembly indicates that the post-tensioning tendons provide a sufficient amount of restoring force to yield the tension angles back in compression and close the gaps at the beam-to-wall interfaces. The total force, P_b in the post-tensioning tendons corresponding to the hysteretic behavior in Fig. 4.4a is shown in Fig. 4.4b. The total post-tensioning force is normalized with respect to the total strength $A_{bp}f_{bpu}$ of the tendons, where $A_{bp}=n_{bt}a_{bt}$. Since the yielding of the post-tensioning tendons is significantly delayed as a result of unbonding, only a small amount of loss in the initial post-tensioning force occurs during the reversed cyclic displacements of the structure.

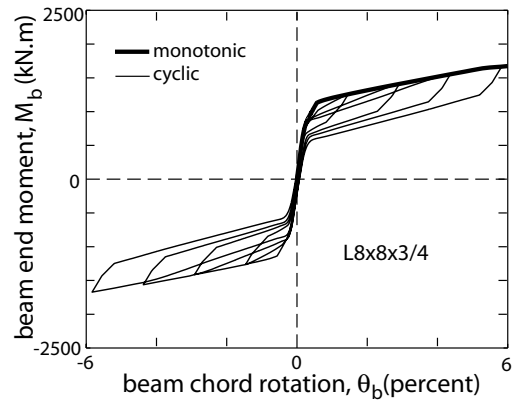
Figs. 4.4c and 4.4d investigate the effect of the top and seat angles on the hysteretic behavior of the subassembly. The moment-rotation behavior in Fig. 4.4c is for a subassembly with smaller angles having a $L8 \times 8 \times 3/4$ cross-section. Similarly, Fig. 4.4d shows the behavior of the prototype subassembly with the angles removed.



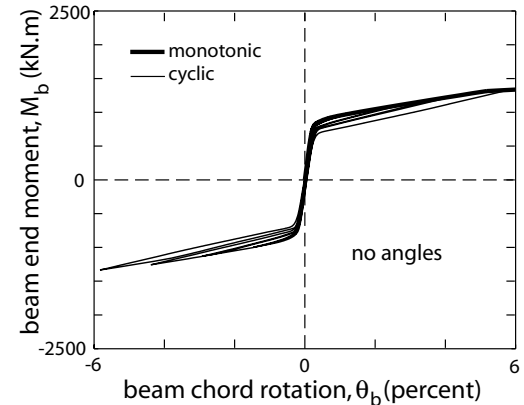
(a)



(b)



(c)



(d)

Fig. 4.4 Subassembly behavior under cyclic loading: (a) with $L8 \times 8 \times 1-1/8$ angles; (b) total force in post-tensioning tendons; (c) with $L8 \times 8 \times 3/4$ angles; (d) without angles

The cyclic behavior of the subassembly without angles is very close to nonlinear-elastic indicating that the angles provide most of the inelastic energy dissipation of the structure and that significant damage is confined to the angles only, which are replaceable after an earthquake. The angle size and amount of post-tensioning can be determined to satisfy different design requirements as described in detail later in the dissertation. A large enough post-tensioning force should be provided to yield the tension angles back in compression during unloading and to develop a sufficient amount of self-centering

capability in the subassembly. If necessary, supplemental energy dissipation devices can be used to increase the energy dissipation of the system.

4.4 Parametric Analyses

This section presents a parametric investigation of the nonlinear moment-rotation behavior of unbonded post-tensioned hybrid coupled wall subassemblages under monotonic loading. Selected structural properties of the prototype subassembly are varied, and then, a monotonic analysis of each subassembly is conducted using the fiber element model. The results are used to determine how the behavior of the system can be controlled by design. The varied properties are: (1) area of post-tensioning tendon, a_{bt} ; (2) initial stress in post-tensioning steel, f_{bpi} ; (3) length of wall, l_w ; (4) thickness of flange cover plate, t_c ; (5) thickness of beam flange, t_{bf} ; (6) depth of beam web, d_{bw} ; and (7) length of beam, l_b .

The subassembly moment-rotation relationships from the parametric investigation are given in Figs. 4.5a-h. Each figure shows the moment-rotation behavior of three parametric subassemblages. Subassembly (1) is the same as the prototype subassembly from Chapter 3 and the properties of Subassemblages (2) and (3) are varied as shown in Table 4.1. The markers in Fig. 4.5 represent the states of behavior identified in Fig. 4.3a.

In Fig. 4.5a, the area a_{bt} and initial stress f_{bpi} of the post-tensioning tendons are varied simultaneously such that the initial post-tensioning force, $P_{bi} = \sum a_{bt} f_{bpi}$ remains constant. The results indicate that the moments $M_{b,dec}$ and $M_{b,sof}$ remain constant when P_{bi} is constant. In Figs. 4.5b and 4.5c, a_{bt} and f_{bpi} are varied one at a time, respectively. There

is an increase in $M_{b,dec}$ and $M_{b,sof}$, and a decrease in $\theta_{b,bfy}$ as a_{bt} is increased. An increase in f_{bpi} results in decreases in $\theta_{b,bfy}$ and $\theta_{b,pty}$, while $M_{b,bfy}$ and $M_{b,pty}$ are not significantly affected.

TABLE 4.1
PARAMETRIC STUDY OF COUPLED WALL SUBASSEMBLAGES

Parameters Varied	Subassembly (1)	Subassembly (2)	Subassembly (3)
Beam post-tensioning tendon area, a_{bt}	420 mm ²	504 mm ² (1.20)	360 mm ² (0.86)
Initial stress in beam post-tensioning steel, f_{bpi}	0.6 f_{bpu}	0.5 f_{bpu} (0.83)	0.7 f_{bpu} (1.17)
Beam post-tensioning tendon area, a_{bt}	420 mm ²	560 mm ² (1.33)	280 mm ² (0.67)
Initial stress in beam post-tensioning steel, f_{bpi}	0.6 f_{bpu}	0.5 f_{bpu} (0.83)	0.7 f_{bpu} (1.17)
Wall length, l_w	3.05 m	3.81 m (1.25)	4.57 m (1.50)
Flange cover plate thickness, t_c	38.1 mm	63.5 mm (1.67)	12.7 mm (0.33)
Beam flange thickness, t_{bf}	37.6 mm	63.0 mm (1.67)	88.4 mm (2.35)
Beam web depth, d_{bw}	502 mm	604 mm (1.20)	705 mm (1.40)
Beam length, l_b	3.05 m	3.81 m (1.25)	4.57 m (1.50)

Note: numbers in parentheses show parameter values for Subassembly (2) or (3) divided by value for Subassembly (1).

As expected, an increase in the wall length, l_w in Fig. 4.5d results in an increase in $\theta_{b,pty}$ since the unbonded length of the post-tensioning tendons is increased. In Fig. 4.5e, the most significant effect of an increase in the flange cover plate thickness t_c is an increase in $\theta_{b,bfy}$. The variables t_{bf} and d_{bw} in Figs. 4.5f and 4.5g represent the beam flange thickness and web depth, respectively. Both parameters affect the stiffness and strength of the subassembly. Finally, Fig. 4.5h shows that the beam length l_b does not have a significant effect on the subassembly moment-rotation behavior, other than a change in $\theta_{b,pty}$ due to a change in the unbonded length of the post-tensioning tendons.

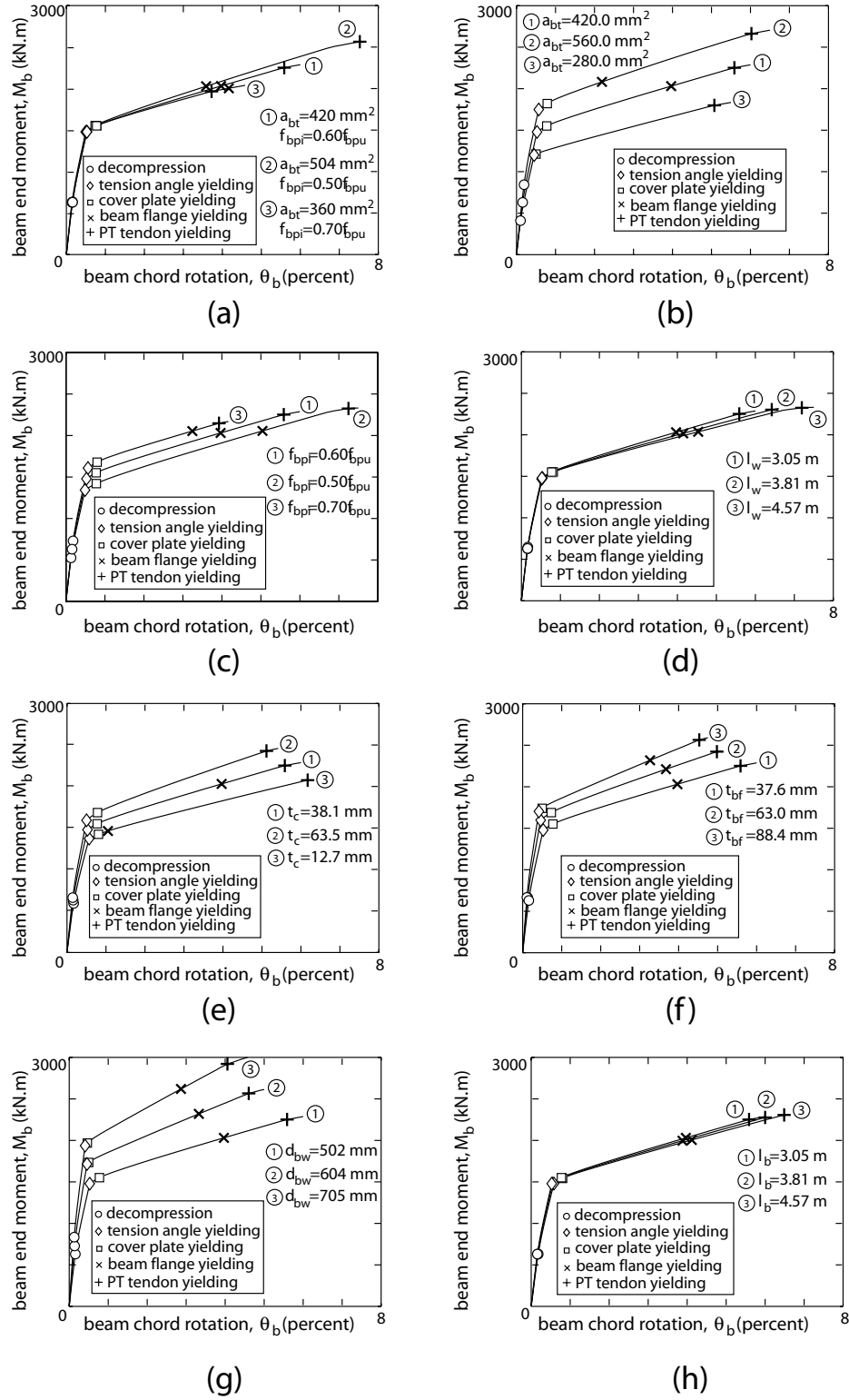


Fig. 4.5 Subassembly moment-rotation behaviors from parametric investigation: (a) a_{bt} and f_{bpi} ; (b) a_{bt} ; (c) f_{bpi} ; (d) l_w ; (e) t_c ; (f) t_{bf} ; (g) d_{bw} ; (h) l_b

Note that the location of the beam post-tensioning tendons is not investigated as a part of the parametric analyses since the elongations in the tendons due to the displacements of the subassembly are the same regardless of the distance of the tendons from the beam centerline (assuming that the tendons are prestressed by the same amount and that the left and right wall regions do not rotate relative to each other as shown in Fig. 4.2). Thus, the subassembly moment-rotation behavior is not affected by the location of the post-tensioning tendons.

The parametric investigation described above provides useful information to control the behavior of unbonded post-tensioned hybrid coupled wall subassemblies in design. For example, the results in Fig. 4.5 show that the coupling moment, shear force, and initial stiffness of the subassemblies can be controlled using the post-tensioning steel area and the beam depth. the coupling shear force, which is equal to $V_b=2M_b/l_b$, can also be controlled using the beam length. the rotation capacity at the pt-yielding state can be controlled by controlling the initial stress and unbonded length of the post-tensioning tendons.

4.5 Chapter Summary

This chapter presents an analytical investigation on the nonlinear behavior of unbonded post-tensioned hybrid coupled wall subassemblies under lateral loads. The effects of structural design parameters such as the amount of post-tensioning, beam properties, and angle properties on the behavior of the subassemblies, including the lateral resistance and energy dissipation is investigated. The following conclusions are made based on the results:

(1) As a result of post-tensioning, the initial stiffness of an unbonded post-tensioned hybrid coupled wall subassembly is similar to the initial stiffness of a comparable embedded steel coupling beam system. Top and seat angles are used at the beam-to-wall interfaces for inelastic energy dissipation and redundancy during an earthquake. The structure can be designed to provide significant and stable levels of coupling over large nonlinear cyclic deformations with most of the damage occurring in the angles, which can be replaced after the earthquake.

(2) The effect of gap opening on the subassembly stiffness is small until the gaps extend over a significant portion of the beam depth.

(3) The behavior of a properly designed and detailed unbonded post-tensioned coupled wall subassembly under lateral loads is characterized by the following five states: (1) decompression; (2) yielding of the angles in tension; (3) yielding of the flange cover plates (if used) in compression; (4) yielding of the flanges in compression; and (5) yielding of the beam post-tensioning tendons.

(4) The total beam post-tensioning force remains relatively constant until the softening state is reached.

(5) The contact depth at the beam-to-wall interfaces remains relatively constant after the softening state is reached.

(6) The post-tensioning force provides a restoring effect that yields the tension angles back in compression, closes the gaps, and pulls the walls and the coupling beam back towards their undisplaced position upon unloading from a large nonlinear deformation. This results in a large self-centering capability of the structure. The initial post-tensioning force is maintained as long as the yielding of the tendons is prevented.

(7) The coupling moment can be controlled by the area of the post-tensioning steel as well as the beam depth, and the yielding of the beam post-tensioning steel can be controlled by the initial stress and unbonded length of the post-tensioning tendons.

(8) As a result of gap opening at the beam-to-wall interfaces, the coupling moment strength of an unbonded post-tensioned steel coupling beam is smaller than the moment strength of an embedded steel coupling beam with the same cross section. This loss in strength is somewhat compensated by the top and seat angles used at the beam ends.

CHAPTER 5

IDEALIZED SUBASSEMBLAGE MOMENT-ROTATION RELATIONSHIP

This chapter presents an idealized beam end moment versus chord rotation relationship for unbonded post-tensioned hybrid coupled wall subassemblages under monotonic lateral loading. Procedures are developed to estimate the structure behavior using basic principles of equilibrium, compatibility, and constitutive relationships. These procedures are used later in the dissertation as design tools and to develop idealized lateral load versus displacement relationships for multi-story coupled wall structures. The chapter is divided into the following sections: (1) linear-elastic behavior; (2) idealized nonlinear relationship; and (3) verification of idealized relationship.

5.1 Linear-Elastic Behavior

The linear-elastic behavior of an unbonded post-tensioned hybrid coupled wall subassemblage under lateral loads can be approximated using the simplified model in Fig. 5.1a. The cross-sectional properties and boundary conditions of the model are determined from the fiber element model in Figs. 3.3a and 3.3b, based on the following general assumptions/approximations:

- (G1) The deformations in the wall-height elements are negligible.
- (G2) The left and right wall regions do not rotate relative to each other.



(b)

132

In the linear-elastic range of behavior, the effects of the post-tensioning tendons and the top and seat angles are ignored. Gap opening at the beam ends causes geometric nonlinear effects on the structure, and thus, is not included in the linear-elastic model.

Due to symmetry, only one half the length of the subassembly is used, from the center of the reaction block (Node 1) to the midspan of the coupling beam (Node 10). The center of the reaction block is fixed and the beam midspan is free. A vertical force V_b is applied at the free end as shown in Fig. 5.1a. The Y-translational DOF of Node 5, which represents the beam-to-wall interface, is restrained. Thus, the model is statically indeterminate to the first degree.

The cross-sectional properties of the model in Fig. 5.1a vary along the length. The properties between Nodes 1 and 5 are the same as the properties used for the wall-contact elements in the fiber element model in Fig. 3.3b. The cross-sectional properties between Nodes 5 and 8 and between Nodes 8 and 10 are determined based on the beam cross section with and without the cover plates (if used), respectively.

The linear-elastic lateral stiffness of the subassembly is defined using the beam end moment versus chord rotation (M_b - θ_b) relationship as:

$$K_{bi} = \frac{M_b}{\theta_b} \quad (5.1)$$

and can be determined using an appropriate linear-elastic structural analysis procedure based on the model in Fig. 5.1a. Closed-form expressions for K_{bi} can also be developed.

Note that a simpler linear-elastic subassembly model can be obtained by ignoring the deformations in the wall-contact elements, resulting in a small overestimation of the initial stiffness as shown in Fig. 3.12. The linear-elastic subassembly model without the

wall-contact elements is shown in Fig. 5.1b. This model is statically determinate. Ignoring the effect of the beam flange cover plates (if any) and including the shear deformations of the beam, the subassembly initial stiffness, K_{bi} can be determined as:

$$K_{bi} = \frac{6E_b I_b}{l_b} \frac{1}{1 + 2\alpha_{bg}} \quad (5.2)$$

where,

$$\alpha_{bg} = \frac{6E_b I_b}{G_b A_{bg} l_b^2} \quad (5.3)$$

with G_b (shear modulus of the coupling beam steel) and A_{bg} (shear area of the coupling beam cross section) given as,

$$G_b = \frac{E_b}{2(1 + \nu_b)} \text{ and } A_{bg} = d_b t_{bw} \quad (5.4)$$

and l_b is the coupling beam span length (as shown in Fig. 5.1), I_b is the moment of inertia, d_b is the depth, and t_{bw} is the web thickness of the coupling beam cross section (ignoring the beam flange cover plates), and ν_b and E_b are the Poisson's ratio and modulus of elasticity of the beam steel, respectively (assumed as $\nu_b=0.3$ and $E_b=199955$ MPa, resulting in $G_b=76907$ MPa).

For the prototype subassembly in Chapter 3, initial linear-elastic stiffness values of $K_{bi}=4.25 \times 10^8$ kN-mm (3.77×10^6 kip-in.) and $K_{bi}=5.01 \times 10^8$ kN-mm (4.43×10^8 kip-in.) result from the models in Figs. 5.1a and 5.1b, respectively, which compare well with the value of $K_{bi}=4.17 \times 10^8$ kN-mm (3.69×10^6 kip-in.) from the DRAIN-2DX fiber element model including the beam cover plates and the wall-contact elements.

5.2 Idealized Nonlinear Relationship

The nonlinear beam end moment versus chord rotation behavior of an unbonded post-tensioned hybrid coupled wall subassembly is idealized using a bilinear relationship. As an example, Fig. 5.2 shows the bilinear moment-rotation relationship estimated for the prototype subassembly in Chapter 3. The idealized moment-rotation relationship is identified by the coupling beam softening state (at $M_{b,sof}$, $\theta_{b,sof}$) and the PT-yielding state (at $M_{b,pty}$, $\theta_{b,pty}$). A procedure to estimate $M_{b,sof}$, $\theta_{b,sof}$, $M_{b,pty}$, and $\theta_{b,pty}$ is developed below using basic principles of equilibrium, compatibility, and constitutive relationships. This estimation procedure can be used as a tool in the seismic analysis and design of coupled wall structural systems, without the need to develop nonlinear fiber element models.

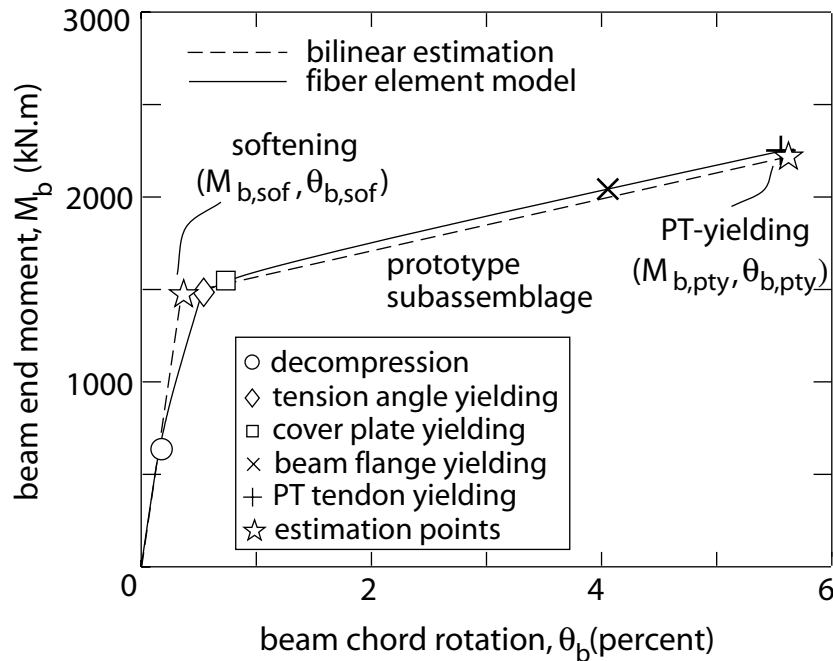


Fig. 5.2 Idealized bilinear subassembly moment-rotation relationship

The following general assumptions/approximations are made for the development of the bilinear subassembly relationship, in addition to assumptions (G1)-(G2) described previously:

(G3) Local and/or global instability of the coupling beam does not occur.

(G4) The post-tensioning anchorages, angle-to-beam and angle-to-wall connections, and cover-plate-to-beam-flange welds (if cover plates are used) are properly designed and detailed for the maximum forces and deformations.

(G5) The coupling beam does not slip with respect to the walls at the beam-to-wall interfaces.

(G6) The cover plates (if used) are sufficiently long such that yielding of the coupling beam does not occur where the plates are terminated.

5.2.1 Beam Softening State

The beam end moment $M_{b,sof}$ and chord rotation $\theta_{b,sof}$ at the softening state of an unbonded post-tensioned hybrid coupled wall subassembly are estimated based on the following assumptions, in addition to the general assumptions (G1)-(G6) above:

(S1) The force in each tension angle is equal to the yield force, T_{ayx} (see Fig. 3.9), and acts at the middle of the horizontal leg of the angle parallel to the beam flange.

(S2) The force in each compression angle is equal to the slip force, C_{asx} (see Fig. 3.9), of the angle-to-beam connection bolts and acts at the middle of the horizontal leg of the angle parallel to the beam flange.

(S3) The stress in the beam post-tensioning tendons is equal to the initial stress, f_{bpi} (as demonstrated in Fig. 4.3b).

The steps used in the estimation of $M_{b,sof}$ and $\theta_{b,sof}$ are presented below:

Step 1

Based on Assumptions (G3), (G4), (S1), (S2), and (S3), and using the free body diagram in Fig. 5.3, estimate the total beam compression force at the beam-to-wall interface as:

$$C_{b,sof} = P_{bi} + T_{ayx} - C_{asx} \quad (5.5)$$

where, P_{bi} is the total initial post-tensioning force as:

$$P_{bi} = \sum a_{bt} f_{bpi} \quad (5.6)$$

Step 2

Estimate the depth of the compression (i.e., contact) region, $c_{b,sof}$ at the beam-to-wall interface using a linear stress distribution based on Assumptions (S4) and (S5). Assuming that the compression region is above the coupling beam web (i.e., $c_{b,sof} \leq t_{bf} + t_c$) and the width of the cover plate is the same as the beam flange width b_{bf} , then, $c_{b,sof}$ can be estimated as:

$$c_{b,sof} = \frac{2C_{b,sof}}{f_{sy} b_{bf}} \quad (5.7)$$

Note that a non-rectangular compression region should be used if the compression region extends into the beam web (i.e., $c_{b,sof} > t_{bf} + t_c$). The cover plate thickness $t_c = 0$ if no cover plates are used on the coupling beam.

Step 3

Estimate the moment $M_{b,sof}$ at the beam-to-wall interface by taking moments about the centerline of the beam as:

$$M_{b,sof} = V_{b,sof} \frac{l_b}{2} = C_{b,sof} \left(\frac{d_{bc}}{2} - \frac{c_{b,sof}}{3} \right) + 0.5(C_{asx} + T_{ayx})(d_{bc} + t_a) \quad (5.8)$$

where, d_{bc} is equal to the total beam depth including the cover plate thicknesses (i.e., $d_{bc}=d_b+2t_c$).

Step 4

Estimate the beam chord rotation at the softening state, $\theta_{b,sof}$ using the initial lateral stiffness, K_{bi} from a linear-elastic analysis of the subassembly (see Section 5.1). Ignore the rotation that occurs due to gap opening since the effect of gap opening on the stiffness of the subassembly before the softening state is small as shown in Fig. 4.3. Thus,

$$\theta_{b,sof} = \frac{M_{b,sof}}{K_{bi}} \quad (5.9)$$

Step 5

The nonlinear behavior of the coupled wall subassembly can also be represented using the coupling shear force versus beam chord rotation relationship. Estimate the coupling shear force at the softening state, $V_{b,sof}$, as:

$$V_{b,sof} = \frac{2M_{b,sof}}{l_b} \quad (5.10)$$

5.2.2 Beam PT-Yielding State

The beam end moment, $M_{b,pty}$ and chord rotation, $\theta_{b,pty}$ at the PT-yielding state of an unbonded post-tensioned hybrid coupled wall subassembly are estimated using an iterative procedure based on the following assumptions, in addition to the general assumptions (G1)-(G6) described previously:

(P1) The beam post-tensioning tendons are stressed to the same initial stress, f_{bpi} .

(P2) Strain hardening of the beam and cover plate (if any) steel in compression is ignored. Thus, the largest compression stress in the beam and cover plates is equal to f_{sy} .

(P3) The compressive stresses in the beam and in the cover plates at the beam-to-wall interfaces have a uniform (i.e., rectangular) distribution.

(P4) An idealized load-deformation relationship is available for the angles in tension.

(P5) The force in each compression angle is equal to the slip force, C_{asx} (see Fig. 3.9), of the angle-to-beam connection bolts and acts at the middle of the horizontal leg of the angle parallel to the beam flange.

Based on these assumptions, Fig. 5.4 shows the PT-yielding-state free body diagram of a coupling beam between the midspan and the beam-to-wall interface. The beam shear force is equal to the coupling shear force at the beam PT-yielding state, $V_{b,pty}$ and the beam axial force at midspan is equal to the total force in the post-tensioning tendons at yield, $P_{b,pty}$. The rectangular compressive stress distribution shown at the beam end is based on Assumptions (P2) and (P3).

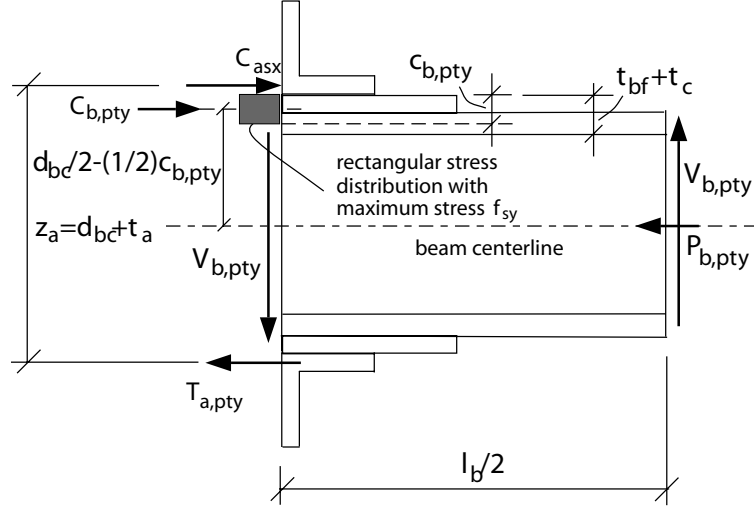


Fig. 5.4 Coupling beam free body diagram at PT-yielding state

The steps used in the estimation of $M_{b,pty}$ and $\theta_{b,pty}$ are presented below:

Step 1

Select an initial value for the tension angle force at PT-yielding, $T_{a,pty}$. Since the tension angles are assumed to yield at the softening state, $T_{a,pty} > T_{ayx}$. An initial value of $T_{a,pty}$ may be selected as:

$$T_{a,pty} = T_{ayx} \quad (5.11)$$

Step 2

Based on the free body diagram in Fig. 5.4, estimate the total beam compression force at the beam-to-wall interface as:

$$C_{b,pty} = P_{b,pty} + T_{a,pty} - C_{asx} \quad (5.12)$$

where, $T_{a,pty}$ is from Step 1. As described in Chapter 4, the post-tensioning tendons go through the same elongation regardless of their locations within the beam depth. Thus, based on Assumption (P1), the tendons yield simultaneously and

$$P_{b,pty} = \sum a_{bt} f_{bpy} \quad (5.13)$$

Step 3

Estimate the depth of the compression (i.e., contact) region, $c_{b,pty}$ at the beam-to-wall interface using a uniform contact stress distribution based on Assumptions (P2) and (P3). Assuming that the compression region is above the coupling beam web and the width of the cover plate (if any) is the same as the beam flange width b_{bf} , then, $c_{b,pty}$ can be estimated as:

$$c_{b,pty} = \frac{C_{b,pty}}{f_{sy} b_{bf}} \quad (5.14)$$

A non-rectangular compression region should be used if $c_{b,pty} > t_{bf} + t_c$. The cover plate thickness $t_c = 0$ if no cover plates are used on the coupling beam.

Step 4

Estimate the elongation of the beam post-tensioning tendons between the initial prestress state and the PT-yielding state as:

$$u_{b,pty} = \frac{(f_{bpy} - f_{bpi}) l_{bpu}}{E_{bp}} \quad (5.15)$$

where, $l_{bpu} = l_b + 2l_w$ is the unbonded length and E_{bp} is the Young's modulus of the tendons.

Step 5

Estimate the width of the beam-to-wall gap at the centerline of the beam, $g_{b,pty}$. Fig. 5.5 shows the gap opening that occurs at the beam-to-wall interface at the PT-yielding state. Since the left and right wall regions do not rotate relative to each other, the centerline gap at the two ends of the beam have the same width, and thus,

$$g_{b,pty} = \frac{u_{b,pty}}{2} \quad (5.16)$$

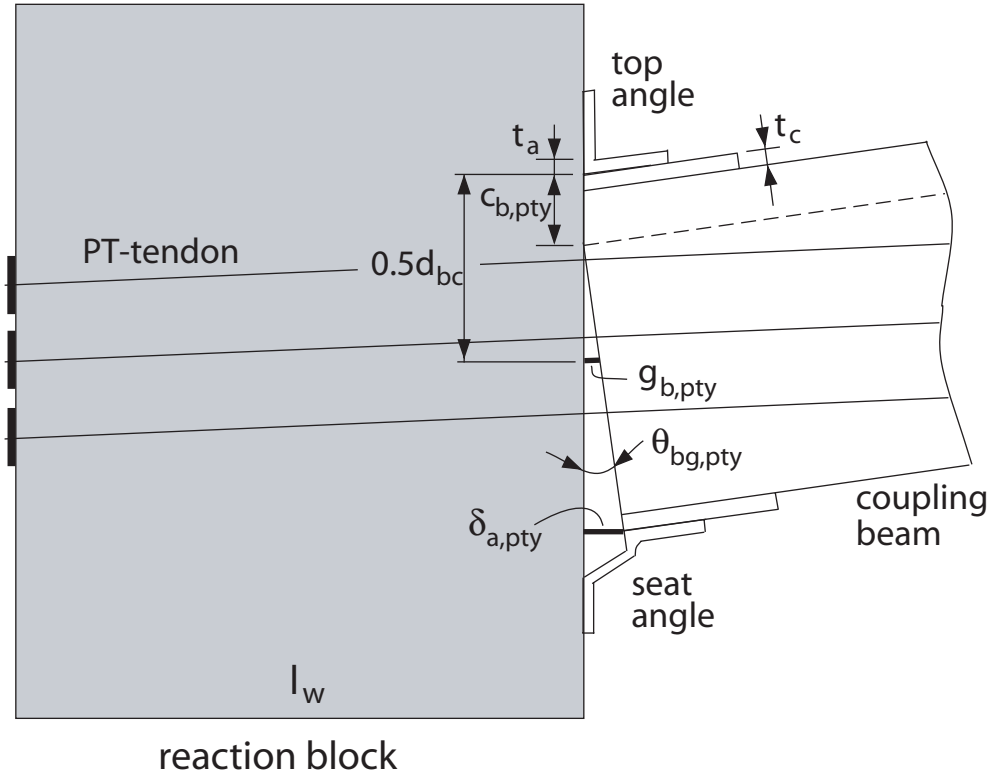


Fig. 5.5 Gap opening at coupling beam PT-yielding state

Step 6

Estimate the elongation of the tendon angle, $\delta_{a,pty}$ due to gap opening. Based on Fig. 5.5:

$$\delta_{a,pty} = \frac{d_{bc} + 0.5t_a - c_{b,pty}}{0.5d_{bc} - c_{b,pty}} g_{b,pty} \quad (5.17)$$

Step 7

Determine the tension angle force $T_{a,pty}$ using the angle deformation $\delta_{a,pty}$ from Step 6 and the idealized angle load-deformation relationship from Assumption (P4). Repeat Steps 1-7 using the value of $T_{a,pty}$ from Step 7 in Step 1 until a satisfactory agreement between the $T_{a,pty}$ values from Steps 1 and 7 is achieved. Analyses of the parametric coupled wall subassemblages from Chapter 4 indicate that convergence can be achieved in four to five iterations.

Step 8

Based on the free body diagram in Fig. 5.4, estimate the moment $M_{b,pty}$ at the beam-to-wall interface by taking moments about the centerline of the beam as:

$$M_{b,pty} = V_{b,pty} \frac{l_b}{2} = 0.5C_{b,pty}(d_{bc} - c_{b,pty}) + 0.5(C_{asx} + T_{a,pty})(d_{bc} + t_a) \quad (5.18)$$

Step 9

Referring to Fig. 5.5, estimate the rotation of the beam due to gap opening at the PT-yielding state as:

$$\theta_{bg,pty} = \frac{g_{b,pty}}{0.5d_{bc} - c_{b,pty}} \quad (5.19)$$

where, $g_{b,pty}$ and $c_{b,pty}$ are determined in Steps 5 and 3, respectively.

Step 10

Estimate the elastic rotation of the beam at the PT-yielding state as:

$$\theta_{be,pty} = \frac{M_{b,pty}}{K_{bi}} \quad (5.20)$$

Step 11

Estimate the total beam chord rotation at the PT-yielding state as:

$$\theta_{b,pty} = 1.075(\theta_{bg,pty} + \theta_{be,pty}) \quad (5.21)$$

where, $\theta_{bg,pty}$ and $\theta_{be,pty}$ are from Steps 9 and 10, respectively.

Based on the analyses of the parametric subassemblages from Chapter 4, a factor of 1.075 is necessary in the estimation of $\theta_{b,pty}$ to account for the additional beam rotation that occurs due to the deformations in the wall-contact regions at the PT-yielding state.

Step 12

Consider second order effects (often referred to as “P- Δ ” effects) as follows:

- If the beam post-tensioning ducts are not oversized, then, the tendons kink at the beam-to-wall interfaces as soon as gap opening occurs and displace parallel to the coupling beam. Thus, the second order effects in the tendons counteract the second order effects in the coupling beam and,

$$M_{b,pty} \text{ (with second order effects)} = M_{b,pty} \text{ (from Step 8)} \quad (5.22)$$

- If the beam post-tensioning ducts are large enough such that the post-tensioning tendons remain straight (i.e., the tendons do not kink at the beam-to-wall interfaces). Then, referring to Fig. 5.6, the displaced shapes of the beam and the post-tensioning tendons differ, resulting in second order effects as:

$$M_{b,pty} \text{ (with second order effects)} = M_{b,pty}(\text{from Step 8}) - \frac{P_{b,pty}\theta_{b,pty}l_b}{2} \left(1 - \frac{l_b}{l_b + 2l_w}\right) \quad (5.23)$$

The parametric analyses from Chapter 4, which assume that the post-tensioning tendons remain straight, indicate that the change in $M_{b,pty}$ due to second order effects results in a negligible change in $\theta_{b,pty}$ and, thus, there is no need to update the rotation $\theta_{b,pty}$ from Step 10. Note also that a consideration of second order effects is not necessary in the estimation of the softening state moment $M_{b,sof}$ since the beam rotation at the softening state (i.e., $\theta_{b,sof}$) is small.

- If the beam post-tensioning ducts are oversized, but not enough to prevent kinking of the post-tensioning tendons during the entire displacement history of the subassemblage, then, an $M_{b,pty}$ value in between the values given by Equations (5.22) and (5.23) should be used.

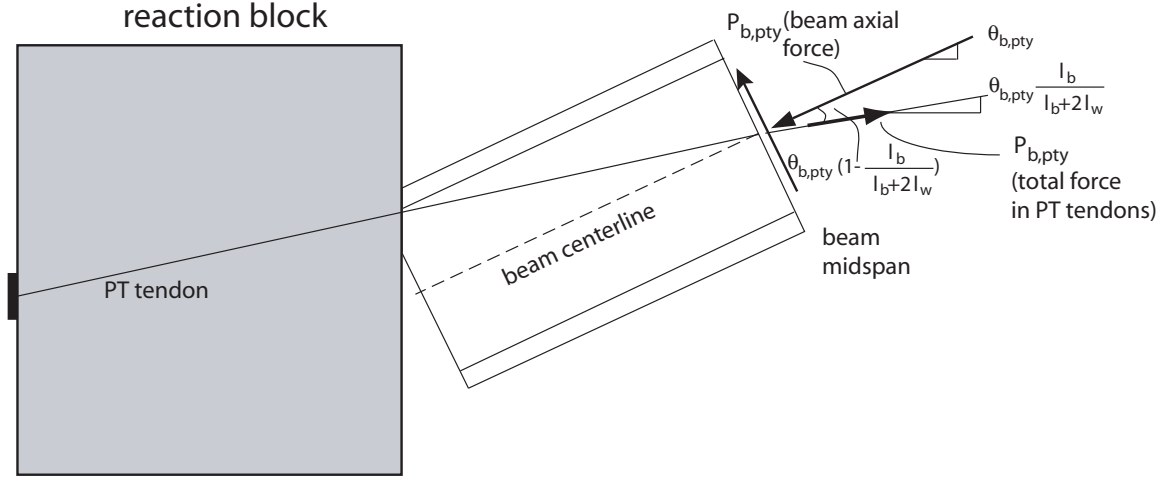


Fig. 5.6 Second order effects

Step 13

Estimate the coupling shear force at the PT-yielding state, $V_{b,pty}$, as:

$$V_{b,pty} = \frac{2M_{b,pty}}{l_b} \quad (5.24)$$

5.3 Verification of Idealized Relationship

The bilinear estimation of the subassembly moment versus rotation behavior described above is verified by comparing the estimated moment and rotation values corresponding to the softening and PT-yielding states with values determined using the fiber element model. The $M_{b,sof}$ and $\theta_{b,sof}$ values from the fiber element model are determined at the “tension angle yielding” state from the subassembly moment-rotation relationship. Fig. 5.7 shows the comparisons for the $M_{b,sof}$ and $M_{b,pty}$ values and Fig. 5.8

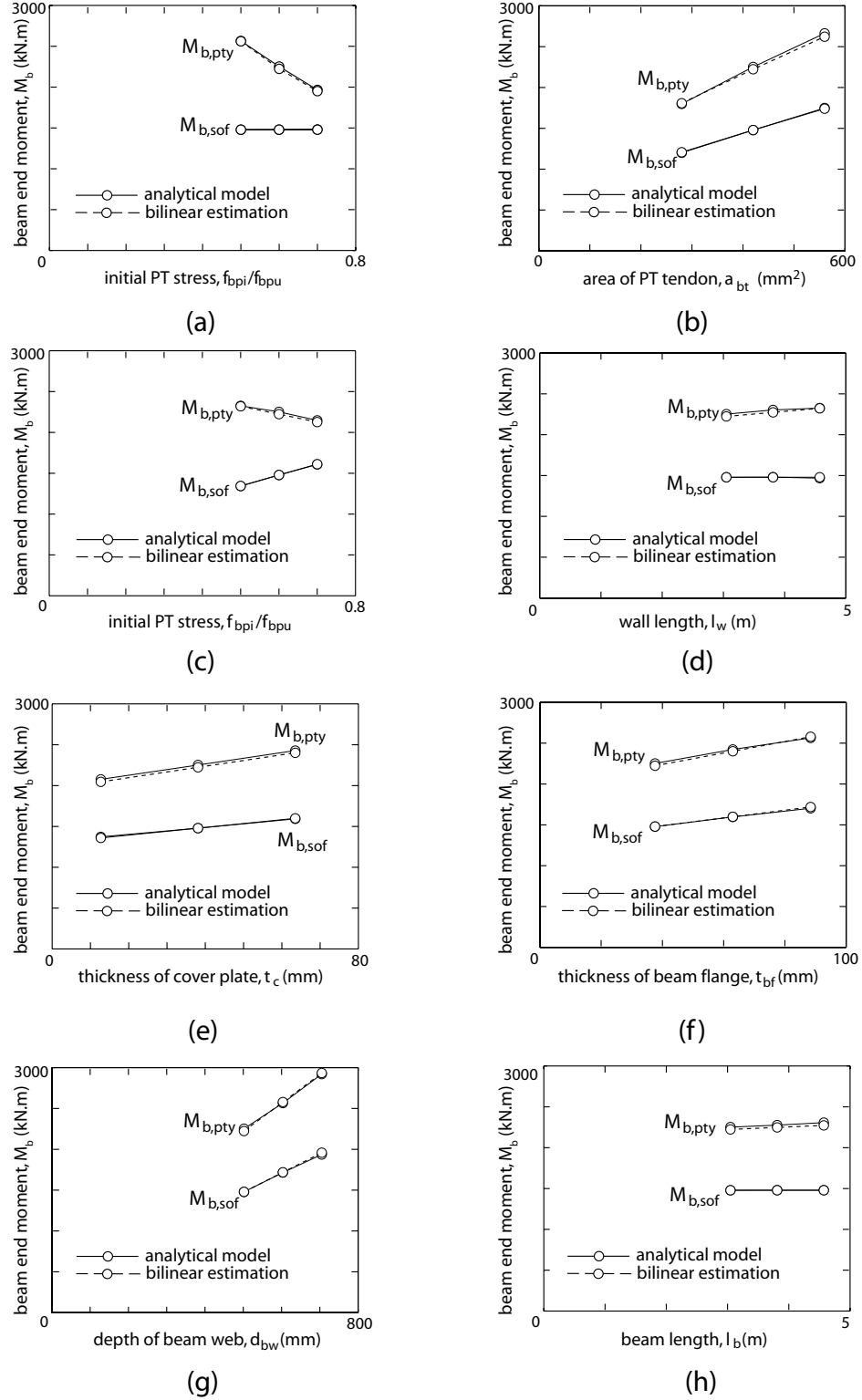
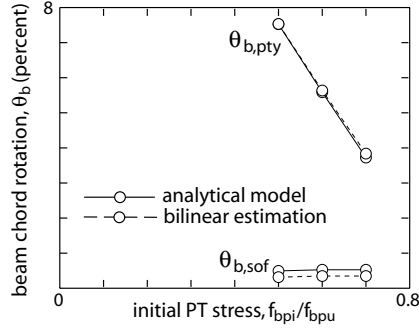
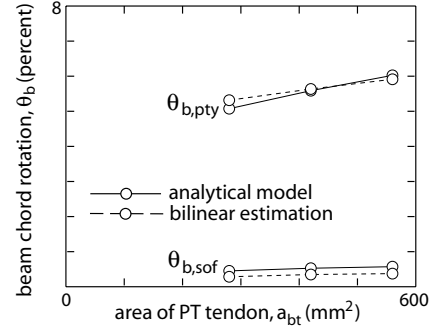


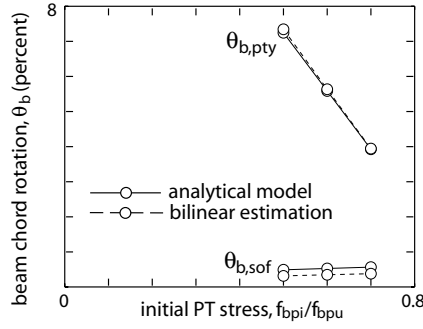
Fig. 5.7 Verification of moment estimations: (a) a_{bt} and f_{bpi} ; (b) a_{bt} ; (c) f_{bpi} ; (d) l_w ; (e) t_c ; (f) t_{bf} ; (g) d_{bw} ; (h) l_b



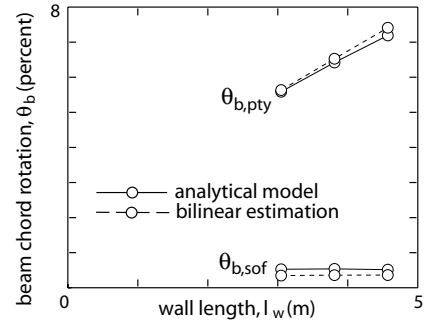
(a)



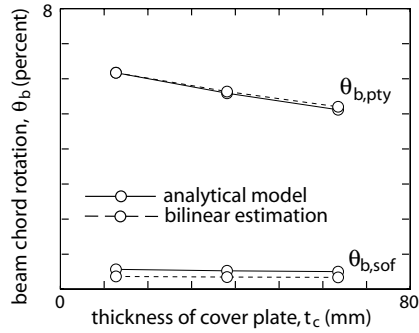
(b)



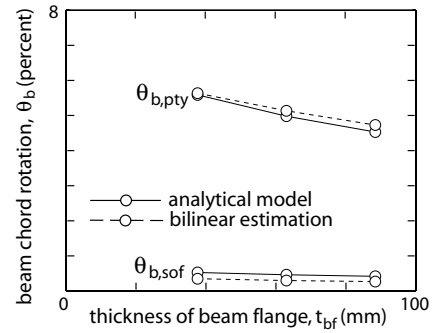
(c)



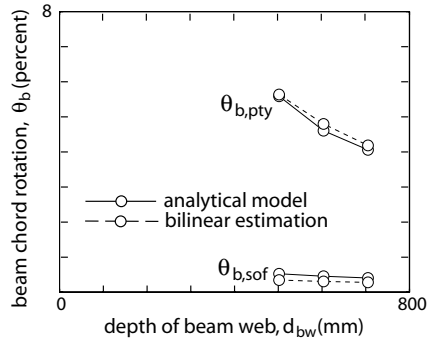
(d)



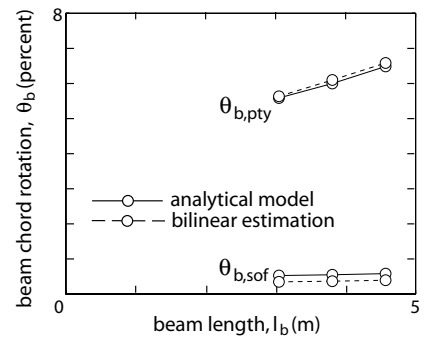
(e)



(f)



(g)



(h)

Fig. 5.8 Verification of rotation estimations: (a) a_{bt} and f_{bpi} ; (b) a_{bt} ; (c) f_{bpi} ; (d) l_w ; (e) t_c ; (f) t_{bf} ; (g) d_{bw} ; (h) l_b

shows the comparisons for the $\theta_{b,sof}$ and $\theta_{b,pty}$ values for the parametric subassemblages in Fig. 4.5. The effect of the wall-contact elements is included in the estimation of K_{bi} (using the model in Fig. 5.1a) and second order effects are included in the estimation of $M_{b,pty}$. The results indicate that the estimated moment and rotation values are remarkably close to the values determined using the fiber element model for a wide range of parameters. The maximum error in the estimation of $M_{b,sof}$, K_{bi} , $M_{b,pty}$, and $\theta_{b,pty}$ is less than 5%. Thus, it is concluded that the estimation procedure described above can be used to conduct approximate, simplified analyses of unbonded post-tensioned hybrid coupled wall subassemblages with different properties.

5.4 Chapter Summary

This chapter describes an analytical procedure to estimate the nonlinear lateral load versus displacement behavior of unbonded post-tensioned hybrid coupled wall subassemblages by quantifying two selected limit states. The estimation procedure, which is verified with results from the DRAIN-2DX program (Prakash et al. 1993), can be used to conduct approximate, simplified analyses of coupled wall subassemblages with different structural properties. This procedure is used later in Chapter 8 to estimate the behavior of multistory coupled wall systems under lateral loads and in the seismic design approach proposed in Chapters 11 and 12.

CHAPTER 6

ANALYTICAL MODELING OF MULTI-STORY COUPLED WALLS

This chapter describes the analytical modeling of multi-story hybrid coupled wall structures as follows: (1) prototype coupled wall structures; (2) analytical modeling assumptions; (3) multi-story coupled wall models; (4) verification of wall models; (5) advantages and limitations of analytical models; and (6) modeling of walls with embedded coupling beams.

6.1 Prototype Coupled Wall Structures

This section describes the design properties of two prototype eight-story unbonded post-tensioned hybrid coupled wall structures. The plan view of the building for which the structures were designed is shown in Fig. 6.1. This plan layout was determined based on the recommendations from the *U.S.-Japan Cooperative Earthquake Research Program on Composite and Hybrid Structures* (Goel and Yamanouchi 1992) funded by the National Science Foundation. The building was designed for a site with a “stiff” soil profile [Site Class *D* in IBC-2000 (ICC 2000)] in a region with high seismicity (e.g., coastal California).

A set of four identical unbonded post-tensioned hybrid coupled wall structures provide the entire lateral load resistance in the east-west direction of the building. The structural walls providing lateral load resistance in the north-south direction of the

building are not addressed in this dissertation. The properties of the prototype coupled wall structures are presented below.

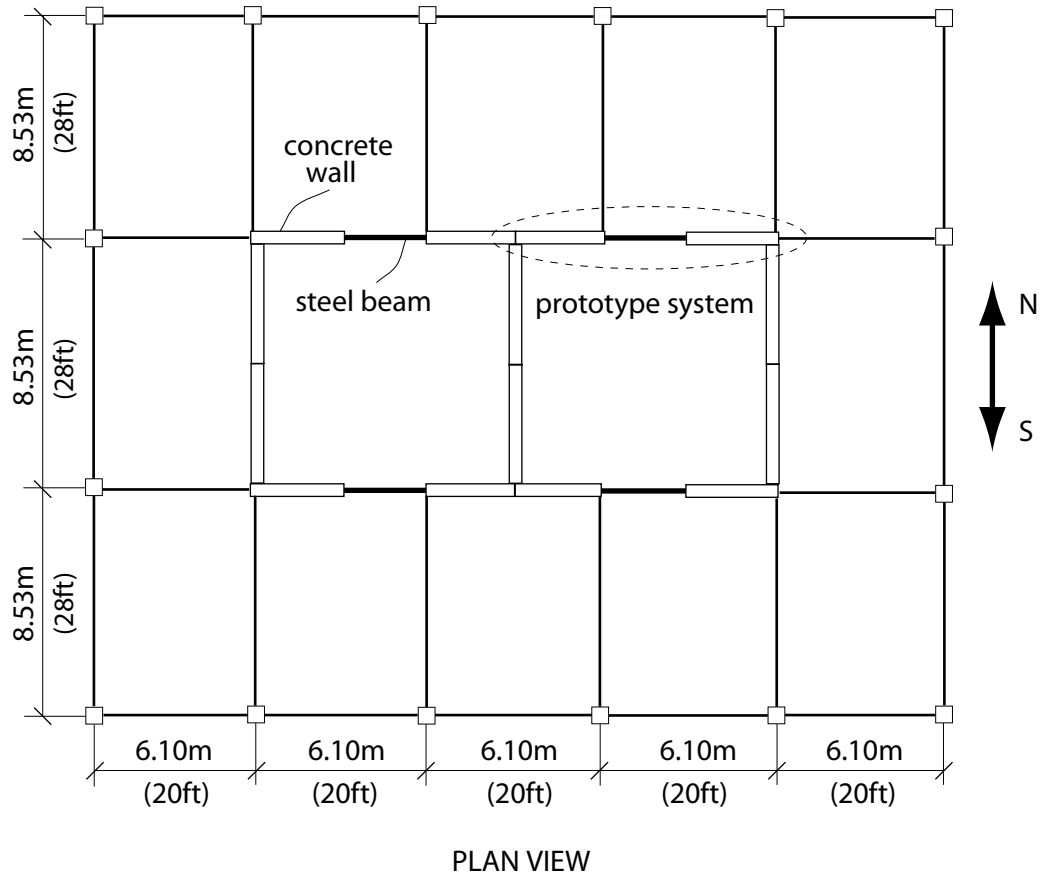


Fig. 6.1 Plan view of prototype structures

6.1.1 Walls

Each prototype coupled wall structure includes two identical concrete walls. The wall height $h_w=32.6\text{m}$ (107 ft) [with 4.88m (16 ft) for the first story and 3.96m (13 ft) for the upper stories], wall length $l_w=3.05\text{m}$ (10 ft), and wall thickness $t_w=356\text{mm}$ (14 in. uniform).

Figure 1: Reinforcement details of the column and slab. The diagram shows a column cross-section with reinforcement details for different floors: roof, 8th floor, 7th floor, 6th floor, 5th floor, 4th floor, 3rd floor, 2nd floor, and foundation. The column is labeled with height $h_w = 32.6\text{m}$. The reinforcement includes mild steel reinforcement (not shown) and spiral reinforcement. The column is divided into sections with lengths l_w , l_b , and l_w . The bottom part shows a slab cross-section with reinforcement details: $18\#7@3\text{in.}$ ($18\text{Ø}22.2\text{mm}@76\text{mm}$) for the top and bottom, and $10\#5@18\text{in.}$ ($10\text{Ø}15.9\text{mm}@457\text{mm}$) for the middle. The slab is labeled with thickness $t_w = 356\text{mm}$ (14in.) and width $l_w = 3.05\text{m}$ (10ft). The reinforcement ratio is given as $\rho_{ws} = 1.94\%$.

(b)

TABLE 6.1

CIP-UPT WALL PROPERTIES

CIP-UPT Wall Properties	
Wall length, l_w	3.05 m (10 ft)
Wall thickness, t_w	356 mm (14 in.)
Wall height, h_w	32.6 m (107 ft)
Wall main flexural reinforcement	mild steel bars (see Fig. 6.2a)
Diameter of boundary flexural reinforcing bars	22.2 mm (7/8 in.)
Area of each boundary flexural reinforcing bar	387 mm ² (0.6 in ²)
Number of boundary flexural reinforcing bars	18
Total area of boundary flexural reinforcement	6968 mm ² (10.8 in ²)
Wall base region spiral diameter, D_{wsp}	296 mm (11.67 in.)
Wall base region spiral wire diameter, d_{wsp}	8.4 mm (0.329 in.)
Wall base region spiral pitch, s_{wsp}	38.1 mm (1.5 in.)
Wall base region spiral reinforcement ratio, ρ_{wsp}	1.94%
Wall base region spiral confined length	508 mm

TABLE 6.2

PRE-UPT WALL PROPERTIES

PRE-UPT Wall Properties	
Wall length, l_w	3.05 m (10 ft)
Wall thickness, t_w	356 mm (14 in.)
Wall height, h_w	32.6 m (107 ft)
Wall main flexural reinforcement	high strength post-tensioning bars (see Fig. 6.2b)
Diameter of wall post-tensioning bars	35 mm (1.375 in.)
Area of each wall post-tensioning bar	1019 mm ² (1.58 in ²)
Number of wall post-tensioning bars in each wall	12
Total area of wall post-tensioning steel in each wall	12232 mm ² (18.96 in ²)
Initial stress in wall post-tensioning steel, f_{wpi}	$0.625f_{wpu}$
Unbonded length of wall post-tensioning bars, l_{wpu}	32.6 m (107 ft)
Wall base region spiral diameter, D_{wsp}	152 mm (6.0 in.)
Wall base region spiral wire diameter, d_{wsp}	10.7 mm (0.422 in.)
Wall base region spiral pitch, s_{wsp}	31.8 mm (1.25 in.)
Wall base region spiral reinforcement ratio, ρ_{wsp}	7.46%
Wall base region spiral confined length	508 mm

The monolithic cast-in-place reinforced concrete walls in Fig. 6.2a are conventional walls with bonded mild steel reinforcement to provide flexural resistance. The precast concrete walls in Fig. 6.2b are similar to the wall shown in Fig. 2.15, and are constructed by joining two-story tall precast concrete wall panels along horizontal joints using high

strength post-tensioning bars running in the vertical direction. The post-tensioning bars are prestressed to $f_{wpi}=0.625f_{wpu}$, where $f_{wpu}=1035\text{MPa}$ (150 ksi) is the design maximum strength of the post-tensioning steel. The stress $f_{wpi}=0.625f_{wpu}$ represents the design initial stress assumed to act in the wall post-tensioning bars just before the application of lateral loads on the walls.

The post-tensioning bars in the precast concrete walls are unbonded over the entire wall height, and, are anchored to the walls only at the roof and foundation levels. The behavior of these walls under lateral loads is governed by the opening of gaps at the horizontal joints between the wall panels and between the wall and the foundation (see Fig. 2.15), similar to the opening of gaps at the ends of the coupling beams. More detailed information on this type of precast concrete wall can be found in Chapter 2.

It is assumed that adequate concrete confinement is provided in the walls using spiral reinforcement near the base (see Fig. 6.2). For Wall CIP-UPT, the center-to-center spiral diameter $D_{wsp}=296\text{ mm}$ (11.67 in.), spiral W8.5 wire diameter $d_{wsp}=8.4\text{ mm}$ (0.329 in.), and pitch $s_{wsp}=38.1\text{ mm}$ (1.5 in.), resulting in a spiral reinforcement ratio, $\rho_{wsp}=1.94\%$ (defined as the ratio of the volume of spiral reinforcement to the volume of spiral confined concrete core). Similarly, for Wall PRE-UPT, the center-to-center overlapping spiral diameter $D_{wsp}=152\text{ mm}$ (6.0 in.), spiral W14 wire diameter $d_{wsp}=10.7\text{ mm}$ (0.422 in.), and pitch $s_{wsp}=31.8\text{ mm}$ (1.25 in.), resulting in $\rho_{wsp}=7.46\%$. The larger amount of concrete confinement used at the base of Wall PRE-UPT is due to the additional concrete compression stresses from the wall post-tensioning.

6.1.2 Coupling Beams

The coupling beams in Walls CIP-UPT and PRE-UPT are assumed to be identical, with properties that remain constant over the height of the structures as shown in Fig. 6.3. The properties of the coupling beams in the multi-story prototype structures are the same as the prototype subassembly in Chapter 3, with the following exceptions: (1) the thickness of the flange cover plates is reduced to $t_c=28.6\text{mm}$ (1.125 in.); (2) the gage length of the angle-to-wall connection bolts measured from the heel of the angle to the center of the innermost angle-to-wall bolts is increased to $l_{gv}=114\text{ mm}$ (4.5 in.); and (3) the area and initial stress of the beam post-tensioning steel are different as described below. More information on the design properties of the coupling beams in Walls CIP-UPT and PRE-UPT is provided below and listed in Tables 6.3-6.5.

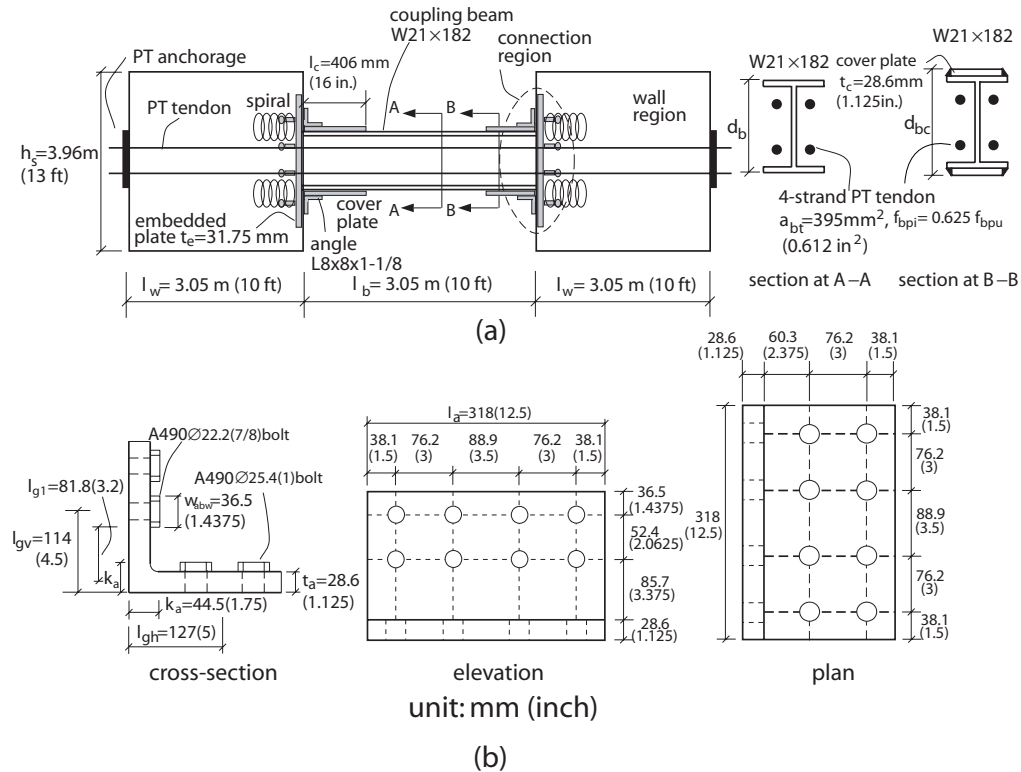


Fig. 6.3 Floor level details: (a) elevation; (b) top and seat angle connections

As shown in Fig. 6.3, each coupling beam in the multi-story CIP-UPT and PRE-UPT systems is post-tensioned using four multi-strand tendons, two tendons on each side of the beam web. Each tendon consists of four 12.7mm (0.5 in.) nominal diameter high-strength seven-wire strands with a total area of $a_{bt}=395\text{mm}^2$. The tendons are prestressed to $f_{bpi}=0.625f_{bpu}$, where $f_{bpu}=1862\text{ MPa}$ (270 ksi) is the design maximum strength of the post-tensioning strands. The stress $f_{bpi}=0.625f_{bpu}$ represents the design initial stress assumed to act in the beam post-tensioning tendons just before the application of lateral loads on the walls.

TABLE 6.3
WALLS CIP-UPT AND PRE-UPT COUPLING BEAM PROPERTIES

CIP-UPT and PRE-UPT Coupling Beam Properties	
Section	W21×182
Beam length, l_b	3.05 m (10 ft)
Beam depth, d_b	577 mm (22.72 in.)
Flange thickness, t_{bf}	37.6 mm (1.48 in.)
Flange width, b_{bf}	318 mm (12.5 in.)
Web thickness, t_{bw}	21 mm (0.83 in.)
Beam cross section area, A_b	34581 mm ² (53.6 in ²)
Beam moment of inertia, I_b	19.7 m ⁴ (4730 in ⁴)
Flange cover plate thickness, t_c	28.6mm (1.125 in.)
Flange cover plate width, b_c	318 mm (12.5 in.)
Flange cover plate length, l_c	406 mm (16 in.)

TABLE 6.4
WALLS CIP-UPT AND PRE-UPT BEAM POST-TENSIONING PROPERTIES

CIP-UPT and PRE-UPT Beam Post-Tensioning Properties	
Beam post-tensioning strand diameter, d_{bp}	12.7 mm (0.5 in.)
Number of strands per beam post-tensioning tendon, n_{bp}	4
Beam post-tensioning tendon area, a_{bt}	395 mm ² (0.612 in ²)
Number of beam post-tensioning tendons, n_{bt}	4
Total beam post-tensioning steel area, A_{bp}	1579 mm ² (2.448 in ²)
Unbonded length of beam post-tensioning steel, l_{bpu}	9.14 m (30 ft)
Initial stress in beam post-tensioning steel, f_{bpi}	$0.625f_{bpu}$

TABLE 6.5
WALLS CIP-UPT AND PRE-UPT BEAM-TO-WALL CONNECTION
TOP AND SEAT ANGLE PROPERTIES

CIP-UPT and PRE-UPT Beam-to-Wall Connection Top and Seat Angle Properties	
Section	L8×8×1-1/8
Angle length, l_a	318 mm (12.5 in.)
Angle leg length, l_{al}	203 mm (8 in.)
Angle leg thickness, t_a	28.6 mm (1.125 in.)
Angle fillet length, k_a	44.5 mm (1.75 in.)
Number of angle-to-wall connection bolts, n_{abw}	8
Number of angle-to-beam connection bolts, n_{abb}	8
Angle-to-wall connection bolt diameter, d_{abw}	22.2 mm (7/8 in.)
Angle-to-beam connection bolt diameter, d_{abb}	25.4 mm (1 in.)
Angle-to-wall connection bolt head width across flats, w_{abw}	36.5 mm (1.4375 in.)
Angle-to-wall connection gage length, l_{gv}	114 mm (4.5 in.)
Angle-to-beam connection gage length, l_{gh}	127 mm (5 in.)

6.1.3 Material Properties and Idealizations

This section describes assumed material properties for: (1) the flexural mild steel reinforcement used in Wall CIP-UPT; (2) the post-tensioning bars used in Wall PRE-UPT; and (3) the spiral confined concrete at the wall bases. Multi-linear idealizations to the assumed smooth uniaxial stress-strain relationships are also provided for modeling purposes.

Some of the design material properties for the prototype structures are listed in Table 6.6. Note that the material properties for the coupling beams, top and seat angles, flange cover plates, wall embedded plates, and beam post-tensioning strands are assumed to be the same as the properties described for the prototype subassembly in Chapter 3 (see Figs. 3.2a and 3.2b). Similarly, the compressive stress-strain relationships of the spiral confined concrete in the wall-contact regions and the unconfined concrete are assumed to be the same as the prototype subassembly in Figs. 3.2c and 3.2d.

TABLE 6.6

WALL MATERIAL PROPERTIES

Wall CIP-UPT Mild Steel Bars		Wall PRE-UPT Post-Tensioning Bars		Wall Base Region Spiral Wire		Wall Base Region Spiral Confined Concrete			
						Wall CIP-UPT		Wall PRE-UPT	
Yield strength, f_{wsy}	414 MPa (60 ksi)	Yield strength, f_{wpy}	828 MPa (120 ksi)	Yield strength, f_{spy}	414 MPa (60 ksi)	Linear-elastic stiffness, E_c	30441 MPa (4415 ksi)	Linear-elastic stiffness, E_c	30441 MPa (4415 ksi)
Yield strain, ϵ_{wsy}	0.00207	Yield strain, ϵ_{wpy}	0.00414	Yield strain, ϵ_{spy}	0.00207	Maximum strength, f_{cc}	63.4 MPa (9.2 ksi)	Maximum strength, f_{cc}	100 MPa (14.5 ksi)
Maximum strength, f_{wsm}	672 MPa (97.5 ksi)	Maximum strength, f_{wpu}	1035 MPa (150 ksi)	Maximum strength, f_{spm}	621 MPa (90 ksi)	Strain at max. strength, ϵ_{cc}	0.00728	Strain at max. strength, ϵ_{cc}	0.0162
Strain at max. strength, ϵ_{wsm}	0.06	Strain at max. strength, ϵ_{wpu}	0.08	Strain at max. strength, ϵ_{spm}	0.08	Ultimate strain, ϵ_{ccu}	0.0182	Ultimate strain, ϵ_{ccu}	0.0385

Fig. 6.4a shows the assumed idealized multi-linear stress-strain relationships for the mild steel reinforcement in Wall CIP-UPT. The design yield strength and maximum strength of the steel are equal to $f_{wsy}=414$ MPa (60 ksi) and $f_{wsm}=672$ MPa (97.5 ksi), respectively.

Similarly, the assumed smooth (dashed line) and idealized bi-linear (solid line) stress-strain relationships for the post-tensioning bars used in Wall PRE-UPT are shown in Fig. 6.4b. The smooth stress-strain relationship is from test results of 25.4 mm (1 in.) diameter Grade 150 hot-rolled threaded post-tensioning bars reported by Dywidag[®] Systems International (2002). The yield strength and maximum strength of the post-tensioning bars are taken as $f_{wpy}=828$ MPa (120 ksi) and $f_{wpu}=1035$ MPa (150 ksi), respectively. The yield strength f_{wpy} is assumed to be equal to the linear limit stress (i.e., the limit of proportionality) of the smooth stress-strain relationship.

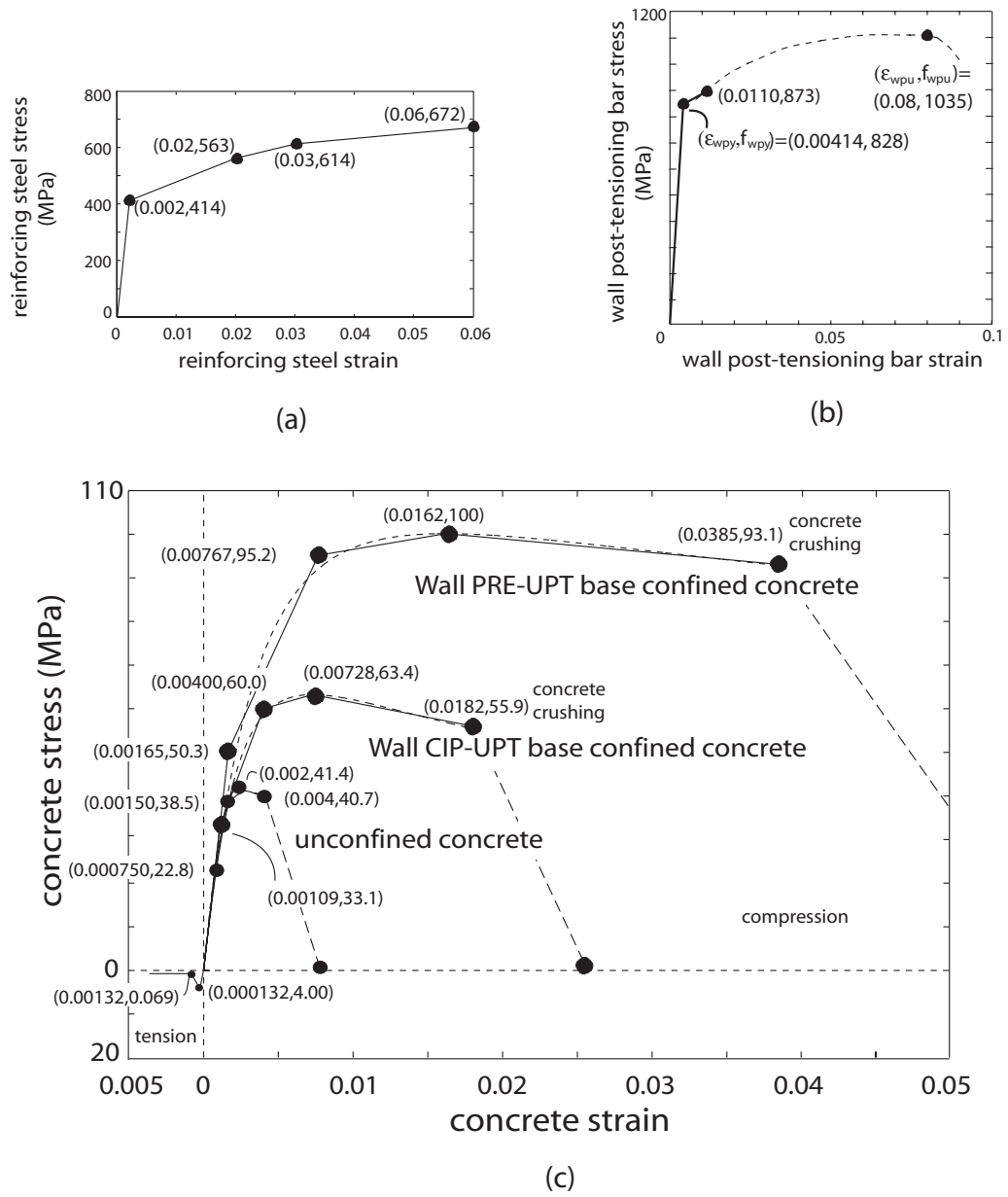


Fig. 6.4 Wall material properties and idealizations: (a) mild reinforcing steel for CIP-UPT system; (b) post-tensioning bar for PRE-UPT system; (c) concrete

Since the wall post-tensioning bars are not bonded to the concrete, the peak strains in the bars during an earthquake are expected to remain small. Thus, the post-yield stiffness of the idealized stress-strain relationship in Fig. 6.4b was determined from the portion of the smooth stress-strain relationship between the yield strain, ϵ_{wpy} , and a

maximum strain of 0.0110 (with a stress of 873 MPa) expected in the wall post-tensioning bars as the structure is displaced laterally. The ratio of the idealized post-yield stiffness to the initial linear-elastic stiffness $E_{wp}=199955$ MPa (29000 ksi) of the post-tensioning bars is equal to 0.0328.

Fig. 6.4c shows the smooth (dashed lines) and idealized multi-linear (solid lines) compressive stress-strain relationships of the spiral confined concrete at the bases of Walls CIP-UPT and PRE-UPT. The unconfined concrete stress-strain relationship is also shown for comparison. The maximum compressive strength of the spiral confined concrete near the base of Wall CIP-UPT is $f_{cc}=63.4$ MPa (9.2 ksi) reached at a strain of $\epsilon_{cc}=0.00728$, and the ultimate (i.e., crushing) strain is $\epsilon_{ccu}=0.0182$. The maximum compressive strength of the spiral confined concrete near the base of Wall PRE-UPT is $f_{cc}=100$ MPa (14.5 ksi) reached at a strain of $\epsilon_{cc}=0.0162$, and the ultimate (i.e., crushing) strain is $\epsilon_{ccu}=0.0385$.

The smooth concrete stress-strain relationships in Fig. 6.4c were determined using a concrete model developed by Mander et al. (1988). The spiral confined concrete stress-strain parameters, which include the maximum strength, f_{cc} , strain at maximum strength, ϵ_{cc} , and ultimate (i.e., crushing) strain, ϵ_{ccu} , were calculated based on the unconfined concrete properties and the amount, distribution, yield strength [assumed as $f_{spy}=414$ MPa (60 ksi)], and strain at maximum strength (assumed as $\epsilon_{spm}=0.08$) of the spiral reinforcement. According to the concrete confinement model by Mander et al. (1988), the ultimate (crushing) strain ϵ_{ccu} of the confined concrete is reached when the spiral reinforcement fractures, resulting in a complete loss of confinement and a sudden loss in

the compression resistance of the concrete. The concrete confinement provided by the wall transverse reinforcement other than the spirals (e.g., wire mesh) was ignored.

As described in more detail later, the tensile strength of the concrete in Wall PRE-UPT is ignored in order to model the gap opening behavior along the horizontal joints of the walls. For Wall CIP-UPT, the tensile strength of the confined and unconfined concrete is assumed to be equal to $f_{ct}=0.6\sqrt{f'_c}=4$ MPa (or $f_{ct}=7.5\sqrt{f'_c}=581$ psi) as shown in Fig. 6.4c.

In general, the slopes of the first segment of the idealized multi-linear stress-strain relationships in Fig. 6.4 match the linear-elastic stiffness of the smooth relationships. Furthermore, the maximum compressive strength, strain at maximum strength, and ultimate strain of the concrete are matched by the idealized stress-strain relationships in Fig. 6.4c.

6.2 Analytical Modeling Assumptions

In addition to the assumptions made for the subassembly model in Chapter 3, the following assumptions are made for the multi-story coupled wall analytical modeling.

(1) The objective of this research is to investigate the behavior of isolated coupled wall structures under earthquake induced lateral loads. The interaction between the coupled walls and other structural members (e.g., slabs supported by the coupling beams and the walls) is not within the scope of the analytical model, and thus, is ignored. Note that the floor and roof slabs may affect the expected and desired behavior of a coupled wall structure; however, this is not investigated in the dissertation.

- (2) The earthquake induced lateral forces are in the plane of the walls.
- (3) The entire seismic force in the direction of the coupled walls is resisted by the coupled walls.
- (4) The seismic forces at each floor and roof level are transferred to the coupled walls from the floor and roof diaphragms by adequate connections between the coupled walls and the diaphragms. For in-plane forces, the floor and roof diaphragms are assumed to be rigid.
- (5) The total seismic lateral force acting on a coupled wall structure at a floor or roof level is distributed equally between the “left” and “right” walls.
- (6) The coupled wall system undergoes in-plane deformations only. Torsional and out-of-plane deformations are not modeled.
- (7) The walls are sufficiently slender such that their nonlinear behavior is governed by axial-flexural deformations. Shear deformations are assumed to be linear-elastic.
- (8) Shear slip at the bases and along the horizontal joints of the walls is prevented by design.
- (9) The foundations are fixed to the ground (i.e., soil-foundation-structure interaction is not considered).
- (10) The mild steel reinforcement in the CIP-UPT system is assumed to be adequately anchored and fully bonded to the concrete, ignoring any slip due to anchorage and/or bond failure.
- (11) The anchorages for the wall post-tensioning bars in the PRE-UPT system are properly designed for the maximum post-tensioning forces.

6.3 Multi-Story Coupled Wall Models

Analytical models for multi-story unbonded post-tensioned hybrid coupled wall structures are constructed by joining fiber element models for the coupled wall subassemblages at the floor and roof levels. The DRAIN-2DX Program (Prakash et al. 1993) is used as the analytical platform. As an example, analytical models for Walls CIP-UPT and PRE-UPT, and the corresponding floor level subassemblage models are shown in Figs. 6.5a and 6.5b, respectively. Note that only selected beam element nodes and wall PT element nodes (in the PRE-UPT system) are shown in the multi-story wall models to maintain clarity. Detailed information on the subassemblage model is provided in Chapter 3.

As shown in Fig. 6.5 and described in Chapter 3, each concrete wall in the CIP-UPT and PRE-UPT systems is modeled using two sets of fiber beam-column elements. The “wall-contact” elements, which model the local behavior of the wall-contact regions to the left and right of the coupling beams, are discussed in detail in Chapter 3. The “wall-height” elements, which model the axial-flexural and shear behavior of each wall along its height, are described in this section. The modeling of the wall unbonded post-tensioning bars in the PRE-UPT system is also described herein.

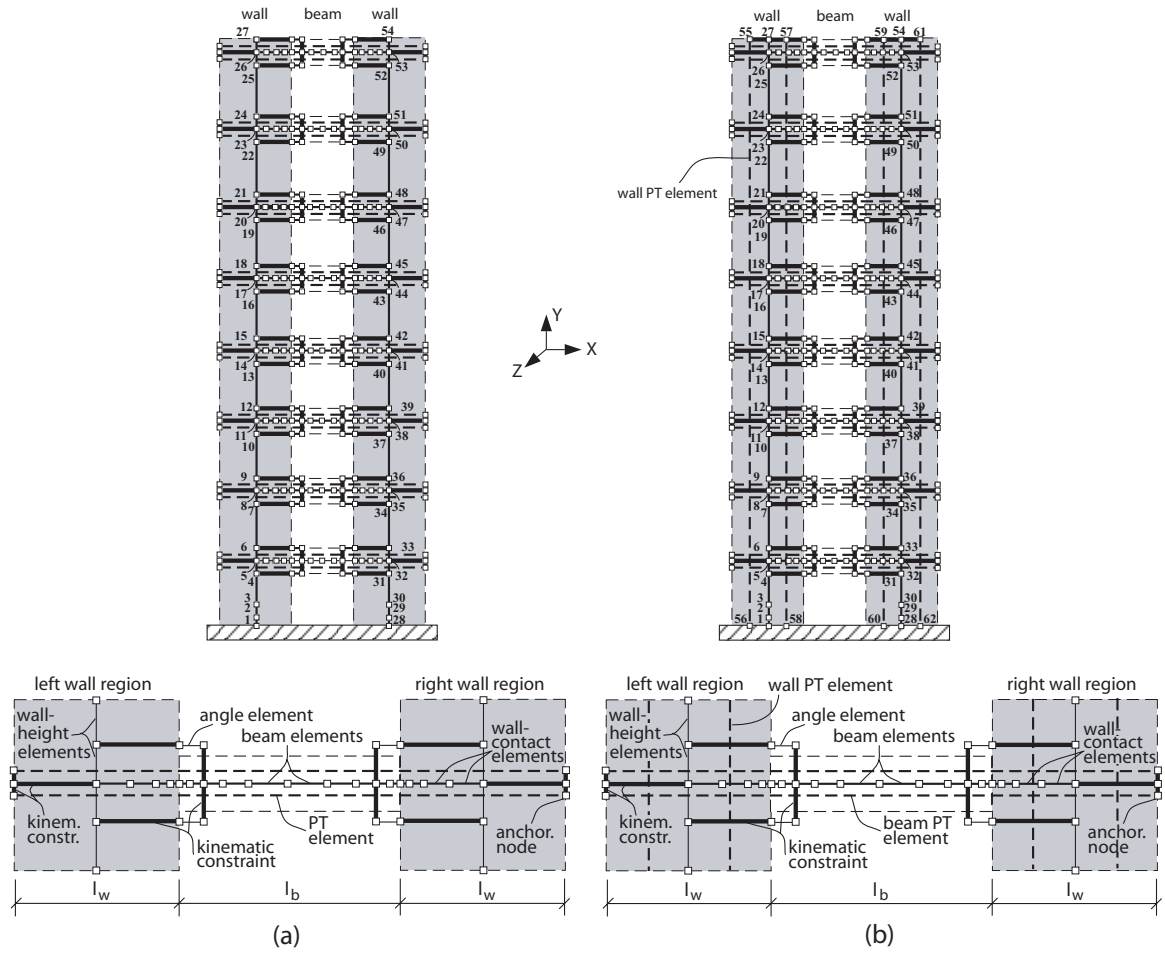


Fig. 6.5 Multi-story coupled wall analytical models:
(a) CIP-UPT system; (b) PRE-UPT system

Each wall-height element consists of a number of parallel steel and/or concrete fibers in the direction of the height of the wall. Each fiber has a location in the wall cross section, a cross-sectional area, and a uniaxial stress-strain relationship. Typically, a larger number of fiber elements/segments/fibers are used near the base of a wall where the nonlinear behavior is expected to concentrate as compared with regions away from the base. The stress-strain relationship of each fiber is a multi-linear idealization of the smooth uniaxial stress-strain relationship for the mild steel, confined concrete, or

unconfined concrete (e.g., cover concrete) in the walls. Second order effects (often referred to as “P- Δ ” effects) in the walls are modeled by the wall-height elements.

6.3.1 Cast-in-Place Concrete Walls in CIP-UPT system

The fiber wall-height elements for the prototype CIP-UPT system are described using Fig. 6.6. A total of 26 elements are used over the height of each wall as shown in Fig. 6.6a. The fiber cross sections (Figs. 6.6b and 6.6c) of the walls include steel fibers to model the flexural mild steel reinforcing bars (with the multi-linear steel stress-strain relationship in Fig. 6.4a) and concrete fibers to model the unconfined and spiral confined concrete (with the multi-linear concrete stress-strain relationships in Fig. 6.4c).

In Figs. 6.6b and 6.6c, “CU” refers to unconfined concrete fibers, “CC” refers to spiral confined concrete fibers, and “S” refers to steel fibers. In the boundary regions near the base of each wall (Fig. 6.6b), spiral confined concrete as well as unconfined concrete and steel fibers are used. Away from the wall base (Fig. 6.6c), only unconfined concrete and steel fibers are used. The actual number of fibers, thickness of each concrete fiber, t_f , and area of each steel fiber, a_f , used in the wall-height elements for the CIP-UPT system are given in Table 6.7. Note that refinement studies using models with larger numbers of elements/segments/fibers than the discretization in Table 6.7 showed no appreciable differences in the analysis results.

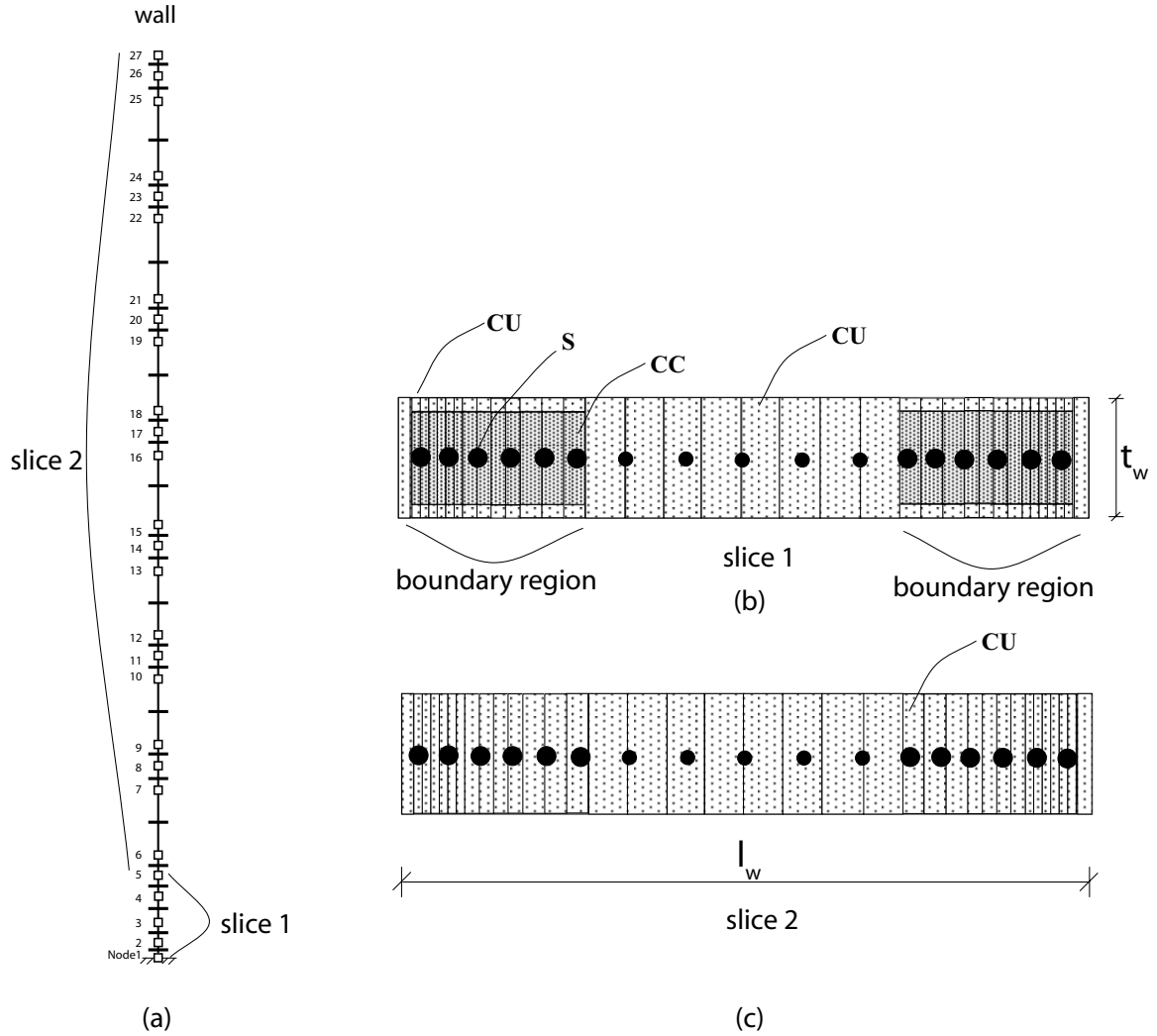


Fig. 6.6 CIP-UPT wall-height elements: (a) elevation; (b) fiber slice schematic near wall base; (c) fiber slice schematic away from wall base

The cyclic behavior of the concrete fibers modeling the spiral confined concrete (CC fiber type) at the base of the CIP-UPT system is shown in Fig. 6.7a. The cyclic behavior of the unconfined concrete (CU) fibers has similar characteristics to the hysteretic model for the confined concrete fibers, as shown in Fig. 6.7b. More details on the cyclic stress-strain characteristics of the concrete fiber in DRAIN-2DX can be found in Kurama et al. (1996) and Kurama (1997).

CIP-UPT SYSTEM WALL-HEIGHT ELEMENT DISCRETIZATION

Notes:

168

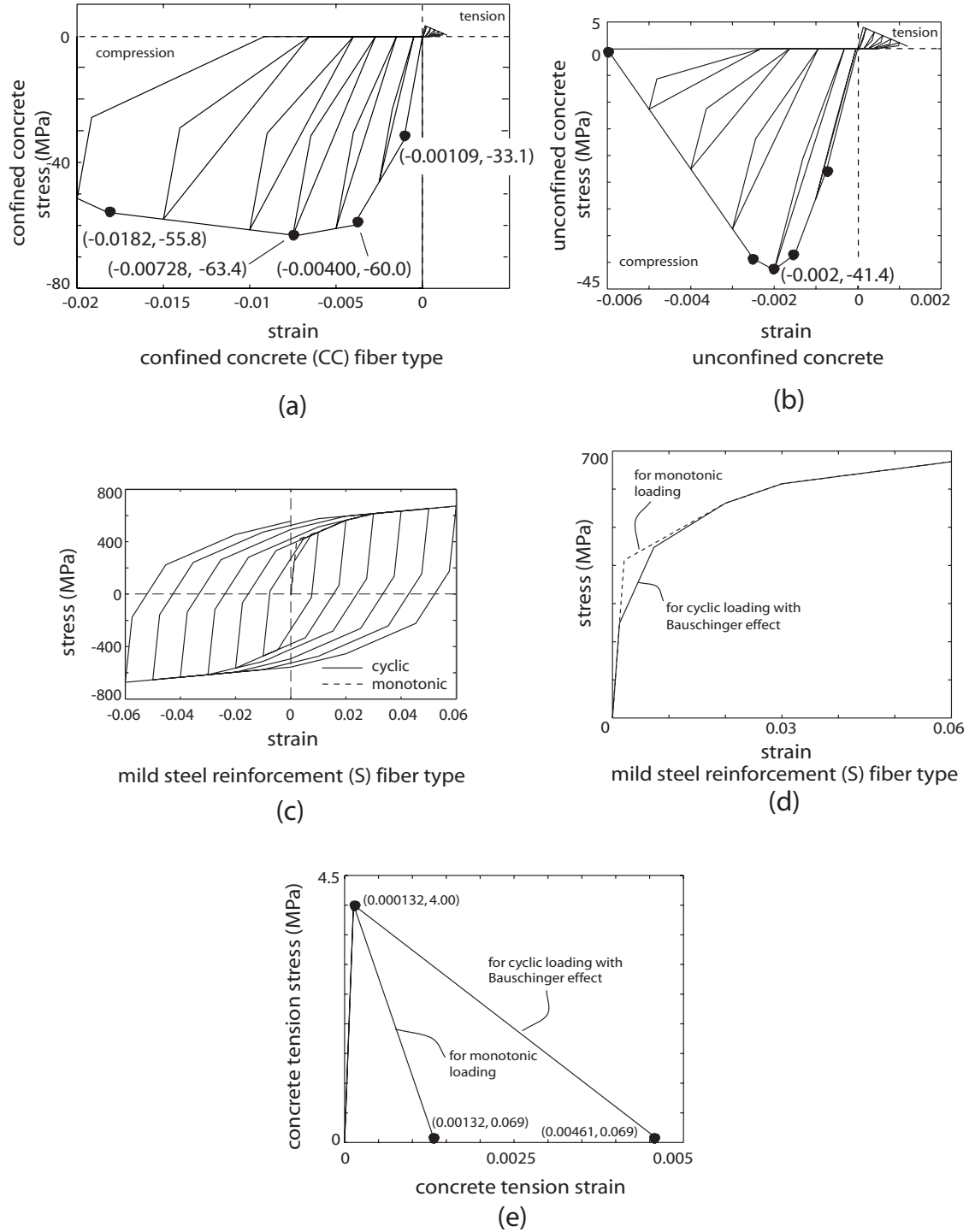


Fig. 6.7 CIP-UPT system cyclic material models: (a) confined concrete (CC) fiber; (b) unconfined concrete (CU) fiber; (c) mild steel reinforcement (S) fiber; (d) steel fiber stress-strain relationship under monotonic loading and envelope relationship under cyclic loading; (e) concrete in tension

Fig. 6.7c shows the cyclic (solid lines) and monotonic (dashed lines) behavior of the steel fibers used to model the mild steel reinforcement (S fiber type) in the CIP-UPT system. Note that in Fig. 6.7c, a lower yield strength is used for the steel fibers under cyclic loading than under monotonic loading in order to model the Bauschinger effect in the reinforcing steel under cyclic loading (see also Fig. 6.7d for a comparison between the monotonic steel stress-strain relationship and the envelope relationship under cyclic loading). The use of a lower yield strength for the reinforcing steel results in an earlier reduction in the stiffness (i.e., softening) of the walls under lateral loading. In order to compensate for this reduction, modifications to the unconfined and confined concrete stress-strain behavior in tension are also made, as shown in Fig. 6.7e, such that the monotonic lateral load behavior of the coupled wall structure using the cyclic and monotonic reinforcing steel fiber models are similar.

6.3.2 Precast Concrete Walls in PRE-UPT system

The modeling of the precast concrete walls in the PRE-UPT system is different than the modeling of the cast-in-place concrete walls in the CIP-UPT system because of the use of unbonded post-tensioning bars in the precast walls and the opening of gaps along the horizontal joints of the walls. This is described in detail in Kurama et al. (1999) and Kurama (2002).

The fiber wall-height elements for the PRE-UPT system are described using Fig. 6.8. Similar to the CIP-UPT system, a total of 26 elements are used over the height of each wall as shown in Fig. 6.8a. The fiber cross sections (Figs. 6.8b and 6.8c) of the precast concrete wall panels include concrete fibers to model the unconfined and spiral

confined concrete (with the multi-linear concrete stress-strain relationships in Fig. 6.4c). The actual number of fibers and thickness of each fiber, t_f used in the wall-height elements for the PRE-UPT system are given in Table 6.8. Refinement studies using models with larger numbers of elements/segments/fibers than the discretization in Table 6.8 showed no appreciable differences in the analysis results.

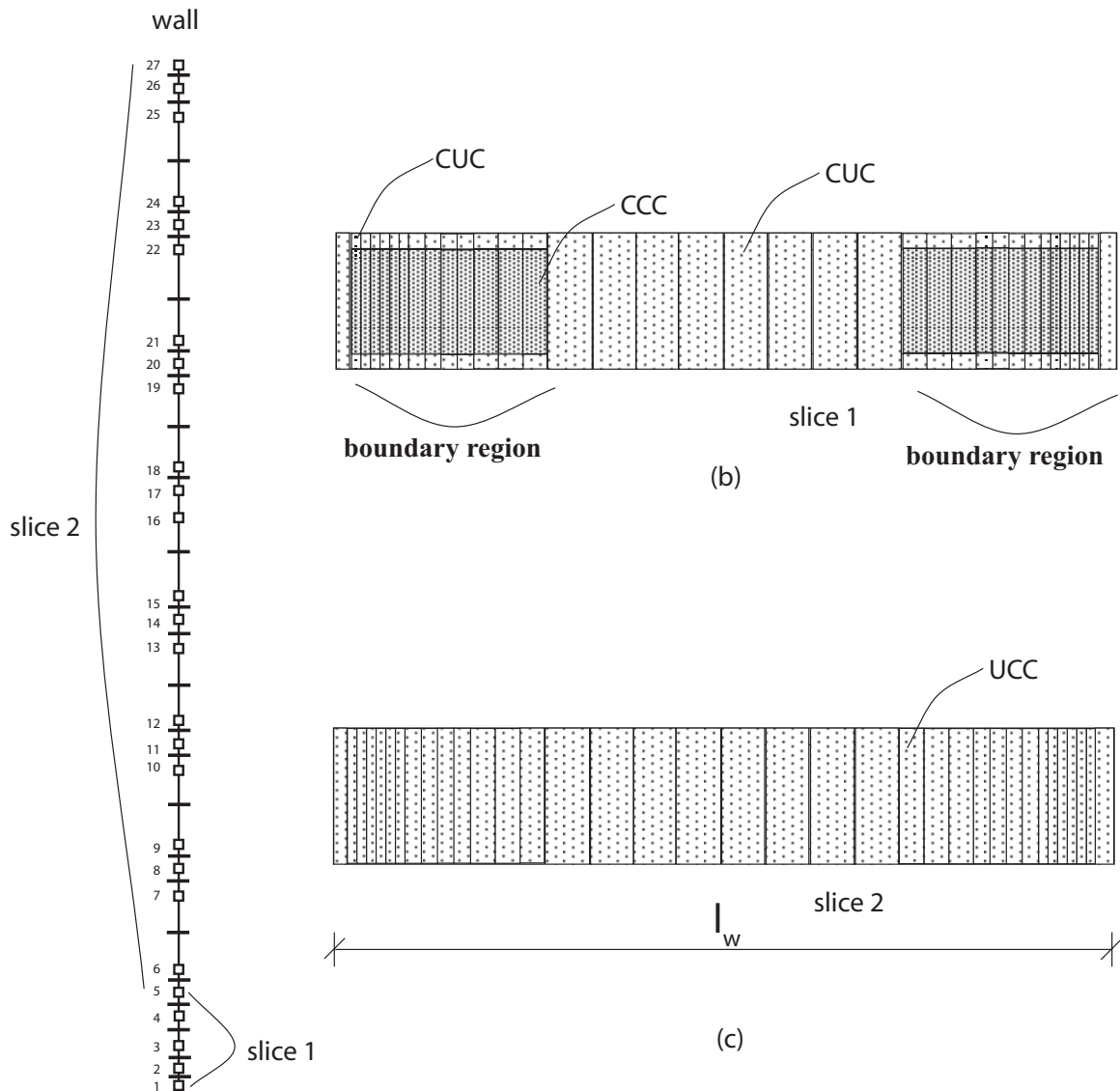


Fig. 6.8 PRE-UPT wall-height elements: (a) elevation; (b) fiber slice schematic near wall base; (c) fiber slice schematic away from wall base

Note that the fiber elements modeling the wall panels in the PRE-UPT system do not contain any steel fibers for two reasons: (1) the post-tensioning bars are unbonded from the wall panels, and thus, are modeled separately using truss elements; and (2) the bonded wall panel steel reinforcement (e.g., wire mesh) is not continuous across the horizontal joints, and thus, does not contribute to the flexural resistance of the wall. The modeling of the post-tensioning bars and the modeling of gap opening along the horizontal joints of the walls are described below.

Modeling of Gap Opening

Gap opening at the horizontal joints, especially between the base panel and the foundation, is one of the most important characteristics governing the behavior of unbonded post-tensioned precast concrete walls. The modeling of gap opening at the horizontal joints is similar to the modeling of gap opening at the joints between the coupling beams and the walls as described in Chapter 3. As a result of the opening of gaps and due to post-tensioning, large compressive stresses develop near the regions of a precast wall panel in contact with another panel or with the foundation, while the tensile stresses in a significant portion of the panel are equal or close to zero (Allen and Kurama 2002). The compression behavior in the contact regions is modeled using the nonlinear uniaxial compressive stress-strain relationships of the concrete fibers. To model the gap opening behavior, the tensile strength and stiffness of the fibers representing the wall panels are set to zero as described in Kurama et al. (1996, 1999) and verified in Kurama (2000).

TABLE 6.8

PRE-UPT SYSTEM WALL-HEIGHT ELEMENT DISCRETIZATION

Element Nodes	Element Length	Number of Segments and Slices	Segment Length/Element Length and Slice Number	Fiber Thickness, t_f mm (in.)	Length of Cross Section	Total Number of Fibers in Slice
1-2 2-3 3-4 4-5	292 mm (11.5 in.) 762 mm (30 in.) 2756 mm (108.5 in.) 721 mm (28.4 in.)	1	1 (Slice 1) (see Fig. 6.8b)	1 CUC fiber; $t_f=31.75(1.25)$ 1 CUC fiber; $t_f=19(0.75)$ 1 CCC fiber; $t_f=19(0.75)$ 5 CUC fibers; $t_f=25.4(1)$ 5 CCC fibers; $t_f=25.4(1)$ 4 CUC fibers; $t_f=50.8(2)$ 4 CCC fibers; $t_f=50.8(2)$ 5 CUC fibers; $t_f=127(5)$ 5 CCC fibers; $t_f=127(5)$ 2 CUC fibers; $t_f=254(10)$	3048 mm (120 in.)	66
5-6 6-7 7-8 8-9 9-10 10-11 11-12 12-13 13-14 14-15 15-16 16-17 17-18 18-19 19-20 20-21 21-22 22-23 23-24 24-25 25-26 26-27	292 mm (11.5 in.) 3378 mm (133 in.) 292 mm (11.5 in.) 292 mm (11.5 in.) 3378 mm (133 in.) 292 mm (11.5 in.) 292 mm (11.5 in.) 3378 mm (133 in.) 292 mm (11.5 in.) 292 mm (11.5 in.) 3378 mm (133 in.) 292 mm (11.5 in.) 292 mm (11.5 in.) 3378 mm (133 in.) 292 mm (11.5 in.) 292 mm (11.5 in.) 3378 mm (133 in.) 292 mm (11.5 in.) 292 mm (11.5 in.) 3378 mm (133 in.) 292 mm (11.5 in.) 292 mm (11.5 in.) 3378 mm (133 in.) 292 mm (11.5 in.) 292 mm (11.5 in.) 3378 mm (133 in.) 292 mm (11.5 in.) 292 mm (11.5 in.) 3378 mm (133 in.) 292 mm (11.5 in.) 345 mm (13.6 in.)	1	1 (slice 2) (see Fig. 6.8c)	1 CUC fiber; $t_f=31.75(1.25)$ 1 CUC fiber; $t_f=19(0.75)$ 5 CUC fibers; $t_f=25.4(1)$ 4 CUC fibers; $t_f=50.8(2)$ 5 CUC fibers; $t_f=127(5)$ 2 CUC fibers; $t_f=254(10)$	3048 mm (120 in.)	36

Notes:

(1) Only fiber discretization for left half of cross section is given for each slice, listed in order from extreme fiber to innermost fiber. Fiber discretization for right half of each cross section is symmetric about mid-length of section. (2) Modeling of left and right walls is the same.

In Figs. 6.8b and 6.8c, “CUC” refers to “compression-only” unconfined concrete fibers and “CCC” refers to compression-only confined concrete fibers. Fig. 6.9a shows the cyclic behavior of the compression-only concrete fibers modeling the spiral confined concrete (CCC fiber type) at the base of the PRE-UPT system. The cyclic behavior of the compression-only unconfined concrete (CUC) fibers has similar characteristics to the hysteretic model for the confined concrete fibers.

Through this model, the gap opening displacements that occur at the horizontal joints of the PRE-UPT system are represented as distributed tensile deformations that occur in the fiber elements over the height of the wall panels. The reduction in the flexural stiffness of the structure as a result of gap opening (Kurama et al. 1999a, 1999b) is modeled by the zero stiffness of the concrete fibers that go into tension when the precompression stresses due to the gravity and post-tensioning forces are overcome by the flexural stresses that develop at the tension sides of the left and right walls due to the lateral loads (i.e., when decompression occurs).

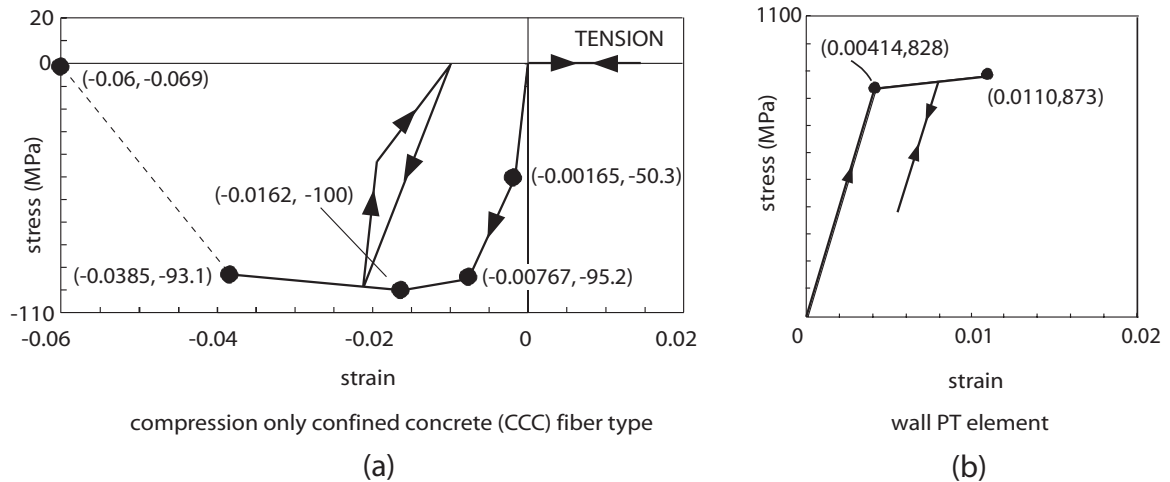


Fig. 6.9 PRE-UPT system cyclic material models:
(a) compression-only confined concrete (CCC) fiber; (b) wall PT element

The process of gap opening/closing under the action of lateral loading/unloading causes softening/re-stiffening at the horizontal joints. This process is captured in the fiber elements by having an increasing number of fibers subjected to tension during loading, and then by having the fibers subjected to tension go back into compression during unloading.

Modeling of Wall Post-Tensioning Bars and Anchorages

The wall unbonded post tensioning bars in the PRE-UPT system are modeled using truss elements, referred to as “wall PT elements,” running over the entire wall height as shown in Fig. 6.5b. Note that only selected wall PT elements are shown in Fig. 6.5b to maintain clarity. The cyclic stress-strain behavior of the truss elements, based on the bilinear relationship in Fig. 6.4b, is shown in Fig. 6.9b. The post tensioning loads are simulated by tensile forces in the truss elements, which are equilibrated by compression forces in the wall-height elements. Note that the compression forces that develop in the wall-height elements result in an elastic shortening and subsequent loss in the forces in the truss elements modeling the post-tensioning bars. Thus, larger tensile forces are applied to the truss elements in order to achieve the desired amount of initial force in the post-tensioning bars after elastic shortening.

Each wall PT element is connected to two nodes representing the anchorages between the post-tensioning bar and the walls (e.g., Nodes 55-56 and 57-58 in Fig. 6.5b). It is assumed that the bars are placed inside oversized ducts in the wall panels, and thus, remain straight during the lateral displacements of the structure. At the bases of the walls,

the wall PT element nodes (Nodes 56, 58, 60 and 62 in Fig. 6.5b) are assumed fixed to the foundation. At the top of the walls (i.e., roof), the displacements of the PT element nodes (Nodes 55, 57, 59 and 61 in Fig. 6.5b) are kinematically constrained to the corresponding wall-height element node (Node 27) to model the anchorages between the post-tensioning bars and the walls (see Fig. 6.5b). Second order effects (often referred to as “P- Δ ” effects) in the post-tensioning bars (due to the relative displacements of the bar nodes in a direction perpendicular to the bar) are modeled in the wall PT elements.

6.4 Verification of Wall Models

Test results of multi-story hybrid coupled wall systems are not available. Thus, the model for the coupled wall subassemblages at the floor levels and the models for the concrete walls are verified separately. The verification of the subassemblage model based on comparisons with ABAQUS results is discussed in Chapter 3, and the verification of the precast concrete wall model can be found in Kurama et al. (1999) and Kurama (2000). These results show that the fiber-element analytical models are capable of adequately predicting both the global (e.g., load-deformation) behavior and the local (e.g., gap opening and contact) behavior of the coupled wall subassemblages and the precast concrete walls. Further verification and improvement of the subassemblage model based on experimental results can be found in Chapters 9 and 10.

The verification of the cast-in-place wall-height element model is done based on previous experiments conducted by Thomsen (1995). Fig. 6.10a shows the elevation and cross section of the wall test specimen used in the verification, which is referred to as Wall RW2 with full details provided in Thomsen (1995). A reversed cyclic lateral force

and a constant vertical force were applied at the top of the wall. The behavior of the wall was dominated by nonlinear axial-flexural deformations rather than shear deformations as described by Thomsen (1995). Fig. 6.10b shows the lateral force versus top displacement relationship of the wall measured during the test and Fig. 6.10c shows the predicted behavior using a fiber element analytical model similar to the model in Fig 6.6. A reasonable comparison between the measured and predicted results is observed. Thus, it is concluded that the analytical model is capable of providing an adequate representation of the nonlinear axial-flexural behavior of monolithic cast-in-place reinforced concrete walls under cyclic lateral loads.

6.5 Advantages and Limitations of Analytical Models

A significant advantage of the fiber element models used in this dissertation is that a reasonably accurate representation of multi-story hybrid coupled wall systems can be developed using only the geometry and dimensions of the structure, and uniaxial stress-strain models for concrete and steel. The model provides an effective tool to conduct static and dynamic analyses of multi-story structures under earthquake-induced loads, accounting for axial-flexural interaction in the wall and beam members, behavior of the top and seat angles, gap opening at the beam and wall joints, and hysteretic behavior of the steel and concrete.

The main limitations of the multi-story coupled wall models presented in this chapter are as follows:

- (1) The fiber element models account for the linear and nonlinear axial-flexural deformations (including gap opening) and linear shear deformations of the walls;

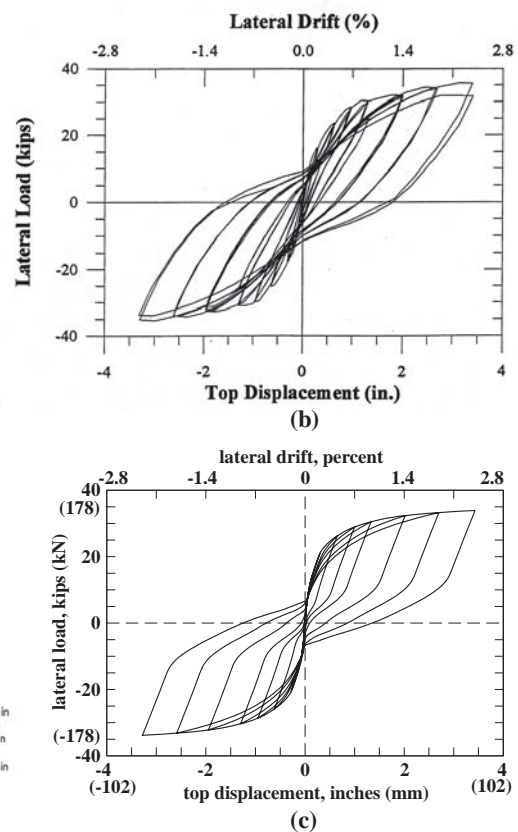
Figure 1 is a schematic diagram of the test apparatus for the rectangular wall specimen. The diagram includes a side elevation and a cross-section of the specimen.

Side Elevation:

- The specimen is a rectangular wall specimen, 48 in. wide.
- It is supported by a pedestal on a strong floor. The pedestal height is 27 in.
- The specimen is anchored to a reaction wall on the left via a hydraulic actuator and load cell.
- The top of the specimen is supported by S.T.S. channels, which are held up by hydraulic jacks and flange load cells.
- High-strength post-tensioning cables run vertically through the specimen.
- The total height of the apparatus is 144 in. (12 in. + 127 in.).
- Dimensions: 48 in. (width), 144 in. (total height), 27 in. (pedestal height), 12 in. (top section height).

Cross-section:

- The specimen is 48 in. wide and 4 in. high.
- Reinforcement includes 8 #3 bars, #2 bars @ 7.5 in. spacing, and 3/16 in. hoops @ 2 in. spacing.
- Dimensions: 48 in. (width), 4 in. (height), 0.75 in. (corner radius), 6 in. (corner radius), 3 @ 7.5 in. (spacing), 3 @ 2 in. (spacing).



178

(2) The degradation (if any) in the flexural stiffness and resistance of the walls due to increasing lateral displacements is modeled; however, any additional degradation under repeated displacement cycles to a constant amplitude is not captured.

(3) Buckling and low cycle fatigue fracture of the mild steel reinforcement are not modeled.

(4) For systems with precast concrete walls, the desired behavior of the walls is governed, primarily, by the opening of gaps at the horizontal joints between the wall panels and between the base panel and the foundation. Shear slip at the horizontal joints should be prevented by design, and thus, is not modeled.

(5) The precast concrete wall model assumes that the post-tensioning bars remain straight during the lateral displacements of the structure. Kinking of the bars at the horizontal joints can occur if the bars come into contact with the ducts inside the wall panels; however, this behavior is not desired and should be prevented by using sufficiently oversized ducts.

6.6 Modeling Of Walls with Embedded Coupling Beams

The modeling of multi-story hybrid coupled wall systems with embedded steel coupling beams is similar to the modeling of the CIP-UPT system described above, except for the use of embedded steel coupling beam subassemblage models at the floor and roof levels as described in Chapter 3.

6.7 Chapter Summary

This chapter describes fiber element analytical models to investigate the nonlinear behavior of multi-story hybrid coupled wall systems. The details of two prototype unbonded post-tensioned hybrid coupled wall structures are also presented. The analytical models are constructed by joining subassemblage models at the floor and roof levels. Systems with monolithic cast-in-place reinforced concrete walls as well as with precast concrete walls are considered. Verification of the cast-in-place reinforced concrete wall model is presented based on comparisons with previous experiments of isolated (i.e., uncoupled) wall specimens.

CHAPTER 7

NONLINEAR BEHAVIOR OF MULTI-STORY COUPLED WALLS

This chapter describes an analytical investigation on the nonlinear behavior of multi-story unbonded post-tensioned hybrid coupled wall systems under lateral loading as follows: (1) overview of analyses; (2) behavior under monotonic loading; (3) behavior under cyclic loading; and (4) parametric investigation. The behavior of unbonded post-tensioned hybrid coupled wall structures is compared with the behavior of structures that use embedded steel coupling beams and structures without coupling.

7.1 Overview of Analyses

The two coupled wall systems (Walls CIP-UPT and PRE-UPT) and the fiber element models described in Chapter 6 are used as the basis for the multi-story coupled wall analyses in this chapter. The analyses are conducted by applying loads on the structures in the following order: (1) beam and wall pier (for the PRE-UPT system) post-tensioning forces; (2) gravity loads applied at the floor and roof levels; and (3) lateral forces applied at the floor and roof levels in displacement control.

The beam and wall PT element forces are applied all at once. Then, the gravity loads, G are applied as 100% of the unfactored design dead load (D) plus 25% of the unreduced unfactored design live load (L) to represent the amount of gravity loads that may be acting on the structure during an earthquake. As shown in Fig. 7.1, the gravity

loads are applied at the wall-height element nodes at the floor and roof levels, with no loads applied along the length of the coupling beams. Table 7.1 provides a summary of the gravity loads applied at the floor and roof levels of the left and right wall piers in the CIP-UPT and PRE-UPT systems. Note that the gravity loads for these two systems are assumed to be the same in order to facilitate comparisons between the behaviors of the two structures.

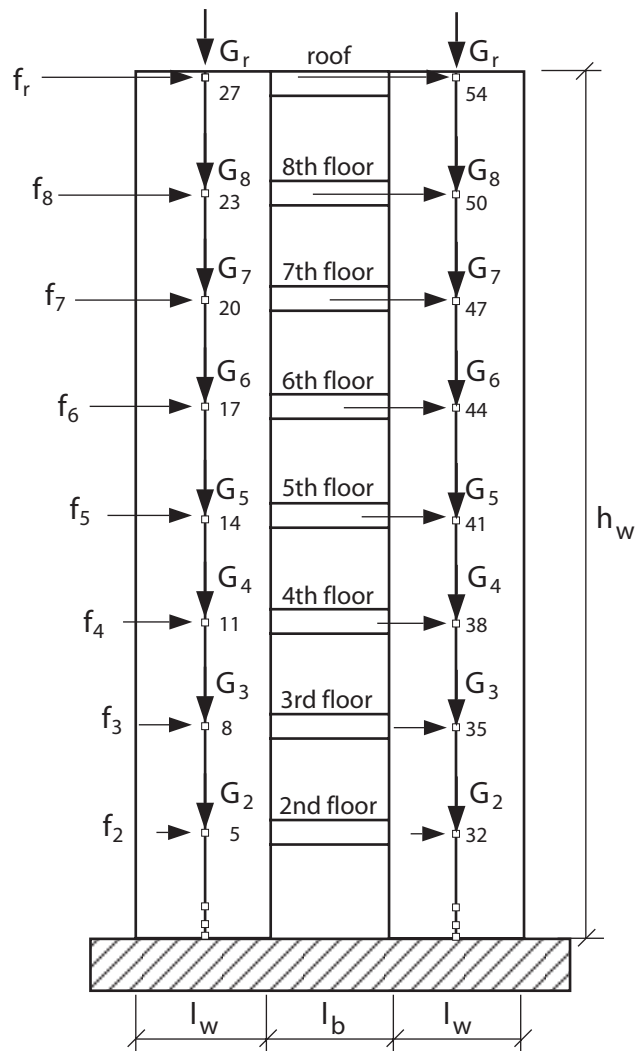


Fig. 7.1 Gravity and lateral forces for multi-story coupled wall analyses

TABLE 7.1

WALL PIER GRAVITY LOADS FOR CIP-UPT AND PRE-UPT SYSTEMS

Level	Gravity Loads, G	
	1.0D (kN)	0.25L (kN)
Roof	207	3.8
8 th floor	258	15.6
7 th floor	258	15.6
6 th floor	258	15.6
5 th floor	258	15.6
4 th floor	258	15.6
3 rd floor	258	15.6
2 nd floor	332	15.6

The displacement controlled nonlinear lateral load analyses are conducted based on the lateral displacement of Node 54 (as shown in Fig. 7.1) with respect to the wall base. An inverse triangular distribution of lateral loads, F (applied from left to right) over the height of the walls is used. For each coupled wall system, the lateral loads are assumed to be equally divided between the left and right walls and are applied at the same nodes as the gravity loads as shown in Fig. 7.1. Note that inertia force distributions significantly different than the assumed inverse triangular lateral load distribution may occur during an earthquake (e.g., Ghosh and Markevicius 1990; Paulay and Priestley 1992; Eberhard and Sozen 1993; Kabeyasawa 1993; Aoyama 1993; Otani et al. 1994; Kurama et al. 1997, 1999b); however, this is not investigated in this chapter.

7.2 Behavior under Monotonic Loading

This section describes the behavior of the prototype CIP-UPT and PRE-UPT coupled wall systems under combined gravity loads and monotonic lateral loads as follows: (1) base shear force versus roof drift behaviors; (2) wall pier deflected shapes; (3) wall pier base flexural steel strains and stresses; (4) wall pier base axial forces; (5) wall

pier base moments; (6) degree of coupling; (7) wall pier base concrete strains; (8) coupling beam shear force versus chord rotation behaviors; (9) coupling beam axial forces; (10) coupling beam end strains; and (11) tension angle force versus deformation behaviors.

7.2.1 Coupled Wall Base Shear Force versus Roof Drift Behaviors

As examples of representative behavior, the thick solid lines in Figs. 7.2a and 7.2b show the coupled wall base shear force versus roof drift ($F-\Delta$) behaviors of the CIP-UPT and PRE-UPT systems, respectively. The roof drift is equal to the average lateral displacement of the left and right side walls at the roof (i.e., at Nodes 27 and 54 in Fig. 7.1) divided by the wall height to the base, h_w .

The prototype CIP-UPT and PRE-UPT systems were designed such that they have similar $F-\Delta$ relationships under monotonic lateral loads as shown in Figs. 7.2a and 7.2b. This was done to facilitate comparisons between the behaviors of the two structures. As the prototype systems displace laterally, they go through a number of states including:

(1) Tension-side wall (left-side wall for lateral loads applied from left to right) softening (Δ markers in Fig. 7.2) – This state is defined as the state when the neutral axis at the base of the tension-side wall reaches the centerline of the wall.

(2) Compression-side wall (right-side wall for lateral loads applied from left to right) softening (+ markers) – This state is defined as the state when the neutral axis at the base of the compression-side wall reaches the centerline of the wall.

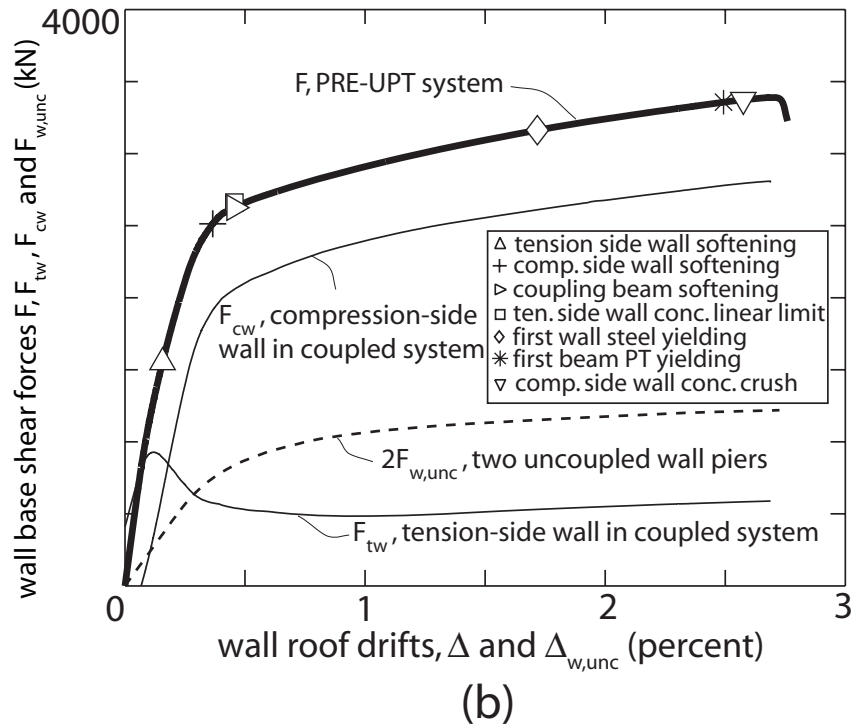
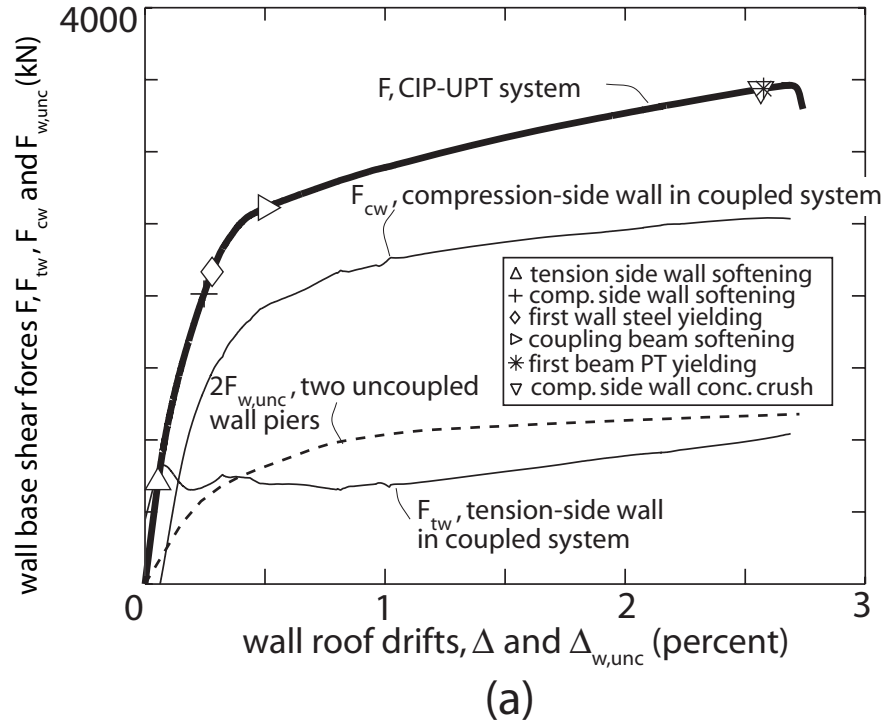


Fig. 7.2 Base shear force versus roof drift behaviors under monotonic lateral loads:
(a) CIP-UPT system; (b) PRE-UPT system

(3) First wall pier steel yielding (\diamond markers) – This state is defined as the first yielding of the wall pier mild flexural reinforcing bars for the CIP-UPT system and the wall pier post-tensioning bars for the PRE-UPT system. Note that the linear limit point on the stress-strain curve is used to identify the yielding of the post-tensioning bars (see Fig. 6.4c).

(4) Coupling beam softening (\triangleright markers) – This state is defined as the state when the average coupling beam shear force in the multi-story structure (i.e., the sum of the shear forces in the coupling beams divided by the number of beams) is equal to $1.05V_{b,sof}$, where $V_{b,sof}$ is the subassembly softening state coupling shear force (see Chapters 4 and 5) and the factor 1.05 is described in Chapter 8.

(5) Tension-side wall concrete linear limit (\square markers) – This state is defined as the state when the maximum confined concrete compression stress at the base of the tension-side wall reaches the linear limit (i.e., limit of proportionality) stress of the confined concrete, f_{cl} .

(6) First beam PT yielding (* markers) – This state is defined as the state when first yielding of the beam post-tensioning tendons at the floor and roof levels occurs (see also Chapter 4).

(7) Compression-side wall concrete crushing (∇ markers) – This state is defined as the state when the extreme strain in the spiral confined concrete at the base of the compression-side wall reaches the crushing strain, ϵ_{ccu} (see Fig. 6.4c).

For each prototype system, the thin solid lines in Figs. 7.2a and 7.2b show the shear forces F_{tw} and F_{cw} at the bases of the tension-side and compression-side walls. Similarly, the dashed lines show the total base shear force versus roof drift relationship ($2F_{w,unc}$, $\Delta_{w,unc}$) of two wall piers without coupling (i.e., two wall piers with no coupling beams). Note that the base shear force versus roof drift relationships of the tension-side and

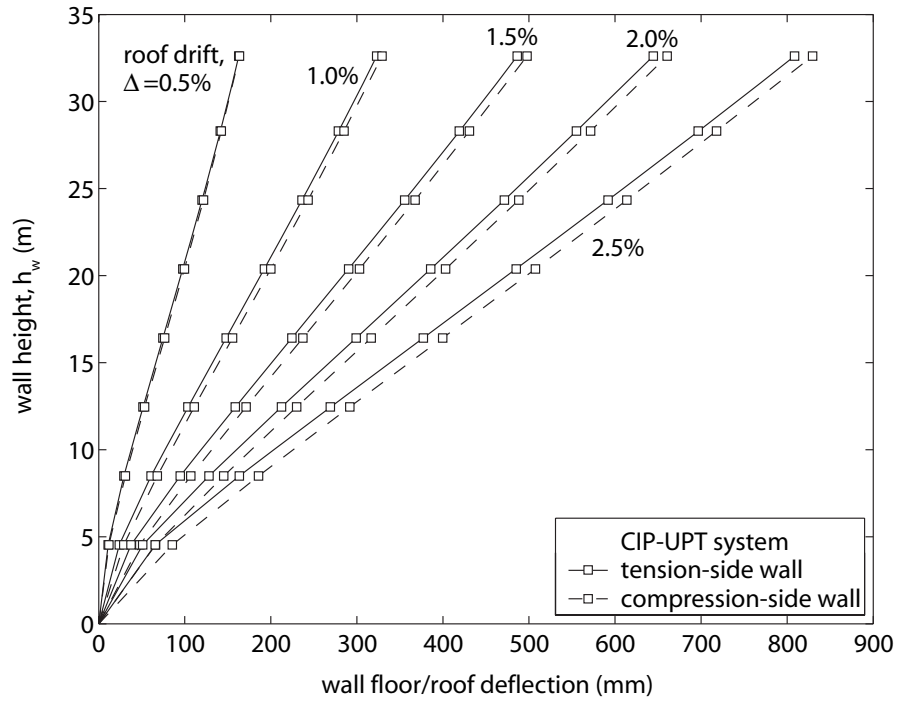
compression-side walls do not pass through the origin since shear forces develop in the walls upon the application of the coupling beam post-tensioning forces, with no external lateral loads. The sum of the tension-side and compression-side wall base shear forces, F_{tw} and F_{cw} is approximately equal to the total coupled wall base shear force, F . In both structures, most of the coupled wall base shear force is resisted by the compression-side wall as a result of the larger compressive axial force that develops as compared with the axial force in the tension-side wall.

7.2.2 Wall Pier Deflected Shapes

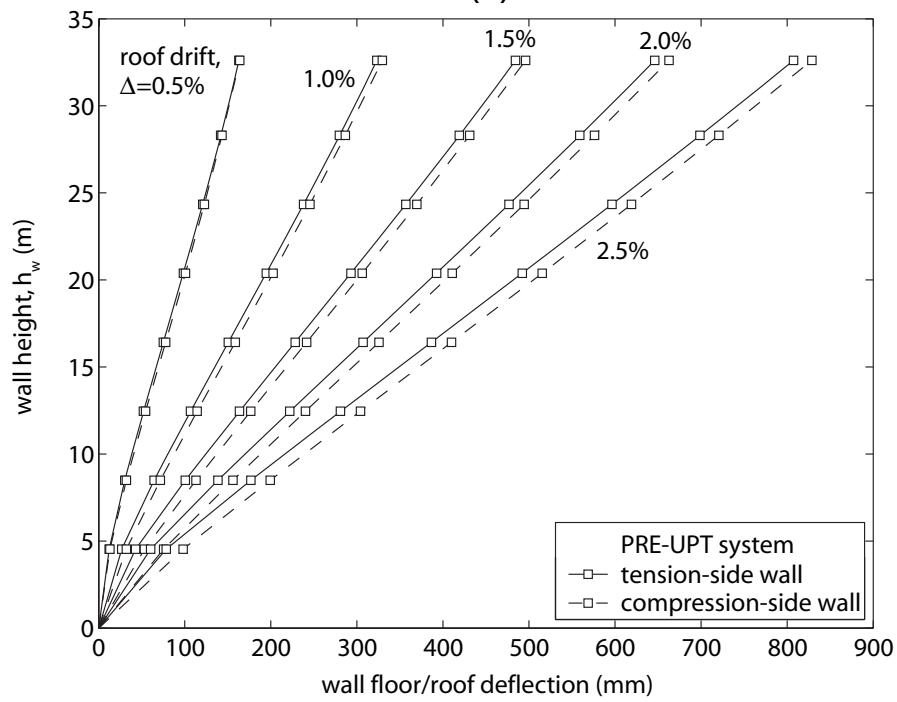
The solid and dashed lines in Figs. 7.3a and 7.3b show the deflected shapes of the tension-side and compression-side walls in the CIP-UPT and PRE-UPT systems, respectively, at coupled wall roof drift values of $\Delta=0.5, 1, 1.5, 2$, and 2.5% . The results demonstrate that the lateral displacements and rotations of the tension-side and compression-side walls are similar.

7.2.3 Wall Pier Base Flexural Steel Strains and Stresses

Fig. 7.4a shows the stresses of the mild reinforcement at four different locations in the tension-side and compression-side walls of the CIP-UPT system, respectively, versus the coupled wall roof drift, Δ . The results indicate that more layers of mild steel reinforcement in the tension-side wall is in tension as compared with the reinforcement in the compression-side wall.



(a)



(b)

Fig. 7.3 Wall deflected shapes: (a) CIP-UPT system; (b) PRE-UPT system

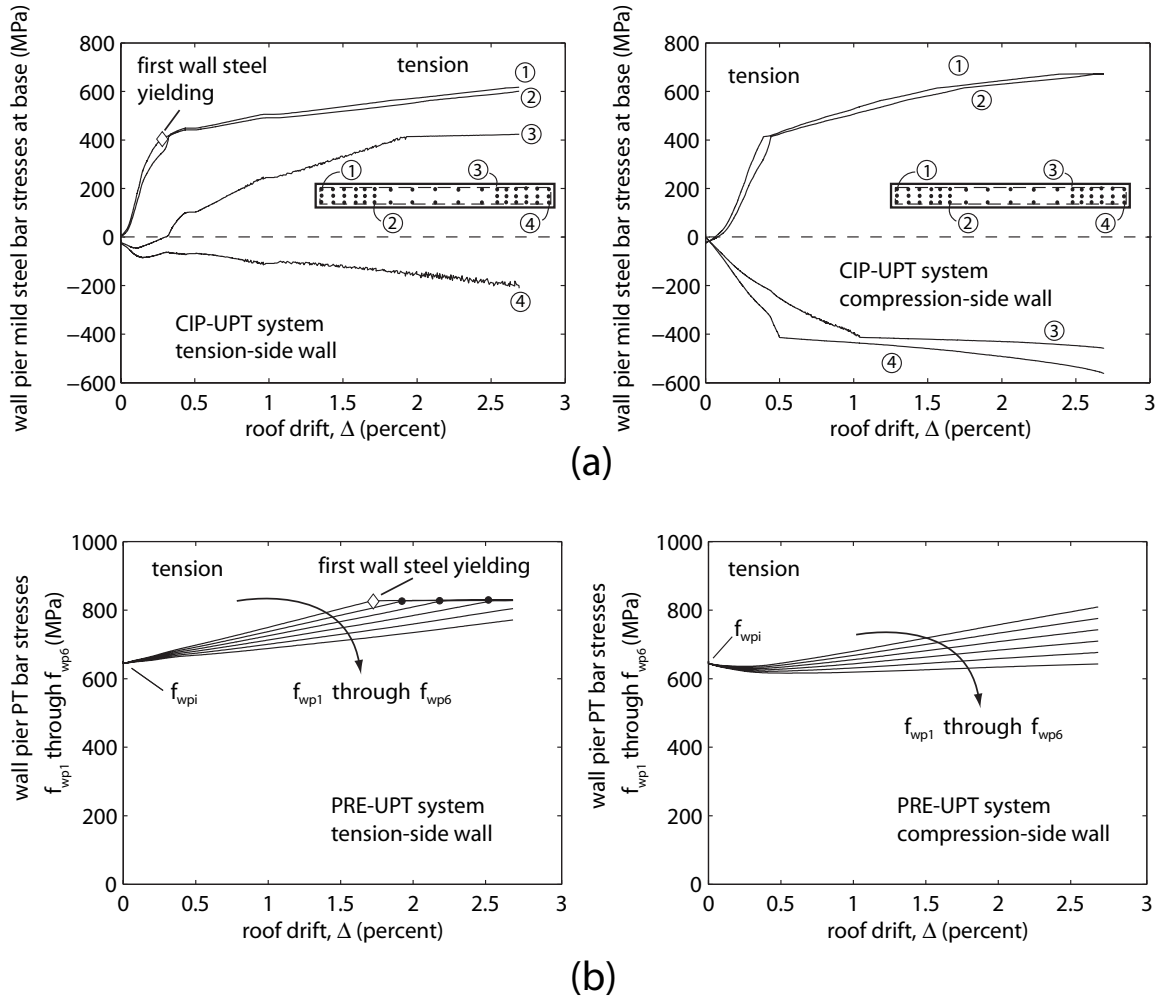


Fig. 7.4 Wall pier flexural steel stresses: (a) CIP-UPT system; (b) PRE-UPT system

Similarly, Fig. 7.4b shows the stresses, f_{wp1} through f_{wp6} in the six pairs of post-tensioning bars (see Fig. 6.2b) in the tension-side and compression-side walls of the PRE-UPT system, respectively, versus the coupled wall roof drift, Δ . The results indicate that the stresses in the post-tensioning bars of the tension-side wall are larger than the stresses in the post-tensioning bars of the compression-side wall. The stresses in the post-tensioning bars located in the compression (i.e., contact) region of the compression-side wall remain close to the initial stress, f_{wpi} .

7.2.4 Wall Pier Base Axial Forces

The solid and dashed lines in Figs. 7.5a and 7.5b show the axial forces N_{tw} and N_{cw} at the bases of the tension-side and compression-side walls in the CIP-UPT and PRE-UPT systems, respectively, versus the coupled wall roof drift, Δ . A positive wall pier axial force represents a compressive force.

Figs. 7.6a and 7.6b show the contributions of the wall pier gravity loads, N_{twg} and N_{cwg} , wall pier post-tensioning forces (for the PRE-UPT system only), N_{twp} and N_{cwp} , and coupling beam shear forces, N_{twb} and N_{cwb} , on the wall pier base axial forces, N_{tw} and N_{cw} in the CIP-UPT and PRE-UPT systems, respectively. Note that the coupling beam shear forces result in tensile axial forces in the tension-side walls and compressive axial forces in the compression-side walls.

The results in Figs. 7.5 and 7.6 show that the post-tensioning of the precast concrete walls in the PRE-UPT system results in significantly larger compressive axial forces than the forces in the cast-in-place concrete walls of the CIP-UPT system. As the structures are displaced laterally, the axial forces in the compression-side walls increase and the axial forces in the tension-side walls decrease due to the coupling beam shear forces. While tensile forces develop at the base of the tension-side wall in the CIP-UPT system, the wall pier axial forces in the PRE-UPT system remain compressive throughout the analysis as a result of the wall post-tensioning forces.

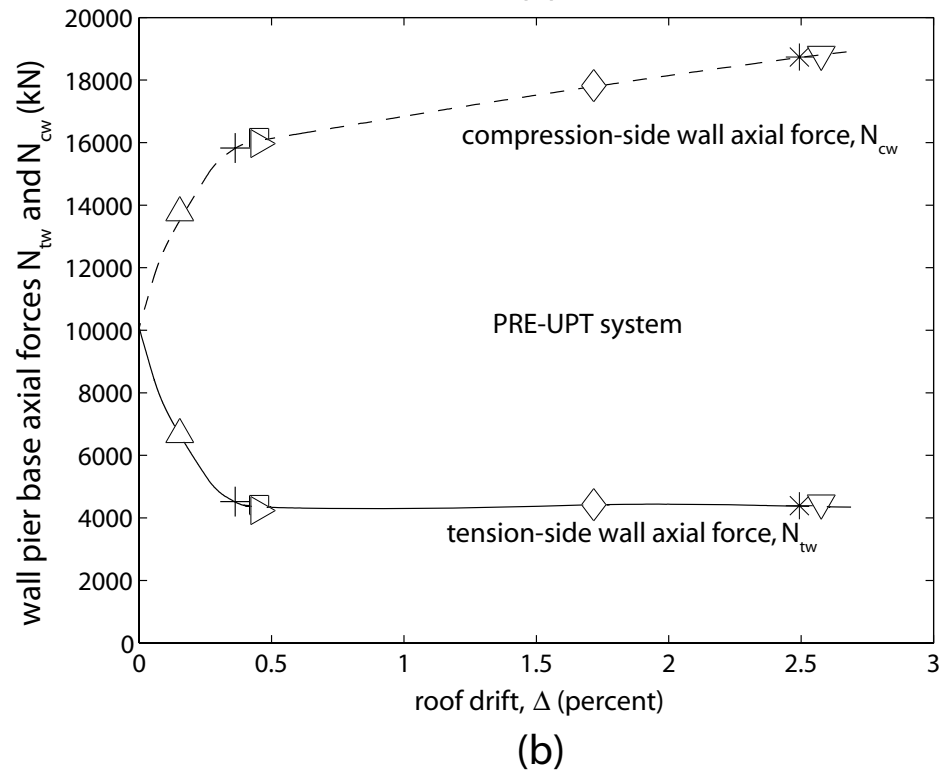
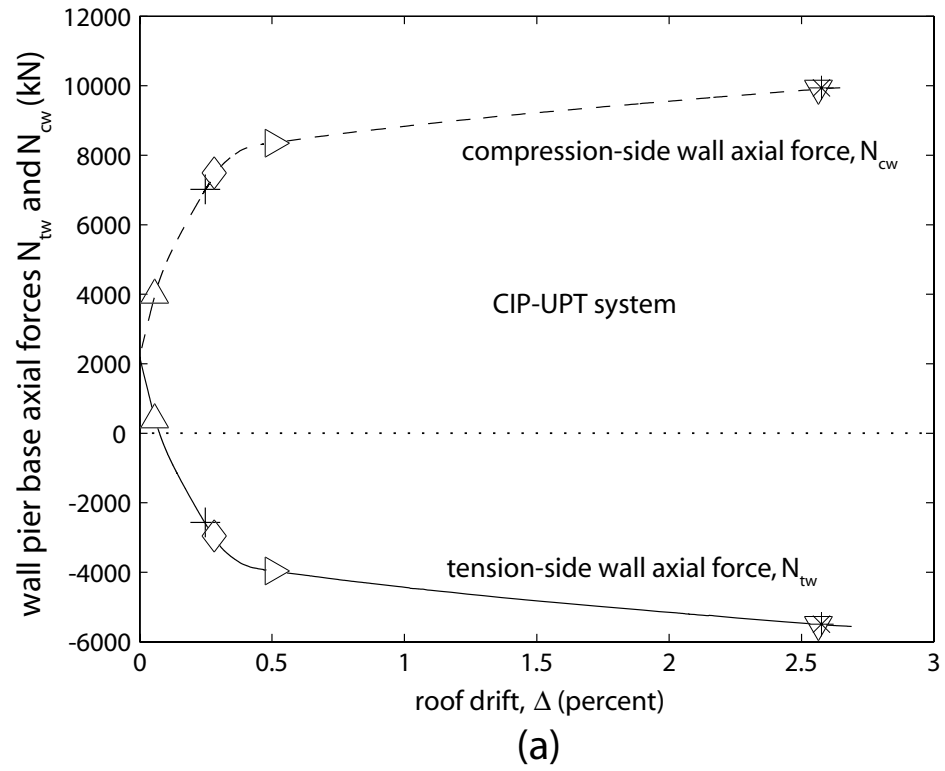


Fig. 7.5 Wall pier base axial forces: (a) CIP-UPT system; (b) PRE-UPT system

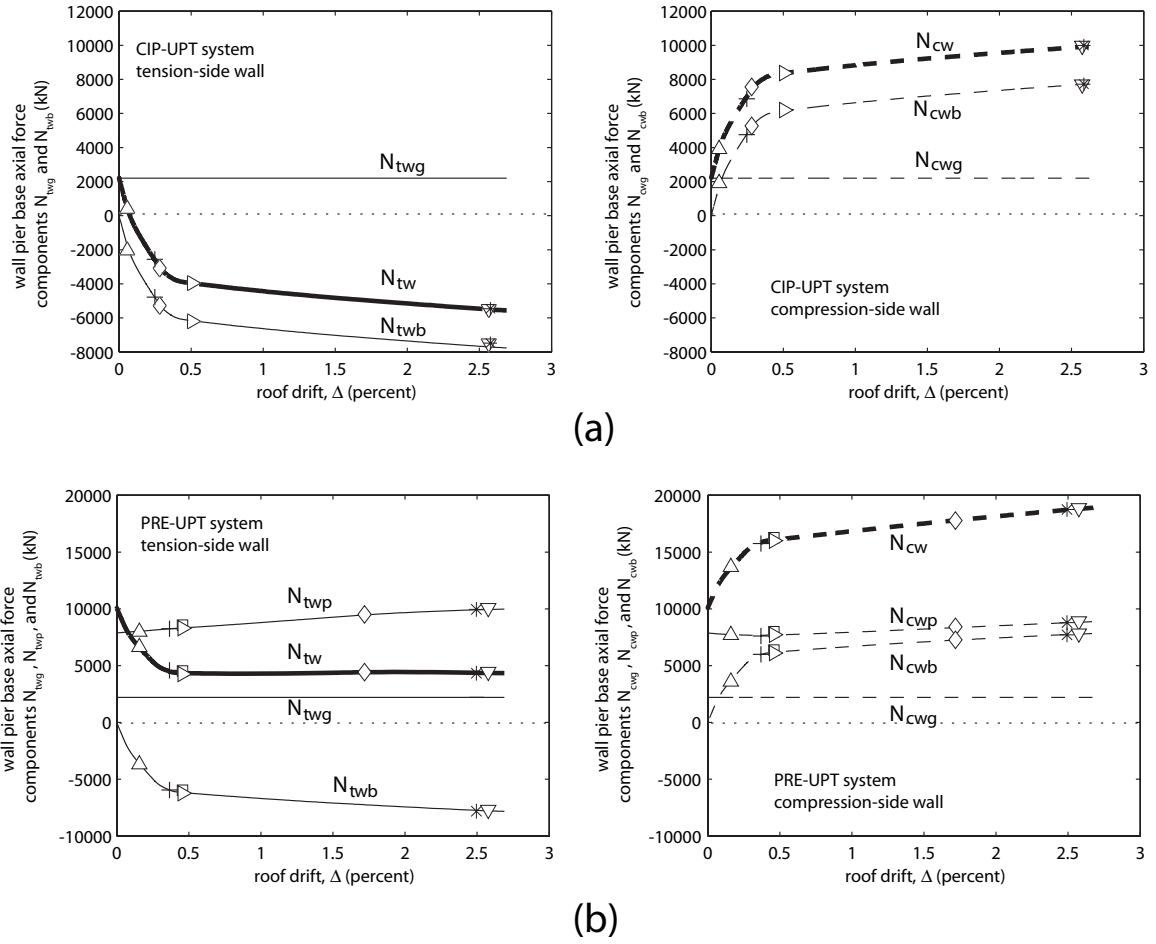


Fig. 7.6 Components of wall pier base axial forces: (a) CIP-UPT system; (b) PRE-UPT system

7.2.5 Wall Pier Base Moments

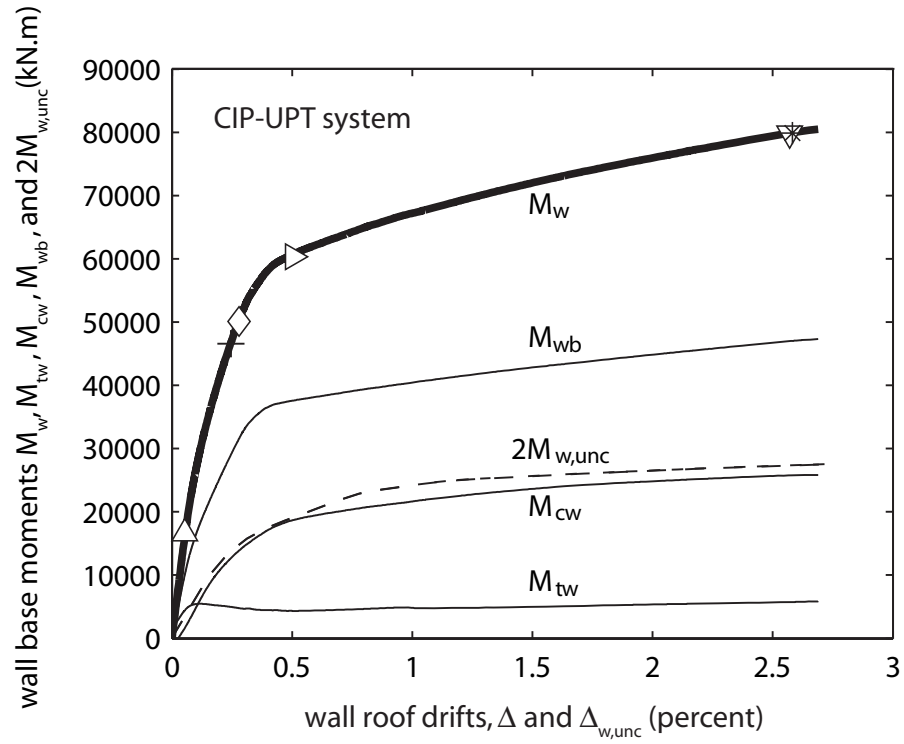
Figs. 7.7a and 7.7b show the contributions of the tension-side wall base moment, M_{tw} , the compression-side wall base moment, M_{cw} and the base moment due to the coupling force couple, M_{wb} to the total coupled wall base moment resistance M_w of the CIP-UPT and PRE-UPT systems, respectively, versus the coupled wall roof drift, Δ . For

comparison the sum of the bending moments, $M_{w,unc}$ at the bases of the wall piers without coupling (i.e., two wall piers with no coupling beams) are also shown in Fig. 7.7a and 7.7b.

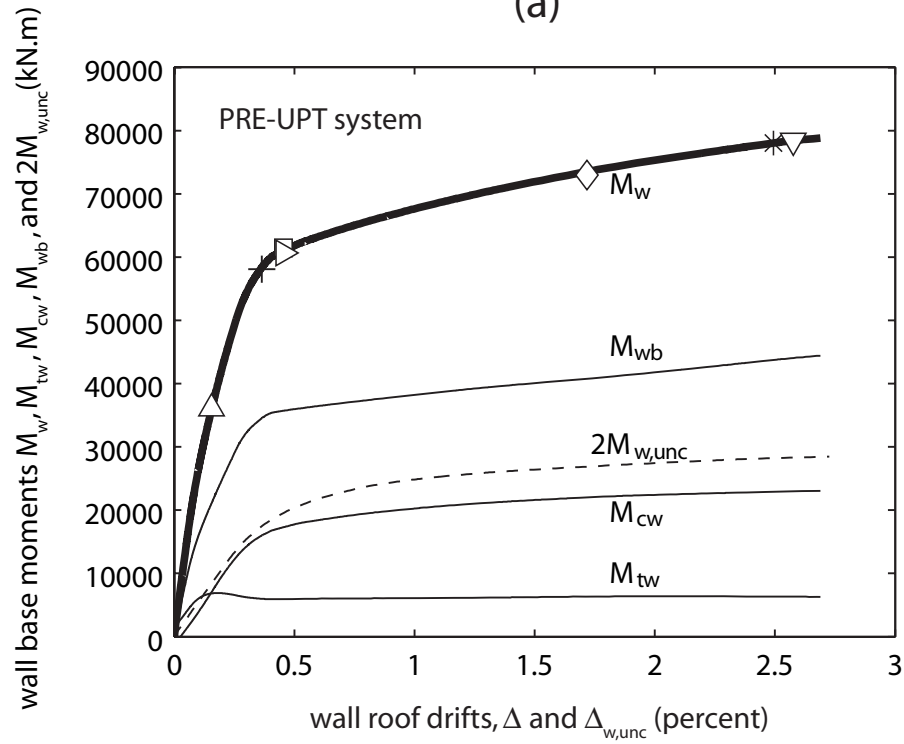
The results in Fig. 7.7 show that most of the coupled wall base moment comes from the coupling force couple, indicating a large degree of coupling in both structures. Similar to the base shear forces in Fig. 7.2, the compression-side wall has a larger contribution to the coupled wall base moment than the contribution of the tension-side wall, as a result of the larger compressive axial forces that develop in the compression-side wall. The base moment versus roof drift relationships for the tension-side and compression-side walls do not pass through the origin since bending moments develop in the walls upon the application of the coupling beam post-tensioning forces, with no external lateral loads.

7.2.6 Degree of Coupling

As shown in Fig. 7.2, coupling of the left and right wall piers results in a significant increase in the lateral strength and initial stiffness of the system as a whole. This increase can be quantified using the degree of coupling, DOC, from Equation (2.2).



(a)



(b)

Fig. 7.7 Wall base moments: (a) CIP-UPT system; (b) PRE-UPT system

Fig. 7.8 shows the degree of coupling [from Equation (2.2)] for the CIP-UPT and PRE-UPT systems (solid and dashed lines, respectively), plotted against the roof drift, Δ . The coupling degree for both systems is around DOC=60% and remains relatively constant as the structures are displaced laterally. Based on recent research by El-Tawil and Kuenzli (2002), the 60% coupling for the prototype walls may be large and can lead to tension forces in the tension-side wall (as shown in Fig. 7.5a for the CIP-UPT system), large compressive and shear forces in the compression-side wall (as shown in Figs. 7.2 and 7.5), and large shear forces at the beam-to-wall interfaces. The design of unbonded post-tensioned hybrid coupled wall structures to achieve a desired target level of coupling is discussed in Chapter 12.

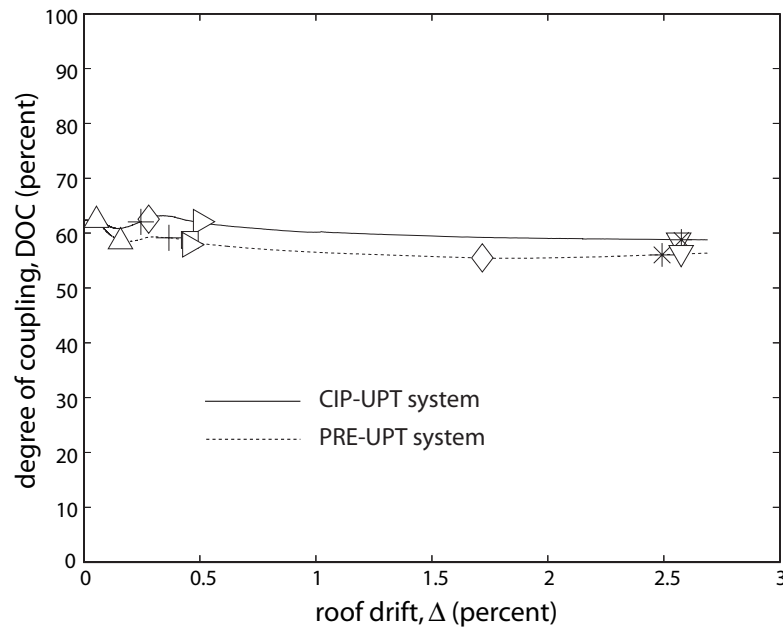


Fig. 7.8 Degree of coupling

7.2.7 Wall Pier Base Concrete Strains

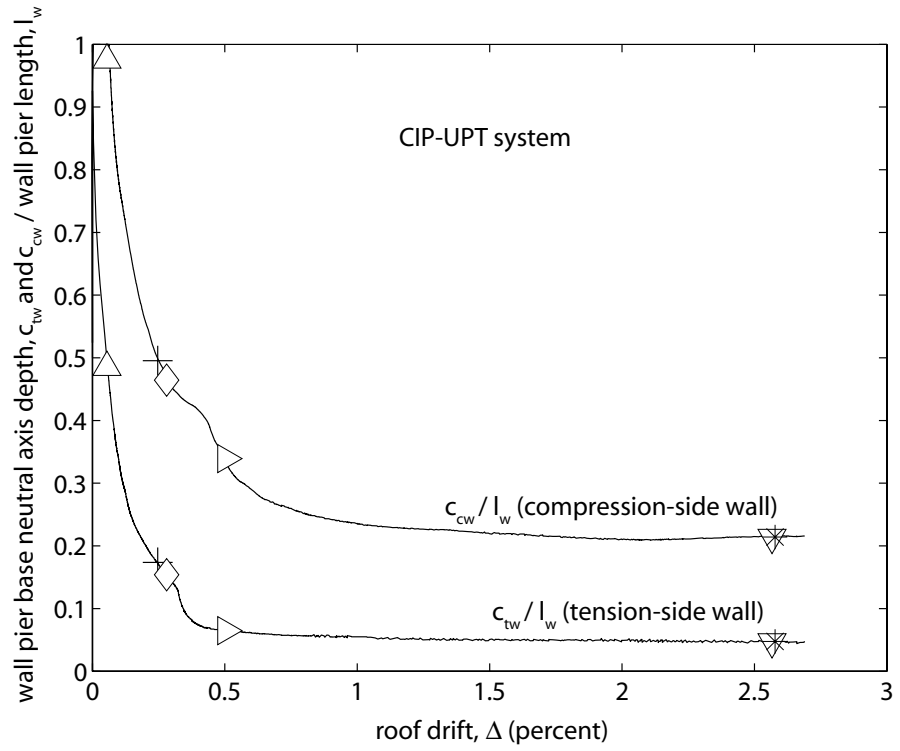
Figs. 7.9a and 7.9b show the neutral axis (i.e., contact) depths c_{tw} and c_{cw} (measured from the compression corners of the wall piers) at the bases of the tension-side

and compression-side walls in the CIP-UPT and PRE-UPT systems, respectively, versus the coupled wall roof drift, Δ . The c_{tw} and c_{cw} values are normalized with respect to the wall pier length, $l_w=3.05$ m (10 ft). The corresponding extreme confined concrete compression strains, ϵ_{tce} and ϵ_{cce} of the tension-side and compression-side wall piers at the base are shown in Figs. 7.10a and 7.10b, respectively, with the confined concrete crushing strains, ϵ_{ccu} shown by the dashed horizontal lines.

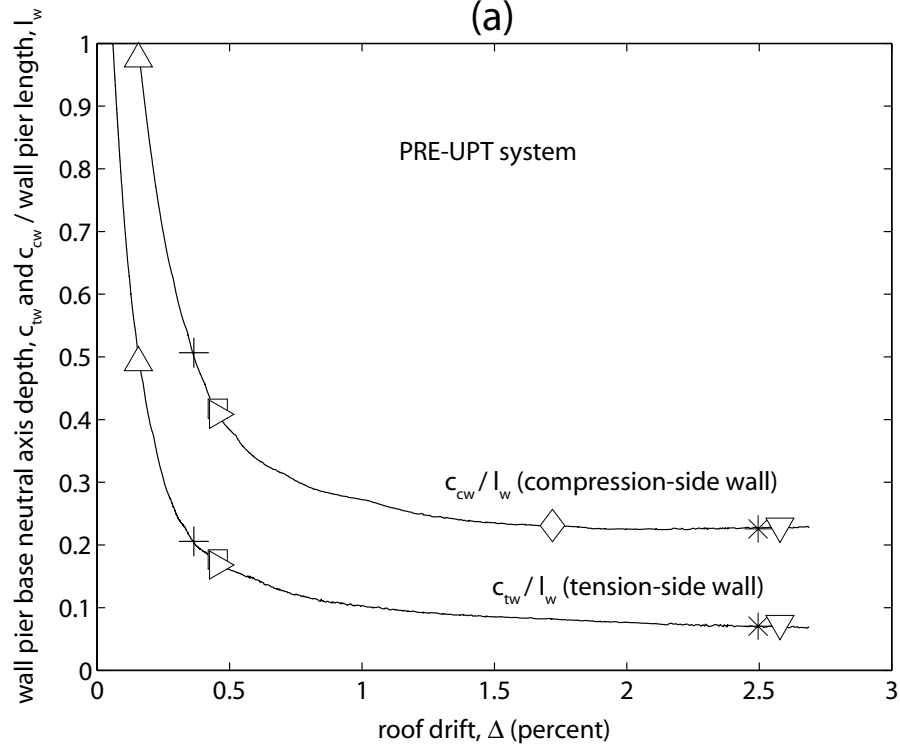
For both structures, the neutral axis depths at the bases of the tension-side and compression-side walls change little at large roof drift values. As expected, the compression-side walls have larger neutral axis depths and larger concrete compression strains than the tension-side walls as a result of the larger compressive axial forces due to the coupling effect. Furthermore, larger wall pier compression strains develop in the PRE-UPT system due to the additional compressive axial forces from the wall post-tensioning bars.

7.2.8 Coupling Beam Shear Force versus Chord Rotation Behaviors

The solid lines in Figs. 7.11a-7.11h show the shear force versus chord rotation (V_b - θ_b) behaviors of the eight coupling beams in the CIP-UPT system, respectively. The solid lines in Figs. 7.12a through 7.12h show similar relationships for the coupling beams in the PRE-UPT system. The chord rotation values for the coupling beams are measured from a tangent drawn at the left end of each beam as shown in Fig. 7.13.



(a)



(b)

Fig. 7.9 Wall pier base neutral axis depths: (a) CIP-UPT system; (b) PRE-UPT system

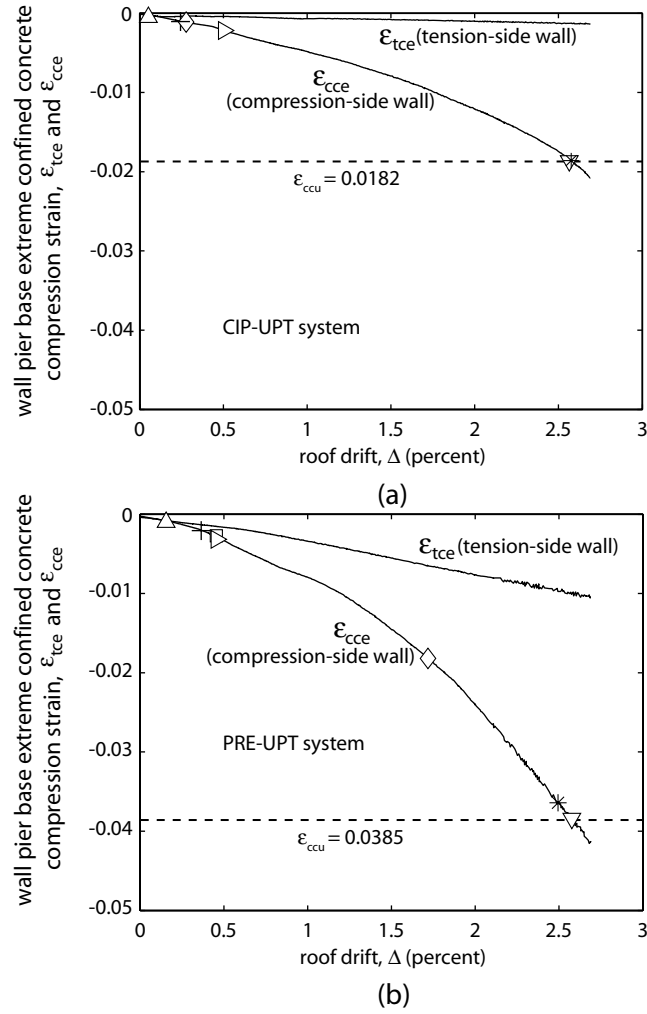


Fig. 7.10 Wall pier base extreme confined concrete compression strains: (a) CIP-UPT system; (b) PRE-UPT system

For comparison, the dashed lines in Figs. 7.11 and 7.12 show the coupling beam shear force versus chord rotation behaviors of isolated subassemblages from the CIP-UPT and PRE-UPT systems, respectively. For both structures, the coupling beams from the multistory and subassemblage models have similar V_b - θ_b behaviors.

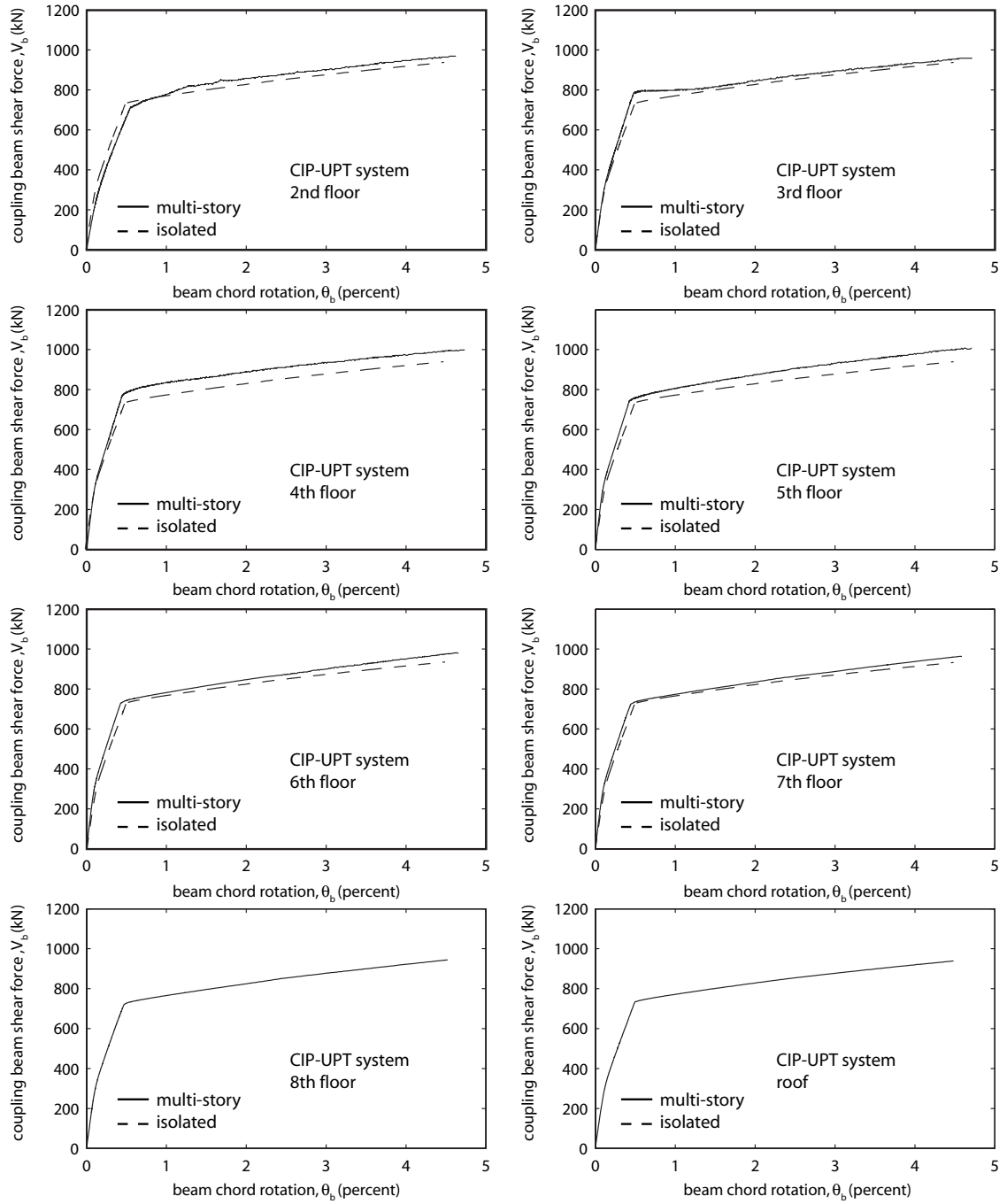


Fig. 7.11 Coupling beam shear force versus chord rotation behaviors for CIP-UPT system

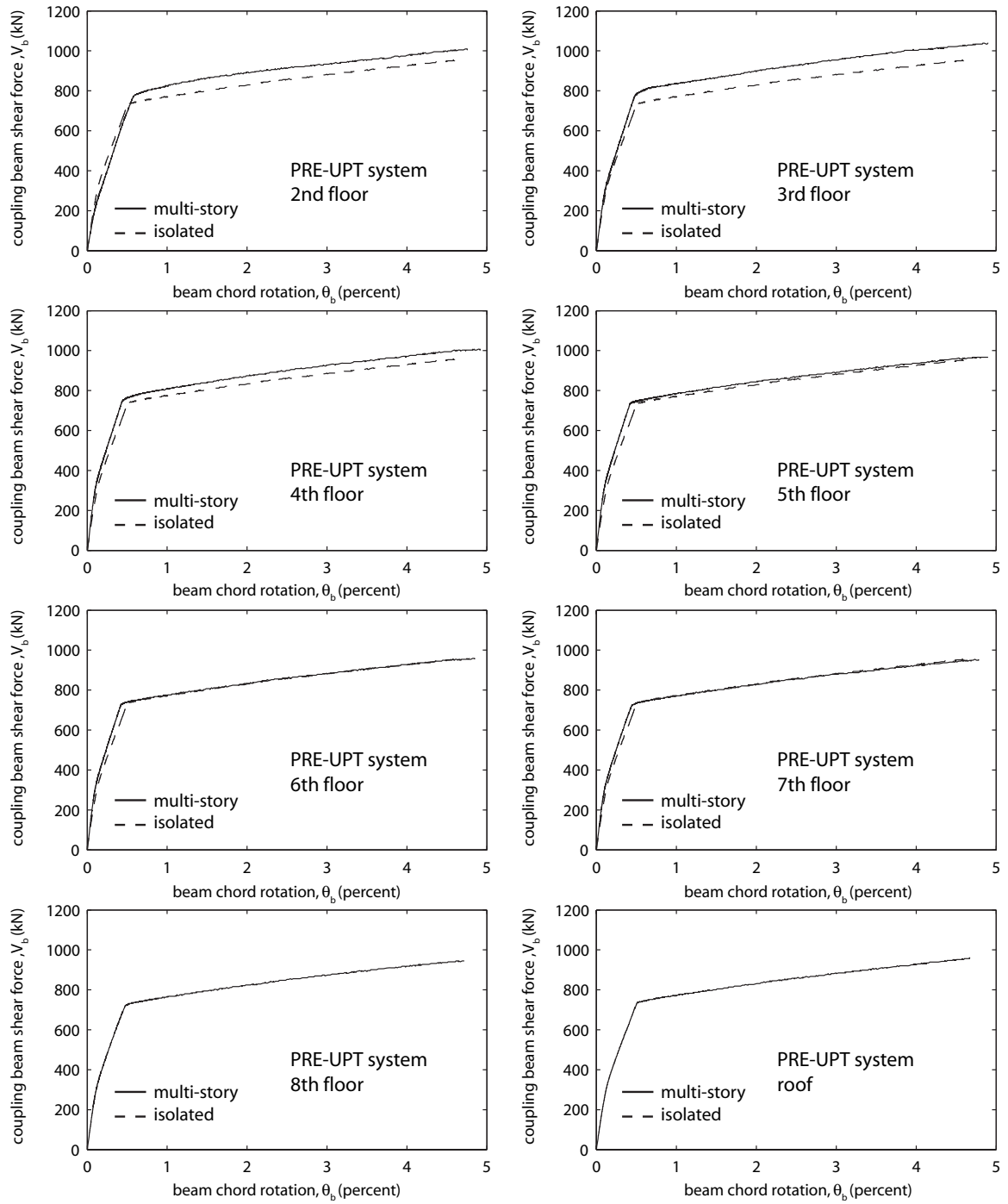


Fig. 7.12 Coupling beam shear force versus chord rotation behaviors for PRE-UPT system

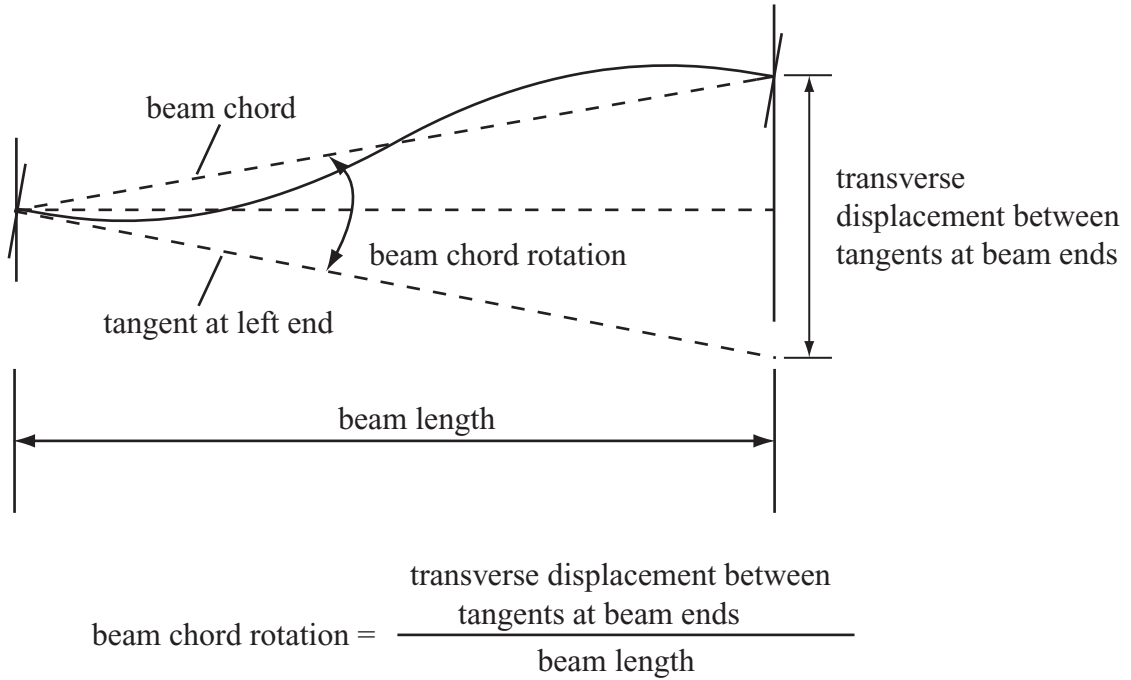


Fig. 7.13 Calculation of coupling beam chord rotation, θ_b in multi-story coupled wall

7.2.9 Coupling Beam Axial Forces

Axial forces develop in the coupling beams of an unbonded post-tensioned hybrid coupled wall structure, primarily, as a result of the post-tensioning forces applied at the floor and roof levels. As described in Chapter 3, the prestressing of the beam post-tensioning tendons is simulated in the coupled wall analytical models by tensile forces in the beam PT elements, which are equilibrated by compression forces in the beam and wall-contact elements. In order to reach equilibrium, the post-tensioning forces result in an elastic shortening of the beam and wall-contact elements, which in turn result in a reduction in the beam PT element forces. Thus, larger tensile forces are applied to the beam PT elements in order to achieve the desired amount of initial post-tensioning forces in the tendons after elastic shortening. For the prototype CIP-UPT and PRE-UPT systems, a total force of $P_{bj}=1868$ kN (420 kips) is applied in the beam PT elements at each floor

and roof level to result, approximately, in the desired total beam initial post-tensioning force of $P_{bi}=n_{bt}a_{bt}f_{bpi}=1837$ kN (413 kips) before the application of lateral loads, where $a_{bt}=395$ mm² is the beam post-tensioning tendon area, $n_{bt}=4$ is the number of beam post-tensioning tendons, and $f_{bpi}=0.625f_{bpu}$ (with $f_{bpu}=1862$ MPa) is the initial stress in the tendons.

The analysis results for the CIP-UPT and PRE-UPT systems indicate that the “fixed” foundation conditions assumed at the bases of the left and right wall piers and the in-plane lateral stiffness of the wall piers affect the transfer of the post-tensioning forces as compressive axial forces into the coupling beams. As an example, Fig. 7.14a shows the axial force, N_b at the midspan of the 2nd floor coupling beam (as marked in Fig. 7.1) of the CIP-UPT system, as well as the total force, P_b in the 2nd floor post-tensioning tendons as the structure is displaced (thick and thin solid lines, respectively). A positive beam axial force indicates a compressive force. Figs. 7.14b-7.14h show similar comparisons between the beam axial forces and the beam PT tendon forces at the upper floor and roof levels. The dashed lines in Fig. 7.14 show the total initial force, P_{bi} (i.e., at $\Delta=0\%$) in the post-tensioning tendons at each floor and roof level, which is approximately equal to the desired initial post-tensioning force of 1837 kN (413 kips).

Fig. 7.14a shows that the initial axial force, N_{bi} in the 2nd floor beam before the application of lateral loads on the structure (i.e., at $\Delta=0\%$), is about 70% of the total initial force, P_{bi} in the 2nd floor post-tensioning tendons. A significant portion of the initial post-tensioning force is not transferred into the beam due to the fixed conditions assumed at the base of the walls. The initial axial forces in the upper level coupling beams are close to the total post-tensioning forces (as shown in Figs. 7.14b-7.14h), indicating that the effect of the foundation/wall stiffness quickly diminishes above the base.

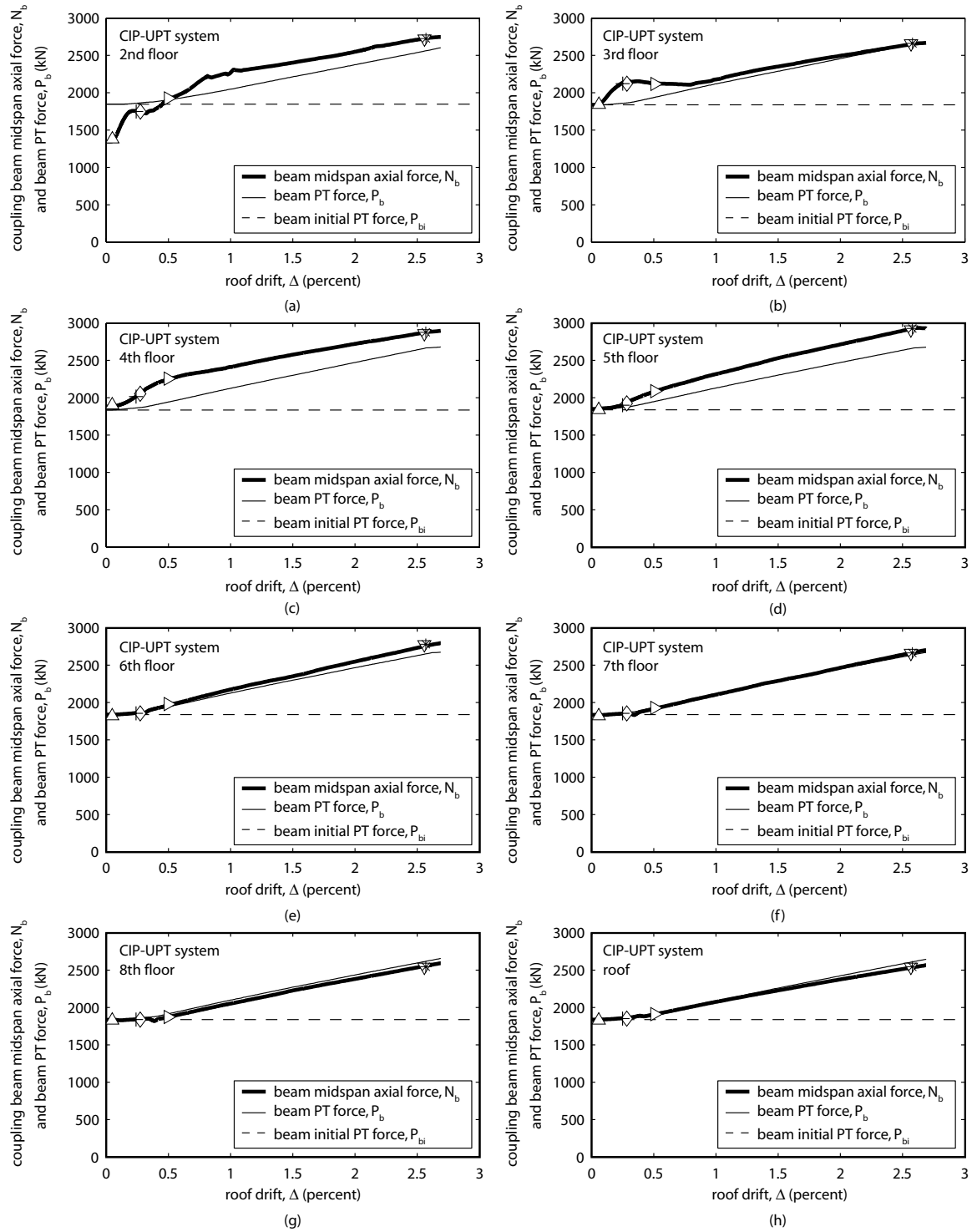


Fig. 7.14 Coupling beam axial forces and post-tensioning forces in CIP-UPT system:
 (a) 2nd floor; (b) 3rd floor; (c) 4th floor; (d) 5th floor; (e) 6th floor;
 (f) 7th floor; (g) 8th floor; (h) roof

Upon lateral displacements of the structure, the fixed foundation conditions restrain the opening of gaps at the ends of the lower level coupling beams, resulting in the development of additional axial forces in the beams as the walls displace. This effect is most pronounced in the 2nd floor beam and results in the development of larger axial forces, N_b in the beam than the total post-tensioning force P_b as shown in Fig. 7.14a.

Note that the results in Fig. 7.14 are based on analyses where the beam PT element forces at the floor and roof levels are applied all at once. These analyses may not reflect actual conditions from practice, where the coupling beam post-tensioning forces would most likely be applied sequentially, beginning from the 2nd floor and ending at the roof level. Based on the principle of superposition, the sequence of post-tensioning over the height of the structure should not affect the axial forces that develop in the coupling beams as long as the structure remains linear-elastic during the post-tensioning process.

Figs. 7.15a and 7.15b demonstrate two different cases where the post-tensioning forces are applied sequentially from the 2nd floor level to the roof and from the roof to the 2nd floor level, respectively, of the CIP-UPT system. Since the DRAIN-2DX analysis program (Prakash et al. 1993) does not allow sequential application of initial element forces, the beam post-tensioning forces in Fig. 7.15 were simulated by external forces applied at the floor and roof levels as shown in Fig. 7.16. The total element force of $P_{bj}=1868$ kN (420 kips) corresponding to the desired initial post-tensioning force of $P_{bi}=1837$ kN (413 kips) was used as the magnitude of these external forces. The structure was assumed to remain linear-elastic (including the beam-to-wall connections) during the entire post-tensioning operation.

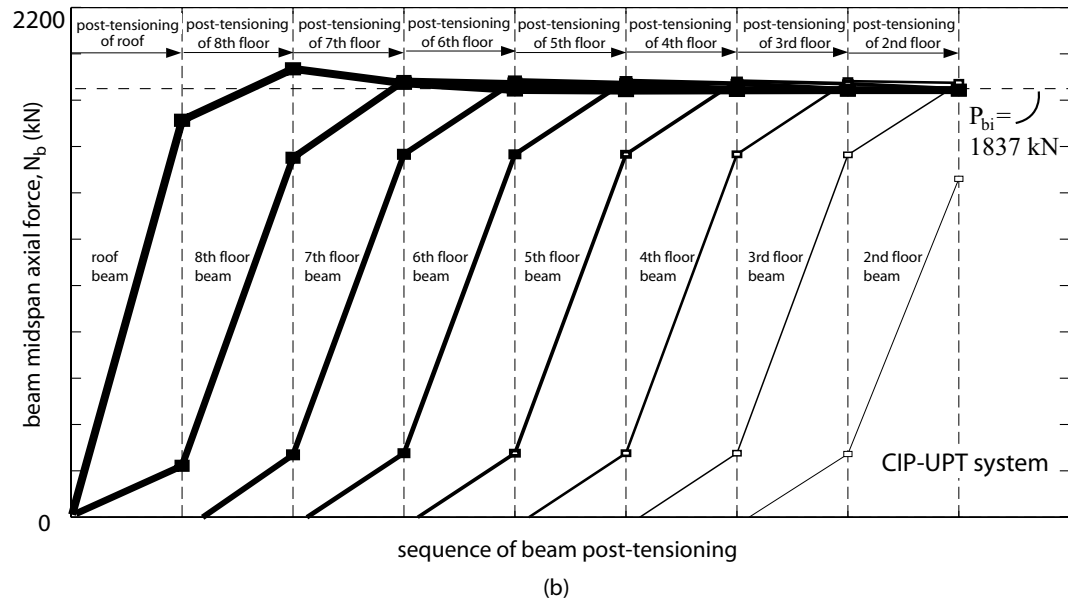
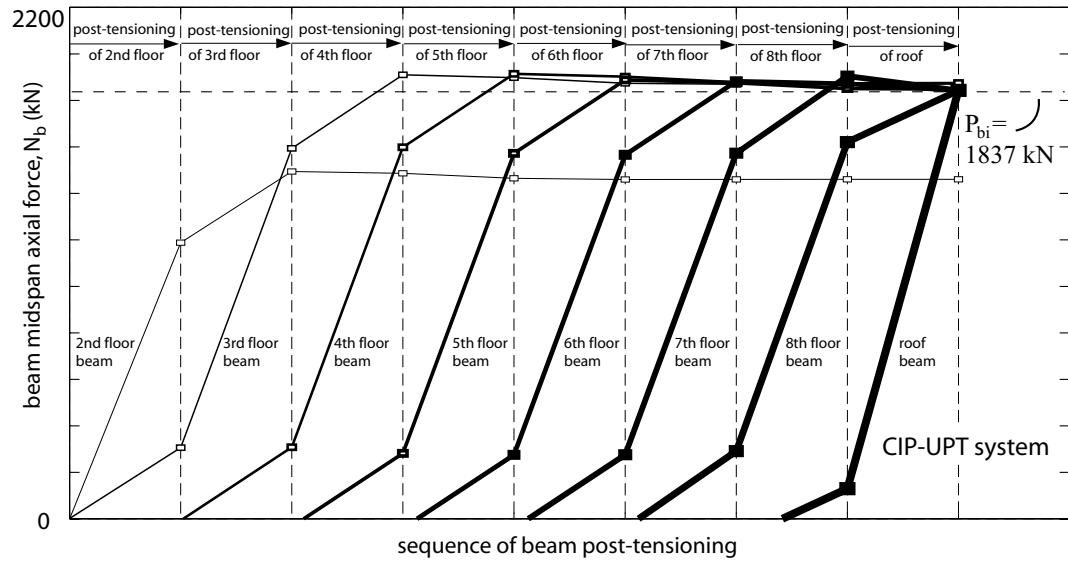


Fig. 7.15 Effect of beam post-tensioning sequence on beam axial forces:
(a) 2nd floor to roof; (b) roof to 2nd floor

In Fig. 7.15a, the thin to thick solid lines represent the application of the external forces in Fig. 7.16 sequentially from the 2nd floor level to the roof. The application of the force at the 2nd floor level results in the development of a compressive axial force in the 2nd floor coupling beam (around $N_b=1200 \text{ kN}$) as well as a compressive force in the 3rd

floor beam (around $N_b=300$ kN). The axial forces in the coupling beams at the 4th floor level and above are little influenced. Upon the application of the external force at the 3rd floor level, the axial force in the 2nd floor beam increases to about $N_b=1500$ kN, the axial force in the 3rd floor beam increases to about $N_b=1600$ kN, and the axial force in the 4th floor beam increases to about $N_b=300$ kN. The axial forces that develop in the coupling beams following the entire post-tensioning sequence over the height of the structure are similar to the forces in Fig. 7.14. The dashed line in Fig. 7.15a represents the desired initial post-tensioning force of $P_{bi}=1837$ kN (413 kips). As discussed previously, the initial (i.e., after all floor and roof level beams are post-tensioned but before the application of lateral forces) compressive force in the 2nd floor beam is significantly smaller than the total force in the 2nd floor post-tensioning tendons due to the fixed boundary conditions at the wall bases.

Similarly in Fig. 7.15b, the external forces are applied sequentially from the roof to the 2nd floor level. By comparing the results in Figs. 7.14, 7.15a, and 7.15b, it is concluded that the axial forces that develop in the coupling beams are not affected by the sequence of post-tensioning over the height of the structure, as long as the structure remains linear-elastic during this process. The results also indicate that the application of post-tensioning at a floor or roof level primarily affects the beam axial forces at that level and the two adjacent levels above and below.

Note that the results in Fig. 7.15 are limited to structures that remain linear-elastic during post-tensioning. While significant material nonlinearity is not expected to occur as a result of post-tensioning, geometric nonlinearity can occur during sequential post-tensioning of an unbonded post-tensioned system if gaps are allowed to open at the ends of the beams that are not yet prestressed. According to Fig. 7.15a, when the 2nd floor coupling beam is post-tensioned, small tensile forces (not shown in the figure) develop in

the 4th floor beam and above. The opening of gaps at the beam ends as a result of these tensile forces, and the effect of these gaps on the subsequent axial forces that develop in the coupling beams upon completion of the entire post-tensioning operation cannot be investigated using a linear-elastic model.

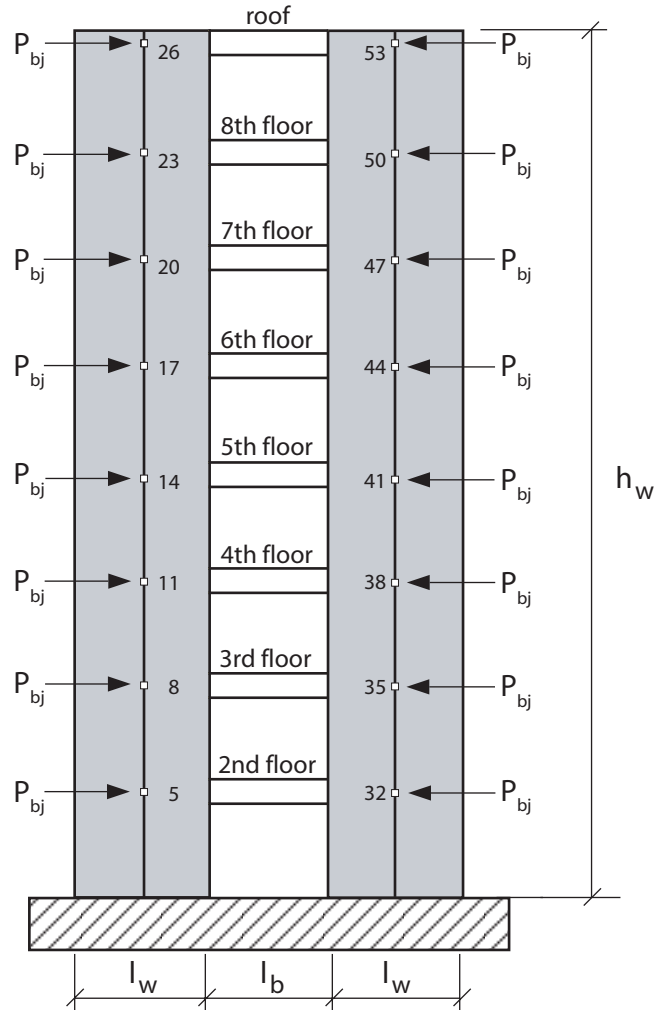


Fig. 7.16 Simulation of beam post-tensioning using external forces

The coupled wall analyses described in the remainder of this dissertation are based on the model where the beam post-tensioning forces are simulated using element forces (not external forces) and applied simultaneously at all floor and roof levels.

7.2.10 Coupling Beam End Strains

Figs. 7.17 and 7.18 show the neutral axis (i.e., contact) depths, c_b at the left ends of the coupling beams in the CIP-UPT and PRE-UPT systems, respectively. The c_b values are normalized with respect to the beam depth, $d_{bc}=634$ mm (24.97 in). The behaviors at the right ends of the coupling beams are similar. The corresponding extreme cover plate steel compression strains, ϵ_{be} at the left ends of the coupling beams are shown in Figs. 7.19 and 7.20, respectively, with the steel yield strain, ϵ_{sy} shown by the dashed horizontal lines. In general, the coupling beams over the height of each structure have similar behaviors.

7.2.11 Tension Angle Force versus Deformation Behaviors

Figs. 7.21 and 7.22 show the force versus deformation behaviors of the tension angles at the left ends of the coupling beams in the CIP-UPT and PRE-UPT systems, respectively. The behaviors of the tension angles at the right ends of the coupling beams are similar. For both structures, the tension angles at the second floor level have the smallest deformations because the fixed boundary conditions at the wall bases restrain the gap opening at the beam-to-wall interfaces.

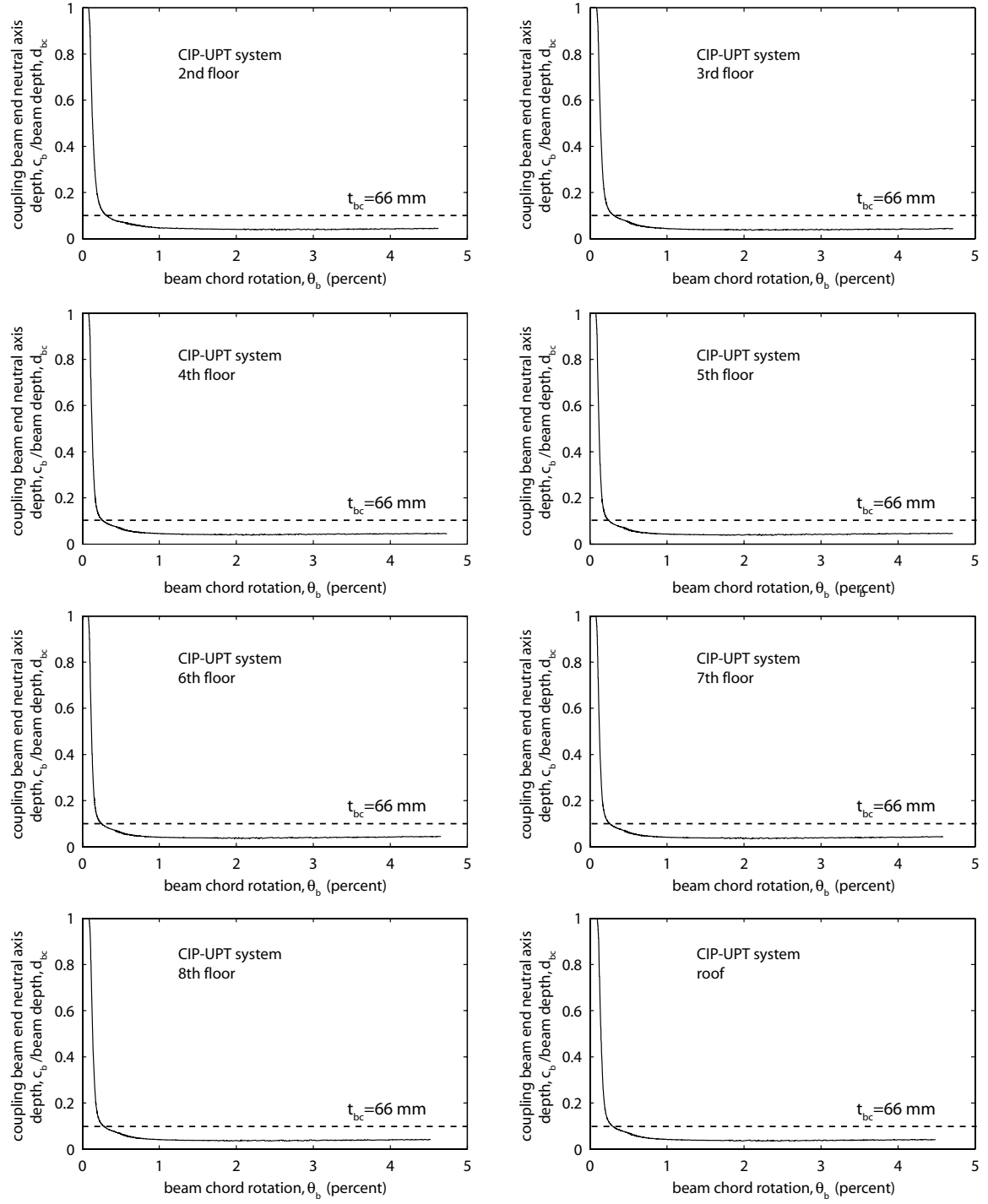


Fig. 7.17 Coupling beam end neutral axis (i.e., contact) depths for CIP-UPT system

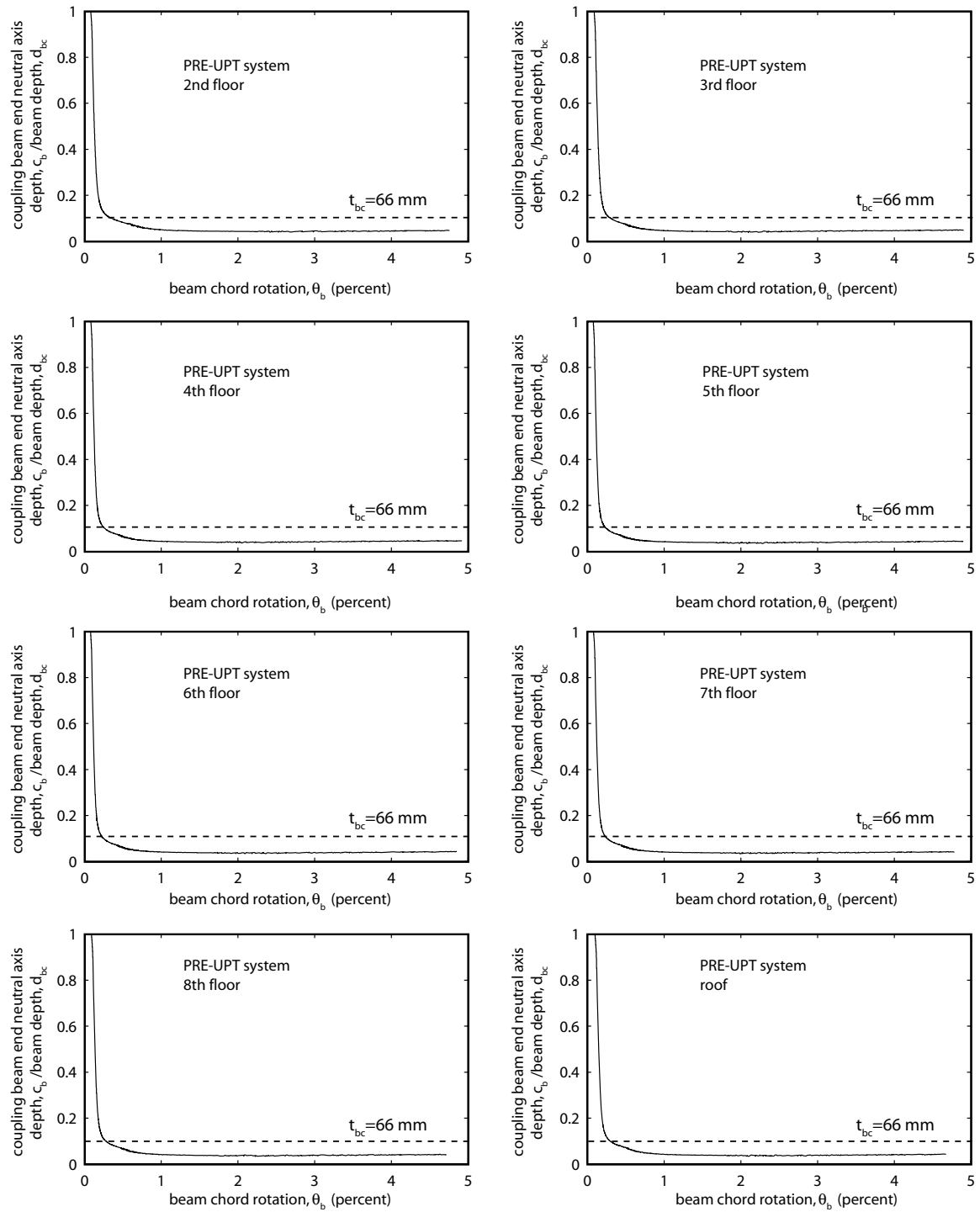


Fig. 7.18 Coupling beam end neutral axis (i.e., contact) depths for PRE-UPT system

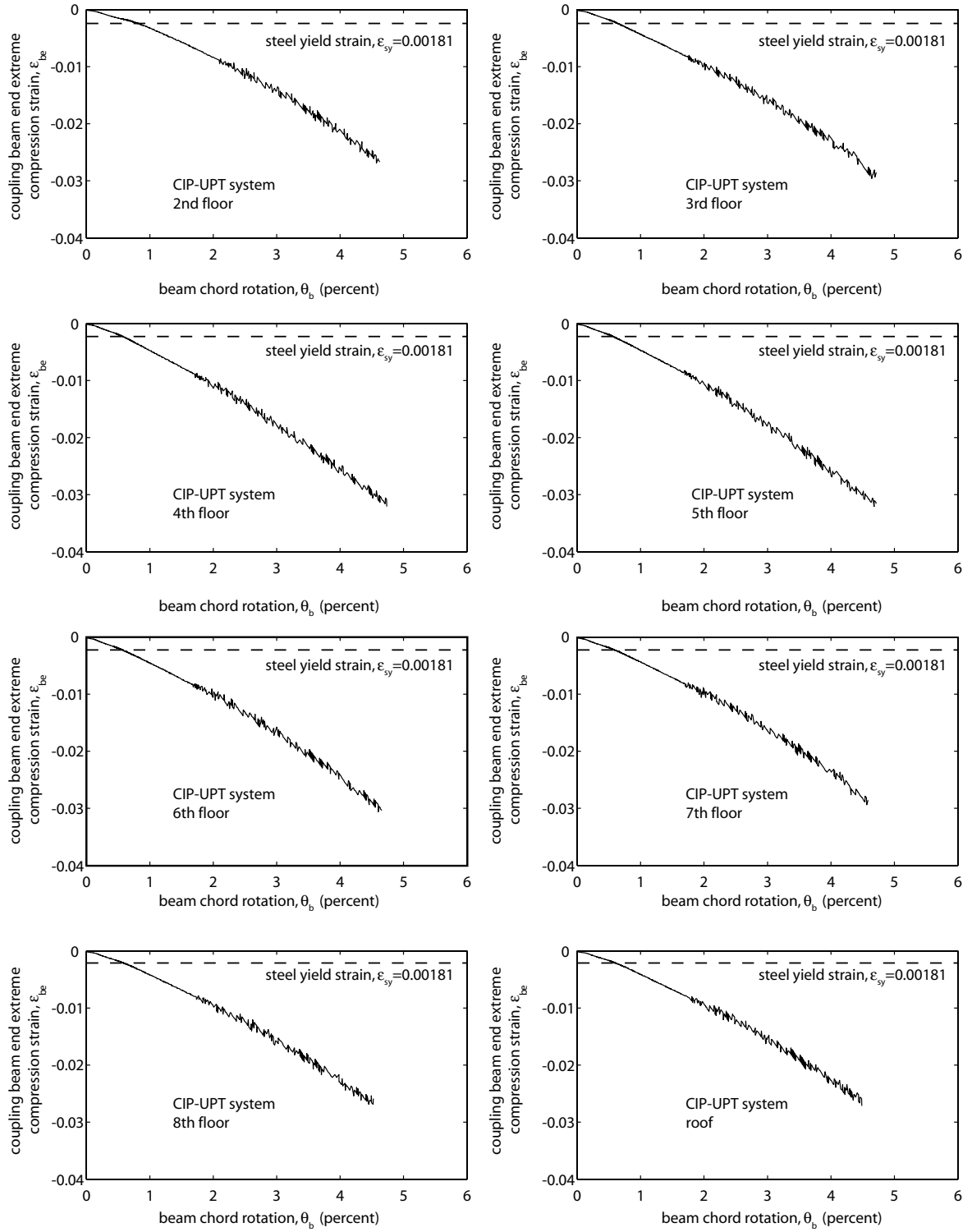


Fig. 7.19 Coupling beam end extreme steel compression strains for CIP-UPT system

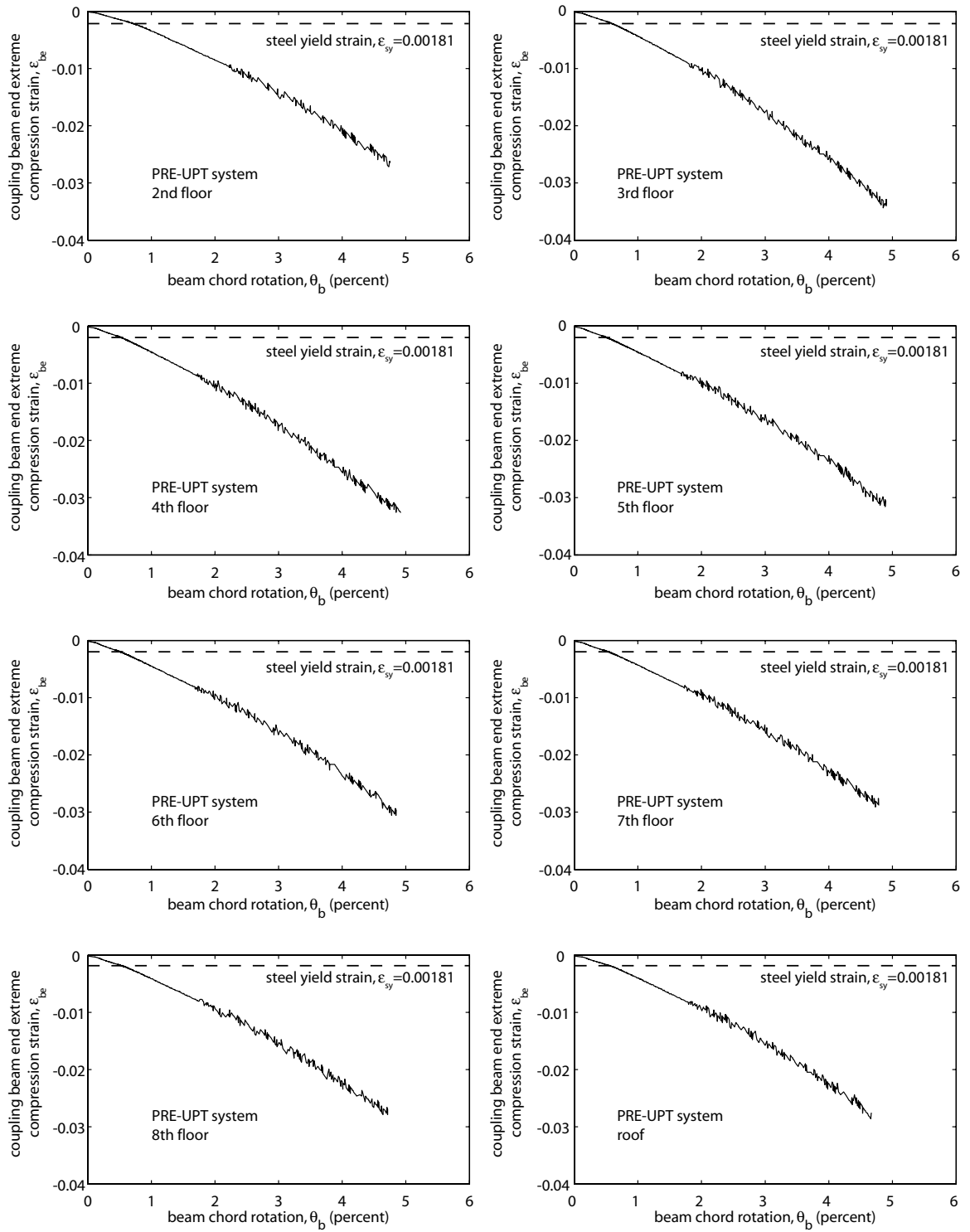


Fig. 7.20 Coupling beam end extreme steel compression strains for PRE-UPT system

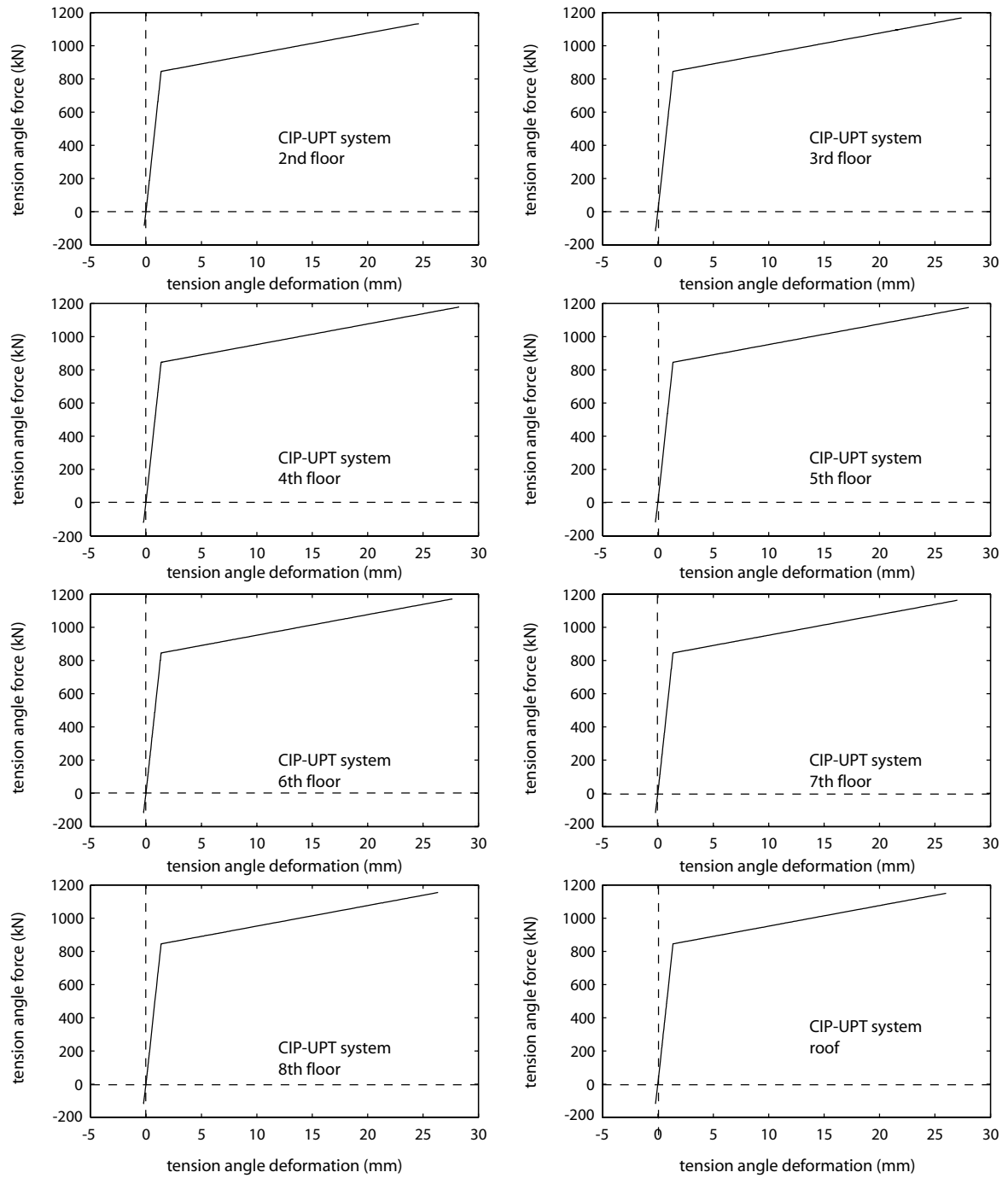


Fig. 7.21 Coupling beam tension angle force-deformation behaviors for CIP-UPT system

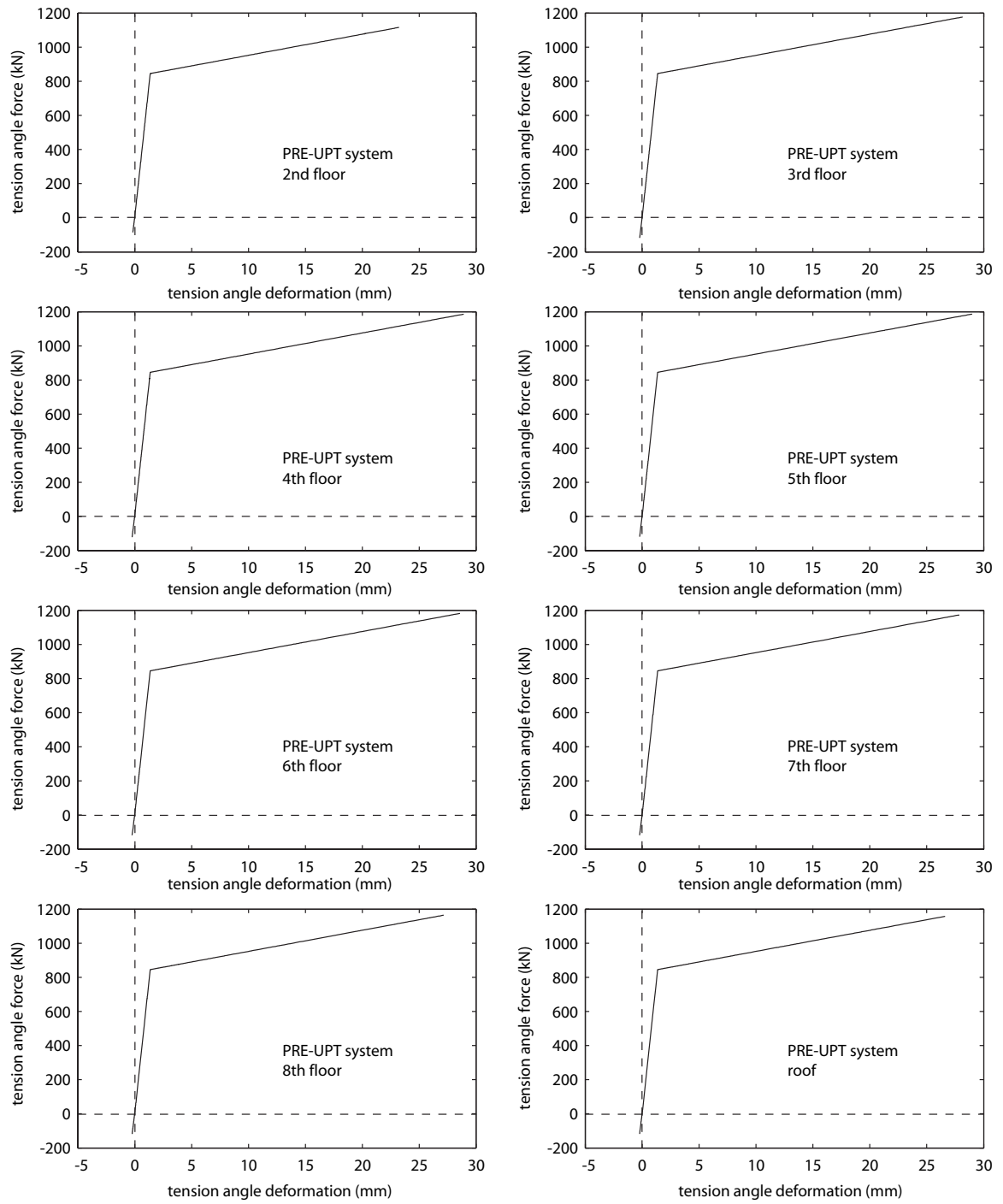


Fig. 7.22 Coupling beam tension angle force-deformation behaviors for PRE-UPT system

7.3 Behavior under Cyclic Loading

This section describes the behavior of the prototype CIP-UPT and PRE-UPT systems under combined gravity loads and reversed cyclic lateral loads. The structures are displaced to roof drift values of $\Delta=\pm 0.5, 1, 1.5, 2,$ and 2.5% , with one cycle of loading at each displacement amplitude. The base shear versus roof drift behavior of the prototype systems is compared with structures that use embedded steel coupling beams. The effect of the top and seat angles on the behavior of the prototype structures is investigated.

7.3.1 Coupled Wall Base Shear Force versus Roof Drift Behaviors

Figs. 7.23a and 7.23b show the base shear versus roof drift ($F-\Delta$) behaviors of the prototype CIP-UPT and PRE-UPT systems, respectively, under combined gravity loads and cyclic lateral loads. The results indicate that the PRE-UPT system has considerable inelastic energy dissipation and a large self-centering capability (i.e., ability to return towards the zero displacement position upon unloading from a nonlinear displacement). The CIP-UPT system has larger inelastic energy dissipation and a somewhat reduced but still large self-centering capability. Both structures have stable behavior under large nonlinear reversed cyclic lateral displacements.

The large self-centering capability of the structures indicate that the beam post-tensioning tendons provide a sufficient amount of restoring force to pull the walls back towards their original undisplaced position upon unloading. The increased self-centering capability of the PRE-UPT system occurs as a result of the additional restoring effect of the post-tensioning bars used as flexural reinforcement in the precast concrete walls. The larger inelastic energy dissipation in the CIP-UPT system occurs, primarily, as a result of

the yielding of the wall mild steel reinforcement near the base of the walls. Note that the unbonded post-tensioning bars used as flexural reinforcement in the precast concrete walls have little contribution to the inelastic energy dissipation of the PRE-UPT system since the yielding of the bars is significantly delayed as a result of unbonding (see Figs. 7.2b and 7.4b).

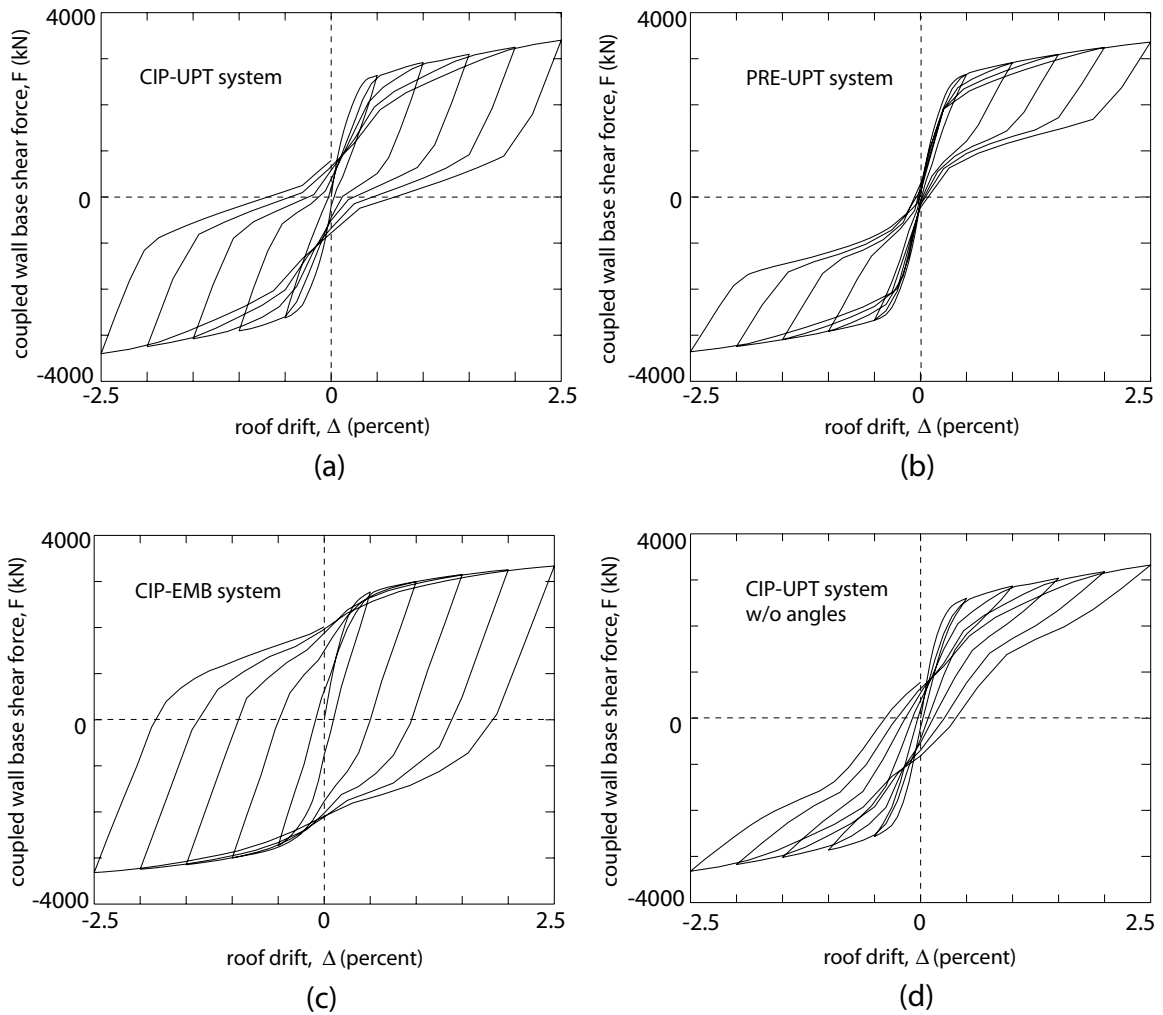


Fig. 7.23 Coupled wall base shear force versus roof drift behaviors under cyclic lateral loads: (a) CIP-UPT system; (b) PRE-UPT system; (c) CIP-EMB system; (d) CIP-UPT system without angles

For comparison, Fig. 7.23c shows the expected behavior of the cast-in-place reinforced concrete walls with embedded steel coupling beams (referred to as the CIP-EMB system) representing conventional construction. Note that the lateral strength of a post-tensioned coupling beam is smaller than the lateral strength of an embedded beam of the same size since the post-tensioned beam cannot develop the full yield and plastic capacity of the cross section as described in Chapter 4. To facilitate a comparative investigation, smaller coupling beams are used in the CIP-EMB system (with W21×93 cross sections) than the beams in the CIP-UPT system (with W21×182 cross sections) such that the monotonic $F-\Delta$ relationships of the two systems are similar. The modeling of the CIP-EMB system is similar to the modeling of the CIP-UPT system (see Chapter 6), except for the use of embedded steel coupling beam subassemblage models at the floor and roof levels as described in Chapter 3. The embedded lengths of the coupling beams in the CIP-EMB system are assumed to be equal to $l_{be}=1.83$ m (6 ft).

Comparing the cyclic behaviors of the CIP-UPT and CIP-EMB systems in Figs. 7.23a and 7.23c, the CIP-EMB system has significantly larger energy dissipation, which occurs as a result of the yielding of the coupling beams. However, the self-centering capability of the CIP-EMB system is small indicating the possibility of significant residual (i.e., permanent) lateral displacements after a large earthquake.

The results in Figs. 7.23a and 7.23b are for systems that include top and seat angles at the beam-to-wall interfaces. To investigate the amount of energy dissipation provided by the angles, Fig. 7.23d shows the behavior of the CIP-UPT system with the angles removed. In this case, the area of the post-tensioning steel in the coupling beams is

doubled [to a value of $a_{bt}=790 \text{ mm}^2$ (1.224 in^2)] such that the monotonic $F-\Delta$ relationship of the system without angles is similar to that of the system with angles.

As expected, the energy dissipation of the system without angles in Fig. 7.23d is significantly smaller than the system with angles in Fig. 7.23a. Since unbonded post-tensioned coupling beams without top and seat angles do not dissipate much energy (see Chapter 4), the energy dissipated in Fig. 7.23d is provided primarily by the inelastic behavior of the walls near the base.

7.3.2 Coupling Beam Axial Forces

Figs. 7.24 and 7.25 show the axial forces, N_b at the midspan of the coupling beams and the total forces in the post-tensioning tendons, P_b respectively, at the floor and roof levels of the CIP-UPT system corresponding to the analysis results in Fig. 7.23a. A positive beam axial force indicates a compressive force. The empty circle and solid circle markers indicate peak roof drift (with $\Delta=\pm 0.5, 1, 1.5, 2, 2.5\%$) and zero roof drift positions, respectively, during the lateral load analysis of the structure. The beam axial forces and post-tensioning forces follow similar trends. The peak forces occur when the structure is displaced to the peak roof drift during each cycle. The peak beam axial forces are similar to or larger than (especially for the second floor level during the small displacement cycles in Fig. 7.24a) the peak post-tensioning forces. The larger peak beam axial forces as compared to the post-tensioning forces are due to the restraining effect of the left and right wall piers on the opening of gaps at the beam ends. Upon returning to the original undisplaced position (with $\Delta=0\%$), the axial forces and post-tensioning forces generally decrease back towards their initial levels of N_{bi} and P_{bi} (horizontal dashed lines)

before the application of lateral forces, except for the second floor beam axial force as shown in Fig. 7.24a.

Upon unloading of the structure from $\Delta=2.0\%$, Fig. 7.24a shows that the axial force in the second floor coupling beam drops well below the initial axial force level of $N_{bi}=1467$ kN even though the total force in the post-tensioning tendons in Fig. 7.25a is close to the initial force, P_{bi} . The smallest axial force reached in the 2nd floor coupling beam upon unloading from $\Delta=2.5\%$ is around $N_b=199$ kN, indicating that the beam has lost most of its initial precompression at this stage of the analysis. This type of behavior is not observed in the upper level coupling beams, which maintain most of their initial axial force, N_{bi} levels throughout the lateral loading history. Note that despite the loss in precompression upon unloading, the peak 2nd floor beam axial forces are similar to or larger than the peak post-tensioning forces upon loading, similar to the behavior shown in Fig. 7.14a.

The horizontal (axial/shear) force equilibrium diagram in Fig. 7.26a is used to explain the reduction of the precompression force in the 2nd floor coupling beam upon unloading under cyclic loading. Only the left wall region above and below a floor/roof level and half of the coupling beam is shown as a free body. The axial force in the coupling beam, N_b is in equilibrium with the total force in the post-tensioning tendons, P_b , the external lateral force, f , applied at the floor level, and the wall top and bottom shear forces, F_{wts} and F_{wbs} . Let the difference between the wall bottom shear force F_{wbs} and the wall top shear force F_{wts} for each floor and roof level be defined as F_{wsi} . The F_{wsi} values for the second floor and roof levels of the CIP-UPT system are compared in Fig. 7.26b (solid and dashed lines, respectively). The empty circle markers and solid circle markers indicate peak roof drift (with $\Delta=\pm 0.5, 1, 1.5, 2, 2.5\%$) and zero roof drift positions, respectively, during the lateral load analysis of the structure.

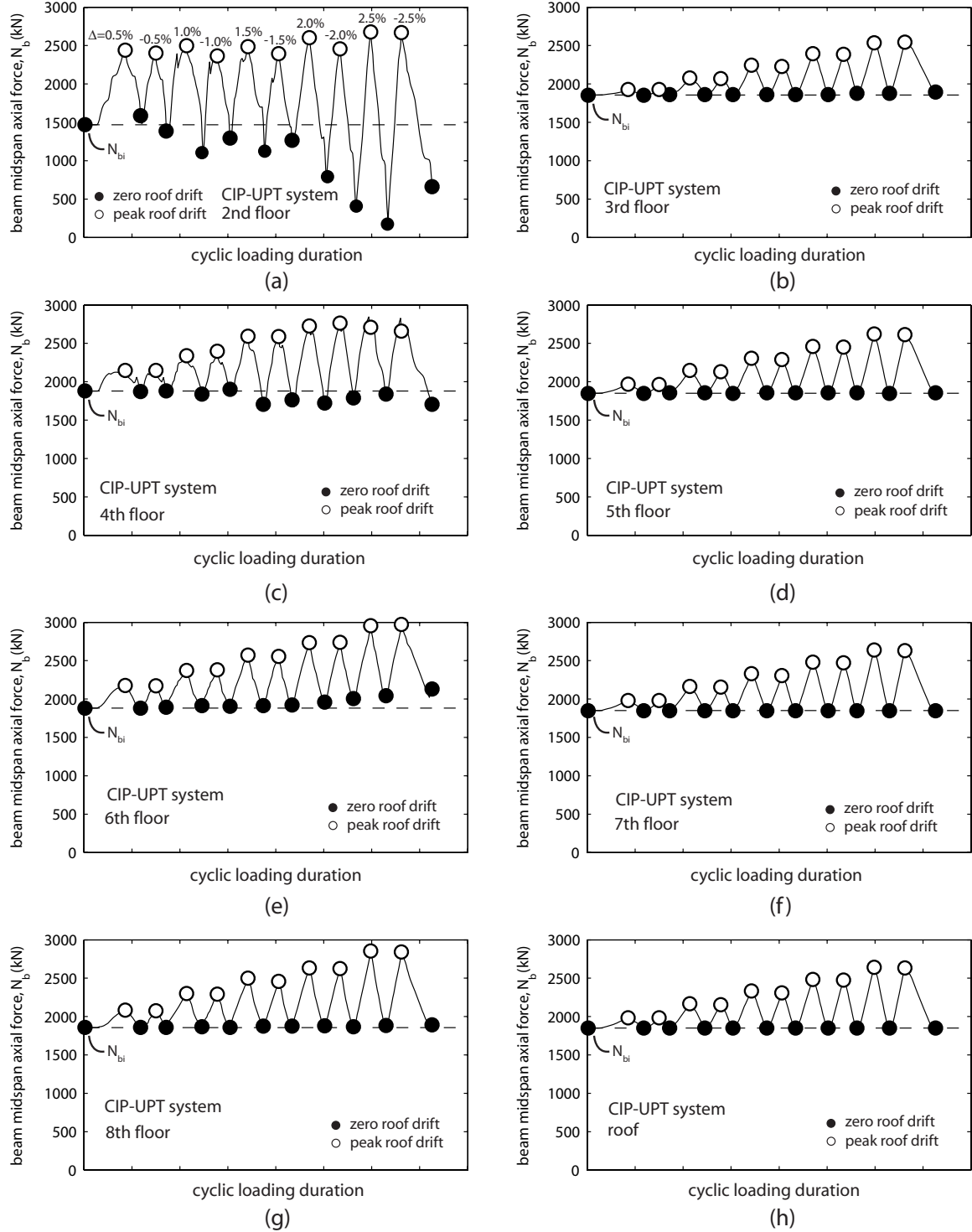


Fig. 7.24 Coupling beam axial forces in CIP-UPT system – cyclic loading:
 (a) 2nd floor; (b) 3rd floor; (c) 4th floor; (d) 5th floor; (e) 6th floor;
 (f) 7th floor; (g) 8th floor; (h) roof

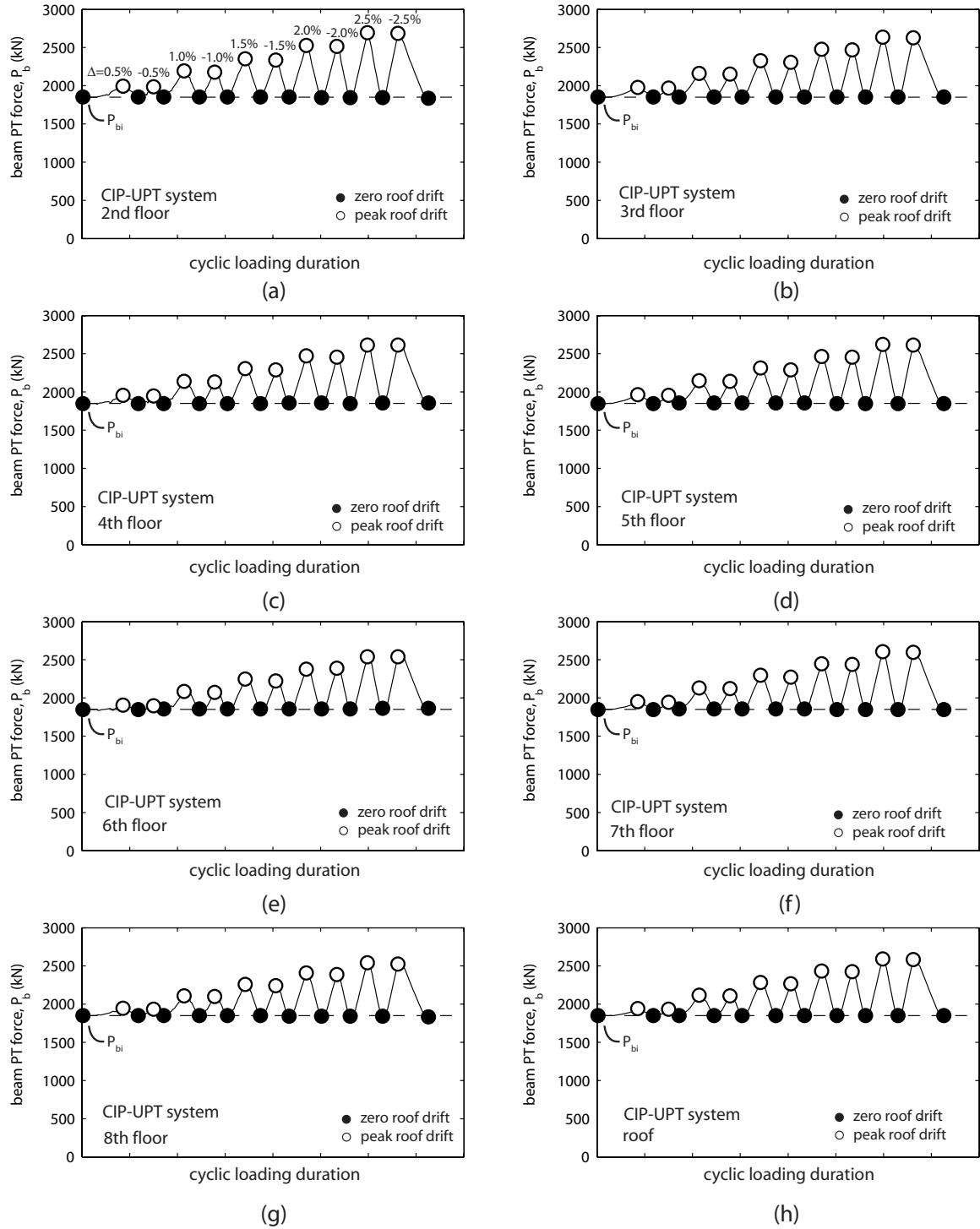


Fig. 7.25 Coupling beam post-tensioning forces in CIP-UPT system – cyclic loading:
 (a) 2nd floor; (b) 3rd floor; (c) 4th floor; (d) 5th floor; (e) 6th floor;
 (f) 7th floor; (g) 8th floor; (h) roof

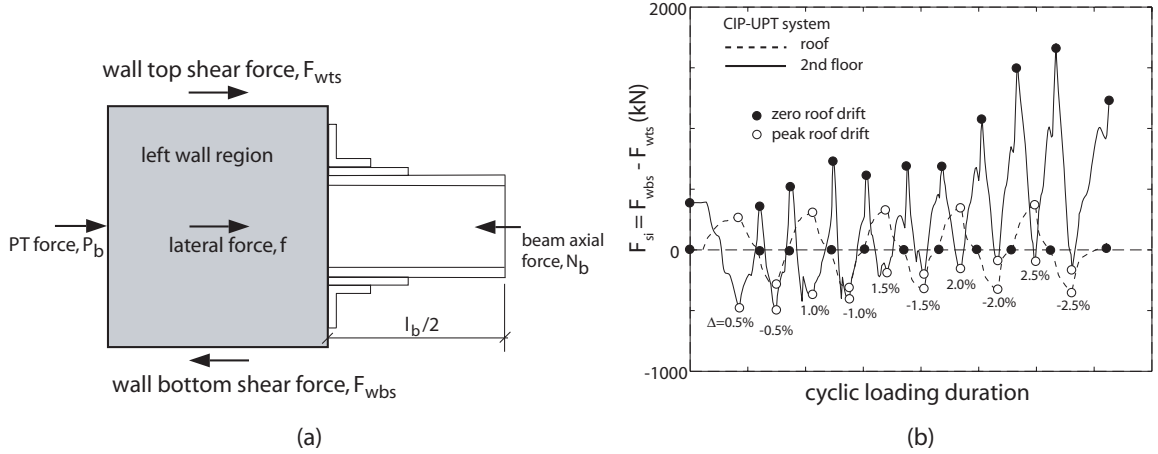


Fig. 7.26 Coupling beam axial forces: (a) equilibrium of horizontal forces; (b) wall floor/roof shear forces

The results in Fig. 7.26b show that, after the application of the initial beam post-tensioning forces and at the beginning of the lateral load analysis, F_{wsi} is equal to zero at the roof level (dashed line) while a non-zero F_{wsi} value is developed at the 2nd floor level (solid line) because of the wall foundation boundary conditions. This non-zero F_{wsi} value is the reason for the difference in the initial beam axial force, N_{bi} and total post-tensioning force, P_{bi} at the 2nd floor level in Figs. 7.14a and 7.24a. The results in Fig. 7.26b show that there is a decrease and then reversal in the 2nd floor F_{wsi} value as the structure is loaded laterally. Upon unloading of the structure back to $\Delta=0\%$, the F_{wsi} value at the 2nd floor level begins to increase, especially following the displacements to $\Delta=2\%$ and 2.5% . This buildup in the F_{wsi} value at $\Delta=0\%$ results in the decrease in the coupling beam axial force, N_b observed in Fig. 7.24a. In comparison, the F_{wsi} value at the roof level (dashed line in Fig. 7.26b) is close to zero upon unloading to $\Delta=0\%$. The behaviors of the upper floor level coupling beams are similar to the roof beam as indicated in Figs. 7.24b-h and 7.25b-h.

7.4 Parametric Investigation

The pushover lateral load behavior of a series of parametric unbonded post-tensioned hybrid coupled wall systems, as determined by varying the structural properties of the CIP-UPT and PRE-UPT systems described above, is investigated in this section. The results are used to determine how the behavior of each system can be controlled by design.

The following parameters are investigated: (1) wall length, l_w ; (2) wall reinforcement ratio, ρ_{ws} or ρ_{wp} (defined as the total area of wall mild steel or post-tensioning steel divided by the wall gross cross section area); (3) wall thickness, t_w (investigated only for systems with cast-in-place concrete wall piers); (4) initial stress in wall post-tensioning bars, f_{wpi} (investigated only for systems with precast concrete wall piers); (5) beam web depth, d_{bw} ; (6) beam post-tensioning tendon area, a_{bt} ; (7) initial stress in beam post-tensioning tendons, f_{bpi} ; (8) beam length, l_b ; and (9) top and seat angle thickness, t_a .

Three coupled wall systems are investigated for each parameter: System (1) is the same as the prototype CIP-UPT or PRE-UPT system and the properties of Systems (2) and (3) are varied as shown in Tables 7.2 and 7.3. All other structural properties of Systems (2) and (3) are the same as System (1). A discussion of the results from the parametric analyses is provided below.

TABLE 7.2

PARAMETRIC CIP-UPT SYSTEMS

Parameter Varied	System (1)	System (2)	System (3)
Wall length, l_w	3.05 m	3.81 m (1.25)	2.29 m (0.75)
Wall flexural reinforcement ratio, ρ_{ws}	1.47%	1.84% (1.25)	2.21% (1.50)
Wall thickness, t_w	356 mm	254 mm (0.71)	457 mm (1.28)
Beam web depth, d_{bw}	502 mm	629 mm (1.25)	375 mm (0.75)
Beam PT tendon area, a_{bt}	395 mm ²	592 mm ² (1.50)	197 mm ² (0.50)
Initial stress of beam PT tendons, f_{bpi}	0.625 f_{bpu}	0.725 f_{bpu} (1.16)	0.525 f_{bpu} (0.84)
Beam length, l_b	3.05 m	3.81 m (1.25)	4.57 m (1.50)
Angle thickness, t_a	28.6 mm	19.1 mm (0.67)	0 mm (0)

Note: numbers in parentheses show parameter values for Systems (2) and (3) divided by value for System (1)

TABLE 7.3

PARAMETRIC PRE-UPT SYSTEMS

Parameter Varied	System (1)	System (2)	System (3)
Wall length, l_w	3.05 m	3.81 m (1.25)	2.29 m (0.75)
Wall flexural reinforcement ratio, ρ_{wp}	1.13%	1.41% (1.25)	1.69% (1.50)
Initial stress of wall PT bars, f_{wpi}	0.625 f_{wpu}	0.725 f_{wpu} (1.16)	0.525 f_{wpu} (0.84)
Beam web depth, d_{bw}	502 mm	629 mm (1.25)	375 mm (0.75)
Beam PT tendon area, a_{bt}	395 mm ²	592 mm ² (1.50)	197 mm ² (0.50)
Initial stress of beam PT tendons, f_{bpi}	0.625 f_{bpu}	0.725 f_{bpu} (1.16)	0.525 f_{bpu} (0.84)
Beam length, l_b	3.05 m	3.81 m (1.25)	4.57 m (1.50)
Angle thickness, t_a	28.6 mm	19.1 mm (0.67)	0 mm (0)

Note: numbers in parentheses show parameter values for Systems (2) and (3) divided by value for System (1)

7.4.1 Base Shear versus Roof Drift Behavior

The base shear versus roof drift behaviors of the parametric coupled wall systems in Tables 7.2 and 7.3 are given in Figs. 7.27 and 7.28, respectively. The markers shown on the figures represent the states of behavior defined in Fig. 7.2.

The base shear versus roof drift behaviors of the parametric coupled wall systems show that the lateral strength of the structures can be controlled by the beam post-tensioning tendon area a_{bt} , beam depth d_{bw} , and angle thickness t_a , as well as the wall length l_w . The yielding of the beam post-tensioning steel, which is significantly delayed

due to the use of unbonded tendons, can be controlled by the initial stress in the post-tensioning steel, f_{bpi} . More information on the parameters that control the behavior of the coupling beams can be found in Chapter 4 and more information on the parameters that control the behavior of unbonded post-tensioned precast concrete walls (e.g., the eccentricity of the wall post-tensioning bars) can be found in Kurama et al. (1996, 1999a).

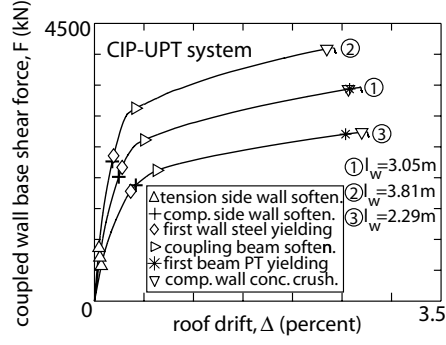
7.4.2 Degree of Coupling

As described previously, the degree of coupling, DOC, is an important factor for the lateral load behavior of coupled wall structures. For this purpose, Tables 7.4 and 7.5 show the degrees of coupling for the parametric coupled wall systems in Tables 7.2 and 7.3. As shown in Fig. 7.8, the degree of coupling varies by a small amount during lateral loading. The degree of coupling values in Tables 7.4 and 7.5 were calculated using Equation (2.2) at a roof drift of $\Delta=0.5\%$.

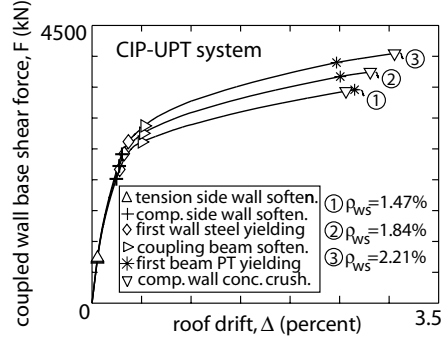
TABLE 7.4
DEGREE OF COUPLING OF PARAMETRIC CIP-UPT SYSTEMS

Parameter Varied	Degree of Coupling, DOC (%)		
	System (1)	System (2)	System (3)
Wall length, l_w	62	58 (0.94)	68 (1.10)
Wall flexural reinforcement ratio, ρ_{ws}	62	59 (0.95)	57 (0.92)
Wall thickness, t_w	62	64 (1.03)	61 (0.98)
Beam web depth, d_{bw}	62	66 (1.06)	56 (0.90)
Beam PT tendon area, a_{bt}	62	65 (1.05)	56 (0.90)
Initial stress of beam PT tendons, f_{bpi}	62	63 (1.02)	60 (0.97)
Beam length, l_b	62	59 (0.95)	56 (0.90)
Angle thickness, t_a	62	55 (0.89)	47 (0.76)

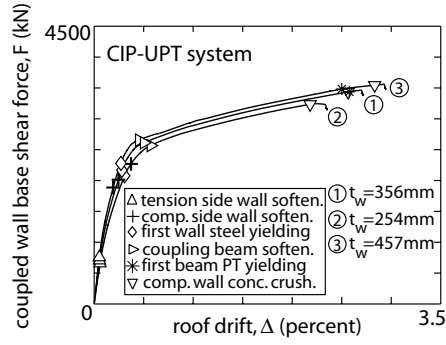
Note: numbers in parentheses show DOC values for Systems (2) and (3) divided by DOC value for System (1)



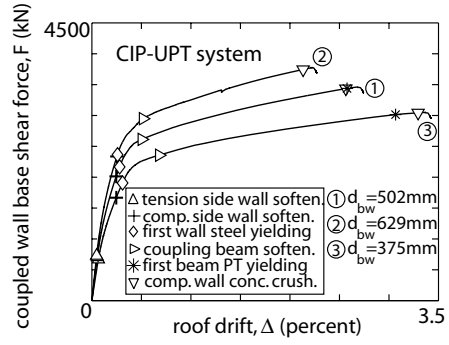
(a)



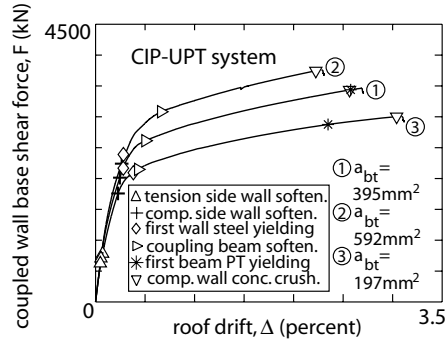
(b)



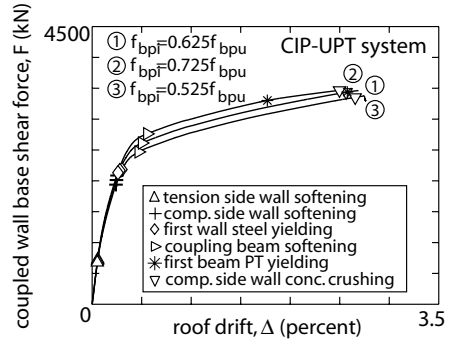
(c)



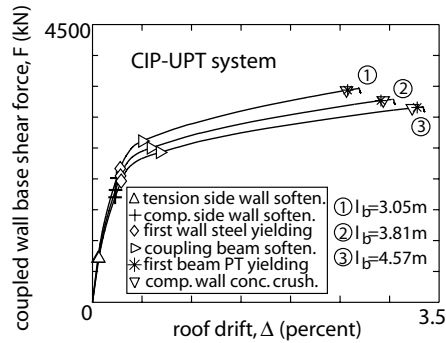
(d)



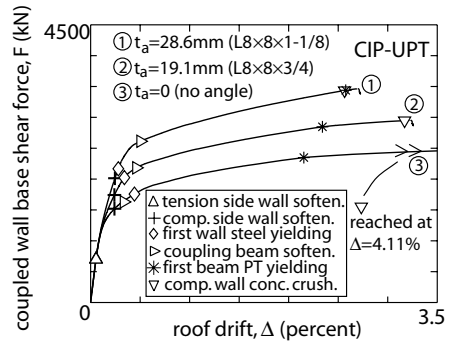
(e)



(f)



(g)



(h)

Fig. 7.27 Base shear versus roof drift behaviors of parametric CIP-UPT systems:

(a) l_w ; (b) ρ_{ws} ; (c) t_w ; (d) d_{bw} ; (e) a_{bt} ; (f) f_{bpi} ; (g) l_b ; (h) t_a

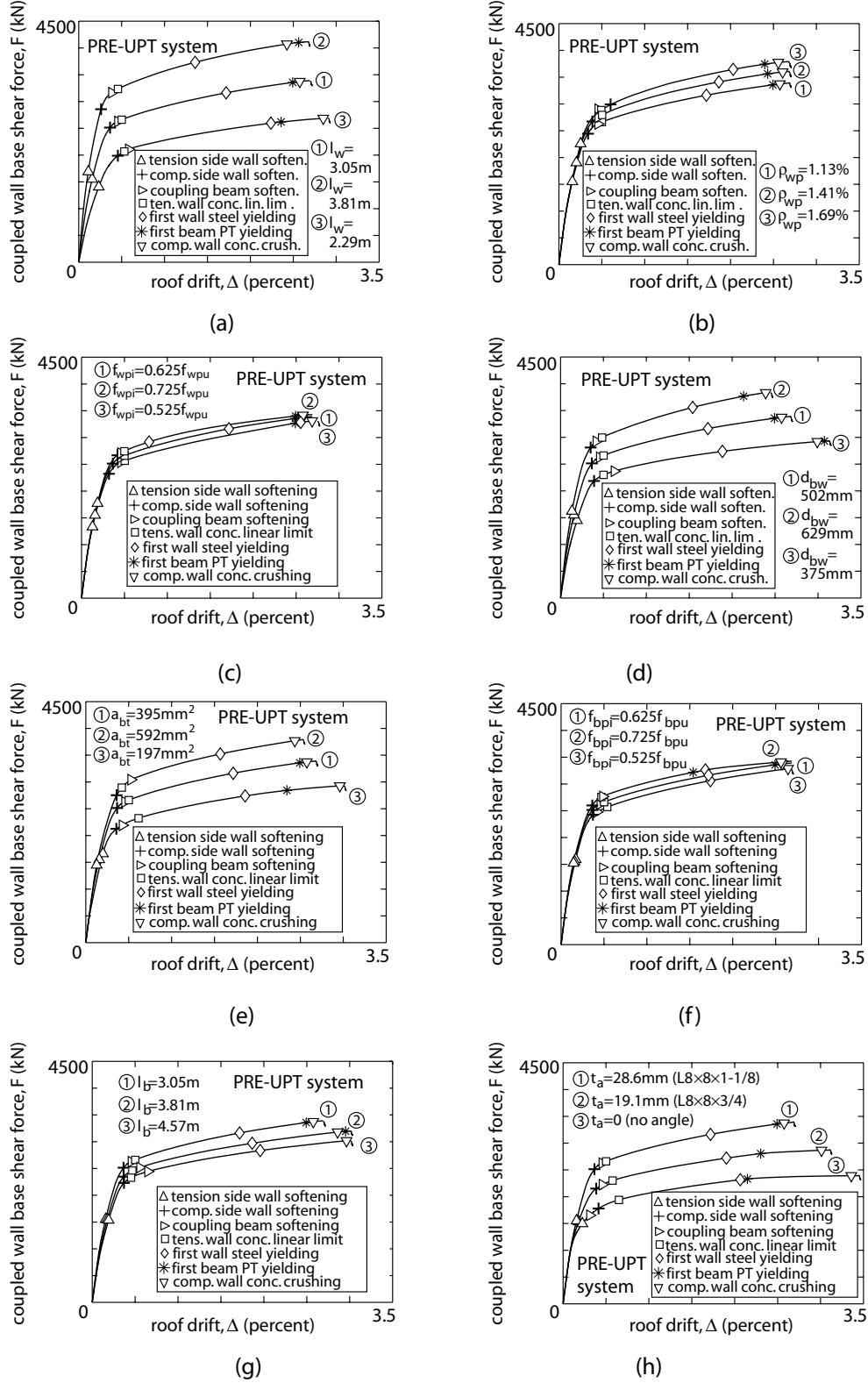


Fig. 7.28 Base shear versus roof drift behaviors of parametric PRE-UPT systems:
(a) l_w ; (b) ρ_{wp} ; (c) f_{wpi} ; (d) d_{bw} ; (e) a_{bt} ; (f) f_{bpi} ; (g) l_b ; (h) t_a

TABLE 7.5

DEGREE OF COUPLING OF PARAMETRIC PRE-UPT SYSTEMS

Parameter Varied	Degree of Coupling, DOC (%)		
	System (1)	System (2)	System (3)
Wall length, l_w	58	54 (0.93)	63 (1.09)
Wall flexural reinforcement ratio, ρ_{wp}	58	55 (0.95)	52 (0.90)
Initial stress of wall PT bars, f_{wpi}	58	56 (0.97)	60 (1.03)
Beam web depth, d_{bw}	58	62 (1.07)	52 (0.90)
Beam PT tendon area, a_{pt}	58	62 (1.07)	52 (0.90)
Initial stress of beam PT tendons, f_{bpi}	58	60 (1.03)	57 (0.98)
Beam length, l_b	58	55 (0.95)	53 (0.91)
Angle thickness, t_a	58	52 (0.90)	44 (0.76)

Note: numbers in parentheses show DOC values for Systems (2) and (3) divided by DOC value for System (1)

In Table 7.4, the degree of coupling for the cast-in-place concrete wall systems (see Fig. 7.27) ranges between 47%-68%. Similarly, the degree of coupling for the precast concrete wall systems in Fig. 7.28 ranges between 44%-63% (see Table 7.5). In Chapter 13, the behavior of coupled wall systems with lower coupling degrees (DOC=30-35%) will be demonstrated. Since the different parameters in Tables 7.4 and 7.5 are varied by different amounts, it is difficult to directly compare the relative effects of these parametric variations on the degree of coupling. However, the results indicate that the wall length, beam depth, and angle thickness have larger influences on the coupling degree than the other parameters investigated. The beam length, beam post-tensioning steel area, wall flexural reinforcement area, and initial stresses in the beam and wall post-tensioning steel have smaller effects, and the wall thickness has the smallest effect on the degree of coupling. The results for the systems with cast-in-place concrete and precast concrete walls are similar.

7.4.3 Coupling Beam Axial Forces

As described previously using Figs. 7.14a and 7.26, a significant portion of the total initial post-tensioning force, P_{bi} at the 2nd floor level is not transferred into the 2nd floor coupling beam as a result of the fixed base conditions assumed for the walls. This effect quickly diminishes above the 2nd floor level. In order to investigate this behavior further, Tables 7.6 and 7.7 show the 2nd floor beam initial axial force, N_{bi} divided by total initial post-tensioning force P_{bi} for the parametric coupled wall structures in Tables 7.2 and 7.3. It is clear that among the parameters investigated, the wall length has the largest influence on the amount of initial axial force transferred into the 2nd floor coupling beam, since it results in the largest effect on the lateral stiffness of the left and right side wall piers.

TABLE 7.6

SECOND FLOOR BEAM INITIAL AXIAL FORCE DIVIDED BY TOTAL INITIAL
PT FORCE IN PARAMETRIC CIP-UPT SYSTEMS

Parameter Varied	N_{bi} / P_{bi}		
	System (1)	System (2)	System (3)
Wall length, l_w	73%	68%	83%
Wall flexural reinforcement ratio, ρ_{ws}	73%	75%	74%
Wall thickness, t_w	73%	77%	74%
Beam web depth, d_{bw}	73%	76%	74%
Beam PT tendon area, a_{bt}	73%	75%	75%
Initial stress of beam PT tendons, f_{bpi}	73%	75%	75%
Beam length, l_b	73%	73%	71%
Angle thickness, t_a	73%	73%	72%

TABLE 7.7

SECOND FLOOR BEAM INITIAL AXIAL FORCE DIVIDED BY TOTAL INITIAL
PT FORCE IN PARAMETRIC PRE-UPT SYSTEMS

Design Parameter	N_{bi} / P_{bi}		
	System (1)	System (2)	System (3)
Wall length, l_w	76%	69%	84%
Wall flexural reinforcement ratio, ρ_{wp}	76%	76%	76%
Initial stress of wall PT bars, f_{wpi}	76%	76%	76%
Beam web depth, d_{bw}	76%	77%	75%
Beam PT tendon area, a_{bt}	76%	76%	76%
Initial stress of beam PT tendons, f_{bpi}	76%	76%	76%
Beam length, l_b	76%	75%	74%
Angle thickness, t_a	76%	74%	72%

7.5 Chapter Summary

This chapter presents an analytical investigation on the nonlinear lateral load behavior of multi-story unbonded post-tensioned hybrid coupled wall structures. The effects of structural design parameters such as the amount of post-tensioning, beam properties, and wall properties on the behavior of the structures, including the degree of coupling, energy dissipation, and lateral displacement capacity is investigated. Systems with precast concrete walls as well as monolithic cast-in-place reinforced concrete walls are considered. The behavior of post-tensioned coupled wall systems is compared with the behavior of systems with embedded steel coupling beams and systems without coupling. Some of the conclusions based on the analysis results are as follows:

1. Post-tensioned steel beams can provide significant and stable levels of coupling between concrete walls over large nonlinear cyclic deformations, similar to the levels of coupling that can be developed using embedded steel beams. As a result of the use of

unbonded post-tensioning steel and the opening of gaps at the beam-to-wall interfaces, little damage is expected to occur in the coupling beams and in the regions of the walls near the beams.

2. As a coupled wall structure is displaced laterally, the axial forces in the compression-side wall increase and the axial forces in the tension-side wall decrease due to the coupling beam forces. This can lead to tension forces in the tension-side wall and large compressive and shear forces in the compression-side wall. Thus, large levels of coupling should be avoided in design.

3. The lateral displacements and rotations of the tension-side and compression-side walls in a coupled wall structure under lateral loading are similar.

4. As compared with embedded steel coupling beams, post-tensioned beams can provide a large restoring force to the walls, reducing the residual lateral displacements upon unloading from a nonlinear displacement. This results in a large self-centering capability of the structure.

5. Unbonded post-tensioned hybrid coupled walls dissipate less energy than walls with embedded steel coupling beams. Most of the energy dissipation is provided by the yielding of the top and seat angles used at the beam-to-wall interfaces and the nonlinear behavior of the walls near the base.

6. Unbonded post-tensioned coupled wall structures with cast-in-place reinforced concrete walls have larger inelastic energy dissipation and a somewhat reduced but still large self-centering capability as compared with structures that use post-tensioned precast concrete walls.

7. In order to achieve the same lateral strength, coupled wall structures with unbonded post-tensioned steel coupling beams require beams of larger cross section than walls with embedded steel coupling beams.

8. The lateral strength of unbonded post-tensioned hybrid coupled walls can be controlled by the area of the beam post-tensioning steel, as well as other parameters such as the wall length, beam depth, and thickness of the beam-to-wall connection angles. The yielding of the post-tensioning steel can be controlled by the initial stress in the steel, and can be significantly delayed due to the use of unbonded tendons.

9. The degree of coupling remains relatively constant as a coupled wall structure is displaced laterally into the nonlinear range.

10. A significant portion of the total initial force in the 2nd floor coupling beam post-tensioning tendons is not transferred into the 2nd floor coupling beam as a result of the fixed base conditions assumed for the walls. The initial axial forces in the upper level coupling beams are close to the total initial post-tensioning forces, indicating that the effect of the foundation/wall stiffness quickly diminishes above the base. The wall pier length has the largest influence on the amount of initial post-tensioning force transferred into the 2nd floor beam, since it results in the largest effect on the lateral stiffness of the wall piers.

11. Upon lateral displacements of the structure, the fixed foundation conditions restrain the opening of gaps at the ends of the 2nd floor coupling beam, resulting in the development of additional axial forces in the beam as the walls displace.

12. During large nonlinear cyclic lateral displacements of an unbonded post-tensioned hybrid coupled wall system, the 2nd floor coupling beam can lose most of its

initial precompression even if the total force in the post-tensioning tendons remains close to the initial force. This behavior is not observed in the upper level coupling beams, which maintain most of their initial axial force levels.

13. The initial axial forces that develop in the coupling beams are not affected by the sequence of post-tensioning over the height of the structure.

CHAPTER 8

IDEALIZED COUPLED WALL LATERAL LOAD-DISPLACEMENT RELATIONSHIPS

This chapter presents idealized base shear force versus roof drift relationships for unbonded post-tensioned hybrid coupled wall structures under monotonic lateral loading. Procedures are developed to estimate the structure behavior using basic principles of equilibrium, compatibility, and constitutive relationships. These procedures are used later in the dissertation as design tools for unbonded post-tensioned hybrid coupled wall structures. The chapter is divided into the following sections: (1) linear-elastic behavior; (2) systems with cast-in-place concrete walls; (3) systems with precast concrete walls; and (4) verification of idealized relationships.

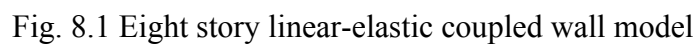
8.1 Linear-Elastic Behavior

For design purposes, the linear-elastic behavior of a multi-story unbonded post-tensioned hybrid coupled wall structure under lateral loads can be determined using a linear-elastic structural analysis program [e.g., SAP2000 (CSI 1999)]. The cross-sectional properties and boundary conditions of the model can be determined from the multi-story coupled wall fiber element model in Fig. 6.5 and from the subassembly linear-elastic model in Fig. 5.1. Note that in the linear-elastic range of behavior, the effects of the beam and wall post-tensioning tendons and the beam-to-wall connection angles can be ignored.

Gap opening behavior at the beam-to-wall joints and at the precast concrete wall panel joints causes geometric nonlinear effects in the structure, and thus, is not included in the linear-elastic model. As a result, unbonded post-tensioned coupled wall systems with precast concrete walls can be modeled the same as systems with monolithic cast-in-place reinforced concrete walls.

In lieu of considering the local deformations in the wall-contact regions as described in Chapter 5 using the subassemblage model in Fig. 5.1a, a simpler linear-elastic analytical model can be developed as shown in Fig. 8.1 for an eight story structure (see also Fig. 5.1b). The deformations in the wall-contact elements are ignored and rigid zones are used between the ends of the coupling beams and the wall centerlines (similar to the model in Fig. 2.4a). Ignoring the flange cover plates (if any) and including shear deformations, the initial linear-elastic stiffness matrix for the steel coupling beams is given as:

$$[K_{bi}] = \begin{bmatrix} \frac{E_b A_b}{l_b} & 0 & 0 & -\frac{E_b A_b}{l_b} & 0 & 0 \\ 0 & \frac{12E_b I_b}{l_b^3 (1 + 2\alpha_{bg})} & \frac{6E_b I_b}{l_b^2 (1 + 2\alpha_{bg})} & 0 & -\frac{12E_b I_b}{l_b^3 (1 + 2\alpha_{bg})} & \frac{6E_b I_b}{l_b^2 (1 + 2\alpha_{bg})} \\ 0 & \frac{6E_b I_b}{l_b^2 (1 + 2\alpha_{bg})} & \frac{4E_b I_b (1 + \alpha_{bg}/2)}{l_b (1 + 2\alpha_{bg})} & 0 & -\frac{6E_b I_b}{l_b^2 (1 + 2\alpha_{bg})} & \frac{2E_b I_b (1 - \alpha_{bg})}{l_b (1 + 2\alpha_{bg})} \\ -\frac{E_b A_b}{l_b} & 0 & 0 & \frac{E_b A_b}{l_b} & 0 & 0 \\ 0 & -\frac{12E_b I_b}{l_b^3 (1 + 2\alpha_{bg})} & -\frac{6E_b I_b}{l_b^2 (1 + 2\alpha_{bg})} & 0 & \frac{12E_b I_b}{l_b^3 (1 + 2\alpha_{bg})} & -\frac{6E_b I_b}{l_b^2 (1 + 2\alpha_{bg})} \\ 0 & \frac{6E_b I_b}{l_b^2 (1 + 2\alpha_{bg})} & \frac{2E_b I_b (1 - \alpha_{bg})}{l_b (1 + 2\alpha_{bg})} & 0 & -\frac{6E_b I_b}{l_b^2 (1 + 2\alpha_{bg})} & \frac{4E_b I_b (1 + \alpha_{bg}/2)}{l_b (1 + 2\alpha_{bg})} \end{bmatrix} \quad (8.1)$$



where,

$$\alpha_{bg} = \frac{6E_b I_b}{G_b A_{bg} l_b^2} \quad (8.2)$$

with G_b (shear modulus of the coupling beam steel) and A_{bg} (shear area of the coupling beam cross section) given as:

$$G_b = \frac{E_b}{2(1 + \nu_b)} \text{ and } A_{bg} = d_b t_{bw} \quad (8.3)$$

and l_b is the coupling beam span length (as shown in Fig. 8.1), I_b is the moment of inertia, A_b is the gross area, d_b is the depth, and t_{bw} is the web thickness of the coupling beam cross section (ignoring the beam flange cover plates), and ν_b and E_b are the Poisson's ratio and modulus of elasticity of the beam steel, respectively (assumed as $\nu_b=0.3$ and $E_b=199955$ MPa, resulting in $G_b=76907$ MPa).

Similarly, the initial linear-elastic stiffness matrix for the concrete walls is given as:

$$[K_{ci}] = \begin{bmatrix} \frac{E_c A_w}{l_w} & 0 & 0 & -\frac{E_c A_w}{l_w} & 0 & 0 \\ 0 & \frac{12E_c I_w}{l_w^3(1+2\alpha_{wg})} & \frac{6E_c I_w}{l_w^2(1+2\alpha_{wg})} & 0 & -\frac{12E_c I_w}{l_w^3(1+2\alpha_{wg})} & \frac{6E_c I_w}{l_w^2(1+2\alpha_{wg})} \\ 0 & \frac{6E_c I_w}{l_w^2(1+2\alpha_{wg})} & \frac{4E_c I_w(1+\alpha_{wg}/2)}{l_w(1+2\alpha_{wg})} & 0 & -\frac{6E_c I_w}{l_w^2(1+2\alpha_{wg})} & \frac{2E_c I_w(1-\alpha_{wg})}{l_w(1+2\alpha_{wg})} \\ -\frac{E_c A_w}{l_w} & 0 & 0 & \frac{E_c A_w}{l_w} & 0 & 0 \\ 0 & -\frac{12E_c I_w}{l_w^3(1+2\alpha_{wg})} & -\frac{6E_c I_w}{l_w^2(1+2\alpha_{wg})} & 0 & \frac{12E_c I_w}{l_w^3(1+2\alpha_{wg})} & -\frac{6E_c I_w}{l_w^2(1+2\alpha_{wg})} \\ 0 & \frac{6E_c I_w}{l_w^2(1+2\alpha_{wg})} & \frac{2E_c I_w(1-\alpha_{wg})}{l_w(1+2\alpha_{wg})} & 0 & -\frac{6E_c I_w}{l_w^2(1+2\alpha_{wg})} & \frac{4E_c I_w(1+\alpha_{wg}/2)}{l_w(1+2\alpha_{wg})} \end{bmatrix} \quad (8.4)$$

where,

$$\alpha_{wg} = \frac{6E_c I_w}{G_c A_w l_w^2} \quad (8.5)$$

with the shear modulus of the wall concrete, G_c given as:

$$G_c = \frac{E_c}{2(1 + \nu_c)} \quad (8.6)$$

and l_w is the wall length (as shown in Fig. 8.1), I_w is the moment of inertia and A_w is the area of the wall cross section, and ν_c and E_c are the Poisson's ratio and modulus of elasticity for the wall concrete, respectively (assumed as $\nu_c=0.18$ and $E_c=30441$ MPa for $f'_c=41.4$ MPa, resulting in $G_c=12901$ MPa).

A Matlab algorithm (2000) was developed using the beam and wall element stiffness matrices above to conduct linear-elastic structural analyses of multi-story coupled wall structures under lateral loads. The initial linear-elastic lateral stiffness of the structure is defined using the base shear versus roof displacement (F-u) relationship as:

$$K_{wi} = \frac{F}{u} \quad (8.7)$$

For the prototype CIP-UPT and PRE-UPT systems described in Chapter 6, an initial linear-elastic stiffness of $K_{wi}=41$ kN/mm (233 kip/in.) results from the Matlab algorithm, which compares well with the value of $K_{wi}=40$ kN/mm (227 kip/in.) from the DRAIN-2DX fiber element model including the beam cover plates and the wall-contact elements.

8.2 Systems With Cast-In-Place Concrete Walls

The nonlinear base shear force versus roof drift (F - Δ) behavior of an unbonded post-tensioned hybrid coupled wall system with monolithic cast-in-place reinforced concrete walls is idealized using a bilinear relationship. As an example, Fig. 8.2 shows the bilinear F - Δ relationship estimated for the prototype CIP-UPT system in Chapter 6. The idealized base shear versus roof drift relationship is identified by the coupled wall softening state (at F_{ws} , Δ_{ws}) and the coupled wall ultimate state (at F_{wu} , Δ_{wu}). A procedure to estimate F_{ws} , Δ_{ws} , F_{wu} , and Δ_{wu} is developed below using basic principles of equilibrium, compatibility, and constitutive relationships. This estimation procedure can be used as a tool in the seismic analysis and design of coupled wall structural systems, without the need to develop nonlinear fiber element models.

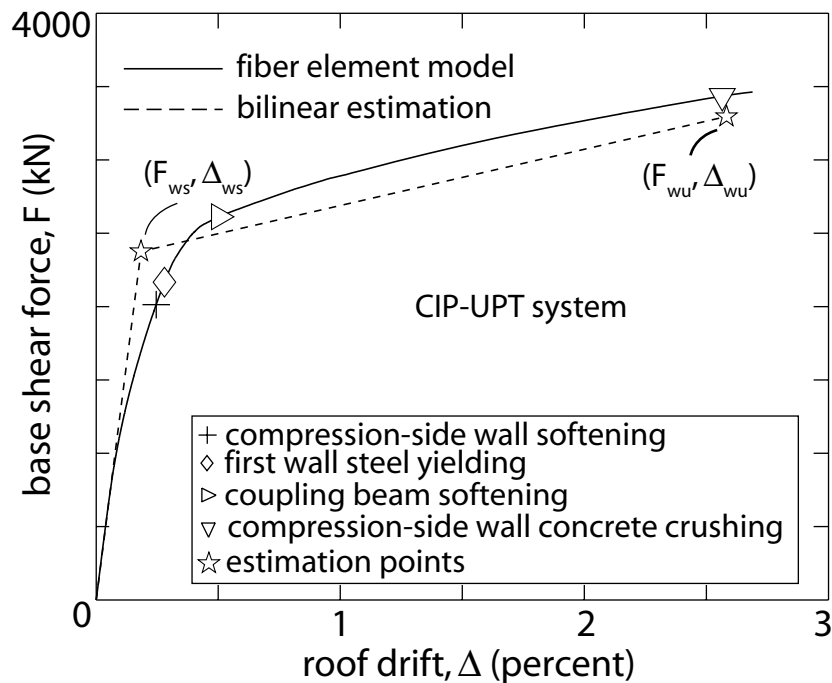


Fig. 8.2 Idealized base shear force versus roof drift relationship for prototype CIP-UPT system

8.2.1 Coupled Wall Softening State

The coupled wall softening state is defined as the state corresponding to a significant reduction in the lateral stiffness of the coupled wall system. For a system with cast-in-place concrete walls, the base shear force F_{ws} and roof drift Δ_{ws} at this state are estimated using an iterative procedure with the following assumptions:

(1) The coupling beams are at the beam softening state and the coupling shear force corresponding to the beam softening state, $V_{b,sof}$, can be estimated as described in Chapter 5. This assumption is justified, on average, based on the \triangleright marker in Fig. 7.2a.

(2) The strain distributions at the bases of the walls are linear.

(3) The concrete compressive stresses at the bases of the walls have linear distributions.

(4) The neutral axis at the base of the compression-side wall (i.e., right side wall for lateral loads applied from left to right) is located at the centerline of the wall (i.e., $c_{cws}=0.5l_w$). The $+$ marker in Fig. 7.2a shows that this assumption is reasonable.

(5) The strain and stress in the extreme flexural reinforcement of the tension-side wall is equal to the yield strain ϵ_{wsy} and stress f_{wsy} , respectively. The \diamond marker in Fig. 7.2a shows that this assumption is reasonable.

As an example, Fig. 8.3a shows a free body diagram to determine the wall softening state for the prototype CIP-UPT system described in Chapter 6. Note that the axial forces and moments developed at the beam ends are not shown in the free body diagram. The steps used in the estimation of F_{ws} and Δ_{ws} are presented below:

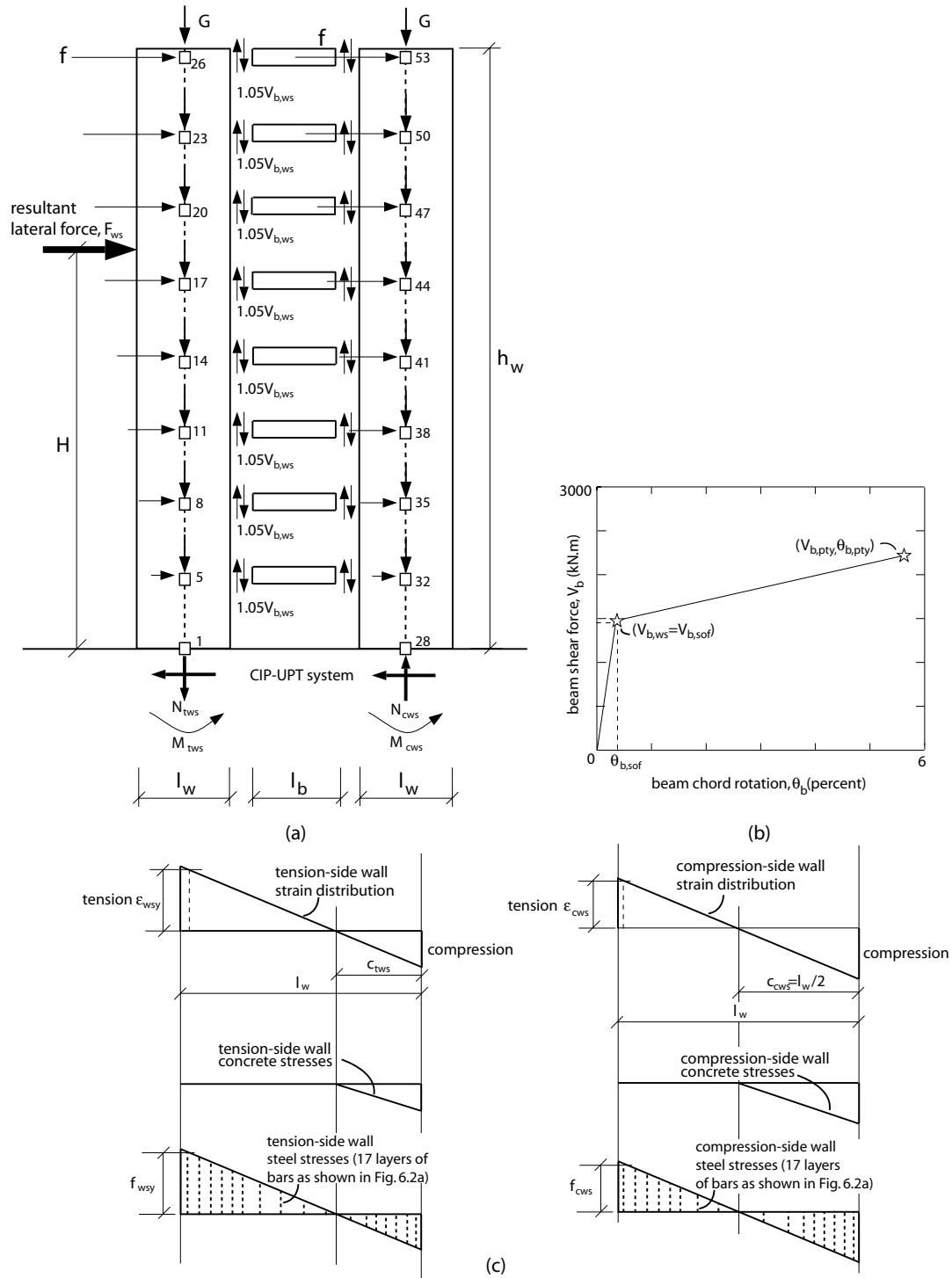


Fig. 8.3 Coupled wall softening state for systems with cast-in-place concrete walls:
 (a) free body diagram; (b) coupling beam shear forces;
 (c) strain and stress distributions at wall bases

Step 1

Estimate the axial forces at the bases of the tension-side and compression-side walls, N_{tws} and N_{cws} , respectively, as:

$$N_{tws} = \sum G - 1.05 \sum V_{b,ws} \quad (8.8a)$$

$$N_{cws} = \sum G + 1.05 \sum V_{b,ws} \quad (8.8b)$$

where, G represents the gravity loads applied at the floor and roof levels and $V_{b,ws}$ represents the shear forces in the coupling beams (see Fig. 8.3a). Based on Assumption (1), the coupling beam shear forces can be calculated as $V_{b,ws}=V_{b,sof}$ (see Fig. 8.3b) corresponding to the beam softening state for an isolated coupled wall subassemblage from Chapter 5 [see Equation (5.10)].

Note that under monotonic lateral loading, the coupling beam shear forces that develop in the lower stories of a multi-story structure are typically larger than the beam shear force estimated using an isolated subassemblage. This is because of the additional axial forces that develop in the lower story beams as shown in Fig. 7.14. The 1.05 factor in Equations (8.8a) and (8.8b) represents this effect, on an average and approximate sense, for the beams used in a multi-story coupled wall system. This factor is discussed further in Chapter 14.

Step 2

Select initial values for the neutral axis depth at the base of the tension-side wall, c_{tws} and the strain in the extreme flexural reinforcement of the compression-side wall, $\epsilon_{cws} < \epsilon_{wsy}$ when the coupled wall softening state is reached.

Step 3

Determine the axial strains and stresses in the concrete and flexural steel at the bases of the tension-side and compression-side walls using Assumptions (2)-(5), and the ϵ_{cws} and ϵ_{cws} values selected in Step 2 (see Fig. 8.3c). Ignore the tensile stresses in the concrete.

Step 4

Use the concrete and steel stresses from Step 3 to determine the axial forces at the bases of the tension-side and compression-side walls, N_{tws} and N_{cws} .

Step 5

Repeat Steps 2-4 until a satisfactory agreement between the N_{tws} and N_{cws} values from Steps 1 and 4 is achieved.

Step 6

Use the concrete and steel stresses from Step 3 to determine the moments at the bases of the tension-side and compression-side walls, M_{tws} and M_{cws} , respectively, by taking moments about the wall centerlines.

Step 7

Using the free body diagram in Fig. 8.3a, determine the total moment at the base of the coupled wall system by taking moments about the system centerline as:

$$M_{ws} = M_{tws} + M_{cws} + 1.05(l_w + l_b) \sum V_{b,ws} \quad (8.9)$$

The total coupled wall base shear force can be determined as:

$$F_{ws} = \frac{M_{ws}}{H} \quad (8.10)$$

where, H is the resultant height of the lateral loads applied on the walls.

Step 8

Determine the degree of coupling at the coupled wall softening state (to be used later) as:

$$DOC_{ws} = \frac{1.05(l_w + l_b) \sum V_{b,ws}}{M_{ws}} \quad (8.11)$$

Note that this definition for the degree of coupling [based on Equation (2.2)] is different from the definition used in Chapter 7 based on the lateral load resistances of the coupled and uncoupled wall systems.

Step 9

Determine the coupled wall roof drift at the wall softening state, Δ_{ws} using the initial lateral stiffness, K_{wi} from a linear-elastic analysis of the structure (see Section 8.1) as:

$$\Delta_{ws} = \frac{F_{ws}}{h_w K_{wi}} \quad (8.12)$$

where, h_w is the wall height.

8.2.2 Coupled Wall Ultimate State

The coupled wall ultimate state is defined as the state corresponding to the crushing of the confined concrete at the base of the compression-side wall. For a system with cast-in-place concrete walls, the base shear F_{wu} and roof drift Δ_{wu} at this state are estimated using an iterative procedure with the following assumptions:

(1) The maximum compression strain in the confined concrete at the base of the compression-side wall is equal to the ultimate (i.e., crushing) strain of the confined concrete, ϵ_{ccu} . This assumption is based on the definition of the coupled wall ultimate state above.

(2) The strain distributions at the bases of the walls are linear.

(3) The height of the “plastic hinge,” h_{wp} at the base of the compression-side wall is equal to the confined thickness of the wall, t_{wc} (i.e., the wall thickness enclosed by the centerline of the reinforcing bars or wires used as concrete confinement).

(4) The coupling degree at the coupled wall ultimate state, DOC_{wu} is the same as the coupling degree at the wall softening state, DOC_{ws} . This assumption is justified based on Fig. 7.8.

(5) The rotations and lateral displacements of the tension-side and compression-side walls are the same. This assumption is justified based on Fig. 7.3a.

(6) The moment at the base of the tension-side wall at the coupled wall ultimate state, M_{twu} is the same as the moment at the wall softening state, M_{tws} . Fig. 7.7a shows that this assumption is reasonable.

As an example, Fig. 8.4a shows the assumed strain and stress distributions [based on Assumptions (1)-(2)] at the base of the compression-side wall when the ultimate state

of the prototype CIP-UPT system is reached. The steps used in the estimation of F_{wu} and Δ_{wu} are presented in the following. Note that the differences between the unconfined cover concrete and the confined concrete are ignored (as shown in Fig. 8.4a) in the procedure below. A revised procedure can be developed by considering the crushing of the unconfined cover concrete in the proposed formulation.

Step 1

Select an initial value for the neutral axis depth at the base of the compression-side wall c_{cwu} , when the coupled wall ultimate state is reached. An initial value of $c_{cwu}=c_{cws}=l_w/2$ may be selected.

Step 2

Determine the axial strains and stresses in the concrete and flexural steel at the base of the compression-side wall using Assumptions (1) and (2), and the c_{cwu} value selected in Step 1 (see Fig. 8.4a). Ignore the tensile stresses in the concrete.

Step 3

Use the concrete and steel stresses from Step 2 to determine the axial force at the base of the compression-side wall, N_{cwu} .

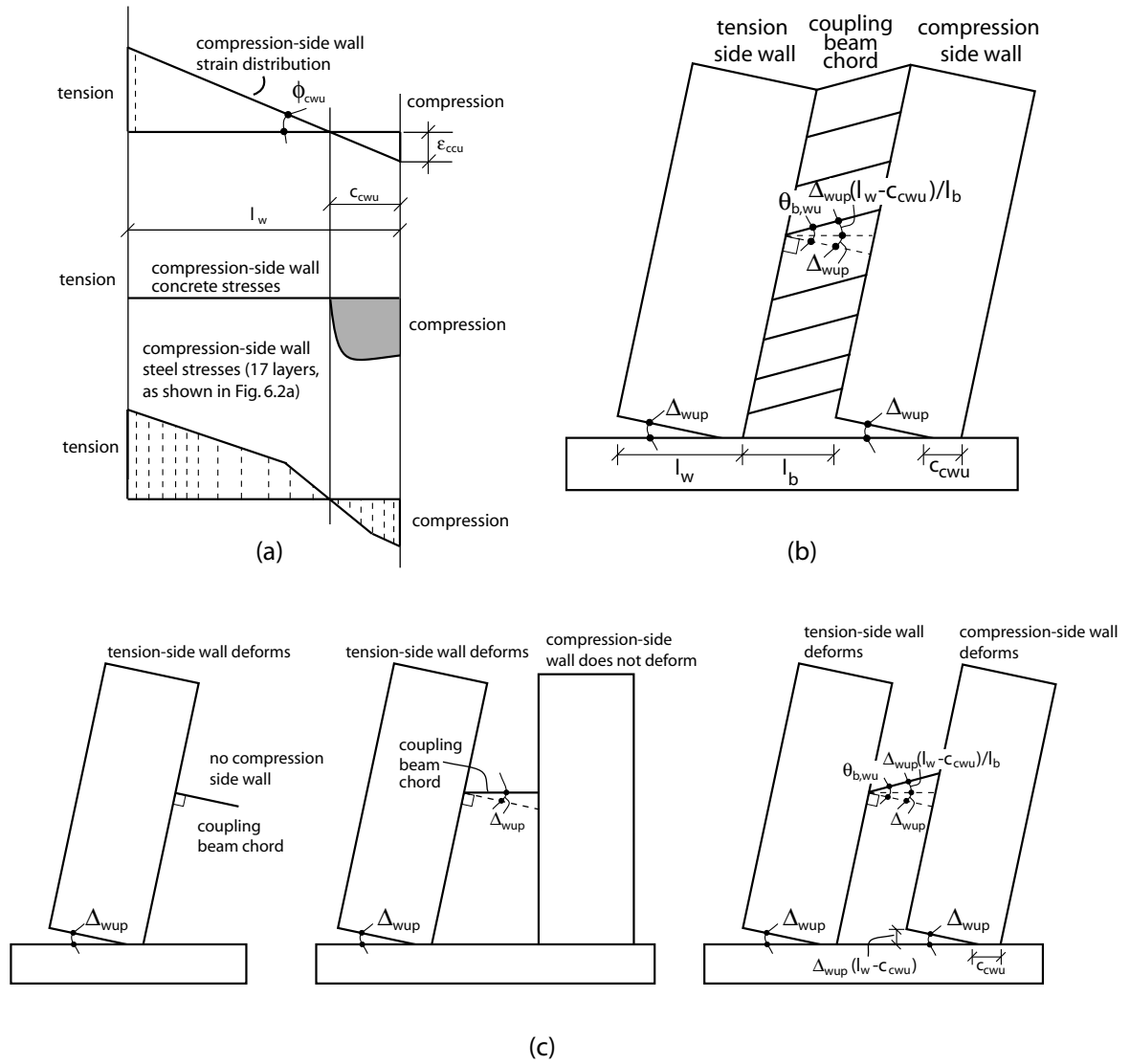


Fig. 8.4 Coupled wall ultimate state for systems with cast-in-place concrete walls: (a) strain and stress distributions at base of compression-side wall; (b) beam chord rotation; (c) components of beam chord rotation

Step 4

Estimate the curvature at the base of the compression-side wall as:

$$\phi_{cwu} = \frac{\epsilon_{ccu}}{c_{cwu}} \quad (8.13)$$

Step 5

Estimate the coupled wall roof drift due to the plastic rotation at the base of the compression-side wall as:

$$\Delta_{wup} = 1.85 \frac{\phi_{cwu} h_{wp}}{DOC_{wu}} \quad (8.14)$$

where, $h_{wp}=t_{wc}$ and $DOC_{wu}=DOC_{ws}$ based on Assumptions (3) and (4), respectively. This equation was determined based on the results obtained from the parametric coupled wall analyses in Chapter 7.

Step 6

Estimate the chord rotation in the coupling beams at the coupled wall ultimate state as:

$$\theta_{b,wu} = \Delta_{wup} \left(1 + \frac{l_w - c_{cwu}}{l_b} \right) \quad (8.15)$$

based on the idealized coupled wall displaced shape in Fig. 8.4b and Assumption (5). Note that the beam chord rotation includes two components; one is Δ_{wup} from Step 5 due to the rotation of the tension-side wall and the other is $\Delta_{wup}(l_w - c_{cwu})/l_b$ due to the rotation of the compression-side wall, as shown in more detail in Fig. 8.4c. The transverse (i.e., vertical) displacements at the ends of the coupling beams supported by the tension-side wall are ignored in the estimation of $\theta_{b,wu}$ in Equation (8.15).

Step 7

Estimate the shear force in the coupling beams $V_{b,wu}$ corresponding to the beam rotation $\theta_{b,wu}$ using the idealized subassembly shear force versus rotation relationship described in Chapter 5 (see Fig. 8.5a).

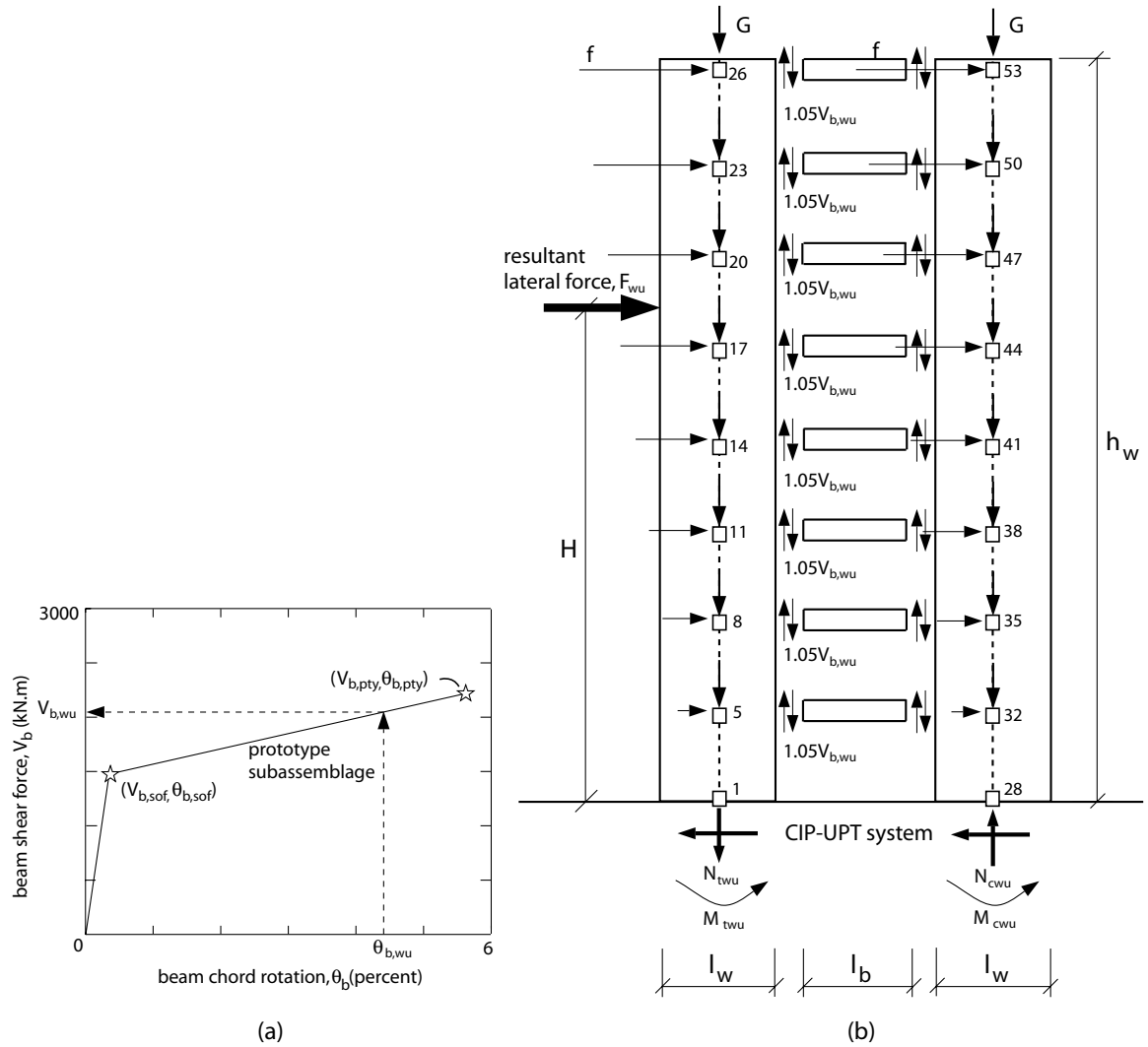


Fig. 8.5 Coupled wall ultimate state for systems with cast-in-place concrete walls:
(a) coupling beam shear forces; (b) free body diagram

Step 8

Determine the total axial force at the base of the compression-side wall as:

$$N_{cwu} = \sum G + 1.05 \sum V_{b,wu} \quad (8.16)$$

based on the free body diagram at the coupled wall ultimate state as shown in Fig. 8.5b. Note that the axial forces and moments developed at the beam ends are not shown in Fig. 8.5b. The 1.05 factor in Equation (8.16) is described in Section 8.2.1 for the coupled wall softening state.

Step 9

Repeat Steps 1-8 until a satisfactory agreement between the N_{cwu} values in Steps 3 and 8 is achieved.

Step 10

Use the concrete and steel stresses from Step 2 to determine the moment at the base of the compression-side wall, M_{cwu} , by taking moments about the centerline of the wall.

Step 11

Using the free body diagram in Fig. 8.5b, determine the total moment at the base of the coupled wall system by taking moments about the system centerline as:

$$M_{wu} = M_{twu} + M_{cwu} + 1.05 (l_w + l_b) \sum V_{b,wu} \quad (8.17)$$

where, $M_{twu} = M_{tws}$ based on Assumption (6).

The total coupled wall base shear force can be determined as:

$$F_{wu} = \frac{M_{wu}}{H} \quad (8.18)$$

where, H is the resultant height of the lateral loads applied on the walls.

Based on the multi-story coupled wall analyses in Chapter 7, second order effects (often referred to as “P-Δ” effects) in the tension-side and compression-side walls have a small influence on the base shear force versus roof drift relationship of the structure, and thus, can be neglected. Note that the second order effects in the coupling beams and the beam post-tensioning tendons are included in the calculation of $V_{b,wu}$ as described in Chapter 5. Note also that a consideration of second order effects is not necessary in the estimation of the coupled wall softening state since the displacements of the structure at the softening state are relatively small.

Step 12

Estimate the coupled wall roof drift as:

$$\Delta_{wu} = \Delta_{wup} + \Delta_{wue} \quad (8.19)$$

where, Δ_{wup} is from Step 5 and Δ_{wue} is the linear-elastic roof drift determined as:

$$\Delta_{wue} = \frac{F_{wu}}{h_w K_{wi}} \quad (8.20)$$

with the initial lateral stiffness of the coupled wall system K_{wi} determined from a linear-elastic analysis of the structure as described in Section 8.1.

8.3 Systems With Precast Concrete Walls

The nonlinear base shear force versus roof drift (F - Δ) behavior of an unbonded post-tensioned hybrid coupled wall system with precast concrete walls is idealized using a trilinear relationship. As an example, Fig. 8.6 shows the trilinear F - Δ relationship estimated for the prototype PRE-UPT system in Chapter 6. The idealized base shear versus roof drift relationship is identified by the coupled wall softening state (at F_{ws} , Δ_{ws}), the wall PT-yielding state (at F_{wy} , Δ_{wy}), and the coupled wall ultimate state (at F_{wu} , Δ_{wu}). A procedure to estimate F_{ws} , Δ_{ws} , F_{wy} , Δ_{wy} , F_{wu} , and Δ_{wu} is developed below using basic principles of equilibrium, compatibility, and constitutive relationships. This estimation procedure can be used as a tool in the seismic analysis and design of coupled wall structural systems, without the need to develop nonlinear fiber element models.

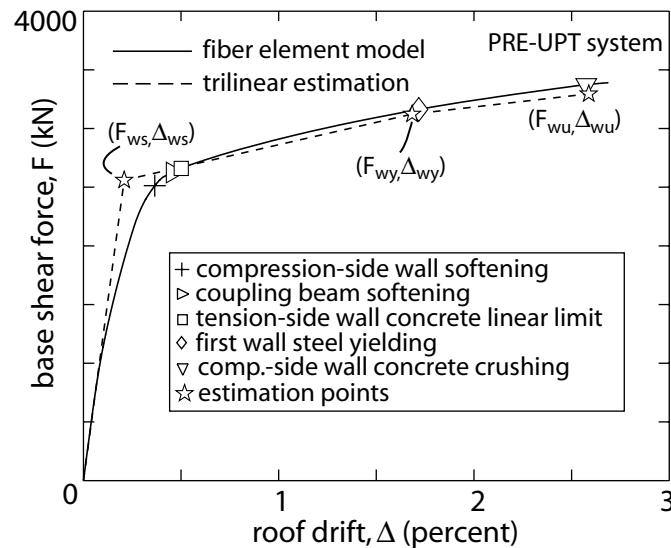


Fig. 8.6 Idealized base shear force versus roof drift relationship for prototype PRE-UPT system

8.3.1 Coupled Wall Softening State

The coupled wall softening state is defined as the state corresponding to a significant reduction in the lateral stiffness of the coupled wall system. For a system with precast concrete walls, the base shear F_{ws} and roof drift Δ_{ws} at this state are estimated using the following assumptions:

(1) Assumptions (1)-(4) from the estimation of the coupled wall softening state for a system with cast-in-place concrete walls, described in Section 8.2.1, are also valid for a system with precast concrete walls. Assumptions (1) and (4) are justified based on the \triangleright and $+$ markers in Fig. 7.2b, respectively.

(2) The stresses in the wall post-tensioning bars are equal to the initial stress f_{wpi} . This assumption is justified based on Fig. 7.4b.

(3) The maximum confined concrete compression stress at the base of the tension-side wall is equal to the linear limit stress of the confined concrete, f_{cl} . This assumption is justified based on the \square marker in Fig. 7.2b.

As an example, Fig. 8.7a shows a free body diagram to determine the coupled wall softening state for the prototype PRE-UPT system described in Chapter 6. Note that the axial forces and moments developed at the beam ends are not shown in the free body diagram. The assumed concrete stress and strain distributions for the tension-side and compression-side walls are shown in Fig. 8.7b. The steps used in the estimation of F_{ws} and Δ_{ws} are presented below:

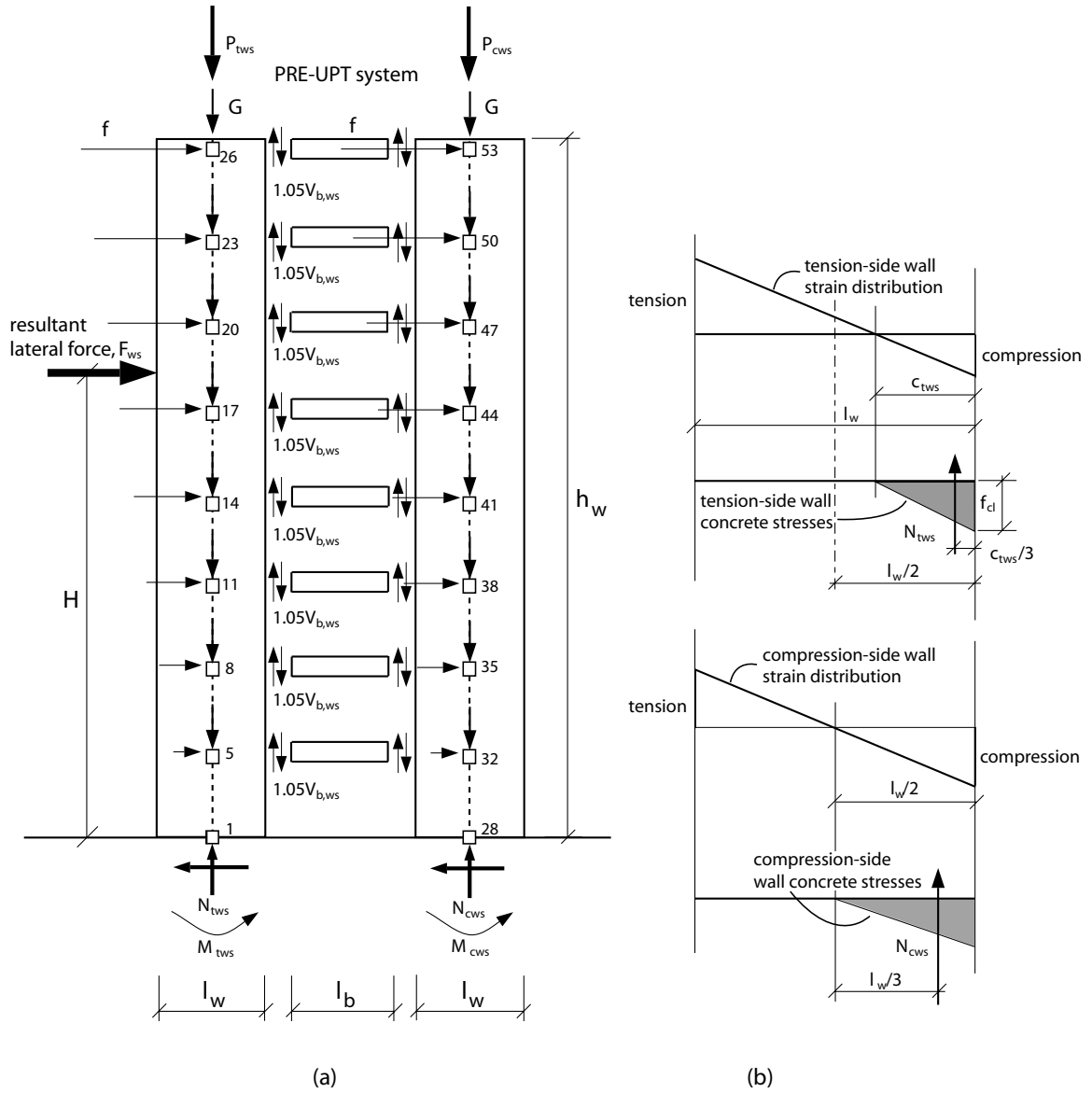


Fig. 8.7 Coupled wall softening state for systems with precast concrete walls:
(a) free body diagram; (b) concrete strain and stress distributions at wall bases

Step 1

Determine the axial forces at the bases of the tension-side and compression-side walls, N_{tws} and N_{cws} , respectively, as:

$$N_{tws} = \sum G - 1.05 \sum V_{b,ws} + P_{tws} \quad (8.21)$$

$$N_{cws} = \sum G + 1.05 \sum V_{b,ws} + P_{cws} \quad (8.22)$$

where, G represents the gravity loads applied at the floor and roof levels, $P_{tws}=P_{cws}=\sum a_{wp}f_{wpi}$ is the total initial post-tensioning force in each wall (a_{wp} is the area of a post-tensioning bar), and $V_{b,ws}$ represents the shear forces in the coupling beams (see Fig. 8.7a). The coupling beam shear forces are calculated as $V_{b,ws}=V_{b,sof}$ (see Fig. 8.3b) corresponding to the beam softening state for an isolated coupled wall subassemblage from Chapter 5 [see Equation (5.10)]. The 1.05 factor in Equations (8.21) and (8.22) is described in Section 8.2.1.

Step 2

Determine the neutral axis (i.e., contact) depth at the base of the tension-side wall (i.e., the depth over which the wall is in contact with the foundation) as:

$$c_{tws} = \frac{2N_{tws}}{f_{cl}t_w} \quad (8.23)$$

For the parametric walls in Chapter 7, $f_{cl}=0.5f_{cc}$ is assumed, where f_{cc} is the maximum compressive strength of the confined concrete.

Step 3

From Fig. 8.7b, determine the moments at the bases of the tension-side and compression-side walls by taking moments about the wall centerlines using Equations (8.24) and (8.25), respectively, as:

$$M_{tws} = N_{tws} \left(\frac{l_w}{2} - \frac{c_{tws}}{3} \right) \quad (8.24)$$

$$M_{cws} = N_{cws} \frac{l_w}{3} \quad (8.25)$$

Step 4

Using the free body diagram in Fig. 8.7a, determine the total moment at the base of the coupled wall system by taking moments about the system centerline as:

$$M_{ws} = M_{tws} + M_{cws} + 1.05(l_w + l_b) \sum V_{b,ws} \quad (8.26)$$

The total coupled wall base shear force can be determined as:

$$F_{ws} = \frac{M_{ws}}{H} \quad (8.27)$$

where, H is the resultant height of the lateral loads applied on the walls.

Step 5

Estimate the coupled wall roof drift at the wall softening state, Δ_{ws} using the initial lateral stiffness, K_{wi} from a linear-elastic analysis of the structure (see Section 8.1) as:

$$\Delta_{ws} = \frac{F_{ws}}{h_w K_{wi}} \quad (8.28)$$

where, h_w is the wall height.

8.3.2 Coupled Wall PT-Yielding State

The coupled wall PT-yielding state for a system with precast concrete walls is defined as the state when the first wall pier post-tensioning bar yields. The base shear F_{wy}

and roof drift Δ_{wy} at this state are estimated using an iterative procedure with the following assumptions:

(1) The maximum stress in the wall pier post-tensioning bars is equal to the yield stress, f_{wpy} (corresponding to the linear limit strain of the post-tensioning steel, see Chapter 6). This assumption is based on the definition of the coupled wall PT yielding state above.

(2) The stresses in the wall pier post-tensioning bars located within the contact depth at the bases of the tension and compression-side walls are equal to the initial stresses, f_{wpi} (i.e., the stresses just before the application of the lateral forces). The results in Fig. 7.4b indicate that this assumption is in general valid.

(3) The rotations and lateral displacements of the tension-side and compression-side walls are the same. This assumption is justified based on Fig. 7.3b.

The steps used in the estimation of F_{wy} and Δ_{wy} are presented in the following. Note that the differences between the unconfined cover concrete and the confined cover concrete are ignored in the procedure below. A revised procedure can be developed by considering the crushing of the unconfined cover concrete in the proposed formulation.

Step 1

Estimate the elongation (due to the lateral displacements of the walls) of the wall pier post-tensioning bar that yields (usually the extreme bar on the tension side of the structure) as:

$$u_{wpy} = \frac{(f_{wpy} - f_{wpi})l_{wpu}}{E_{wp}} \quad (8.29)$$

where, $l_{wpu}=h_w$ is the unbonded length and E_{wp} is the Young's modulus of the wall pier post-tensioning bars.

Step 2

Select initial values for the neutral axis (i.e., contact) depths at the bases of the tension-side and compression-side walls, c_{twy} and c_{cwy} , respectively, when the coupled wall PT-yield state is reached. Initial values of $c_{twy}=c_{tws}$ and $c_{cwy}=c_{cws}=l_w/2$ may be selected.

Step 3

Estimate the coupled wall roof drift at the coupled wall PT-yielding state as:

$$\Delta_{wy} = \frac{u_{wpy}}{d_{wp1} - c_{twy}} \quad (8.30)$$

where, d_{wp1} is the distance of the first post-tensioning bar that yields from the compression corner of the tension-side wall as shown in Fig. 8.8a and u_{wpy} and c_{twy} are from Steps 1 and 2, respectively.

Step 4

Based on the idealized coupled wall displaced shape in Fig. 8.8a (see also Figs. 8.4b and 8.4c), estimate the chord rotation in the coupling beams as:

$$\theta_{b,wy} = \Delta_{wy} \left(1 + \frac{l_w - c_{cwy}}{l_b} \right) \quad (8.31)$$

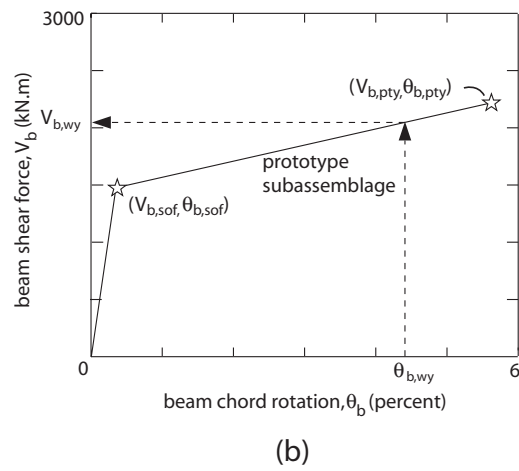
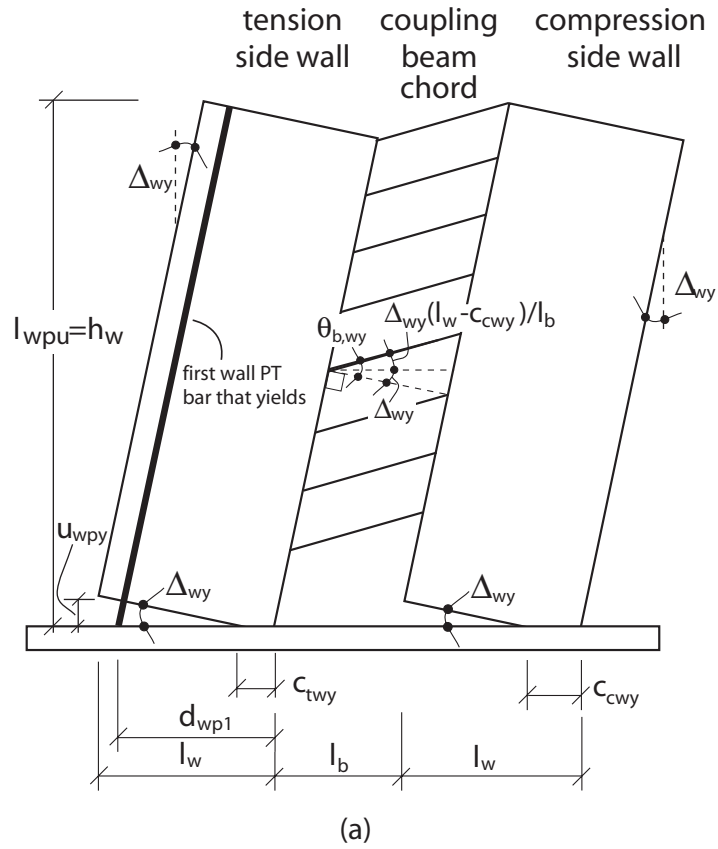


Fig. 8.8 Coupled wall PT-yielding state for systems with precast concrete walls:
 (a) idealized coupled wall displaced shape; (b) beam shear forces

Note that the transverse (i.e., vertical) displacements at the ends of the coupling beams supported by the tension-side wall are ignored in the estimation of $\theta_{b,wy}$ in Equation (8.31).

Step 5

Estimate the shear force in the coupling beams $V_{b,wy}$ corresponding to the beam rotation $\theta_{b,wy}$ using the idealized subassembly shear force versus rotation relationship described in Chapter 5 (see Fig. 8.8b).

The third term on the right hand side of Equation (8.33) for the compression-side wall post-tensioning bars accounts for the shortening of the post-tensioning bars due to the coupling forces transferred to the wall pier at each floor and roof level (see the free body diagram of the coupled wall system at the wall PT-yielding state in Fig. 8.9a). Note that a similar term to account for the elongation of the tension-side wall post-tensioning bars due to the coupling forces is not included in Equation (8.32) in order to determine a conservative (i.e., lower) value for the stresses in the post-tensioning bars.

Step 6

Estimate the stress of each post-tensioning bar in the tension-side and compression-side walls using Equations (8.32) and (8.33), respectively, as:

$$f_{twp} = f_{wpi} + \frac{E_{wp}A_{wy}(d_{wp} - c_{twy})}{l_{wpu}} \quad (8.32)$$

$$f_{cwp} = f_{wpi} + \frac{E_{wp}A_{wy}(d_{wp} - c_{cwy})}{l_{wpu}} - \frac{1.05V_{b,wy}E_{wp}\sum h_b}{l_{wpu}(A_{wc}E_c + A_{wp}E_{wp})} \quad (8.33)$$

where, d_{wp} is the distance of each bar from the compression corner of the wall pier, A_{wc} is the net concrete area of the wall pier cross section, E_c is the Young's modulus of concrete, and $A_{wp} = \sum a_{wp}$ is the total area of the post-tensioning steel in the wall pier cross section. Note that $f_{wpy} \geq f_{twp} \geq f_{wpi}$ and $f_{wpy} > f_{cwp} \geq f_{wpi}$. In Equation (8.33), h_b is equal to the height of each coupling beam from the base of the wall, with the term $\sum h_b$ calculated as the sum of the h_b values for the coupling beams over the height of the structure.

Step 7

Determine the axial forces at the bases of the tension-side and compression-side walls, N_{twy} and N_{cwy} , respectively, as:

$$N_{twy} = \sum G - 1.05 \sum V_{b,wy} + P_{twy} \quad (8.34)$$

$$N_{cwy} = \sum G + 1.05 \sum V_{b,wy} + P_{cwy} \quad (8.35)$$

based on the free body diagram of the coupled wall system at the PT-yielding state as shown in Fig. 8.9a. Note that the axial forces and moments developed at the beam ends are not shown in Fig. 8.9a. In Equations (8.34) and (8.35), $P_{twy} = \sum a_{wp} f_{twp}$ and $P_{cwy} = \sum a_{wp} f_{cwp}$ are the total forces in the post-tensioning bars of each wall pier, G represents the gravity loads applied at the floor and roof levels, and $V_{b,wy}$ represents the shear forces in the coupling beams. The 1.05 factor is described in Section 8.2.1.

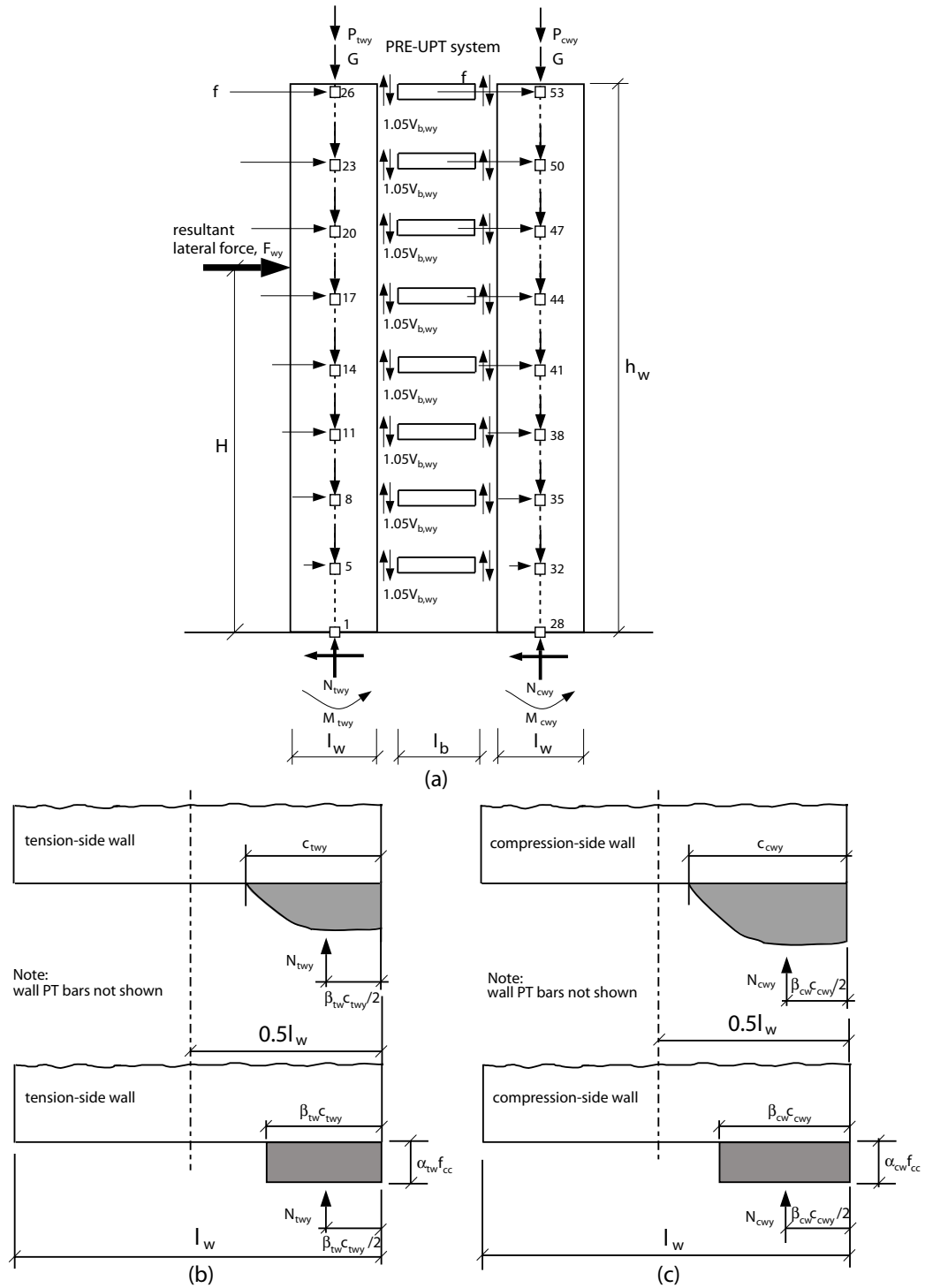


Fig. 8.9 Coupled wall PT-yielding state for systems with precast concrete walls:
 (a) free body diagram; (b) concrete stress distributions at base of tension-side wall;
 (c) concrete stress distributions at base of compression-side wall

Step 8

Estimate the neutral axis depths at the bases of the tension-side and compression-side walls using assumed equivalent rectangular compression stress distributions as:

$$c_{twy} = \frac{N_{twy}}{\alpha_{tw}\beta_{tw}f_{cc}t_{wc}} \quad (8.36)$$

$$c_{cwy} = \frac{N_{cwy}}{\alpha_{cw}\beta_{cw}f_{cc}t_{wc}} \quad (8.37)$$

where, α_{tw} and β_{tw} are confined concrete compression stress block parameters (Mander et al. 1988, Paulay and Priestley 1992) for the tension-side wall, and α_{cw} and β_{cw} are confined concrete compression stress block parameters for the compression-side wall. It is assumed that significant nonlinear behavior (but no crushing) occurs in the confined concrete at the bases of the tension-side and compression-side walls when the coupled wall PT-yielding state is reached. Figs. 8.9b and 8.9c show the smooth compression stress distributions and the assumed equivalent rectangular stress distributions for the tension-side and compression-side walls, respectively. For the parametric coupled wall structures investigated in this chapter, confined concrete compression stress block parameters of $\alpha_{tw}=0.68$, $\beta_{tw}=0.73$, and $\alpha_{cw}=0.87$, $\beta_{cw}=0.83$ were used.

Step 9

Repeat Steps 2-8 using the values of c_{twy} and c_{cwy} from Step 8 in Step 2 until a satisfactory agreement between the c_{twy} and c_{cwy} values from Steps 2 and 8 is achieved.

Step 10

Determine the moments at the bases of the tension-side and compression-side walls, M_{twy} and M_{cwy} , respectively, by taking moments about the wall pier centerlines as:

$$M_{twy} = 0.5N_{twy}(l_w - \beta_{tw}c_{twy}) + \sum[a_{wp}f_{twp}(d_{wp} - 0.5l_w)] \quad (8.38)$$

$$M_{cwy} = 0.5N_{cwy}(l_w - \beta_{cw}c_{cwy}) + \sum[a_{wp}f_{cwp}(d_{wp} - 0.5l_w)] \quad (8.39)$$

where, d_{wp} is the distance of each post-tensioning bar from the compression corner of the wall pier. Note that the wall pier post-tensioning bars are not shown in Figs. 8.9b and 8.9c for clarity.

Step 11

Using the free body diagram in Fig. 8.9a, estimate the total moment at the base of the coupled wall system by taking moments about the system centerline as:

$$M_{wy} = M_{twy} + M_{cwy} + 1.05(l_w + l_b)\sum V_{b,wy} \quad (8.40)$$

The total coupled wall base shear force can be determined as:

$$F_{wy} = \frac{M_{wy}}{H} \quad (8.41)$$

where, H is the resultant height of the lateral loads applied on the walls.

Based on the multi-story coupled wall analyses in Chapter 7, second order effects (often referred to as “P- Δ ” effects) in the tension-side and compression-side walls have a small influence on the base shear force versus roof drift relationship of the structure, and thus, can be neglected. Note that the second order effects in the coupling beams and the beam post-tensioning tendons are included in the calculation of $V_{b,wy}$ as described in Chapter 5. Note also that a consideration of second order effects is not necessary in the

estimation of the coupled wall softening state since the displacements of the structure at the wall softening state are relatively small.

8.3.3 Coupled Wall Ultimate State

The coupled wall ultimate state is defined as the state corresponding to the crushing of the confined concrete at the base of the compression-side wall. For a system with precast concrete walls, the base shear F_{wu} and roof drift Δ_{wu} at this state are estimated using the following assumptions:

(1) Assumptions (1), (2), (3), and (5) from the estimation of the coupled wall ultimate state for systems with cast-in-place concrete walls are also valid for a system with precast concrete walls.

(2) The neutral axis depth at the base of the compression-side wall at the coupled wall ultimate state is the same as the neutral axis depth at the coupled wall PT-yield state (i.e., $c_{wu}=c_{wy}$). This assumption is justified based on Fig. 7.9b.

As an example, Fig. 8.10 shows the assumed strain and stress distributions at the base of the compression-side wall when the ultimate state of the prototype PRE-UPT system is reached. The steps used in the estimation of F_{wu} and Δ_{wu} are presented in the following. Note that the differences between the unconfined cover concrete and the confined concrete are ignored (as shown in Fig. 8.10) in the procedure below. A revised procedure can be developed by considering the crushing of the unconfined cover concrete in the proposed formulation.

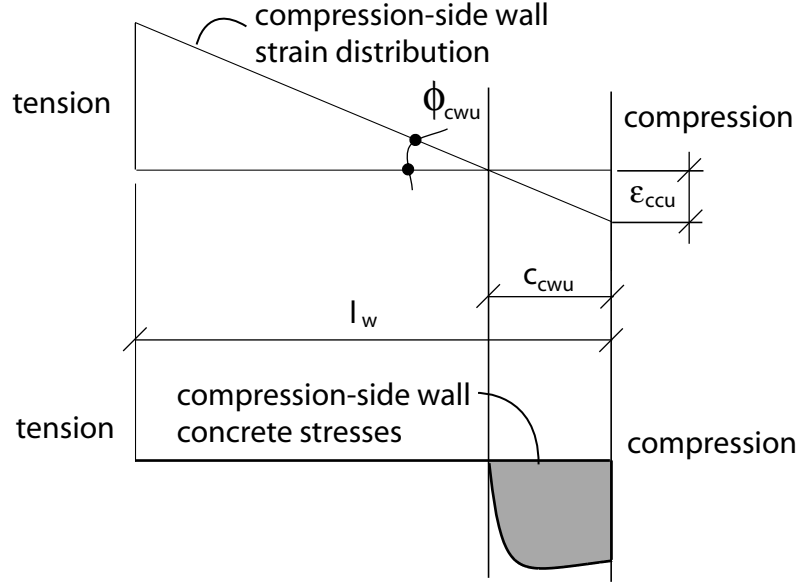


Fig. 8.10 Coupled wall ultimate state for systems with precast concrete walls – strain and stress distributions at base of compression-side wall

Step 1

Estimate the curvature at the base of the compression-side wall as:

$$\phi_{cwu} = \frac{\epsilon_{ccu}}{c_{cwu}} \quad (8.42)$$

Step 2

Estimate the coupled wall roof drift due to gap opening at the base of the compression-side wall as:

$$\Delta_{wug} = 1.5\phi_{cwu}h_{wp} \quad (8.43)$$

where, $h_{wp}=t_{wc}$. This equation was determined based on the results obtained from the parametric coupled wall analyses in Chapter 7.

Step 3

Estimate the coupled wall base shear force at the coupled wall ultimate state as:

$$F_{wu} = F_{wy} + 0.5(\Delta_{wug} - \Delta_{wy}) \frac{F_{wy} - F_{ws}}{\Delta_{wy} - \Delta_{ws}} \quad (8.44)$$

Equation (8.44) assumes that the slope of the idealized base shear force versus roof drift relationship from the coupled wall PT yielding state to the coupled wall ultimate state is one half of the slope from the coupled wall softening state to coupled wall PT yielding state.

Step 4

Estimate the coupled wall roof drift as:

$$\Delta_{wu} = \Delta_{wug} + \Delta_{wue} \quad (8.45)$$

where, Δ_{wug} is from Step 2 and Δ_{wue} is the linear-elastic roof drift determined as:

$$\Delta_{wue} = \frac{F_{wu}}{h_w K_{wi}} \quad (8.46)$$

with the initial lateral stiffness of the coupled wall system K_{wi} determined from a linear-elastic analysis of the structure as described in Section 8.1.

8.4 Verification of Idealized Relationships

The idealized F- Δ relationships described above are verified by comparing the estimated base shear force and roof drift values with values determined using the fiber element model from Chapter 6. A Matlab (2000) algorithm was developed to carry out the estimation procedures. Fig. 8.11 shows the comparisons for F_{ws} and F_{wu} , and Fig. 8.12

shows the comparisons for Δ_{ws} and Δ_{wu} for the parametric coupled wall systems with cast-in-place concrete walls in Fig. 7.27. Similarly, Fig. 8.13 shows the comparisons for F_{ws} , F_{wy} , and F_{wu} , and Fig. 8.14 shows the comparisons for Δ_{ws} , Δ_{wy} , and Δ_{wu} for the parametric coupled wall systems with precast concrete walls in Fig. 7.28.

The F_{wu} and Δ_{wu} values from the fiber element model correspond to the crushing of the confined concrete at the base of the compression-side wall (based on the definition of the wall ultimate state) as indicated by the ∇ markers in Figs. 7.27 and 7.28. Similarly, the F_{wy} and Δ_{wy} values correspond to the initiation of yielding in the wall post-tensioning bars (based on the definition of the wall PT-yielding state) as indicated by the \diamond markers in Fig. 7.28.

The F_{ws} and Δ_{ws} values from the fiber element model correspond to a significant reduction in the lateral stiffness of the coupled wall system. This state was determined based on the assumptions used in the estimation of the coupled wall softening state as follows. For each coupled wall system, the base shear corresponding to three states were determined using the fiber element model. The F_{ws} value was taken as the average of the maximum and minimum base shear forces from these three states. The Δ_{ws} value was taken as the roof drift corresponding to F_{ws} . Figs. 8.15a and 8.15b show the procedure to determine F_{ws} and Δ_{ws} for the prototype CIP-UPT and PRE-UPT systems, respectively.

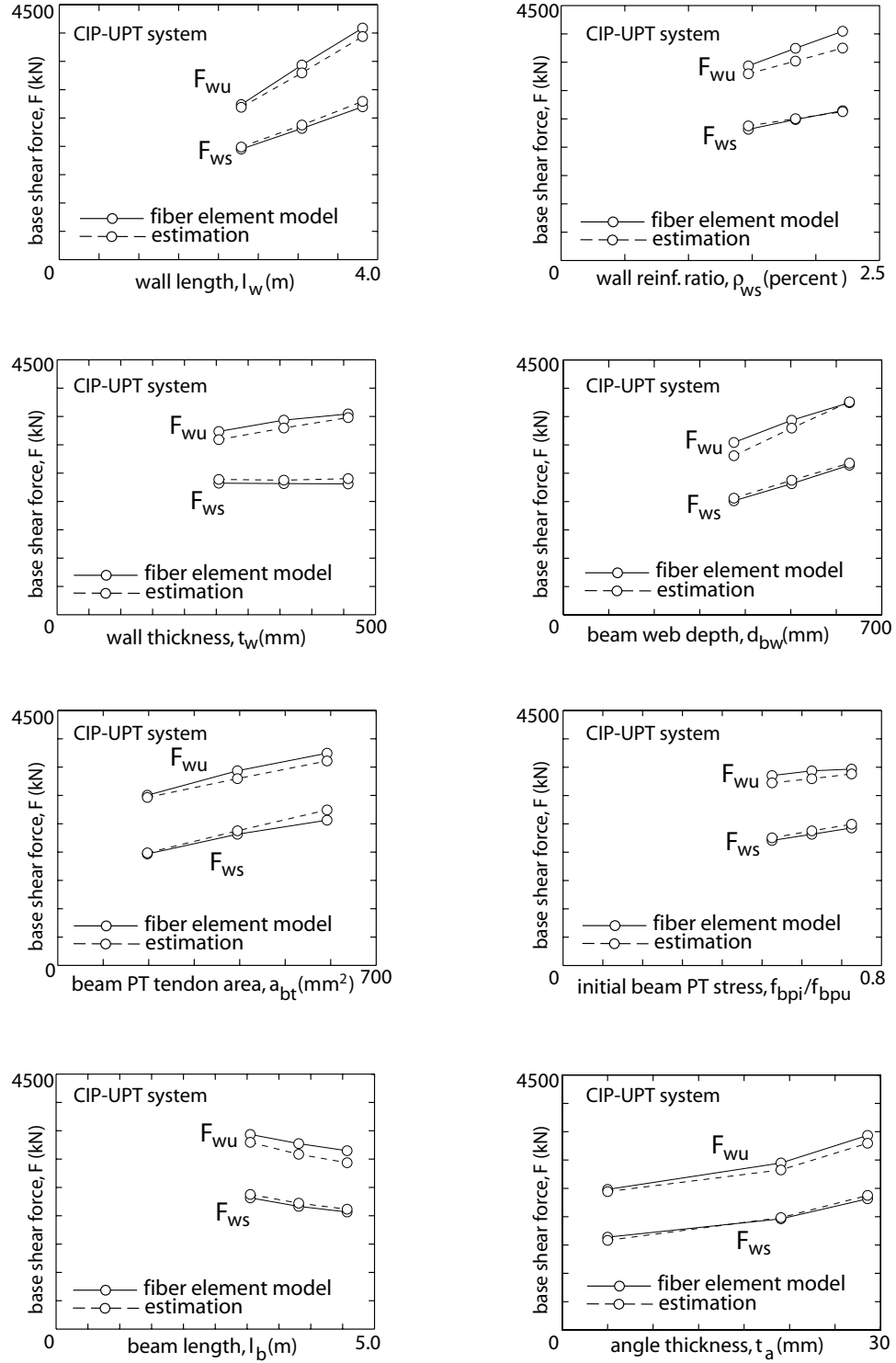


Fig. 8.11 Verification of idealized relationship for systems with cast-in-place walls – F_{ws} and F_{wu}

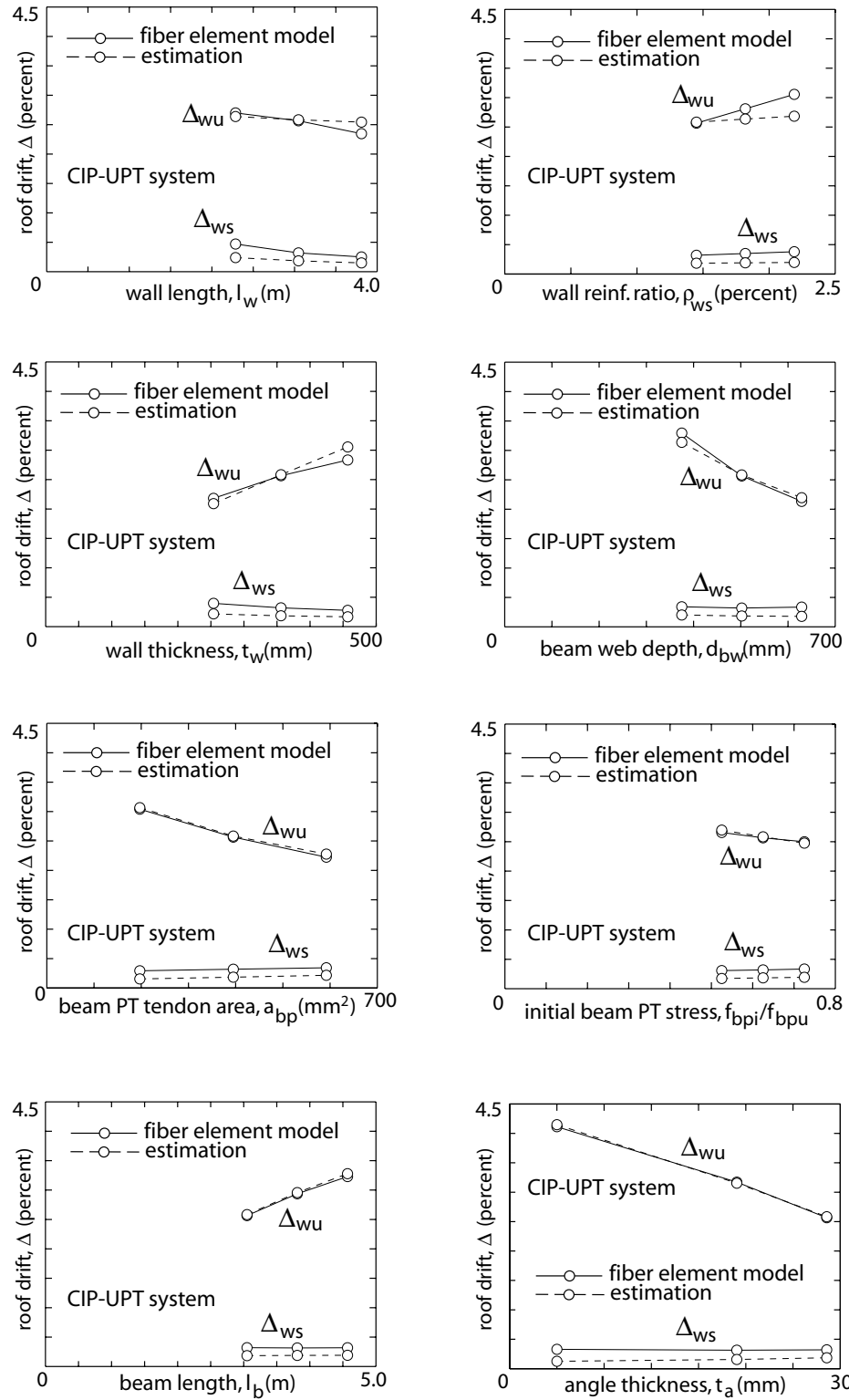


Fig. 8.12 Verification of idealized relationship for systems with cast-in-place walls – Δ_{ws} and Δ_{wu}

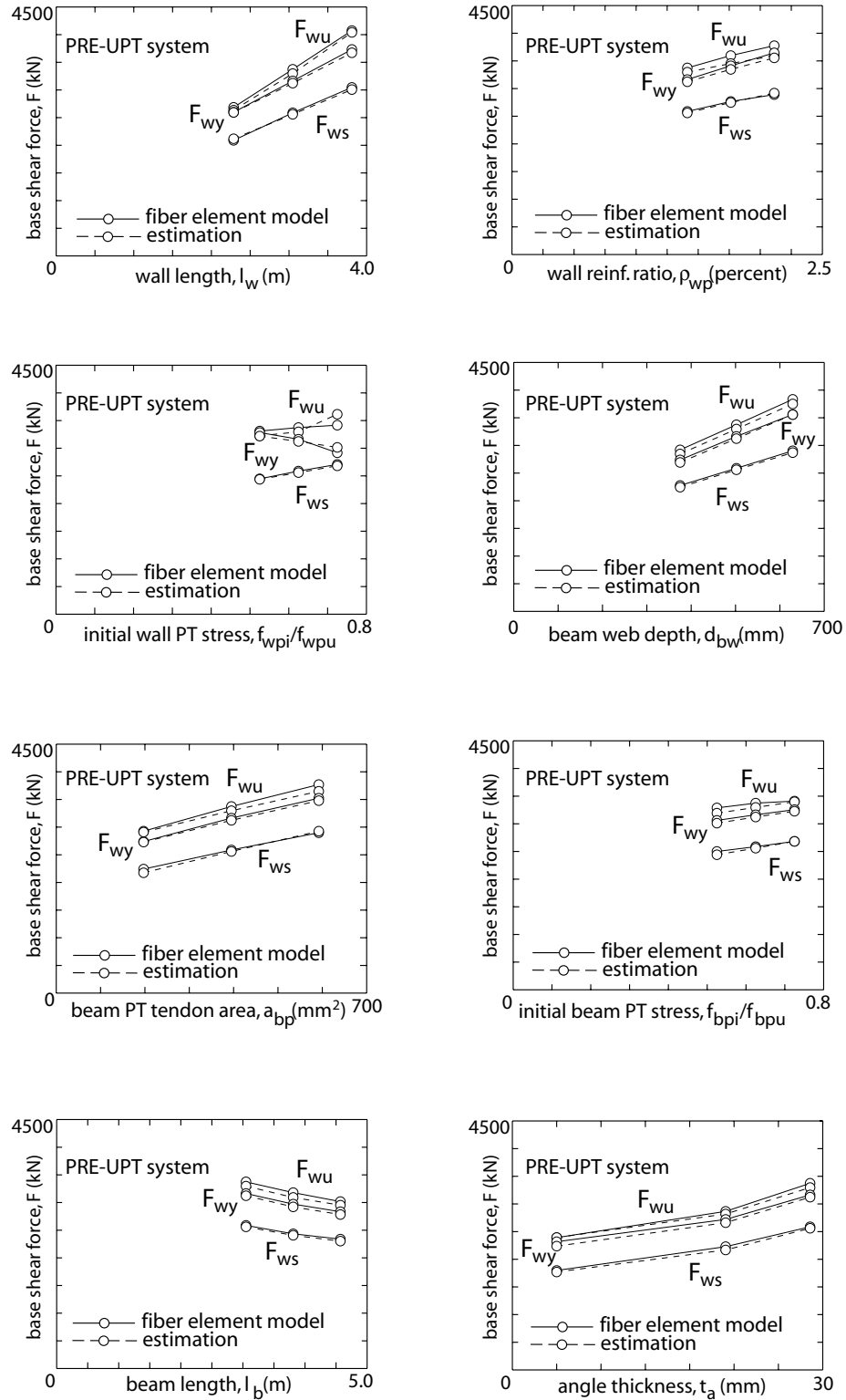


Fig. 8.13 Verification of idealized relationship for systems with precast walls – F_{ws} , F_{wy} , and F_{wu}

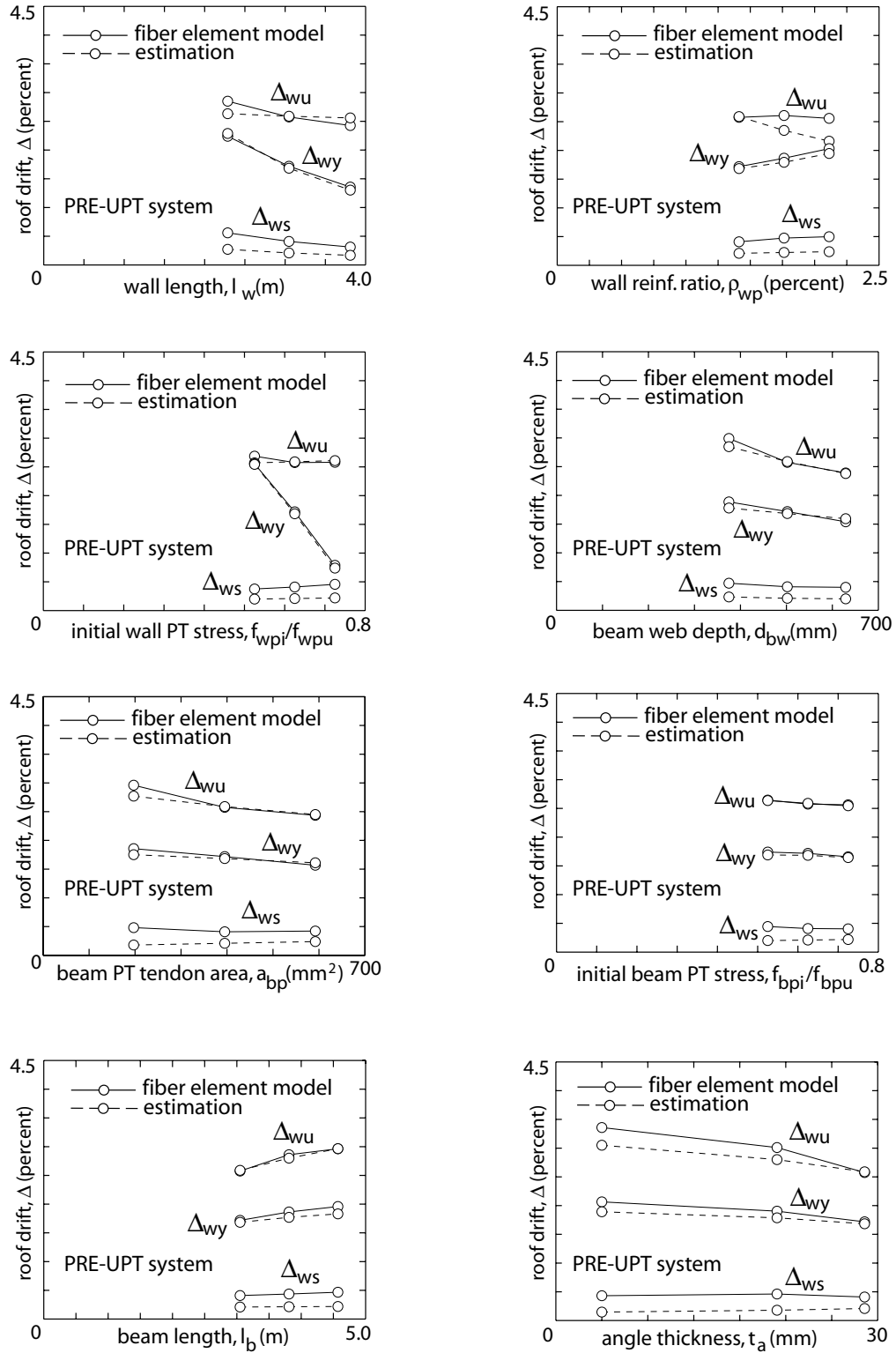
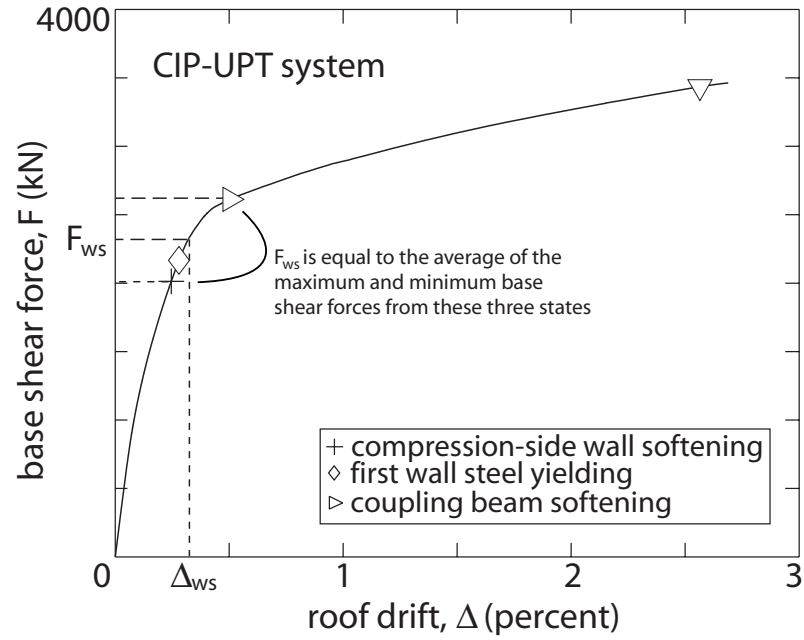
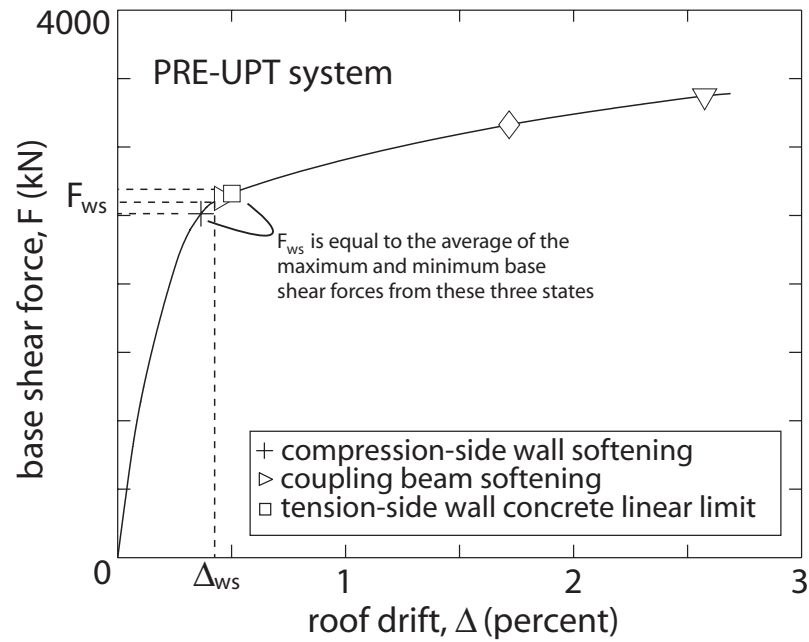


Fig. 8.14 Verification of idealized relationship for systems with precast walls – Δ_{ws} , Δ_{wy} , and Δ_{wu}



(a)



(b)

Fig. 8.15 Determination of coupled wall softening state in fiber element model:
 (a) systems with cast-in-place concrete walls; (b) systems with precast concrete walls

For coupled wall systems with cast-in-place walls, F_{ws} values for the following states were used in accordance with Assumptions (1), (4), and (5) from the estimation of the coupled wall softening state: (1) softening of the compression-side wall, which is reached when the neutral axis at the base of the wall reaches the centerline of the wall (+ marker); (2) first yielding of the wall pier steel, which is reached when the extreme reinforcement in the tension-side wall yields (\diamond marker); and (3) softening of the coupling beams, which is reached when the average coupling beam shear force in the structure (i.e., the sum of the shear forces in the coupling beams divided by the number of beams) is equal to $1.05V_{b,sof}$, where $V_{b,sof}$ is the softening state coupling shear force for an isolated floor-level coupled wall subassembly (see Chapters 4 and 5) and the factor 1.05 is described previously.

For coupled wall systems with precast concrete walls, the first two states are the same as the first and third states listed for systems with cast-in-place walls above. In accordance with Assumption (3) from the estimation of the coupled wall softening state for systems with precast concrete walls, the third state was taken as the state when the maximum confined concrete compression stress at the base of the tension-side wall reaches the linear limit stress of the confined concrete, $f_{cl}=0.5f_{cc}$ (\square marker).

The comparisons in Figs. 8.11 through 8.14 show that the estimated coupled wall base shear force and roof drift values are close to the values determined using the fiber element model for a wide range of parameters. The wall-contact elements and the beam flange cover plates were ignored in the estimation of K_{wi} (using the model in Fig. 8.1). The maximum error in the estimation of K_{wi} is less than 5%, the maximum error in the estimation of M_{ws} , M_{wy} , and M_{wu} is less than 7.5% and the maximum error in the estimation of Δ_{wy} and Δ_{wu} is less than 15%. Thus, it is concluded that the estimation

procedures described above can be used to conduct approximate analyses of unbonded post-tensioned hybrid coupled wall systems with different properties.

These approximate analyses can be used for two purposes: (1) to evaluate the behavior of a given system under lateral loads; and (2) as part of a design approach that requires the estimation of the nonlinear lateral load versus displacement relationship of the structure. Note that while the proposed analysis procedures involve a significant number of steps (some of which are iterative), the calculations can be coded into a computer algorithm, for example using Matlab (2000). This allows for push-over analyses of multi-story coupled wall systems in seismic evaluation/design, without the need to develop a sophisticated analytical model (e.g., the fiber element model). A performance-based seismic design approach using the above estimation procedures is described in Chapters 11 and 12.

8.5 Chapter Summary

This chapter describes analytical procedures to estimate the linear and nonlinear lateral load versus displacement behavior of multi-story unbonded post-tensioned hybrid coupled wall structures by quantifying selected limit states for the walls. The estimation procedures, which are verified with results from the DRAIN-2DX program (Prakash et al. 1993), can be used to conduct approximate analyses of coupled wall systems with cast-in-place reinforced concrete and precast concrete walls as part of a performance-based seismic evaluation and design approach as demonstrated in Chapters 11 and 12.

CHAPTER 9

SUBASSEMBLAGE EXPERIMENTS

This chapter describes the results from eleven half-scale experiments to investigate the nonlinear behavior of unbonded post-tensioned hybrid coupled wall subassemblages. Each test specimen includes a steel coupling beam and the adjacent concrete wall regions at a floor level. The experiments were conducted in the Structural Systems Laboratory at the University of Notre Dame by two other graduate students, Michael A. May and Brad D. Weldon, as part of their research towards a Master of Science Degree in Civil Engineering. A large portion of the material presented in this chapter is based on their work (May et al. 2006).

The chapter is divided into the three main sections: (1) experimental program; (2) results of experiments; and (3) recommendations for application. The results from the experimental investigation described in this chapter are used in the remainder of this dissertation as follows. Chapter 10 provides comparisons between the test results and analytical predictions and makes revisions to the analytical models developed previously in the dissertation. Then, Chapters 11 and 12 propose a design approach to ensure the desirable behavior of the proposed coupling system and describe the design of two prototype coupled wall systems. Finally, Chapters 13 through 15 evaluate the seismic response of the prototype structures based on nonlinear static and nonlinear dynamic analyses under earthquake-induced loads, including a critical evaluation of the proposed design approach.

9.1 Experimental Program

Fig. 9.1 shows a photograph of the half-scale test set-up. Eleven specimens were tested (Tests 1-11) with the following parameters: beam cover plate, beam post-tensioning steel area, angle leg thickness, angle vertical leg gage length, and beam depth. Test 3 was designed to represent a half-scale model of the prototype subassembly described in Chapter 3. The other test specimens were determined based on parameter variations from Test 3 and were not necessarily designed for all of the anticipated forces and deformations. This allowed the experimental program to demonstrate a number of critical failure modes for the proposed system. More details on the test specimens are provided below, with variations between the specimens summarized in Table 9.1.

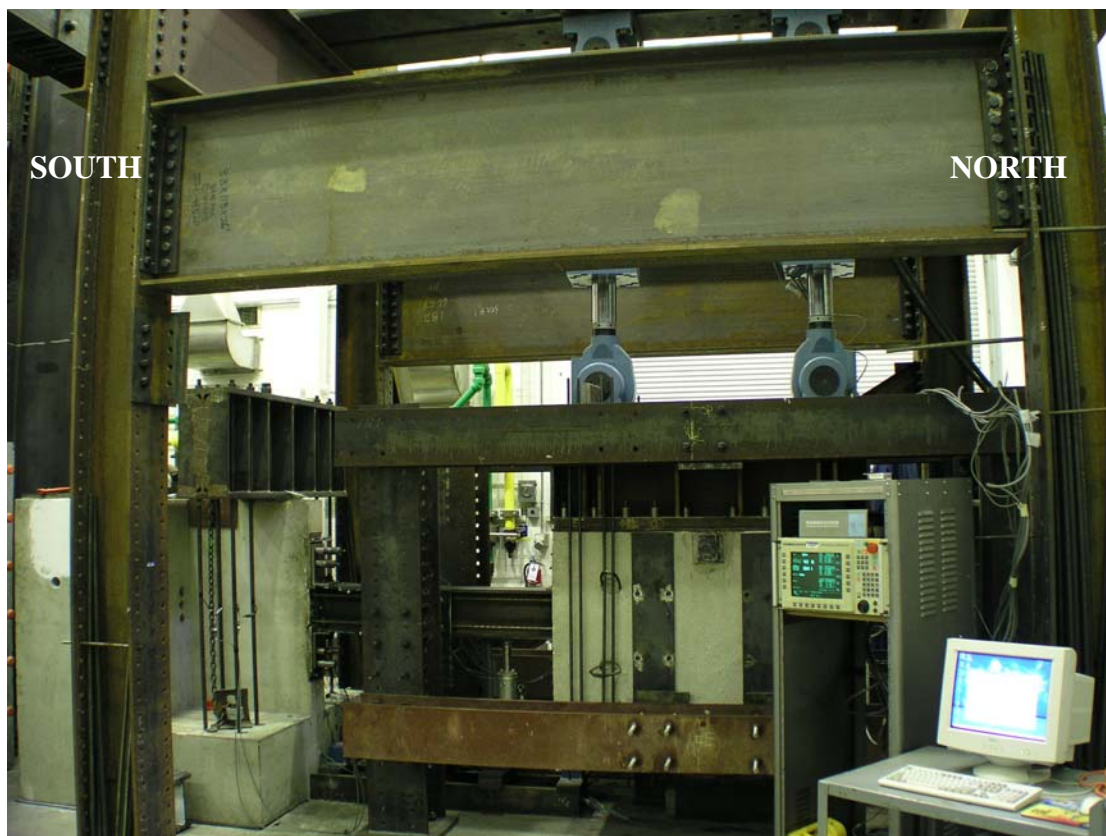


Fig. 9.1 Photograph of test set-up

TABLE 9.1
SUBASSEMBLAGE TEST SPECIMENS

Test No.	Test Date	Loading Type	^a Coupling Beam	Cover plates (mm)	^b Angles	^c l _{gv} (mm)	^d Σa _{bp} (mm ²)	$\frac{e P_{bi}}{P_{bu}}$	$\frac{f P_{bi}}{A_{bfc} f_{by}}$	$\frac{g P_{bm}}{A_{bfc} f_{by}}$	$\frac{h P_{by}}{A_{bfc} f_{bm}}$	Test Parameter
1	3/13/02	Cyclic	W10x68	203x124 x19.1	-	-	560	0.55	0.25	0.37	0.30	No angles
2	3/18/02	Cyclic	W10x68	203x124 x19.1	-	-	560	0.54	0.24	0.38	0.30	Retest beam
3	4/8/02	Cyclic	W10x68	203x124 x19.1	Four L8x4x1/2	95.3	560	0.52	0.23	0.35	0.30	Base test
4	7/18/02	Monot.	W10x68	203x124 x19.1	Two L8x4x1/2	95.3	-	-	-	-	-	Angle test
5	2/12/03	Cyclic	W10x68	-	Four L8x4x1/2	114	560	0.53	0.47	0.70	0.60	No cover plates
6	3/12/03	Monot.	W10x68	-	Two L8x4x1/2	114	-	-	-	-	-	Angle test
7	5/15/03	Cyclic	W10x68	-	Four L8x4x5/8	114	560	0.56	0.50	0.70	0.60	Thicker angles
8	5/29/03	Monot.	W10x68	-	Two L8x4x5/8	114	-	-	-	-	-	Angle test
9	6/5/03	Cyclic	W10x68	-	Four L8x4x5/8	114	840	0.55	0.74	0.96	0.90	Larger PT area
10	11/14/03	Cyclic	W14x99	-	Four L8x4x5/8	138	560	0.52	0.46	0.68	0.60	Larger beam depth
11	11/25/03	Cyclic	W14x99	-	Four L8x4x5/8	138	-	-	-	-	-	Angle test

Notes:

^aU.S. shape. Coupling beam flanges were saw cut to a width of 159 mm to satisfy similitude requirements.

^bU.S. shape.

^cAngle vertical leg gage length measured from center of innermost angle-to-wall connectors to heel of angle.

^dΣa_{bp}=total area of coupling beam post-tensioning steel.

^eP_{bi}=total initial force measured in coupling beam post-tensioning strands; P_{bu} = Σa_{bp}f_{bpu}, where f_{bpu}=design maximum strength of post-tensioning strands (1862 MPa).

^fA_{bfc}=cross section area of one beam flange, A_{bf} plus cover plate, A_c (if any); f_{by}= measured yield strength of coupling beam steel (386 MPa), where, difference between measured yield strengths of beam steel and cover plate steel in Tests 1-3 is ignored.

^gP_{bm}=maximum total force measured in coupling beam post-tensioning strands.

^hP_{by} = Σa_{bp}f_{bpy}, where f_{bpy}=design “yield” strength corresponding to linear limit stress (i.e., limit of proportionality) of beam post-tensioning strand stress-strain relationship (1689 MPa); f_{bm}=measured maximum strength of coupling beam steel (524 MPa), where, difference between measured maximum strengths of beam steel and cover plate steel in Tests 1-3 is ignored.

9.1.1 Test Set-Up

Figs. 9.2a and 9.2b show the side view and end view, respectively, of the test set-up, which includes two reinforced concrete wall regions placed at each end of a steel coupling beam. The left (south) wall region, referred to as the “reaction block,” is fixed to a 1524 mm (60 in.) thick strong floor in the laboratory. The right (north) wall region, referred to as the “loading block,” is connected to two hydraulic actuators hanging from a stiff steel loading frame. The actuators are used in displacement control to move the loading block up or down without rotating it; thus, modeling the idealized displaced shape of the subassembly with respect to the reference line in Fig. 1.3b.

The loading block is free to move in the horizontal (north-south) direction. Out-of-plane displacements are not modeled in the test program. An inner steel bracing frame (see Fig. 9.3, not shown in Fig. 9.2) is used to prevent out-of-plane movement of the loading block at three points, and of the coupling beam at the midspan on each side. At each bracing point, steel bracing plates are adjusted up against corresponding bracing plates on the coupling beam and the loading block. Grease is applied between the matching bracing plates to allow in-plane movements of the beam and the loading block, while out-of-plane displacements are prevented.

Note that the subassembly test set-up in Fig. 9.2 does not model the wall pier shear forces that develop in a multi-story structure, and thus, does not capture the effect of the wall piers on the coupling beam axial forces during the application of post-tensioning as well as the application of lateral loads on the structure. As discussed in

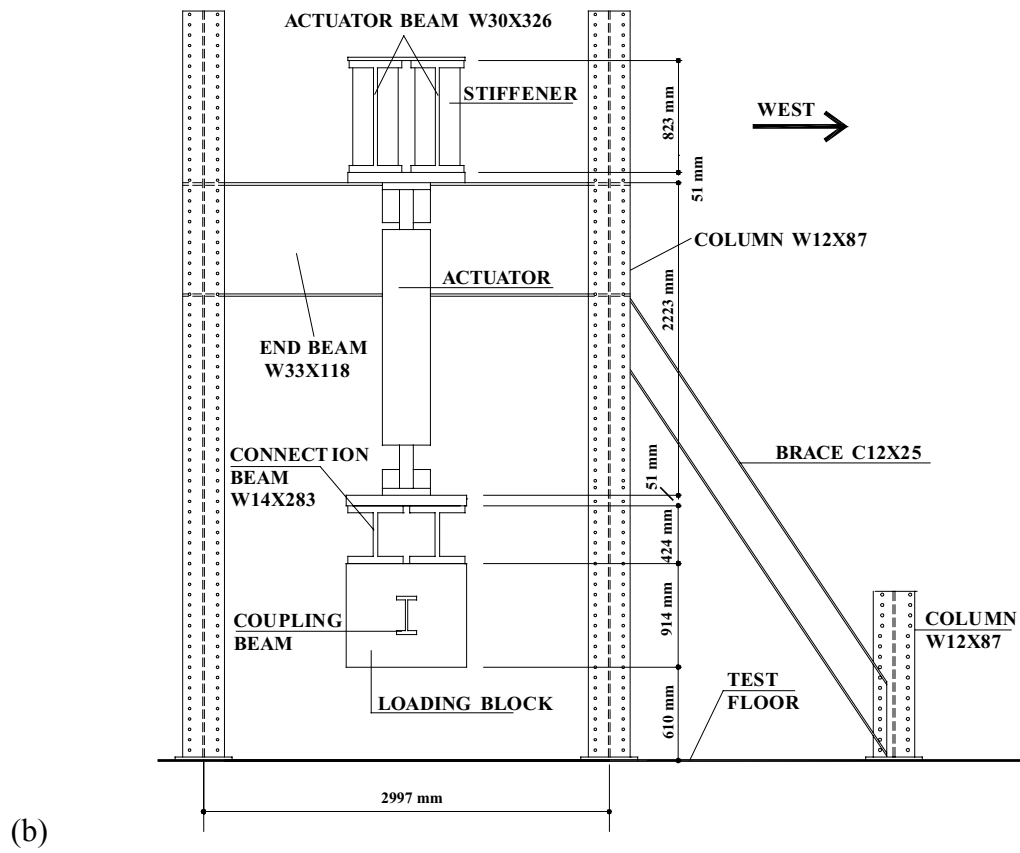
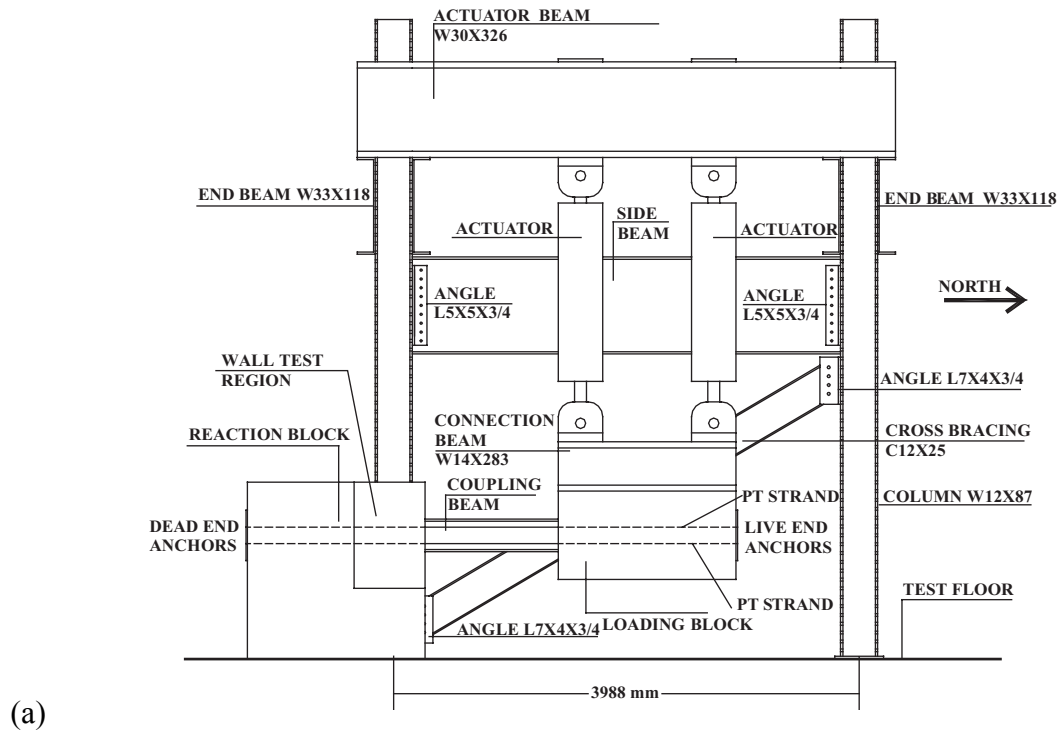


Fig. 9.2 Elevation of experimental set-up: (a) side view; (b) end view

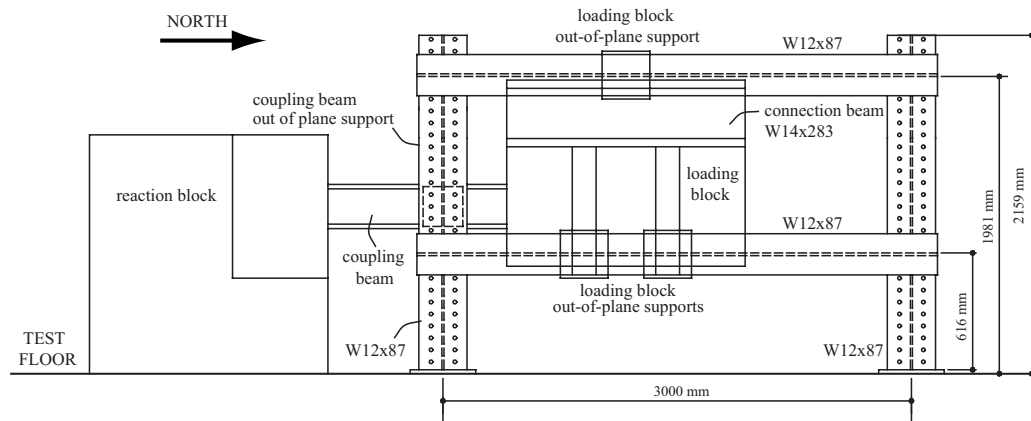


Fig. 9.3 Bracing frame side view

Chapter 7, the effect of the wall piers on the coupling beam axial forces may be significant in the lower floor beams in a multi-story structure; however, they are negligible for the coupling beams in the upper floor and roof levels.

9.1.2 Loading Block and Reaction Block

Fig. 9.4 shows a more detailed view of the test structure. The horizontal lengths of the loading and reaction blocks are equal to $l_w=1524$ mm (60 in.; one half the length of the full-scale prototype wall described in Chapter 3). The loading block is used to transmit the forces from the actuators to the coupling beam and is connected to the actuators via two W14×283 (see Fig. 9.2) steel connection beams bolted to the actuators. The loading block has a uniform width (thickness) of 889 mm (35 in.) along its length (see Fig. 9.5) in order to accommodate the connections to the two actuators and to prevent damage to the block during testing.

A total of twenty-eight 15.2 mm (0.6 in.) diameter post-tensioning strands, each prestressed to approximately 89 kN, are used to secure the loading block to the two

connection beams. The strands run through 25.4 mm (1 in.) diameter vertical ducts in the loading block and are anchored to the bottom flanges of the connection beams (dead end) and to four 1524 mm by 102 mm by 19 mm (60 in. by 4 in. by 3/4 in.) plates embedded to the bottom of the loading block (live end). In addition to the strands, eight high strength steel threaded rods prestressed to approximately 156 kN each, are used near the coupling beam end of the loading block to increase the clamping force between the block and the connection beams.

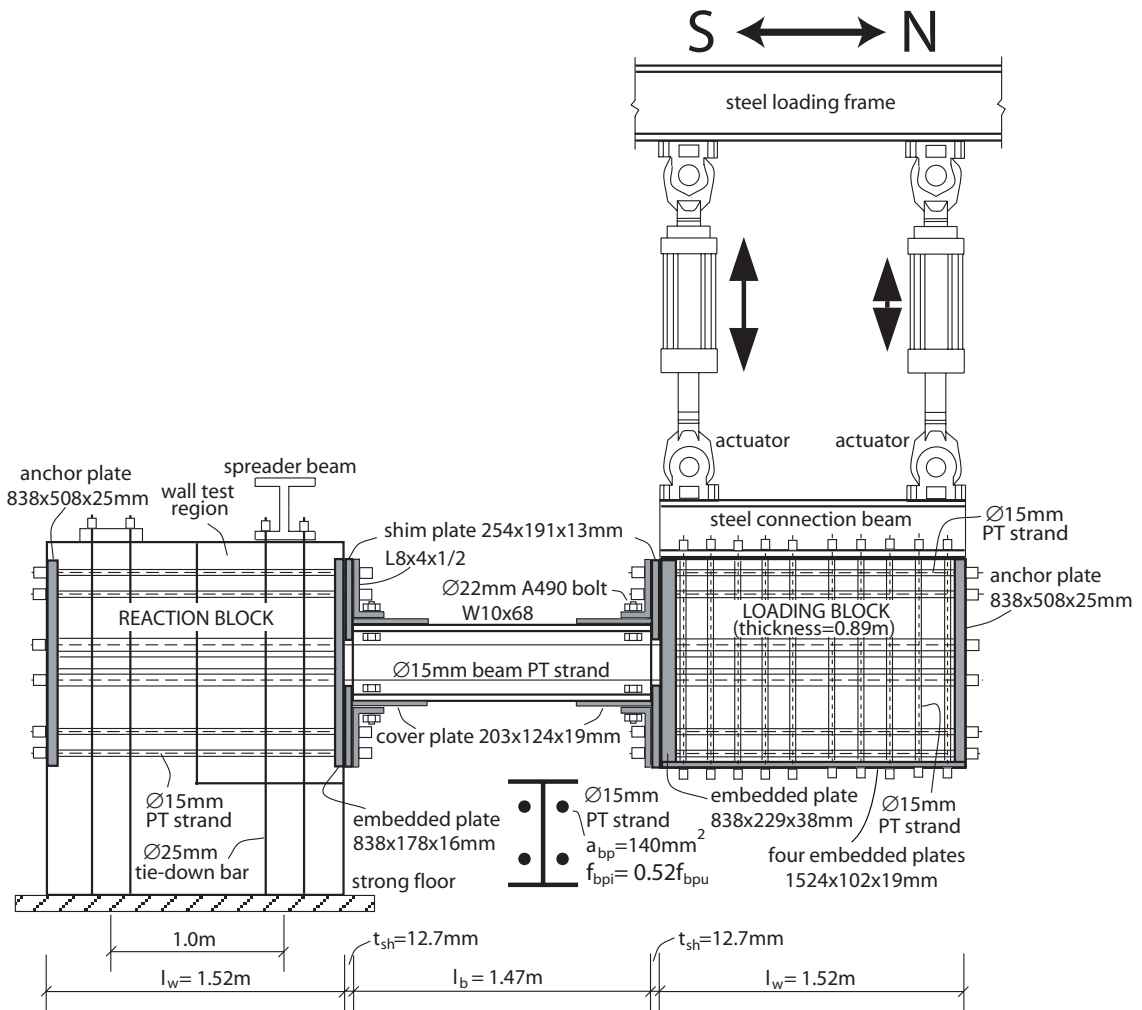


Fig. 9.4 Test structure

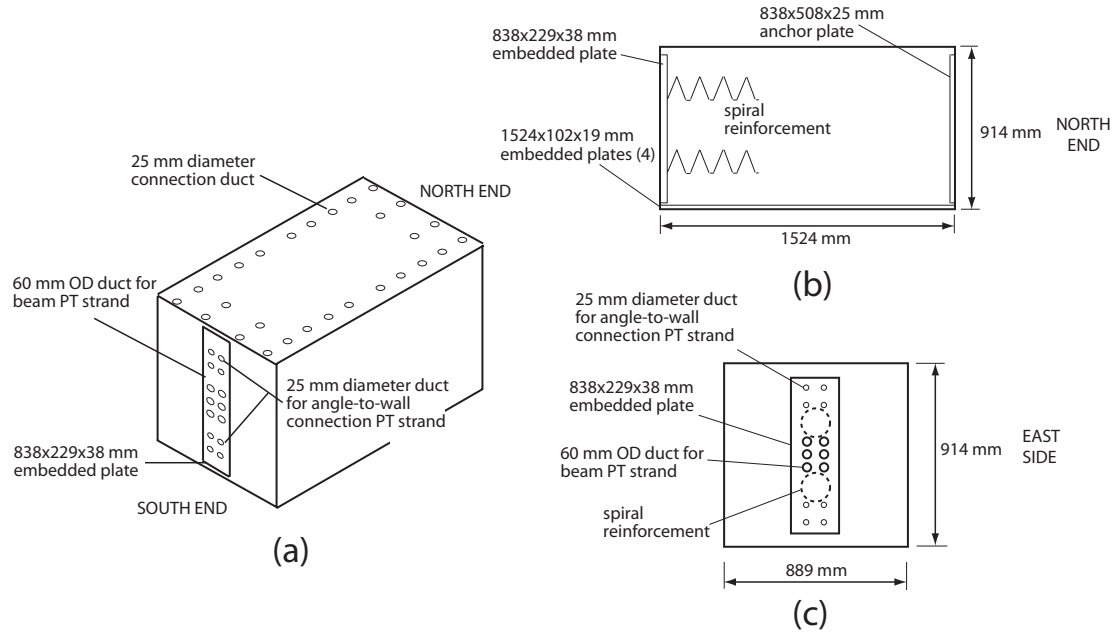


Fig. 9.5 Loading block: (a) 3D view; (b) side view; (c) south end view

Unlike the loading block, the reaction block does not have a uniform thickness (see Fig. 9.6). Adjacent to the coupling beam, the width of the reaction block is 191 mm (7.5 in.), modeling the thickness of the prototype wall in Chapter 3. This region of the reaction block, referred to as the “wall test region,” is 762 mm (30 in.) long and 1219 mm (48 in.) high. Note that half-scale similitude requires a wall thickness of $t_w=178$ mm (7 in.); however, a slightly larger thickness was necessary to accommodate the placement of oversized post-tensioning ducts in the block with adequate concrete cover and reinforcement. The other regions of the reaction block are 1473 mm (58 in.) wide to provide lateral stability to the block and to allow tie down to the laboratory strong floor [at a spacing of 1000 mm (39.4 in.) between four groups of four anchors]. Fig. 9.7 shows a photograph of the steel form used to cast the reaction block.

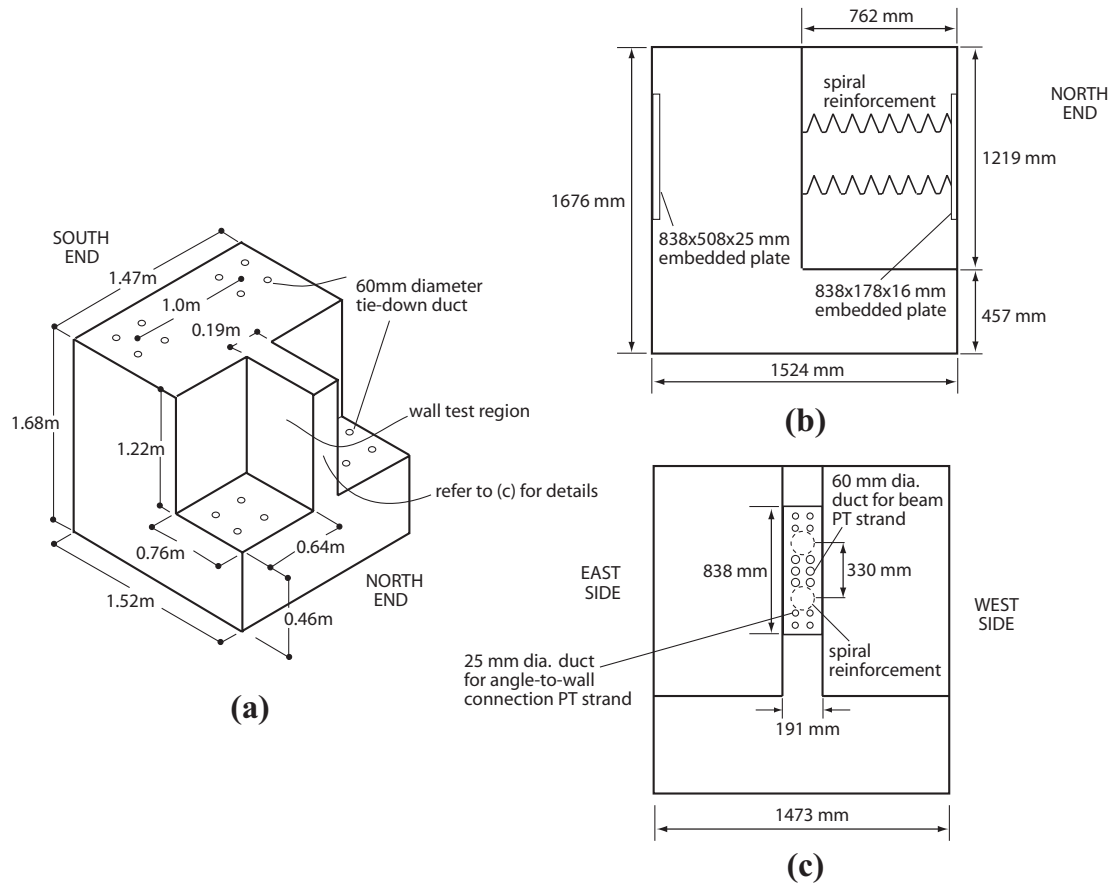


Fig. 9.6. Reaction block: (a) 3D view; (b) side view; (c) north end view



Fig. 9.7 Photograph of steel form for casting of reaction block

9.1.3 Coupling Beams

Steel U.S. wide-flange shapes (Table 9.1) are used for the coupling beams. The beam length is equal to $l_b \approx 1473$ mm (58 in.; one half the full-scale prototype beam length). In order to satisfy half-scale similitude requirements with the prototype beam (with a W21 \times 182 cross-section), the flanges of the test beams were saw cut to a width of $b_{bf} = 159$ mm (6.25 in.; one half the full-scale flange width). Figs. 9.8 and 9.9 show the beam-end-view and beam-side-view, respectively, of the test set-up near the wall test region. The ends of the beams were trimmed (after welding of the flange cover plates, if any) using a saw cutter to achieve even contact surfaces at the beam-to-wall interfaces.

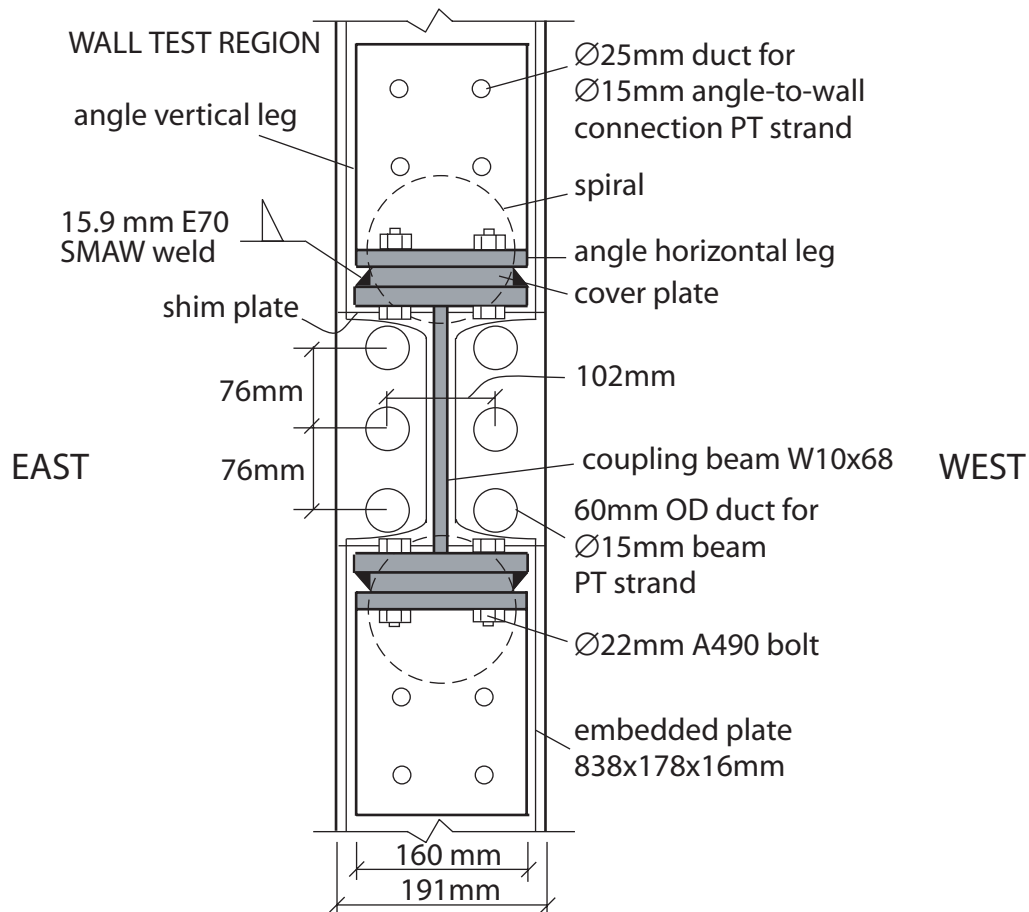


Fig. 9.8 Beam end view

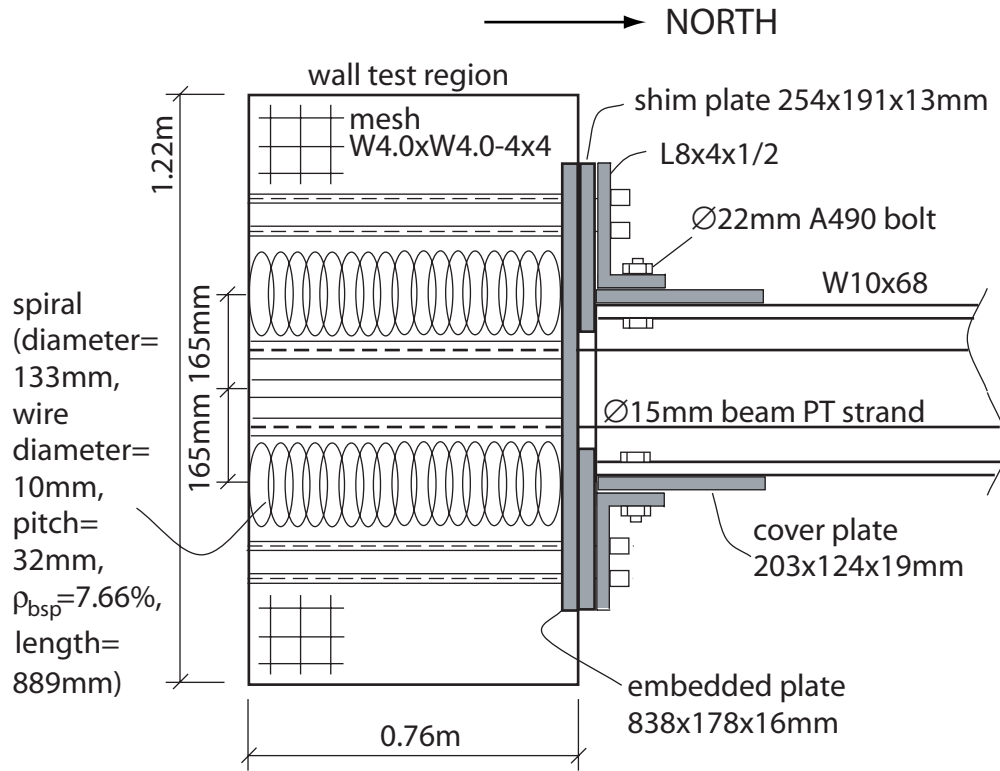


Fig. 9.9 Beam side view

9.1.4 Beam Post-Tensioning Strands

Seven-wire strands, each strand with a nominal diameter of $d_{bp}=15.2$ mm (0.6 in.) and area of $a_{bp}=140$ mm² (0.217 in²), are used to apply the beam post-tensioning force. Six test specimens had two pairs of strands (placed on either side of the coupling beam web as shown in Fig. 9.9), one specimen had three pairs of strands, and four specimens had no post-tensioning strands. The resulting total post-tensioning steel area, $A_{bp}=\Sigma a_{bp}$, in each specimen is given in Table 9.1. Note that the post-tensioning steel area required for similitude with the full-scale prototype beam (see Chapter 3) is equal to 630 mm² (0.977 in²), which is slightly larger than the area provided in Test 3 (560 mm²). Each post-

tensioning strand is run through an oversized Dywidag Spiro[®] duct [with 60.1 mm (2.37 in.) outside diameter] inside the reaction and loading blocks, and is anchored to the far ends of the blocks using steel wedge/barrel anchorage systems (Fig. 9.10). The strands are not bonded to the blocks or connected to the beam between the anchors. Embedded steel anchor plates are used at the far ends of the reaction and loading blocks (see Fig. 9.4) to distribute the forces from the beam post-tensioning tendons. The post-tensioning operation is carried out from the north end of the loading block (live end).

9.1.5 Beam-to-Wall Connection Regions

The beam-to-wall connection regions (see Fig. 9.9) include embedded steel plates, wire mesh reinforcement, and spiral reinforcement inside the loading and reaction blocks; and flange cover plates (in Tests 1-4; see Table 9.1), shim plates, and top and seat angles at the beam ends. Each of these beam-to-wall connection components is described in more detail below. A photograph of the wall test region (adjacent to the beam-to-wall interface) before the casting of the concrete is provided in Fig. 9.11.



Fig. 9.10 Photograph of post-tensioning anchorage system



Fig. 9.11 Photograph of wall test region prior to casting of concrete

Embedded Plates – Embedded steel plates, placed flush with the outside of the reaction and loading blocks during casting (with nominal welded studs), are used to distribute the contact stresses in the concrete. The embedded plate inside the reaction block has a thickness of $t_e = 16.0$ mm (0.625 in.; one half the embedded plate thickness in the full-scale prototype wall) and a width of 178 mm (7 in.). A thicker 38 mm (1.5 in.) plate is used in the loading block to prevent damage to the block during testing.

Spiral Reinforcement – Spiral reinforcement (Fig. 9.12) is used behind the embedded plates to resist and distribute the compression stresses without excessive deformations in the concrete. Two spirals are placed horizontally in each of the reaction and loading blocks, one spiral near each coupling beam flange as shown in Figs. 9.9 and 9.11. The spiral center-to-center diameter $D_{bsp} = 133$ mm (5.25 in.), spiral smooth wire diameter $d_{bsp} = 10$ mm (0.4 in.), and spiral pitch $s_{bsp} = 32$ mm (1.25 in.), resulting in a spiral reinforcement ratio, $\rho_{bsp} = 7.66\%$. Note that this spiral reinforcement ratio is

significantly larger than the value of $\rho_{bsp} = 5.57\%$ used in the prototype subassemblage in Chapter 3. The length of the spiral is 889 mm (35 in.) inside the reaction block and 305 mm (12 in.) inside the loading block. In addition, W4.0×W4.0-4×4 welded wire mesh [with 5.72 mm (0.22 in.) wire diameter] is used on both faces of the 191 mm (7.5 in.) thick wall test region of the reaction block, with a concrete cover of 12.7 mm (0.5 in.) to the center of the wire mesh.

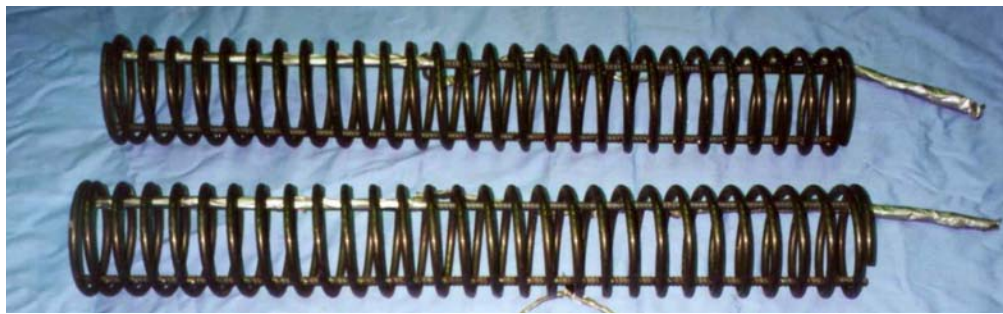


Fig. 9.12 Photograph of spiral reinforcement used inside wall test region

Flange Cover Plates – Beam flange cover plates with thickness of $t_c=19.1$ mm (0.75 in.), width of 124 mm (4.875 in.), and length of $l_c=203$ mm (8 in., one half the full-scale cover plate length) are used in Tests 1-4 to strengthen and stabilize the coupling beam flanges in compression. As shown in Figs. 9.8 and 9.9, the cover plates are placed flush with the beam ends and are fillet welded to the flanges using 15.9 mm (0.625 in.) E70 SMAW (Shielded Metal Arc Welding) welds along all edges except at the beam ends.

Shim Plates – Previous experiments of post-tensioned steel moment frame systems (Ricles et al. 2001, 2002) have shown that yielding and permanent deformation of the beam flanges in compression may result in a loss of contact at the flanges upon unloading to the zero displacement position, leading to a reduction in the initial lateral stiffness of

the structure under reversed cyclic loading. Shim plates are used between the coupling beam flanges and the embedded plates in the walls (see Fig. 9.13) in order to force the bearing between the coupling beam and the walls to occur at the flanges (so that one or both flanges remain in contact with each wall during the reversed cyclic displacements of the structure). The shim plates are welded to the embedded plates and are terminated at the beam web (Figs. 9.8 and 9.9), thus preventing contact between the web and the concrete blocks. The shim plates in the test specimens have a thickness of $t_{sh}=12.7$ mm (0.5 in.), width of 191 mm (7.5 in.), and length of 254 mm (10 in.). In practical applications, shim plates may also be used for construction/tolerance purposes.

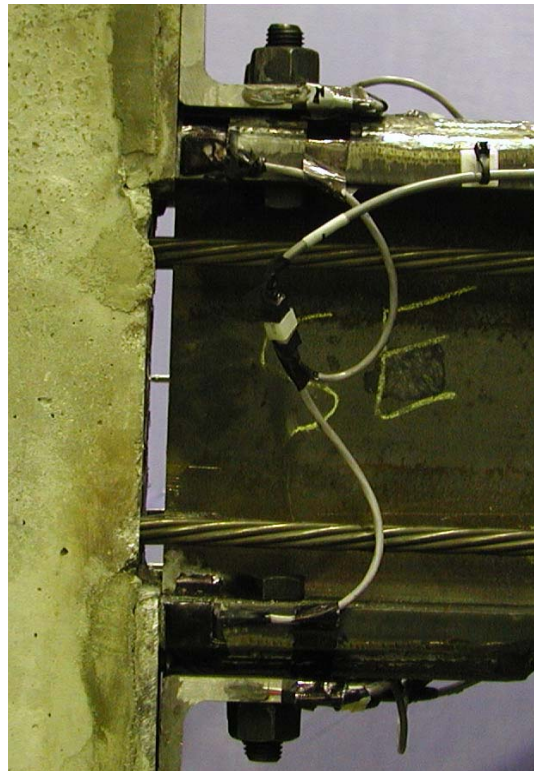


Fig. 9.13 Photograph showing shim plates at beam-to-reaction-block interface

Top and Seat Angles – Top and seat angles are used at the beam ends to yield and dissipate energy under cyclic loading. The angles in Tests 3-6 have L8×4×1/2 cross-sections and the angles in Tests 7-11 have L8×4×5/8 cross-sections. The angle length is equal to the beam flange width of $b_{bf}=159$ mm (6.25 in). As shown in Figs. 9.8 and 9.9, the angles are oriented such that the shorter leg, which is parallel to the beam flange, is bolted to the beam flange using two A490 Ø22.2 mm slip critical bolts (inside oversized 27.0 mm diameter holes) in Tests 3-9 (see Fig. 9.14) and two Ø25.4 mm slip critical bolts (inside standard 27.0 mm diameter holes) in Tests 10 and 11. The bolts are installed using the “turn-of-nut pretensioning method” described in the Manual of Steel Construction Load and Resistance Factor Design (AISC 2001).



Fig. 9.14 Photograph showing angle-to-beam and angle-to-wall connections

The connection between the vertical leg of each angle and the reaction block or the loading block is achieved using two (Tests 6, 10, and 11, see Fig. 9.14) or four (Tests 3-5 and 7-9) 15.2 mm (0.6 in.) diameter seven-wire unbonded post-tensioning strands, each

prestressed to 0.4-0.5 times the design maximum (i.e., peak) strength of the post-tensioning steel [$f_{bpu}=1862$ MPa (270 ksi)]. The connection gage lengths, l_{gv} for the vertical legs of the angles (i.e., the length between the center of the innermost angle-to-wall connectors and the angle heel) are given in Table 9.1. The purpose of the longer angle vertical legs is to allow for parameter variations in l_{gv} . Each post-tensioning strand in an angle-to-wall connection is passed through a 25.4 mm (1 in.) diameter duct and is unbonded along its length (i.e., the length of the concrete block) to prevent the yielding of the connection strand as the angles are pulled by the beam during testing. Each strand is anchored at the ends of the concrete block using steel wedge/barrel anchorage systems, thus putting the concrete into compression. The post-tensioning operation for the angle-to-wall connection strands is carried out from the outer end of each block.

Note that it would also be possible to use bolted or welded angle-to-wall connections. These connection types were not used in this research to prevent the development of large tensile stresses in the concrete. Furthermore, yielding and fracture of the angle-to-wall connection bolts/welds may be possible, thus reducing the ductility of the connection and preventing the angles from yielding and dissipating energy effectively.

9.1.6 Loading

Two 979 kN (220 kip) servo-controlled hydraulic actuators are connected to the top of the loading block (Fig. 9.4) and are operated in displacement control to move the block up or down at a rate of approximately 12.7 mm per minute. The two actuators are moved by the same displacement (resulting in actuator forces in opposite directions), thus

restraining the block from rotating in the vertical plane (i.e., the plane of the test set-up) to achieve the idealized displaced shape in Fig. 1.3c. A two-channel Schenck Pegasus 5910 Digital Controller and a computer are used to send the displacement command signal to the two actuators near-simultaneously and prevent significant lag between the actuators.

Fig. 9.15 shows the cyclic actuator displacement history in Tests 5, 7, 9, 10 and 11, which consists of a series of 6-cycle sets with target amplitudes corresponding to beam chord rotation values (i.e., relative vertical displacement between the coupling beam ends divided by the beam length) of $\theta_b=0.125, 0.25, 0.5$, and 0.75% , followed by 3-cycle sets each with amplitudes of $\theta_b=1, 1.5, 2, 3, 4, 5, 6, 7$, and 8% . After 1% rotation, three smaller cycles with a target amplitude of $\theta_b=0.25\%$ are imposed between two consecutive large rotation cycle sets. A slightly different displacement history was used in Tests 1 and 3, consisting of 3-cycle sets with target amplitudes of $\theta_b=0.10, 0.25, 0.50, 0.75, 1, 2, 3, 4, 5, 6, 7$, and 8% . After 1% rotation, one small cycle at $\theta_b=0.25\%$ was imposed between two consecutive large rotation cycle sets. Selected displacement cycles from Test 1 were used in Test 2, consisting of 3-cycle sets with target amplitudes of $\theta_b=0.10, 0.25, 0.50, 0.75, 1, 2, 4, 6$, and 8% .

The beam and angle post-tensioning strands are prestressed using a mono-strand hydraulic jack (Fig. 9.16). Table 9.1 shows the total initial forces (after short-term losses) measured in the beam post-tensioning strands, P_{bi} normalized by the total design maximum strength $P_{bu}=\sum a_{bp}f_{bpu}$. Due to the relatively short length of the strands in the

half-scale test specimens, considerable prestress was lost upon seating of the post-tensioning anchors during post-tensioning. As a result, the average initial stresses in the beam post-tensioning strands are smaller than the design initial stress of $0.60f_{bpu}$ in the prototype subassemblage.

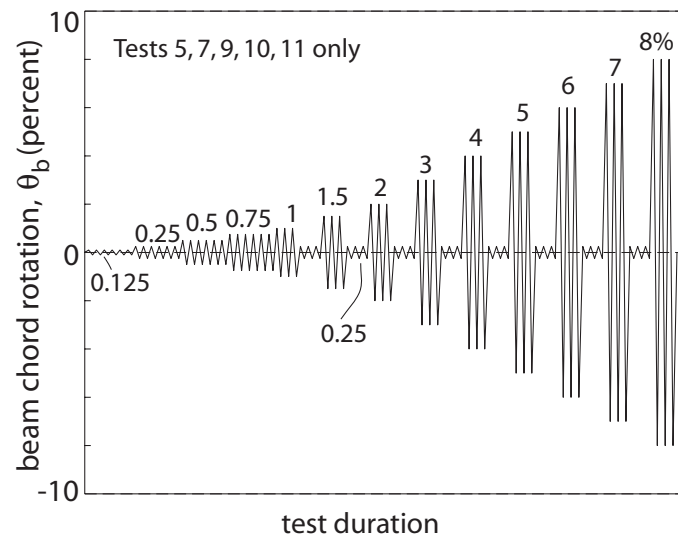


Fig. 9.15 Displacement history



Fig. 9.16 Photograph of mono-strand post-tensioning jack and pump

A nominal compression (i.e., downward) axial force is applied to the 191 mm (7.5 in.) thick wall test region of the reaction block (adjacent to the coupling beam) using eight 25.4 mm (1 in.) diameter vertical tie-down steel bars (Fig. 9.4) that bolt the block to the strong floor [through 60 mm (2.36 in.) diameter ducts] on either side of the wall test region. Each tie-down rod is pre-tensioned to about 89 kN (20 kips) resulting in a total force of about 712 kN (160 kips) in the wall test region. This axial force stayed relatively constant during each test. Eight additional tie-down bars are used through the 1473 mm (58 in.) wide region of the reaction block to secure it to the strong floor.

9.1.7 Material Properties

American Society for Testing and Materials (ASTM) standards were followed to determine the properties of the coupling beam steel, cover plate steel, angle steel, spiral steel, and post-tensioning strand (ASTM 370), and the wall concrete (ASTM C39/C 39M).

Coupling beam steel

The material samples for the coupling beam steel (ASTM A572 Grade 50 steel) were saw cut from the flange in the direction along the length of the beam. A total of three samples (only for the W10×68 section) were machined into standard (ASTM .505) 12.8 mm (0.5 in.) round specimens with 50.8 mm (2 in.) gage length.

Fig. 9.17 shows the measured monotonic tensile stress-strain relationships of the three specimens, as obtained from an Instron Model 5590-67HVL hydraulic universal testing machine with 267 kN (60 kip) capacity. The strains were measured using an

Instron Model 2630-114 extensometer with 50.8 mm (2 in.) gage length. The failure of all three specimens occurred within this gage length.

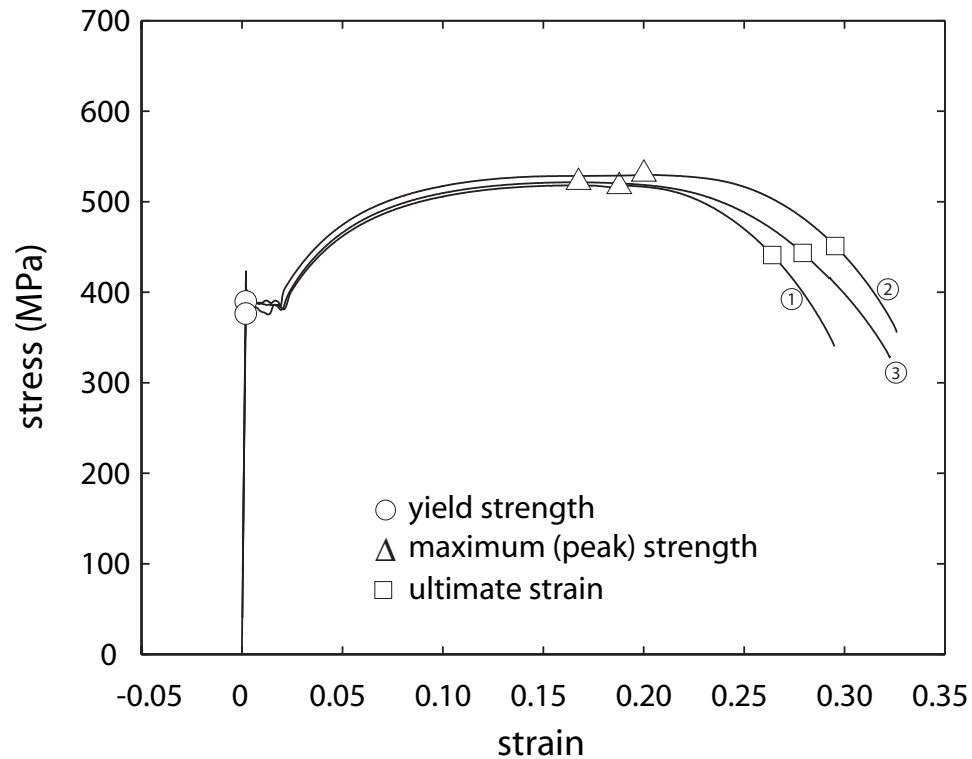


Fig. 9.17 Beam steel stress-strain behavior

Table 9.2 summarizes the material properties of the coupling beam steel specimens. The samples show a distinct yield point. The yield strength was determined as the lower yield point on the measured stress-strain relationship. The yield strain was determined by dividing the yield strength with the Young's modulus. The Young's modulus was calculated based on the slope from two points on the linear-elastic portion of the measured stress-strain relationship. The \circ , Δ , and \square markers in Fig. 9.17 correspond to the yield strength, maximum (peak) strength, and ultimate strain values, respectively, in Table 9.2.

TABLE 9.2

BEAM STEEL (W10×68) MATERIAL PROPERTIES

Specimen No.	f_{by} (MPa)	ϵ_{by} (%)	f_{bm} (MPa)	ϵ_{bm} (%)	f_{bu} (MPa)	ϵ_{bu} (%)
1	390	0.19	519	16.5	441	26.5
2	386	0.18	531	16.3	451	30.0
3	383	0.20	521	16.8	443	28.1
Average	386	0.19	524	16.5	445	28.2

Notes:

f_{by} =lower yield strength; $\epsilon_{by}=f_{by}$ divided by measured Young's modulus (\circ markers in Fig. 9.17).

f_{bm} =maximum (i.e., peak) strength; ϵ_{bm} =strain at f_{bm} (Δ markers in Fig. 9.17).

$f_{bu}=0.85f_{bm}$; ϵ_{bu} =ultimate strain at $0.85f_{bm}$ (\square markers in Fig. 9.17).

Cover plate steel

The material samples for the coupling beam flange cover plate steel (ASTM A572 Grade 50 steel) were saw-cut in the longitudinal direction (i.e., in the direction along the length of the beam). A total of three samples were machined into standard (ASTM .505) 12.8 mm (0.5 in.) round specimens with 50.8 mm (2 in.) gage length, similar to the coupling beam material.

Fig. 9.18 shows one of the specimens after failure and Fig. 9.19 shows the measured monotonic tensile stress-strain relationships of the three specimens, as obtained from an Instron Model 5590-67HVL hydraulic universal testing machine with 267 kN (60 kip) capacity. The strains were measured using an Instron Model 2630-114 extensometer with 50.8 mm (2 in.) gage length. The failure of all three specimens occurred within this gage length.

Table 9.3 summarizes the material properties of the cover plate steel specimens. The samples show a distinct yield point. The yield strength was determined as the lower yield point on the measured stress-strain relationship. The yield strain was determined by dividing the yield strength with the Young's modulus. The Young's modulus was calculated based on the slope from two points on the linear-elastic portion of the measured stress-strain relationship. The \circ , Δ , and \square markers in Fig. 9.19 correspond to the yield strength, maximum (peak) strength, and ultimate strain values, respectively, in Table 9.3.



Fig. 9.18 Cover plate steel specimen

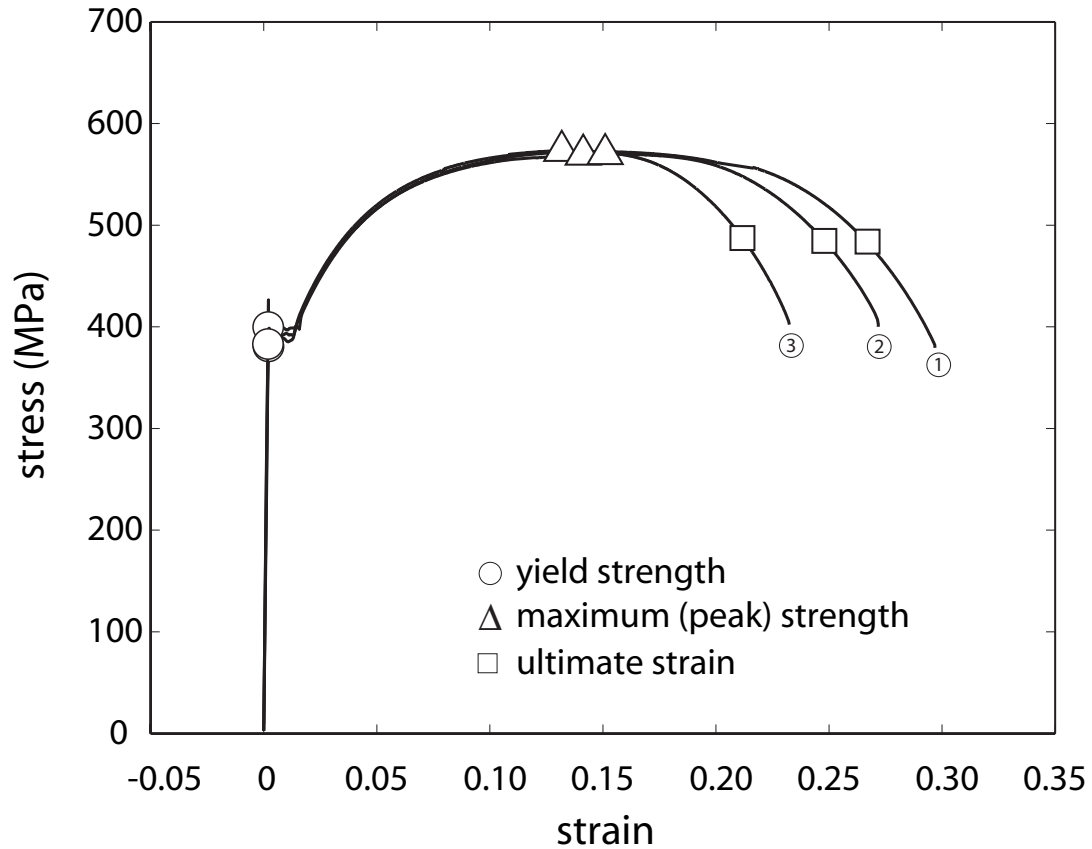


Fig. 9.19 Cover plate steel stress-strain behavior

TABLE 9.3

COVER PLATE STEEL MATERIAL PROPERTIES

Specimen No.	f_{ry} (MPa)	ϵ_{ry} (%)	f_{rm} (MPa)	ϵ_{rm} (%)	f_{ru} (MPa)	ϵ_{ru} (%)
1	399	0.19	572	14.3	486	26.9
2	380	0.20	570	15.1	485	24.8
3	383	0.17	573	15.2	487	21.2
Average	387	0.19	572	14.9	486	24.3

Notes:

f_{ry} =lower yield strength; $\epsilon_{ry}=f_{ry}$ divided by measured Young's modulus (○ markers in Fig. 9.19).

f_{rm} =maximum (i.e., peak) strength; ϵ_{rm} =strain at f_{rm} (△ markers in Fig. 9.19).

$f_{ru}=0.85f_{rm}$; ϵ_{ru} =ultimate strain at $0.85f_{rm}$ (□ markers in Fig. 9.19).

Angle steel

The material samples for the angle steel (ASTM A36-96) were saw-cut from the longer (i.e., vertical) leg in the direction perpendicular to the angle length. A total of nine samples (three samples each for two heats of L8×4×1/2 angles and three samples for the L8×4×5/8 angles) were machined into 6.40 mm (0.25 in.) round specimens (proportional to standard ASTM .505 specimens because of the limited angle thickness) with 50.8 mm (2 in.) gage length. The L8×4×1/2 angles in Test 3 were from the first heat and the angles in Tests 4-6 were from the second heat.

Fig. 9.20 shows one of the specimens during testing and Figs. 9.21a-c show the measured monotonic tensile stress-strain relationships of the nine specimens, as obtained from an Instron Model 5590-67HVL hydraulic universal testing machine with 267 kN (60 kip) capacity. The strains were measured using an Instron Model 2630-114 extensometer with 50.8 mm (2 in.) gage length. The failure of all three specimens occurred within this gage length.

Table 9.4 lists the material properties of the angle steel specimens. The samples show a distinct yield point. The yield strength was determined as the lower yield point on the measured stress-strain relationship. The yield strain was determined by dividing the yield strength with the Young's modulus. The Young's modulus was calculated based on the slope from two points on the linear-elastic portion of the measured stress-strain relationship. The ○, Δ, and □ markers in Fig. 9.21 correspond to the yield strength, maximum (peak) strength, and ultimate strain values, respectively, in Table 9.4.



Fig. 9.20 Angle steel specimen

TABLE 9.4

ANGLE STEEL MATERIAL PROPERTIES

Specimen No.	L8x4x1/2 Angle – 1 st heat					
	f_{ay} (MPa)	ϵ_{ay} (%)	f_{am} (MPa)	ϵ_{am} (%)	f_{au} (MPa)	ϵ_{au} (%)
1	324	0.18	472	15.3	401	21.3
2	317	0.17	476	22.8	405	31.4
3	308	0.24	469	20.3	399	29.3
Average	316	0.20	472	19.5	402	27.3
Specimen No.	L8x4x1/2 Angle – 2 nd heat					
	f_{ay} (MPa)	ϵ_{ay} (%)	f_{am} (MPa)	ϵ_{am} (%)	f_{au} (MPa)	ϵ_{au} (%)
1	334	0.19	486	16.2	413	19.8
2	321	0.16	487	19.3	414	26.7
3	327	0.17	483	20.9	411	28.8
Average	327	0.17	485	18.8	413	25.1
Specimen No.	L8x4x5/8 Angle					
	f_{ay} (MPa)	ϵ_{ay} (%)	f_{am} (MPa)	ϵ_{am} (%)	f_{au} (MPa)	ϵ_{au} (%)
1	376	0.21	548	16.9	467	24.8
2	374	0.28	544	15.2	462	22.1
3	380	0.37	548	15.2	466	19.8
Average	377	0.29	547	15.8	465	22.2

Notes:

f_{ay} =lower yield strength; ϵ_{ay} = f_{ay} divided by measured Young's modulus (○ markers in Fig. 9.21).

f_{am} =maximum (i.e., peak) strength; ϵ_{am} =strain at f_{am} (Δ markers in Fig. 9.21).

f_{au} =0.85 f_{cm} ; ϵ_{au} =ultimate strain at 0.85 f_{am} (□ markers in Fig. 9.21).

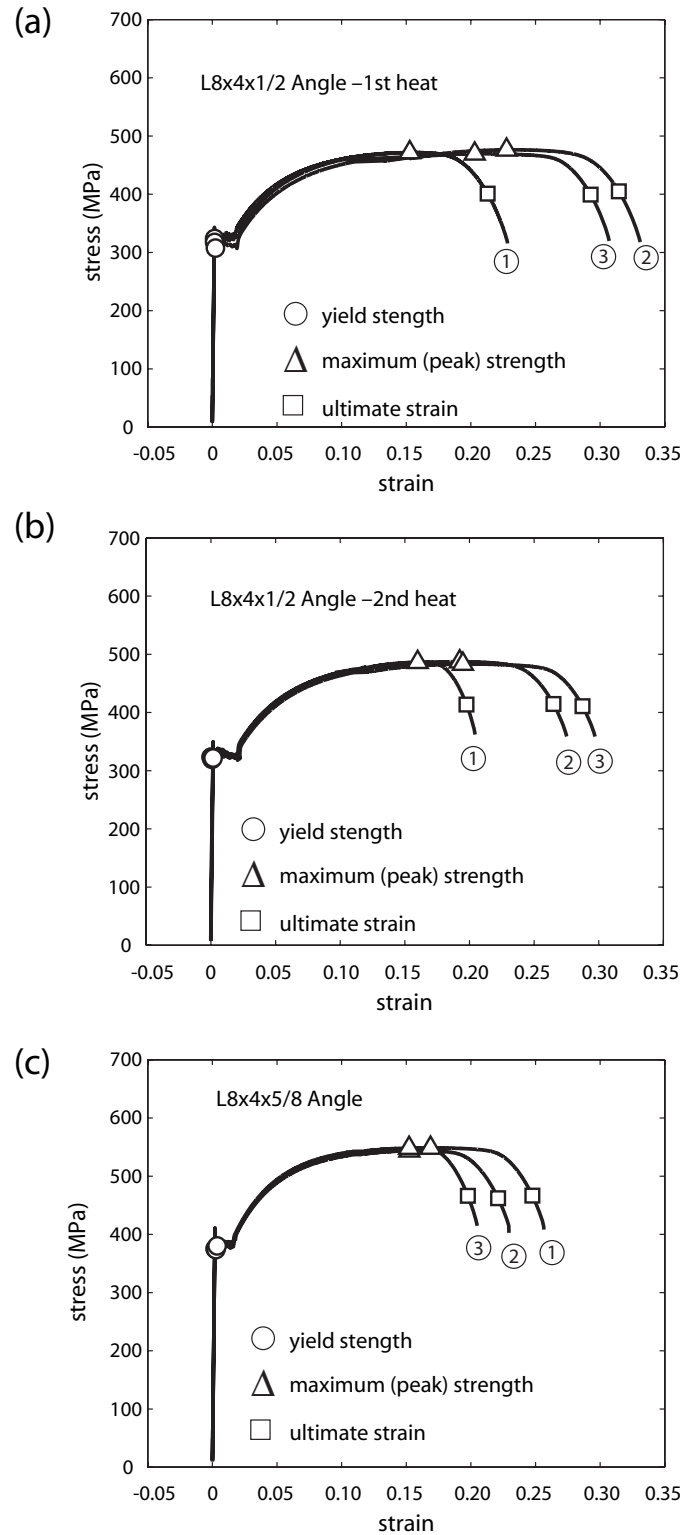


Fig. 9.21 Angle steel stress-strain behavior: (a) L8x4x1/2 – first heat; (b) L8x4x1/2 – second heat; (c) L8x4x5/8

Spiral wire steel

The monotonic tensile stress-strain relationships of three spiral wire steel (ASTM A82) samples were obtained by using a 2669 kN (600 kip) SATEC Model 600XWHVL universal testing machine. The strains were obtained using an MTS Model 634.25E-24 extensometer with a 50.8 mm (2 in.) gage length.

In order to ensure failure to occur within the extensometer gage length, the cross-section of each wire specimen was reduced by hand-grinding a short length of the wire. The diameter of the reduced cross-section, where necking and fracture occurred, was used to calculate the stresses from the measured forces. Fig. 9.22 shows the three specimens that were tested and Fig. 9.23 shows the measured stress-strain relationships for the specimens. The material properties from the tests are summarized in Table 9.5. The \circ , Δ , and \square markers in Fig. 9.23 correspond to yield strength, maximum (peak) strength, and ultimate strain values, respectively, in Table 9.5.

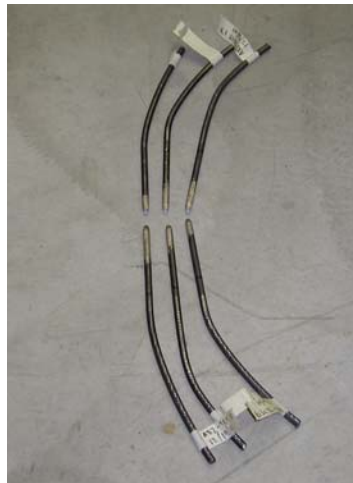


Fig. 9.22 Spiral wire specimens

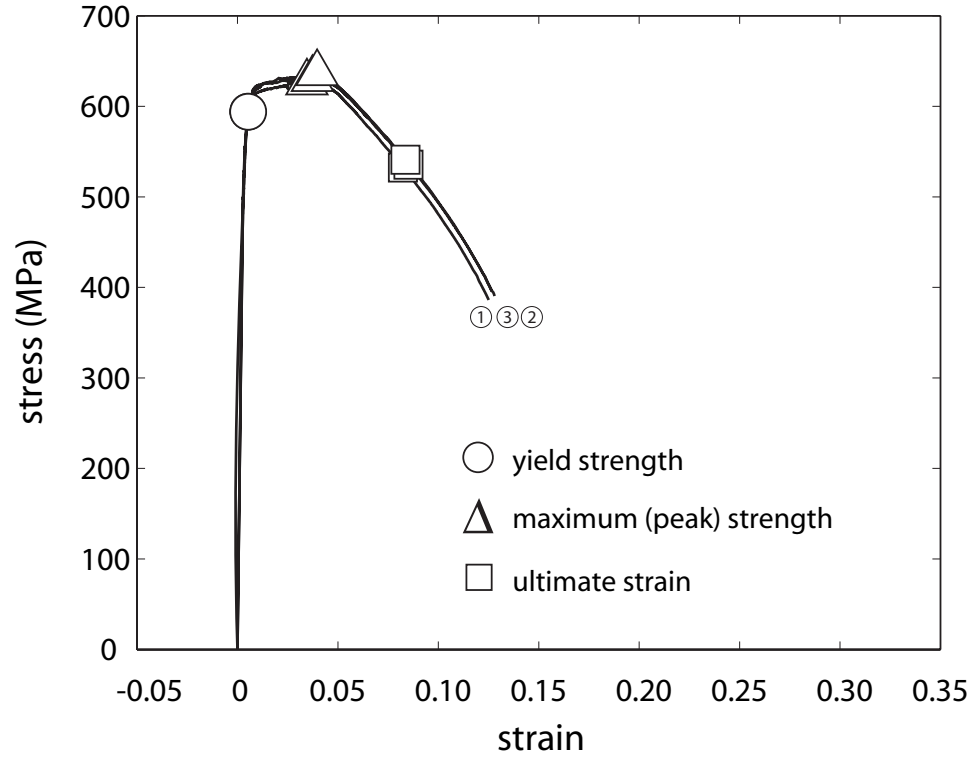


Fig. 9.23 Spiral wire stress-strain behavior

TABLE 9.5

SPIRAL WIRE STEEL MATERIAL PROPERTIES

Specimen No.	Reduced diameter (mm)	E_{sp} (MPa)	f_{spy} (MPa)	ϵ_{spy} (%)	f_{spm} (MPa)	ϵ_{spm} (%)	f_{spu} (MPa)	ϵ_{spu} (%)
1	10	183669	595	0.52	626	3.45	532	8.24
2	10	179663	594	0.53	630	3.73	536	8.51
3	10	176360	594	0.54	637	3.96	541	8.36
Average	10	179897	594	0.53	631	3.71	536	8.37

Notes:

E_{sp} =Measured Young's modulus.

f_{spy} , ϵ_{spy} ="yield" strength and strain based on a 0.2% strain off-set at zero stress (\circ markers in Fig. 9.23).

f_{spm} =maximum (i.e., peak) strength; ϵ_{spm} =strain at f_{spm} (Δ markers in Fig. 9.23).

$f_{spu}=0.85f_{spm}$; ϵ_{spu} =ultimate strain at $0.85f_{spm}$ (\square markers in Fig. 9.23).

Note that the spiral wire specimens were bent prior to testing (see Fig. 9.22), as a result of being stored in a spool. The stress-strain relationships in Fig. 9.23 and the values in Table 9.5 show the behaviors of the specimens after they were straightened under tensile loading; with the initial linear-elastic portion of the curves determined from the measured linear-elastic unloading stiffnesses of the straightened specimens. In order to determine the point on the original stress-strain curves (not shown in Fig. 9.23) where the samples were straightened, eight unloading-reloading cycles were applied – the cycles were set to load to 414 MPa, unload to 276 MPa, reload to 441 MPa, unload to 303 MPa, and continue similar cycles at 28 MPa increments until a stress of 607 MPa was reached. The unloading stiffness from each of these cycles was determined and then compared with the “linear-elastic” Young’s modulus, E_{sp} determined from an additional (ninth) unloading-reloading cycle from a strain of 0.035.

Since the Young’s modulus, E_{sp} determined during unloading from a strain of 0.035 corresponded to a straight specimen, it was assumed that the complete straightening of the specimen occurred at a stress when the unloading stiffness interpolated from the first eight unloading-reloading cycles equaled the unloading stiffness, E_{sp} from the cycle at 0.035 strain (see Fig. 9.24). The portion of the measured stress-strain curve before this stress was ignored and the linear-elastic origin for each curve was determined by unloading from this point with a slope equal to E_{sp} .

The strain values listed in Table 9.5 were calculated from this revised origin for the data. Note that, since the stress-strain relationships in Fig. 9.23 do not show a distinct yield point, the “yield” strength and strain were determined based on a 0.2% strain off-set at zero stress upon unloading from the yield point using the measured Young’s modulus, E_{sp} .

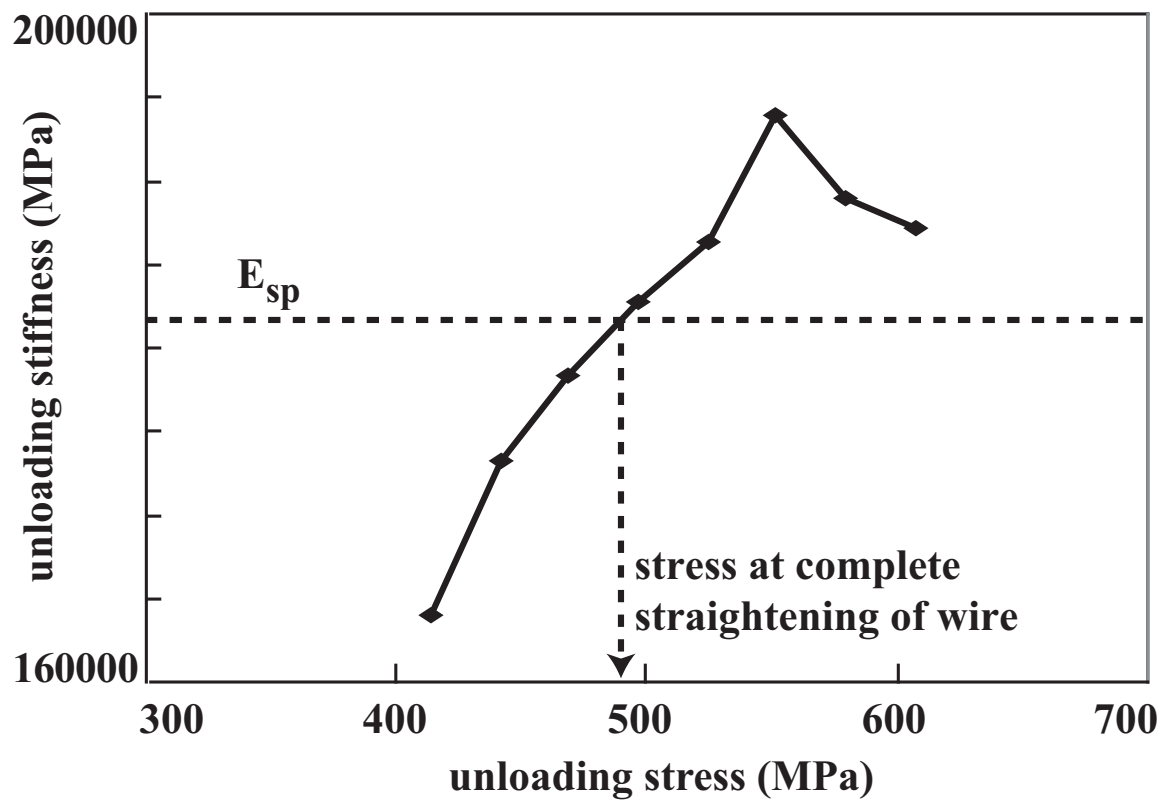


Fig. 9.24 Unloading stiffness of spiral wire steel

Post-tensioning strand

Fig. 9.25 shows the monotonic tensile stress-strain relationships of three single strand post-tensioning steel specimens (ASTM A416 low-relaxation seven-wire strands),

as obtained from a 2669 kN (600 kip) SATEC Model 600XWHVL universal testing machine. The strains were obtained using an MTS Model 634.25E-24 extensometer with a 50.8 mm (2 in.) gage length.

Single strand steel wedge/barrel anchors (see Fig. 9.10) were used to pull the post-tensioning strands until failure, resulting in anchor conditions similar to those in the coupled wall subassembly experiments. The strand specimens were approximately 1.5 m (60 in.) long between anchors and were carefully aligned between the loading heads of the testing machine (see Fig. 9.26). No prestress was applied on the strands prior to loading. The failure of all three specimens occurred due to the fracture of a post-tensioning wire (one wire in a seven-wire strand) inside an anchor, at an average stress of $f_{bpu}=1698$ MPa (246 ksi), well below the design maximum strength of $f_{bpu}=1862$ MPa (270 ksi). Table 9.6 summarizes the material properties for the post-tensioning strand specimens. The \circ and Δ markers in Fig. 9.25 correspond to the limit of proportionality point and the maximum (peak) strength/ultimate strain values, respectively, in Table 9.6. Note that the ultimate strain, ϵ_{bpu} at wire fracture of the post-tensioning strands is reached when the peak stress, f_{bpu} is reached.

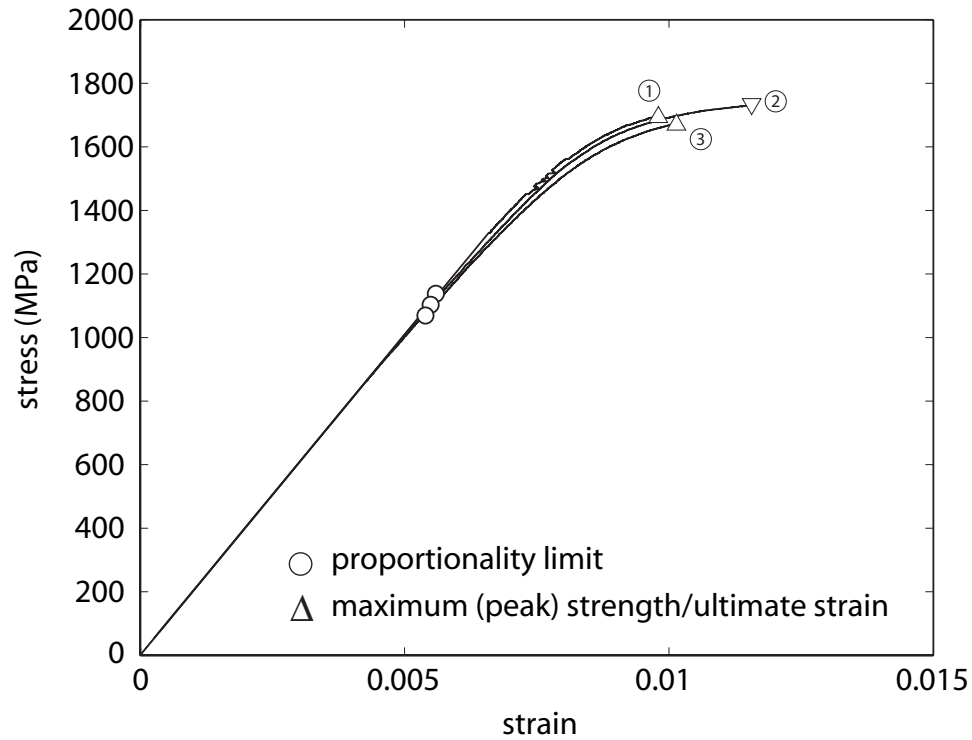


Fig. 9.25 Post-tensioning strand stress-strain behavior

Note that the stress-strain relationships in Fig. 9.25 do not show the initial portions of the measured curves where the post-tensioning strand specimens had reduced stiffness. The specimens do not show a distinct yield point. The linear-elastic origin for each curve was determined by unloading from the limit of proportionality point with a slope equal to the measured Young's modulus. The Young's modulus was calculated based on the slope from two points on the linear-elastic portion of the measured stress-strain relationship. The stress-strain relationships in Fig. 9.25 and the values in Table 9.6 were calculated from this revised origin for the data. The strain at the limit of proportionality was determined by dividing the stress at the limit of proportionality with the measured Young's modulus.

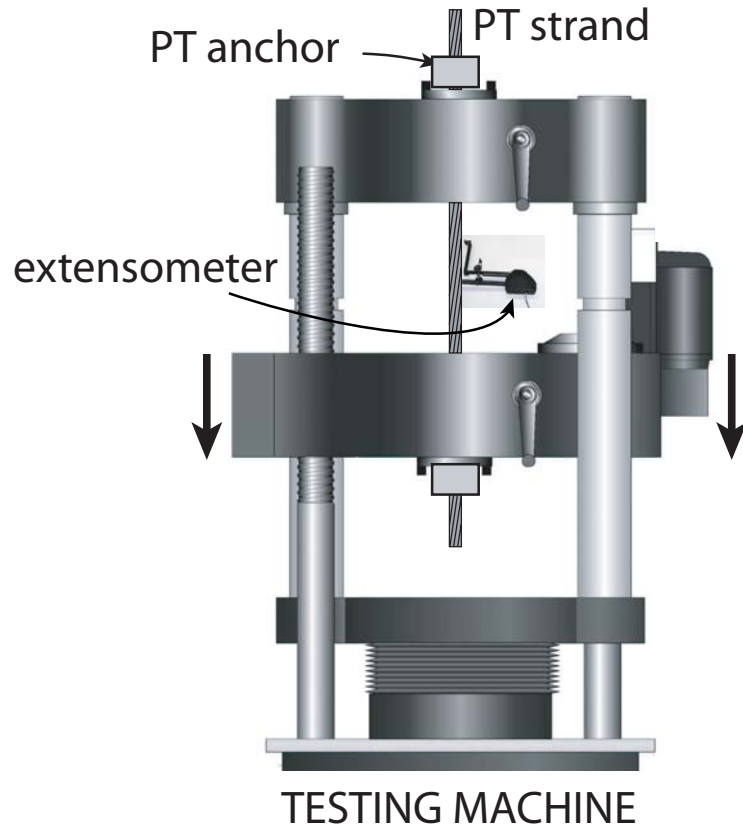


Fig. 9.26 Post-tensioning strand test setup

TABLE 9.6

POST-TENSIONING STRAND PROPERTIES

Specimen No.	f_{bpy} (MPa)	ϵ_{bpy} (%)	f_{bpu} (MPa)	ϵ_{bpu} (%)
1	1138	0.56	1696	0.98
2	1103	0.55	1724	1.16
3	1069	0.53	1674	1.01
Average	1103	0.55	1698	1.05

Notes:

f_{bpy} =limit of proportionality; $\epsilon_{bpy}=f_{bpy}$ divided by measured Young's modulus (\circ markers in Fig. 9.25).

f_{bpu} =maximum (i.e., peak) strength; ϵ_{bpu} =ultimate strain at f_{bpu} (Δ markers in Fig. 9.25).

Wall concrete

The compressive strengths of the unconfined concrete used in the reaction and loading blocks were obtained by conducting three standard 152×305 mm (6x12 in.) cylinder tests using a 2669 kN (600 kip) SATEC Model 600XWHVL universal testing machine. Table 9.7 shows the results obtained from the concrete cylinder tests and Fig. 9.27 shows two sample cylinders after failure. The concrete cylinders were cast at the same time as the reaction and loading blocks and were kept under the same conditions as the blocks until testing.

TABLE 9.7
CONCRETE PROPERTIES

Specimen No.	Block	Cast Date	Test Date	f'_c (MPa)
1	Loading Block	02/07/2001	11/29/2001	65.7
2	Reaction Block	02/07/2001	11/29/2001	66.8
3	Reaction Block	02/07/2001	10/17/2003	67.6

Note: f'_c =maximum (i.e., peak) strength of unconfined loading block or reaction block concrete.

9.1.8 Instrumentation

A National Instruments SCXI data acquisition system and a desktop computer were used to achieve close-to-simultaneous scanning, conditioning, and recording of the data measured during each test. The test instrumentation includes load cells that are numbered with a prefix of LC, displacement/rotation transducers that use a prefix of DT, and strain gages that have a prefix of SG as follows (Fig. 9.28)



Fig. 9.27 Concrete cylinder specimens

Load cells

Load cells – (1) two load cells (LC1 and LC2) to measure the actuator forces; (2) up to six load cells (LC3-LC8) to measure the forces in the beam post-tensioning strands; (3) up to two load cells (LC9-LC10) to measure the forces in the angle-to-wall connection post-tensioning strands; and (4) eight load cells (LC11-LC18) to measure the vertical forces applied to the wall test region of the reaction block.

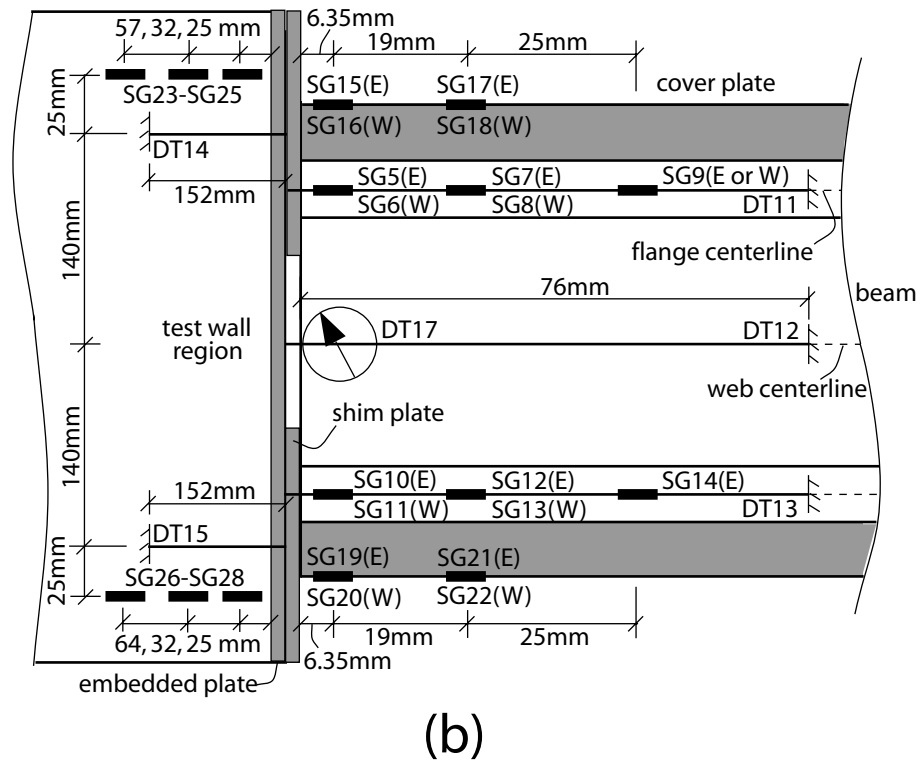
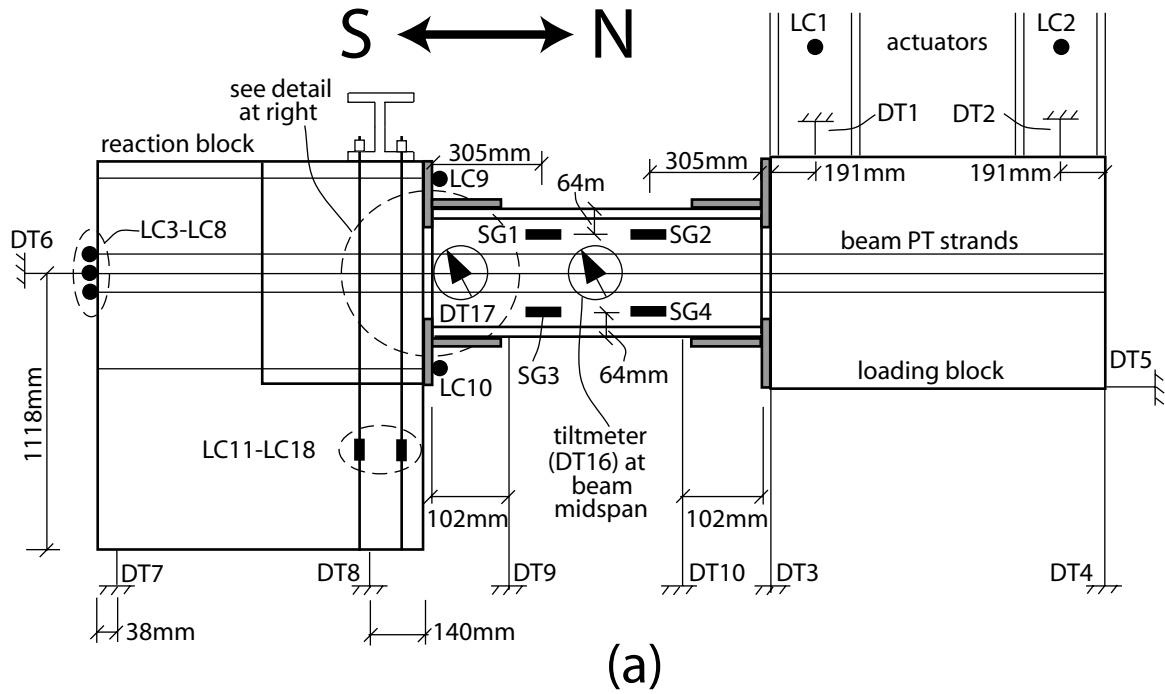


Fig. 9.28 Instrumentation: (a) overall view; (b) beam-to-wall joint region

The post-tensioning strand load cells LC3-LC10 were manufactured and calibrated at the University of Notre Dame by instrumenting a second post-tensioning barrel using four strain gages (Fig. 9.29a). During testing, the load cell barrel is placed between the post-tensioning anchor barrel and the bearing plate (Fig. 9.29b), placing the load cell in compression. The post-tensioning load cells were calibrated using a 2669 kN (600 kip) SATEC Model 600XWHVL universal testing machine. Following several cycles of shake-down loading under various orientations of each load cell, eight increments of load up to 267 kN (60 kips) in compression were used to relate the force from the testing machine to the readings from the four strain gages. The load cells showed linear behavior within the calibration load range. More information on the post-tensioning load cells can be found in May et al. (2006).

Load cells LC11-LC18 each consisted of a single electrical resistance strain gage attached to a steel tie-down bar (a total of 8 bars) used to apply the vertical force in the wall test region.

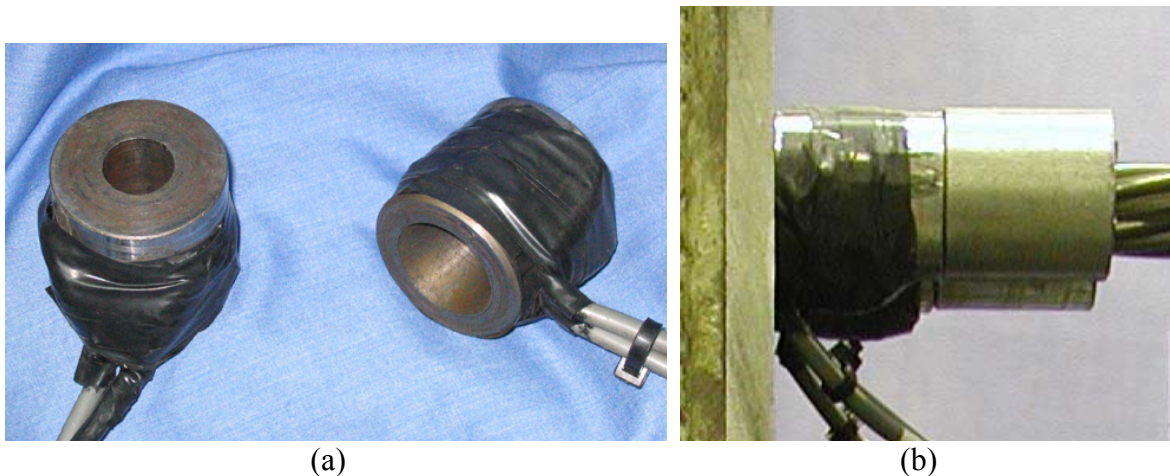


Fig. 9.29 Measurement of post-tensioning forces:
(a) load cells; (b) placement of load cells

Displacement/rotation transducers in the vertical plane

Displacement/rotation transducers in the vertical plane – (1) two displacement transducers (DT1 and DT2) to measure the actuator axial displacements; (2) three displacement transducers (DT3-DT5) to measure the loading block displacements; (3) three displacement transducers (DT6-DT8) to measure the reaction block displacements; (4) two displacement transducers (DT9 and DT10) to measure the coupling beam vertical displacements; (5) three displacement transducers (DT11-DT13) to measure the gap opening displacements between the coupling beam and the reaction block; (6) two displacement transducers (DT14 and DT15) to measure the local horizontal deformations in the high compression regions of the wall test region in the reaction block; and (7) up to two tiltmeters (DT16-DT17) to measure the coupling beam rotations at the midspan and at the reaction block end. Displacement transducers DT3-DT10 were string pots and displacement transducers DT11-DT15 were Linear Variable Displacement Transducers (LVDTs). Fig. 9.30 shows DT11-DT15 at a displaced position of the beam during Test 1.

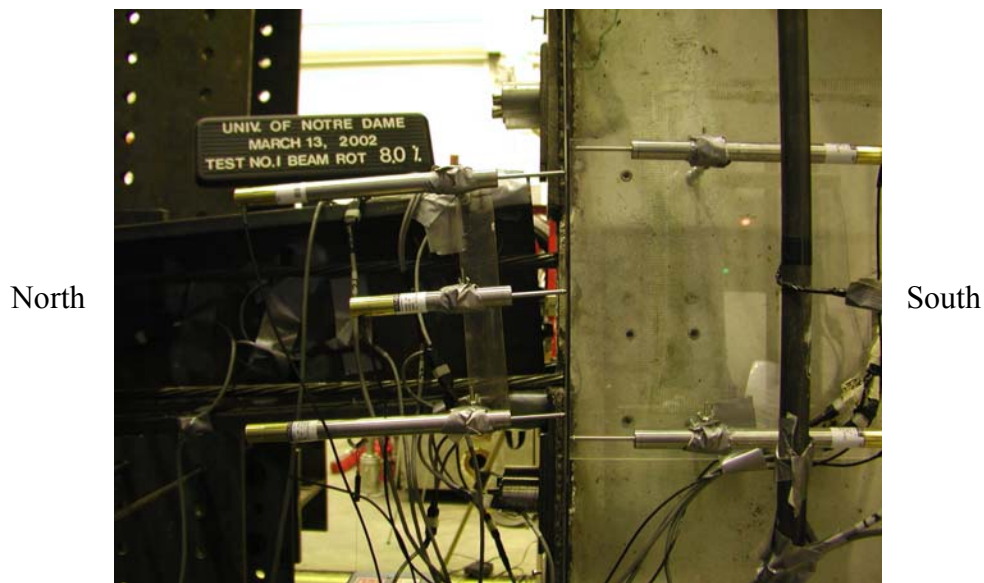


Fig. 9.30 DT11-DT15 at displaced position of coupling beam during Test 1

Electrical resistance strain gages

Electrical resistance strain gages – (1) four strain gages (SG1-SG4) to measure the horizontal strains of the coupling beam web along its length; (2) up to eighteen strain gages (SG5-SG22) to measure the horizontal strains in the coupling beam flanges and cover plates at the reaction block end (the letters “E” and “W” in Fig. 9.28 indicate gages placed on the east and west sides of the beam, respectively); and (3) six strain gages (SG23-SG28) to measure the strains in the confined concrete regions of the wall test region. Gages SG23-SG28 were attached to horizontal 9.5 mm (0.375 in.) diameter deformed steel reinforcing bars tied to the spiral reinforcement inside the concrete. 120 ohm strain gages with a gage factor of 2.0 were used for all strain gage applications.

9.1.9 Test Procedure

The procedure for testing a subassembly requires a two day process. The first day involves the alignment of the coupling beam and the loading and reaction blocks, application of the gravity load to the wall test region of the reaction block, post-tensioning of the beam, and connection of the top and seat angles at the beam-to-wall interfaces. On the second day, the actual testing of the structure occurs by moving the loading block vertically through a predetermined displacement history.

On the first day of preparations, the initial step is to determine the self weight of the loading block and the portion of the self weight of the beam that rests on the loading block. This step is completed by lifting the loading block using the two servo-controlled hydraulic actuators. The actuators are displaced upward until the loading block is off of its temporary support jacks on the laboratory floor. The reading from each of the two

actuator load cells is then recorded. The recorded load from each actuator is used in the following day to subtract out the self weight of the system.

The next step is to make sure that the coupling beam, the loading block, and the reaction block are properly aligned. The loading block is rested back on three temporary support jacks and the hydraulic actuators are turned off. The positions of the loading block and the coupling beam are adjusted on the support jacks until the entire subassembly is aligned using a laser alignment tool. The seat angles are used as temporary supports for the beam at the two ends.

Following proper alignment of the structure, all of the instrumentation is zeroed or initialized. The vertical forces on the wall test region of the reaction block are applied (by tightening the nuts on the tie-down bars) or checked from a previous test based on the measurements from LC11-LC18. Then, the post-tensioning of the coupling beam to the reaction and loading blocks is carried out by first applying a small amount of stress to each of the main strands until the gaps (necessary for construction tolerances) between the coupling beam and the reaction and loading blocks are closed and the subassembly is snugly connected. The LVDTs that measure the gap opening displacements between the coupling beam and the reaction block (DT11-DT13) are re-zeroed, so that the LVDT measurements do not include the gap that exists between the beam and the reaction block before post-tensioning. After the LVDTs have been re-zeroed, the four main beam post-tensioning strands are stressed up to their full desired value of about $0.50-0.55f_{bpu}$. The post-tensioning strand load cells (LC3-LC6) are used to determine when the desired prestress level has been reached. Finally, the positions of the two servo-controlled hydraulic actuators are recorded.

The top and seat angles at the ends of the coupling beam are bolted to the beam flanges and then connected to the reaction block and the loading block using unbonded post-tensioning strands. The angle connections are tightened after the post-tensioning of the main coupling beam strands to ensure that most of the initial post-tensioning force is transferred into the coupling beam. The angle-to-beam connection bolts are tightened to slip-critical level by using the “turn-of-nut pretensioning method” described in the LRFD Manual of Steel Construction (AISC 2001).

On the day of the test (i.e., second day), the first step is to initialize all instruments based on the measurements from the previous day. The two actuators are then moved to their positions recorded during the setup on the previous day. The servo-controller is then switched to load control and the self-weight forces recorded during the previous day are applied on the actuators to remove the effect of self-weight from the specimen. The actuator positions are recorded again and the coupling beam chord rotation and the beam shear force and moment are zeroed. The string pots and tiltmeters are also re-zeroed at this stage. The servo-controller is put back into displacement control mode and, if necessary, the actuators are moved back to their positions recorded just after the application of the self-weight forces. The structure is now ready to run the predetermined displacement history.

A summary of the complete procedure used to set up and conduct the tests is given below.

Day 1 (preparation day)

1. Determine actuator forces due to self weight of subassemblage
2. Level and align coupling beam and loading block using temporary floor jacks

3. Zero/initialize all instrument readings

- Post-tensioning strand load cells
- String pots
- LVDTs measuring gap opening
- LVDTs measuring deformations in wall test region
- Tiltmeters
- Strain gages

4. Apply/check vertical forces on wall test region of reaction block

5. Apply a small amount of prestress to main post-tensioning strands until coupling

beam is snugly connected to reaction and loading blocks

6. Re-zero LVDTs used to measure gap opening

7. Apply full coupling beam post-tensioning force

8. Record actuator positions

9. Tighten angle-to-beam connection bolts to slip-critical level

10. Prestress angle-to-wall connection strands

Day 2 (test day)

1. Initialize all instruments

2. Move actuators to position recorded on step 8 of Day 1

3. Switch to load control

4. Apply self weight forces recorded on step 1 of Day 1

5. Record actuator positions

6. Zero beam rotation and beam shear/moment

7. Re-zero string pots and tiltmeters
8. Switch to displacement control
9. Move actuators to position recorded in step 5 of Day 2
10. Run predetermined displacement history

9.2 Results of Experiments

The experimental results are evaluated below as follows: (1) behavior of properly-designed subassemblages; (2) effect of coupling beam flange cover plates; (3) effect of angle thickness; (4) effect of beam post-tensioning steel area; and (5) effect of beam depth.

9.2.1 Behavior of Properly Designed Subassemblages (Tests 1-4)

The behavior of properly-designed unbonded post-tensioned hybrid coupled wall subassemblages is evaluated below using the results from Tests 1-4 (Table 9.1). In Test 1, top and seat angles were not used at the beam-to-wall connections to study the behavior of the subassemblage and to verify the analytical models without the angles. In Test 2, the coupling beam used in the first test was retested after replacing the post-tensioning strands. In Test 3, a new beam with top and seat angles at the beam-to-wall connections was used. Test 4 was a monotonic test with only two tension angles and no beam post-tensioning steel to obtain more information on the angle behavior.

Preliminary tests of a subassemblage without top and seat angles showed slip of the coupling beam at the beam-to-wall interfaces. To prevent the beams in Tests 1 and 2 from slipping, restraining plates with thickness of 9.5 mm (0.375 in.) were connected to the

shim plates above and below the beam. The restraining plates did not have any effect on the behavior of the subassemblages other than prevent slip of the beam with respect to the wall blocks. The coupling beam in the other tests (except Test 10 as described later) did not slip (since top and seat angles were used in these tests); and thus, restraining plates were not necessary.

Figs. 9.31a-c show the coupling shear force versus rotation (V_b - θ_b) behaviors from Tests 1-3, respectively. The force V_b is determined from the actuator forces and the rotation θ_b is the coupling beam chord rotation determined from transducers DT9 and DT10 measuring the vertical displacements of the beam at the ends. Only the first cycle during each set of displacement cycles of equal amplitude is shown, except where significant differences occur in the subsequent cycles.

Fig. 9.31a shows that the behavior of the subassemblage without angles is essentially bilinear-elastic, caused mainly by gap opening at the beam ends. A small amount of reduction (i.e., loss) in prestress occurred during the test as discussed in more detail later. The reduction in prestress resulted in a small reduction in the V_b resistance; however, it did not cause a reduction in the strength of the specimen (see Fig. 9.31a). Failure of the subassemblage occurred when one of the seven wires in the top west beam post-tensioning strand fractured at the end of the second cycle to $\theta_b=-8\%$ in the negative (i.e., counter clockwise) direction. The fracture occurred inside a post-tensioning anchor (similar to the failures in the material tests), where the anchor teeth grip the strand at the live (north) end, at a stress of 1466 MPa [212.6 ksi, well below the average maximum strength of $f_{bpu}=1698$ MPa (246.3 ksi) from the material tests], and resulted in a small reduction in V_b . The largest stress reached in the four beam post-tensioning strands during the test was 1576 MPa (228.5 ksi). The subassemblage was unloaded and the

experiment was terminated after the strand fracture. No damage was observed in the reaction block or the loading block during the test, allowing both blocks to be reused in all of the subsequent Tests 2-11.

The coupling beam used in Test 1 did not receive any damage other than a small amount of compression yielding in the cover plates at the beam ends. To demonstrate this, the beam was retested after replacing the post-tensioning strands. Note that only selected displacement cycles from Fig. 9.15 were used in this second test. The behavior of the retested beam in Fig. 9.31b is very similar to the behavior of the original beam in Fig. 9.31a. The small differences observed between the two tests are possibly because all or most of the compression yielding in the beam cover plates occurred in Test 1 and no further appreciable beam yielding took place in Test 2. The results demonstrate that unbonded post-tensioned hybrid coupled wall subassemblages can go through large nonlinear reversed cyclic displacements without receiving significant damage in the walls or the beams. The beams do not need to be replaced after a large earthquake as long as the yielded or fractured strands are replaced.

Figs. 9.31a and 9.31b show that there is a small increase in the “post-softening” stiffness (i.e., stiffness after the softening state, see Chapter 4) of the subassemblage after about $\theta_b=4\%$ to 5% rotation. This occurred as a result of the “kinking” of the beam post-tensioning strands when they came into contact with the oversized post-tensioning ducts at the beam-to-wall interfaces, leading to increased second-order effects in the strands. Kinking of the strands did not have any undesirable effects on the behavior of the structure (note that the strand fracture in Test 1 occurred inside an anchor and not along the length of the strand). The post-tensioning strands in Test 2 did not fracture, and the test was terminated after unloading from the third cycle to $\theta_b=8\%$, without failure.

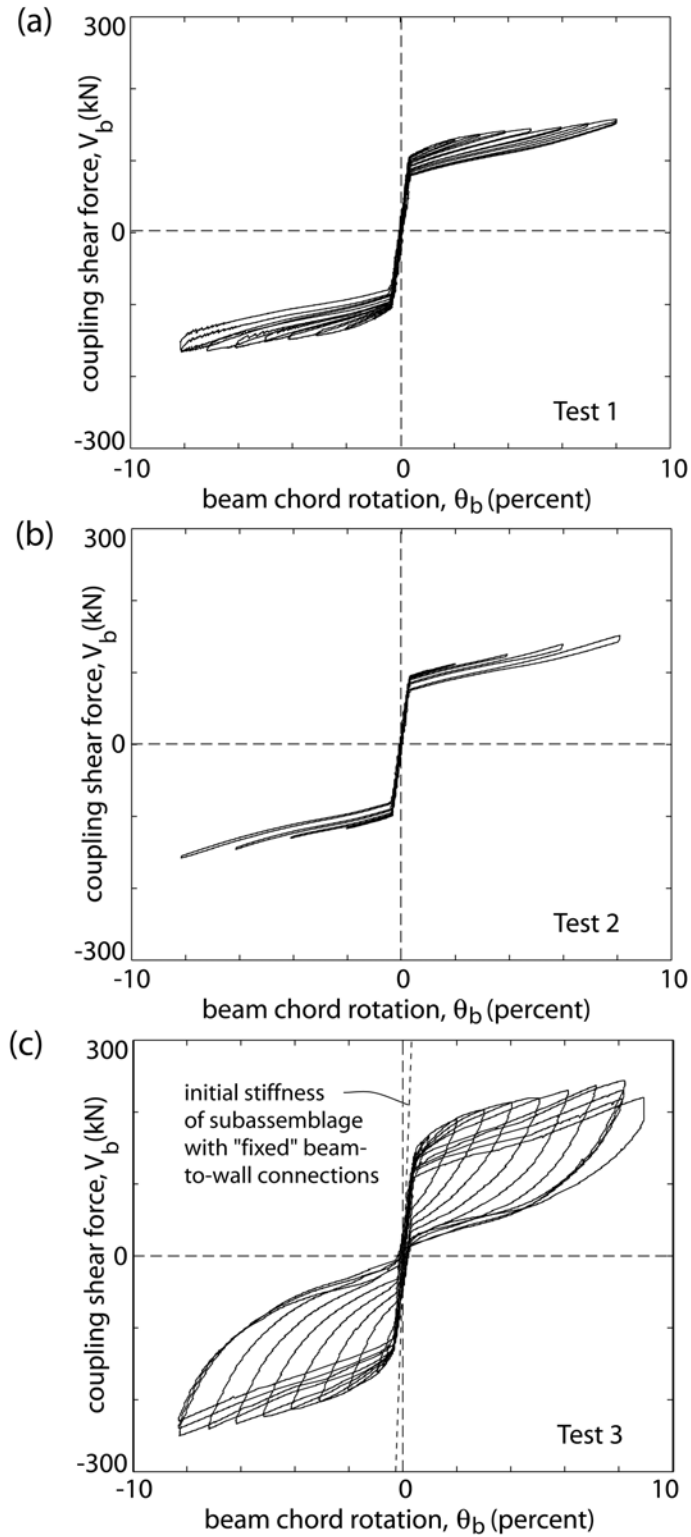
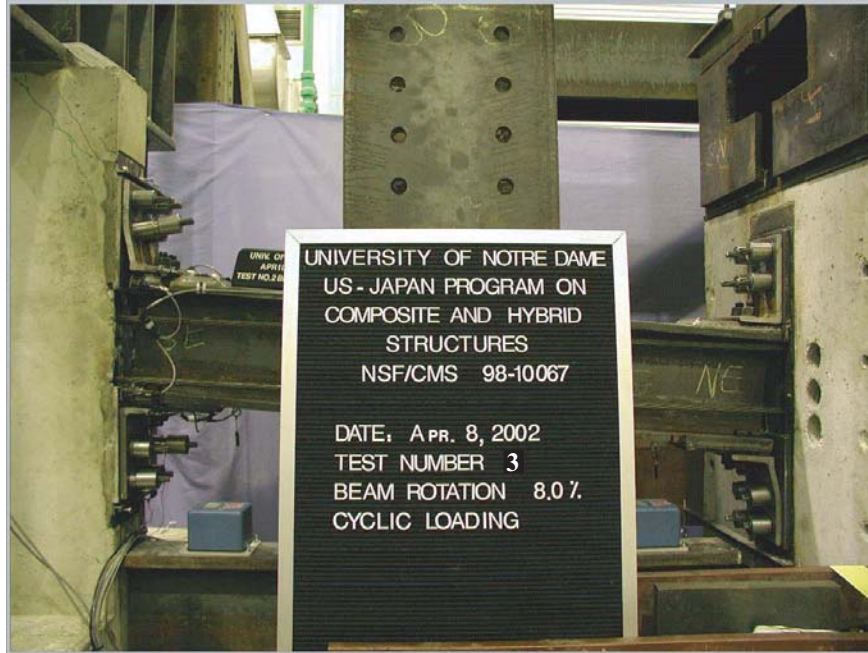


Fig. 9.31 Measured coupling shear force versus beam chord rotation (V_b - θ_b) relationships: (a) Test 1; (b) Test 2; (c) Test 3

Fig. 9.31c shows the V_b - θ_b behavior of the subassembly with top and seat angles from Test 3. As described earlier, this specimen is a half-scale model of the prototype subassembly described in Chapter 3. The hysteresis loops indicate desirable seismic characteristics with stable behavior up to $\theta_b=8\%$ rotation and significant energy dissipation. Comparing Figs. 9.31a and 9.31c, the increase in strength and energy dissipation occurs as a result of the angles.

Fig. 9.32a shows the overall displaced shape of the beam in Test 3 at $\theta_b=+8\%$ rotation in the positive (i.e., clockwise) direction and Fig. 9.32b shows a close-up view of the test region near the reaction block at $+8\%$ rotation. The displaced shape of the subassembly is similar to the displaced shape with respect to the reference line in Fig. 1.3c, with most of the beam rotation occurring as a result of the gaps at the beam ends. The rotation of the beam with respect to the walls results in the yielding of the top and seat angles in tension and compression as shown in Figs. 9.32a and 9.32b.

The straight dashed line in Fig. 9.31c shows the theoretical initial (i.e., linear-elastic) stiffness of the same subassembly assuming fixed beam-to-wall connections (representing an embedded steel beam). As a result of post-tensioning, the measured initial stiffness of the test beam before the initiation of gap opening is similar to the initial stiffness of an embedded beam. The hysteresis loops in Fig. 9.31c indicate that the beam post-tensioning strands provide a restoring force such that the gaps are closed upon unloading, thus pulling the beam towards its undeformed position with little residual displacement (i.e., large self-centering capability). The initial stiffness of the subassembly is preserved even after unloading from very large nonlinear rotations.



(a)



(b)

Fig. 9.32 Test 3: (a) displaced shape – overall; (b) displaced shape – local

The sum of the coupling beam post-tensioning forces, P_b in Test 3 (normalized with the total design maximum strength of the post-tensioning strands, $P_{bu} = \sum a_{bp} f_{bpu}$) is plotted in Fig. 9.33. Before the initiation of gap opening, the total force in the post-tensioning strands is similar to the initial post-tensioning force, P_{bi} . As the specimen is displaced, the strand forces increase, thus resisting gap opening. Prestress losses are observed upon unloading from increased displacements; however, these losses are small because of the use of unbonded post-tensioning strands. Unlike Test 1, fracture of the post-tensioning strands did not occur in Test 3.

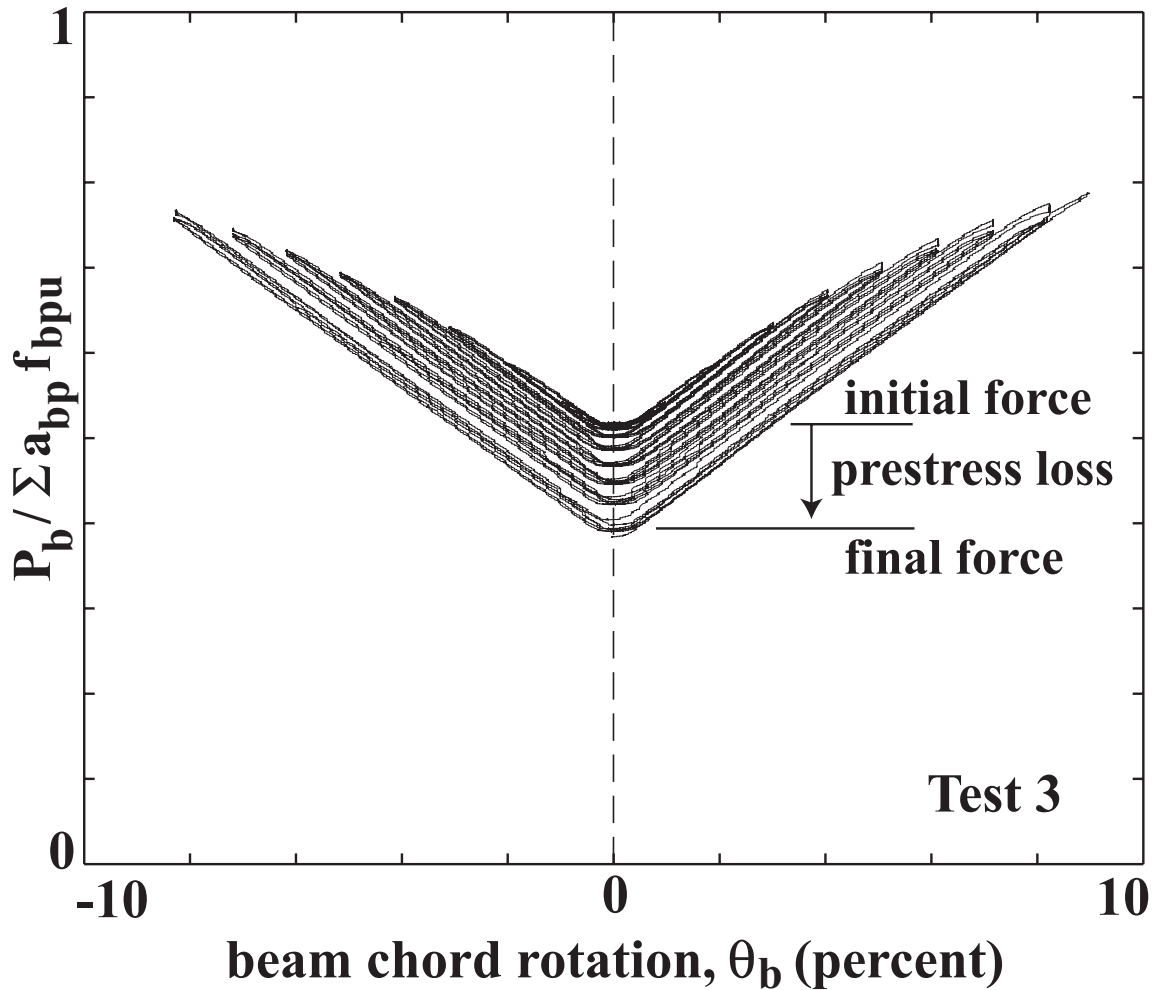


Fig. 9.33 Test 3 - total beam post-tensioning force

Fig. 9.34 shows the depth of contact, c_b between the coupling beam and the reaction block in Test 3, as determined from displacement transducers DT11-DT13 at the beam end (see Fig. 9.28). The contact depth is normalized with respect to the depth of the beam including the cover plates, $d_{bc}=302$ mm (11.89 in.). Each circular marker represents the measured contact depth upon first loading to a peak θ_b value in the positive or negative direction during the displacement history followed in the test. Under small rotations of the beam, the entire beam depth is in contact with the reaction block (note that the beam depth between the shim plates is not in contact). The initiation of gap opening (i.e., decompression) occurs before $\theta_b=0.25\%$ and results in a rapid reduction of the contact depth. Values of c_b below the horizontal dashed line indicate that the contact depth is within the shim plate. A contact depth of $c_b=12.5$ mm (0.49 in., approximately 0.66 times the cover plate thickness, t_c) is reached at $\theta_b=2\%$, beyond which the contact depth changes relatively little.

To investigate the amount of yielding in the coupling beam flanges in Test 3, the deformations were measured using strain gages SG5-SG14 located at the flange centerline. As an example, the thick solid line in Fig. 9.35 shows the top flange strains in SG5 at the beam end (see Fig. 9.28). Application of the initial post-tensioning force results in a compressive strain at the beginning of the test. The strain readings cycle but remain compressive as the beam is rotated in the positive and negative directions. As a result of gap opening, the compression strain in SG5 drops to a minimum value during the first cycle to $\theta_b=+0.25\%$. Upon reversed loading to $\theta_b=-0.25\%$, the strain in SG5 reaches the measured average (from three specimens) yield strain of $\varepsilon_{by}=-0.0019$

(indicated by the thick dashed horizontal line). As shown in Fig. 9.35, there is an accumulation of plastic (i.e., residual) compressive strains in the beam flange upon unloading from θ_b values beyond -0.25%. The largest strain measured in SG5 is -0.0035 (approximately equal to $1.8\varepsilon_{by}$). It is concluded that the amount of yielding in the flanges of the beam in Test 3 was negligible.

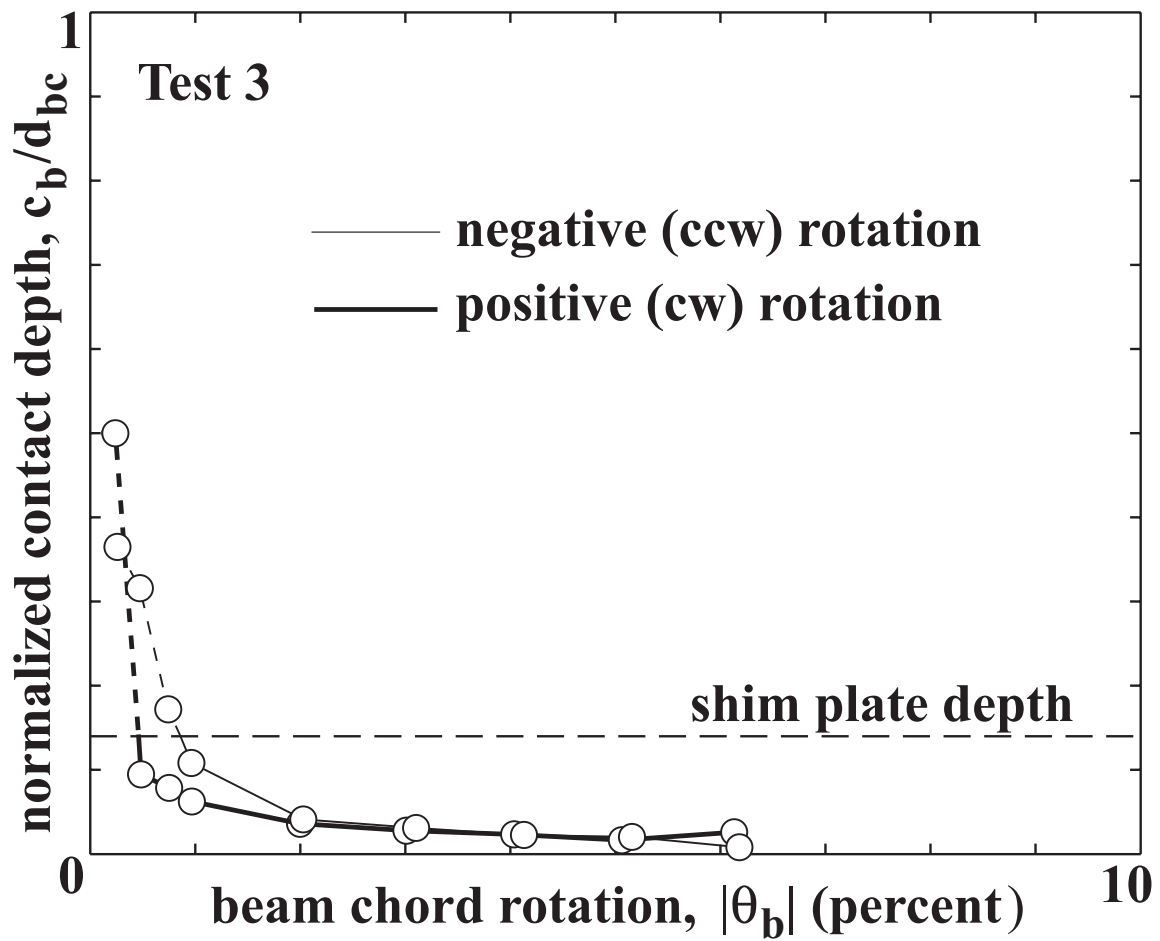


Fig. 9.34 Test 3 - contact depth

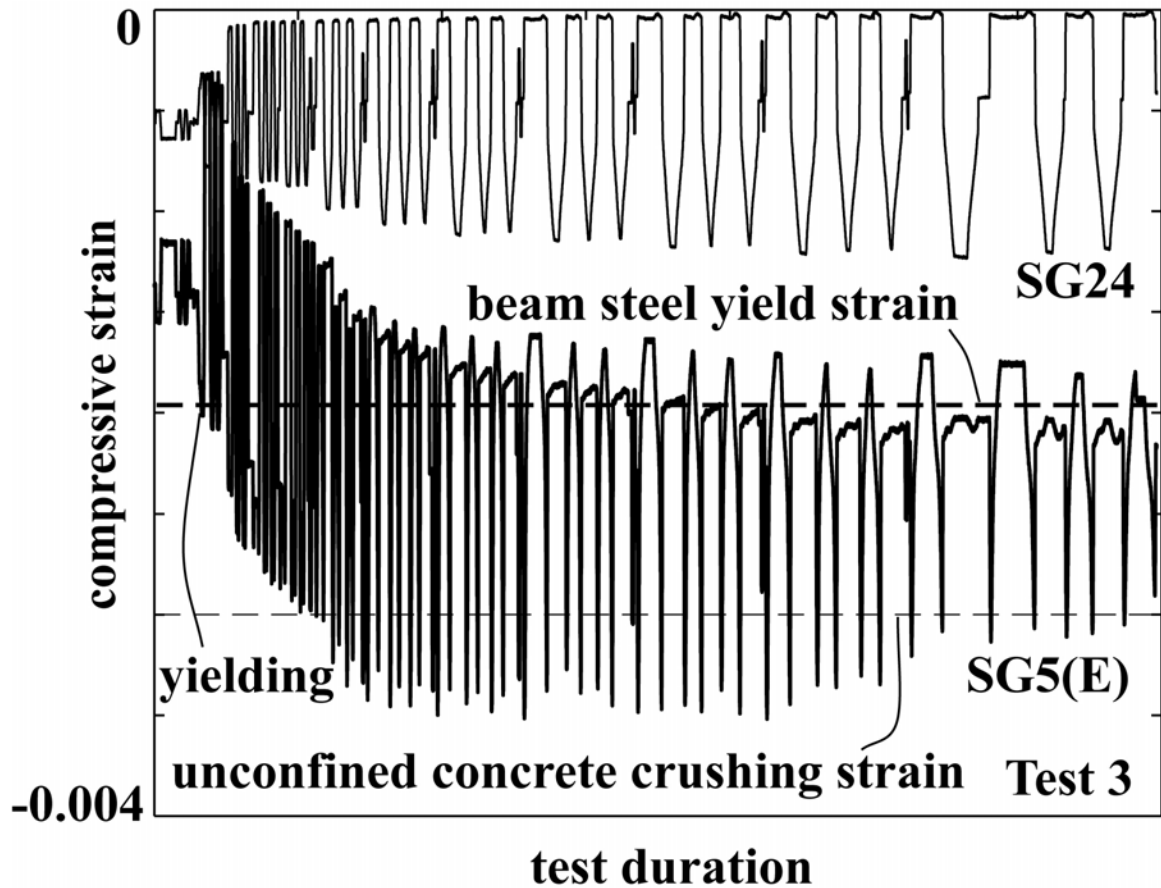


Fig. 9.35 Test 3 - beam flange steel and wall concrete strains

Similarly, in order to investigate the performance of the reaction block, the deformations in the 191 mm (7.5 in.) thick wall test region were measured using DT14-DT15 and SG23-SG28 (see Fig. 9.28). As an example, the thin solid line in Fig. 9.35 shows the strains from SG24, which remain compressive during the test. The thin dashed horizontal line corresponds to the assumed unconfined concrete spalling/crushing strain of -0.003. It is concluded that the wall test region did not receive any damage during the test, including cracking and/or spalling of the cover concrete (see Fig. 9.32b).

Initiation of low cycle fatigue cracks was observed in the vertical legs of the tension angles at about $\theta_b=7\%$. The cracks occurred at the critical section adjacent to the

fillet. The specimen was able to sustain three displacement cycles at $\theta_b=8\%$ with a steady, but not excessively large, reduction in strength and post-softening stiffness (see Fig. 9.31c). This reduction in stiffness and strength occurred due to increased cracking and necking of the vertical legs of the tension angles. Failure of the specimen eventually occurred as a result of the complete fracture of the vertical leg of the seat angle at the north (right) end of the beam when $\theta_b=+9\%$ was reached for the first time. The resistance of the specimen at this stage was, approximately, 90% of the peak resistance. Fig. 9.36 shows the fractured angle at $\theta_b=+9\%$. All four angles had sustained significant damage at this stage resulting in a considerable amount of energy dissipation as shown in Fig. 9.31c. The subassembly was unloaded and the test was terminated upon fracture of the first angle.

As shown in Fig. 9.32b, the angle-to-wall connections performed extremely well, allowing the angles to go through large nonlinear deformations without damaging the concrete. The integrity of the angle-to-wall connections was preserved during the entire test since the connection strands did not yield. The angle-to-beam connections also behaved satisfactorily, with no slip between the angles and the beam up to $\theta_b=5\%$ and negligible slip afterwards, indicating that the slip-critical bolts were adequate. Slip between the coupling beam and the reaction and loading blocks did not occur demonstrating that the angles provided adequate vertical support to the beam together with friction resistance due to the beam post-tensioning force.

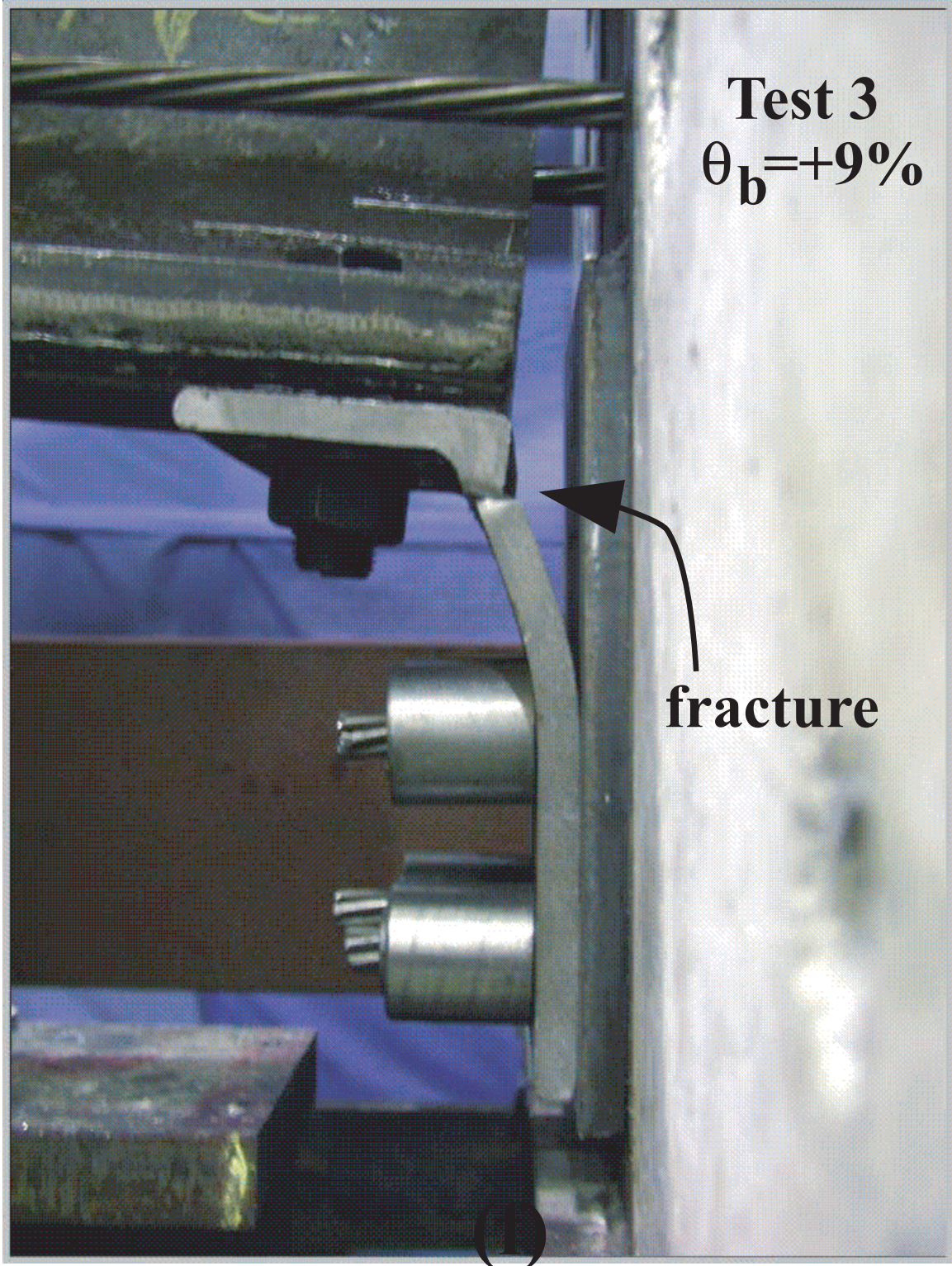


Fig. 9.36 Test 3 – angle fracture

Fig. 9.37a shows the set-up for Test 4, where a subassembly with only two tension angles and no beam post-tensioning steel was tested monotonically. The coupling beam from Test 3 was re-used in Test 4 with two new angles. Since no post-tensioning strands were used in the coupling beam, the entire lateral resistance of the subassembly was from the two angles in tension. Fig. 9.37b shows the displaced shape from a similar test (Test 6) upon loading to $\theta_b=+8\%$ and upon subsequent unloading to zero rotation. The permanent gaps at the beam ends demonstrate the role of the beam post-tensioning force in yielding the tension angles back in compression and closing the gaps upon unloading. The monotonic $V_b-\theta_b$ relationships from Test 4, as well as from two other similar monotonic tests (Tests 6 and 8 as will be described later), and one cyclic test with four angles and no beam post-tensioning steel (Test 11), are shown in Fig. 9.37c. The tensile “yield” strengths of the angles were determined from these curves and were used to develop/verify analytical models for the angles. Unlike the cyclic loading experiments, the angles in the monotonic experiments did not show any evidence of deterioration/failure.

9.2.2 Effect of Coupling Beam Flange Cover Plates (Tests 5-6)

A coupling beam with no flange cover plates was used in Test 5 to explore the need for the cover plates in strengthening and stabilizing the flanges. As a second difference, the gage length l_{gv} for the angle vertical legs in Test 5 was longer than the gage length in Test 3 by an amount equal to the cover plate thickness of $t_c=19.1$ mm (0.75 in., Table 9.1). The measured $V_b-\theta_b$ behavior from Test 5, shown in Fig. 9.38a, illustrates the stable behavior of the structure. Failure of the subassembly occurred as a result of the complete fracture of the vertical leg of the top angle at the north end of the beam when

$\theta_b = -7\%$ was reached for the third time, after which the subassembly was unloaded and the experiment was terminated. The angle-to-beam and angle-to-wall connections performed as desired, with no slip or failure during the entire test.

As compared with Test 3 (Fig. 9.31c), the peak coupling shear strength and energy dissipation from Test 5 (Fig. 9.38a) are smaller. This is possibly due to the increase in the angle gage length, which led to a reduction in the angle contribution to the coupling resistance. To investigate the effect of the gage length on the angle behavior, a second monotonic angle test (Test 6) was conducted, with the smaller angle strength demonstrated as shown in Fig. 9.37c. The coupling beam from Test 5 was re-used in Test 6, with no beam post-tensioning strands and after replacing the angles.

To investigate the nonlinear behavior in the coupling beam from Test 5, Fig. 9.38b shows the flange strains at the top south end of the beam (from strain gages SG5, SG8 and SG9 at the flange centerline). The strain readings remain compressive (similar to Fig. 9.35) and increase under negative θ_b (i.e., when the loading block is moved upward), and decrease under positive θ_b . The circular markers show the maximum and minimum readings in strain gage SG5 (at the beam end) corresponding to peak θ_b values in the negative and positive directions, respectively. The flange strain reaches the beam yield strain $\epsilon_{by} = -0.0019$ (indicated by the dashed horizontal line) at approximately $\theta_b = -1.5\%$, after which there is an accumulation of plastic (i.e., residual) strains upon unloading. The delayed flange yielding in Test 5 as compared with Test 3 could be due to uneven initial contact at the beam-to-wall interfaces. The largest strain measured in SG5 is -0.012 (approximately equal to $6\epsilon_{by}$). The measurements from the three gages indicate that the beam strains quickly diminish away from the beam end. It is concluded that the lack of cover plates resulted in an increase in the beam flange strains (as compared with Test 3, Fig. 9.35); however, this did not have any adverse effects on the performance of the beam.

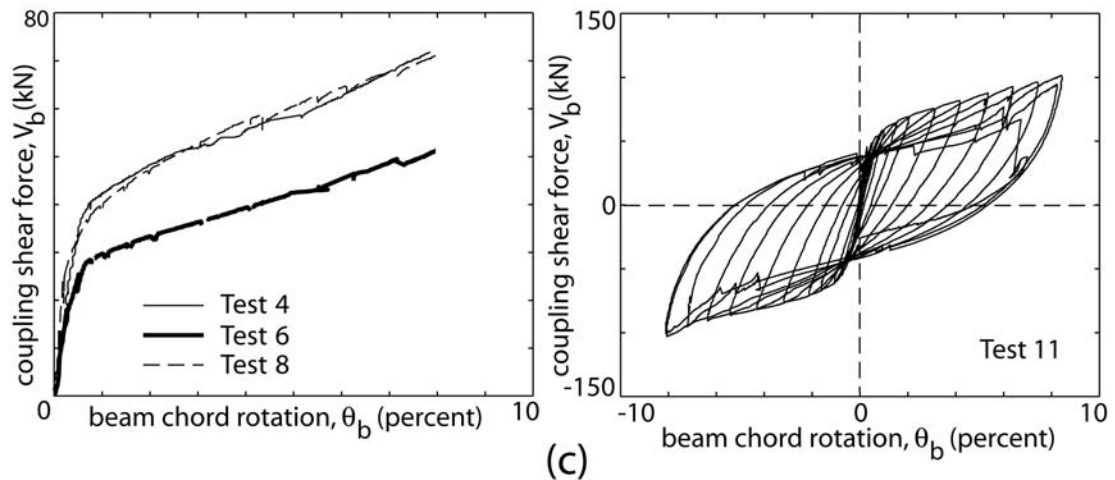
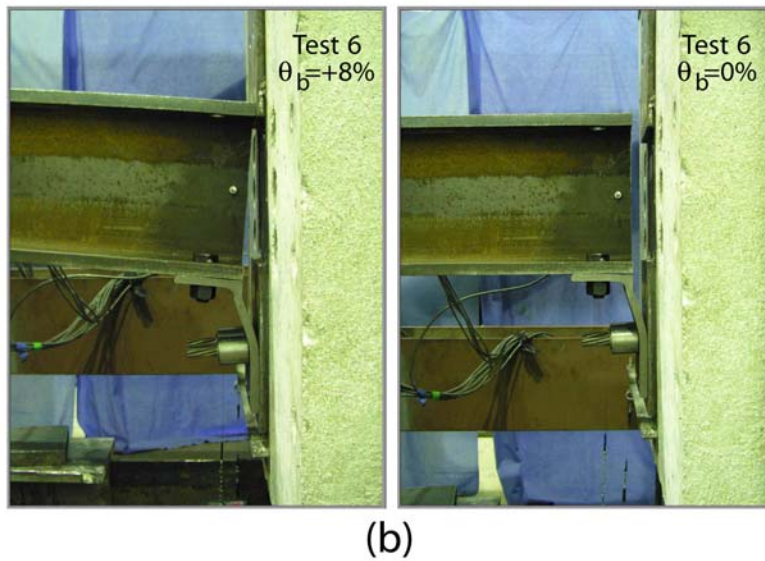
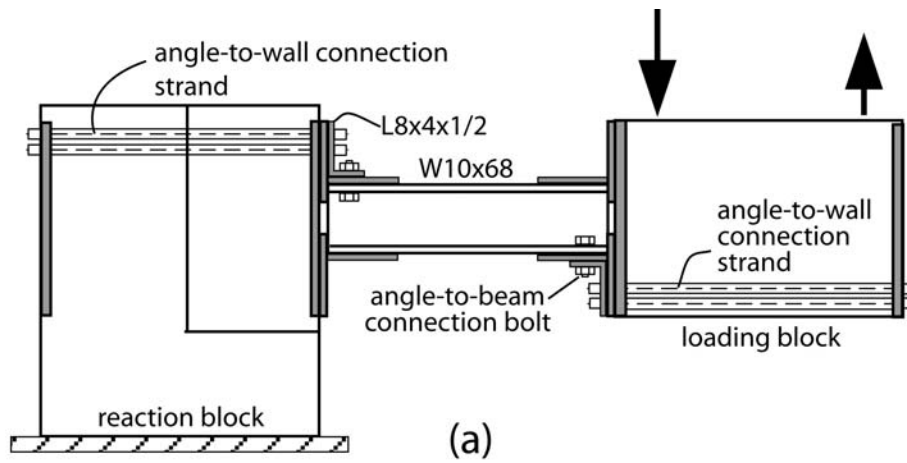


Fig. 9.37 Angle behavior (Tests 4, 6, 8, and 11): (a) test set-up; (b) deformed shape; (c) V_b - θ_b relationships

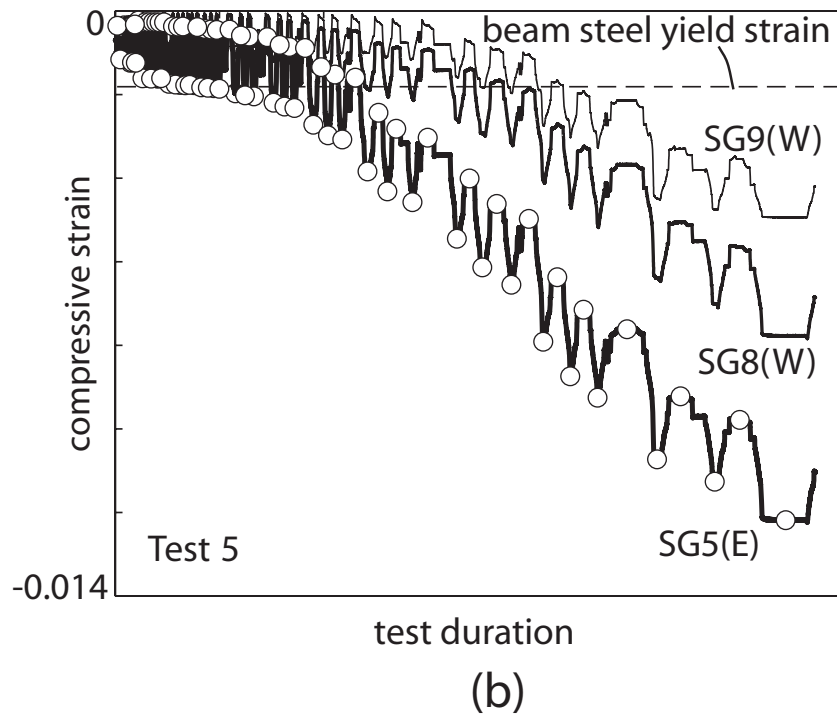
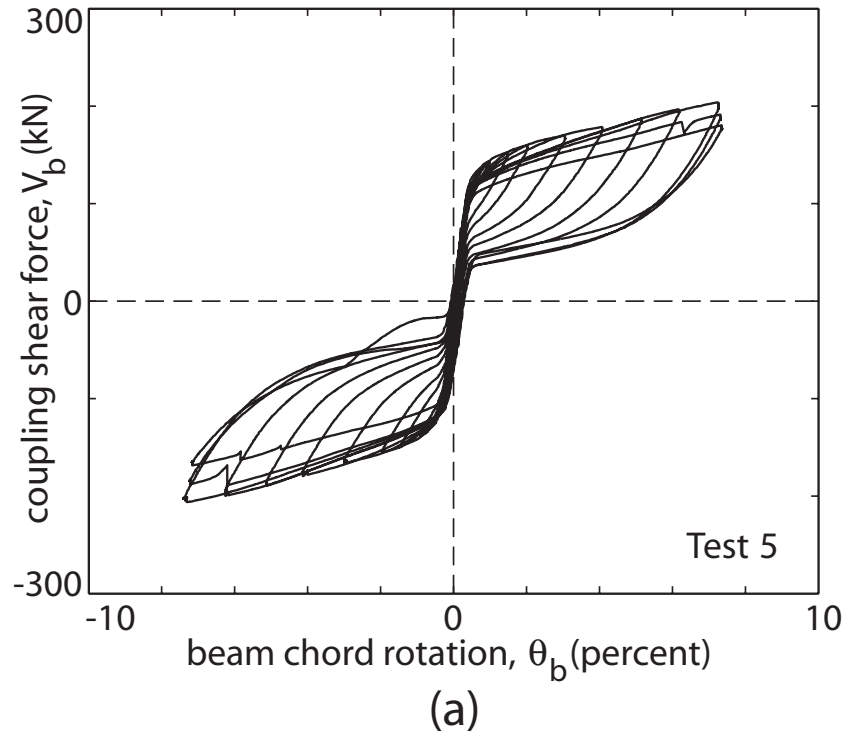


Fig. 9.38 Test 5: (a) V_b - θ_b relationship; (b) beam flange steel strains

9.2.3 Effect of Angle Thickness (Tests 7-8)

The primary variable between Tests 7 and 5 is the thickness of the top and seat angles; thicker L8×4×5/8 angles were used in Test 7 as compared with L8×4×1/2 angles in Test 5. Fig. 9.39 shows the measured V_b - θ_b hysteresis loops from Test 7, which demonstrate desirable characteristics with stable behavior up to $\theta_b=6\%$, large self-centering capability, and increased energy dissipation. Initiation of low cycle fatigue cracking was apparent in the vertical legs of the tension angles at $\theta_b=6\%$, resulting in a reduction in the coupling resistance and post-softening stiffness. Failure of the specimen occurred as a result of the complete fracture of the vertical leg of the seat angle at the north end of the beam when $\theta_b=+7\%$ was reached for the second time.

Compared with Test 5, the increase in the coupling strength and energy dissipation in Test 7 (see Figs. 9.38a and 9.39) occurred as a result of the thicker top and seat angles. This is shown using the results from a third monotonic angle test (Test 8) in Fig. 9.37c. The coupling beam from Test 7 was re-used in Test 8, with no beam post-tensioning strands and after replacing the angles.

As indicated by the self-centered hysteretic behavior in Fig. 9.39, the beam post-tensioning force in Test 7 was sufficient to yield the tension angles back in compression and close the gaps. The beam flanges remained stable during the entire test. The angle-to-wall connections also behaved satisfactorily, with no evidence of yielding in the connection strands or damage in the concrete blocks.

Different from the previous tests, slipping of the angle horizontal legs with respect to the coupling beam was more evident at rotations larger $\theta_b=6\%$, indicating that the slip critical capacity of the angle-to-beam bolts was not sufficient beyond this rotation. The

slip behavior resulted in the spikes in the hysteresis loops of Fig. 9.39. Early stiffening of the hysteresis curves at small rotations during unloading is also evident in Fig. 9.39, which occurred as the slipped angles came into contact with the loading and reaction blocks prior to the closing of the gaps at the beam ends.

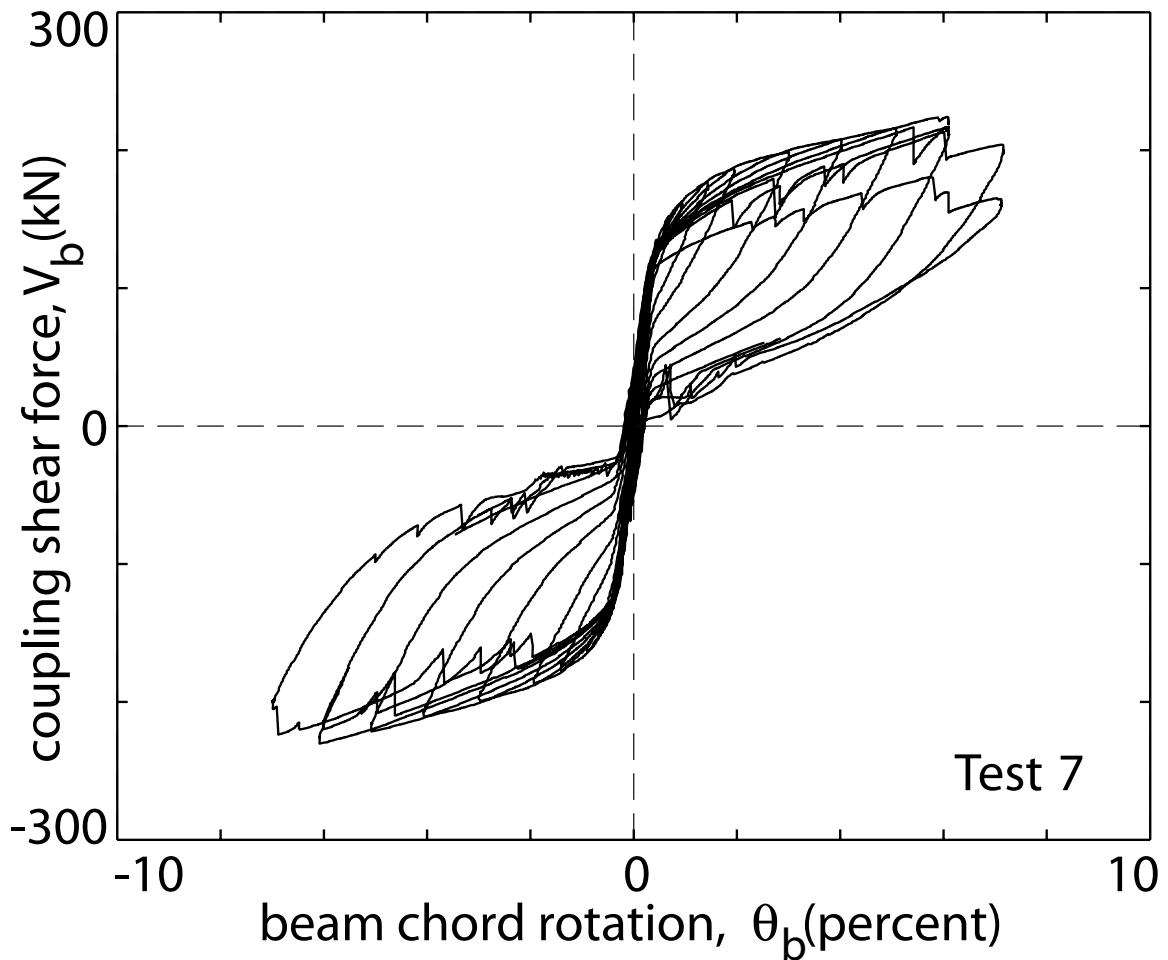


Fig. 9.39 V_b - θ_b relationship from Test 7

9.2.4 Effect of Beam Post-Tensioning Steel Area (Test 9)

Test 9 differs from Test 7 in the total area of the beam post-tensioning steel; six 15.2 mm diameter strands were used in Test 9 as compared with four strands in Test 7

(Table 9.1). No modifications were made in the angle-to-beam connections. Figs. 9.40a and 9.40(b) show the measured V_b - θ_b hysteresis loops and the total normalized beam post-tensioning force from Test 9, respectively. The results demonstrate stable behavior up to $\theta_b=7\%$ rotation and increased self-centering capacity. The strength of the subassembly is also increased as compared with Test 7. Slip in the angle-to-beam connections of Test 9 was more evident as compared with Test 7, (with first slip occurring at $\theta_b=4\%$) and resulted in the jagged hysteresis loops in Fig. 9.40a. The initiation of low cycle fatigue cracking in the angle vertical legs was apparent at $\theta_b=6\%$. Ultimate failure of the specimen occurred as a result of the complete fracture of the vertical leg of the seat angle at the south end of the beam when $\theta_b=-8\%$ was reached for the second time.

Table 9.1 shows the nominal beam flange initial stress after gap opening, calculated by normalizing the total measured initial force in the post-tensioning strands $P_{bi}=\sum a_{bp}f_{bpi}$ by $A_{bfc}f_{by}$, where A_{bfc} is the cross section area of one flange plus cover plate (if any) and f_{by} is the measured beam steel yield strength. Note that, for simplicity, the small difference between the measured yield strengths of the beam steel and cover plate steel in Tests 1-3 was ignored in this calculation. As a result of the larger beam post-tensioning force, the nominal flange initial stress in Test 9 is significantly larger than the initial stress in the other test beams. Fig. 9.40c shows the strain measurements from SG6, SG8, and SG9 in the top flange at the south end of the beam in Test 9. Flange yielding is increased significantly (with a maximum compression strain of, approximately, -0.084 , which is equal to $44\varepsilon_{by}$) as a result of the larger post-tensioning force; however, the beam remained stable during the test. As compared with Tests 3 (Fig. 9.33), 5, and 7, a larger

amount of prestress was lost during Test 9 (Fig. 9.40b), possibly because of the increased compression yielding, and thus, shortening of the beam. Minor spalling of the cover concrete in the wall test region occurred at the level of the beam flanges approximately 76 mm (3 in.) away from the beam-to-wall interface. The reaction block was patched and reused in the subsequent tests. It is concluded that the increased post-tensioning force resulted in increased, but still small levels of damage in the coupling beam and the wall concrete.

9.2.5 Effect of Beam Depth (Tests 10-11)

The main difference between Tests 10 and 7 is the coupling beam depth; a W14×99 beam was used in Test 10 as compared with a W10×68 beam in Test 7 (Table 9.1). The flanges of both beams were saw cut to a width of 159 mm (6.25 in.) as described earlier. Additional differences are: (1) the gage length, l_{gv} for the angle vertical legs in Test 10 (138 mm, 5.44 in.) was longer than the gage length in Test 7 (114 mm, 4.5 in., see Table 9.1); (2) two A490 Ø25.4 mm slip critical bolts were used in the angle-to-beam connections of Test 10 as compared with two A490 Ø22.2 mm bolts in Test 7; and (3) two post-tensioning strands were used in the angle-to-wall connections of Test 10 as compared with four strands in Test 7.

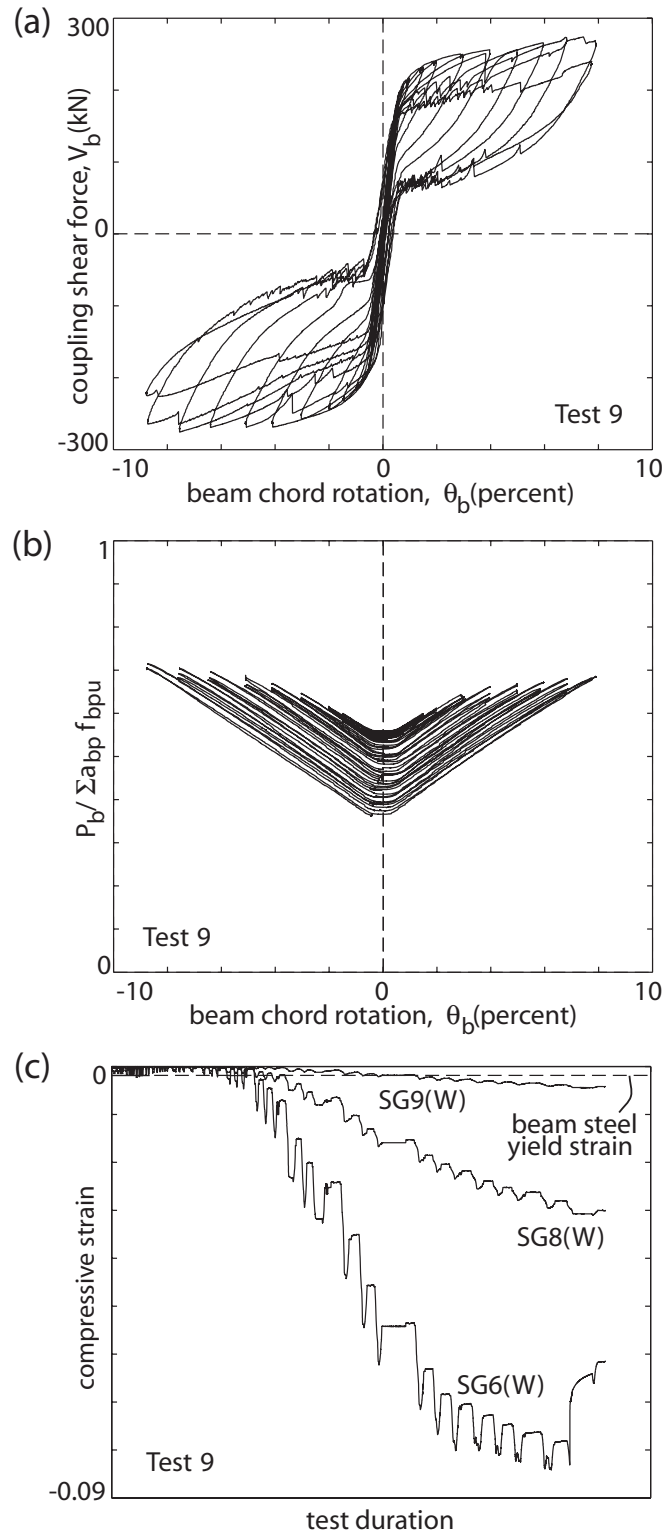


Fig. 9.40 Test 9: (a) V_b - θ_b relationship; (b) total beam post-tensioning force; (c) beam flange steel strains

Figs. 9.41a and 9.41b show the measured V_b - θ_b hysteresis loops and the total normalized beam post-tensioning force from Test 10, respectively. Although the subassembly performed well up to $\theta_b=5\%$, the behavior of the structure beyond this rotation was dominated by the failure of the beam post-tensioning strands. A wire in the bottom east post-tensioning strand fractured at a stress of 1364 MPa (well below the average maximum strength of $f_{bpu}=1698$ MPa from the material tests) at the end of the first cycle to $\theta_b=+5\%$, followed by simultaneous fractures of one wire each in the top east strand (at a stress of 1465 MPa) and top west strand (at a stress of 1497 MPa) at the end of the first cycle to $\theta_b=+6\%$, and subsequent post-tensioning wire fractures in the bottom east strand (second fracture) and bottom west strand (at a stress of 1525 MPa) during the second cycle to $\theta_b=+7\%$ and third cycle to -7% , respectively.

All strand wire fractures occurred inside the post-tensioning anchors, where the anchor teeth grip the strands at the live (north) end. The effects of these fractures on the V_b - θ_b hysteresis loops and on the total beam post-tensioning force are evident from Figs. 9.41a and 9.41b. As shown in Table 9.1, the initial stresses in the beam post-tensioning strands used in Test 10 were similar to the initial stresses in the previous tests. However, the largest stress reached in the strands during Test 10 was 1627 MPa, significantly higher than the stresses reached during the other tests. The increase in the gap widths as a result of the increase in the beam depth in Test 10 resulted in increased elongations, and thus, increased stresses in the post-tensioning strands.

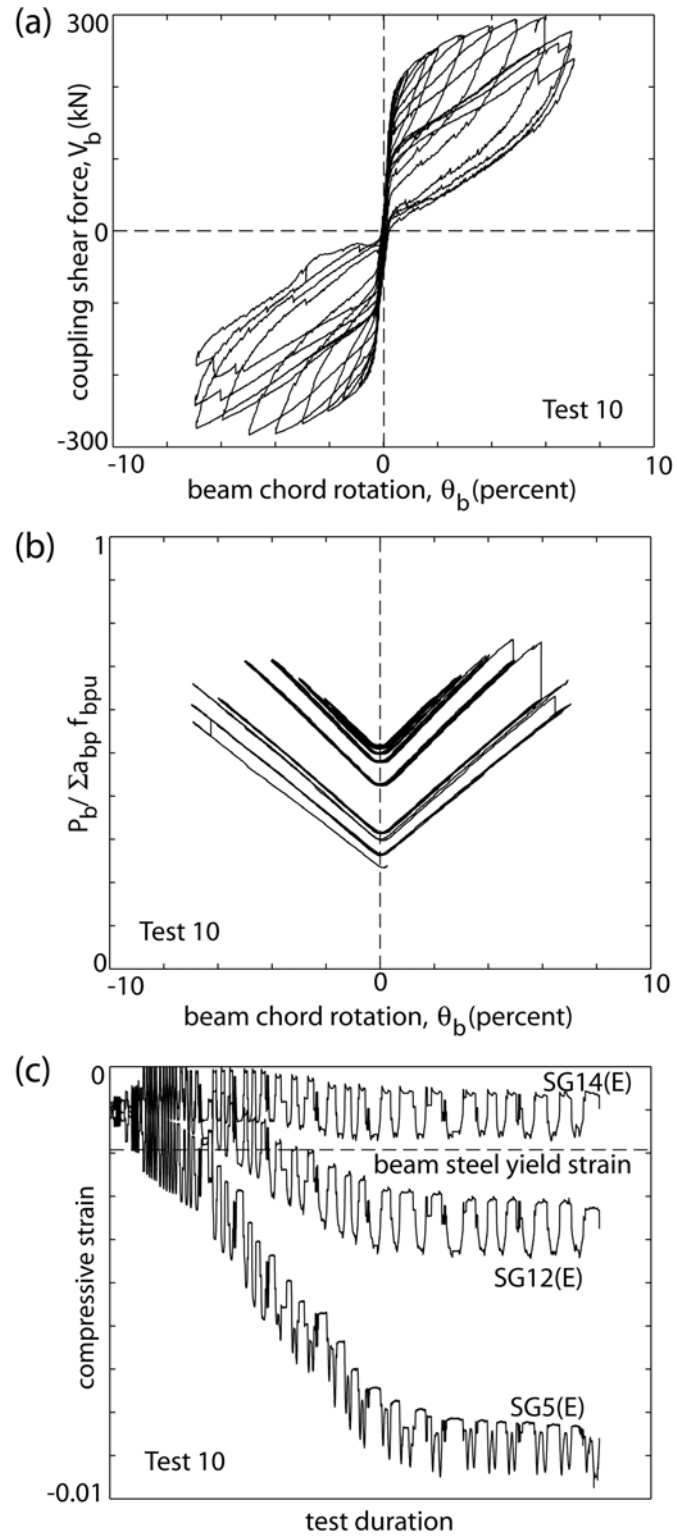


Fig. 9.41 Test 10: (a) V_b - θ_b relationship; (b) total beam post-tensioning force; (c) beam flange steel strains

Other than the premature strand failures, the results from Test 10 demonstrated the increased coupling shear strength due to the increased beam depth. Slip in the angle-to-beam connections was not observed due to the use of the larger bolts. The angle-to-wall connections also behaved well; however, a small amount of slip between the beam and the wall blocks occurred during second loading to $\theta_b = -5\%$, after a significant loss in the beam post-tensioning force due to strand fracture. It is possible that the slip occurred as a result of a reduction in the friction resistance at the beam-to-wall interfaces due to the loss in the total post-tensioning force.

Despite the fracture of multiple post-tensioning strand wires, the subassemblage maintained all or most of its coupling strength. Significant low cycle fatigue deterioration in the top and seat angles was observed upon first loading to $\theta_b = 7\%$. The ultimate failure of the specimen occurred as a result of the complete fracture of the vertical leg of the seat angle at the south end of the beam when $\theta_b = -7\%$ was reached for the third time. Fig. 9.41c shows the strains from beam flange gages SG5, SG12, and SG14. The strain in SG5 reached the beam steel yield strain at $\theta_b = -0.25\%$ (with a maximum compression strain of, approximately, -0.0097 , which is equal to $5.1\varepsilon_{by}$).

Test 11 was conducted to investigate the behavior of the angles in Test 10. The coupling beam from Test 10 was re-used with no beam post-tensioning strands and after replacing the angles. Different from the previous angle Tests 4, 6, and 8, the subassemblage in Test 11 had all four angles and was tested cyclically under the same displacement history as Test 10. Fig. 9.37c shows the measured V_b - θ_b hysteresis loops. The stiffening behavior at large displacements occurred as the compression angles came into contact with the reaction and loading blocks. Failure occurred as a result of the

complete fracture of the seat angle at the north end of the beam during loading to $\theta_b=+8\%$ for the third time. While the fracture of the angles in all of the previous tests occurred in the vertical leg as shown in Fig. 9.36, the failure of the angle in Test 11 occurred in the horizontal leg. As a result of the different angle failure mechanisms, it is questionable how well the results from Test 11 represent the behavior of the angles in Test 10, especially at large beam rotations.

9.3 Recommendations for Application

Based on the test results described above, it is concluded that properly-designed unbonded post-tensioned hybrid coupled wall subassemblages (e.g., Test 3) offer significant advantages for seismic regions, such as a self-centering capability and an ability to undergo large nonlinear rotations without significant damage (except in the sacrificial top and seat angles). The beam post-tensioning anchors and the angle-to-wall and angle-to-beam connections are critical components that can adversely affect the performance of these structures. Anchor types other than the steel wedge/barrel system used in this experimental program may improve the performance of the post-tensioning strands. It may also be possible to grout a short length of the post-tensioning tendons near the anchors to prevent premature fracture of the strands inside the anchors. Kinking of the post-tensioning strands during the experiments did not have any adverse effects on the performance of the strands.

The slip critical angle-to-beam connections used in the test specimens worked well. Slip at the angle-to-beam connections in Tests 7 and 9 was observed at relatively large rotations; however, Test 10 showed that it is possible to prevent this slip by ensuring that

the total slip capacity of the connection is larger than the maximum tension force developed in the angles. If the required slip capacity cannot be achieved using a bolted angle-to-beam connection, it may also be possible to weld the angles to the beam flanges. The post-tensioned angle-to-wall connections performed well, with no yielding in the connection strands and no damage in the concrete.

The beam-to-wall connections should be designed to transfer the maximum coupling shear forces without slip. Significant loss of the beam post-tensioning force in Test 10 resulted in a loss in the friction resistance against slip at the beam ends. It may be possible to increase the contribution of the top and seat angles against slip by fillet welding the vertical legs of the angles to the walls. It is important that this weld does not prevent the development of a ductile yield mechanism in the angle.

The experimental results showed that the use of cover plates on the coupling beam flanges is not necessary for nominal flange initial stress values (see Table 9.1) of up to 75% of the steel yield strength, as long as compact sections are used for the beams. The use of confinement reinforcement inside the wall contact regions and steel plates at the beam-to-wall interfaces is necessary to prevent damage to the wall concrete. The shim plates used in the experiments ensured contact between the beam flanges and the walls throughout the cyclic displacement history; and thus, their use in practice is recommended.

9.4 Chapter Summary

This chapter describes an experimental program on the nonlinear behavior of unbonded post-tensioned hybrid coupled wall subassemblages. The test results demonstrate that the proposed system can be designed to have excellent stiffness, strength, ductility, and energy dissipation characteristics under large reversed cyclic loading. The post-tensioning anchors and the angle-to-wall and angle-to-beam connections are critical components that can adversely affect the performance of the structure.

As a result of post-tensioning, the initial linear elastic stiffness of an unbonded post-tensioned hybrid coupled wall subassemblage is similar to the initial stiffness of a subassemblage with an embedded steel beam. The nonlinear deformations of properly designed systems occur primarily as a result of the opening of gaps at the beam ends. The post-tensioning force provides a restoring effect that closes these gaps and pulls the walls and the beam back towards their original undisplaced position upon unloading from a large nonlinear deformation, resulting in a self-centering capability. The structure can be designed to provide significant and stable levels of coupling with most of the damage occurring in the beam-to-wall connection angles, which can be replaced after an earthquake. It is concluded that unbonded post-tensioned steel beams provide an effective and feasible means to couple reinforced concrete walls.

CHAPTER 10

REVISED ANALYTICAL MODEL

This chapter makes modifications to the analytical models developed previously for unbonded post-tensioned hybrid coupled wall subassemblages to better capture the experimental measurements and observations from Chapter 9. These revised models are used in the remainder of this dissertation for the modeling, design, and analysis of coupled wall structures. The chapter is divided into the following sections: (1) revised subassemblage model; (2) evaluation of revised subassemblage model; and (3) revised idealized moment-rotation relationship.

10.1 Revised Subassemblage Model

This section makes modifications to the fiber element coupled wall subassemblage analytical model in Chapter 3, based on the experimental results from Chapter 9. The revised model is shown in Figs. 10.1a and 10.1b. The modeling of the wall-height elements and gap opening/closing behavior at the beam-to-wall interfaces remain unchanged. The modeling of the coupling beams and wall-contact regions, the beam post-tensioning tendons, and the top and seat angles are revised as follows. The assumptions for the subassemblage model can be found in Chapter 3.

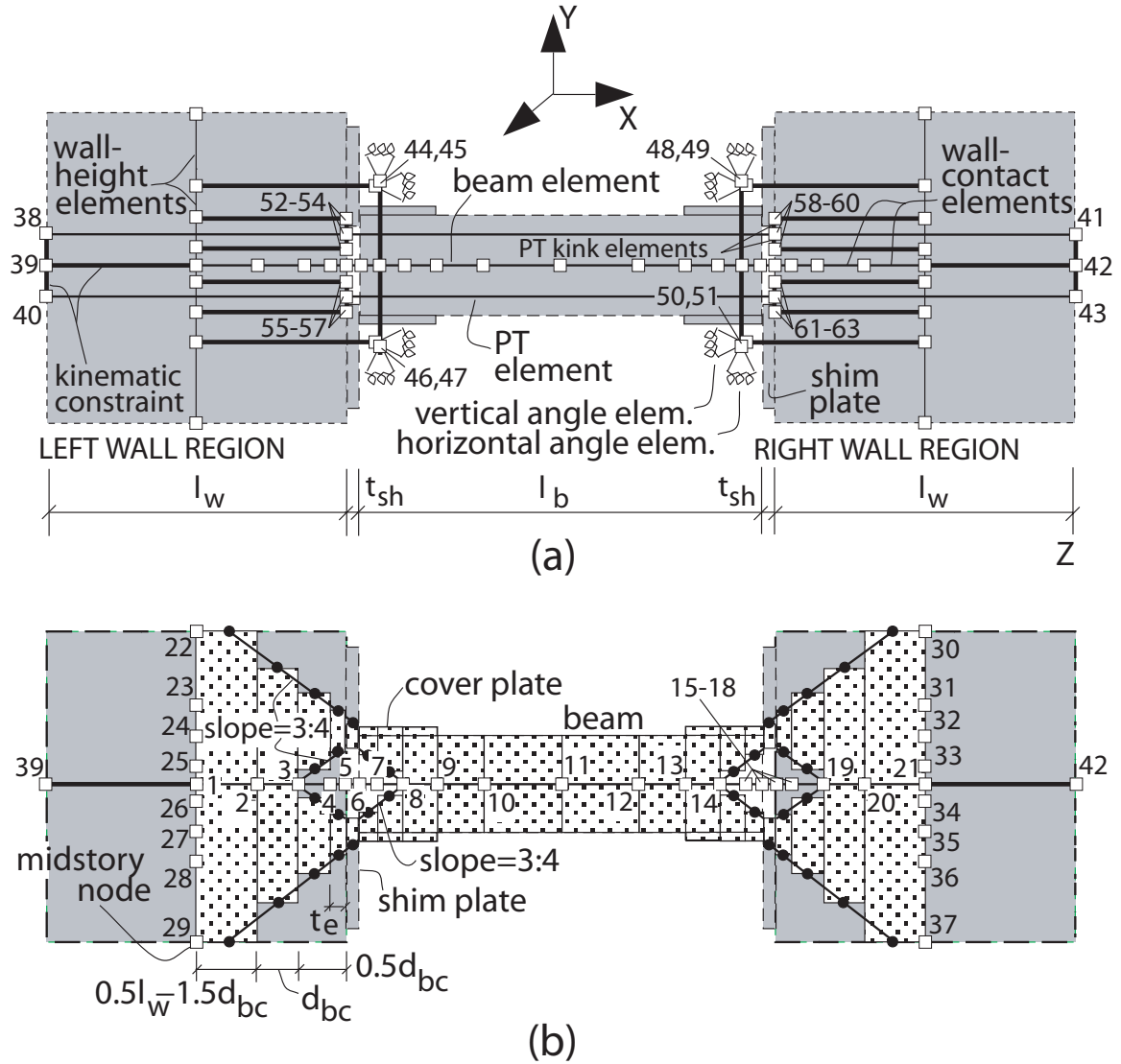


Fig. 10.1 Revised analytical model: (a) subassembly;
(b) wall-contact elements and beam elements

10.1.1 Modeling of Coupling Beams and Wall-contact Regions

As described in Chapter 9, the use of shim plates at the beam-to-wall interfaces is recommended to prevent contact between the coupling beam web and the walls, so that one or both flanges of the beam remain in contact with each wall during the reversed cyclic displacements of the structure, even after the yielding of the flanges in

compression. In practical applications, shim plates may also be used for construction/tolerance purposes.

The experiments described in Chapter 9 show that the shim plates may have a significant effect on the behavior of the subassemblies by limiting the contact depth at the beam-to-wall interfaces. The previous analytical model shown in Fig. 3.3a and 3.3b does not include the shim plates, allowing full contact between the beam and the walls at zero rotation. Three changes are made in the revised model to account for the shim plates (Fig. 10.1b): (1) the thickness of the shim plates is included in the model; (2) an “effective” beam cross-section is used in the fiber elements near the beam ends instead of the full cross-section; and (3) the “effective” cross-section of the wall-contact elements in Fig. 3.3b is revised. The dotted regions in Fig. 10.1b show the effective cross-sections used in the beam and wall-contact elements in the revised model, including the shim plates.

The depth of the effective beam cross-section adjacent to the shim plates is assumed to be equal to the depth (including the cover plates, if any) in contact with the shim plates (i.e., the depth between the shim plates is not included in the effective beam depth). The effective beam depth is assumed to increase away from the shim plates with a slope of 3:4 as shown in Fig. 10.1b. The shim plates are modeled as part of the wall-contact elements. The effective depth for the wall-contact elements is determined with a 3:4 slope spread away from the shim plates, similar to the effective beam depth. The compressive contact stresses in the beam and walls decrease away from the shim plates as a result of an increase in the depth of the compression region. The increase in the depth of

the effective beam and wall cross-sections represents this increase in the depth of the compression regions away from the shim plates.

The widths of the effective wall and beam cross sections are assumed to be equal to the wall thickness and beam flange/web width, respectively. The beam elements include second order effects due to the rotation of the beam with respect to the walls. The discretization of the fiber elements along the length of the beam is flexible with the following exceptions: (1) there are two beam nodes (Nodes 7 and 15 in Fig. 10.1b) located at the same X-coordinates as the angle element nodes (the angle element nodes are constrained to these beam nodes as described later); and (2) new fiber elements or segments are used where the effective beam depth becomes equal to the full depth of the beam and where the beam cover plates (if any) are terminated (in order to define the change in beam geometry). Furthermore, the length of the first beam fiber element segment adjacent to the shim plates is important in estimating the maximum compression deformations that occur at the beam ends. Similar to the previous model in Chapter 3, a length of $l_{b,cr}=2c_{b,sof}$ (Fig. 3.6) is used in this research, where $c_{b,sof}$ is the estimated depth of the compression (i.e., contact) region at the beam softening state.

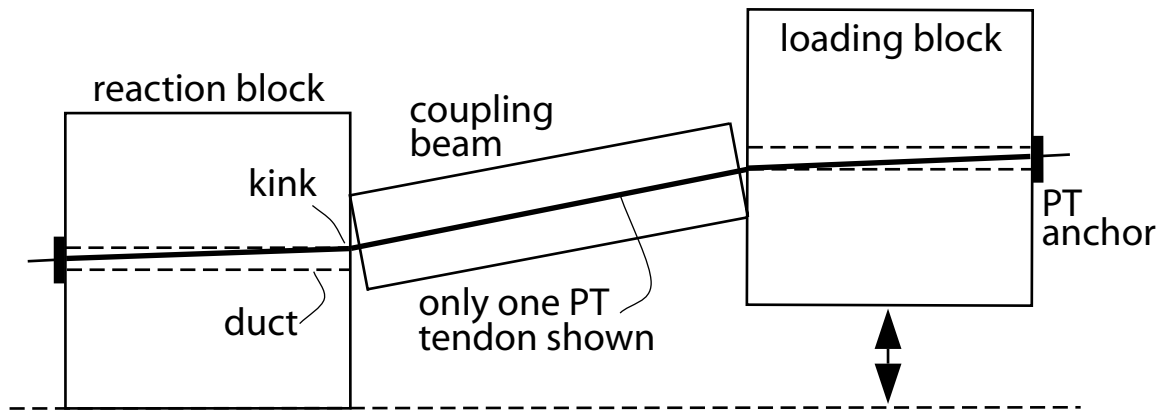
Fiber wall-contact elements are used between the center of the left wall region (Node 1) and the beam-to-shim-plate interface (Node 6). The Y-translational DOF of Node 6 is kinematically constrained to Node 1. The rotational and X-translational DOFs of Node 6 are not constrained. It is assumed that no slip occurs at the beam-to-shim-plate interface. The discretization of the wall-contact elements between Nodes 1 and 6 is flexible with the following exceptions: (1) the length of the first wall-contact element segment adjacent to Node 6 is equal to the shim plate thickness; and (2) new fiber

elements or segments are used to define changes in the properties of the effective wall cross-section (e.g., to model the wall embedded plates). The modeling of the right wall region is similar to the left wall region.

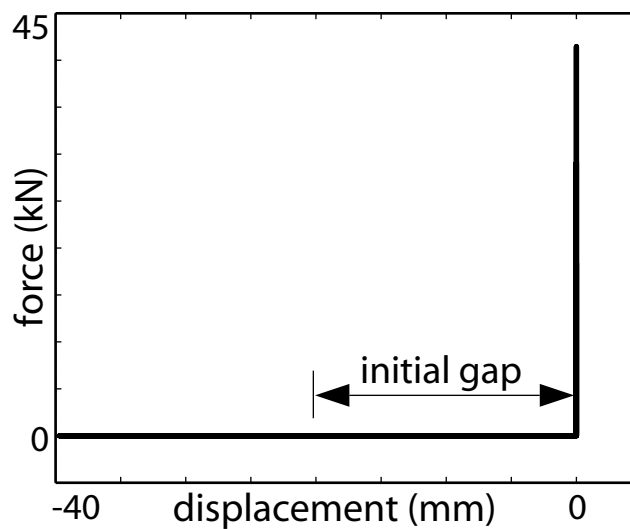
10.1.2 Modeling of Beam Post-Tensioning Tendons

As shown in Fig. 10.1a, three truss elements (e.g., see elements between Nodes 38-53-59-41) are used to model a beam post-tensioning tendon in the revised model, whereas only one truss element is used to model each tendon in the previous model (Fig. 3.3a). The objective of this modification is to model the kinking of the post-tensioning tendons at the beam ends, which occurs when the displacement of the structure is large enough to cause the tendons to come into contact with the post-tensioning ducts (Fig. 10.2a). As observed in the subassembly experiments described in Chapter 9, kinking of the beam post-tensioning tendons results in an increase in the coupling resistance and stiffness due to increased second order effects in the tendons.

In the revised analytical model, the truss elements representing a beam post-tensioning tendon are connected to each other at nodes (e.g., Node 53) located at the beam-to-wall interfaces. These nodes are free to move in the horizontal direction (since the post-tensioning tendons are unbonded), but are kinematically constrained from moving in the vertical direction by gap/contact “PT kink” elements above and below. Each PT kink element is connected to a second node (e.g., Node 52), which is kinematically constrained to a wall-height element node at the same elevation (Node 24).



(a)



(b)

Fig. 10.2 Kinking behavior: (a) idealized deformed shape;
(b) gap/contact PT kink element

The force-displacement relationship of the gap/contact PT kink elements is shown in Fig. 10.2b. An initial gap is defined to model the distance between the outside of the post-tensioning tendon and the inside of the post-tensioning duct. The initial gap is zero if the ducts are not oversized with respect to the tendon diameter. The forces in the PT kink elements are initially zero. Contact between the post-tensioning tendons and the ducts occurs when the displacement of the structure is large enough to close the initial gap.

Once in contact, the PT kink elements constrain further vertical displacements of the post-tensioning truss element nodes at the beam-to-wall interfaces, modeling the effect of kinking. Second order effects are included in the truss elements to capture the increase in the coupling resistance and stiffness of the subassembly due to kinking.

10.1.3 Modeling of Top and Seat Angles

In the previous analytical model, the contribution of the top and seat angles to the coupling resistance was represented using fiber elements placed parallel to the coupling beam (see Chapter 3). Based on the experimental results from Chapter 9, three modifications are made to this model: (1) zero-length translational spring elements are used to model the angles instead of fiber elements; (2) the hysteretic model for the angle elements placed parallel to the coupling beam is revised; and (3) the shear force in the horizontal legs of the angles is modeled.

In the revised model, each angle is represented using two translational zero-length spring elements in the X- and Y-directions, respectively (Fig. 10.1a). The first spring element, which is placed in the horizontal (i.e., X) direction parallel to the beam, represents the axial force in the horizontal leg of the angle and is referred to as the “horizontal angle element.” The second element, referred to as the “vertical angle element,” is in the vertical (i.e., Y) direction and represents the shear force in the angle horizontal leg. Both elements are connected to the same pair of nodes (e.g., Nodes 44 and 45) with identical coordinates at the centroid of the angle-to-beam connection bolts and at the same elevation as the middle of the angle horizontal leg thickness. It is assumed that the angle-to-wall and angle-to-beam connections are properly designed for the maximum

angle forces and deformations. Based on this assumption, one of the angle nodes (e.g., Node 44) is kinematically constrained to a wall-height element node at the same elevation (Node 23) and the other angle node (Node 45) is kinematically constrained to a corresponding beam node (Node 7).

The behavior of an angle as it is loaded by the beam is governed by many factors including the angle leg thickness, and the number, size, layout, and gage length of the angle connectors. Fig. 10.3a shows the idealized deformed shape of a seat angle as it is pulled and rotated by the coupling beam. It is assumed that the failure of the angle occurs through the formation of two plastic hinges in the vertical leg. As described in Sims (2000), other angle failure modes (e.g., an additional plastic hinge in the horizontal leg) may be possible; however, this was not observed in the subassembly experiments presented in Chapter 9, and thus, is not modeled. The relatively short connection gage length for the horizontal legs of the angles in the half-scale test specimens may have played a role in the observed angle failure mode. Full scale subassembly tests need to be conducted to investigate the possibility of other angle failure mechanisms.

Fig. 10.3a shows the angle free body diagram between the plastic hinge adjacent to the angle fillet on the vertical leg and the centroid of the angle-to-beam connector bolts on the horizontal leg. Using equilibrium of the angle forces, it can be shown that:

$$T_{ayx} = V_{ap} \quad (10.1)$$

$$T_{ayy} = \frac{M_{ap} + V_{ap}(k_a - \frac{t_a}{2})}{l_{gh} - \frac{t_a}{2}} \quad (10.2)$$

where, T_{ayx} is the axial force in the angle horizontal leg, T_{ayy} is the shear force in the horizontal leg, M_{ap} is the plastic hinge moment and V_{ap} is the plastic shear force in the

vertical leg including shear-flexure interaction, k_a is the distance from heel to toe of fillet of the angle, l_{gh} is the gage length of the angle-to-beam connectors (measured from heel of the angle to the centroid of the angle-to-beam connector bolts), and t_a is the angle leg thickness. The angle moment M_a at the centroid of the angle-to-beam connector bolts is ignored.

Horizontal angle element force-deformation model

The force-deformation relationship of the horizontal angle element is shown in Fig. 10.3b, where the hysteretic characteristics were determined based on the subassembly experiments as described later. A new type of zero-length spring element was developed in DRAIN-2DX to model the hysteretic behavior in Fig. 10.3b. Under tensile loading, the “yield” strength, $T_{ayx}=V_{ap}$ [see Equation (10.1)] and initial stiffness, K_{aixt} are determined the same as the previous model in Chapter 3 using a method developed by Kishi and Chen (1990) and Lorenz et al. (1993). In this model, the vertical leg is assumed to be fixed along the innermost edge of the line of angle-to-wall connectors and is pulled horizontally by the coupling beam flange like a cantilever. The rotation of the horizontal leg with respect to the vertical leg, which occurs as a result of the rotation of the beam with respect to the walls, as shown in Fig. 10.3a, is ignored. The “yield” strength, T_{ayx} is reached when the two plastic hinges in Fig. 10.3a develop, considering the interaction between the bending moment and shear force in the vertical leg.

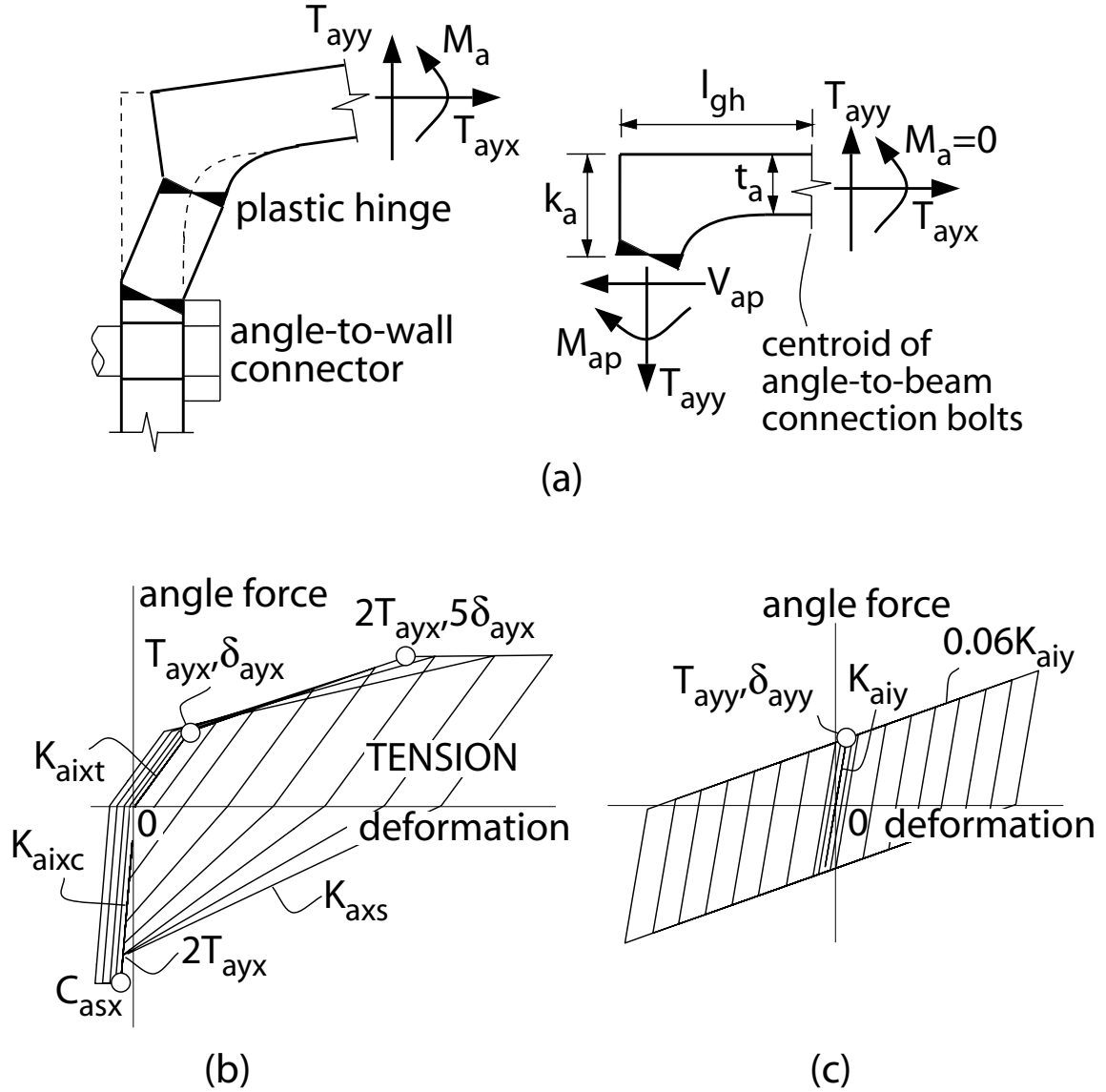


Fig. 10.3 Angle model: (a) angle displacements and forces;
(b) horizontal angle element; (c) vertical angle element

Based on the subassembly experiments, it is assumed that the maximum strength of the horizontal angle element in tension is equal to 2 times the yield strength, T_{ayx} , and is reached at an angle deformation of 5 times the yield deformation, $\delta_{ayx} = T_{ayx}/K_{aixt}$.

Under compression, the initial stiffness of an angle as it is pushed back horizontally toward the wall by the coupling beam is assumed to be equal to:

$$K_{aixc} = \frac{1}{40} \frac{E_a A_a}{l_{gh}} \geq K_{aixt} \quad (10.3)$$

where, E_a is the Young's modulus for the angle steel, A_a is the gross cross-section area of the angle horizontal leg. The angle unloading stiffness from a tensile force is assumed to be the same as the initial stiffness in tension, K_{aixt} , and the stiffness upon crossing the zero-force axis is assumed to be equal to the “shooting” stiffness, K_{axs} .

The angle force-deformation behavior is assumed to shoot towards the smallest of the following three forces on the initial linear-elastic loading branch in compression: (1) a compressive force with magnitude equal to the unloading force in tension; (2) the compression force reached assuming $K_{axs}=K_{aixt}$; and (3) the “yield” strength of the angle in compression. The yield strength of the angle in compression is assumed to be equal to the slip force, C_{asx} of the angle-to-beam connection bolts. The development of the full bearing capacity of the angle horizontal leg cross-section is not expected, and, is not modeled since analyses and experiments of coupled wall subassemblages show that extremely small deformations occur in an angle once the beam flange comes into contact with the wall.

Note that slip of the angle-to-beam connector bolts can also occur when the angle is pulled away from the wall (i.e., tension loading direction in Fig. 10.3b); however, this is not a desirable type of behavior since it would be difficult to control the amount of slip. In Fig. 10.3b, the slip critical capacity of the angle-to-beam bolts, C_{asx} is larger than the assumed angle capacity in tension, $2T_{ayx}$, and thus, slip does not occur in tension. A design approach to achieve the desired behavior of the angles is described in Chapter 12.

Vertical angle element force-deformation model

The vertical angle element models the shear force in the angle horizontal leg using an elasto-plastic force-deformation behavior as shown in Fig. 10.3c. The “yield” force T_{ayy} is determined from Equation (10.2), with M_{ap} and V_{ap} calculated as recommended by Kishi and Chen (1990) ignoring the rotation of the horizontal angle leg with respect to the vertical leg. Assuming that T_{ayx} and T_{ayy} are reached at the same coupling beam chord rotation and that the rotation of the beam occurs about the compression corner, the initial stiffness, K_{aiy} of the vertical angle element can be determined as:

$$K_{aiy} = K_{aixt} \frac{T_{ayy}}{T_{ayx}} \frac{d_{bc}}{l_{gh}} \quad (10.4)$$

where, d_{bc} is the depth of the coupling beam including the cover plates (if any). The post-yield stiffness of the vertical angle element is assumed to be equal to 6% of the initial stiffness, K_{aiy} .

Note that the modeling of the angles as described above assumes that the contributions of the vertical and horizontal angle elements can be superposed, even though this assumption is in general not valid in the nonlinear range. Note also that the contribution of the vertical angle element to the subassembly behavior is small as compared with the horizontal angle element, and thus, can be ignored. The evaluation of the revised analytical model below includes the vertical angle elements to achieve better comparisons with the experimental results; however, these elements are ignored in the multi-story analyses in the remainder of this dissertation.

10.2 Evaluation of Revised Subassemblage Model

This section provides a critical evaluation of the revised analytical model based on the subassemblage experiments in Chapter 9. Comparisons between experimentally measured and analytically predicted behaviors are presented with respect to the following: (1) coupling shear force versus chord rotation behaviors; (2) coupling beam post-tensioning forces; (3) behavior at coupling beam ends; (4) behavior along beam span; and (5) behavior of top and seat angles. The analytical models use the material test results from Chapter 9.

10.2.1 Coupling Shear Force versus Chord Rotation Behaviors

Fig. 10.4 shows the predicted coupling shear force versus chord rotation (V_b - θ_b) behaviors for Tests 1, 3, 5, 7, 9, and 10 using the revised analytical model. The measured behaviors in Chapter 9 are not plotted with the predicted results to maintain clarity in the hysteresis curves. Note that the analytical cycle rotation amplitudes are very close to but not the same as the actual rotations reached during each experiment. For comparison, Fig. 10.5a shows the predicted behavior for Test 3 using the previous model from Chapter 3. The previous model is able to capture the envelope of the measured V_b - θ_b behavior; however, the behavior of the specimen during unloading is not represented well. The force-deformation behavior of an angle element during Test 3 using the previous model and the behavior of a horizontal angle element from the revised model are shown in Figs. 10.5b and 10.6a, respectively. The improved hysteretic characteristics of the revised model in Fig. 10.4b as compared with Fig. 10.5a are primarily due to the differences in the modeling of the angles as well as the other modifications presented previously.

For comparison, the force-deformation behavior of a vertical angle element from the revised analytical model for Test 3 is shown in Fig. 10.6b; and Fig. 10.6c shows the predicted $V_b-\theta_b$ behavior for Test 3 using the revised analytical model with the vertical angle elements removed. It is observed that the vertical angle elements have relatively a small effect on the behavior of the structure.

The results in Fig. 10.4 indicate that the revised analytical model provides a good representation of the global behavior of the test specimens across the entire parameter range. The increase in the coupling resistance and stiffness due to the kinking of the post-tensioning strands in Test 1 is captured. Note that this effect is not evident in the $V_b-\theta_b$ behaviors of the other test specimens since the kinking of the post-tensioning strands occurs at large rotations (due to the use of oversized post-tensioning ducts) and the increase in stiffness due to kinking is counteracted by the reduction in stiffness due to deterioration in the top and seat angles. The failure of the test specimens (i.e., reduction in the coupling resistance) due to low cycle fatigue fracture of the angles or due to fracture of the post-tensioning strands is not captured by the analytical model. Slip at the beam-to-wall interfaces or at the angle-to-wall and angle-to-beam connections is also not included in the model.

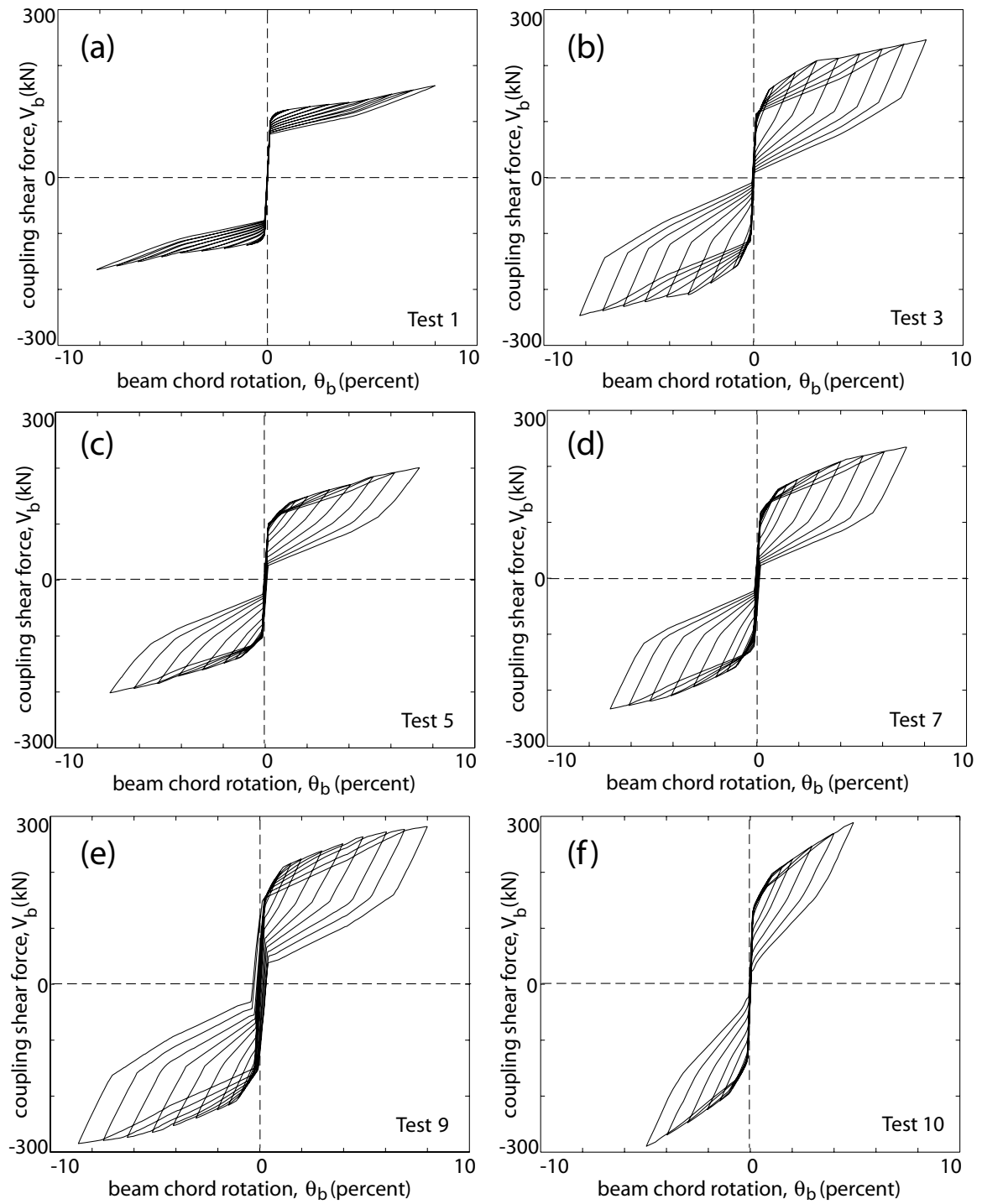


Fig. 10.4 Coupling shear force versus rotation (V_b - θ_b) behaviors: (a) Test 1; (b) Test 3; (c) Test 5; (d) Test 7; (e) Test 9; (f) Test 10

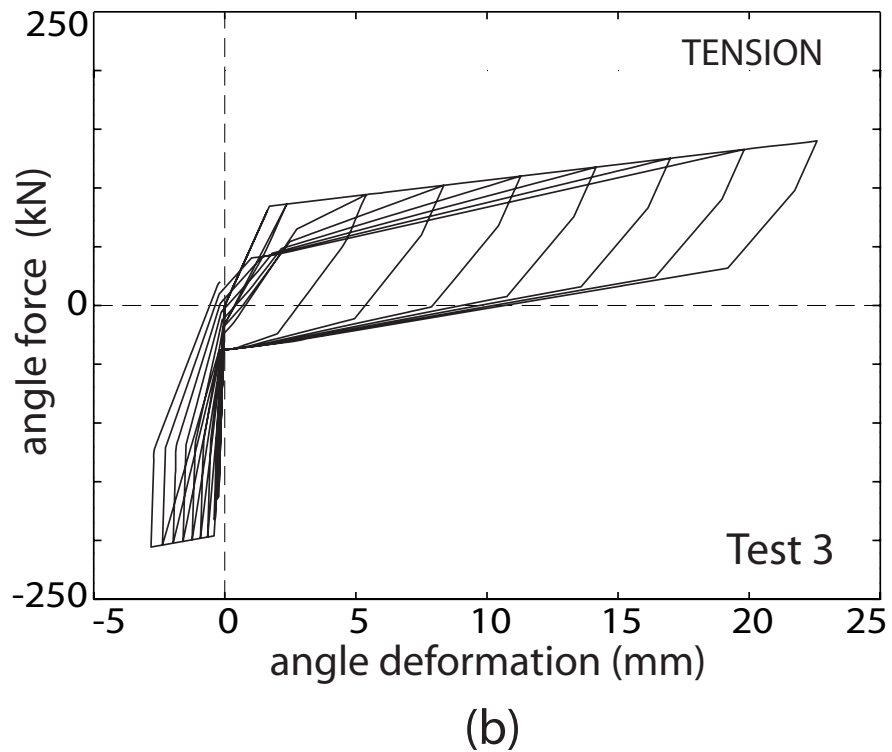
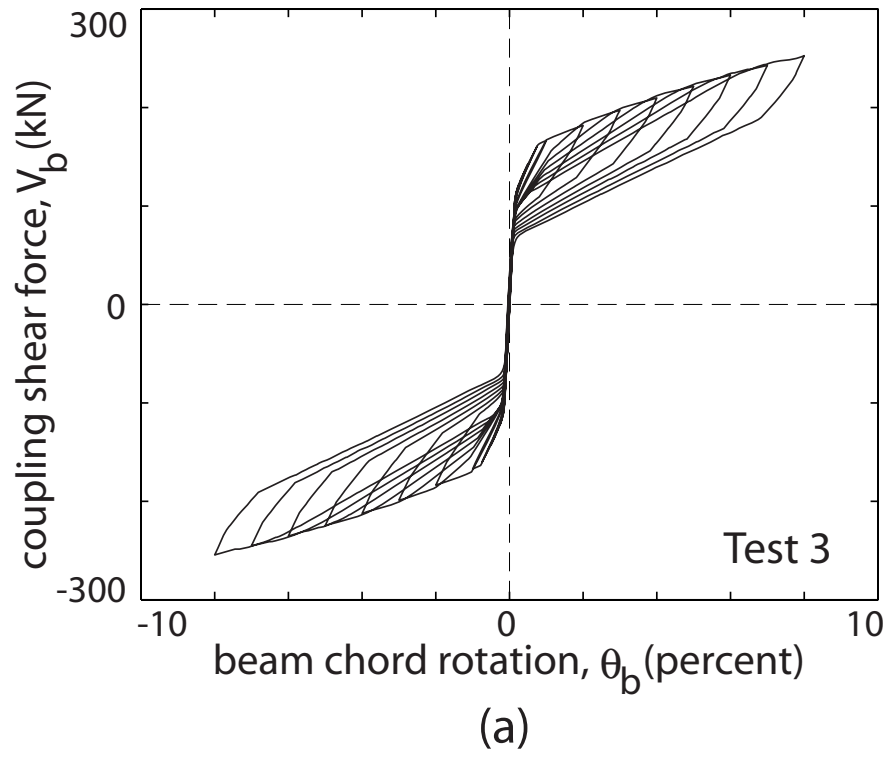


Fig. 10.5 Test 3 predictions using the previous model:
 (a) V_b - θ_b behavior; (b) angle behavior

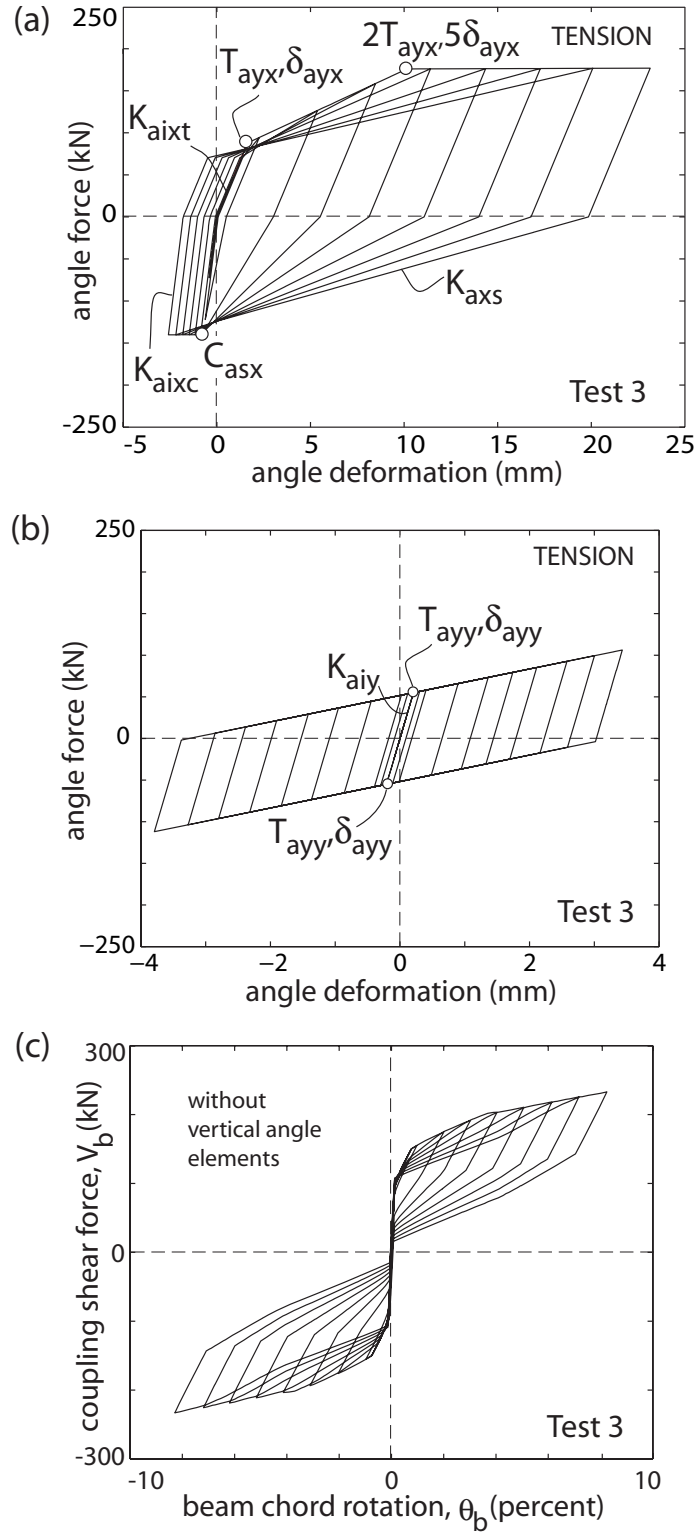


Fig. 10.6 Test 3 predictions using the revised model: (a) horizontal angle element; (b) vertical angle element; (c) model with vertical angle elements removed

10.2.2 Coupling Beam Post-Tensioning Forces

Fig. 10.7 shows the predicted results for the total post-tensioning forces (i.e., sum of the forces in the post-tensioning strands) from Tests 3, 9, and 10 using the revised analytical model. The total post-tensioning force is normalized by the design maximum strength of the strands, $P_{bu} = \Sigma a_{bp} f_{bpu}$, where $a_{bp} = 140 \text{ mm}^2$ (0.217 in^2) is the area of a single strand and $f_{bpu} = 1862 \text{ MPa}$ (270 ksi) is the design maximum strength of the post-tensioning steel. Comparisons of the predicted forces with the measured forces in Chapter 9 indicate that the analytical model is capable of predicting not only the increase in the post-tensioning force due to the displacements of the subassembly, but also the loss in the post-tensioning force (upon unloading to zero displacement) due to nonlinear behavior in the structure. The fracture of the post-tensioning tendons in Test 10 is not modeled.

The results in Fig. 10.7 show that the analytical model overestimates slightly the increase in the total beam post-tensioning force as the subassembly is displaced. To investigate this difference, Fig. 10.8 compares the measured and predicted displacements of the loading block in the horizontal direction as the beam is rotated. The positive displacements indicate that the loading block moves away from the reaction block. These horizontal displacements, which occur primarily due to the opening of gaps at the beam-to-wall interfaces, are directly related to the total elongations of the post-tensioning strands, and thus, the post-tensioning forces. Note that the measured displacements in Fig. 10.8 are upon first loading to peak θ_b values during the loading history followed in each test. The displacements corresponding to the same θ_b amplitude in the positive and negative loading directions are averaged. The comparisons indicate that the analytical model overestimates the horizontal displacements of the loading block at large rotations,

and thus overestimates the elongations of the post-tensioning tendons, resulting in the overestimated post-tensioning forces in Fig. 10.7.

10.2.3 Behavior at Coupling Beam Ends

To evaluate the capability of the revised analytical model in predicting the behavior at the coupling beam ends, Fig. 10.9 compares the measured and predicted results for the “average” compressive strains in the beam contact regions from Tests 1, 3, 5, 7, 9, and 10. Beam cover plate (for Test 1) and flange (for Tests 3, 5, 7, 9, and 10) strain gages SG5-SG22 were used for this purpose, with locations as given in Chapter 9.

The procedure to calculate the average strains from the measured data is demonstrated using strain gages SG15-SG22 in Fig. 10.10. The following steps are used: (1) for each strain gage, take the average of the peak compression strain values (occurring at peak θ_b values; e.g., see \square markers in Fig. 10.10a for SG22 during Test 1) from the three cycles during each set of displacement cycles; (2) take the average of the average peak compression strains from the gages located at the same distance from the beam end (i.e., average from strain gages SG15, SG16, SG19 and SG20 located 6.35 mm from the beam end, and strain gages SG17, SG18, SG21 and SG22 located 25.35 mm from the beam end, as shown in Fig. 10.10b); (3) assume a uniform strain distribution over the “influence length” for each set of strain gages (i.e., uniform strain distribution over a length of 15.85 mm for SG15, SG16, SG19 and SG20 and over a length of 19 mm for SG17, SG18, SG21 and SG22); (4) use the uniform strain distributions to calculate the total compressive deformation at the end of the beam (over a total length of 34.85 mm for strain gages SG15-SG22 in Fig. 10.10b); and (5) calculate the average strains by dividing the total deformation with the total length considered (i.e., 34.85 mm in Fig. 10.10b).

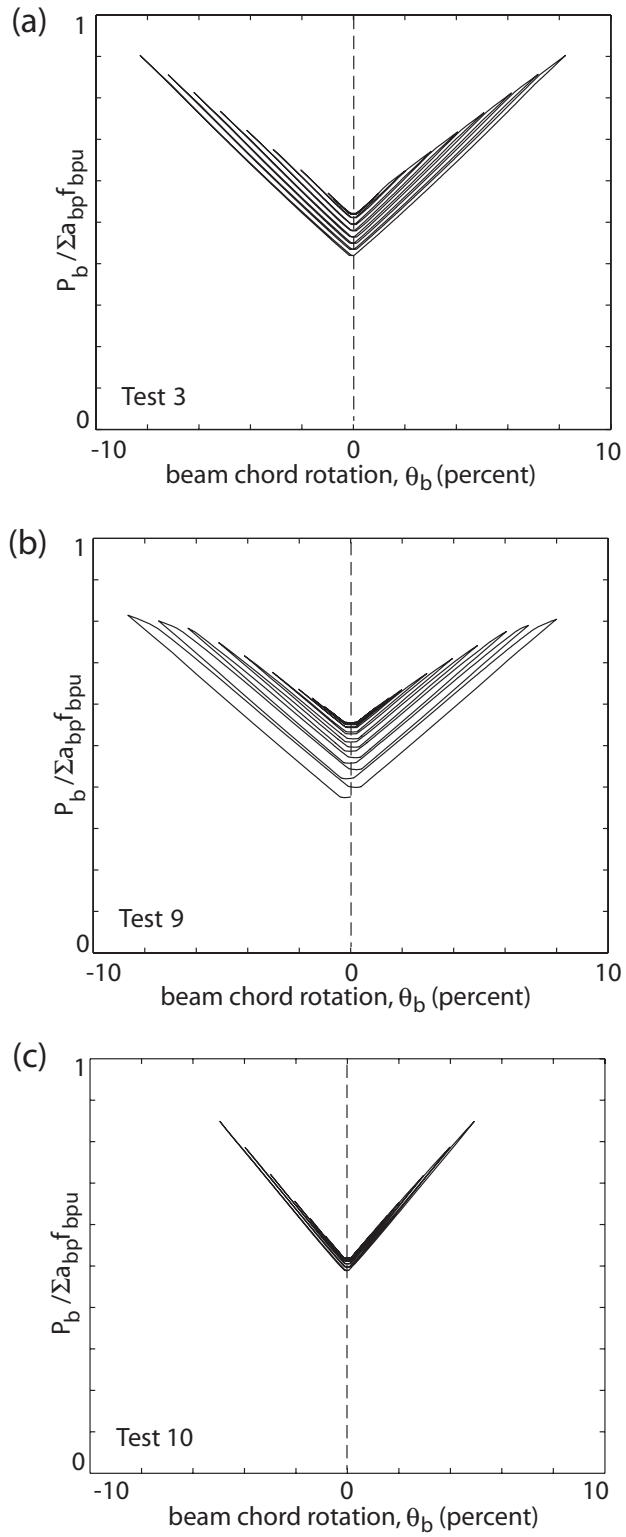


Fig. 10.7 Post-tensioning forces: (a) Test 3; (b) Test 9; (c) Test 10

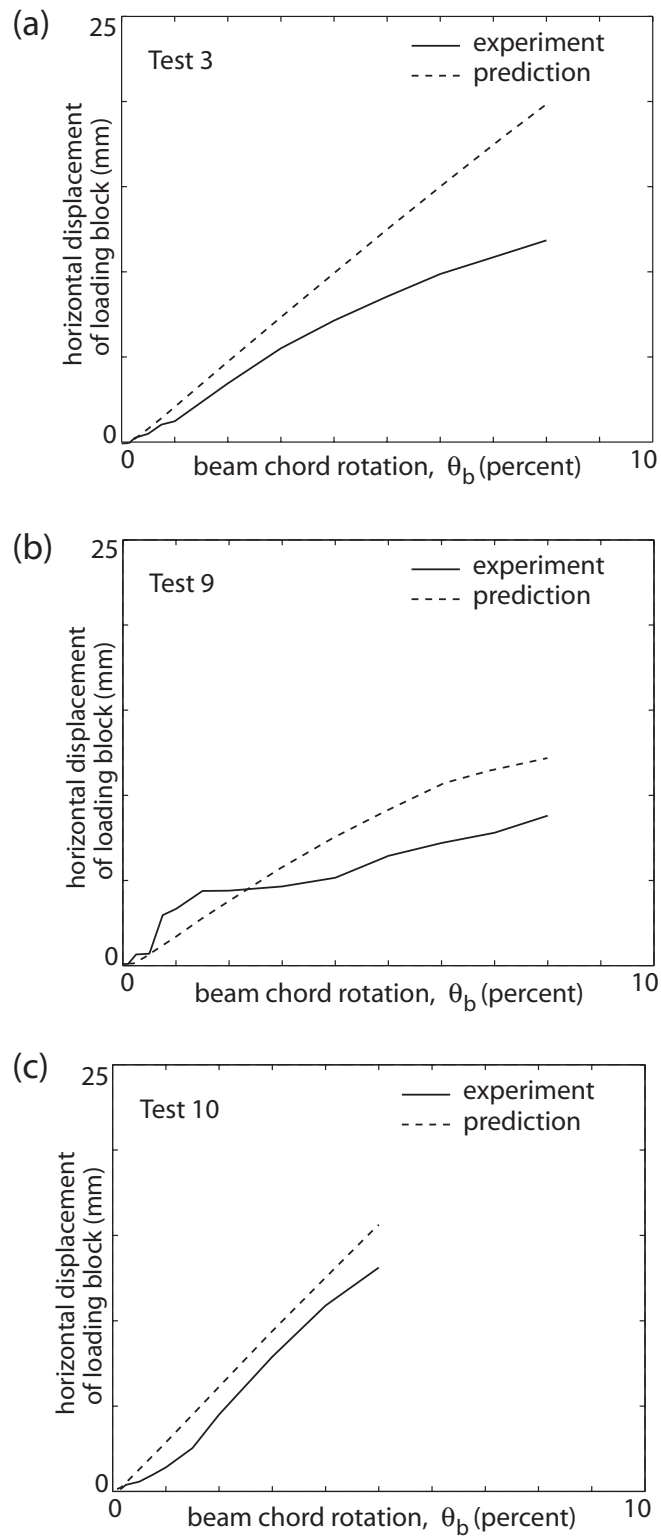


Fig. 10.8 Horizontal displacements of loading block: (a) Test 3; (b) Test 9; (c) Test 10

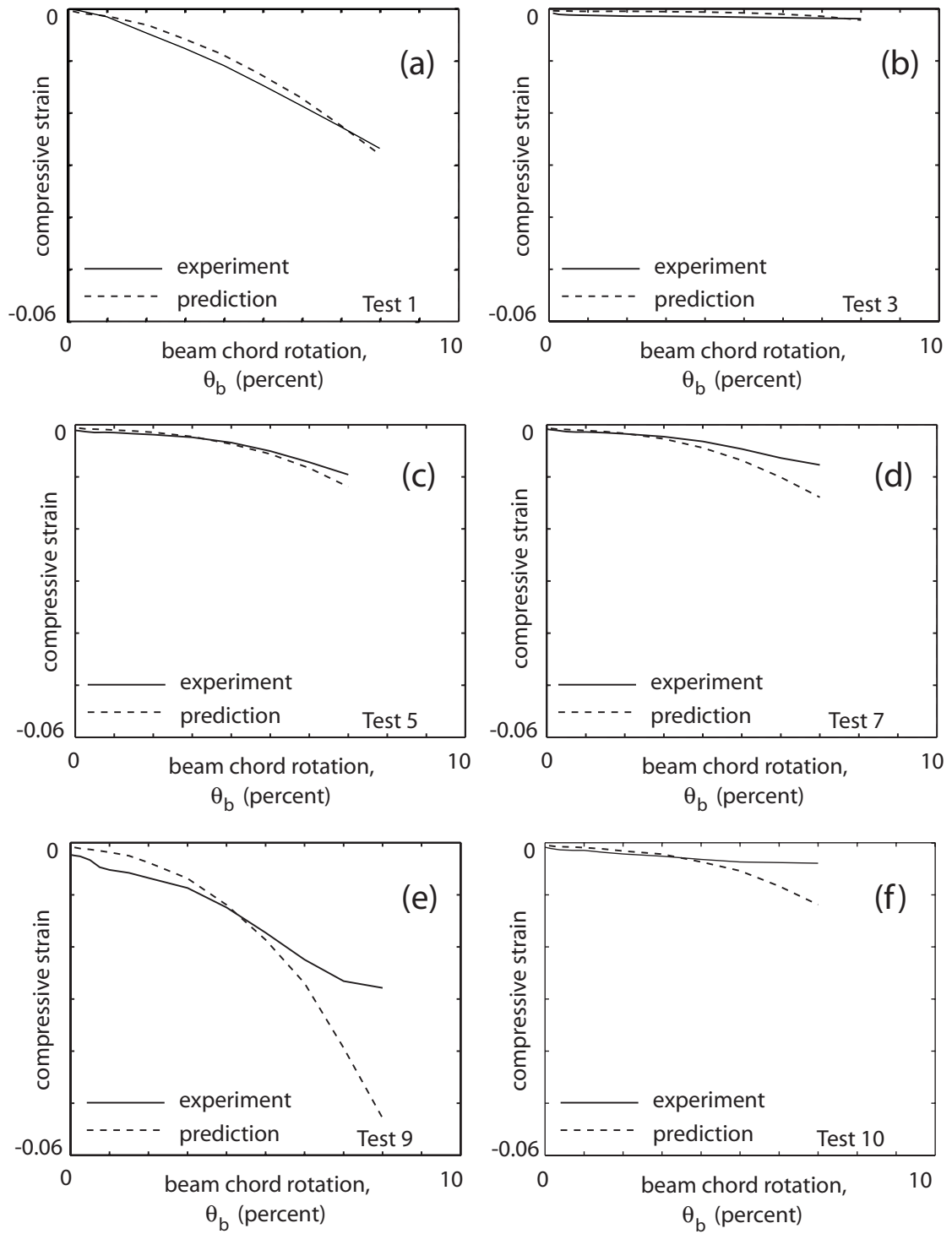
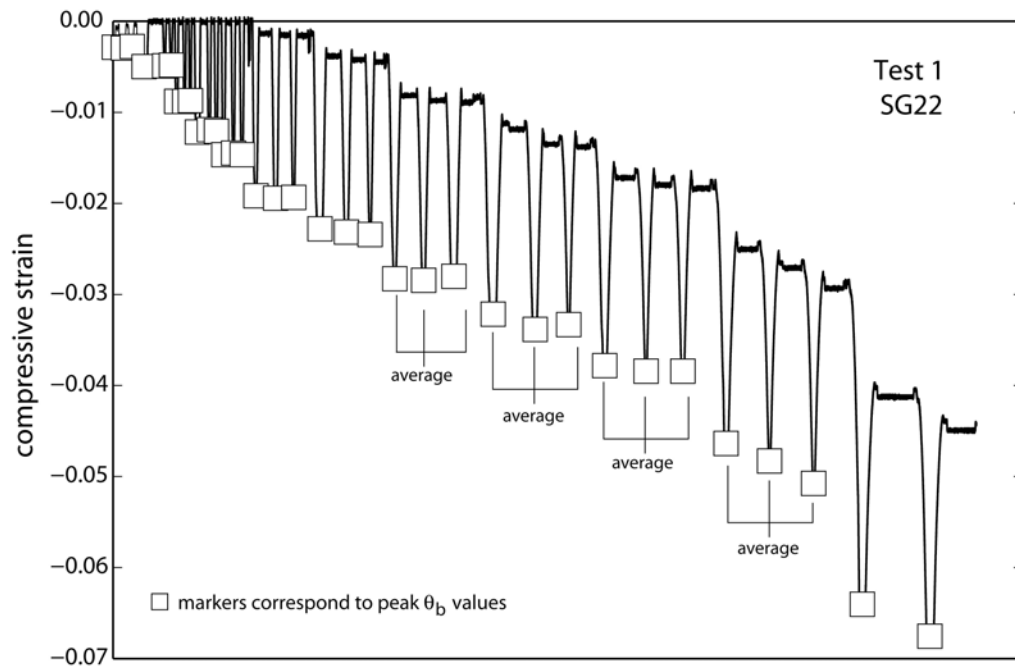
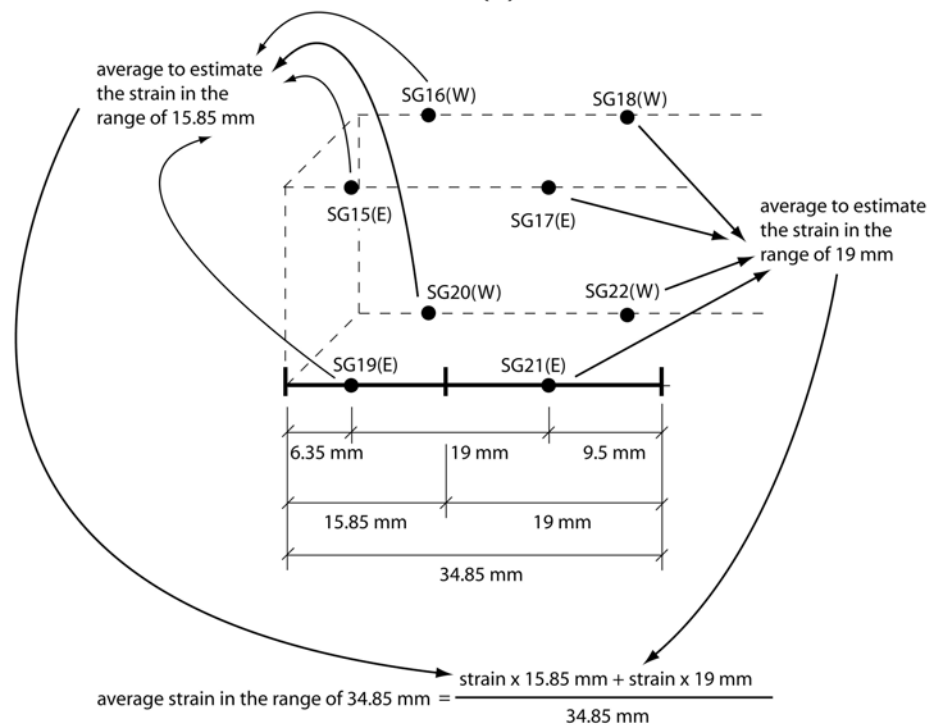


Fig. 10.9 Beam cover plate/flange strains: (a) Test 1; (b) Test 3; (c) Test 5; (d) Test 7; (e) Test 9; (f) Test 10



(a)



(b)

Fig. 10.10 Average compressive strains at beam end: (a) SG22 from Test 1;
(b) calculation of average strain

The predicted “average” strains for the same length of cover plate or flange are determined using the analytical model. The comparisons in Fig. 10.9 indicate that, while there are discrepancies between the measured and predicted values, the analytical model is capable of providing a satisfactory representation of the contact behavior at the beam ends. No attempt is made to compare the measured and predicted strains at individual gage locations, since the measured strains varied considerably due to uneven contact at the beam ends.

10.2.4 Behavior Along Beam Span

To evaluate the capability of the revised analytical model in predicting the behavior of the coupling beams along the span, Fig. 10.11 compares the measured and predicted “average” maximum and minimum compressive strain values in strain gages SG1-SG4 from Tests 1, 3, 5, 7, 9, and 10. The locations of strain gages SG1-SG4 are given in Chapter 9.

Note that when θ_b is positive (i.e., clockwise rotation), maximum compression strains of similar value are measured in gages SG2 and SG3, and minimum compressive strains of similar value are measured in gages SG1 and SG4. This is because of the symmetric double curvature loading condition that develops along the length of the beam (with zero curvature at beam midspan) as the subassembly is displaced laterally. As the beam is cycled in the positive and negative loading directions, the maximum and minimum readings in these gage pairs alternate. The measured strains in Fig. 10.11 are calculated as the average maximum and minimum readings from all four gages upon first loading to the peak θ_b values in the positive and negative directions during the

displacement history followed in each test (see Fig. 10.12). The comparisons indicate that, while there are discrepancies between the measured and predicted results, the analytical model provides reasonable estimates of the beam web strains along the span.

10.2.5 Behavior of Top and Seat Angles

Fig. 10.13 shows the measured versus predicted V_b - θ_b behaviors from Tests 4, 6, and 8. As described in Chapter 9, these experiments were conducted under monotonic loading using subassemblages with two angles in tension and no beam post-tensioning strands. The predicted curves up to the “yield” point of the angles (circular markers in Fig. 10.13) indicate that the method developed by Kishi and Chen (1990) provides reasonable estimates for the initial stiffness, $K_{a_{ixt}}$ and yield strength, T_{ayx} of the test specimens. The post-yield stiffnesses of the angles under monotonic loading were determined from the experimental results in Fig. 10.13.

Under reversed cyclic loading, the post-yield behavior of the top and seat angles is complicated due to kinematic hardening of the steel and low cycle fatigue of the angle vertical legs. Low cycle fatigue of the angles did not occur in Tests 4, 6, and 8 since the loads were applied monotonically. Furthermore, the angles in Test 11, which was conducted under reversed cyclic loading, formed a different failure mechanism than the other cyclic tests as described in Chapter 9. In the absence of a reliable method to predict the post-yield behavior of the angles under reversed cyclic loading, the following approach was taken.

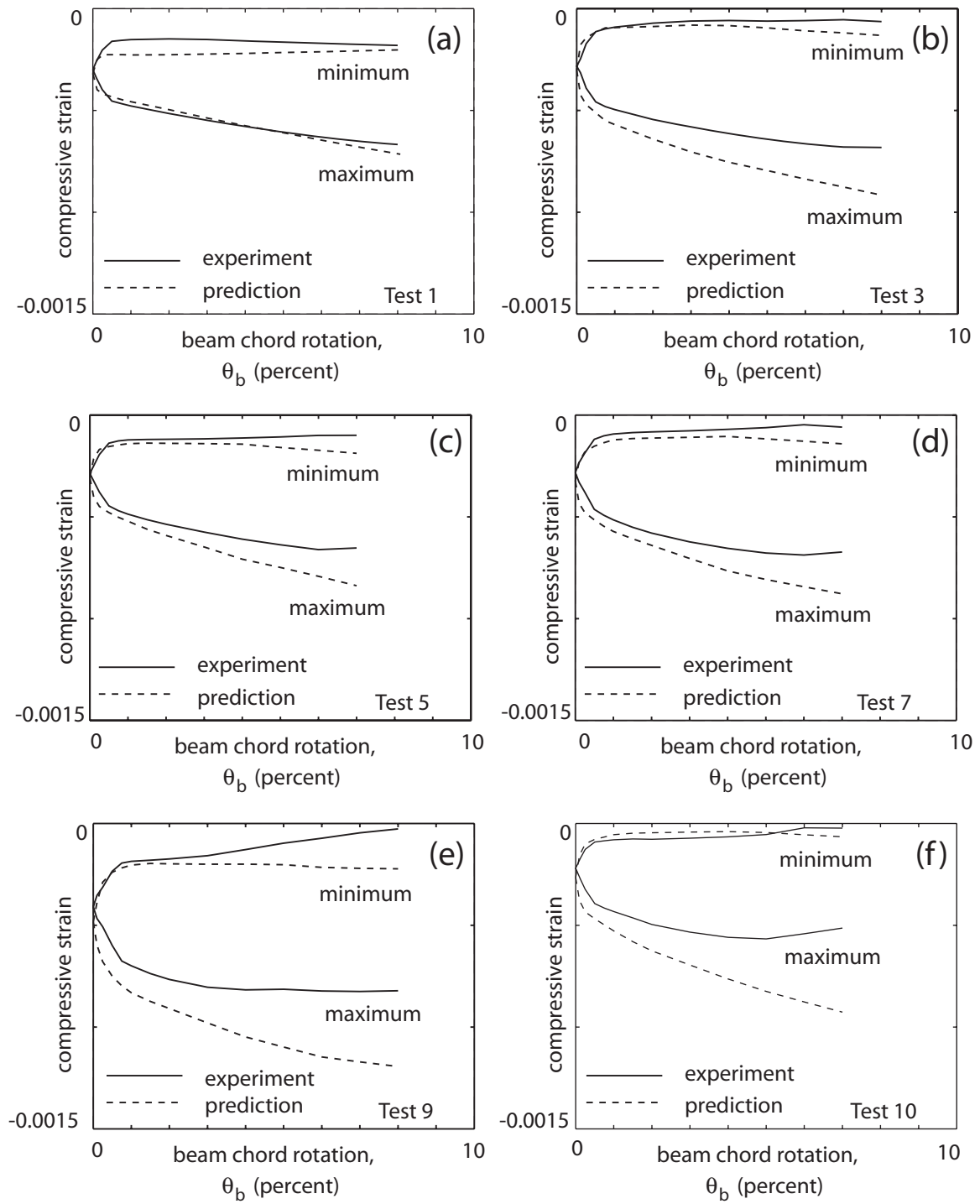
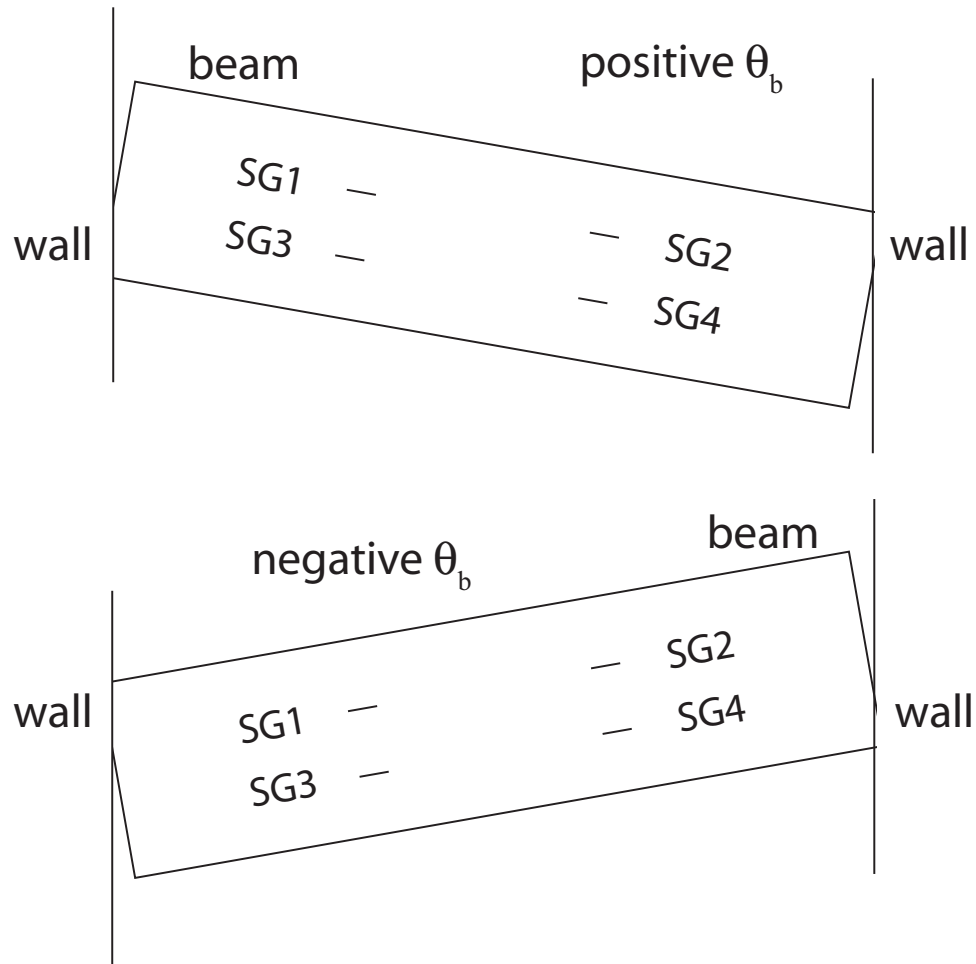


Fig. 10.11 Beam web strains: (a) Test 1; (b) Test 3; (c) Test 5; (d) Test 7; (e) Test 9; (f) Test 10



$$\text{average maximum compression strain} = \frac{(\text{SG2} + \text{SG3})_{\text{at positive } \theta_b} + (\text{SG1} + \text{SG4})_{\text{at negative } \theta_b}}{4}$$

$$\text{average minimum compression strain} = \frac{(\text{SG1} + \text{SG4})_{\text{at positive } \theta_b} + (\text{SG2} + \text{SG3})_{\text{at negative } \theta_b}}{4}$$

Fig. 10.12 Calculation of average compressive strains in beam web

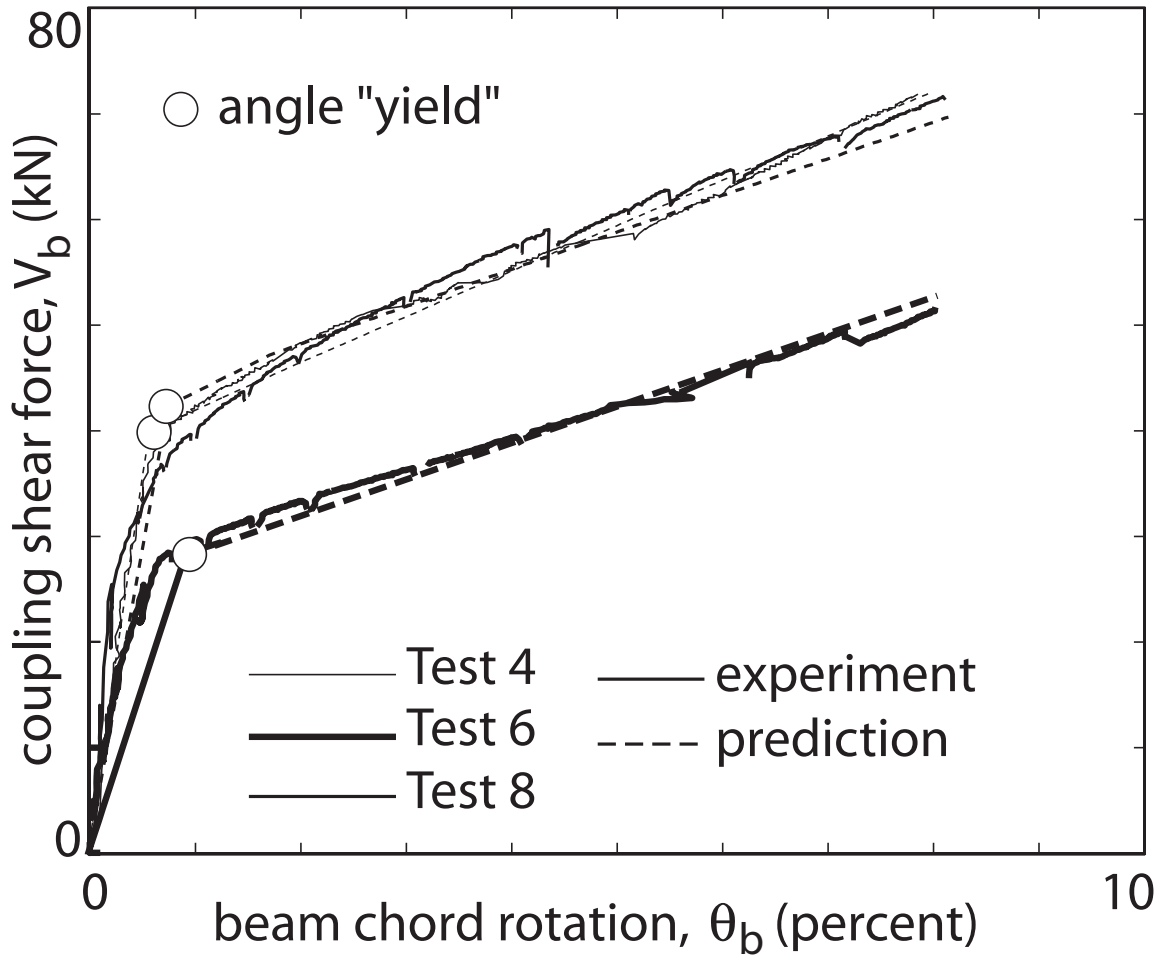


Fig. 10.13 Angle behavior under monotonic loading - Tests 4, 6, and 8

As described in Chapter 9, the only significant difference between Tests 1 and 3 is the use of four top and seat angles at the beam ends. The contribution of these angles to the coupling resistance was determined by “subtracting” the V_b - θ_b relationship of Test 1 from that of Test 3 as shown in Fig. 10.14a. The resulting V_b - θ_b behavior for a cycle of loading to $\theta_b = \pm 6\%$ is shown by the thick line in Fig. 10.14b.

For comparison, the predicted difference between Tests 1 and 3 using the angle models in Figs. 10.3b and 10.3c is shown by the thin line in Fig. 10.14b. The results indicate that the revised angle model provides a reasonable representation of the behavior

of the angles under cyclic loading. Failure of the angles due to low cycle fatigue is not modeled.

10.3 Revised Idealized Moment-Rotation Relationship

This section makes modifications to the idealized bilinear subassembly beam end moment versus chord rotation (M_b - θ_b) relationship in Chapter 5 based on the revised subassembly model described above. The most significant update to the idealized moment-rotation relationship is the use of the horizontal angle element force-deformation model in Fig. 10.3b. This modification is necessary to better capture the measured behavior from the subassembly experiments as demonstrated in Figs. 10.5 and 10.6. The contribution of the vertical angle elements (see Fig. 10.3c) to the subassembly behavior is ignored.

The revised moment-rotation relationship is identified by the following two limit states, similar to the previous relationship in Chapter 5:

- (1) Beam softening state (at $M_{b,sof}$, $\theta_{b,sof}$).
- (2) Beam PT-yielding state (at $M_{b,pty}$, $\theta_{b,pty}$).

10.3.1 Beam Softening State

The coupling beam end moment, $M_{b,sof}$ and chord rotation, $\theta_{b,sof}$ at the beam softening state of an unbonded post-tensioned hybrid coupled wall subassembly are estimated as described in Chapter 5 with the following modifications:

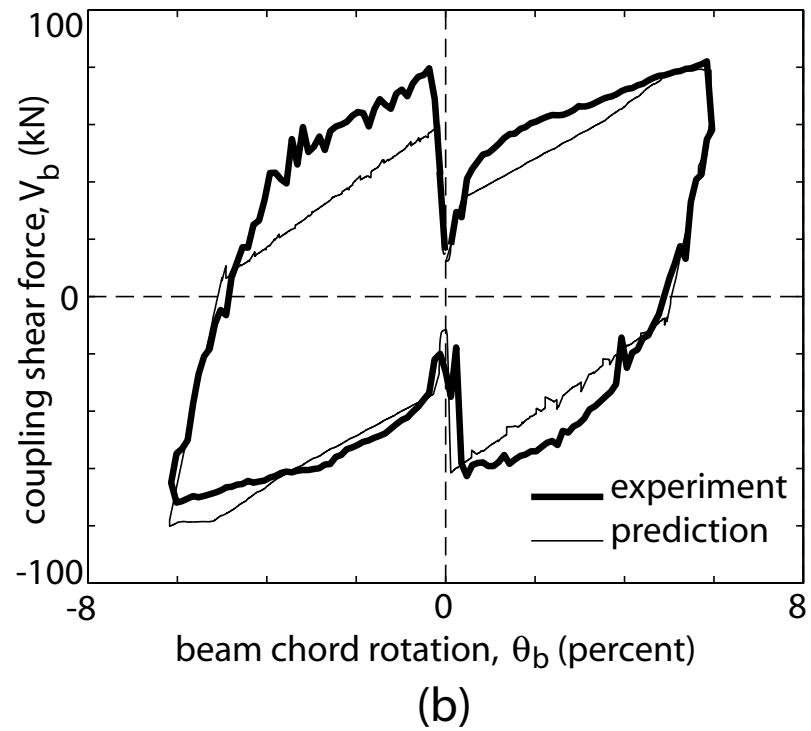
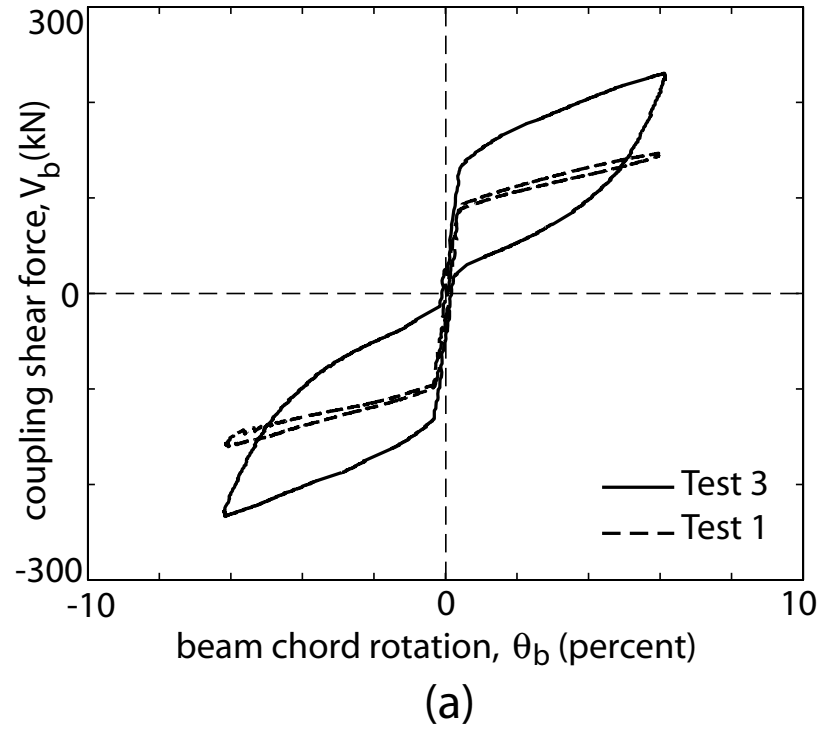


Fig. 10.14 Angle behavior under cyclic loading: (a) Tests 1 and 3; (b) difference between Tests 1 and 3 during $\theta_b=6\%$ cycle

(1) The force in each tension angle is equal to $1.5T_{ayx}$, where T_{ayx} is the yield strength of the horizontal angle elements as shown in Fig. 10.3b.

(2) The force in each compression angle is equal to $(1/40)f_{ay}A_a \leq C_{asx}$, where f_{ay} is the angle steel yield strength and C_{asx} is the slip force for the angle-to-beam connector bolts as shown in Fig. 10.3b.

The subassembly initial stiffness, K_{bi} can be determined ignoring the deformations in the wall-contact regions as described in Chapter 5.

10.3.2 Beam PT-Yielding State

The coupling beam end moment, $M_{b,pty}$ and chord rotation, $\theta_{b,pty}$ at the beam PT-yielding state of an unbonded post-tensioned hybrid coupled wall subassembly are estimated as described in Chapter 5 with the following modifications:

(1) The maximum strength of the angles in tension is reached and maintained (i.e., angle failure does not occur) before the yielding of the beam post-tensioning tendons. Thus, the force in each tension angle at the PT-yielding state is equal to $2T_{ayx}$, where $2T_{ayx}$ is the maximum strength of the horizontal angle elements as shown in Fig. 10.3b.

(2) The force in each compression angle is equal to C_{asx} , where C_{asx} is the slip force for the angle-to-beam connector bolts as shown in Fig. 10.3.

The steps used in the estimation of $M_{b,pty}$ and $\theta_{b,pty}$ are presented below. Note that different from Chapter 5, the revised procedure does not require an idealized load-deformation relationship for the angles in tension since the force in each tension angle is assumed to be equal to $2T_{ayx}$. Thus, there is no need for iteration to estimate $M_{b,pty}$ and $\theta_{b,pty}$.

Step 1

Estimate the total beam compression force at the beam-to-wall interface as:

$$C_{b,pty} = P_{b,pty} + 2T_{ayx} - C_{asx} \quad (10.5)$$

where, $P_{b,pty}$ is the total force in the post-tensioning tendons. As described in Chapter 5, the post-tensioning tendons go through the same elongation regardless of their locations within the beam depth. Thus, the tendons yield simultaneously and

$$P_{b,pty} = P_{by} = \sum a_{bt} f_{bpy} \quad (10.6)$$

Step 2

Estimate the depth of the compression (i.e., contact) region, $c_{b,pty}$ at the beam-to-wall interface using a uniform contact stress distribution. Assuming that the compression region is above the coupling beam web and the width of the cover plate (if used) is the same as the beam flange width b_{bf} , then, $c_{b,pty}$ can be estimated as:

$$c_{b,pty} = \frac{C_{b,pty}}{f_{by} b_{bf}} \quad (10.7)$$

A non-rectangular compression region should be used if $c_{b,pty} > t_{bf} + t_c$. The cover plate thickness $t_c = 0$ if no cover plates are used on the coupling beam.

Step 3

Estimate the coupling beam end moment at the beam PT-yielding state, $M_{b,pty}$ by taking moments about the centerline of the beam as:

$$M_{b,pty} = V_{b,pty} \frac{l_b}{2} = 0.5 C_{b,pty} (d_{bc} - c_{b,pty}) + 0.5 (C_{asx} + 2T_{ayx}) (d_{bc} + t_a) \quad (10.8)$$

Step 4

Estimate the elongation of the beam post-tensioning tendons between the initial prestress state and the PT-yielding state as:

$$u_{b,pty} = \frac{(f_{bpy} - f_{bpi})l_{bpu}}{E_{bp}} \quad (10.9)$$

where, $l_{bpu} = l_b + 2l_w$ is the unbonded length and E_{bp} is the Young's modulus of the post-tensioning tendons.

Step 5

Estimate the width of the beam-to-wall gap at the centerline of the beam, $g_{b,pty}$.

Fig. 5.5 shows the gap opening that occurs at the beam-to-wall interface at the PT-yielding state. Using symmetry,

$$g_{b,pty} = \frac{u_{b,pty}}{2} \quad (10.10)$$

Step 6

Estimate the rotation of the beam due to gap opening at the PT-yielding state as:

$$\theta_{bg,pty} = \frac{g_{b,pty}}{0.5d_{bc} - c_{b,pty}} \quad (10.11)$$

where, $g_{b,pty}$ and $c_{b,pty}$ are determined in Steps (5) and (2), respectively.

Step 7

Estimate the elastic rotation of the beam at the PT-yielding state using the subassemblage linear-elastic stiffness, K_{bi} as:

$$\theta_{be,pty} = \frac{M_{b,pty}}{K_{bi}} \quad (10.12)$$

Step 8

Estimate the total beam chord rotation at the PT-yielding state as:

$$\theta_{b,pty} = 1.075(\theta_{bg,pty} + \theta_{be,pty}) \quad (10.13)$$

where, the factor 1.075 is described in Chapter 5, and $\theta_{bg,pty}$ and $\theta_{be,pty}$ are from Steps (6) and (7), respectively.

Step 9

Consider second order effects on $M_{b,pty}$ as described in Chapter 5.

Step 10

Estimate the coupling shear force at the beam PT-yielding state, $V_{b,pty}$, as:

$$V_{b,pty} = \frac{2M_{b,pty}}{l_b} \quad (10.14)$$

10.4 Chapter Summary

This chapter uses the experimental results from Chapter 9 to make necessary modifications to the fiber element subassembly analytical model described in Chapter 3.

The revised analytical model is critically evaluated by comparing the analytical estimations with the experimental measurements. The idealized coupling beam end moment versus chord rotation relationship developed in Chapter 5 is also modified based on the experimental results.